20th INTERNATIONAL CONFERENCE ON MACHINE DESIGN AND PRODUCTION

CONFERENCE PROCEEDINGS

Editorial Board

M. Cemal ÇAKIR
Barış ÇETİN
S. Engin KILIÇ
E. İlhan KONUKSEVEN
Bahram LOTFİ
Ramazan H. NAMLU
Ali ORAL
İ. Etem SAKLAKOĞLU
Ulvi ŞEKER
Damla TOPALLI
Hakkı Özgür ÜNVER
Volkan ESAT
Selcuk HIMMETOĞLU

umtik 2024

14-17 August 2024

ANKARA- TURKIYE

MATIMAREN
DEPARTMENT OF MECHANICAL ENGINEERING
MIDDLE EAST TECHNICAL UNIVERSITY
ANKARA-TURKEY

Dedicated to the memory of

Metin AKKÖK, Ferenc ERDELYI

and all other IPC members we have lost in previous Years.

All rights of this book are reserved by the Middle East Technical University.
None of the papers printed in this book may be reproduced without the prior permission, in writing, from the Author(s) of the paper(s) and the editors of the book. The papers can however be cited by giving the source.

This book can be obtained from the following addresses:

Mechanical Engineering Department
ATILIM University
06830 Ankara- Turkey

UMTIK
Mechanical Engineering Department
Middle East Technical University
06800 Ankara- Turkey

Cover Print:

METU- Ankara

Printing and Binding:

METU- Ankara

Printed by:

METU- Ankara

ISBN

Organizing Committee

M. Cemal ÇAKIR”	(Uludağ, Dept. of Mechanical Eng.)	cemal@uludag.edu.tr
Barış Çetin	(FNSS)	cetin.baris@fnss.com.tr
S. Engin KILIÇ	(Atılım, Dept. of Manufacturing Eng.)	engin.kilic@atilim.edu.tr
E. İlhan KONUKSEVEN	(METU, Dept. of Mechanical Eng.)	konuk@metu.edu.tr
Bahram LOTFI	(TOBB ETÜ, Dept. of Mechanical Eng.)	blotfi@etu.edu.tr
Ramazan Hakkı NAMLU	(Atılım, Dept. of Mechanical Eng.)	ramazan.namlu@atilim.edu.tr
Ali ORAL	(Balıkesiri, Dept. of Mechanical Eng.)	a.oral@balikesir.edu.tr
İ. Etem SAKLAKOĞLU	(Ege University Dept. of Mechanical Eng.)	i.e.saklakoglu@ege.edu.tr
Ulvi ŞEKER	(Gazi, Dept. of Mechanical Eng.)	useker@gazi.edu.tr
Damla TOPALLI	(Atılım, Dept. of Computer Eng.)	damla.topalli@atilim.edu.tr
Hakkı Özgür ÜNVER	(TOBB ETÜ, Dept. of Mechanical Eng.)	hounver@etu.edu.tr

Organizing Committee of “Commemoration of Professor Memiş ACAR Day”

Volkan ESAT	(METU NCC, Dept. of Mechanical Eng.)	evolkan@metu.edu.tr
Selcuk HIMMETOĞLU	(Hacettepe, Dept. of Mechanical Eng.)	s.himmetoglu@hacettepe.edu.tr
Ulaş Yaman	(METU, Dept. of Mechanical Eng.)	uyaman@metu.edu.tr

Contact: umtik@metu.edu.tr **Tel:** +90 312 586 8888

International Program Committee

Erdem	ACAR	TÜRKİYE
Serpil	ACAR	UNITED KINGDOM
Samet	AKAR	TÜRKİYE
M. Oktay	ALNIAK	TÜRKİYE
Ali M.	ALSAMHAN	SAUDI ARABIA
Yusuf	ALTINTAŞ	CANADA
Carla	ANFLOR	BRASIL
Ömer	ANLAĞAN	TÜRKİYE
Ahmet Hakan	ARGEŞO	TÜRKİYE
Özgür	ASLAN	TÜRKİYE
Hediye	ATİK	TÜRKİYE
Paulo Jorge	BÁRTOLO	SINGAPORE
Bekir	BEDİZ	TÜRKİYE
Erhan	BUDAK	TÜRKİYE
Mehmet	ÇELİK	TÜRKİYE
Barış	ÇETİN	TÜRKİYE
Shun Fung	CHIU	THE PHILIPPINES
Ender	CİĞEROĞLU	TÜRKİYE
Leo	COURTY	FRANCE
Samad	DADVANDIPOUR	HUNGARY
Yılser	DEVRİM	TÜRKİYE
László	DUDÁS	HUNGARY
Ferenc	ERDELYI	HUNGARY
Abdülkadir	ERDEN	TÜRKİYE
Zühal	ERDEN	TÜRKİYE
Kaan	ERKORKMAZ	CANADA
Tahir	FİDAN	TÜRKİYE
Faby	FONG	TAIWAN R.O.C.
Necdet	GEREN	TÜRKİYE
Greg	GIBBONS	UNITED KINGDOM
Jui-Pin	HUNG	TAIWAN R.O.C.
Wen-Yuh	JYWE	TAIWAN R.O.C.
Bilgin	KAFTANOĞLU	TÜRKİYE
Çetin	KARATAŞ	TÜRKİYE
Yiğit	KARPAT	TÜRKİYE
Şükran	KATMER	TÜRKİYE

Takeo	KATO	JAPAN
Yusuf	KAYNAK	TÜRKİYE
Zafer	KAZANCI	UNITED KINGDOM
Behzat Bahadır	KENTEL	TÜRKİYE
Z. Murat	KILIÇ	UNITED KINGDOM
Gökhan	KİPER	TÜRKİYE
Bahattin	KOÇ	TÜRKİYE
Ramji	KOONA	INDIA
Gökhan	KÜÇÜKTÜRK	TÜRKİYE
İsmail	LAZOĞLU	TÜRKİYE
Kuan-Ming	LI	TAIWAN R.O.C.
Yangmin	LI	HONG KONG
Raphael	LORAIN	FRANCE
Ming-Chyuan	LU	TAIWAN R.O.C.
Tzuo Liang	LUO	TAIWAN R.O.C.
Kei	MATSUOKA	JAPAN
Yoshiyuki	MATSUOKA	JAPAN
Pınar	MENGÜÇ	TÜRKİYE
Tomoyuki	MIYASHITA	JAPAN
Tuğrul	ÖZEL	USA
Gökhan	ÖZGEN	TÜRKİYE
Emre	ÖZLÜ	TÜRKİYE
Fahrettin	ÖZTÜRK	TÜRKİYE
Katta Durga	PRASAD	INDIA
Ferit	SAİT	TÜRKİYE
İbrahim Etem	SAKLAKOĞLU	TÜRKİYE
Durmuş Tayyar	ŞEN	TÜRKİYE
Eiji	SHAMATO	JAPAN
Sergey	SHEVTSOV	RUSSIA
Vadim S.	SILBERSCHMIDT	UNITED KINGDOM
Uğur	ŞİMŞİR	TÜRKİYE
Meng-Shiun	TSAI	TAIWAN R.O.C.
Cihan	TURHAN	TÜRKİYE
Ali	ÜNÜVAR	TÜRKİYE
Min	WAN	P.R.C.
Selçuk	YAHŞİ	TÜRKİYE
Ulaş	YAMAN	TÜRKİYE
Tanfer	YANDAYAN	TÜRKİYE
Hakan	YAVAŞ	TÜRKİYE
Wong Kuan	YEW	MALAYSIA
Çağrı Vakkas	YILDIRIM	TÜRKİYE
Ali Rıza	YILDIZ	TÜRKİYE
Bülent	YILMAZ	TÜRKİYE
Oğuzhan	YILMAZ	TÜRKİYE
Michael	ZAEH	GERMANY
Erdem	ACAR	TÜRKİYE
Serpil	ACAR	UNITED KINGDOM
Samet	AKAR	TÜRKİYE
M. Oktay	ALNIAK	TÜRKİYE
Ali M.	ALSAMHAN	SAUDI ARABIA
Yusuf	ALTINTAŞ	CANADA
Carla	ANFLOR	BRASIL
Ömer	ANLAĞAN	TÜRKİYE
Ahmet Hakan	ARGEŞO	TÜRKİYE
Özgür	ASLAN	TÜRKİYE

SUPPORTING MUNICIPALITIES AND ASSOCIATIONS

ATILIM UNIVERSITY

TÜBİTAK

MAKİNA İHRACATÇILARI BİRLİĞİ

MATİMAREN

SILVER SPONSORS

BELGIN OIL

KALYON PV

HAIMER

FNSS

BRONZE SPONSORS

GENBA

TEI

INSIZE

BVS CRANES Bülbüloğlu VİNÇ

YÜNEL

MVD

YILDIRIM GRUP

MANUS

Conference Secretariat

ORIGIN EMC



Çamlık Mahallesi, Dinç sok. Muyar Plaza No: 4 D: 25 P.O. Box: 34774 Ümraniye, İSTANBUL
TEL: +90 216 372 23 30

www.originemc.com.tr
info@originemc.com.tr

Contact Address

http://www.umtik.com
umtik@metu.edu.tr

PREFACE

It is a great pleasure to welcome you to the 20th International Conference on Machine Design and Production. It has been 40 years since we organized the first UMTIK conference in 1984 in the Mechanical Engineering Department of the Middle East Technical University in Ankara. This conference will be the 15th of the international and the 20th of all UMTIK conferences which were organized every two years since then without interruption, except for the year 2020, due to the worldwide pandemic.
The first day of UMTIK 2024 will be “The Commemoration Day of Professor Metin Akkök”; it is dedicated to the memory of the late Professor Metin Akkök who was one of the original initiators and organizers of the inaugural UMTIK Conference and continued to make significant contributions to the subsequent UMTIK conferences until his passing on May 11, 2023. The first-day program will start by welcoming and opening speeches to UMTIK 2024 which will be followed by the commemoration of Professor Metin Akkök. There will be a Welcome Cocktail in the evening.

During the four-day UMTIK conference, there will be:

- 11 keynote speeches by the eminent international and national researchers on leading topics such as digital machining, additive manufacturing, structural dynamics, innovative design, research for value generation, environment friendly manufacturing and future for young engineers.

- 21 sessions under 12 themes such as automotive engineering, metal cutting, simulation and modeling, intelligent systems, additive manufacturing, biomedical and engineering applications, artificial intelligence in design and manufacturing, mechanics, tribology, and sustainable manufacturing.

- 6 special sessions on various topics from dynamics and machining stability for flexible systems to design science and time axis design, design and human interface to sustainable design and operation.

- 11 sponsor sessions (industry speakers) to introduce themselves to other companies and academics for future collaborations.

- Two industrial panels to discuss 1) the development of a national CNC controller for the future of Turkish CNC machine tools industry, and 2) the use and applications of TRIZ (innovative problem-solving theory).

- The Gala Dinner on the third day of the conference by the beautiful Mogan lake of Ankara.

We extend our sincere gratitude to Mr. Yalçın Zaim, Chairman of the Board of Trustees at Atılım University, Prof. Dr. Serkan Eryılmaz, Rector of Atılım University, and Prof. Dr. Yılser Devrim, Dean of the Faculty of Engineering, for all their support. Additionally, we express our thanks to Prof. Dr. Esra Gül Dardağan Kibar, Dean of the Faculty of Law, for her hospitality in allowing us to use the facilities of the Faculty of Law. Furthermore, we thank Mr. Ozan Budak, Director of Corporate Communication and Promotion, Mr. Kemal Şenoğlu, former Director of Cultural and Social Affairs, Mr. Hüseyin Dölen, Director of Distance Education, and all the staff of Atılım University for their support.

We hope all the participants will feel the warm and positive atmosphere at Atılım University. We highly acknowledge the Honorary Conference Chairs for their kind support: Presidents of the four universities, Professor Serkan Eryılmaz of Atılım University, Professor Hasan Ali Karasar of

Kapadokya University, Professor Türkay Dereli of Hasan Kalyoncu University and Professor İhsan Sabuncuoğlu of TED University.

We would like to thank the honorary keynote speaker, Professor Yusuf Altıntaş and the other keynote speakers, Professor Bilgin Kaftanoğlu, Emeritus Professor H. Nevzat Özgüven, Professor İsmail Lazoğlu, Professor Bahattin Koç, Professor Charlie C. L. Wang, Professor Tomoyuki Miyashita, Professor Birol Kılkış, Assoc. Prof. Tanfer Yandayan, Mr. Mümtaz Afşin Esi, Mr. Fuat Tiniş.

We would like to express our sincere appreciation to Mr. Berkin Bilge and Mr. Burak Can Çiçek for their efforts in organizing and moderating the industrial panels on the second and the fourth days of the conference. The panelists, special session organizers, session chairs, authors and all the participants are highly acknowledged for their invaluable contributions.

Asst. Prof. Bahram Lotfi and Asst. Prof. Ramazan H. Namlu are gratefully acknowledged for their tremendous time and effort in every phase of the conference organization and in the editorial work of the Proceedings and the Abstracts Book.

Last but not the least, we would like to thank TÜBİTAK “The Scientific and Technological Research Council of Türkiye”, “Turkish Machinery Exporters Union”, silver and bronze sponsors, members of the International Program Committee, Conference Secretariat “ORIGINEMC”, Scientific Secretariat (Research Assistants Yunus Emre Nehri and Mehmet Furkan Özbey) and all who contributed to the success of UMTIK 2024.

We wish all the participants a highly memorable time during their stay in Ankara.

The Organizing Committee
UMTIK 2024,
August 14th – 17th
2024
Ankara, Türkiye

CONTENTS **PAGE**

GREEN INDUSTRIAL PARKS, CARBON TAXES, AND GLOBAL WARMING 19
Birol KILKIŞ

Design Science and Time-axis Design
Design of the Deployment of Membranes on Satellites 37
Teru NATORI, Tomoyuki MIYASHITA

Numerical Approach of Time-axis Design Method - Validation through an Application for Chair Design 51
Akinari HIRAO, Takeo KATO, Yoshiyuki MATSUOKA

Design and Human Interface
Multilingual Communication Robot Using Language Detection System 65
Kei MATSUOKA, Yuki KIDA, Takeo KATO, Tetsuro OGI

Human Relationship Felt in Communication Using Tele-Immersion Avatar Robot 75
Tetsuro OGI, Yuki KIDA

Simple Reaction Test with Mouse Clicks Using 500 Hz Monitors. Is A 500 Hz Monitor Effective for Esports? 85
Yuya ASHIZAWA, Hideo MIYACHI

Seating Positions and Behaviors in Virtual Space 99
Toma SHIBANO, Hideo MIYACHI, Sumire HIROTA

Architecture of Autonomous Avatar and VR Simulator for Various Training Purposes and Situations 111
Tomohiro TANIKAWA

Sustainable design and operation in the built environment (II)
Thermal Management of a Multi-Functional Battery Case 127
İbrahim DİKER, O. Cem GÖKCİLER, Göktürk M. ÖZKAN, Durmuş Can ACER, Ahmet ÇETİN, Necdet GEREN

Machine Design, Sustainability, Manufacturing and Tribology
An Experimental Investigation on the Energy Requirement of Different Materials Manufactured on a CNC 145
Ural ULUER, Metin AKKÖK, Sadık Engin KILIÇ, Dr. Ulaş YAMAN

Water Jet Guided Laser Micro Drilling of an Aerospace Alloy 155
Levent SUBAŞI, Mustafa GÖKLER, Dr. Ulaş YAMAN

Integration of 6-Axis Hexapod with Nanosecond Laser for Micro Machining 169
Aykut BAKAN, Yigit KARPAT

Milling Force Estimation Using Angular Domain Harmonics with Cutting and Edge Coefficients 183
Mert İLME, Hakan ÇALIŞKAN

Fracture Mechanics and Damage Modelling
Evaluation of Different Damage Models Applied for Extruded 6xxx Series Aluminum 193
Seda YILDIZ, Hüseyin LEKESİZ

Evaluating Steel/Adhesive Interfacial Failure using Pull-Off Tests 207
Fatih İBRAHIMOĞLU, Ata KHABAZ-AGHDAM, Şehram DIZECI

Damage Detection on Beam Structures using Ho-Kalman Identification Method 213
Ömer Dehan ÖZBOZ, Özkan ALTAY, Ahmet Murat ÖZBAYOĞLU, Hakkı Özgür ÜNVER

Additive Manufacturing
The Additive Manufacturing Process and Its Challenges in Human Prosthesis Development: Preliminary Studies 233
Carla ANFLOR, Euclides SANTANNA, Karla SARTIN

Simulation and Modelling-I
Methodology for The Optimized Arrangement of Microelectronic Components on The Printed Circuit Board from a Mechanical Perspective 243
Fahri Berk BİLBAY, Mustafa Cemal ÇAKIR

The Influence of Metal Forming on Crashworthiness 259
Murat BÜYÜK, V. Emre SAVAŞ

Intelligent Systems in Production
Implementation of the Kanban System on a Machine Assembly Line 271
Hafize DURMAZ, Hasan ÇAKIR, Alper YETER, MUSTAFA BAKKAL

Engineering Applications
Design, Analysis and Verification of EMC with Various Ball and Trapezoidal Drives 285
Berk KURT, Ömer Faruk UYSAL, Tolga CANKURT

Biomedical Applications

THE DESIGN OF A ROTATING MODULAR UPPER LIMB PROSTHETIC WRIST UNIT 301
A. Ali GÜRLER, E. İlhan KONUKSEVEN

Automotive Engineering-I

Development of a Roll Over Prevention Control Strategy for an Articulated Bus Equipped with On-Board Electric Motors 319
Kerem BAYAR

Planetary Gearbox Design for Hybridization of a Prototype Powertrain 339
Özgür AKDENİZ, Ali EMİN

Automotive Engineering-II

A Lightweight Multifunctional Battery Case 357
Necdet GEREN, Orhun Cem GÖKCİLER, Mehmet Burak İBEKCI, Çağrı UZAY, Melih BAYRAMOĞLU

Design and Analysis of Suspension and Steering System for an Electric Vehicle 373
Umut Berke HAKTANIR, Emre ÇELİKCAN, Umut NAZLIER, Berkay KANDEMİR, Özgür AKDENİZ, Ali EMİN

Improvements on the Lightweight Shell of an Electric Vehicle 387
Mustafa EROL, Cemal Emre HOKKAÖMEROĞLU, Özgür AKDENİZ

Dynamic Height Adjustment and Obstacle Climbing Capabilities of A 6x6 Unmanned Ground Vehicle with Advanced Hydropneumatics Suspension Systems 401
Melikşah BEŞİR, Eren DOYMUŞ, İsmail Melih CANBOLAT, Ahmet H. ALKAN, Erhan Ilhan KONUKSEVEN

TÜRKÇE BİLDİRİLER

Malzeme ve Malzeme Mekaniği-I

Ağir Ticari Araçlarda Kardan Mili U-Sacinin Güçlendirilmesi 425
Umut Can GÖLBAŞI, Murat ÖZBAKIŞ, Onur ŞEN

Makine Tasarımı I

Abkant Preslerde Dinamik Bombeleme Sisteminin Tasarim Kriterleri ve Avantajlari 437
Abdullah ÖZKAN, Mustafa GÜLTEKİN

Eklemeli İmalat

3B Yazici İle Üretilen Parçalarin Farkli Baski Yönlerindeki Dayaniminin Deneysel ve Nümerik İncelenmesi 447
Emre Can HASKİLİT, Habip Gökay KORKMAZ, Remzi Ecmel ECE, Serkan TOROS, Fahrettin ÖZTÜRK

Martenzitik Paslanmaz Çeliklerin Lazer Dolgu Kaynağinda Örtüşme Oraninin Kalinti Gerilmeye Etkis 463
Meryem ALTAY, Hakan AYDIN, Adem KARŞI

Makina Tasarımı II
Temassiz Enerji Sistemi ile Çalişan 70 Ton Transfer Arabasi 471
Yalçın Y. GÜLER, Mehmet KOÇHİSARLI, Aydoğan AKÇA, Ece KARSLI, Engin TEKİN, Sibel Sain ÖZDEMİR

Yüksek Hacimli Talaş Kaldirma Kapasitesine Sahip Freze Tezgahi İçin Takim Değiştirme Sisteminin Geliştirilmesi 487
Can TUNCER, Talat Yiğit GENCEL, Enver YALÇIN, Ali ORAL

Sistematik Konstrüksiyon Yaklaşımıyla Lineer Ray Tapası Montaj Aparatı Tasarımı 497
H. Aytuğ KURT, Alper YETER, Mustafa BAKKAL

Büyük Boyutlu Freze Tezgahları İçin Hidrolik Döner-İş Bağlama Sisteminin Geliştirilmesi 515
Mehmet UĞUR, Talha GİRGİN, O. Talha DİNÇER, Cengiz OĞUZER, Ali ORAL

Mühendislik Uygulamaları
İnce Cidarli Çelik Tübüler Direklerin Dinamik Performansi Üzerine Pasif Sarkaç Ayarli Kütle Sönümleyicilerin Etkilerinin Deneysel İncelenmesi 525
Sertaç ÖZDEMİR, Rafet AKTEPE, Alper ALDEMİR, Erdem ACAR

Akıllı Mücevherlerde İnovasyon: Teknoloji ve Tasarımın Birleşimi 543
Sevban AKIN, Hüseyin Özkal ÖZSOY

Automotive Engineering I
Ürün Doğrulama ve Saha Testlerinde Kullanima Yönelik Android Tabanli Canli Veri Toplama Arayüzü Geliştirme 561
Sedat TARAKÇI, Oğuzhan ALDEMİR, Efe IŞIK

Talaşlı İmalat
Alüminyum 7075 T6 Malzemesinin Frezelenmesinde Kesme Parametrelerinin En İyilenmesi 569
Sinan GÖKÇE, Semin KAYA

Sertleştirilmiş Çeliklerin Frezeleme İşlemlerinde Kesici Takim Karbür Kalitesi ve Kaplamanin İşleme Performansina Etkisi 579
Hasan KUŞ, Çağla Gökbulut AVDAN, Çağlar YAVAŞ

PAPERS

GREEN INDUSTRIAL PARKS, CARBON TAXES, AND GLOBAL WARMING

B. **KILKIŞ**, *birol.kilkis@ostimteknik.edu.tr* OSTIM Technical University**,** 06374, Ankara, Türkiye

ABSTRACT

Based on carbon dioxide emissions, this paper focuses on global warming, associated environmental issues, and climate crisis, related to industrial parks facing carbon taxes. Two primary components of carbon dioxide emissions are recognized, namely 1- direct emissions and 2- nearly avoidable emissions due to availability destructions in industrial processes and manufacturing activities. The latter emission responsibility has been linked to availability (exergy) destructions taking place in any process as an extension of the Second Law of thermodynamics. Green industrial parks are defined and rated with a new metric called Exergy Star. Eco-industrial park concept derived by the United Nations International Development Organization is expanded and redefined. The carbon tax at the border under way by the European Union is criticized in terms of its concealed dangers for industrial parks in Türkiye, specifically, for the OSTİM techno city. In this respect, the emissions-based carbon taxes versus added values in terms of the final products are formulated with sustainability and rationality of energy use and shown that carbon taxes will limit the product development for decarbonization in the industry and reduce the added value potential, while European countries largely will benefit from carbon taxes.

Keywords: Industrial parks, Global warming, Paris Agreement, Availability, Exergy analysis, Carbon tax, Manufacturing, availability, sustainability, energy rationality

1. INTRODUCTION

1.1. Global Crisis and Thermodynamics

The United Nations (UN) has issued seventeen *Sustainable Development Goals*. Only one of them (13*, Climate Action*) is related to energy, global warming, and CO_2 emissions. Climate action, according to the UN, is only related to direct CO_2 emissions measured onsite, as shown on the right-hand-side of Figure 1 (Power plant stack). This relationship is described with the First Law of thermodynamics, involving energy efficiency and conservation of energy. However, energy has another vital component, namely the useful work potential (availability). Energies

are not the same, they have different availability. If the so-called exergy is not balanced among the supply and demand energies, then nearly avoidable ΔCO_2 emissions, which may not be observed and measured on site but appears and measurable in the atmosphere, take place somewhere else for offsetting the destruction at the original source point. This is shown in Figure 2. The inset in Figure 2 and the Figure 3 explains this concept.



Figure 1.Seventeen SDG (Sustainable Development Goals) By The United Nations Targets Are Necessary But Not Sufficient.

<https://www.un.org/sustainabledevelopment/wp-content/uploads/2023/09/Goal-13_Fast-Facts.pdf>

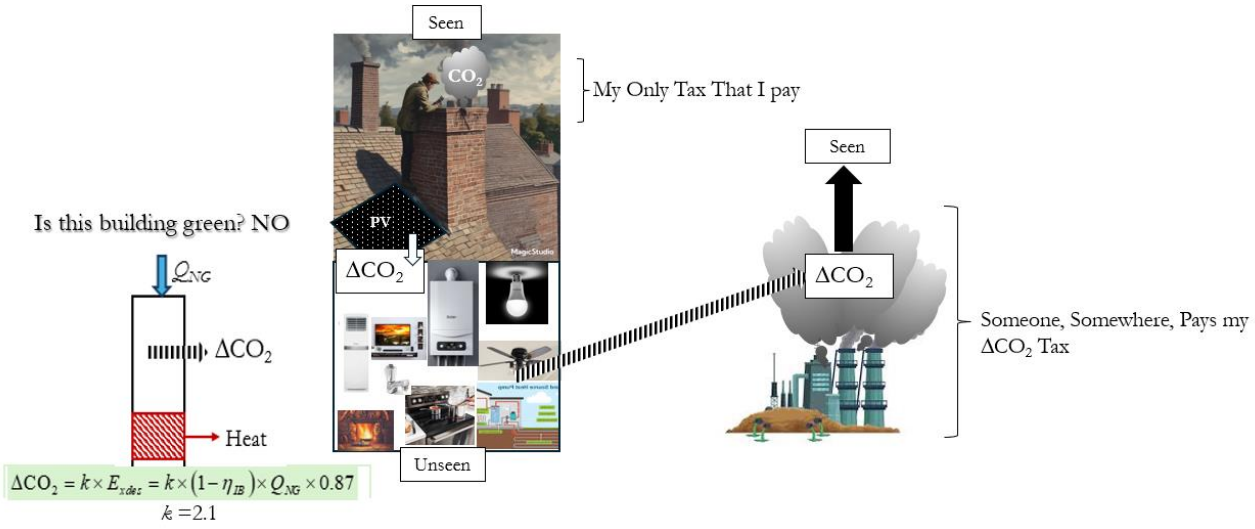


Figure 2. Seen and Unseen CO_2 Emissions in Carbon Taxes

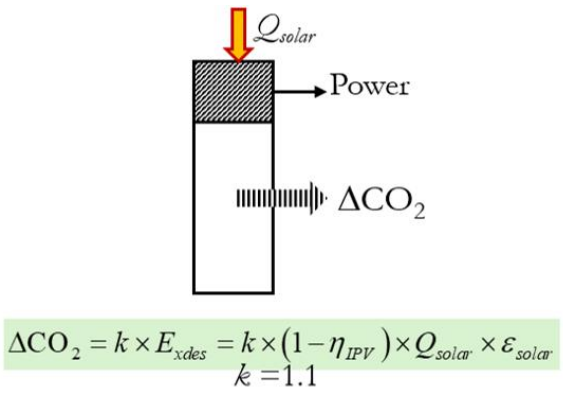
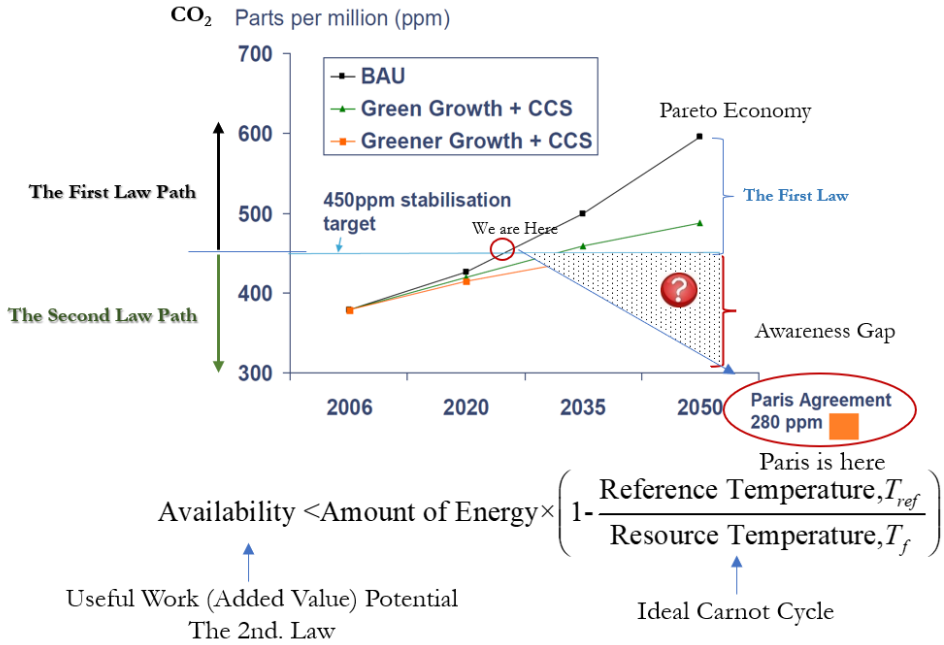


Figure 3. A Solar PV System and ΔCO_2 Emission Responsibility

The first one (in Figure 2) depicts a gas boiler with a First Law efficiency of (η_{IB}), which generates thermal exergy but misses the opportunity of generating electric power, upstream. 0.87 kW-h_{ex}/kW-h_{en} is the unit exergy of natural gas. The Second one (Figure 3) depicts a solar PV panel, which generates electric power at a modest First Law efficiency (η_{IPV}) and destroys the useful work potential downstream in the form of heat to the environment, which also adds to the formation of heat islands. Instead, the waste heat could be collected and utilized (Solar Photo-voltaic-thermal, PVT). Unit exergy of solar energy is in the range of 0.55 kW-h_{ex}/kW-h_{en}. The term (k) is the proportionality constant, which relates the destruction of the useful work potential (added value, quality of energy, exergy).

Because the ΔCO_2 concept is not accounted for the global warming analyses and mitigation efforts, the CO2 concentration in the atmosphere keeps rising despite all First Law-related activities, measures, and all directives. This awareness gap shown in Figure 4 may only be closed by the Second Law. Otherwise, current system will also have implications on unfair distribution of carbon taxes because one's ΔCO_2 emissions responsibilities will be paid by somewhere, by someone, who offsets the exergy destructions (Figure 3).



$$\Delta CO_2 = k \times Availability\ Destruction$$

Figure 4. Availability (Added Value Potential) of Energy in Global Crisis

1.2. Global Crisis and the Industry

Another problem is that electricity is regarded as the only energy form. In fact, according to the International Energy Agency (IEA), the share of electricity in final energy consumption is estimated to have reached only to 20% in 2023, up from 18% in 2015. The highest increase in

global electricity demand belongs to the industry (Figure 5). Yet the waste heat in the built environment is not generally recognized as a (Secondary) green source of energy, if not wasted. At the same time, the industry is the largest producer of waste heat but is not regarded as a marketable commodity. Figure 5 shows an IEA depiction of electric demand. Even though the electricity comes from purely renewables, Figure 6 shows that there is a substantial ΔCO_2 remainder, which is not considered. The same also holds for carbon tax directives and rules.

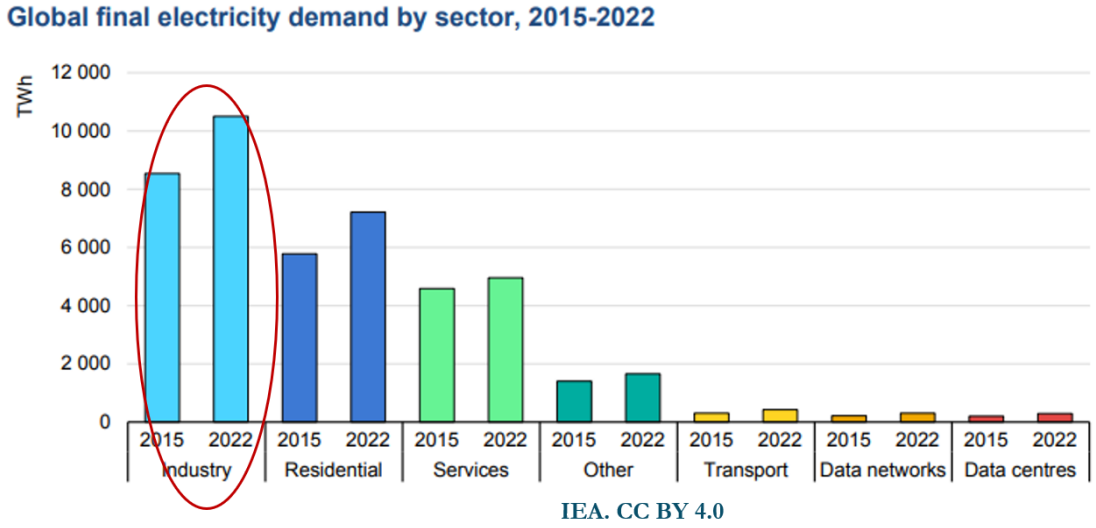


Figure 5. The Highest Increase in Global Electricity Demand Belongs to the Industry

1.3. The Urgency Of A New Carbon Market

At the heart of global resource use are fundamental inequalities: low-income countries consume six times less materials and generate 10 times less climate impacts than those living in high-income countries. Despite this fact, developing countries will face the highest Carbon Tax (CBAM) at the Border to be imposed by the European Union. Global Temperature keeps rising despite First-Law measures, like energy efficiency, energy savings, use of renewable energy resources and waste heat, and energy storage to shave off the peak loads, circular economy, reducing wastes, recycling, carbon capture. Current Seventeen SDG Targets are necessary but not sufficient.

The European Union takes a series of measures and releases directives and restrictions concerning the global warming [1]. Carbon Border Adjustment Mechanism (CBAM). In this context, the European Union has declared a comprehensive policy and strategy package in 2019. The most important section is the Carbon Border Adjustment Mechanism (CBAM), which will virtually affect all the countries, worldwide, with direct or indirect trade connections with the EU Countries [2]. Aligning with the Paris Agreement, the objective is to keep the global warming temperature below 1.5°C until 2053 by reducing greenhouse gas emissions. Accordingly, the concentration of CO2 gas in the atmosphere is expected to decrease to about 280 ppm (parts per million). Human-induced greenhouse gas emissions cause global warming

leading to several global challenges, such as ozone layer depletion [3], wide climatic and meteorological disasters of unusual magnitude, deterioration in ecosystems, decline in agriculture and animal husbandry, decrease in clean water resources, air quality, and increase in magnitude and frequency of pandemics [4, 5]. Causes for all such problems include CO2 emissions due to fossil fuel use, inefficiencies, and primarily but most often ignored quality mismatches among different energy source, equipment, and systems. The latter, which is two to five times more than direct missions at the source is often ignored as shown in Figure 6. Every thousand Gton of CO_2 released into the atmosphere causes the global average temperature to increase by 0.45°C, and an average of 37 Gton of CO2 gas continues to be released every year because of energy use alone [6, 7]. The total annual global CO2 emission is around 60 Gton CO_2/year. Among the root causes that have the ability to explain most of these emissions measured in the air, it is the ignorance of the fundamental fact on that all energy sources and applications are not equal on earth, and they have different qualities, which means ability to do useful work and to add value. Humanity must duly respect all energy sources and the environment In Asian and Near Eastern culture, respect for energy and water resources are among these. Western culture, on the other hand, lacks this quality awareness and views energy as a commodity that can only be bought and sold on the stock exchange. In addition, the current western culture depends on the Pareto principle and the free market rules (linear economy) and tries to solve the global warming in a narrow mold. However, global warming is a three-dimensionally complex problem. In this respect, although the amount of CO2 in the atmosphere can be measured accurately (Visible), many root causes on earth remain ignored and unaccounted for. Consequently, adequate, and sustainable solutions cannot be implemented. Figure 6 clarifies this problem. In essence, only the Eastern culture can solve the unawareness issue and sustainably develop and implement realistic solutions by giving attention to the quality of energy rather than quantity of energy. Emissions due to quality mismatches are invisible to us on earth.

Within the framework of the EU's Green Transformation Strategy, it is aimed to reduce carbon emissions by 55% compared to 1990 levels in 2030 and to become the first climate neutral continent in 2050. The tools and measures to achieve these limited targets, however, are concerned with direct emissions only, as seen in Figures 1 and 2. In recent years, it is observed that even these modest goals will not be achieved with today's technology. Unless wide awareness of CO_2 emissions due to quality mismatches is established and implemented, it will not be possible to satisfy the Paris Agreement. Despite the importance of recognizing the quality (Exergy) mismatches and trying to solve them with sustainable and fair measures, the West, keeps trying to reach the Paris Agreement by 2050, by simply activating impositions such as carbon tax at the border and carbon trading rules, all based on linear economy only. Without solid scientific foundations, these measures are insufficient, unfair, and unpractical.

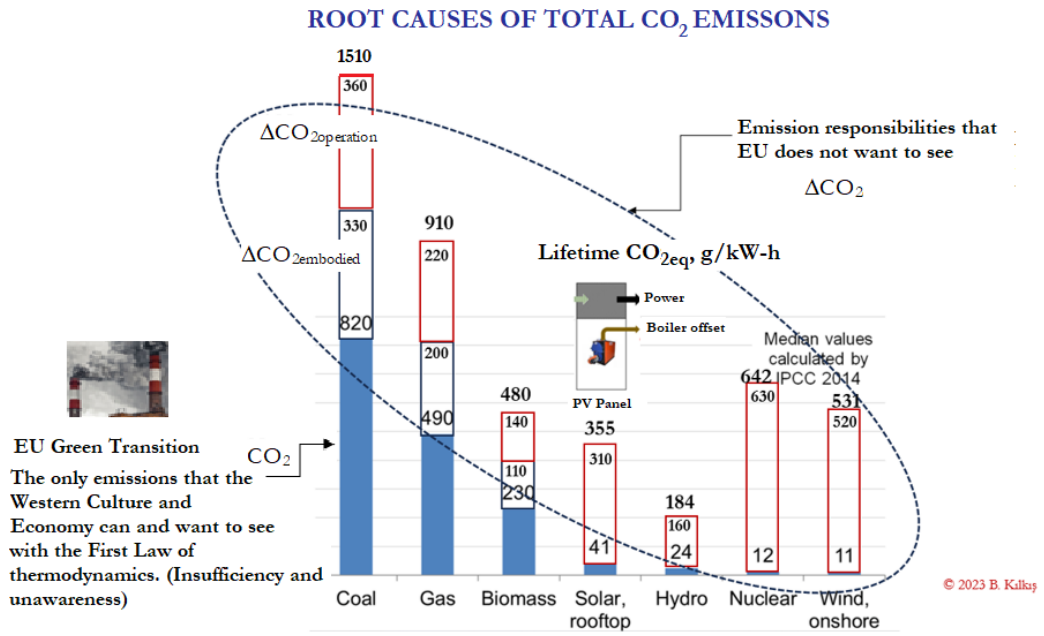


Figure 6. Visible and Invisible Emission Responsibilities of Different Energy Sources [8]

2. THE NEW MODEL

Among the Western solutions in agriculture and animal husbandry, only agricultural insurances and limited financial supports within the linear economy rules and interest stand out. These are far from being permanent solutions to global warming and, in fact, confine the agriculture and animal husbandry in a vicious circle [9, 10, 11]. In a proper response by the East with effective and sustainable solutions against such ineffectiveness and inconveniences across the globe, integrated farming cooperatives along the beltway must be established in close coordination and integration of light agricultural industry and rural communities, attached to these cooperatives, which generate and share their own energy [12]. Inconsistencies and insufficiencies in the European Union's decarbonization initiatives are reaching significantly unreasonable levels. For example, according to a law that is on the agenda to be implemented in Denmark, animal owners will be charged a carbon tax of one hundred Euros for one cow, for every year. Farm animals existed throughout the history and their global warming effects were not an issue until the industrial revolution, but now the blame is being put on them. This bill shows the West's inadequacy against global warming. If this tax is implemented in a broader sense, such an irrational tax may be demanded from animal owners when exporting meat or live animals to the West. Moreover, animal husbandry is at the forefront in all Turkic States and other Eastern countries and grossly supports their economies.

A cow owner may not get free by just paying 100 Euros every year for the same cow. If farmer collects the manure and utilizes it to generate heat and electricity in a biogas facility as an effective remedy against global warming, the farmer may have to pay a second tax for the CO2

coming out from the exhaust of the biogas facility (cogeneration), since the positive energy flow chain is not foreseen in the tax law and the anthropogenicity is not considered. The Danish bill does not look at the continuation of the energy chain by saying the tax is per cow, whatever you do, and does not consider positive appraisal stages. It looks at each system one by one. In the contrary, the same farmer when selling a product produced by using his electricity and heat to the EU countries, another carbon tax will be collected at the border. Electricity and fertilizer products are at the top of the border carbon tax list. While the EU struggles with such inconsistencies, we should focus on realistic, innovative, and rational solutions with cultural fairness and greater respect to our future and environment and create our own carbon market against their impositions. There must be a regional carbon trading at the border system with Belt Road alternatives. Only with these methods can we eliminate the dangers that the West will bring to Türkiye, the Turkic States, and all Belt Road countries.

If this tax is considered as scientifically consistent by some circles in the EU, then it is necessary to look at the environmental footprint of an F-35 jet aircraft belonging to the Royal Danish Air Force in proportion to this tax. This single aircraft will emit 3.5 tons of CO2 from its turbine exhausts by spending fossil fuel in just 15 minutes in a hovering position over the ground. This emission is equivalent to the cumulative CO2 emissions of three cows for a complete year. As a result, if this aircraft repeats this vertical take-off hovering and landing action 15 times in a year, it will have to pay a tax of 4500 Euros. This amount excludes the tax liability of the same aircraft during level flights during the year. In the same context, since Afşin-Elbistan-A lignite thermal power plant generates approximately 4 billion kW-h of electricity annually, it may have to pay 0.2 billion Euros in taxes- equivalent to two million cows annually. If this electrical energy is exported to neighboring countries (bordering EU countries such as Greece and Bulgaria), a tax will be imposed at the border in proportion to the portion exported.

As a result, while EU countries keep themselves busy by taking precautions against global warming with such inconsistencies, particularly important opportunities arise for us. By conducting algorithmic studies about new carbon market models, we should reach a position that enables us to collect carbon taxes, instead of them at the new border against the EU impositions, as opposed by the Belt Road and the Turkic States. This will be possible because the new model will recognize and respect the virtues of energy quality, of which the EU does not want to see. With such a realistic and fair approach, the Eat will protect their trade rights and all sectors, including livestock and agriculture, from unfair carbon competition, and will set a role model for Western countries by achieving the Paris Agreement targets on time and will ahead of them. This leadership will also reflect on political power. It is obvious that the goals

of the Paris Agreement cannot be achieved if the so-called linear, or circular, one-dimensional economy, which ties everything to money, continues to be in force.

Among these problems, the biggest threat from the West will apply to Turkic States and all Belt Road countries, except certain developed countries (such as China and India, the Russian Federation is already subject to disproportionate sanctions.) Figure 7 shows the major threat. The basic economy of Asian countries is based on agriculture, animal husbandry, mining, and semi-finished goods. According to Figure 7, which represents today's conflict between West and East, EU countries dominantly practice extended R&D activities and novel engineering designs. These activities have low CO_2 emission responsibilities and high ΔCO_2 responsibilities due to the nature of such practices. Despite this controversy, they generate exceedingly high added values and high selling prices. In essence, the EU countries simply assemble and touch them up the semi-finished products with high ΔCO_2 emissions that they conceal and keep untaxed, yet unfairly attribute CO_2 emissions to other countries and charge high carbon taxes at their border. Other countries, on the other hand, mostly sell their semi-finished products to EU countries with a small profit margin, consuming much energy, practicing some production line developments, and emitting larger amount of CO_2, thus facing large carbon taxes. As a result, these counties will not have a net profit, as shown on the left-hand-side of Figure 7. In fact, the fundamental problem is not limited to CO_2. Factors such as water (such as cotton production), labor, land, and environment (such as toxic waste) should also be considered cumulatively. The Final Production Ratio, FPR of Turkic states and Belt Rad countries must reach to at least 60% in their industry and farming, from today's average ratio of approximately 35%. Only if this gap is closed, then these countries may achieve sustainable decarbonization and net profitability targets in accordance with the Paris Agreement. Otherwise, commodities produced along the Belt Road, including Turkic states, will face carbon taxes at the EU border. The EU will sell back finished products with minimal emissions but with high revenues. For example, if a cow is exported and returns as a meat product, cow tax will be charged on departure and little or no tax will be charged upon arrival at the border. EU countries need us as intermediate producers to keep their advantage and maintain their large profits, . In fact, this is an opportunity to close the gap by leaping to finished products rather than keeping on semi-finished products or raw material.

A new and joint Belt Road customs line must be drawn. According to Figure 7, EU countries have low CO_2 emissions but high and hidden (Untaxed) ΔCO_2 emissions. Because ΔCO_2emissions are recorded somewhere else, or even by some other countries, which offset the quality mismatches of the original location face unfair taxes. This another issue that must

be taken care of to eliminate this taxing problem. New belt and road customs line must be flexible to recognize the origin of ΔCO_2, not the final offset point.

To overcome all these difficulties, a series of sustainable measures must be taken, and Belt Road boundaries must be adaptively protected. A final product requires low exergy compared to semi products. They keep using power etc. just for assembly etc. Semi products have more exergy balance. For example, yes mining uses power but the product has high exergy. For example, coal has minimum ε_x of 0.85 kW-h_{ex}/kW-h_{en}, electric power used has 0.95 kW-h_{ex}/kW-h_{en}. For low ΔCO_2 another approach may be to have low *k* values.

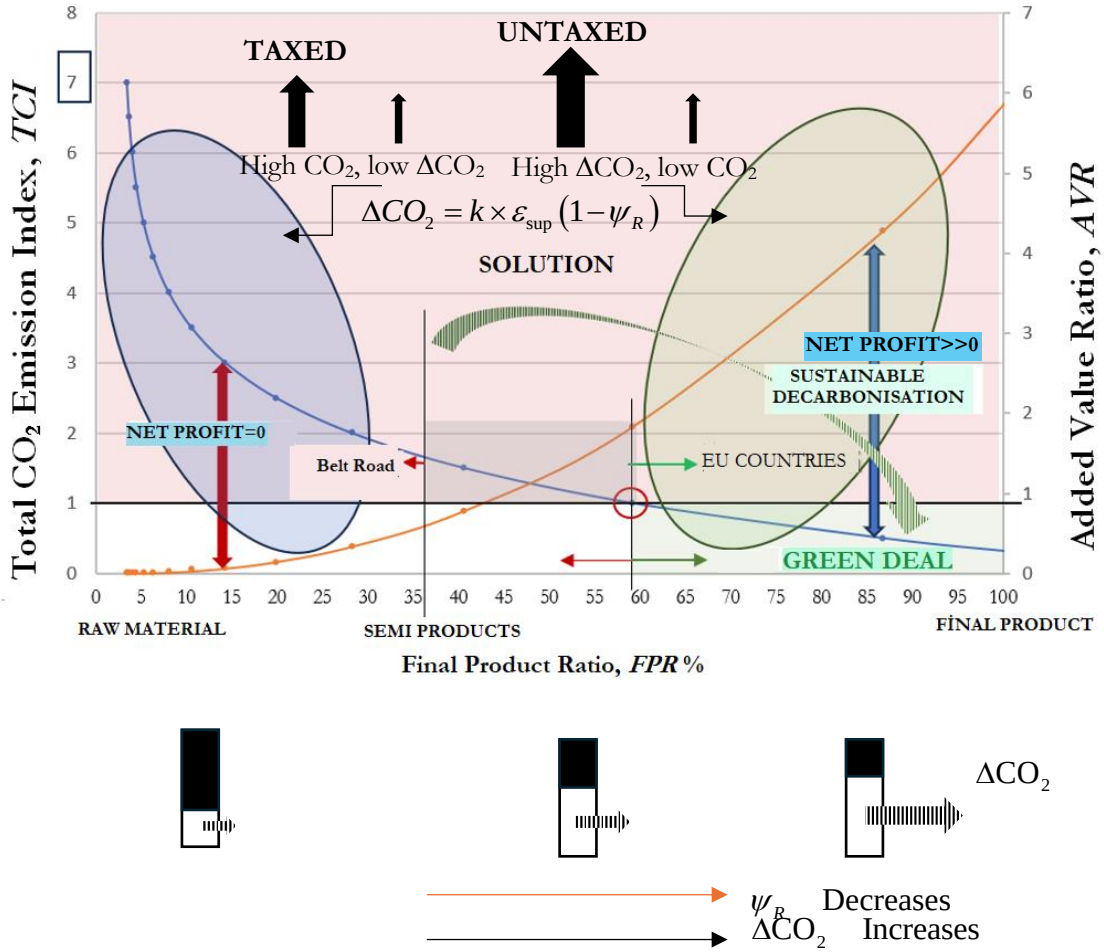


Figure 7. Negative Impact of Carbon Tax on the Border fort the Belt Road Industries and Agriculture and the Solution with Final Products [8]

The following equations provide the new metrics for evaluating the carbon footprint of the built environment. *SEI* is the Sustainable Environment Index, which involves both the First Law efficiency, Exergy rationality, and *ODI* (Ozone Depletion Index). Ozone Depletion Index is a combination of Ozone Depletion Potential (*ODP*) and the Global Warming Potential (*GWP*). Coefficients *w*, *y*, and *z* in Equation 2 depend on the climatic conditions and the type of refrigerant leaking from systems and equipment, like heat pumps. Heat pumps are touted to

be one of the best assets for nearly total electrification and green energy in the quest of decarbonization, which are not. Yet, the sales are exponentially increasing and the carbon footprint (Equation 3) of heat pumps in this respect must be seriously considered. Typically, the correlation constants, namely *w, y, and z are* 0.1, 0.045, and 0.01, respectively. The term (*y*) includes the effect of water vapor release.

(1)

$$ODI = \frac{wGWP^{y}}{(1-ODP)} \times \left(\frac{ALT}{1}\right)^{z} \qquad \{0 \le ODP < 1\} \qquad (2)$$

$$\Delta CO_{2refrigerant} = \left(GWP_{refrigerant} + 1000\Delta CO_{2-HP}\right) \times \left(\frac{LR \times R_c}{E_{X-HP}}\right) \qquad (3)$$

Here, $E_{X\text{-}HP}$ is the exergy delivered by the heat pump during its annual operating hours, *LR* is the leakage ratio of the refrigerant *R* is the refrigerant charge of the heat pump.

$$FPR = \left[\frac{\left(e^{-a \times TCI}\right)}{b} + c\right] \times 100 \qquad \{\text{Finished Product Ratio, see Figure 7}\} \qquad (4)$$

$$AVR = d\left(e^{-f \times TCI}\right) \qquad \{\text{Added Value Ratio, see Figure 7}\} \qquad (5)$$

The terms *a*, *b*, *c*, and *f* in Equations 4 and 5 are the coefficients depending upon the industry specifics.

$$TCI = \sum CO_2 / 0.63 \qquad (6)$$

The term (0.63) is the reference unit ΔCO_2, considering that the average unit exergy supply, $\varepsilon_{sup\text{-}ref}$ is 0.8 kW-h_{ex}/kW-h_{en} for the current global energy mix and the reference $\psi_{R\text{-}ref}$ is 0.21:

$$\Delta CO_{2-ref} = \varepsilon_{\sup-ref}\left(1-\psi_{R-ref}\right) = 0.80 \times (1-0.21) = 0.632 \text{ kg } CO_2/\text{kW-h}_{ex} \qquad (7)$$

3. CASE STUDIES

3.1. Geothermal Energy

Geothermal energy is considered to be green and carbon free, except embodiments and non-condensable gases, provided that proper environmental protection measures and re-injection processes are accomplished. Yet, Figure 8 shows several ΔCO_2 responsibilities, although it might be argued that the geothermal power plant uses part of its own electricity production. However the electric power demand of the cooling fans means reduction in the grid power supply from the geothermal plant, which translates to more fuel demand at the power plant leading to more emissions there. According to Figure 8, geothermal brine is cooled in the open-to-atmosphere pool, discharging heat and chemicals to the environment, leading to a heat island in the vicinity, and water loss. Due to the concerns about the loss of electric power

generation potential during the lifetime of the geothermal reservoir, financers like the World Bank do not permit the utilization of the waste heat and enforce to send the heat back to the reinjection wells at 90°C, minimum. This is understandable from the viewpoint of today's simple economy. However, according to the Second Law, at an expense of a certain amount of compromise in power exergy generation potential, an optimum waste heat utilization rate may be determined, which maximizes the total exergy generated and utilized in the built environment, leading to minimum carbon footprint, while a district heating system is implemented. *Y* is the total life expectancy of only power generation and *X* is the reduction in the life expectancy of the reservoir due to lowering the return temperature to the injection well at T_{inj} to accommodate the utilization of thermal exergy before reinjection. This imposes the following optimization condition:

$$(Y-X)\left[0.95\times\eta_{IT/orc}+\eta_{IHE}\times(1-\eta_{IT/orc})\times\left(1-\frac{T_{inj}}{363\ \mathrm{K}}\right)\right]>Y\times0.95\times\times\eta_{IT/orc} \quad (8)$$

s.t. $T_{inj}\geq 310\mathrm{K}$

After simplification:

$$\left(1-\frac{X}{Y}\right)\left[0.95\times\eta_{IT/orc}+(1-\eta_{IT/orc})\times\eta_{HE}\times\left(1-\frac{T_{inj}}{363\ \mathrm{K}}\right)\right]>0.95\times\times\eta_{IT/orc} \quad (9)$$

Where, the reduction of the reservoir life, *Y* depends on the reinjection temperature, T_{inj}, to be chosen, below 90°C, which is the standard reinjection temperature required by the creditors.

$$\left(\frac{X}{Y}\right)=a\times\left(363-T_{inj}\right)^{b} \quad (10)$$

$$\left(1-a\times\left(363-T_{inj}\right)^{b}\right)\times\left[0.95\times\eta_{IT/orc}+(1-\eta_{IT/orc})\times\eta_{HE}\times\left(1-\frac{T_{inj}}{363\ \mathrm{K}}\right)\right]>0.95\times\times\eta_{IT/orc}$$

{Equations 9 and 10 combined} (11)

Figure 9 shows a typical result for *a* = 0.2 and *b* = 0.1, $\eta_{IT/ORC}$ = 0.2 (power generation efficiency of turbine and ORC mix), η_{IHE} = 0.9 (heat exchanger efficiency). ORC stands for organic Rankine-Cycle turbine. Note that, Equation 11 does not involve any economic concerns.

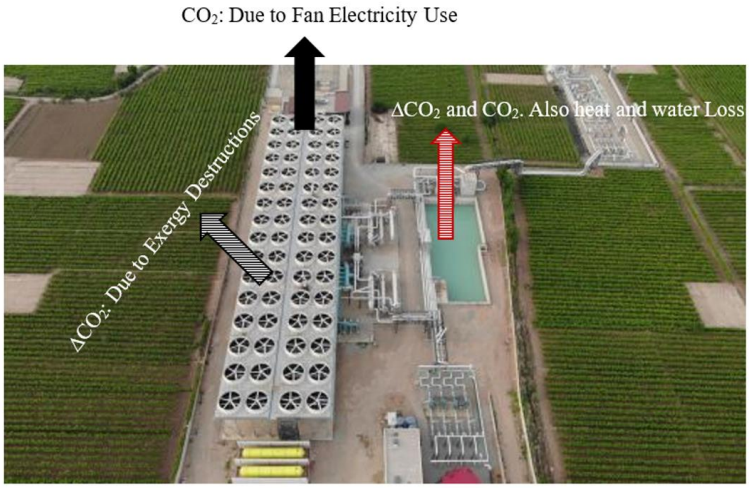


Figure 8. A Geothermal Power Plant with Dry Cooling with Electric Fans and Open Pond

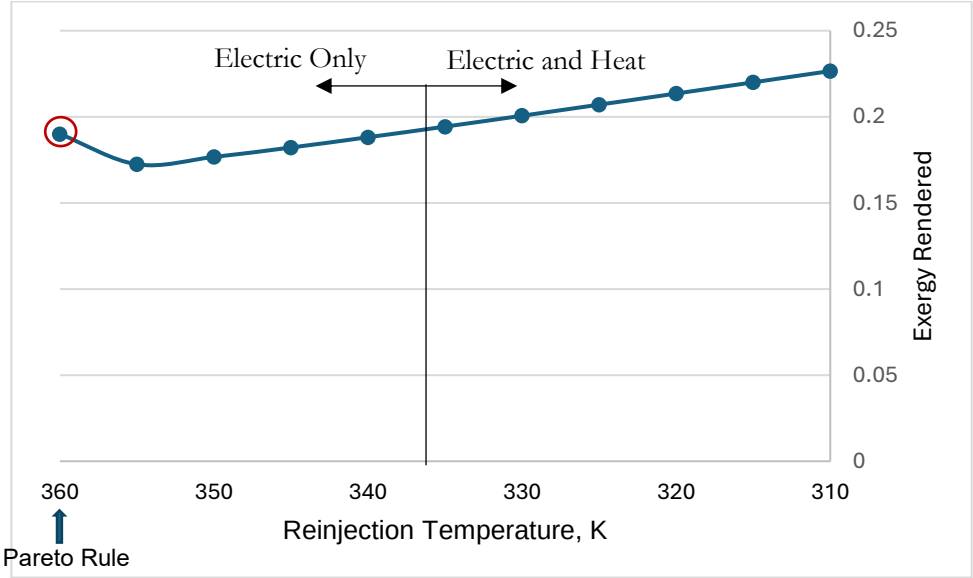


Figure 9. Power or Heat or Both?

According to Figure 9, the maximum exergy rendered throughout the life of the reservoir is at the point T_{inj}=337 K with (X/Y) = 0.187, which means that the life expectancy is shorter by this ratio, but maximum exergy is rendered by about 20% more when compared with no heat generation case. Today's linear, Pareto-based simple economy, however, does not yield any maxima at stays at X = 0 (the origin of the curve), which renders less total exergy, even the life expectancy of the reservoir is the longest. This typical result shows that analyses must be based on the Second Law, instead of simple economy. For example, at almost all global average power- to-heat market price ratios along the life expectancy of the reservoir, the solutions will always stay at the origin (T_{inj} = 363 K) and the geothermal heat would be wasted.

3.2. Afşin Elbistan Power Plant and TOKİ Buildings

Figure 10 shows the plan view about the Afşin-Elbistan lignite power plant, which is cooled by the Ceyhan River's fresh and cold water at its source. This water is transported by pipelines about 30 km long, driven by electric pumps (Figure 10). The return warmer water is discharged to the river. Yet the TOKİ buildings constructed after the 2023 major earthquake in the region is somewhere at the midway, only 5 km away, but the design and construction remained blindfolded to this waste heat source. These new apartments are heated by natural gas boilers. Figure 11 shows an alternative solar green prosumer building, which exchanges heat with the alternative district heating system. District heating system also involves an agricultural complex and light industry to support the local economy. The conceptual hybrid agricultural park and light industrial park is shown in Figure 12. The agricultural park is part of the slow city concept. It consists of renewable energy systems. Irrigation wells are operated by DC powered pumps, connected to wind turbines and solar PVT cells. The pumped ground water is circulated first in the PVT cells at an optimum rate, which maintains the solar cell efficiency, warms the irrigation water below the excess vaporization temperature for plant growth, and minimum pump power demand. Excess power is stored to hydrogen and stored. Fuel cells convert hydrogen to electric power with reject heat, which is reclaimed and utilized in crop drying and similar light industry in the agricultural park. Heat pups may be used for cooling purposes in greenhouses and dwellings in a district heating and cooling system.

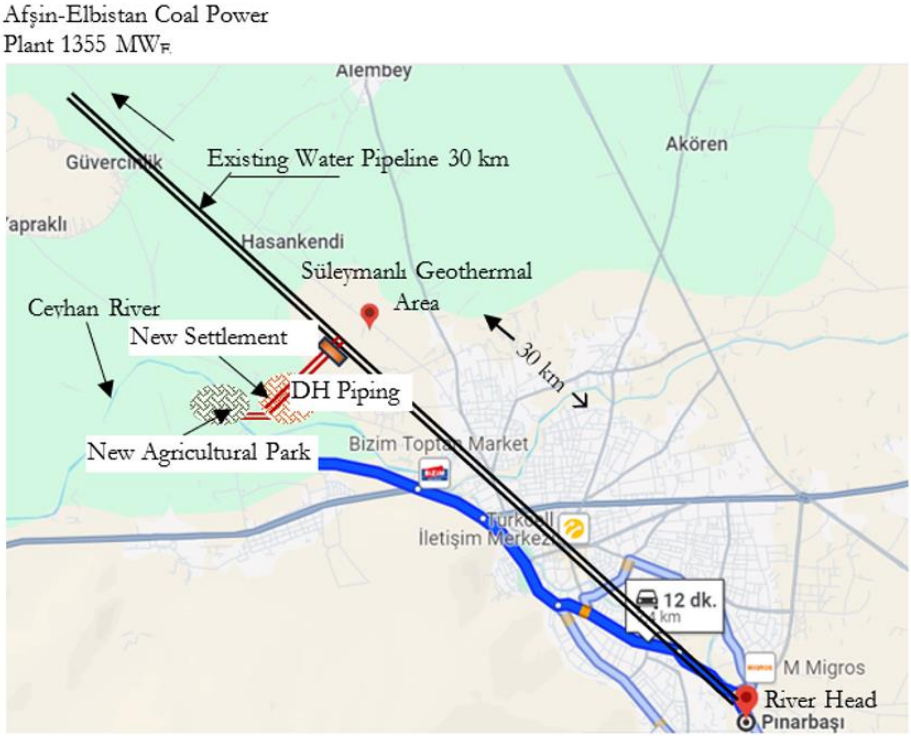


Figure 10. What is Missing?

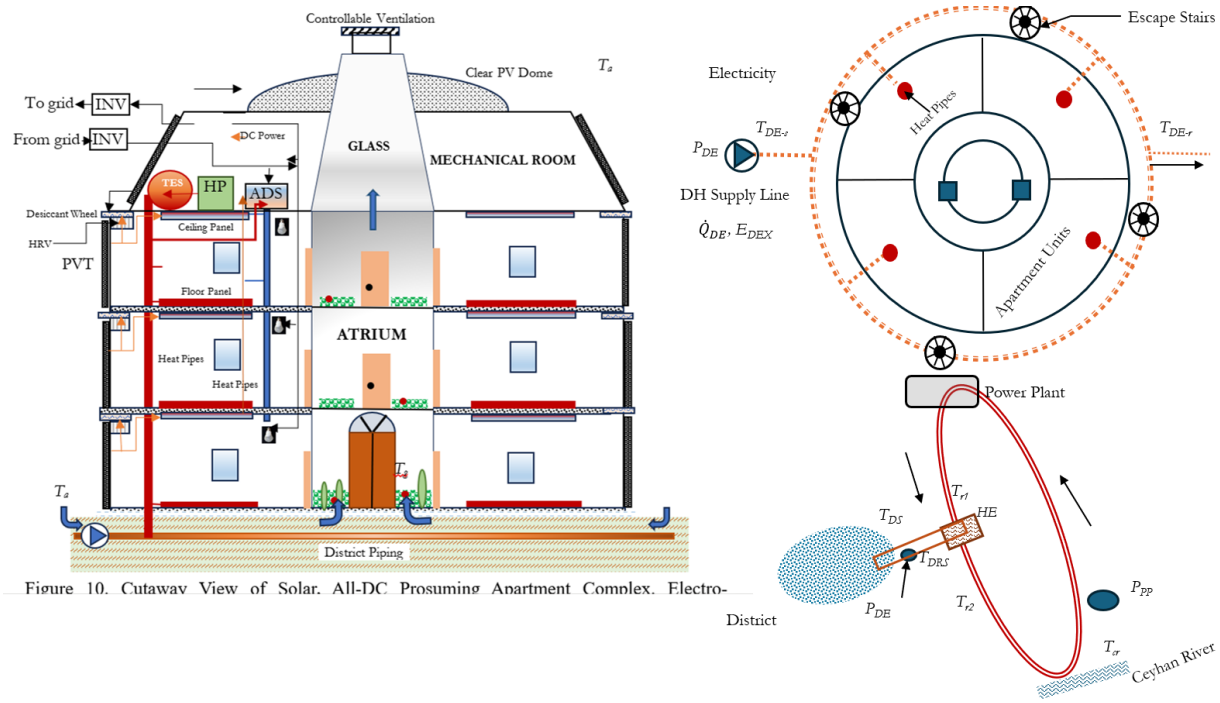


Figure 10. Cutaway View of Solar, All-DC Prosuming Apartment Complex, Electro-

Figure 11. A Better Decarbonization Solution With Solar Green Prosumers and the Waste Heat of the Power Plant

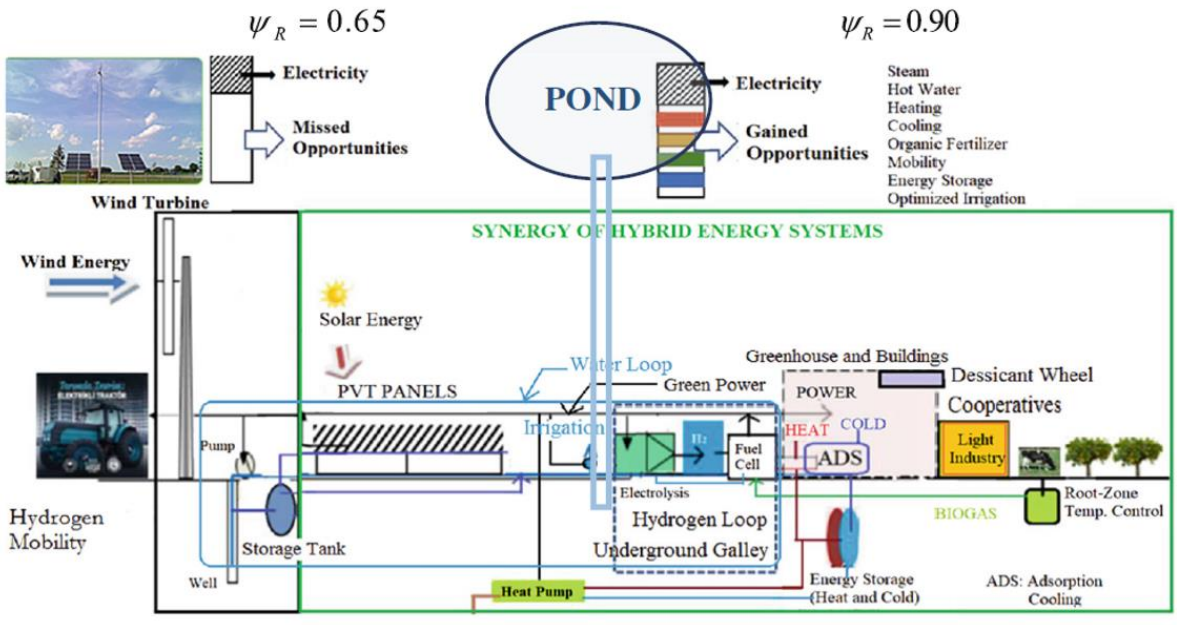


Figure 12. Meeting of the Agriculture and Industry in a Green City

To solve the implications of the current carbon tax schema of the European Union a series of counter measures may be taken. These are short listed below.

4. CONCLUSIONS

To solve the implications of the current carbon tax schema of the European Union a series of counter measures may be taken. These are short listed below.

- Creation of a Joint Scientific and Technological Strategy Center
- Development and implementation of cross-country coordinated state farms based on renewable and waste energy [12, 13].
- Making the Common Central Bank functional (competing with the EU Central Bank)
- Establishing a competing fund to the IMF
- Developing and implementing a common carbon market model
- Developing a carbon tax algorithm
- Implementation of a banking system competing with the World Bank (WB)
- Expanding and coordinating Shanghai Cooperation Organization and the Belt Road initiative
- Establishment of a new and protectionist customs union between East and West
- Preparation and implementation of new criteria for carbon markets (based on the value of energy), realistic laws and directives
- Preparation of scientifically valid and fair CO_2 emission accounting standards challenging the ISO standards
- Accelerating and supporting the transition of all Eastern countries from semi-finished products to finished products (Figure 7)
- New location adaptive carbon taxes including both ΔCO_2 and CO_2
- Issuing standards specific to Belt Road countries in the field of Green Building and Green Industry certification, like exergy star and TSE Safe and Green Building Program of TSE.

Once these measures and others, likewise, are implemented, the benefits will be multiple. These are namely, 1-the fundamental root causes and locations may be determined about ΔCO_2 and sustainably rational measures may be taken towards satisfying the Paris Agreement goals., 2- Fair carbon takes in a constructive manner may be established, 3- By doing so, the economic development of the countries by shifting them to finished products will be accelerated, 4- the SDG 17 of the United Nations will be more meaningful, comprehensive, end constructive by factoring in ΔCO_2.

5. REFERENCES

1. **Ersen, P. (2024),** “Avrupa Yeşil Mutabakatı: Temel Bilgiler ve Türkiye’nin Uyumu, BAZ Girişim”, < https://www.bazgirisim.com/avrupa-yesil-mutabakati-temel-bilgiler-ve-turkiyenin-uyumu/>
2. T. C. Avrupa Birliği Başkanlığı. (2024). “Sınırda Karbon Düzenleme Mekanizması (SKDM)”. <https://www.ab.gov.tr/sinirda-karbon-duzenleme-mekanizmasi-skdm-_53747.html>

3. **Kilkis, B. (2019),** "The Importance of Exergy Rationality And Storage For 100% Renewable Targets In Decoupling Sustainable Development And Ozone Depletion", Workshop on Considering Unlocking Energy Efficient Opportunities And Exploring Low GWP Non-HFC Alternative Technologies In The Cooling Sector And Safety Standards While Phasing-Down HFC Under The Kigali Amendment, UNIIO, September 16-17, 2019, Antalya, Türkiye.
4. **Kılkış, B. (2020),** "Küresel Salgının Hatırlattıkları, İklimsel Isınma ve Klima Sistemleri", Tesisat Mühendisliği Dergisi, MMO, Sayı 177/Özel Sayı-Haziran 2020, s: 16-24.
5. **Kılkış, B. (2021)."** Küresel Kapitalizmde Küresel Salgınlar, İklimsel Isınma ve Atmosfer", BRIQ Working Paper Series, No: 2, Kuşak ve Yol Çalışmaları Uygulama ve Araştırma Merkezi (KUYÇAM), İstinye Üniversitesi. E-ISSN 2718-0581 e.
6. IPCC. (2023). "Climate Change 2023 Synthesis Repor"t, WMO, UNEP, ISBN: 978-92-9169-164-7, DOI: 10.59327/IPCC/AR6-978929169164
<https://www.ipcc.ch/report/ar6/syr/downloads/report/IPCC_AR6_SYR_FullVolume.pdf>
7. Architecture2030. (2024). ""Why the Built Environmen?"
<https://www.architecture2030.org/why-the-built environment/#:~:text=Of%20those%20total%20emissions%2C%20building,for%20an%20additional%2015%25%20annually.>
8. **Kılkış, B. (2024).** "Hemp, Energy And Environment, Technology of Hemp", Int. Interdisciplinary Research Conference, 21-22 May 2024, OSTIM, Ankara Türkiye.
9. **Kılkış, B. (2020).** "Tarım Sigortalarında Doğal Afetler, İklimsel Isınma ve Enerji Sinerjisi", T. C. Tarım ve Orman Bakanlığı-TARSİM, Rapor, 15 s. Ankara, Türkiye
10. Aydınlık Gazetesi. (2020). "Sigortalama Yetmez Yeşil Tarım Atağı Şart!", Haber, 6 Aralık
11. **Kılkış, B. (2020),** "Tarım Sigortalarında Doğal Afetler", Aydınlık Gazetesi, 1-2, 29 Mayıs
12. **Kılkış, B. (2022),** "Yeşil Hidrojen: Kuşak ve Yol Girişimi'nin Ortak Bağı". Kuşak ve Yol Girişimi Dergisi (BRIQ), 3(3), s: 6-20.
<https://briqjournal.com/sites/default/files/yazi-ici-dosyalar/2022-06/CILT3_SAYI3_TR_FINAL_SON_1-15.pdf>
13. **Kılkış, B. (2024),** "Exergy-Based Slow-City/Agriculture Mechanization With Circular Hydrogen and Renewable Energy Systems", E. Cavallo et al. (Eds.): ANKAgEng 2023, LNCE 458, pp. 112–125, 2024. <https://doi.org/10.1007/978-3-031-51579-8_12>

6. WEB LITERATURE

https://en.wikipedia.org/wiki/Eco-industrial_park

https://www.unido.org/sites/default/files/files/2020-05/International_Guidelines_for_Industrial_Parks_EN_0.pdf?_token=1788844873

https://www.greenindustryplatform.org/themes/eco-industrial-parks

https://www.project-syndicate.org/commentary/green-industrial-parks-could-help-accelerate-decarbonization-by-ricardo-hausmann-2023-07

https://www.rmit.edu.vn/news/all-news/2024/mar/a-greener-tomorrow-with-sustainable-industrial-parks

https://www.globalnature.org/en/industrial-parks-phase-1

https://smartcitysweden.com/best-practice/424/haraholmen-a-green-industrial-park-where-sustainability-is-key/

https://www.unido.org/our-focus-safeguarding-environment-resource-efficient-and-low-carbon-industrial-production/eco-industrial-parks

DESIGN OF THE DEPLOYMENT OF MEMBRANES ON SATELLITES

Teru NATORI, *teruteru.natori@toki.waseda.jp* Waseda University, Tokyo, Japan

Tomoyuki MIYASHITA *tomo.miyashita@waseda.jp* Waseda University, Tokyo, Japan

ABSTRACT

In recent years, the development of small satellites has become increasingly active. However, this has led to an increase in the amount of space debris. As a countermeasure, satellites are required to be equipped with a deorbit mechanism. One of the deorbit mechanisms for satellites is to deploy a membrane to reduce the velocity. This research proposes a method to determine the deployment of the membrane by the change in the rotation of the satellite. The validity of the method is demonstrated through modelling and numerical analysis, and its feasibility is demonstrated by designing the system.

Keywords: Satellite, Membrane, De-orbit

1. INTRODUCTION

Since the successful launch of the first satellite, Sputnik 1, in 1957, the number of satellites launched has continued to increase, although their purposes have changed. One factor behind the increase in the number of satellites launched in recent years is the increasing development of small satellites, which can be developed at low cost and in a short period of time, due to the miniaturization and high performance of the electronic components installed on satellites.

On the other hand, the increase in the number of satellite launches has led to an increase in space debris, which is man-made objects orbiting the Earth without a purpose, including satellites that have completed their missions and the parts of rockets. Currently, there are approximately 100 million pieces of space debris with diameters ranging from 1 to 10 cm. Although most of the space debris is small, it moves at high speeds of around 7 to 8 km per second, and a large amount of energy is generated when it collides with something. In fact, there have been cases where operational satellites have been rendered non-functional by collisions with space debris, and space debris is now considered a problem. In order to prevent the increase of space debris, guidelines have now been established that require low-earth orbit satellites to deorbit or enter a graveyard orbit within 25 years of completing their missions [1].

To achieve this, satellites are sometimes equipped with a deorbit mechanism. A deorbit mechanism is a mechanism that quickly removes a satellite from its orbit after it has finished operating. This makes it possible to re-enter the atmosphere and burn up the satellite, allowing it to be operated without increasing space debris.

A representative deorbit mechanism is membrane deployment [2], [3]. This involves installing a folded membrane on the satellite, which is deployed at the end of the mission. When the membrane is deployed, the satellite experiences slight resistance from the atmosphere in Earth orbit, causing it to slow down. This causes the satellite to lose altitude, shortening the time it takes to re-enter the atmosphere, making deorbit possible. Other methods include using electromagnetic tethers [4]. Grant Bonin, Jesse Hiemstra, Thomas Sears and Robert Zee [5] had also shown that membrane deorbiting is effective for satellites with orbital altitudes of less than 1,000 km. There is a need to install such de-orbit mechanisms on satellites and take steps to prevent the increase of space debris.

In this de-orbiting mechanism, various methods were used to confirm whether the de-orbiting membrane had been deployed. B. Cotton, I. Bennett, and R. Zee [6] confirmed this on the CANX-7 satellite using a door switch and reel sensor and publicly available orbital information. In the door switch and reel sensor method, the door switch was used to check whether the door was open, and the reel sensor was used to determine whether the reel was extended long enough to deploy the sail. In the publicly available orbital information method, sail deployment was determined from the orbital drop caused by sail deployment. Alperen PALA, Toshinori KUWAHARA, Takumi SAITOU, Hiroki UTO, and Yoshihiko SHIBUYA [7] used a camera and publicly available orbital information to determine the deployment of the membrane on the ALE-1 satellite. In the camera method, the state of the membrane when deployed was photographed with a camera and the data was sent to the ground for confirmation.

This method of using public orbital information is common and has the advantage that it allows confirmation without having to install a device on the satellite to check the membrane deployment. However, since the confirmation takes time, there remains the issue that it is not possible to confirm whether the membrane has been deployed immediately after sending the membrane deployment command. Therefore, this research proposes a method to confirm the deployment of the membrane by observing the change in satellite rotation that occurs as the membrane is deployed. This aims to make it possible to determine the membrane deployment at low cost and in a short time, which are advantages of small satellites.

2. SATELLITE OVERVIEW

2.1 Waseda-Sat-Zero-II

First, this chapter describes the satellites used in the analysis. The analysis will be carried out using the satellite Waseda-Sat-Zero-II. The satellite Waseda-Sat-Zero-II was selected as the fourth satellite in JAXA's Innovative Satellite Technology Demonstration Project, and as of 2024, it is being developed at Waseda University's Miyashita Laboratory. Waseda-Sat-Zero was selected as the third satellite in the Innovative Satellite Technology Demonstration Project, was also developed by the Miyashita Laboratory, and was launched in 2022, but did not reach operational status due to a rocket launch failure, so this satellite is being developed as a second attempt. The external design diagram of the satellite is shown in Figure 1.

The external view of the Waseda-Sat-Zero-II case is shown in Figure 2, and its specifications are shown in Table 1. The external view of the top cover is shown in Figure 3, and its specifications are shown in Table 2. The satellite is completed by attaching the top cover, side panels, deployment membrane, convex mechanism, antenna, and base to this case.

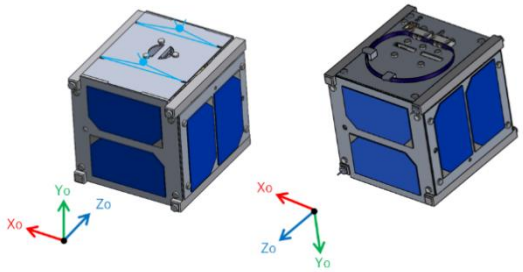


Figure 1 External view of Waseda-Sat-Zero

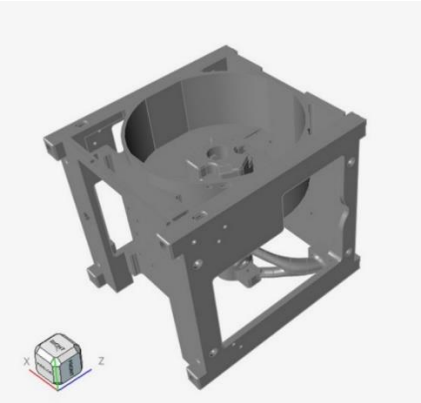


Figure 2 Waseda-Sat-Zero-II case

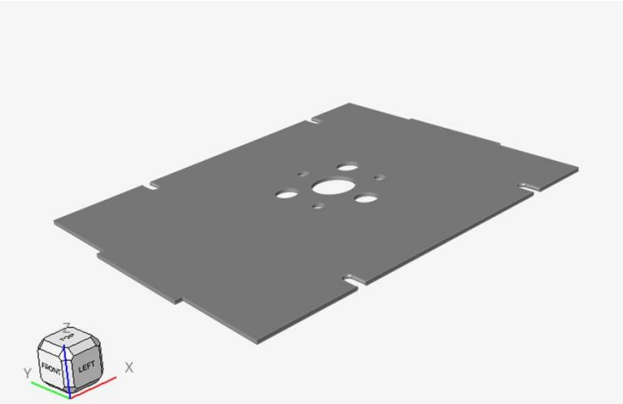


Figure 3 Waseda-Sat-Zero-II top cover

Table1 Satellite Case Specifications

Size	x	0.100 m
	y	0.102 m
	z	0.113 m
Mass		0.376 kg
Mass moment of inertia	I_{xx}	0.001 kg*m^2
	I_{yy}	0.001 kg*m^2
	I_{zz}	0.001 kg*m^2
	I_{xy}	-9.583^{-6} kg*m^2
	I_{xz}	1.342^{-6} kg*m^2
	I_{yz}	1.878^{-5} kg*m^2

Table 2 Top Cover Specifications

Size	x	0.102 m
	y	0.082 m
	z	0.001 m
Mass		0.022 kg

2.2 Membrane Deployment Mission

One of the missions of this satellite is to demonstrate membrane deployment technology. This has two purposes. One is to demonstrate the technology to deploy a membrane using a hyper-elastic wire. This will reduce the number of parts in the deployment structure, and we aim to demonstrate safe, low-cost, and short-term satellite production. This purpose will be demonstrated by deploying a membrane stored in a satellite in space using a folding method determined by calculation. The other one is to lower the altitude and de-orbit the satellite by reducing its speed through atmospheric resistance caused by the deployed membrane. The aim is to remove a satellite that has completed its mission from orbit quickly without it becoming debris. This will be demonstrated by deploying the membrane.

The membrane of this satellite is composed of hyper-elastic wire, solar cells, and polyimide film, and is folded by multiple spiral folds. The membrane is connected to the extension mast using a trilane knot, and is stored in the satellite by being pressed down by the top cover. The convex tape connected to the membrane is stored by wrapping it around the axis. Both the convex tape and the top cover are fixed in place by string when stored. The membrane deploys by melting the string that secures the top cover and the convex tape when a command is received. When the string is melted, the convex tape advances first. This force pushes the membrane out, and the membrane unfolds due to the stretching force of the convex tape and the force of the hyper-elastic wire.

2.3 Membrane Deployment Experiment

This chapter shows the actual membrane deployment experiment. First, Figure 4 shows a successful deployment experiment. In this deployment experiment, the string is melted from the state shown in the left figure of Figure 4, the membrane deploys as shown in the center figure of Figure 4, and the convex tape advances as shown in the left figure of Figure 4. Next, Figure 5 shows a failed membrane deployment experiment. In this case, the membrane does not deploy as shown in the left figure of Figure 5, and only the convex tape is extended as shown in the right figure of Figure 5.

As explained in the membrane deployment experiment, there are three possible states for the deployment of the membrane. The first is the state shown in the left figure of Figure 4, where neither the convex tape nor the membrane is deployed. The second is the state shown in the right figure of Figure 5, where only the convex tape is extended, and the membrane is not deployed. The third is the state shown in the right figure of Figure 4, where the convex tape has advanced, and the membrane is also deployed. The purpose of this study is to determine which of these states exists from the difference in rotation in each state.

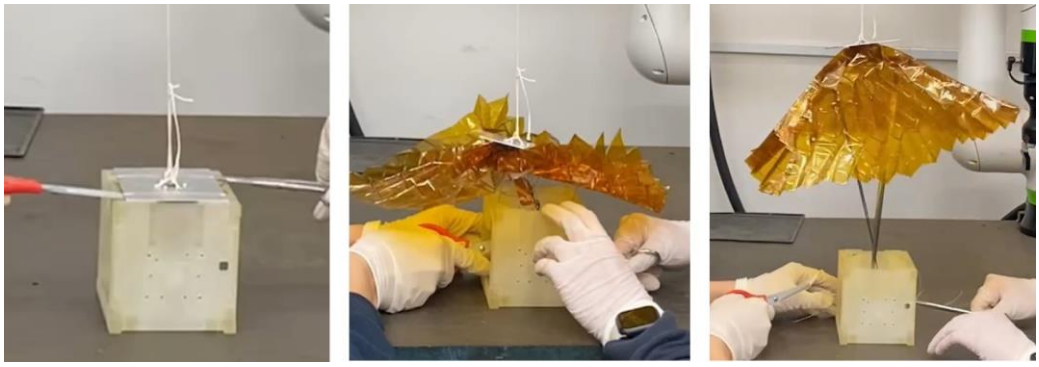


Figure 4 Successful Membrane Deployment Experiment

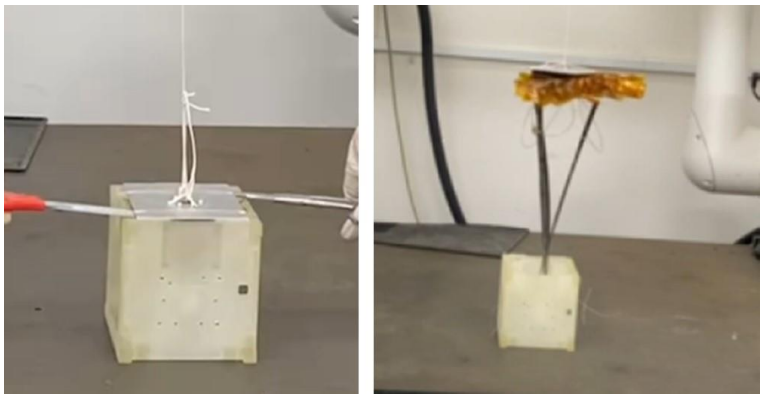


Figure 5 Failure Membrane Deployment Experiment

3. MODELING AND ANALYSIS

Model and analyze the three conditions described in Chapter 2.3

3.1 Before Membrane Deployment

The rotational motion of the satellite before membrane deployment is modeled as shown in Figure 6. The rotational equation of motion can be expressed by the following equation.

$$I_{xx}\dot{\omega_x} + \left(I_{zz} - I_{yy}\right)\omega_y\omega_z = M_{nsx} \quad (1)$$

$$I_{yy}\dot{\omega_y} + (I_{xx} - I_{zz})\omega_z\omega_x = M_{nsy} \quad (2)$$

$$I_{zz}\dot{\omega_z} + \left(I_{yy} - I_{xx}\right)\omega_x\omega_y = M_{nsz} \quad (3)$$

Therefore, the angular acceleration can be expressed by the following equation:

$$\dot{\omega_x} = \frac{M_{nsx} - (I_{zz} - I_{yy})\omega_y\omega_z}{I_{xx}} \quad (4)$$

$$\dot{\omega_y} = \frac{M_{nsy} - (I_{xx} - I_{zz})\omega_z\omega_x}{I_{yy}} \quad (5)$$

$$\dot{\omega_z} = \frac{M_{nsz} - (I_{yy} - I_{xx})\omega_x\omega_y}{I_{zz}} \quad (6)$$

Here, moments related to rotational motion could include forces from the attitude control mechanism, but since Waseda-Sat-Zero-II does not have an attitude control mechanism, these will be ignored in this case. The satellite rotation is analyzed using equation (4), (5), (6). The values of the variables used in the analysis are given in Table 3 and are taken from the Waseda-Sat-Zero-II casing data. Since ω_{x0}, ω_{y0}, and ω_{z0} cannot be determined from the Waseda-Sat-Zero-II information, the angular velocity around the spacecraft axis of the QSAT-EOS [8] satellite, which has already been launched, is used.

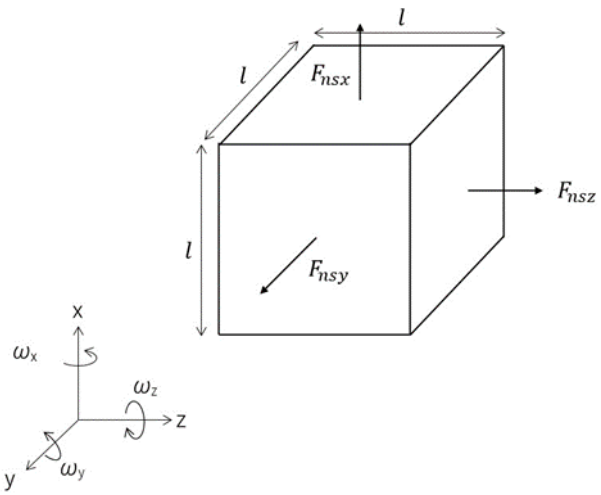


Figure 6 Model Before Membrane Deployment

Table 3 Values to Use in Analysis

Variable name	Values
ρ	1 * 10^{-12} kg/m^3
Cd	2.2
A	l*l m^2
l	0.1 m
I_{xx}	0.001 kg m^2
I_{yy}	0.001 kg m^2
I_{zz}	0.001 kg m^2
ω_{x0}	-0.14 °/s
ω_{y0}	1.09 °/s
ω_{z0}	-2.02 °/s

3.2 After Membrane Deployment

The rotational motion of the satellite after the membrane is deployed is modeled as shown in Figure 7. The rotation is analyzed using the same equations of motion as in Chapter 3.1. The values used in the analysis are shown in Table 4. The mass moment of inertia I_{xx}, I_{yy}, and I_{zz} are calculated as follows, assuming that the satellite is equipped with a membrane surface and top cover with the thickness of the top cover, as shown in Figure 8.

$$I_{xx} = I_{xxsat} + \frac{Mr_p^2}{2} \tag{7}$$

$$I_{yy} = I_{yysat} + M\left(\frac{r_s^2}{4} + \frac{d^2}{12}\right) l_s \tag{8}$$

$$I_{zz} = I_{zzsat} + M\left(\frac{r_s^2}{4} + \frac{d^2}{12}\right) l_s \tag{9}$$

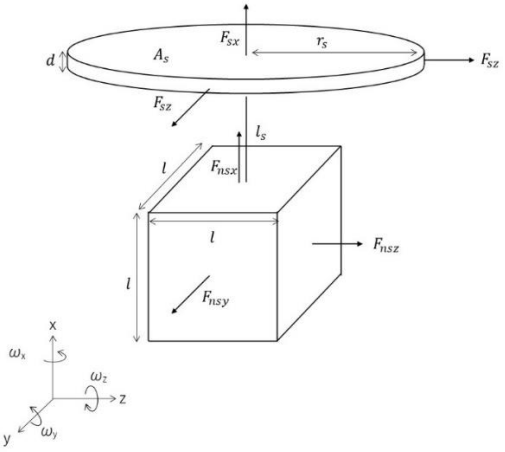


Figure 7 Model After Membrane Deployment

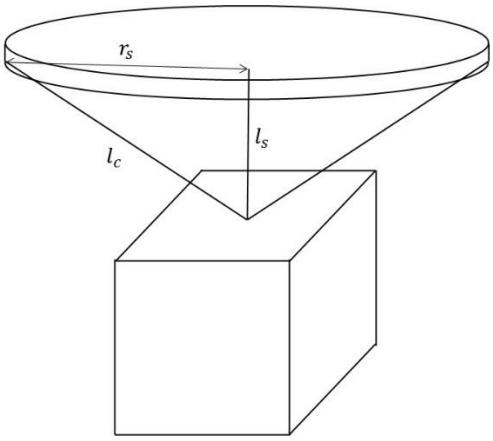


Figure 8 Relationship Between Convex Tape Length And l_s

Table 4 Values To Use In Analysis

Variable name	Values
ρ	$1 * 10^{-12}$ kg/m^3
Cd	2.2
A	l*l m^2
l	0.1 m
I_{xx}	Equation (7)
I_{yy}	Equation (8)
I_{zz}	Equation (9)
ω_{x0}	-0.14 °/s
ω_{y0}	1.09 °/s
ω_{z0}	-2.02 °/s
ls	Figure 8
rs	0.3 m
d	0.001 m

3.3 Extension Of The Convex Tape

The rotational motion of the satellite with only the convex tape extended is modeled as shown in Figure 9. The rotation is analyzed using the same equation of motion as in Chapter 3.1. The values used in the analysis are shown in Table 5. The mass moment of inertia is calculated using the same method as in Chapter 3.2.

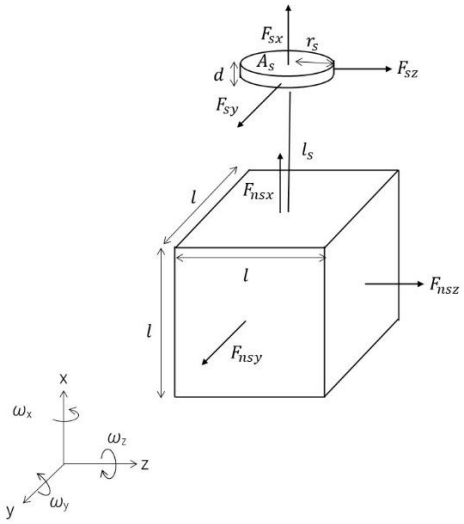


Figure 9 Model Only the Convex Tape is Extended

Table 5 Values to Use in Analysis

Variable name	Values
ρ	$1 * 10^{-12}$ kg/m^3
Cd	2.2
A	l*l m^2
l	0.1 m
I_{xx}	Equation (7)
I_{yy}	Equation (8)
I_{zz}	Equation (9)
ω_{x0}	-0.14 °/s
ω_{y0}	1.09 °/s
ω_{z0}	-2.02 °/s
ls	Figure 8
rs	0.3 m
d	0.001 m

3.4 Result

The rotational changes of the satellite are calculated by numerical analysis using these rotational equations of motion. The numerical analysis was performed using the Runge-Kutta method. The analysis time was set to 90 minutes, which is the period of Waseda-Sat-Zero-II. The analysis span was set to 0.1 s. The analysis results for each axis are shown in Figure 10, 11 12. The analysis results show that the deployment of the membrane causes changes in the satellite's rotation, demonstrating the validity of the proposed method.

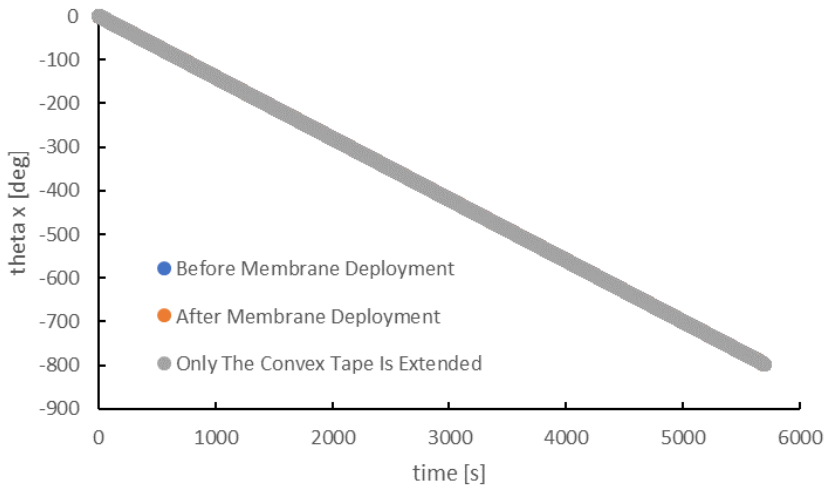


Figure 10 Angle change around the x-axis

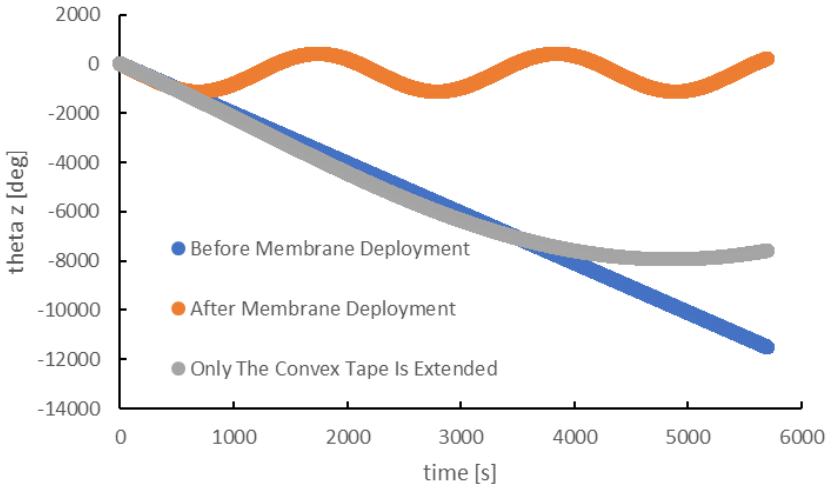


Figure 11 Angle change around the y-axis

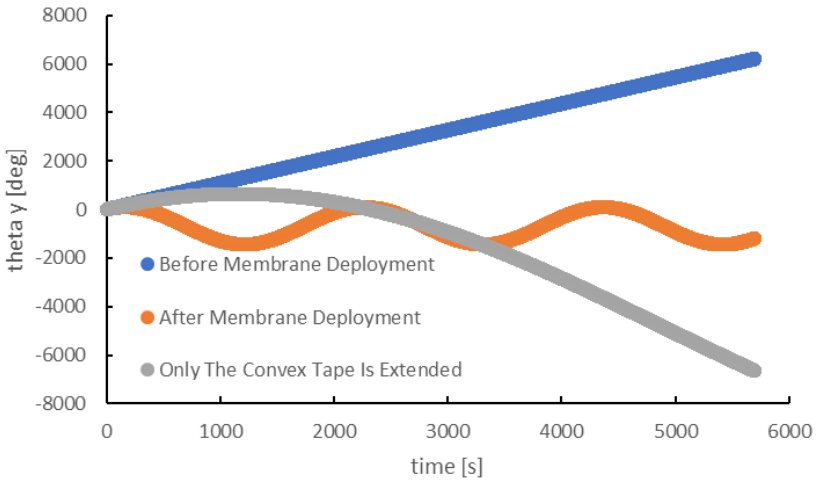


Figure 12 Angle change around the z-axis

3.5 Discussion

The results of this experiment showed that the deployment status of the membrane causes changes in the satellite's rotation. Therefore, it is thought that the deployment status of the membrane can be determined by reading the satellite's rotation using a magnetic sensor. Therefore, using the results of this experiment, we will consider whether it is possible to determine membrane deployment from the values of the magnetic sensor installed on the Waseda-Sat-Zero-II. To take advantage of the advantages of microsatellites, commercially available equipment will be used for the Waseda-Sat-Zero-II. The flash memory used is the SST25VF080B-50-4C-PAE, which has a storage capacity of 8 Mbit. The magnetic sensor used is the HMC5883L, which can measure with an accuracy of 1 to 2 degrees. Since the value read by the sensor is 2 bytes, the number of magnetic data that can be stored on the satellite Waseda-Sat-Zero-II is 500. Taking into account the balance with other data, this time we will consider the optimal interval for collecting data, assuming that 180 data points will be collected per axis.

The data obtained when the data interval for measuring the magnetic data is set to 0.1 s, 0.2 s, 0.5 s, 1 s, and 2 s will be compared for data before the membrane is deployed, after the membrane is deployed, and when only the convex tape is advanced. When the data acquisition, interval is set to 2 s, data can be acquired up to 360 s. The final values of the data obtained will also be compared. Table 6 shows data for the x-axis, Table 7 shows data for the y-axis, and Table 8 shows data for the z-axis. This table shows that by collecting data 180 times at a data acquisition interval of 1 second, a difference of more than 2 degrees, which is the accuracy of the magnetic sensor, is achieved, making it sufficient to determine the deployment of the membrane. This demonstrates the feasibility of the proposed method.

Table 6 Comparing Angles around the x-axis

Data span s	Before Membrane Deployment deg	After Membrane Deployment deg	Only The Convex Tape Is Extended deg
0.1	-2.52	-2.52	-2.52
0.2	-5.04	-5.04	-5.04
0.5	-12.60	-12.60	-12.60
1	-25.20	-25.20	-25.20
2	-50.40	-50.40	-50.40

Table 7 Comparing Angles around the z-axis

Data span s	Before Membrane Deployment deg	After Membrane Deployment deg	Only The Convex Tape Is Extended deg
0.1	19.62	18.64	19.48
0.2	39.24	35.26	38.68
0.5	98.10	72.63	94.59
1	196.20	91.38	182.07
2	392.40	-34.18	335.17

Table 8 Comparing angles around the z-axis

Data span s	Before Membrane Deployment deg	After Membrane Deployment deg	Only The Convex Tape Is Extended deg
0.1	-36.36	-36.87	-36.43
0.2	-72.72	-74.69	-73.02
0.5	-181.80	-192.73	-183.64
1	-363.60	-397.84	-370.77
2	-727.20	-786.29	-754.40

4. CONCLUSION

This research proposed a method to determine the deployment of the membrane used for deorbiting from the rotation of the satellite.

The social background is that the intensification of the development of small satellites has led to an increase in debris, which has made it necessary to install a membrane for deorbiting on satellites, and to confirm the deployment of the membrane. The conventional method was to check using public orbit information. However, this method had issues with the time required for confirmation. Therefore, this study focused on the rotation of the satellite and aimed to propose a method to check the deployment of the membrane from the change in rotation before and after the deployment of the membrane.

To demonstrate the validity of the proposed method, we first calculated the force applied to the satellite and derived the equation of motion. We then provided information necessary for numerical analysis of the satellite used in the demonstration. A numerical analysis was performed using this information and the derived equation of motion. The analysis was performed on three types of models: a model before the membrane was deployed, a model with only the convex tape extended, and a model with the convex tape advanced and the membrane deployed.

The results of the numerical analysis showed that there was a change in rotation in the three assumed types of models, demonstrating the validity of the method proposed in this research. In addition, the data acquisition interval for the magnetic sensor used on the satellite and the sensor suitable for flash memory were determined to be 1 second, and the number of acquired data items was determined to be 180. This demonstrated the feasibility of the research.

REFERENCES

1. **Inter-Agency Debris Coordination Committee (2007)**, “IADC Space Debris Mitigation Guidelines”, in IADC-02-01.

2. **Chiara Palla, Jenny Kingston, and Stephen Hobbs (2017)**, “DEVELOPMENT OF COMMERCIAL DRAG-AUGMENTATION SYSTEMS FOR SMALL SATELLITES”, Proc. 7th European Conference on Space Debris, Darmstadt, Germany.

3. **Palla, C., Kingston, J. (2016),** “Forecast analysis on satellites that need de-orbit technologies: future scenarios for passive de-orbit devices”. CEAS Space J 8, 191–200.

4. **Stankey, H. C. and Hoyt, R. P. (2021),** “In-Flight Performance of the Terminator Tape End-of-Life Deorbit Module,” 35th Annual Small Satellite Conference, Logan Utah.

5. **G. Bonin, Hiemstra, T. Sears and R. Zee (2013)**, “The CanX-7 Drag Sail Demonstration Mission: Enabling Environmental Stewardship for Nano- and Microsatellites”, Proceedings of the 27th Annual AIAA/USU Conference on Small Satellites, Logan.

6. **B. Cotton, I. Bennett, R. Zee (2017),** " On-Orbit Results from the CanX-7 Drag Sail Deorbit Mission.", 31st Annual AIAA/USU Conference on Small Satellites, Logan, Utah.

7. **Alperen PALA, Toshinori KUWAHARA, Takumi SAITOU, Hiroki UTO, Yoshihiko SHIBUYA (2022),** “Space Demonstration of Boom Extension and De-orbit Sail Deployment of the Separable De-orbit Mechanism of Micro-satellite ALE-1”, Trans. JSASS Aerospace Tech. Japan, Vol. 20, pp. 65-72.

8. **Masayuki KATAYAMA, Shinji HOKAMOTO, Shigeru ASO and Hiroshi HIRAYAMA (2020)**,” Study on Deorbit of a Microsatellite Considering the Solar Activity Effect on Atmospheric Density”, AEROSPACE TECHNOLOGY JAPAN, THE JAPAN SOCIETY FOR AERONAUTICAL AND SPACE SCIENCES, pp.47-55.

NUMERICAL APPROACH OF TIMEAXIS DESIGN METHOD - VALIDATION THROUGH AN APPLICATION FOR CHAIR DESIGN

Akinari HIRAO, *hirao@shibaura-it.ac.jp* Shibaura Institute of Technology, 135-8548, Tokyo, Japan

Takeo Kato, *kato@mech.keio.c.jp* Keio University, 223-8522, Yokohama, Japan

Yoshiyuki Matsuoka, *matsuoka@mech.keio.c.jp* Keio University, 223-8522, Yokohama, Japan

ABSTRACT

Timeaxis design is a design theory that deals with time axis and enables sustainable design by responding to changes in the required characteristics of products as they are used over time. The authors have developed a Timeaxis design method that considers a multi-time-scale model. This method is applied to actual product design considering a time axis by defining elements based on value changes along a time axis based on a multi-space design model, defining each relationship as a mapping function between spaces, and solving it by multi-objective optimization. In this study, an overview of the method is presented, and the effectiveness of the method is verified by applying it to the design of a chair that can be used over a long period of time as a child grows up, as an example of time-axis design.

Keywords: Timeaxis design, Multispace design model, Chair design

1. INTRODUCTION

In modern society, the cycle of mass production and consumption has been conducted based on the pursuit of productivity and cost reduction. To realize such manufacturing, it is important to respond to changes in the required characteristics (target characteristics) of artifacts as they change with time. For this reason, timeaxis design [Matsuoka, 2012], a design theory and methodology that deals with time axis, has been attracting attention.

One of the fundamental theories in timeaxis design is the multi-timescale model [Matsuoka, 2018]. This model integrates models of different time systems, such as the short time-scale model, the medium time-scale model, and the long time-scale model, as shown in Figure 1.

By representing time-varying design elements (all matters to be considered in the design in question) and the relationships among elements as a multi-timescale model, it is possible to design according to the time-varying target characteristics for the artifacts described above. For example, it is possible to derive appropriate design solutions for design problems with a trade-off relationship between the target characteristics of different artifacts at different timescales (“multi-timescale problems”).

The authors proposed a numerical solution method for time-axis design considering multi-time scales by applying a multi-space design model [Matsuoka, 2012] and a multi-objective optimization method to handle trade-off problems [Hirao et al., 2019].

In this study, the numerical approach for timeaxis design is introduced, and the effectiveness of the method is verified by applying it to the design of a chair that can be used over a long period as the child grows.

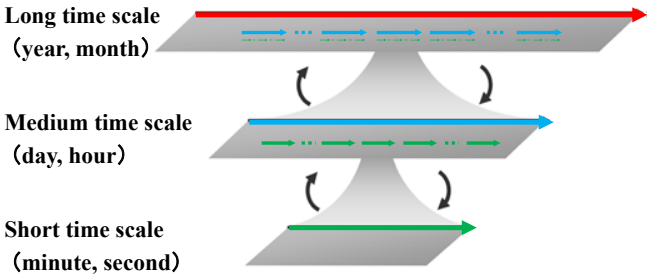


Figure 1. Multi-time scale model.

2. OVERVIEW OF NUMERICAL APPROACH OF TIMEAXIS DESIGN METHOD

1. **Multispace Design Model:** In this method, a multispace design model is applied as a framework for comprehensively expressing design elements. The multispace design model is a design theory proposed by Matsuoka [Matsuoka, 2010]. As shown in Figure 2, it consists of design elements including the design object, a thinking space that expresses design thinking to manipulate the elements, and a knowledge space that is the source of the thinking. The following is an overview of each space.

Thinking space consists of psychological space and physical space. The psychological space consists of the value space and the meaning space, and the physical space consists of the state space and the attribute space. Each of these four spaces will be explained.

Value space: This space expresses elements that express value from various perspectives, such as cultural value and inductive value, and the relationship between them.

Meaning space: This space expresses elements that express the functionality and image of the design object and the relationship between them.

State space: This space represents a field, which is a set of elements that express the environment, and conditions related to the time and space where the design object is placed, and elements that express the physical characteristics that are expressed when the design object is placed in a certain field and the relationship between them.

Attribute space: Elements expressing geometric and physical characteristics of the design object, such as dimensions and materials, as shown in the drawing, and the relationship between them.

This method comprehensively extracts target characteristic systems and their factor systems in multi-timescale problems by organizing psychological elements, which are the required characteristics of each timescale, as design goals and physical elements related to them as design variables.

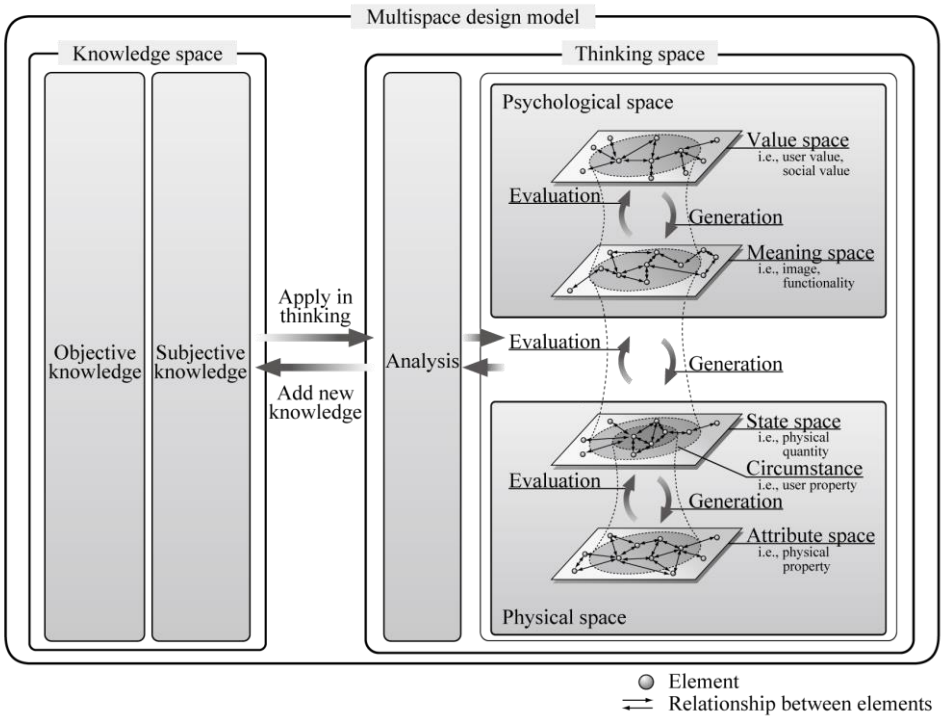


Figure 2. Multispace design model.

2. **Numerical Solution by Multi-objective Optimization:** A multi-objective optimization method is a method for deriving a feasible solution to a vector minimization problem with multiple objective functions in a trade-off relationship, where one objective function cannot be improved without modifying the other objective functions.

The multi-timescale model in Figure 1 shows that the short and medium timescales are part of the medium and long timescales, respectively, and that the short scale occurs repeatedly in

the long scale. To simultaneously evaluate target characteristics on multi-time scales, the method introduces time as a variable to evaluate multiple objective functions on the same time scale in a multi-objective optimization formulation.

In the next step, formulate the problem as a design problem by introducing the concept of four spaces in the multi-space design model to the multi-objective optimization problem that introduces the concept of the time-axis.

The value element is designated as $\boldsymbol{v}(t)$, the meaning element as $\boldsymbol{m}(t)$, the state element as $\boldsymbol{s}(t)$, the circumstance element as $\boldsymbol{c}(t)$, and the attribute element (as a design variable) as $\boldsymbol{a}(t)$ for the time-varying case, and $\boldsymbol{a}$ for the time-invariant case. Since there may be multiple design elements in each space, they are represented as vectors. The mapping function between each space is denoted by $\boldsymbol{f_{m\to v}(m,t)}$, $\boldsymbol{f_{s\to m}(s,t)}$, $\boldsymbol{f_{a,c\to s}(a,c,t)}$, and the relationship between these functions is shown in Figure 3.

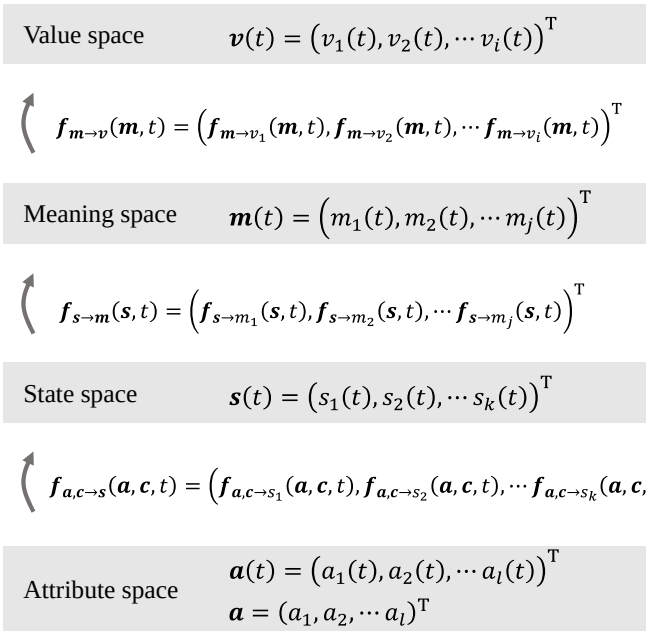


Figure 3. Conceptual drawing of reasoning between design elements in multi-time scale problem.

The figure shows that these functions represent the mapping from bottom to top (i.e., design evaluation) in the multi-space design model, from attributes to values. Once these functions are defined, we can derive the meaning elements to optimize the value elements, and then derive the state elements and attribute elements, in that order, to obtain the final design solution.

In this case, the meaning elements that optimize the value elements can be expressed as in Equation (1).

$$\begin{aligned}&\text{Find } \boldsymbol{m}(t)\\&\text{to minimize } \boldsymbol{v}(t) = \boldsymbol{f}_{\boldsymbol{m}\to v}(\boldsymbol{m}, t)\\&= \begin{Bmatrix} \boldsymbol{f}_{m\to v_1}(\boldsymbol{m}, t_{v_1}) w_{v_1}(t), & \boldsymbol{f}_{m\to v_2}(\boldsymbol{m}, t_{v_2}) w_{v_2}(t), \\ \cdots, & \boldsymbol{f}_{m\to v_0}(\boldsymbol{m}, t_{v_0}) w_{v_0}(t) \end{Bmatrix}\end{aligned} \tag{1}$$

Where t_{v_i} in Equation (1) represents the time parameter of the timescale for the *i*-th value design element. $w_{v_i}(t)$ represents the weight function for the *i*-th value design element.

Next, by successively substituting the meaning element $\boldsymbol{m}(t)$ in Equation (1) with the mapping functions between the spaces shown in Figure 3, i.e., the mapping function between the meaning space and the state space, and the mapping function between the state space and the attribute space and field, the semantic element that optimizes the value element can be expressed as in Equation (2) with the attribute and circumstance elements.

$$\begin{aligned}&\text{Find } \boldsymbol{a}(t)\\&\text{to minimize}\\&\boldsymbol{v}(\boldsymbol{t}) = \boldsymbol{f}_{\boldsymbol{m}\to v}\left(\boldsymbol{f}_{\boldsymbol{s}\to \boldsymbol{m}}\left(\boldsymbol{f}_{\boldsymbol{a}\to \boldsymbol{s}}(\boldsymbol{a}, t)\right)\right)\end{aligned} \tag{2}$$

This is thought to make it possible to view optimization problems that span multi-spaces, such as the case of deriving attribute elements that optimize the required meaning elements, as a single optimization problem, and to perform design (mapping from physical space to psychological space).

3. **Numerical Solution by Multi-objective Optimization:** The procedure (flowchart) for solving the multi-time scale problem formulated in the previous section is shown in Figure 4.

First, based on the concept of the multi-space design model, the necessary design elements are clarified.

Next, among these design elements, target characteristics and design variables are determined.

Then, an objective function that expresses the relationship between design goals, design variables, and time parameters is derived using a physical model and experimental data. If the physical model or experimental data used as a reference does not include a time parameter, it is necessary to set a weight function that defines the relationship between the objective function, the time parameter objective function, and the time parameter. For example, if the target characteristic is a characteristic such as human sensitivity, then a weight function should be set such as the change in (human) sensitivity on the timescale of the target characteristic.

Furthermore, to handle multiple objective functions, the time parameters of each objective function's timescale are aligned, and multi-objective optimization is performed to obtain a design solution.

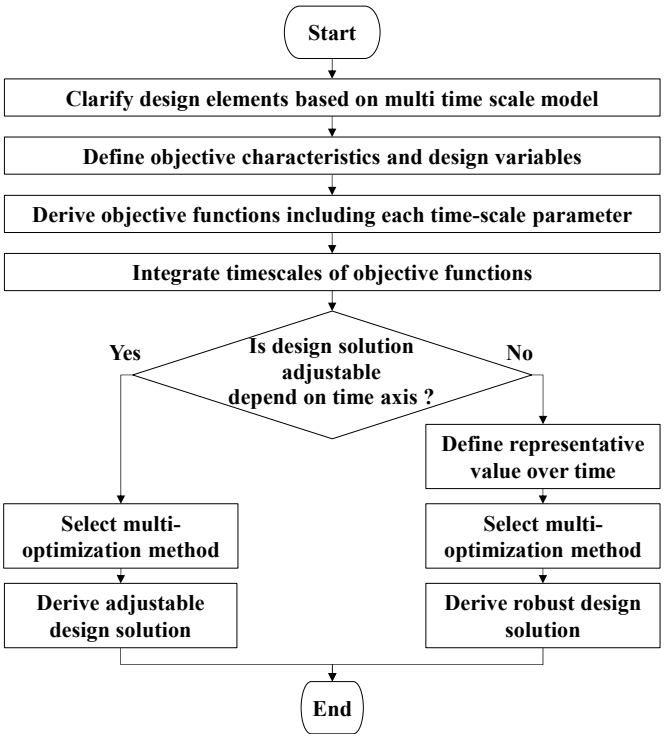


Figure 4. Flowchart of proposed timeaxis design method.

3. OVERVIEW OF NUMERICAL APPROACH OF TIMEAXIS DESIGN METHOD

Many infant chairs are designed to change the height of the seat and footrest to accommodate the changing physique of the child as the child grows. One of the most famous chairs is the "Tripp Trapp "designed by Peter Opsvik, shown in Figure 5. The design concept of this chair is intended for use by adults as well [Opsvik, 2009].

The chair is a design validation of ergonomic aspects and attachment regarding adaptation with growth [Salvador, 2014], [Salvador et al. 2014], [Salvador, 2018], [Salvador, 2018], and can be said to be a design case of timeaxis design concept.

This study attempts to validate the method by applying the numerical solution method for timeaxis design described in the previous chapter to ”Tripp Trapp” design.



Figure 5. “Tripp Trapp” Chair.

1. **Construction of the Elements Inter-relationship Diagram:** The elements inter-relationship diagram for infant chairs was created as shown in Figure 6.

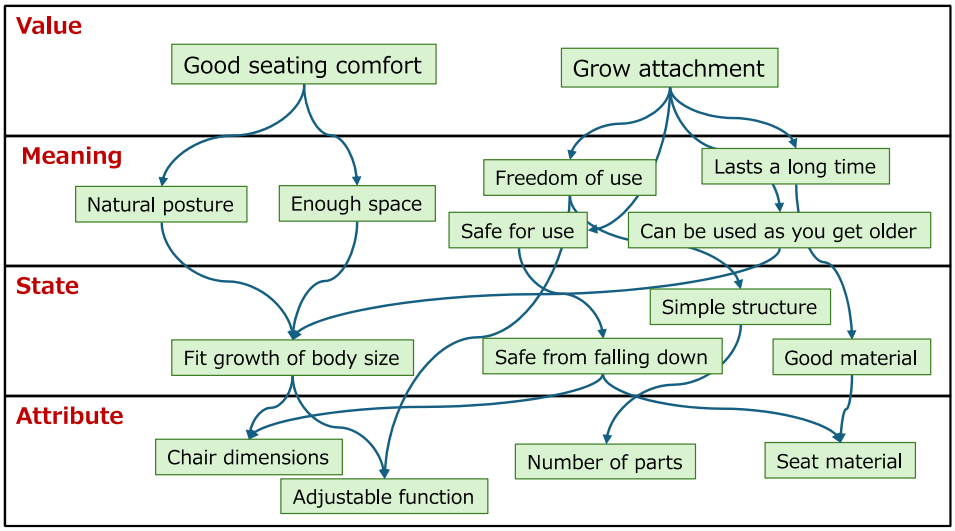


Figure 6. The elements inter-relationship diagram for infant chairs.

In addition to comfort as a basic function of the chair, the value elements include fostering attachment through long-term use, which is an element of time-axis design.

The semantic elements include the basic elements of seating comfort, such as sitting comfortably and fitting the body, while the attachment element assumes that the chair can accommodate changes in body dimensions due to growth, as a condition for long-term use.

In the above-mentioned numerical solution method for timeaxis design, each element is formulated as a mapping function based on subjective evaluation results, etc., and solved analytically. However, in this validation, since there is no data to formulate a mapping function between spaces, the mapping function in physical space and making it an optimization problem were used.

2. **Problem definition:** The “TrippTrapp” chair shown in Figure 5 has a simple chair structure consisting of two wedge-shaped side frames sandwiched between two boards (seat and footrest) whose height and front-back position can be changed. Therefore, the width direction, which is the distance between the side frames, is unified as one.

Schematically speaking, the design can be made by determining the dimensions in a two-dimensional sagittal plane as shown in Figure 7.

Therefore, the following design variables were used in this study.

- Depth of the seat and footrest.
- Number and pitch of fixing grooves for the seat and footrest.

- Diagonal angle of the side frames.

- Length of the legs.

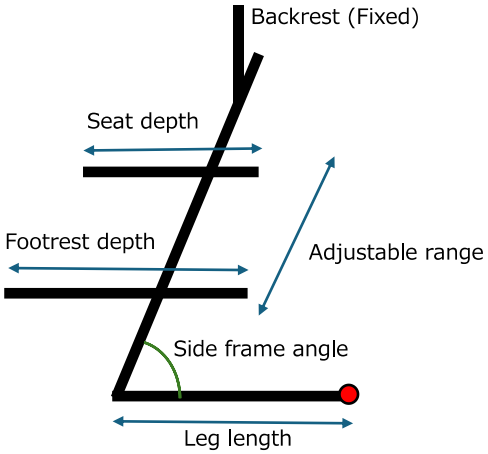


Figure 7. Schematic structure of the chair.

3. **Problem definition:** In this section, the design variables presented in the previous section are determined using various findings corresponding to the mapping function.

In previous studies, there are no examples of research on chair seating comfort for infants.

Therefore, in this study, we assume that the findings obtained in studies with adults can be used regardless of the age of the subjects.

The standard height of the table used with the chairs is 700 mm.

1. Seating comfort elements:

- Body dimension

The change in body size with growth has a significant effect on sitting comfort. For this reason, regression equations of body size on age or body height were developed using published anthropometric body size data [MHLW, 2001] [MEXT, 2022] [Kouchi and Mochimaru, 2005] [HQL, 2008], and used in the following calculations. The details of the regression equations are omitted due to space limitations of this proceedings.

In this study, the design is intended for children from one-year-olds who can sit up by themselves to 17 years olds who have grown almost as tall as adults.

- Width of seat and footrest (inside dimensions of side frames)

In the width direction, the chair structure is unified by one dimension, but it is necessary to cover the maximum value of the target seated person. Therefore, the maximum width of the buttocks of a 17-year-old in the sitting position is 401 mm, so the width should be 420 mm to

allow room for clothing. In this study, the design is intended for children from one-year-olds who can sit up by themselves to 17 years olds who have grown almost as tall as adults.

- Seat height

The “Sashaku” concept has been proposed as a guideline for determining the optimal seat height [Noro, 1994]. This is defined by the following equation.

$$Seat\ height = Table\ height - \frac{0.55 \times body\ height}{3} \quad (3)$$

Using this concept, the seat height for a one-year-old girl with the smallest body size is 687 mm. This is the highest seat position.

Next, the maximum body size for which a footrest is used is determined.

Since a footrest is not necessary when a person's feet reach the floor when seated, the seat height is smaller than the height difference between the knees and the soles of the feet when a comfortable seat height is set using the differential scale. This was obtained by creating a regression equation based on the height on the difference scale and the knee-to-floor height and found to be the case for a body height of 1277 mm or taller. This is equivalent to an age of 8 years, which means that a footrest is not necessary for children over 8 years of age. Therefore, if a footrest is used until the child is 7, the seat height is 475mm based on the same differential scale formula.

Therefore, the seat height should be able to be changed within the range of 475 to 687 mm.

In this case, considering that the seat height can be changed from 1 to 7 years of age, 14 steps would be necessary if it is changed every half a year.

However, dividing the seat height range into 14 steps would result in a pitch of about 15 mm, which is too small considering that the thickness of the board is 10 mm. Therefore, it would be appropriate from a design standpoint to provide adjustment from the upper side at a pitch of 20 mm or more, which is about twice as high, and to provide the lowest step at a lower level that is not assumed to be used as a footrest.

- Seat and footrest depth

The "Tripp Trapp" chair has two boards positioned in the depth direction to adjust the depth of the seat and footrest.

In this study, the shorter board is defined as the seat, and the longer board is the footrest. Naturally, as the body size increases, the longer board becomes the seat, and when the footstool is not used, it can be placed on the backside.

The dimensions of the longer board should be such that the legs can be accommodated when used as a footrest, while the shorter board should be comfortable for a larger stature.

Footrest depth: When seated, if the legs cannot reach the seat and the user hangs down, the thighs are compressed at the end of the seat surface, inhibiting blood flow and causing discomfort. Therefore, the depth of the footrest should be at least longer than the foot size (foot length). In the previous section, we defined the maximum size for using a footrest for a 7-year-old child. A 7-year-old boy's foot length is 193mm, so about 200mm is necessary.

Seat depth: Takamatsu et al. analyzed the mechanism for determining the comfortable seat length and found that 75% of the thigh length is the appropriate seat tip position for seating [Takamatsu et al.] Adding the seated hall and tumescent distance to 75% of the thigh length for a 17-year-old, which is the maximum body size for seating, yields 435 mm.

2. Safety related elements:

The chair should not fall over and collapse when the user is seated in the chair.

Therefore, in this study, the value is maximized when the moment around the rear end of the legs of the chair while seated is positive and maximal.

3. Attachment related elements:

In this study, as an element of timeaxis design, it is assumed that a child's chair can be used as he or she grows older, thereby fostering attachment to the chair. In other words, the value of the chair as defined above should be maximized even if the body dimensions change as the child grows.

4. **Multi-objective optimization:** In the previous section, the design variables have been determined based on the elemental relationship diagram created in Figure 6, based on the knowledge of each element. Many of the variables were determined without solving a multi-objective optimization problem because they could be determined by the dimensions of the largest or smallest body size.

The variables that have not been determined so far are the angle of the side frames and the length of the legs. These two variables are to be solved in a multi-objective optimization problem to maximize their value concerning safety and attachment.

The objective function is to maximize the moment around the back end of the chair leg while seated, a measure of safety-related tipping, at all ages.

The constraint in the optimization is that the moment be positive at all ages.

In calculating the moments, the body weight at each age was a load, and the chair's weight was calculated from the dimensions of the parts using the specific gravity of the wood (0.56 g/cm^3).

4. RESULTS AND DISCUSSION

Table 1 shows the values of the design variables for the children's chairs obtained in this study and the “Tripp Trapp” chair.

Table 1. Comparison of the design variables.

Design valuables	Unit	This method	Tripp Trapp
Seat width	mm	420	420
Seat depth	mm	435	375
Footrest depth	mm	200	230
Seat adjustment range	mm	475~687	125~615
Seat adjustment pitch	mm	Over 20	35
Number of adujustment	Notch	14	14
Side frame angle	degree	52.1	58
Leg length	mm	500	470

The values for seat width were the same. The seat depths differed by 60 mm. This difference may be due to the difference in the degree of coverage for the seat length of large-size persons. The “Tripp Trapp” chair has a shorter seat depth than this study, designed to cover a 17-year-old person of the same size. The footrest depth was 7 mm, which is a larger margin than that in the present study.

The adjustment range of the seat height is much wider, but this is due to the difference in how much the mounting groove is placed below the lower limit of the required dimension, and the range is almost the same. Although the number of adjustment steps is the same, the pitch reflects the difference in the range described above, resulting in the different values.

Finally, the two indices determined by the multi-objective optimization were almost equivalent.

In summary, the design variables determined by this method can be considered almost equivalent to the Opsvik design values. In other words, although the timeaxis design method was not used, it was considered a design concept, and it can be inferred that the design values were determined by Opsvik's skill. In other words, it can be considered that the timeaxis design can be performed analytically by using this method.

In this study, the design was conducted for the target age group up to 17 years old, but the dimensions could be different if the target physique coverage range is changed, and the age

group is made younger. It is also possible to obtain different solutions by changing the weights of the objective function in multi-objective optimization.

In this study, we used Japanese physique statistics, but the “Tripp Trapp” chair designed in Norway as a product is sold globally, and physique statistics for each country should be used. Therefore, it can be inferred that the results may differ when assuming countries with different average body sizes. However, considering the growth process, the dimensions would be different if the age corresponding to attachment is changed, i.e., Japanese 17 years old, which was assumed to be the maximum body size in this study, because it corresponds to the different ages at which the same height is reached. However, this is not a problem for the main target age of the chair, which is the period of growth of body size. This is supported by the fact that the same specifications are sold globally.

5. CONCLUSION

In this study, the concept and numerical solution of timeaxis design considering multi-time scale problems are outlined, and the method is verified on the subject of a child's chair that can be used continuously as the child grows up.

As a result, we were able to obtain a design solution that is almost equivalent to the design of the “Tripp Trapp” chair, which is well known as a long-selling children's chair, and the method was verified.

In the future, we would like to apply the method to other design problems to further validate and establish the method.

ACKNOWLEDGEMENTS

The authors thank Mr. Tasuku Kagami, Mr. Yuto Tanida, Mr. Yuto Ieda, Mr. Tsuyoshi Shikida for contributions of making the elements inter-relationship diagram with discussions in our seminar class of Graduate School of Science and Technology, Keio University.

REFERENCES

1. **Matsuoka, Y. (2012),** "Dawn of Timeaxis Design”, Maruzen Publishing Co., Ltd. , pp.95-104 (In Japanese).

2. **Matsuoka, Y. (2018),** "Timeaxis Design for Product Creation x Product Usage", Journal of Japan Society for Design Engineering, Vol.53, No.2, pp.129-133 (In Japanese).

3. **Matsuoka, Y. (2012),** "Multispace Design Model Towards Integration between Industrial Design and Engineering Design", Proceedings of Design Research Society 2012, pp.1158-1164.

4. **Hirao, A., Kato, T. and Matsuoka, Y. (2019),** "Timeaxis Design Method for multi-time scale problem", Proceedings of Design Symposium 2019, pp.238-241 (In Japanese).

5. **Matsuoka, Y. (2010),** "Design Science", Maruzen Publishing Co., Ltd.

6. **Opsvik, P. (2009),** "Rethinking Sitting", W.W. Norton, New York.

7. **Salvador, C. (2014),** "Apart from traditional design approaches: Peter Opsvik's path", Proceedings of 9th International Committee Design History and Design Studies, pp.681-686.

8. **Salvador, C., Vincente, J. and Martins, J. P. (2014)**, "Ergonomics in Children's Furniture - Emotional Attachment", Proceedings of 5th International Conference on Applied Human Factors and Ergonomics AHFE 2014, pp.5478-5485.

9. **Salvador, C. (2018),** "Ergonomics in the Design Process - Study of Adaptability of Evolutive High Chairs", Advances in Ergonomics Design, pp.773-779.

10. **Salvador, C. (2018),** "Adapting Furniture to the Child - Ergonomics as a Main Tool in a Design Project", Proceedings of IEA 2018, 1294-1305.

11. **Ministry of Health, Labour and Welfare (MHLW), Japan, (2001),** "Report of the Physical Growth Survey of Infants and Toddlers", https://www.mhlw.go.jp/houdou/0110/h1024-4c.html#hyo1-4.

12. **Ministry of Education, Culture, Sports, Science and Technology (MEXT), Japan, (2022),** "School Health Statistics Survey", https://www.e-stat.go.jp/stat-search/files?page=1&layout=datalist&toukei=00400002&tstat=000001011648&cycle=0&tclass1=000001211780&tclass2=000001211781&tclass3val=0.

13. **Kouchi, M. and Mochimaru, M., (2005),** "AIST Anthropometric Database", National Institute of Advanced Industrial Science and Technology, H16PRO 287.

14. **Research Institute of Human Engineering for Quality of Life (HQL), Japan, (2008),** "Database of Children's Body Dimensions", https://www.hql.jp/database/cat/size/children.

15. **Takamatsu, A., Yoshizawa, N., Egami, M. and Hirao, A. (2013),** "Analysis of Seat Cushion Characteristics for Adjusting Wide Range of Occupants' Physique", Proceedings of Japanese Society of Automotive Engineers, No.105-13, pp.1-6.

MULTILINGUAL COMMUNICATION ROBOT USING LANGUAGE DETECTION SYSTEM

Kei MATSUOKA, *matsuoka.kei@kagawa-u.ac.jp* Kagawa University, 760-8521, Takamatsu, Japan

Yuki KIDA, *ykida@keio.jp* Keio University, 223-8526, Yokohama, Japan

Takeo KATO, *kato@mech.keio.ac.jp* Keio University, 223-8522, Yokohama, Japan

Tetsuro OGI, *ogi@sdm.keio.ac.jp* Keio University, 223-8526, Yokohama, Japan

ABSTRACT

In a conventional multilingual information system, the user must actively choose the language. Therefore, in this study, a multilingual communication robot system that realizes natural communication using multiple languages for various foreign visitors was developed. In this system, when a user approaches a guide robot, the language used in the user's smartphone is automatically acquired using iBeacon, and the robot can talk to the user using the user's language. Using this method in this study, the guide robot was able to spontaneously guide the user in the language used by the user.

Keywords: Communication Robot, Multilingual Communication, Language Detection System

1. INTRODUCTION

In recent years, there has been a growing anticipation of an increase in foreign visitors, driven in part by the resurgence of travel following the decline of the COVID-19 pandemic. However, the hospitality industry is currently ill-prepared to offer seamless multilingual services to these international guests due to a shortage of personnel proficient in diverse languages. This situation has hindered the smooth provision of guidance and information crucial for enhancing visitor experiences.

Simultaneously, advancements in AI technology have paved the way for practical applications in natural language communication through IT devices, hinting at a potential solution. The development of guide robots and digital signage holds promise in realizing multilingual services; however, existing implementations have not seamlessly integrated into real-life

scenarios. One prominent issue is the reliance on users to initiate interactions with these systems, which often requires them to manually select their preferred language, posing a significant cognitive barrier.

The primary objective of this research is to bridge this gap by developing a system capable of facilitating multilingual communication between foreign visitors and humanoid guide robots. Unlike existing setups where users must initiate language selection, the proposed system automates this process based on the user's first language, streamlining the interaction. In addition, these research endeavors to establish a robust system architecture that autonomously triggers guidance, paving the way for smoother user experiences.

This research builds upon prior studies in communication robotics [1-9] and multilingual systems [10-14], recognizing the effectiveness of robots in guiding foreign visitors and the problem of current digital signage-based solutions. By integrating language detection capabilities into guide robots, facilitated through beacon technology and smartphone applications, the envisioned "multilingual communication robot system" aims to revolutionize visitor experiences in locations such as airports, hotels, and shopping malls. Through sensory evaluation experiments, the efficacy and user satisfaction of this system will be assessed, contributing to the advancement of multilingual service offerings in the hospitality sector.

3. METHOD

This chapter describes the multilingual communication robot system to be developed. In this system, the "guide robot" recognizes the language to communicate from the user's smartphone and provides guidance by using user's language. The following components were used in the system.

1) Pepper, a humanoid robot made by Softbank Robotics;

2) Aplix MyBeacon, MyBeacon® Pro MB004Ac (-12dBm);

3) Apple iPhone.

Overall System Configuration

In this research, three subsystems consisting of "multilingual control server", "smartphone application" and "guide robot" shown in Figure 1, are linked to each other.

First, the language data and the individual identification of the smartphone, namely the Unique Device Identifier (UDID) received from the "smartphone application" (described later), are recorded as text data in the "multilingual control server" via a PHP program. The stored information is then read by a system (described later) mounted on the "guide robot", and the

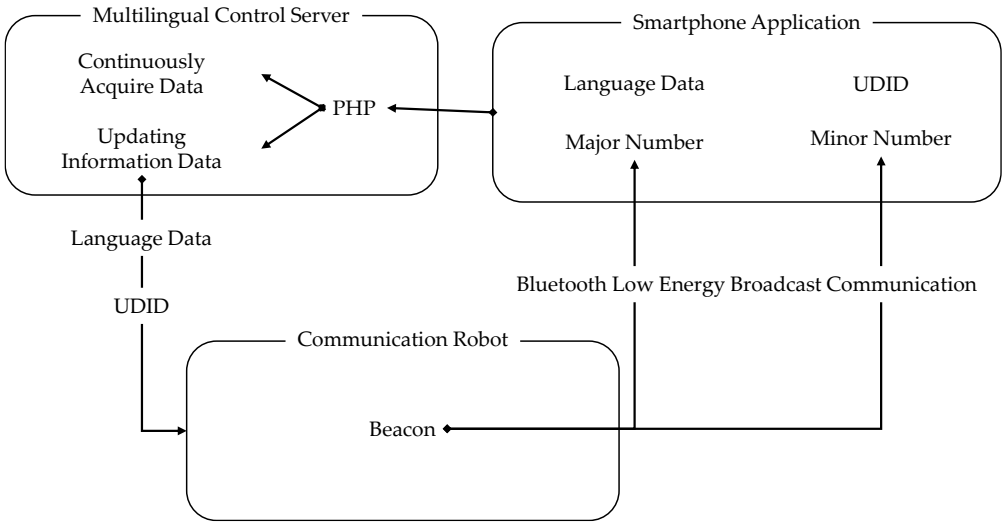


Figure 1. Overall System Configuration

information is divided according to its category to perform language recognition.

Next, the “smartphone application” transmits the language data and UDID of the smartphone to the aforementioned “multilingual control server” through background processing when it receives the signal of Bluetooth low-energy broadcast communication, namely iBeacon. By installing the beacon on the “guide robot”, the robot can automatically and smoothly recognize the user’s language by accessing “multilingual control server” when the user approaches.

Finally, a humanoid robot Pepper (SoftBank robotics) was adopted as the “guide robot”. Pepper is equipped with sensors on the head, chest, hands, and legs, enabling various movements with 20 motors. This system uses a stereo camera (RGB camera) built into Pepper’s head to perform face tracking (described later) to recognize the user. The language data and UDID are obtained from the “multilingual control server” and automatically switches the language to communicate.

Multilingual Control Server

The “multilingual control server” plays an important role in connecting the “smartphone application” and the “guide robot”. As the information to be acquired, “major number”, “minor number”, “UDID”, and “language data” are recorded. Using the extracted data, system health can be confirmed by checking whether the system is operating properly or not. Here, “UDID” can identify the user, and “language data” can understand the language used by the identified user. This information is sent to the database server as a single line of character string information via PHP and is saved as two separate files: one for collecting all logs and the other

for enabling the robot to obtain the required data. The former is set to continuously acquire data, enabling us to manage various user attributes. The latter is set to repeat overwriting and updating information, enabling the robot to prevent continuous guidance from the same person.

Smartphone Application

For the “smartphone application”, iPhone was adopted to use iBeacon, a beacon-compatible system that can perform background processing. The advantage of this application is that the user does not need to touch the app except for setting the location information and notification function to always on. In addition, by bringing the smartphone toward the “guide robot” in which the beacon is installed, the smartphone receives the signal from the beacon and sends the data of “language data” and “UDID” to the “multilingual control server”. When the user approaches the detection area of the “guide robot”, the robot acquires “language data” and “UDID” from the “multilingual control server” and begins the guidance. The detection area of the robot is placed inside the detection area of the beacon.

With these functions, the user only needs to perform the initial setting of the location information and the notification function. Hence, it is expected to reduce the burden and simplify guidance usability.

Guide Robot

In the “guide robot”, the function that performs the processes of providing guidance with smooth language switching (Figure 2) was implemented using Choregraphe. Choregraphe is a GUI-based development environment and visual programing language customized for Pepper that allows developers to develop applications without the need for knowledge of classical programing languages. The details of each process are described below:

Process 1: In the “storage variable setting,” variable items, generally called global variables, are installed. The “guide robot” Pepper has a memory area called ALMemory, which mainly stores data obtained from the sensors. By adding an optional memory, it is possible to create a data storage area that can be treated as a global variable. In this system, a memory area for storing “language data” and “UDID” is created.

Process 2: “Face tracking” has the function of the “guide robot” Pepper tracks the approaching user’s face from the RGB camera on the head. By initializing the camera, the face can be tracked at the same time as the system operation. In addition, the approach of the user is recorded in ALMemory, and with this as a trigger, the system activates “getting server information” and “wait processing” described later.

Process 3: In the “getting server information” step, the information in the “multilingual control server” is accessed, and all the character string information, including the four types of

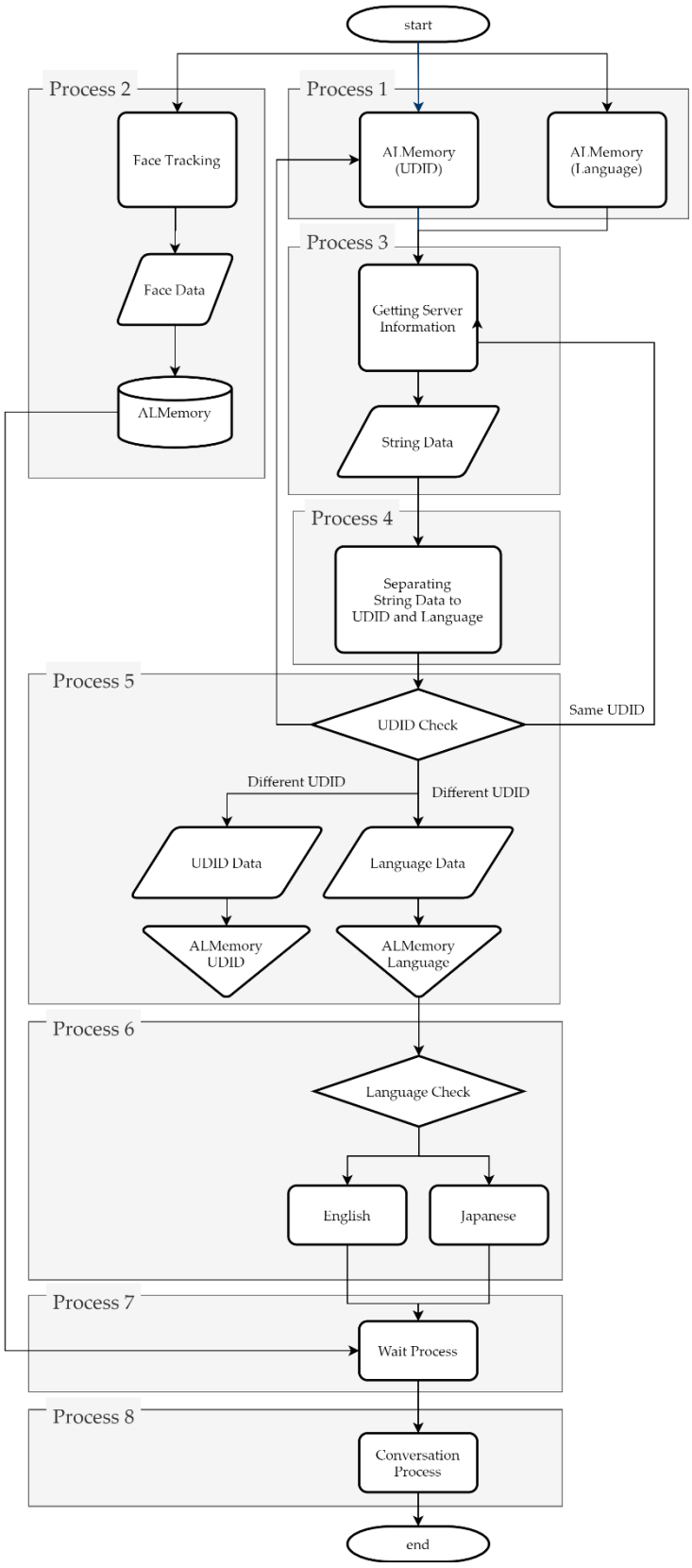


Figure 2. Processes of the Communication Robot

information, is obtained. In this situation, since there is still only one line of character string data that cannot be utilized, it is necessary to go through the data division function described later.

Process 4: In the “character string data division” to “language data” and “UDID”, the location in the string data corresponding to “language data” and “UDID” is set for the data obtained from the server, and each data point is divided. Thus, “language data” and “UDID” can be used as variables in subsequent processing.

Process 5: In “branching processing”, processing is performed using the acquired “language data” and “UDID”. First, it is determined whether the obtained data are the same “UDID”. If the same, it is determined to be the same user, and the process returns to the next loop of “setting server information” stage. If the “UDID” is different, the “language data” is identified, and the process proceeds to “language mode setting” for the detected language.

Process 6: “Language mode setting” is a process for setting the language for the utterance (speech) of the “guide robot” Pepper. Once a language is set, all speech will be spoken in the same language until it is reset.

Process 7: In the “wait process”, the process is terminated when the language is set to “language mode setting” and the “guide robot” Pepper detects the user. In this process, if one or both do not proceed, it is set to wait mode. This makes it possible to reduce malfunctions.

Process 8: The “guidance process” is the phase where it is confirmed that the “waiting process” has been completed, and guidance of the “guide robot” is activated.

Based on these processes, this research constructed a system architecture in which the robot automatically switches the language according to the user and provides guidance information.

4. EXPERIMENT

In this section, an evaluation experiment was performed to confirm the effectiveness of the constructed system. As a condition of this experiment, the subject was asked to walk slowly (0.9 to 1.2 m / s) from a position 10 m away from the “guide robot” Pepper until he/she gets 0.5 m close to the robot, as shown in Figure 3. This was performed five times, and a sensory evaluation experiment was then performed using a five-stage Ricardian scale. The subjects were six males and four females in their 20s and 50s, and the 10 subjects were five Japanese students and five international students using English. The evaluation items are shown in Table 1.



Figure 3. Evaluation Experiment of Guide Robot

Table 1. Evaluation Experiment Question Item

Q1. Would you be grateful if the robot comes close to you in public space and provides information?
1. Highly ungrateful 2. Ungrateful 3. Neither 4. Grateful 5. Highly grateful
Q2. Was the distance of the robot appropriate when it started talking to you?
1. Very inappropriate 2. Inappropriate 3. Neither 4. Appropriate 5. Very appropriate
Q3. Please answer if you marked "inappropriate" or "very inappropriate" in Q2. How did you feel about the distance?
1. Too close 2. Too far
Q4. How did you feel about the timing of the robot begins talking to you?
1. Very inappropriate 2. Inappropriate 3. Neither 4. Appropriate 5. Very appropriate
Q5. Please answer if you marked "inappropriate" or "very inappropriate" in Q4. How did you feel about the timing?
1. Too early 2. Too late

Table 2. Evaluation Results

Nationality	Age	Gender	Q1	Q2	Q3	Q4	Q5
Japan	20's	Male	4	4		4	
Japan	40's and beyond	Male	4	4		4	
Japan	40's and beyond	Male	3	4		2	2
Japan	40's and beyond	Female	3	2	1	4	
Japan	30's	Male	4	2	1	2	2
USA	20's	Male	4	3		2	1
China	20's	Female	3	4		2	1
China	20's	Female	4	4		3	
China	20's	Female	4	4		4	
Korea	20's	Male	3	4		4	
		Average	3.60	3.50		3.10	
		Standard Deviation	0.49	0.81		0.94	

5. RESULT AND DISCUSSION

This section describes the results and discussion of the evaluation experiment performed in the previous section. Table 2 shows the evaluation results. Regarding the robot's spontaneous provision of information in public spaces, the result of Q1 will indicate whether the proposed system is effective for accommodating the problem in the introduction is that the mental threshold of talking to the robot from the user's side and receiving guidance is still high.

Regarding the user's personal space in communication with the robot in Q2, although there may be some individual differences, more than half of the respondents answered that it was somewhat appropriate. This result indicates the validity of the "guide robot" starting the guidance at a distance of 0.5 m or more. Two Japanese respondents replied to Q3 that the robot was too close, as shown in Table 2. This suggests that the personal space of the users may be wider than previously considered and suggests the necessity of analyzing the sense of distance in future research.

Regarding whether the moment the robot started communicating was appropriate or not in Q4, half of the respondents answered that it was somewhat appropriate. Of the four respondents who thought it was inappropriate, two Japanese responded that the moment was too late and two international students answered that the moment was too early, as shown in Table 2. This result suggests that adjusting the response speed may improve the evaluation, depending on the language used.

These results suggest that communication between the robot and providing guidance to the user might be effective. The results also implied the necessity of adjusting the personal space and reaction speed.

6. CONCLUSION

The culmination of this research has led to the successful development of a multilingual communication robot system aimed at facilitating seamless interactions between robots and foreign visitors speaking various languages. Through sensory evaluation experiments, the efficacy and performance of the system were thoroughly assessed, demonstrating its effectiveness in fostering effective communication.

The findings from the evaluation experiments highlighted the system's capability to engage users effectively, paving the way for enhanced spontaneous communication between robots and humans. Particularly noteworthy was the automated language switching and speech capabilities of the robot, which significantly reduced the cognitive load on users and promoted smoother interactions.

ACKNOWLEDGEMENT

This research was partially supported by JKA promotion funds from KEIRIN RACE 2019M-176.

REFERENCES

1. **Ichiryu, A. and Shiizuka, H., (2008),** English talking-robot and its impression of scenarios, Research reports of the Kogakuin University, Vol. 105, pp 187-190 [in Japanese].

2. **Yamaoka, F. and Kanda, T., et al., (2007),** Interacting with a Human or a Humanoid Robot?, IPSJ journal, Vol. 48, No. 11, pp 3577-3587 [in Japanese].

3. **Koizumi, S. and Kanda, T., et al., (2006),** Preliminary Field Trial for Teleoperated Communication Robots, ROMAN 2006 - The 15th IEEE International Symposium on Robot and Human Interactive Communication, Hatfield, doi: 10.1109/ROMAN.2006.314409.

4. **Pandey, A.K. and Gelin, R., (2018),** A Mass-Produced Sociable Humanoid Robot: Pepper: The First Machine of Its Kind, IEEE Robotics & Automation Magazine, Vol. 25, No. 3, pp. 40-48

5. **Aaltonen, I. and Arvola, A., et al., (2017),** Hello Pepper, May I Tickle You?: Children's and Adults' Responses to an Entertainment Robot at a Shopping Mall, HRI '17: Proceedings of the Companion of the 2017 ACM/IEEE International Conference on Human-Robot Interaction, Vienna, pp.53–54

6. **Rae, I. and Takayama, L., et al., (2013),** The influence of height in robot-mediated communication, HRI '13: Proceedings of the 8th ACM/IEEE international conference on Human-robot interaction, Tokyo, pp.1-8

7. **Fujie, S. and Matsuyama, Y., et al., (2012),** Conversation Robot Participating in and Promoting Human-Human Communication, IEICE TRANSACTIONS on Fundamentals of Electronics, Communications and Computer Sciences, Vol. A-95, No. 1, pp. 37-45 [in Japanese]

8. **Kato, S. and Ohshiro, S., et al., (2004),** “Development of a communication robot Ifbot”, IEEE International Conference on Robotics and Automation, 2004. Proceedings. ICRA '04. 2004, New Orleans, Vol. A-95, No. 1, doi: 10.1109/ROBOT.2004.1307230

9. **Matsusaka, Y. and Tojo, T., et al., (2003),** “Conversation robot participating in group conversation”, IEICE TRANSACTIONS on Information and Systems, Vol. E86-D, No. 1, pp. 26-36 [in Japanese]

10. **Ogi, T., and Ito, K., et al., (2016),** “Multilingual Digital Signage Using iBeacon Communication”, 19th International Conference on Network-Based Information Systems (NBiS 2016), pp. 387-392

11. **Ogi, T., and Ito, K., et al., (2017),** “Multilingual Information Service Based on Combination of Smartphone and Digital Signage”, 20th International Conference on Network-Based Information Systems (NBiS 2017), pp. 644-653

12. **Ukegawa, S., and Sato, A., et al., (2017),** “Multilingual Tourist Information Providing System Based on iBeacon Communication”, Proceeding of Human Interface 2017, pp. 791-794 [in Japanese]

13. **Matsuda, S., Hayashi, T., et al., (2017),** “Development of the “VoiceTra” Multi-Lingual Speech Translation System”, IEICE Transactions on Information and Systems, Vol. E100.D, No. 4, pp. 621-632

14. **Isotani, R., and Matsuda, S., et al., (2013),** “Operation of a Nation-Wide Field Experiment of Speech-to-Speech Translation and Adaptation of Speech Recognition Models Using its Log Data”, The IEICE transactions on information and systems, Vol. 96, No. 1, pp. 209-220 [in Japanese]

HUMAN RELATIONSHIP FELT IN COMMUNICATION USING TELE-IMMERSION AVATAR ROBOT

Tetsuro OGI, *ogi@sdm.keio.ac.jp*, Keio University, 223-8526, Yokohama, Japan

Yuki KIDA, *ykida@keio.jp,* Keio University, 223-8526, Yokohama, Japan

ABSTRACT

In this study, a tele-immersion avatar robot that allows remote users to communicate with local users with high presence sensation while feeling that their body was unified into the robot present at the local site was developed. The avatar robot is equipped with audiovisual information transmission function, body movement control function, and voice conversation function. An evaluation experiment using the developed avatar robot in research presentation was conducted, and a questionnaire for remote users and local users regarding the psychological human relationship that was felt during the communication was conducted to evaluate the proposed system.

Keywords: Avatar robot, Tele-immersion, Remote communication, Human relationship

1. INTRODUCTION

Since the COVID-19 pandemic, video conferencing tools such as Zoom and Teams have been used worldwide. However, though current video conferencing tools can be used for meetings in conference rooms and lectures in classrooms, it is difficult to use them for communication in mechanical design and manufacturing because objects and environments in the real world cannot be shared [1][2]. On the other hand, in recent years, avatar robots have often been used as communication devices in the real world. For example, avatar-in's “newme” which serves customers at airports and “OriHime” which is used by disabled people to provide service in coffee shops are used [3][4]. However, in these systems, since remote users operate the avatar robots through PC screens, it is difficult for them to feel that they actually present and act in the places where the avatar robots exist.

In order to solve these problems, in this study, we have developed a tele-immersion type avatar robot that allows remote users to communicate with local users with a high presence sensation,

as if they were in the robot. By using the tele-immersion avatar robot, it is expected that remote users will be able to communicate with local users naturally as a first-person experience.

In general, it is said that communication has two aspects, transmission of information and building of human relationship [5]. The use of avatar robots makes it possible to transmit information through conversation and gestures, but what kind of human relationship is built? Can a remote user build a human relationship with a local user, or does a local user build a human relationship with the avatar robot or with a remote user? In this study, we conducted a communication experiment using the prototype of tele-immersion avatar robot, and evaluated the psychological human relationship built through the communication.

In the following paper, we describe the concept of a tele-immersion avatar robot, the system configuration of the developed avatar robot, and the evaluation of human relationship built in a communication experiment.

2. CONCEPT OF TELE-IMMERSION AVATAR ROBOT

In order to realize a tele-immersion avatar robot, a remote user must be able to communicate with other people as a first-person experience, while feeling as if he or she were not operating a robot, but becoming a robot itself. To achieve this concept, it is necessary for the user to receive information sensed by the robot's eyes and ears as if he or she sensed it using his or her own organs, move the robot's body freely as if it were his or her own body, and talk with the other person using the robot's voice as if it were his or her own voice. In other words, it will be necessary to develop technologies of audiovisual information transmission, body movement control, and voice conversation, that will enable natural communication as a first-person experience.

Figure 1 shows the concept of a tele-immersion avatar robot. The visual and audio function as a first-person experience is to generate the sensation of seeing with your own eyes and hearing with your own ears by using the robot's sensors. Namely, when you turn to the right, you can see an image of the robot's right side, and when you turn to the left, you can see an image of the robot's left side. Therefore, it is necessary for the remote user to be able to freely look around the scene around the robot.

Next, the body control function as a first-person experience is to move the robot's body freely as if it were your own body. When you raise your right hand, the robot also raises its right hand, and when you point at an object you are looking at, the robot also points at the same object. Therefore, it is necessary for the remote user to control the movement of the avatar robot

according to his or her body movement. The conversation function as a first-person experience is the ability to generate the robot's speech as if it were your own speech.

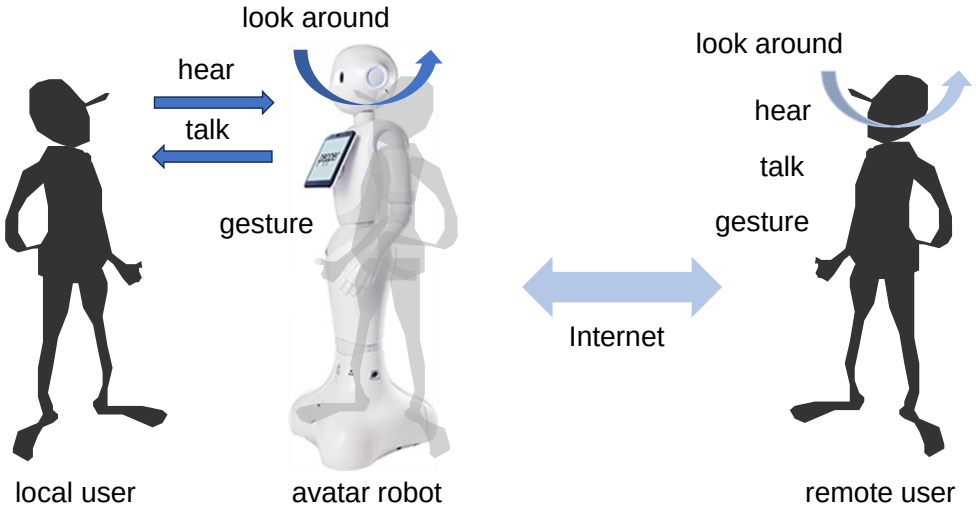


Figure 1. Concept of Tele-Immersion Avatar Robot

.

In the field of tele-existence robots, research on remote robot control as a first-person experience is being conducted, and robots that combine technologies of master-slave arm and visual information transmission have been developed [6][7]. Compared to these studies, the avatar robot developed in this research aims at communicating with humans in the real world. Therefore, it is expected that a human relationship among remote user, local user and avatar robot is constructed, by enabling the remote user to talk with the local user via the avatar robot, and the local user to talk with the remote user via the avatar robot. Namely, it is required that the avatar robot has individuality, expresses personality, and transmit emotions through the communication. In this study, an evaluation experiment using a prototype of avatar robot was conducted, to investigate the question of who the users feel they are talking to, that affects the consciousness of constructing human relationship.

3. SYSTEM CONFIGURATION

In this study, Softbank's communication robot Pepper was used as the base avatar robot. Pepper is a 121cm tall humanoid robot that can be programmed to talk and make gestures, and is used in various applications, such as guiding visitors at museums, promoting sales in shopping malls, and providing care in nursing homes [8][9]. In this study, Pepper was used as an avatar robot that was controlled by a remote user [10].

Audiovisual Information Transmission Technology

In order for a remote user to obtain audiovisual information by using the eyes and ears of an avatar robot like his or her own sensory organs, it is necessary for the user to be able to look around freely and hear the corresponding sounds as if he or she were in the robot's location [11]. Though Pepper which was used as the avatar robot is originally equipped with two cameras on the forehead and mouth and four microphones on the head to obtain audiovisual information, the viewing angles of these built-in cameras are small. In order for a remote user to look around using the built-in cameras, it is necessary to control the movement of the robot's head in real time according to the user's head movement, which causes a time delay in displaying image. Therefore, in this study, a Ricoh's THETA V was attached to Pepper as an external 360-degree camera, allowing the remote user to quickly look around the surroundings independent of the robot's head movement.

THETA V is a camera that can capture 4K resolution 360-degree video and 4-channel spatial audio, and it was used attached to the monitor on Pepper's chest. The 360-degree video and audio captured by THETA is sent from a USB-connected small stick PC (Intel Compute Stick m3) to the remote user's HMD via P2P (peer to peer) communication of WebRTC (Web Real-Time Communication) using NTT Communications' SkyWay. The remote user uses a HMD of Oculus Quest 2, and the received 360-degree video image is texture mapped in real time onto a virtual sphere model constructed in A-Frame. In this way, the remote user can look around Pepper's surroundings freely using the HMD's web browser, independent of Pepper's head movements. Figure 2 shows the system configuration of the audiovisual information transmission.

Body Movement Control Technology

Next, in order for a remote user to control the avatar robot's body as if it were his or her own body, it is necessary for the user to control the movement of the robot's body in real time

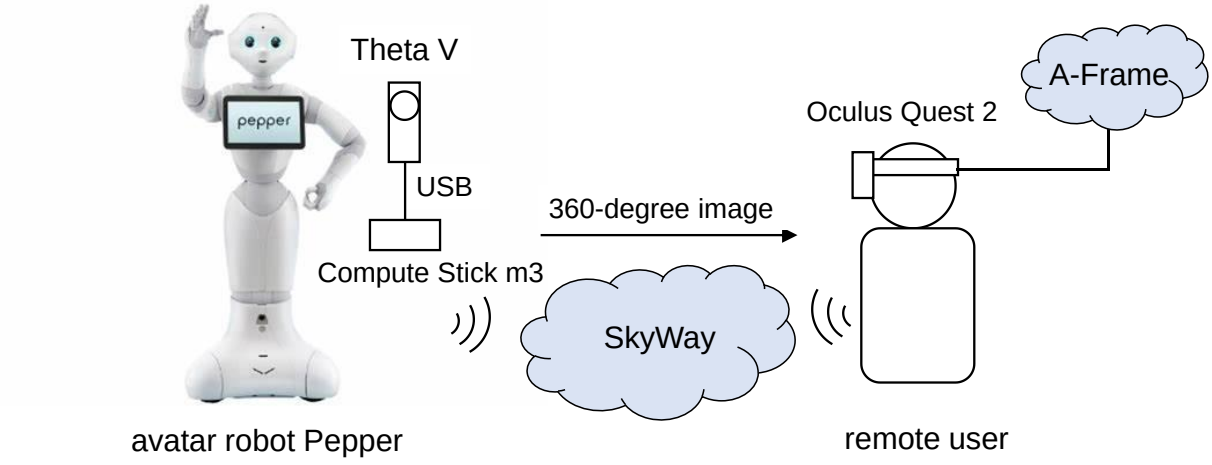


Figure 2. System Configuration of Audiovisual Information Transmission

according to his or her gestures. Therefore, in this study, a method of controlling the robot's posture according to the measurement of the user's gesture with a sensor was implemented. As a sensor to measure the user's gestures, Microsoft's Kinect was used. Kinect projects an infrared pattern onto the user's body, generates depth image by analyzing the captured infrared image, and estimates the user's posture referring to the body model data constructed based on machine learning. In this study, this function was used to calculate the position and angle of each joint of the user and control the corresponding joints of the robot. However, a human arm has three degrees of freedom at the shoulder, two degrees of freedom at the elbow, and two degrees of freedom at the wrist, while Pepper's arm has two degrees of freedom at the shoulder, two degrees of freedom at the elbow, and one degree of freedom at the wrist, and robots and humans have different degrees of freedom and range of motion in their joints. Therefore, the measured user's posture data cannot be used directly, and it was converted into joint angles within the ranges of the robot's motion and used for the control. This made it possible to directly control Pepper's posture by the movements of the head, arms, and waist of the remote user. Figure 3 shows the measured posture of the user and controlled posture of the robot.

Voice Conversation Technology

In order for a remote user to freely talk with a local user using a robot's voice, it is necessary to make the robot talk the remote user's speech. One method of outputting voice from a robot is to transmit the remote user's voice directly, but it would be felt unnatural to output the human’s voice directly because the voice of Pepper is characteristic and well-known. Therefore, in this study, a method of making the robot talk using Pepper's voice tone was used.

In this method, the remote user's voice is converted into text information by voice recognition function and it is transmitted to the robot through the server, and the robot vocalizes the



Figure 3. Measured User’s Posture and Controlled Robot’s Posture

received text information in the robot's voice. Web Speech API was used to recognize the remote user's voice, and the voice data is sent from the remote user's PC to the server through the web browser and it is recorded as text information on the server. Pepper constantly checks the server and vocalizes the recorded text when new text information is recorded.

At this time, the remote user's voice is once converted into text, it would be possible to perform text information processing such as automatic translation. In this system, a mechanism to perform machine translation between Japanese and English using DeepL API on the server was implemented. Pepper originally has conversation function using Japanese, English, Chinese, etc., by switching language modes. Therefore, it is possible to make Pepper speak in Japanese what the remote user speaks in English or speak in English what the remote user speaks in Japanese. Figure 4 shows the screen image of voice conversation interface using Web Speech API and DeepL API.

By using these functions of audiovisual information transmission, body movement control, and voice conversation, a remote user can use Pepper's body as a tele-immersion avatar robot.

4. EVLUATION EXPERIMENT ON HUMAN RELATIONSHIP

An evaluation experiment was conducted to investigate the psychological human relationship that is built when the developed avatar robot is used. As an experiment, we asked graduate students to make a presentation to introduce their research using the avatar robot in a university orientation for new students. The students who explained research operated the avatar robot from the next room as remote users, and the students who listened to the explanation faced the avatar robot as local users. The avatar robot was operated to explain research while pointing at posters, and the new students who listened to the explanation asked questions to the avatar robot after the explanation. The students who listened to the explanation knew in advance who was operating the avatar robot. Each experiment time was

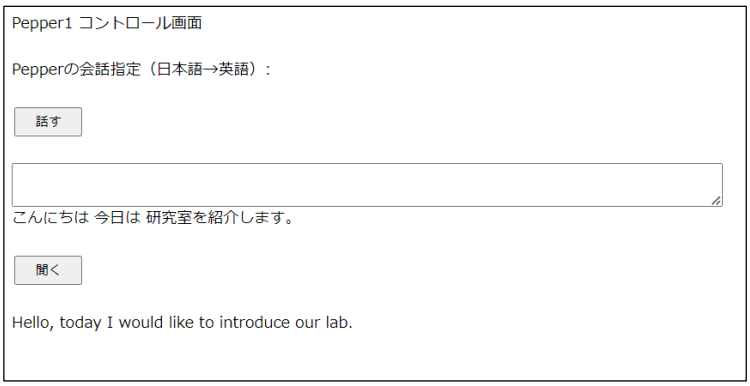
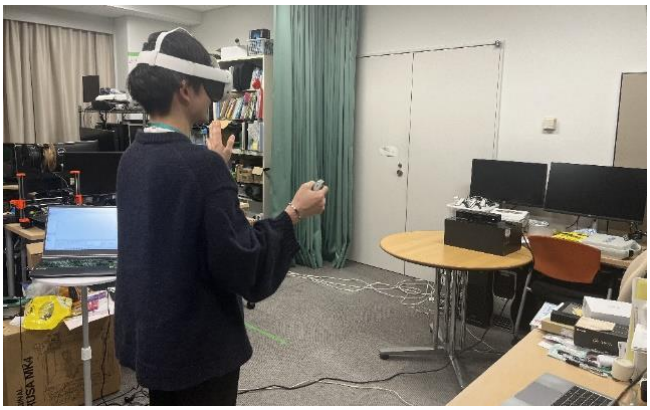


Figure 4. Voice Conversation Interface using Web Speech API and DeepL API

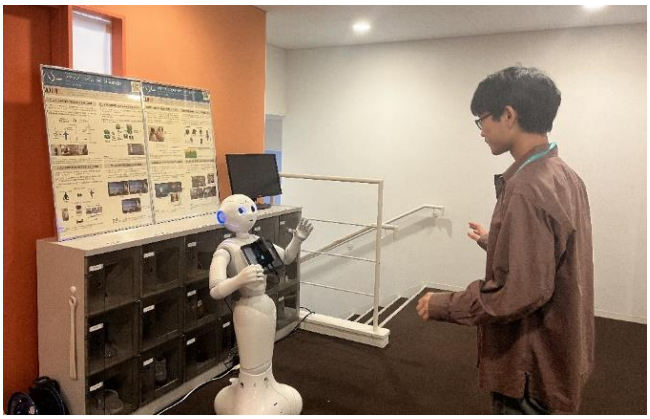
about 5 minutes including the explanation and the Q&A session, and after the experiment, the subjects of the remote users and the local users were asked to answer the questionnaire using 5-point Likert scale as shown in Table 1. The numbers of subjects who gave the explanation and who listened to the explanation were 10, respectively. Figure 5 shows the remote user and local user in the experiment.

Table 1. Questionnaire for Remote Users and Local Users

Q1: I felt I was in the same place as the other person.
Q2: I felt the robot I was controlling was in the same place as the other person.
Q3: I felt I moved my body.
Q4: I felt I moved a robot's body
■ Questions for local user
Q5: I felt I talked with a robot.
Q6: I felt I talked with a remote user.



remote user



local user

Figure 5. Remote User and Local User in the Evaluation Experiment

Figures 6 shows the results of the questionnaire answered by remote users and answered by local users. The results by remote users show that there was a significant difference between Q1 and Q2, but no significant difference between Q3 and Q4 according to the t-test. This result indicates that the remote users who operated the avatar robot felt more that they themselves were in the same place with the other person than that the robot was in the same place with the other person, and felt that they were controlling the movement of both the robot body and their own body. On the other hand, the results by the local users show that there was a significant difference between Q5 and Q6 according to the t-test, and this result indicates that the local users felt more that they were talking with the robot in front of them than that they were talking with the remote user.

5. DISCUSSIONS

The results of the evaluation experiment showed that by using the tele-immersion avatar robot, remote users felt that they existed at the local site as if their body was unified into the robot body, and they were moving the robot body in the same way as moving their own body. This means that the remote users were able to perform the tele-immersive communication as a first-person experience that was the purpose of this study. However, it was shown that the local users felt they were communicating with the robot in front of them, rather than with the remote user, even though they knew who was operating the robot. Namely, it can be thought that the avatar robot was personified and it was felt to have a certain personality through the tele-immersion function.

In the tele-immersion avatar robot, the remote user feels that he or she is communicating with the local user, but the local user feels that he or she is communicating with the personified

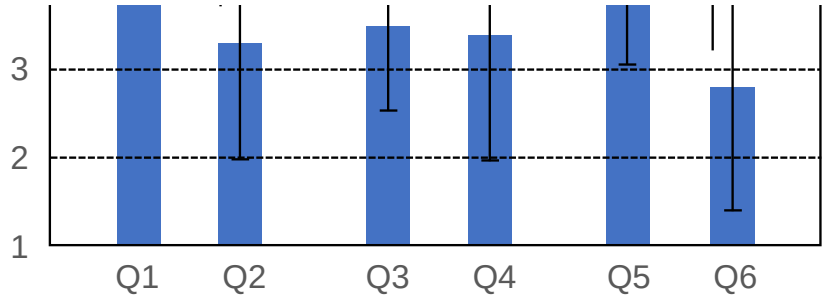


Figure 6. Results of Questionnaire in Evaluation Experiment

avatar robot, not with the remote user. Therefore, when using a tele-immersion avatar robot, the remote user must consider how to make the robot express the same characteristics and personality as himself or herself, or what kind of characteristics and personality to be given to the robot. It was also shown that the local users were able to communicate effectively with the avatar robot which was personified. It would be an interesting research topic to consider whether the avatar robot must be a humanoid robot or whether any object can be used for communication by being personified [12].

From the free comments in the questionnaire, some subjects pointed out that there was a time lag in the response of the avatar robot, which sometimes made the communication unnatural. It is thought this was because the remote user's speech was converted into text in order to be spoken in the robot's voice. To solve this problem, future work will include introducing a method to change the tone of the remote user's voice into the robot's voice in real time.

6. CONCLUSIONS

In this study, a tele-immersion avatar robot that allows remote users to communicate with local users with high presence sensation, as if they were unified into the robot was developed. In order to realize a tele-immersion avatar robot, some functions of transmitting 360-degree camera images, controlling robot's movements based on user's gestures, and talking according to user's speech were introduced. Evaluation experiment using the avatar robot was conducted and the results showed that remote users felt a tele-immersive sensation, that is they felt they were in the place where the avatar robot existed and their gestures naturally controlled the movements of the avatar robot. On the other hand, it was also shown that local users who faced the avatar robot felt that the avatar robot itself had a personality and had a sense of talking with the robot itself. Future research topics will include what kind of personality can be given to the robot by remote users, and what kind of appearance can be used as an avatar robot, in order to build an effective human relationship between the avatar robot and the local user.

ACKNOWLEDGEMENT

This study was partially supported by JKA promotion funds from KEIRIN RACE 2022M-272 and 2024M-549.

REFERENCES

1. **Akutsu, T. and Ogi, T., (2023),** “Differences in Nonverbal Behavior in Online Communication”, International Conference on Design and Concurrent Engineering 2023 & Manufacturing Systems Conference 2023 (JSME iDECON/MS 2023).

2. **SPATHIS, P., DEY, R., (2021),** “Online Teaching amid COVID-19: The Case of Zoom”, 2021 IEEE Global Engineering Education Conference (EDUCON).

3. **FUKABORI, A., KAJITANI, K., (2018), “**ANA AVATAR**”**, Journal of the Robotics Society of Japan, Vol.36, No.10, pp.663-667.

4. **Takeuchi, K., Hatada, Y., Yamazaki, Y., Yoshifuji, K., (2024),** “Empirical Studies on Remote Customer Service using Telepresence Robot “OriHime” by People Who Have Difficulty Going Out”, IPSJ Digital Practice, Vol.5, No.2. (in Japanese)

5. **Scollon, R., and Scollon, S.W., (1995),** “Intercultural Communication: A Discourse Approach”, Oxford: Blackwell.

6. **INOUE, Y., KATO, F., TACHI, S., (2019),** “Master-Slave Robot Hand Control Method based on Congruence of Vectors for Telexistence Hand Manipulation”, 2019 IEEE International Symposium on Measurement and Control in Robotics (ISMCR).

7. **ABE, H., MIURA, M., ABE, T., SUGANUMA, T., (2018),** “A Telexistence System Using Remote Control Robot and Omnidirectional Camera with QoE Control”, 2018 IEEE 7th Global Conference on Consumer Electronics (GCCE).

8. **DRAGHICI, B.G., DOBRE, A.E., MISAROS, M., STAN, O.P., (2022),** “Development of a Human Service Robot Application Using Pepper Robot as a Museum Guide”, 2022 IEEE International Conference on Automation, Quality and Testing, Robotics (AQTR).

9. **YANG, C.Y., LU, M.J., TSENG, S.H., FU, L.C., (2017),** “A Companion Robot for Daily Care of Elders based on Homeostasis”, SICE Annual Conference.

10. **KIDA, Y., MATSUOKA, K., OGI, T., (2023),** “Evaluation of Conveying Spatial Information by Pointing Gestures of a Tele-Immersion Robot Avatar”, International Conference on Design and Concurrent Engineering 2023 & Manufacturing Systems Conference 2023 (JSME iDECON/MS 2023).

11. **OGI, T., FUEKI, Y., (2016), “**Development of HMD-based Tele-Immersion System for Collaborative Work”, International Design and Concurrent Engineering Conference 2016 (iDECON 2016).

12. **KINOSHITA, T., MIKAMI, A., KIDA, Y., YAKOH, T., OGI, T., (2023),** “Evaluation of Generating Avatar Sensation Using 360° Camera Image and Audio”, JSME D&S 2023. (in Japanese)

SIMPLE RECACTION TEST WITH MOUSE CLICKS USING 500 Hz MONITOR ~IS A 500 Hz MONITOR EFFECTIVE FOR ESPORTS?

Yuya ASHIZAWA, *g2172004@tcu.ac.jp* Tokyo City University, 2248551, Yokohama, Japan

Hideo MIYACHI, *miyachi@tcu.ac.jp* Tokyo City University, 2248551, Yokohama, Japan

ABSTRACT

We are interested in the skills people improve through eSports. In this context, we have focused on the use of high-frequency monitors for eSports and have investigated the effects of high-frequency monitors on eSports. In a previous study, we found that in a simple reaction test, even ordinary people without special training could perceive a 360 Hz monitor and react faster than a 60 Hz monitor. Also, in a slightly more complex cursor aiming test, in which the cursor is placed on a target, the high-frequency monitor was found to have an advantage in game scores. Since the latest 500 Hz monitors will begin shipping in Japan in 2023, we conducted a simple reaction test and a cursor aiming test using these monitors. The results showed that a 500Hz monitor allowed participants to react faster in a simple reaction test. However, no significant effect was observed for the 500Hz monitor in the mouse cursor aiming test. It was suggested that the advantage of high-frequency monitors in eSports depends on the content of the game.

Keywords: High-refresh rate monitor, eSports, Simple reaction time

1. INTRODUCTION

Is eSports a Game or a Sport? This is the research question that this study aims to answer. e-sports' adoption for the Olympics is also controversial. The debate over the Olympics is too complex for the author to comment on. However, it is easy to imagine a mother scolding her child in an ordinary Japanese household, saying, "You will not be happy if you keep playing games. If e-sports is a sport, then there must be some skill that can be developed through it. If the skills are not related to specific game content, but are useful in general society, such as reflexivity, communication skills, and logical thinking, society will encourage e-sports, and children can acquire valuable skills through e-sports while having fun. eSports can be played

even by old people with declining physical fitness, and remote participation allows people in underpopulated areas and those in urban areas to participate equally. In addition, if the relationship between e-sports and human skills can be clarified, appropriate handicaps can be set, thereby creating an environment where everyone can enjoy life regardless of age, physical fitness, or region. Therefore, our e-sports research was started with the goal of discovering the abilities that can be trained through e-sports.

The first of these efforts was to investigate human adaptability to high-frequency monitors. Monitors connected to office computers typically operate at 60 Hz, but monitors used for eSports operate at higher frequencies than 60 Hz. However, monitors for eSports use a higher frequency than 60Hz. We have conducted a simple response test and a cursor aiming test using a 360 Hz monitor released in Japan in 2020 as a prior study. The results showed that in both tests, people can use high-frequency monitors to their advantage in eSports

In this study, we report the results of the same two tests conducted in the previous study using a 500 Hz monitor, which will be available in Japan in 2023. This experiment examined the advantage of the monitor in terms of whether people can effectively use the high-frequency monitor, so it did not measure the human skills that can be acquired in e-sports, as mentioned above. However, we believe that these are important basic data to measure the increase in the speed of human response to games.

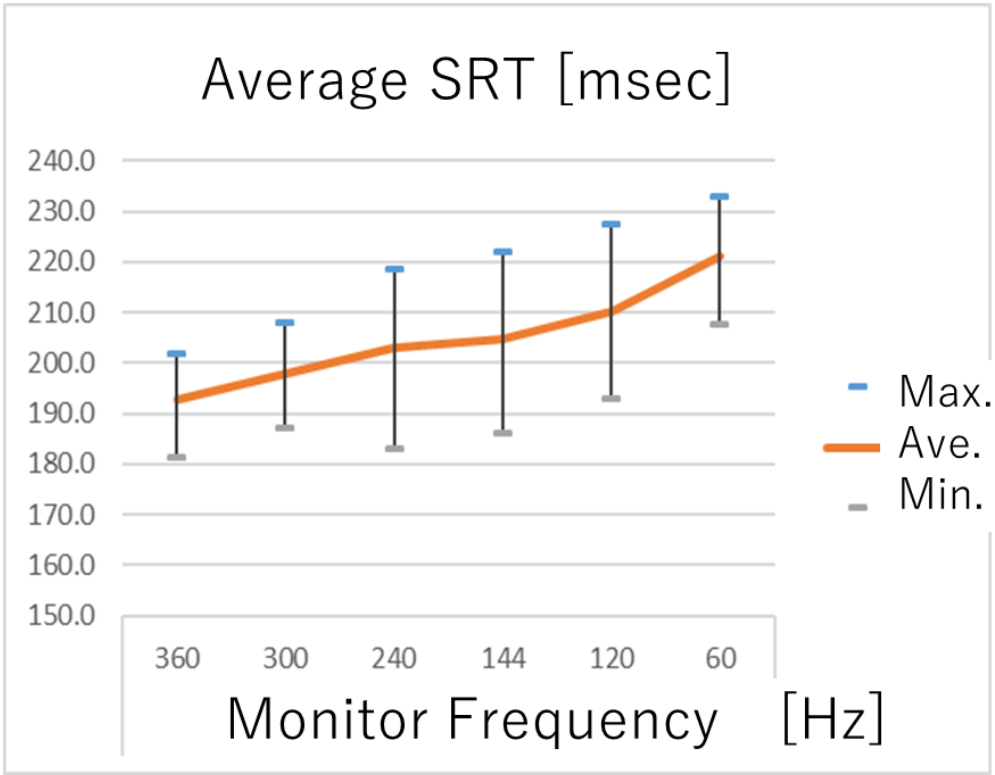


Fig.1 Average SRT versus monitor frequency from 60 Hz to 360 Hz.

2. RELATED STUDIES

（1）Simple Reaction Test

The first test conducted was a simple reaction test [2]. Only the results are described here; the details of the test method are described below. 7 participants measured the simple reaction time while changing the frequency of the monitor from 60 to 360 Hz, and the results are shown in Fig.1. The figure shows that the reaction time became slower as the frequency decreased. This is not a measure of human ability. Assuming that people respond in the same time on average when a sufficiently large number of trials are conducted, the delay in response when the monitor frequency is lowered may be due to a corresponding delay in the display. At this time, the participants were not students practicing e-sports. However, both the average reaction time of the seven participants and the average reaction time of the individual participants were slower on the slower frequency monitors. This indicates that people can recognize and react to 360 Hz displays without special training.

（2） Mouse Cursor Aiming Test

Next, we tested the effect of monitor frequency in a more complex game than the simple response test. The game used was SPHERETRACK90 in AimLab. In this game, a sphere (target) moves randomly in a 3D space for 1 minute while the target moves as shown in Fig.2. The game has a mode in which the player moves the viewpoint to keep the target in the center of the screen. This action is called "adjusting the aim. Ten students played the game. The display frequency setting of the game was controlled by fixing the frequency setting of the monitor at the maximum 360 Hz and changing the maximum frame rate setting of the game from 60 Hz to 144, 240, and 360 Hz. They played the game four times, one at a time, starting with the lowest rate, and measured 10 sets (40 plays in total). Figure 2 shows the average scores of the seven players over 40 plays at frequencies normalized by their own scores at 60 Hz. The dashed line shows their scores and the solid line shows the average of the seven players.

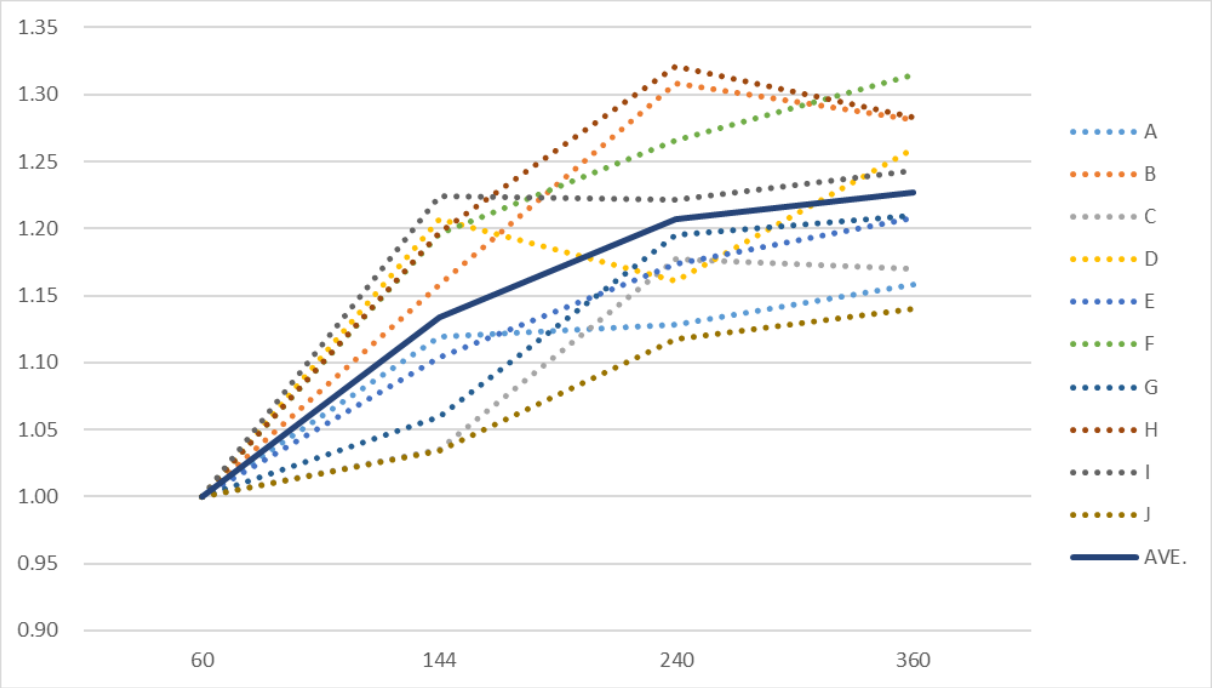


Fig.2 Average SRT versus monitor frequency from 60 Hz to 360 Hz.

The scores tended to be higher as the refresh rate increased, indicating that monitors with higher refresh rates have an advantage in this game. Testing for differences in these means showed significant differences between 60Hz and 144Hz and between 144Hz and 240Hz, but no significant differences between 240Hz and 360Hz. This suggests that as games become more complex, the benefits of high-frequency monitors may be limited in their effective range.

（3） Apex Legends

Previous tests were games played by one person. Next, we investigated the effect of monitor frequency on games played by two players [4]. Apex Legends is a first-person battle royale game available on PC, Nintendo Switch, Playstaion and XBOX. The PlayStation version is played in 54 countries worldwide. Battle Royale is a game type in which multiple players (one person or team) gather on a playing field (map), defeat their enemies in battle, and the last surviving player is the winner.

The experiment used a shooting range in the practice mode of Apex Legends. Two people enter the shooting range for a one-on-one match. Both characters and weapons were the same. The rule was that no ability other than shooting was used in the fight. Four participants played against each other in the experimental environment. The fights were four-player round-robin, with each match being one-on-one. The two opponents stood at designated positions in the shooting range as Apex Legends players and began fighting on verbal cues from the experimenter.

Table.1 Number of wins and win rate per opponent for 4 players using 240 Hz

		60 [Hz]					
		a	b	c	d	TOTAL	Win [%]
240 [Hz]	A		1	0	5	6	20.0%
	B	9		1	9	19	63.3%
	C	7	8		8	23	76.7%
	D	7	2	1		10	33.3%
		23	11	2	22	58	48.3%

Table 1 shows the number of wins and win percentage for each player with 240 Hz for each opponent (10 matches each). The total number of fights was 120, with 58 wins and a 48% win rate. This means that the winning percentage was 52% when fighting on a 60 Hz monitor. In this experiment, users with 240 Hz monitors did not have an advantage in the game. Rather, the win rate for players using the 240 Hz monitor was slightly lower than the win rate for players using the 60 Hz monitor. For the participants in this experiment and for the experimental conditions, the high frequency monitor did not provide an advantage that would have affected wins or loses beyond the skill of the players

Since the skills among the opponents could not be the same, it was first decided to use the results of the match using a 240 Hz monitor of the same frequency as the reference win rate. The reference win rates for participants: B and C, who were the top performers in Experiment 1, were 38% for B and 63% for C. These two players played each other 20 times at 240 Hz.vs. 20, 30, 45, and 60 Hz monitors, exchanging fast/slow. The win rate at each frequency, normalized by the reference win rate, is shown in Fig. 3. When both B and C used 240 Hz monitors, the normalized win rate exceeded 1.1 to 1.2 in both cases where the opponent used a 20 Hz to 60 Hz monitor. This indicates that in the B vs. C matchup, the high-frequency monitor contributes about 20 to 40% to the win rate.

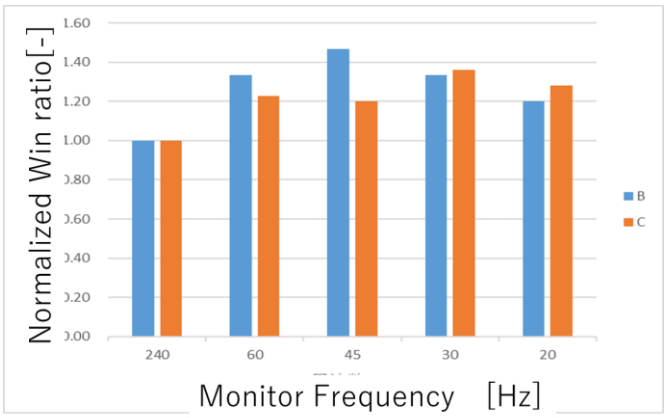


Fig.3 Normalized win rates for B versus C at each frequency

These results (1), (2) and (3) show that high-frequency monitors have an advantage in simple games, but as the game becomes more complex, the advantage decreases. In competitive games, it becomes more difficult for differences in frequency to contribute to winning over differences in skill. However, it was suggested that in a match between people of exactly the same skill, the player with the higher frequency monitor would have an advantage.

At the time the previous study was conducted, the 360 Hz monitor was the fastest, but since a 500 Hz monitor became available in Japan in 2023, a simple reaction test and a mouse cursor aiming game test were conducted using this monitor. Apex Legend was not tested with a 500 Hz monitor because the game does not run at 500 Hz.

3. SIMPLE REACTION TEST USING 500Hz MONITOR

(1) Measurement Systems

The program for this experiment was built on Unity. The time measured in this experiment is described in Fig. 4.

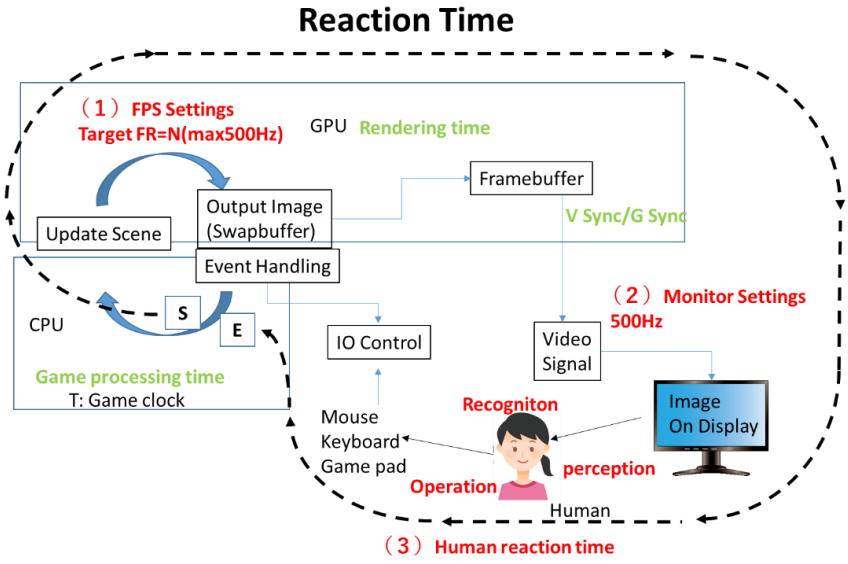


Fig.4 Program design and reaction time measured by this program.

(a) FPS settings

Unity has a parameter called target frame rate. Setting it in N means that Unity's update function will be called once every 1/N seconds. The experimental program changes the window color between 1 and 3 seconds after the left mouse clicking by participants. The changing time is determined by random function. The measurement of reaction time is started at the changing time which is indicated the letter "S" in Fig. 4. At the same time, Unity demands to change the color of the window from white to blue. The color of the frame buffer, which is the background

of the window, is changed by graphics processing according to the Unity's request. The time of rendering depends on the content of the graphics processing, but the graphics load is light in this experiment. We have confirmed the work is enough completed within 1/500 sec. V-Sync in Unity settings is set to ON to prevent rendering from exceeding the monitor's drawing speed.

(b) Monitor settings

The 500 Hz monitor has an ability to work in frequency from 60 to 500 Hz. Within this experiment, the setting is fixed in 500 Hz, the maximum speed. The control on display update speed is controlled by setting the Unity target framerate. The monitor is equipped with a G-Sync chip to synchronize with NVIDEA's graphics board, eliminating timing discrepancies between updates the video signal and LCD monitor.

(c) Human reaction time

The human sees the color change of the monitor, recognizes it, makes the decision to press the button, and clicks the right mouse button by a finger. When Unity receives this mouse event, the measurement of reaction time is completed at the letter "E" illustrated in Fig. 4. The reaction time measured in this experiment indicates the time from the letter "S" to "E" in Fig. 4.

Human response time depends on person and the measuring time is not constant but varies from one measurement to another. The purpose of this experiment is not to measure the reaction time of person. The purpose is to demonstrate the effectiveness of high-frequency monitors in eSports. Assuming that a reaction time for each person is constant on average, the average simple reaction time measured in this experiment will be also constant. However, if the participants could recognize the difference of update speed between monitors and operate button clicking enough fast response to the 500Hz monitor, the reaction time on faster monitor should be shorter than the time on slower monitor.

(2) Experimental procedure

The experiment was conducted as shown in Fig.5. The participants sat in a chair in front of a desk with 500Hz monitor and a mouse. The system specifications of this experiment are listed in Table.2. The computer was a GALLERIA Intel Core i9-14900KF and the monitor was an Alienware 500 Hz gaming monitor.

The measurement begins by the participants clicking the mouse at their own timing. In this experiment, the target frame rates were set to 60 Hz, 240 Hz, and 500 Hz. The number of measurements at each frequency was 20. The experiment started with a setting of 60Hz, and then the frequency was increased to 240Hz and 500Hz. After that, the participants took a break for about one minute, and then the experiment started again with a setting of 500Hz, and the frequency was decreased to 240Hz and 60Hz. Each participant was measured 40 times at

each frequency, for a total of 120 times. The participants were five male and female of university students (aged 20-22).

Table.2 System specification for the experiment

Computer	Vender	GALLERIA
	CPU	Interl Core i9 14900KF
	OS	Windows 11 home edition
	Memory	32GB
	Graphics Board	NVIDIA GeForce RTX 4080
Monitor	Vender	Dell Alienware
	Refrash rate	500Hz
	Response time	0.5ms (GtG Min) 1ms (GtG) (fastest mode)

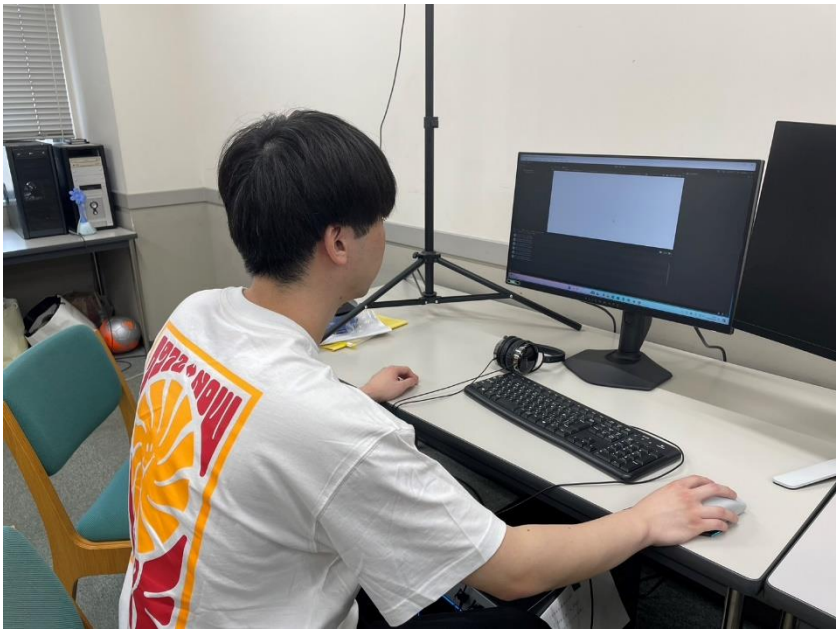


Fig.5 Experimental environment

(3) Experimental results

The same data analyzing methods used in the previous study were applied to this experiment. First, the differences between higher (up) and lower (down) set frequencies were examined to confirm that there was no bias between the two. The 20 reaction times for one measurement at each frequency included values that were obviously fast (likely to have clicked on the prospect) and values that were obviously slow (likely to have been unfocused) based on the average of the reaction times for that participant. Therefore, the 20 reaction times for each measurement were sorted in order of fastest to slowest, and the 10 fastest values from the fourth fastest were considered valid data. Each participant has 20 valid data for two times for up and down at each frequency. The average times are shown in Table.3.

Table.3 Average simple reaction times for five participants at three different monitor frequencies

[msec]

Frequencies	Subject ID					AVERAGE
	A	B	C	D	E	
60Hz	250.267	247.380	257.266	280.893	245.890	256.339
240Hz	236.726	246.962	195.854	237.168	216.904	226.723
500Hz	213.067	225.558	189.833	225.857	209.922	212.847

The results in Table 2 show a tendency to respond faster at 240 Hz than at 60 Hz, but participant B has a smaller difference in average reaction time between 60 Hz and 240 Hz, and participant E has a smaller difference in average reaction time between 240 Hz and 500 Hz. Therefore, we normalized these averages to each participant's average reaction time at 60 Hz as 1.0. A graph of the five participants' averages of the normalized mean is shown in Fig.6. Error bars indicate 95% confidence intervals. The vertical axis is the mean value at each frequency, with the response time at 60 Hz as 1.0, and the horizontal axis is the frame interval [msec]. The means were also the result of the t-test, and the Bonferroni (Bonferroni) correction after the t-test, both of which showed a dominance difference in the 5% test between the normalized means at the three frequencies.

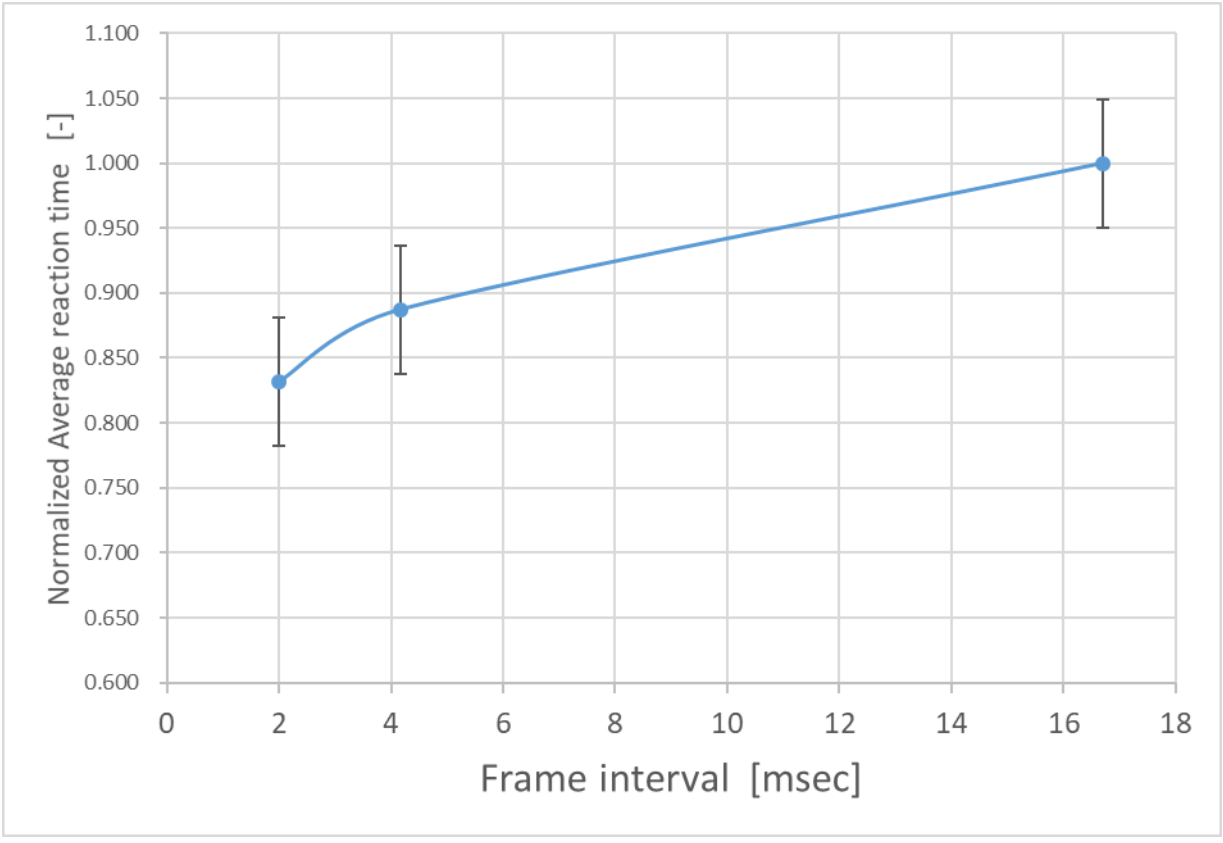


Fig.6 Normalized average reaction time versus frame interval

(4) Discussion

The results of this study showed a tendency for reaction times to become faster depending on frequency, similar to the results of previous studies that measured frequencies from 60 Hz to 350 Hz. The average reaction time was faster at 500 Hz than at 240 Hz, suggesting that people recognize and respond to the switching speed at 500 Hz. Assuming that a person's average reaction time is constant when measured a sufficient number of times, the difference in reaction time measured at each frequency would indicate a delay in the display time of the system. As shown in the measurement in Fig. 4, there is a delay of one frame interval in the display. Since mouse clicks are handled with a maximum of one frame interval and a minimum of no delay, we can assume that the average delay here is 0.5 frame interval. 1.5 delays should appear in the measured response time when the two delays are combined. Table.4 shows the difference between the average reaction times of the five participants for the frequencies 500 Hz and 240 Hz and 240 Hz and 60 Hz. Compared to the calculated differences, both are about 10 msec faster. This implies a possible 10msec of monitor-independent delay. Alternatively, it cannot be ruled out that since the frequencies were verbally communicated during the experiment, this may have manifested a mental bias to think that one must respond faster at faster frequencies.

Table.4 Measured and theoretical values of reaction time delay due to differences in monitor frequencies reaction time lag

[msec]

Rection Time lag	Subject ID					Average	Expected	Average - Expected
	A	B	C	D	E			
60Hz - 240Hz	13.541	0.418	61.412	43.725	28.986	29.616	18.750	10.866
240Hz - 500 Hz	23.659	21.404	6.021	11.311	6.982	13.875	3.250	10.625

4. MOUSE CURSOR AIMING TEST USING 500Hz MONITOR

AimLab's SPHERETRACK90 mode was used in the previous study, while the 500 Hz test used the HEADSHOT(standard) mode. In SPHERETRACK90, the target appears anywhere in 3D space, whereas in HEADSHOT, the target appears in a horizontal straight line, as shown by the white arrow in Fig. 7. SPHERETRACK90 is a game in which the player keeps aiming at a target that keeps moving. HEADSHOT, on the other hand, is a game in which the target is aimed and fired at a stationary target. If the shot hits, the target immediately appears at the next location. If the shot misses, the target continues to fire until it is hit. This is repeated for one minute.



Fig.7 Target movement in HEADSET mode

Five participants played the game four times at each frequency in the order of 60 Hz, 240 Hz, and 500 Hz. The frequency settings were set to the specified frequency for all three game parameters: Maximum Frame Rate, Display Refresh Rate and Max UI Frame Rate. The viewing angle of the game was set to 110°. "Sensitivity," the amount of viewpoint movement per 1 dpi (dpi: dots per inch), was set by each player. Participants were given approximately 2 minutes to practice before the experiment began. During this time, participants could set their "sensitivity," which could not be changed until the end of the experiment. The DPI of the mouse used was DPI4 16000, and the function to change the speed of the cursor movement according to the mouse movement: "mouse acceleration" was set to off.

The average scores of the experimental participants normalized by their own scores at 60 Hz are shown in Fig. 8. Some participants scored higher using the 500 Hz monitor than they did using the 250 Hz monitor, while others scored lower. The average scores of the five participants tended to increase as the frequency increased, but the test did not reveal any significant difference between 240 Hz and 500 Hz.

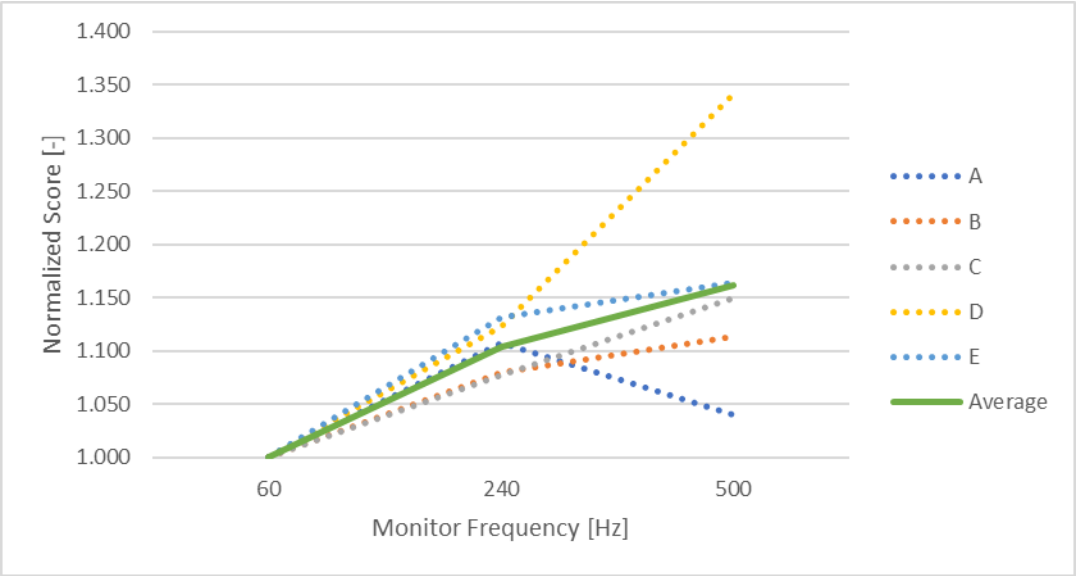


Fig.8 Average score normalized per participant and average score for all participants at 60,250,500 Hz

5. CONCLUSION

A simple reaction test and a mouse cursor aiming test was conducted using 500 Hz monitors. The results showed that, as in the tests up to 360 Hz, reaction time was faster with the 500 Hz monitor than with 60 Hz or 240 Hz. This suggests that people perceive the display at 500 Hz and respond faster to it. The faster the frequency of the monitor, the faster the person can see the image. However, the actual reaction time is faster than the theoretical delay calculated from this. This is in agreement with previous studies. This could be due to a delay that is not included in the theoretical value, or it could be due to the fact that the test was conducted by verbally presenting the frequencies, which may have influenced the feeling of having to respond faster to a faster frequency.

In the mouse cursor aiming test, the score was higher when using a 240Hz monitor than when using a 60Hz monitor, but no difference in score was observed between using 240Hz and 500Hz. The mouse cursor aiming test is more complex than the simple reaction test. As the game becomes more complex, it is suggested that not everyone can take advantage of the benefits of a high-frequency monitor in games with a frequency higher than 360Hz.

REFERENCES

1. **Tom Warren(2022) :** Asus announces world’s first 500Hz Nvidia G-Sync gaming display/144Hz isn’t enough anymore, Article of theverge.com, Online article, https://www.theverge.com/2022/5/24/23139263/

2. **Koshiro Murakami, Hideo Miyachi(1983) :** A Study on the Impact of High Refresh-Rate Displays on Scores of eSports, Lecture Notes in Networks and Systems, Vol., 313, pp.283-288
3. **Koshiro Murakami, Kazuya Miyashita, Hideo Miyachi** (2020): A Study on the Relationship Between Refresh-Rate of Display and Reaction Time of eSports, 3PGCIC2020, pp.339-347、DOI= https://doi.org/10.1007/978-3-030-61105-7_34
4. **Hideo Miyachi, Teruki Sawa(2024):** Impact of High Refresh Rate Display on eSports, proc. of The Ninth International Symposium on BioComplexity 2024 (ISBC 9th 2024), pp.1310-1313

SEATING POSITIONS AND BEHAVIORS IN VIRTUAL SPACE

Toma SHIBANO, *g2172062@tcu.ac.jp* Tokyo City University, 2248551, Yokohama, Japan

Hideo MIYACHI, *miyachi@tcu.ac.jp* Tokyo City University, 2248551, Yokohama, Japan

Sumire HIROTA, *sumire@tcu.ac.jp* Tokyo City University, 2248551, Yokohama, Japan

ABSTRACT

The purpose of this study was to investigate seating behaviors in VR office and to explore the appropriate design for the VR office, comparing with the results of Sommer's (1965) study in real settings. In 1st experiment, 19 pairs of male students were asked to perform the competitive and cooperative work in 2 VR offices for each. The results were different from the ones by Sommers (1965). Experiment 1 showed that the type of work had a different effect on seating position, with competing favoring a position near the front and cooperation favoring a position directly next to the front. In Experiment 2 the confederate seated the seat specified beforehand. As a result, regarding the angle between the gazes of each other, Sommer's two assertions that Opposite was preferred in Competing and Side by Side was preferred in Cooperating were not followed up in the VR space. The times for seating and the reasons to choose the seat were also measured in experiment 2. The reasonable design of the table in the VR office was discussed.

Keywords: VR office, seating behaviors, cooperating, competing

1. INTRODUCTION

The seating arrangement of a restaurant is an important factor in determining the ambience of a restaurant. A restaurant where all seating is at the counter is suitable for a single person eating lunch, but not for a dinner where groups meet for socializing. The relationship between seating arrangement and place is discussed in the field of architecture, which includes not only restaurants but also educational and general workplaces [1,2].

Seating arrangements are deeply related to the conditions at the time, rather than to good or bad arrangements, and human seating behavior has long been discussed in the field of environmental psychology[3-5]. However, experiments on seated behavior require the

construction of an experimental environment, which is costly, and there are difficulties in getting participants to the experimental site. However, today, with the development of VR technology, these constraints could be solved by conducting seating experiments in a virtual space such as a metaverse. We have therefore conducted a seating experiment in a virtual space in which two persons were asked to seat at a rectangular table with six seats , that was the same as Sommer's [6].

2. SOMMER(1965)'S EXPERIMENT

Sommer(1965) presented respondents with a picture of a rectangular table with six seats(Fig.1) and asked them to choose their preferred one from 6 seating positions, when they imagined to perform one of 4 tasks with other person; conversing, cooperating, co-acting and competing. The results showed that the preferred seating arrangement differed according to the type of tasks(Table 1). In the positioning illustrated on the right side of Fig. 1, "Side by side (B)" was selected by 51% of the cooperating group, accounting for about half of the six seating arrangements, and "Opposite (E)" was selected by 41% of the competing group, being the most preferred of the six seating arrangements.

Sommer suggested that this depends on the angle formed by the frontal orientation of the two seats. Though competing groups sit on opposite sides, cooperating groups preferred to sit side-by-side, where their gaze was in the same direction, and conversational groups chose Corner, where their gaze was orthogonal.

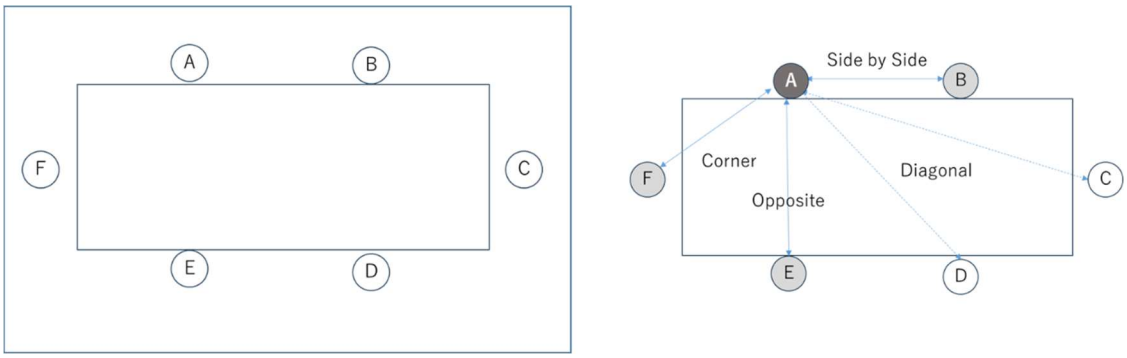


Fig.1 Picture of the rectangular table and seating arrangement used by Sommer in his experiments, and the results of his seating experiments.(The results were arranged and rewrite by Miyachi et al.)

Table 1. Sommer(1965)'s experimental results

Note. The table were rearranged by Miyachi et al.

	Relation	Combination	Competing	Cooperating
Near	Opposite	AE=BD	41	25
	Side by Side	AB=DE	8	51
	Corner	AF=BC=CD=EF	7	19
Distant	Opposite	CF=FC	18	0
	Diagonal	AD=BE	20	5
	Diagonal	AC=BF=CE=DF	5	0

2. OUR EXPERIMENT in VIRTUAL SPACE

A virtual space as shown in Fig. 2 was used for the experiment. A rectangular table with six seats was placed in the center of the meeting room in the virtual space. Two participants as two avatars started their seating behaviors by standing side-by-side at the "starting position" behind the table illustrated in Fig.2.

Assuming that the seating behaviors by two persons depends on the distance between two and the angle formed by their line of sight, the seating arrangement in this experiment was shown in Fig.3. It was a symmetrical seating arrangement, with two people seated along the long sides of the table and one person seated along the short sides of the table, as same as Sommer(1965)'s experiment. Moreover in our experiments all seating positions were strictly designed. Using seat A as the reference, the distances to its front (E), side (B) and diagonal side (F) seats were the same. If the distance from the reference seat to the front seat was D, the distance to the diagonal side (D) was 1.41 D and the distance to the long diagonal side (C) was 1.94 D. The angles from the reference seat to all five seats were different: when the front (E) was 0 degrees and positive anti-clockwise, the short diagonal side (F) was -60 degrees, the front (E) was 0 degrees, the diagonal front (D) was 45 degrees, the long diagonal side (C) was 65 degrees and the side (B) was 90 degrees.

3. IMPLEMENTATION OF EXPERIMENT ENVIRONMENT

The virtual space in Fig. 2 was modeled on the game engine Unity. It was exported to a social VR application: VRchat. Participants in the experiment entered the virtual space as avatars in a seated position wearing a head-mounted display type MetaQuest2, as shown in Fig. 4. The avatar can move around in the virtual space using a controller held in both hands. The operation of the avatar in the virtual space can be practiced for a sufficient amount of time using a different content from the office room used for the experiment.

The pair of the participants proceeded with the experiment in separate rooms .Thus, they could not see other's faces nor hear other's voices during the experiment, even when the head-mounted display was removed. As for the appearance of the avatars, a male avatar and a

neutral avatar whose face was covered by a mask were used, but since the difference between the avatars did not affect the experimental results, the appearance of the avatars is not discussed in this paper.

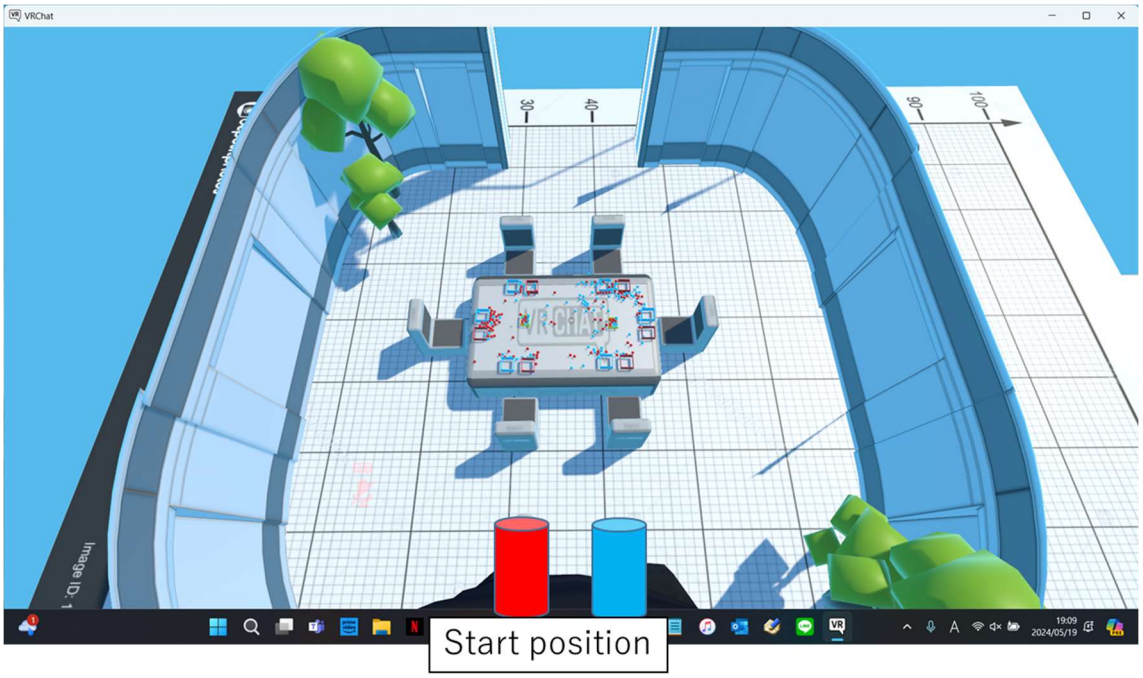


Fig.2 Appearance of the virtual space used in the experiment.

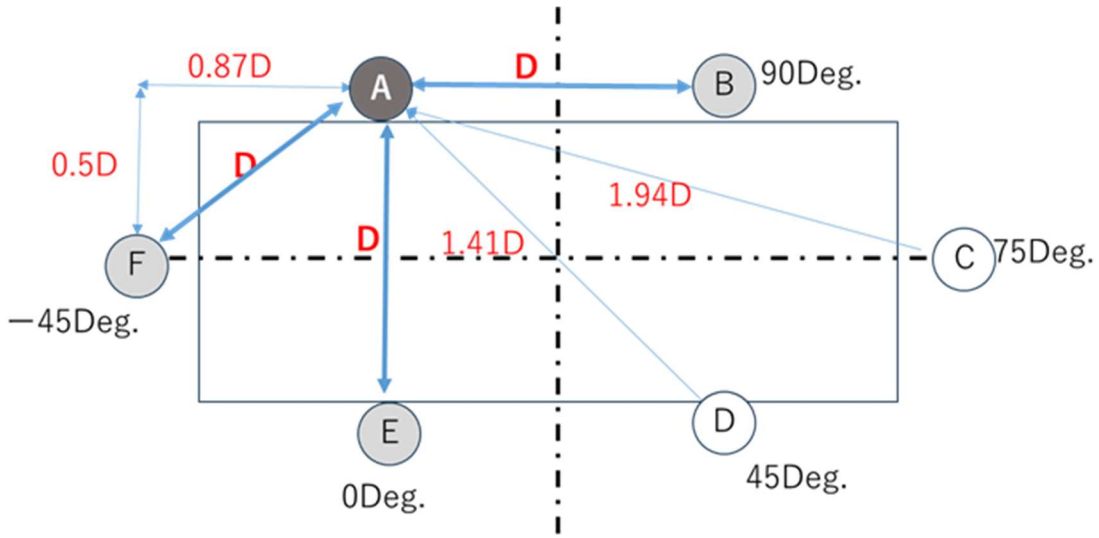


Fig.3 6 Design of seating arrangements in experiment 1.

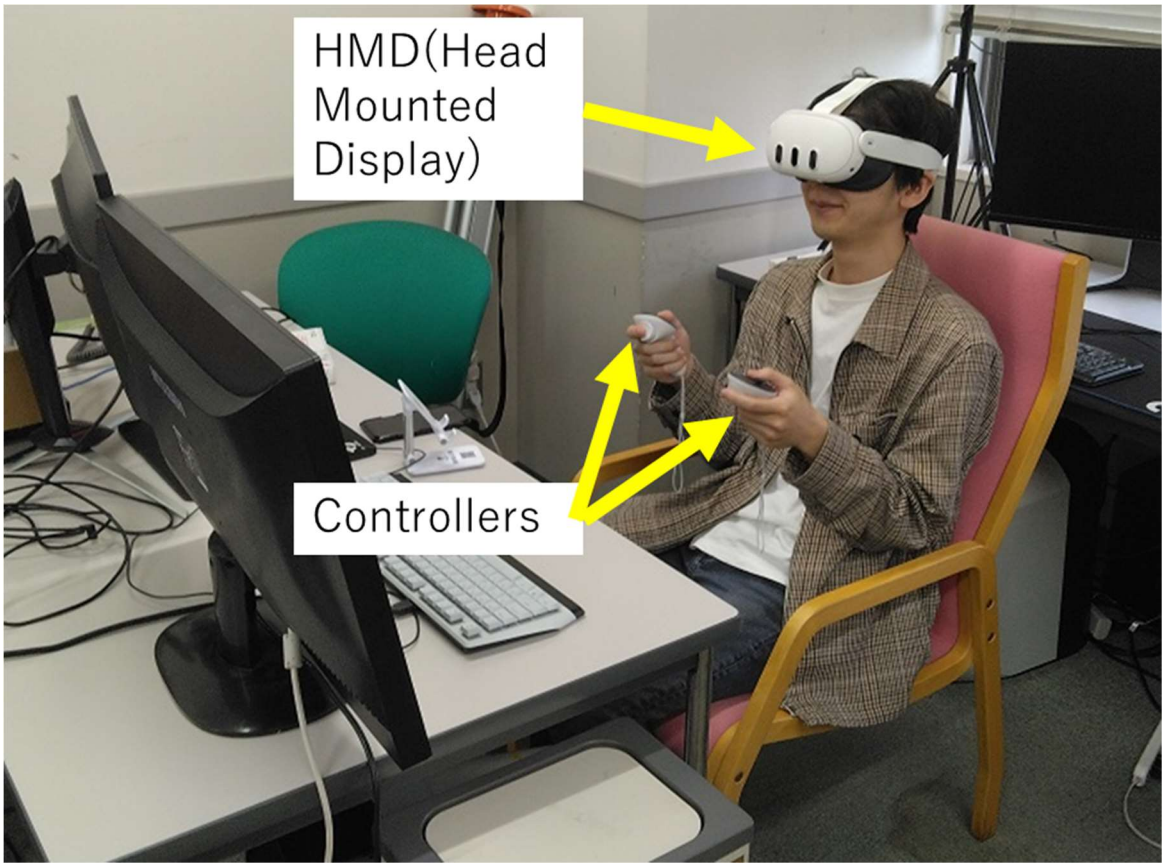


Fig.4 Participants in the experiment acting in a virtual space.

4. EXPERIMENT PROCEDURE

This study will test the seating behavior of two participants in a "cooperation" and a "competing" condition; the only difference between two conditions was the verbal instructions given to the participants before the seating behavior begun. In the "cooperation" condition, participants were told by the experimenter to "cooperate with each other to perform the task," and in the "competing" condition, they were told to "compete with each other to perform the task. The task was to classify and place the red and blue balls generated on the table into the red and blue boxes, respectively, as shown in Fig. 5. Each participant was asked to perform the task independently. Even in the condition of cooperation, the balls cannot be given to the other person or placed in the other person's box. Therefore the tasks in the two conditions were exactly the same. Although the task was performed, the behavior up to seating was observed in this experiment, and the behavior of performing the task itself was outside the scope of the experiment. The experiment procedure is described in Table.1.

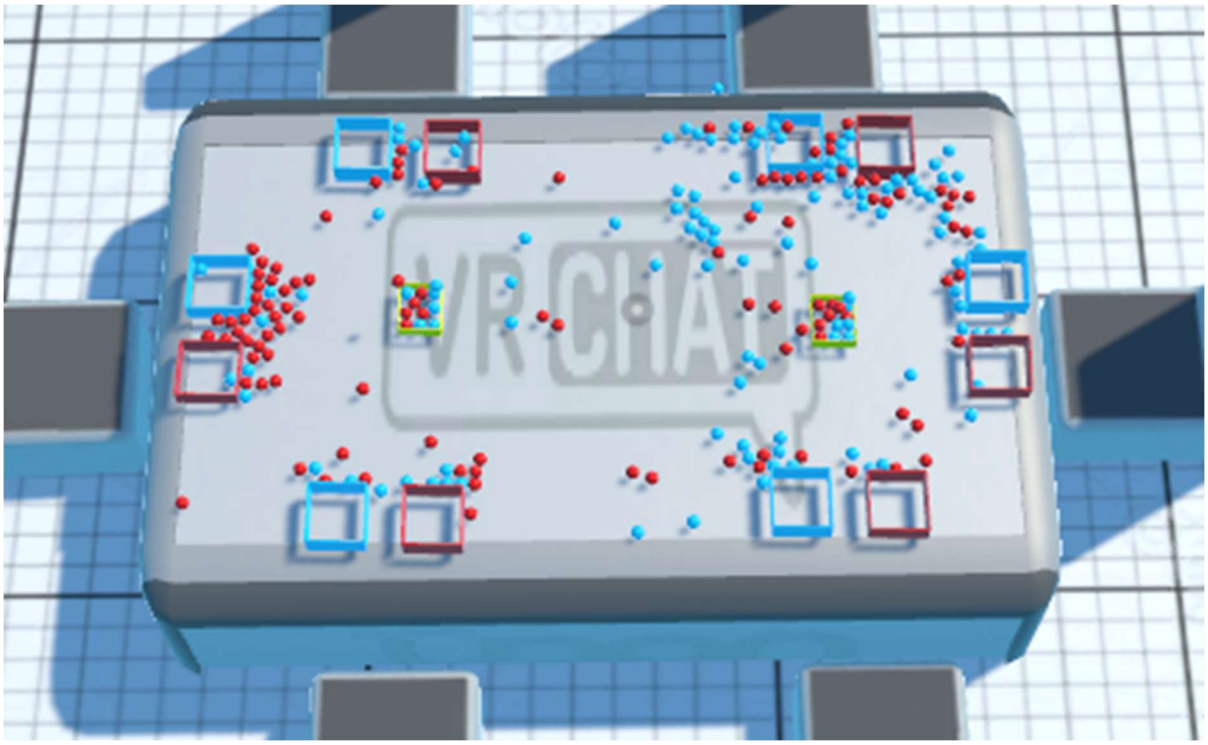


Fig. 5 Red and blue balls and boxes used in the games for the task

Table. 1 Procedure in Experiment 1

Number	Task
1	Enter the experimental room, seat, and wearing the head-mounted display
2	Maniplulation practiec in virtual space
3	Explanation of the experiment, singing of the consent from(HMD wil be removed during this time).
4	Instruction of Experiment 1
5	Task execution
6	Break (about 1min.)
7	Instruction of Experiment 2
8	Task execution
9	Removing the HMD and answering the questionnaire

5. RESULTS OF EXPERIMENT 1

Participants in Experiment 1 were 38 male college students recruited from a university free posting website. From this group, the experiment was conducted with 19 pairs, each pair consisting of two participants who were not acquainted with each other. Participants were paid the gratuities. In competing, AE and CF, which were the frontal positions, were avoided, with the majority of cases sitting in a side or diagonal position (17%-33%). The diagonal arrangement across the corner of the table was the most preferred at 33%. In cooperating, AD positioning was the most preferred at 42%, followed by AE and AF at 17%. These results differed from Sommer's results, which showed that the close frontal Opposite (AE) was more

often chosen in the competitive situation and the side by side (AB) directly next to each other in the cooperative situation.

Table. 2 Seating Behaviors in Experiment 1

[%]

Relation		Combination	Sommer(1965)		Exp.1	
			Competing	Co-oporating	Competing	Co-oporating
Near	Opposite	AE=BD	41	25	0	17
	Side by side	AB=DE	8	51	25	8
	Corner	AF=BC=CD=EF	7	19	33	17
		sum	56	95	58	42
Far	Opposite	CF=FC	18	0	0	8
	Diagonal	AD=BE	20	5	17	42
	Diagonal	AC=BF=CE=DF	5	0	25	8
		sum	43	5	42	58

6. EXPERIMENT 2

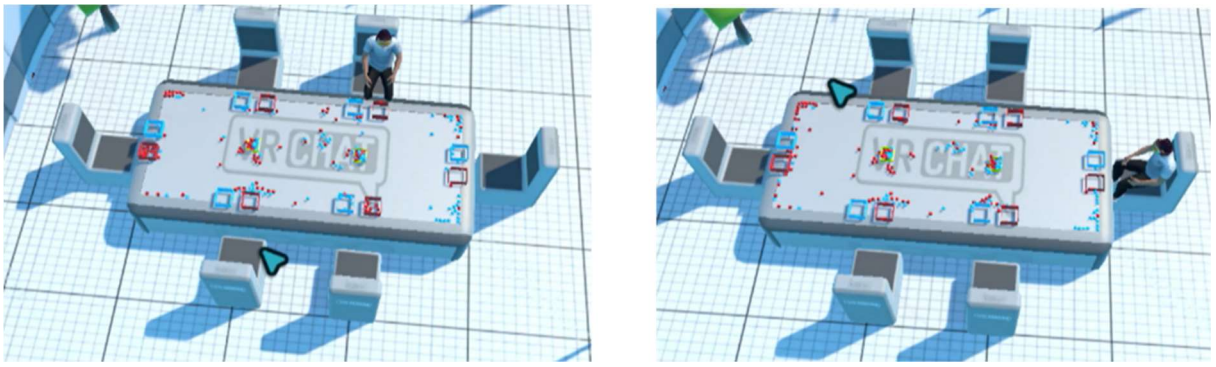
Unlike Sommer's results, Experiment 1 showed that the type of work had a different effect on seating position, with competing favoring a position near the front and cooperation favoring a position directly next to the front. This indicates that VR spaces may have different effects on human seating behavior than real spaces. Previous research in environmental psychology has suggested that distance to humans and eye contact are important factors influencing seating position. The reason why interpersonal distance is influential is that, as pointed out by E. Hall (1966) [7], not only visual distance but also warmth and smell generated by the partner's body are cues in the real environment. In addition, past research has shown that gaze has a strong influence on proxemics (Kleinke, 1986, for a review of psychological research on gaze) [8]. auditory cues were also absent in the experiment. Therefore, it is possible that visual cues, including eye contact, played a stronger role in the results of Experiment 1 than in the real space, and that the participants in the competitive condition, in which they were more aware of their partner, preferred the front location where the partner was completely in view, while in the cooperative condition, in which they were less aware of their partner, they preferred the side location where the partner was out of view rather than in view.

However, it was not clear from the results of Experiment 1 whether angle(gaze) or visually perceived distance worked more strongly depending on seating position. Therefore, in Experiment 2, with confederate's seat fixed, the goal was to determine whether perceived distance or angle had a stronger influence.

7. PROCEDURE OF EXPERIMENT 2

The experimental space in VR and the experimental environment were the same as those described in 2 and 3. However, it differed from Experiment 1 in that the confederate was seated in Seat B in advance. Seat B was the opposite side of the entrance or seat C on the far right, as shown in Fig. 6. This avatar was controlled by the experimenter. The avatar remained seated during the seating behavior and did not move its head or look at the other avatar, but simply remained still, like a puppet, waiting to be seated. It then performed the task on cue, which was outside the scope of the experiment.

As in Fig. 2, the participants begun the seating behavior by standing in the center of the front side of the Fig.2. Though in Fig. 2, two participants stand side by side, in this experiment, at the start, one participants stood in the middle position of the two participants in Fig.2. After being instructed by the experimenter to perform the cooperating task, the participant performed the seating behavior and then perform the cooperating task after seated. Once the task was completed, the participant put off HMD, and took a break. Next, the participant was instructed to put on the HMD and performs the competing task. And the participant performs the seating behavior and the competing task after seated. After completing the task, the participant puts off HMD and the other avatar was revealed to be operated by the experimenter. Finally, the participant filled out a Google Form questionnaire in the experiment room. In this questionnaire, the participant described the reason for seating with an open-ended question.



Pre-seated avatar sits in seat B. (b) Pre-seated avatar sits in seat C

Fig. 6 Scene at seating behavior starting

8. RESULTS OF EXPERIMENT 2

The participants in this experiment were seven male university students who were recruited as volunteers by those involved in the experiment. Each of these seven participants was paired with the confederate and were asked to seat freely and perform the competitive/cooperative tasks. The results were shown in Table 4. Of the seven pairs, four pairs started the experiment with the scene in Fig. 5(a), and three pairs started with the scene in Fig. 5(b).

Table. 3 Experiment procedure in experiment 2

Number	Task
1	Enter the experimental room, seat, and wearing the head-mounted display
2	Maniplulation practiec in virtual space
3	Explanation of the experiment, singing of the consent from(HMD wil be removed during this time).
4	Instruction of Experiment 1 （cooperating). *confederate was already seated in B
5	Task execution
6	Break (about 1min.)
7	Instruction of Experiment 2(competing) *confederate was already seated in B
8	Task execution
9	Removing the HMD and answering the questionnaire
10	debreifing

Table. 3 Seating Behavior in Experiment 2

[%]

Relation		Combination	Sommer(1965)		Exp.1 (n=38)		Exp.2 (n=7)	
			Competing	Co-oporating	Competing	Co-oporating	Competing	Co-oporating
Near	Opposite	AE=BD	41	25	0	17	14	43
	Side by side	AB=DE	8	51	25	8	0	0
	Corner	AF=BC=CD=EF	7	19	33	17	57	29
		sum	56	95	58	42	71	71
Far	Opposite	CF=FC	18	0	0	8	14	14
	Diagonal	AD=BE	20	5	17	42	0	14
	Diagonal	AC=BF=CE=DF	5	0	25	8	14	0
		sum	43	5	42	58	29	29

(1) Distance and angle (Gaze)

Regarding distance, Near was preferred in cooperating tasks as similar to Sommer's results. Near was the dominant position in this experiment at 71%. However, Near was also selected 71% of the time for Competing.

Regarding the angle between the gazes of each other, Sommer's two assertions that Opposite was preferred in Competing and Side by Side was preferred in cooperating were not followed up in the VR space. The order of cooperating and competing was fixed; cooperating first and competing later. This series of experimental procedure is shown in Table.3.

(2) Time for seating behavior

In experiment 2, the time for seating behavior was measured. As each participant performed seating behavior twice, the times were measured in 14 times. However, one experiment failed the measurement due to an accident. The measured time ranged from 3.5 seconds to 28.6 seconds, with the average time of the 13 experiments being 11.6 seconds. The average time for the first and the second were different, 15.3 seconds for the first (cooperating) and 7.4 seconds for the second (competing). This means that the seating behavior was not the same

between the first and the second time. It was found that the order of the task needed to be reversed.

(3) Details of reason for seating

Table 5 shows the reasons for the conscious choices made by the participants in the experiment. There were five reasons for selection. Reasons related to positional relationship with the other person include (A) selecting a seat where I can see the other person, (B) selecting a seat facing the other person, (C) selecting a seat near the other person.

Reasons A and B were related to the visual contact pointed out by Sommer. Five cases were for reason A, but the selected position were not the same. The number of selections for Opposite and Diagonal was almost equal. Among 4 cases of selecting B, three cases were for cooperating tasks which was more than for competing tasks. It differs from Sommer's results. In 3 cases for C, the Corner was preferred. In the design, Opposite and Corner has the same distance, but it seems that the Corner feel closer than Opposite crossing the table.

Reasons not related to positional relationship with the other person include (D) selecting a seat close to the entrance, and (E) selecting a seat that seems advantageous for the game. Three cases were for reason D. The closest seats to the entrance were D and E, which were equidistant from the entrance. In the case of the pre-seated person in C at the end of the table, both D and E become diagonal position, so any discussion of the angle is meaningless. In the case of the pre-seated person in B, D and E are Opposite, so a discussion of the angle is possible. Three cases for reason E were selected in competing condition. One participant wanted to steal the opponent's ball and two participants stated that it looks to be more balls around seat C, regardless of the opponent's seat.

Table.5 Experiment participant's intended reason for seating

		Relationship with the partner			Environmental reason	
		Easy to see	Partiner's front	Close to partner	Close to entrance	Game advantage
cooperating	opposite	1	3			
	diagonal	1		1	2	
competing	opposite	2	1			
	diagonal	1		2	1	3

9. CONCLUSION

The seating behavior in VR space does not conform to Sommer’s rules. In experiment 1, there was no difference in the distance between the seats selected in either Co-operating or Competing. In experiment 2, the results were consistent with Sommer's results that Near seats were preferred in Co-operative, but close seats were also preferred in Competing, so it

indicates that there is no close relationship between task condition and distance on seating behavior in VR space.

On the other hand, the angle had characteristics that differ from real space in VR space. Sommer's conclusion that side-by-side, where the gazes face in the same direction, is preferred in cooperating, was not supported in VR space. Furthermore, side-by-side is not selected in VR space regardless of the task. Table 5 showed that participants wanted to see the other person regardless of the seat selection. In the case of VR, the field of view is narrowed by wearing an HMD, and it is thought that side-by-side is eliminated as a choice because it becomes very difficult to see the other person.

By asking about the reasons for their choices, issues with the experimental method were also made clear. Operating in a VR space is difficult even with some practice, so consideration should be given to the location of the entrance so as not to affect seating behavior. As the game itself sometimes affected the seating behaviors, information related to advantages and disadvantages in the game should not be given. The time for seating behavior showed a time difference between the first and second times, it indicated that the order of the tasks might have affected seating behavior.

REFERENCES

1. **Robson,S.K.A. (2008),** Scenes from a restaurant: Privacy regulation in stressful situation, Journal of Environmental Psychology,Vol.28,pp 373-378
2. **Muto, H. et al (1996)**, Study on space for intellectual creation, part 3：Effect for intellectual creation activity through movement of meeting or refreshment space, Summaries of Technical Papers of Annual Meeting, Architectural Institute of Japan, Architectural Planning and Design 1, pp.781-782（in Japanese）
3. **Cook,M. (1970)**, Experiments on orientation and proxemics, Human Relations, Vol.23,No.1,pp 61-76
4. **Solverstein,C.G., & Stang, D.J. (1976)**, Seating position and interaction in triads: A field study, Sociometry, Vol.39,No.2, pp 166-169
5. **Becker, F. D., Gield, B., Froggatt, C. C (1983)**, Seating Position and Impression Formation in an Office Setting, Journal of Environmental Psychology, Vol.3, pp.253-261
6. **Sommer, R. (1965)**, Further studies of small group ecology, Sociometry, Vol. 28, pp 337-348

7. **Hall, E,T, (1996)**. The Hidden Dimension: An Anthropologist Examines Man's Use of Space in Private and Public; Anchor Books; Doubleday &Company Inc.: New York, NY, USA.
8. **Kleinke, C. L. (1986)**, Gaze and eye contact: A research review, Psychological Bulletin, Vol.100, No.1, 78–100, https://doi.org/10.1037/0033-2909.100.1.78

The study was approved by Ethics Review Committee on Human Research of Tokyo City University (No.2022-h12）

Architecture of Autonomous Avatar and VR Simulator for Various Training Purposes and Situations

Tomohiro TANIKAWA, *tani@cyber.t.u-okyo.ac.jp* The University of Tokyo, 1138656, Tokyo, Japan

ABSTRACT

In mechanical design, it is extremely important to consider what kind of interactions with people will occur in the usage situation. However, the evaluation from the viewpoint of the human interface, i.e., how people will use the machine, is currently conducted by actually using the machine by people. We propose the use of VR to reproduce the situation in which the machine will be used, and to verify. In this paper, we present a pilot implementation of a VR simulator and an architecture for autonomous avatars. In this paper, we present a pilot implementation of a VR simulator and an architecture for autonomous avatars that can simulate not only physical simulations, but also take into account human emotions and attention.

Keywords: Human Factor, Behavior Simulation, Virtual Reality

1. INTRODUCTION

Virtual reality has been applied in various manufacturing industries. In particular, in machine design, physical simulation has enabled the creation and evaluation of mock-ups from a first-person perspective, manufacturing and maintenance/inspection training, and design support for manufacturing plants. Currently, Japan's industrial structure is changing, with a shift to service industries in addition to manufacturing, and human factors are playing an increasing role in industry, not only in the handling of physical objects.

In conventional VR in the manufacturing industry, simulation of objects plays a major role, but in the service industry, VR systems that encompass people are needed in many cases where people are involved. In addition, the importance of education and training systems that include people is being recognized not only in the service industry but also in various other industrial fields. In Japan in particular, there is a need to improve the working environment from the perspective of workers, such as reducing long working hours and caring for emotional labor as part of the workplace environment. In addition, the utilization of a wide range of human

resources and the improvement of work efficiency and productivity have become pressing issues due to the declining labor force caused by the falling birthrate and aging population. Therefore, this study reports on a VR simulator (Figure 1) that can handle various situations involving people and for training purposes, and on a VR system architecture that enables autonomous avatars to realize training involving people.

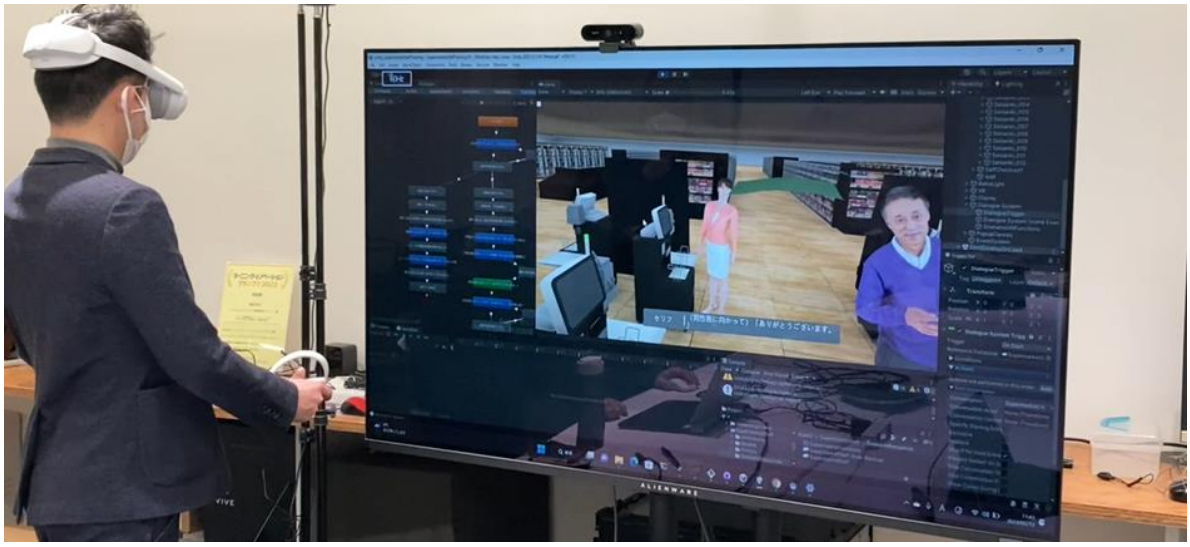


Figure 1 VR Customer Service Training System.

2. VR Simulator

VR Simulator for Manufacturing industries

There are many things that cannot be learned without actual experience in the manufacturing field. For example, there are procedures to assemble things and situations to inspect machines that require learning while working, rather than learning in a classroom, and VR will be optimal for such applications. In addition, training can be conducted more efficiently by recording the work procedures of skilled workers and using them as references; target machines and parts can be reproduced in VR space, and manufacturing and maintenance/inspection training can be conducted safely and in a manner that is nearly realistic [1-3]. In addition, by utilizing VR technology and physical simulation, more accurate simulations can be performed from the design stage. In the case of simulations using models and rapid prototyping, it is difficult to represent things at full-scale, and errors between the actual product and the model are inevitably large. On the other hand, VR space can be used to represent the actual size of the product, making it possible to create a highly accurate simulation that is closer to reality.

VR Simulator of Human Activities

In recent years, simulations of human and vehicle flows in planned cities and buildings have come to be used in the design of cities and buildings [4.5]. By modeling people's movements and behavior patterns and reproducing them on a computer, it is possible to predict human flows and plan congestion and efficient routes under specific conditions. For example, it is used for events to predict in advance the flow of people and congestion in a venue to ensure safety and efficiency. Furthermore, crowd simulations are being introduced as VR simulators with the aim of providing users with a highly immersive experience. In order to realize a realistic world, it is necessary not only to provide a space and manipulable objects, but also to have people, such as virtual characters and crowds. In games, virtual characters are assigned roles and speak and move according to scenarios, and similar mechanisms are used in VR systems. On the other hand, in metaverse and online games, not only virtual characters but also real people log into the same space as avatars and interact with each other through the avatars in the same way as in real space.

VR Simulator for Service Industries

Customer service, which is the target of the service industry, is based on human-to-human communication, which is fundamental to human life. Service providers need to respond appropriately to customer requests without causing discomfort to the customer, as well as to respond based on consideration and care for the customer's situation as appropriate. Training in such customer service has traditionally been provided through on-the-job learning in the field or under the guidance of an instructor. Video/video-based training is also becoming more common. The global pandemic of a new coronary infection (COVID-19) has had a significant impact on forms of customer service and response, and remote customer service and remote training are becoming more common.

Furthermore, with the recent development of network technology and virtual reality technology, progress has been made in the shared virtual space, the metaverse, which is becoming a new field for customer service. At the same time, new business training attempts using VR technology have begun. Furthermore, the introduction of artificial intelligence technology into work training is expected to solve the situation where it is difficult in terms of time and space to prepare a real environment for assumed training situations, and also to make it possible to repeat specific training situations based on the trainee's training status and level of proficiency in order to effectively acquire work skills in customer service. The VR simulator is expected to make it possible for trainees to learn customer service skills effectively. Therefore, the authors have been studying a mechanism to enable the deployment of VR simulators from the manufacturing industry to the service industry [6.7].

3. Autonomous Avatar and VR Training System

In the development of such a VR work training system, the introduction of AI technology and an autonomous avatar driven by AI are necessary for the progression of training scenarios and the evaluation of training results. The following technical items can be processed by AI to enable automated training and evaluation, and the functionality of the system as a VR-based system can be utilized more effectively.

- The system analyzes the trainee's speech, analyzes its content, and recognizes it, thereby generating a corresponding response on the part of the customer.
- Recognize the trainee's response (speech, movement, etc.) and emotional state to the client's response, and adjust the progression of the training scenario based on these responses.
- Recognizing the trainee's response (speech, movement, etc.) and emotional state to the customer's reaction, and based on these series of situations, evaluate the appropriateness of the response from the perspective of job skills.
- Based on the trainee's speech, which stage of the service process is in progress in the training scenario is ascertained, and changes in the trainee's response patterns and emotional state are analyzed and their characteristics are evaluated.

Based on the above, the following stages can be considered for the use of AI in VR training systems.

Phase 1 Avatar that plays back the measured data as is

Phase 2 Avatars that actually have direct human control over their movements.

Phase 3 Avatars that utilize actual measurement data and are indirectly controlled by humans according to the situation.

Phase 4 Avatar that utilizes actual measurement data and reacts simply by motion recognition and voice recognition.

Phase 5 Avatars that automatically generate advanced recognition and response based on analysis of measured data

As the phase progresses, AI will be actively utilized, enabling the development of operational training systems that can respond to more advanced situations and accordingly.

Phase 1: VR training systems that allow users to experience 360-degree full-circumference images captured by a 360-degree camera using an HMD are well-known. These systems provide a highly realistic experience of what it would be like to actually be that person. However,

because the system plays back the captured images as they are, the interaction is limited to looking around, and the training content cannot be changed in response to the user's manipulation or speech.

Phase 2: The trainee operates the staff avatar and another person operates the customer avatar, and they interact with each other in the VR environment. It is a remote VR system in which multiple people share the same VR environment via a network, and it is a method that is ready to be deployed for business training on the metaverse due to its high affinity with the metaverse. In reality, the human client is the trainer, which makes it possible to respond flexibly to the trainer's situation and responses, but it is necessary to prepare a person to respond to each training session. Therefore, the response may vary from person to person, resulting in variations in the content and quality of the training.

Phase 3: Using pre-recorded data and motion capture data, a person monitors the trainee's situation and speech content, and controls the scenario content and the client avatar's reactions as appropriate. Since human recognition of speech and motion is performed, it is possible to flexibly respond to situations in which the meaning is the same but the way of saying it is different. As in Phase 2 above, human intervention has the disadvantages of human resources and inconsistency in response, but since human intervention is provided as an educator, it may be effective depending on the purpose of the work training.

Phase 4: Similar to Phase 3, the system uses pre-recorded recording data and motion capture data, recognizes the trainee's situation and speech content using speech and motion recognition programs, and enables the client avatar to respond using pre-defined speech and motion based on a stimulus-response model (Figure 2). The system is complete within the VR system, allowing for fast response times. In order to realize flexible responses according to the content of the training, it is necessary to create scenarios according to what kind of voice, behavior, and emotional state the avatar is in. On the other hand, if the scenarios are well-developed, it is possible to create customer avatars that make the user feel as if they are responding in the same way as real people.

Phase 5: A mechanism for a fully autonomous avatar, which is the final goal of the project(Figure 3). This is a method to realize a complex AI avatar. In order to link the AI part, which performs complex analysis, and the VR system, which requires responsiveness without delay, it is necessary to use a stimulus-response model that prioritizes responsiveness, which was used in Phase 4, and also to use advanced judgment in accordance with the situation. In addition, by automatically generating scenarios based on customer service data collected in advance and utilizing them in the VR business training system, a more flexible business training system that can respond to trainees and changing situations can be realized.

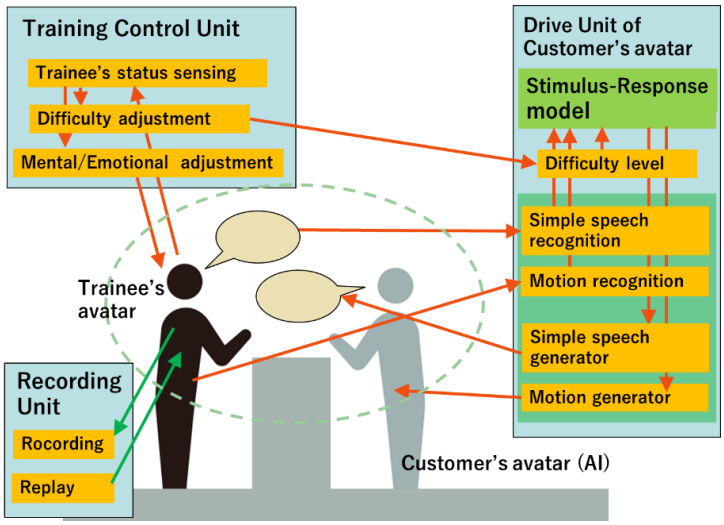


Figure 2 System diagram of VR Training system (Phase 4)

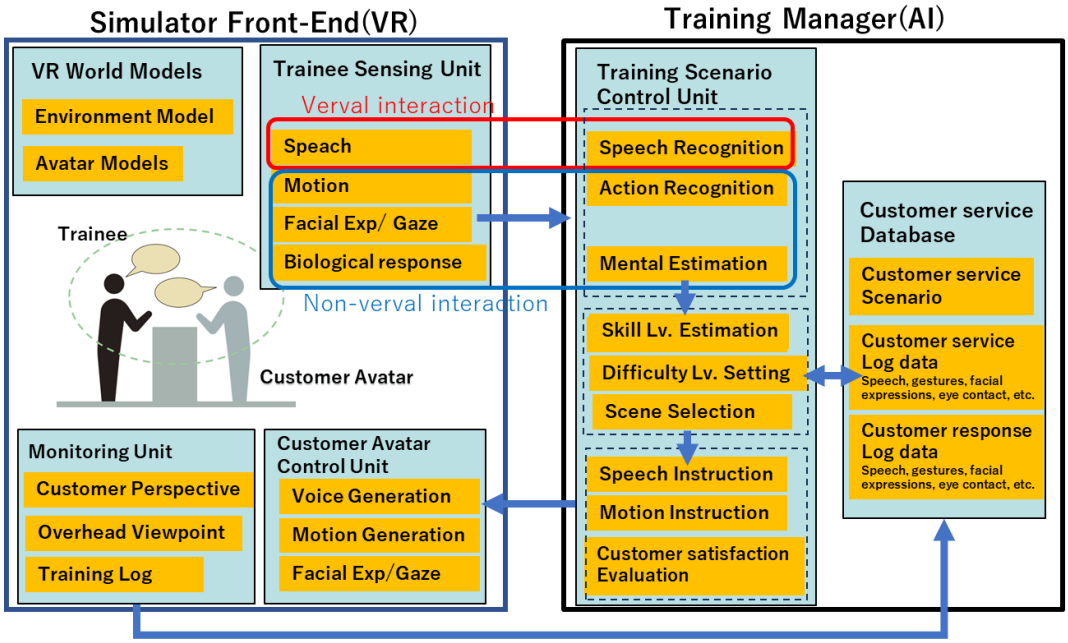


Figure 3 System diagram of VR Training system (Phase 5)

In training that takes advantage of the features of VR, it is possible to replay, rewind to the point of failure, and replay from the customer's point of view, etc., and educational effects and clarification of problems that exceed those of training using actual workplaces can be expected. In addition, in business training using the VR business training system, all the actions and responses of the trainer and customer avatars, as well as their biometric information and emotional states, can in principle be collected, since everything is used to realize the VR experience. In steps (1) to (4), the customer avatars and the trainer's level of customer service are evaluated and managed by human intervention, so they can be effectively used as training data for building an AI. Therefore, the introduction and continued use of the VR business training system can be expected to improve the AI and the content of business training.

3. Prototype VR Training System

Based on the above concept, a prototype system including hardware and software was constructed to provide training for service industry workers (Figure 4)[8]. The simulator is based on a scenario in which the trainee is working as a staff member of a company, and is trained to perform customer service tasks on an autonomously operating customer avatar. In order to effectively train service skills, the simulator estimates the trainee's psychological state during the experience and evaluates the service skills. A simulator that utilizes VR technology for business training requires an environment/avatar model, a verbal interaction module, a nonverbal interaction module, and an evaluation module (Figure 5). This is because the service industry requires both verbal and non-verbal skills, and because role-play training with an AI as a teacher can remove temporal and spatial constraints by using an autonomous avatar as the opponent.

The evaluation module should be developed with an eye to assessing training proficiency, but the evaluation of non-verbal interaction performance, in particular, varies from company to company, making a uniform evaluation difficult. Therefore, it is essential to construct a recording system that allows a skilled teacher to review video records of training and logs of movement and interaction in the system after training and give feedback. In addition, the evaluation module includes an evaluation of the trainee's psychological state, such as stress, etc. The autonomous avatar equipped with AI changes its next response based on the trainee's response skill and psychological state, such as stress value.

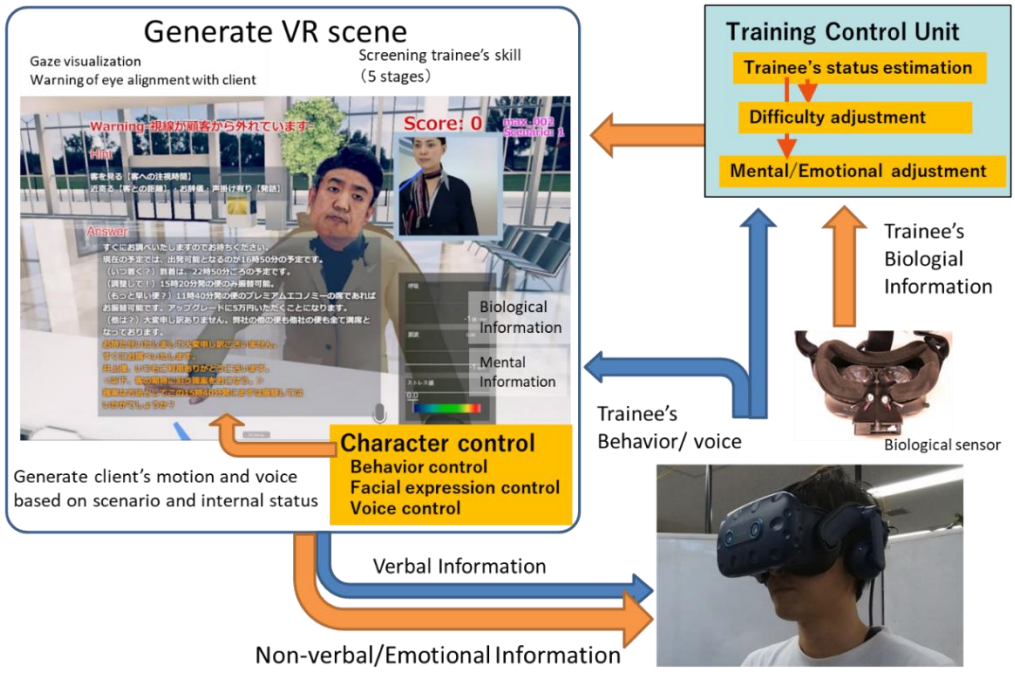


Figure 4 VR Training System for Service Industries

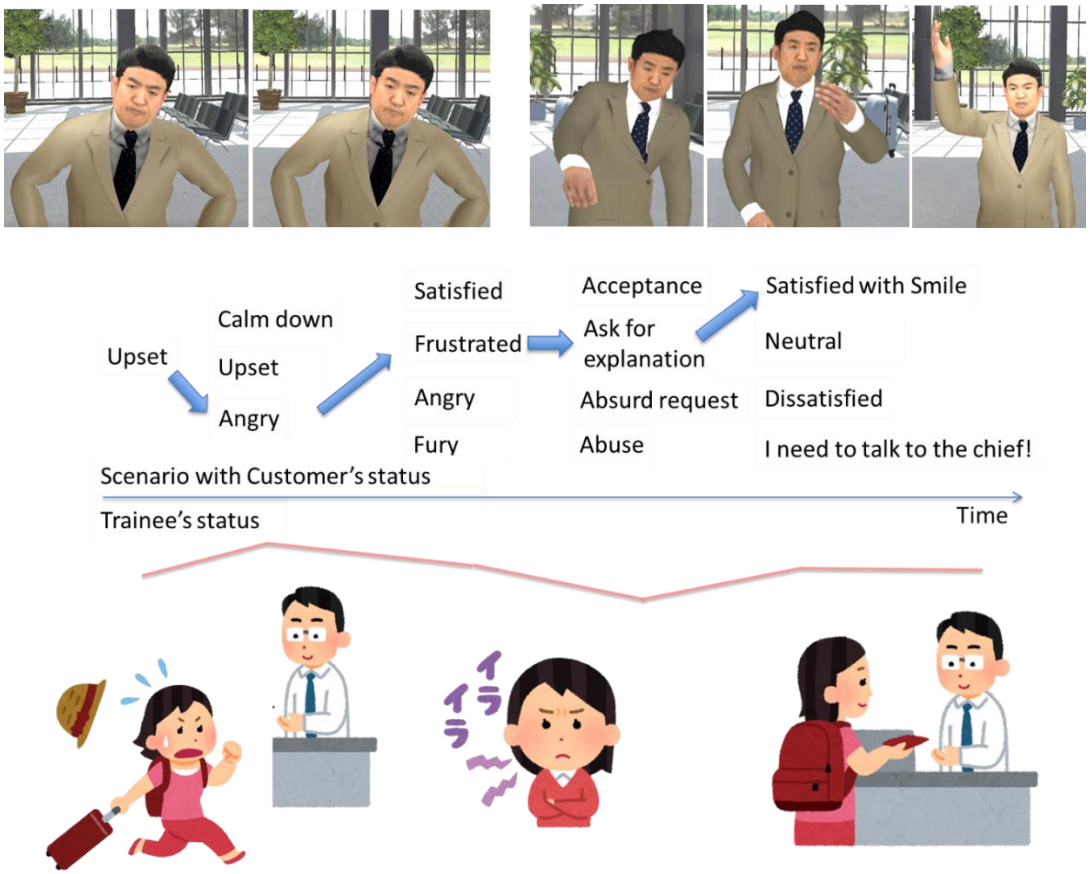


Figure 5 Internal state and Behavior of Autonomous Customer's Avatar

3.1 VRESS: VR Editable Scenario System

A VR system for training customer service operations needs to realize training in skills involving emotions and feelings (emotional skills), which are extremely important in terms of service quality, in order to understand the intentions and feelings of customers and respond appropriately. However, the content of each industry is very different, and there is a wide range of content to be trained, making the cost of development, operation, and customization difficult. The creation of VR content requires knowledge and specialized skills in game engines and programming. In order to enable users to experience various situations in their work, it is necessary to gather personnel who are familiar with the content of service work, who can think about VR training content and scenarios, and who can produce VR content, and to spend time building the system. In addition, when modifying an existing VR system or updating hardware or game engines, specialized skills are also required, and this requires a request to the developer for modification, which is costly and time-consuming. Therefore, we thought that a platform that enables VR content creation and modification using a method called low-code

development, which enables modularization of necessary functions and content creation using GUI, as in the case of web application development, would be effective. In this platform, VR parts (3D models, motion, sound, etc.) and templates are prepared in advance, and by combining them on the GUI with mouse operations, application development and modification become possible.

In this study, we implemented the system as a "VR Editable Scenario System: VRESS," which can be built in low code. The overall structure of the platform is shown in the figure. The VR system is a composite of space, people, and things, and was designed so that each can be handled as separately as possible. The training space and human models are prepared as 3DCG models, and events and human behaviors are managed based on scenarios (Figure 6). The core of the platform is a scenario editor that allows users to create scenarios by arranging and integrating each scene using a GUI. A VR scene is an assortment of various elements such as environment information, character information, and event information (what happens when you do what). On conventional platforms, all of these elements are registered one by one in unity and implemented by writing scripts, making it difficult to grasp the whole picture even for minor scenario modifications. On the other hand, the low-code platform allows scenario editing through a GUI, which facilitates on-the-spot modification.

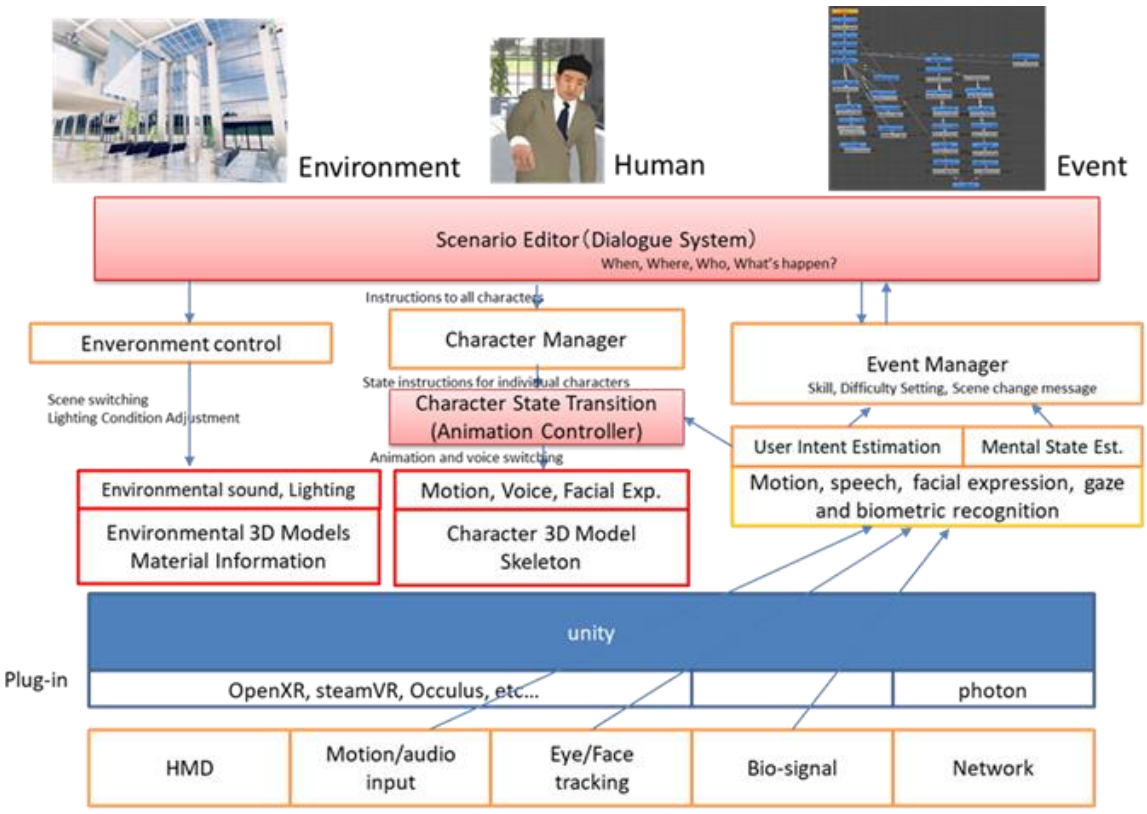


Figure 6 Overview of Proposed Low-code VR Platform VRESS

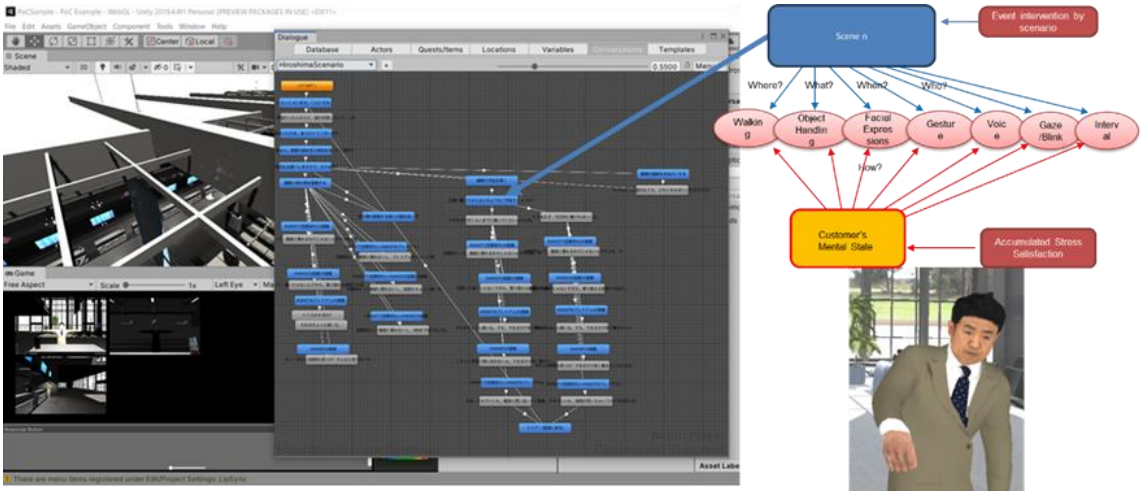


Figure 7 Relationship between Editable Scenario System and segmented VR Scenes.

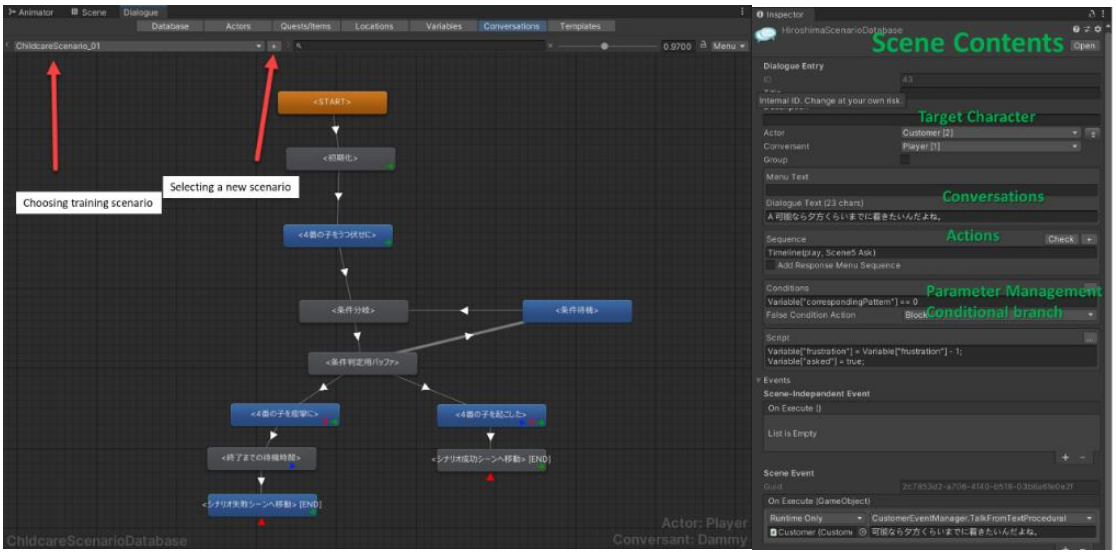


Figure 8 (left) Scenario Editor (right) Inspector of each node.

3.2 Scenario Editor Function

The scenario editor, which can be edited via GUI, was implemented by customizing the Dialogue System [9]. As shown in Figure 7, when the project is opened, there is a scenario editor area with individual scenes that have been segmented in advance and are connected to each other as nodes. Each scene can be configured to specify which characters are to be moved and what they are to say, as well as how stress values and customer satisfaction levels are to be changed. Scenarios can be extended by right-clicking to add a scene as a node, or by creating a link from an existing node. Scenarios can be modified intuitively by deleting and re-linking. Each node can specify which person performs which action, which sound, etc., and

can be used to change the parameters of the person's state or to perform conditional branching by writing simple scripts for judging events or changing states.

3.3 People Manager and Event Manager

In addition, we have developed VR-specific functions that cannot be realized with the standard Dialogue System and added them as an event manager. The customer service training VR system commonly requires functions to handle both verbal and non-verbal interactions. For verbal interaction, we implemented a function that performs speech recognition using the Web Speech API via Websocket [10] and determines whether the user has given the expected response. For nonverbal interactions, we implemented a function that recognizes eye gaze and movement in unity, senses biometric signals and estimates stress state in an external program, receives them in unity via UDP communication, sets the difficulty level, and determines whether to proceed with the scene or not.

In addition, functions (functions) added as project-specific functions, such as the behavior and state of characters, are grouped under the person manager. For example, in the case of a training system for a nursery school, various behaviors of young children were added in the form of "since they have not been added to the existing platform," and can be called from the scenario editing screen. In addition, the person's state can be set to transition using unity's Animation Controller function.

4. CASE STUDIES

Preliminary Through preliminary demonstrations and interviews, we asked four companies that showed interest to cooperate in participating in the demonstration experiment, and based on the interviews, we implemented and experienced the VR training system. (Figure 1).

4.1 Implementation of a business training VR system

Figure 9 shows the implementation screens of VR training systems developed simultaneously using this platform for completely different industries, such as retail, passenger, and daycare, respectively. Each of them has a scenario editing screen on the left, where scenarios for each industry are edited. The VR training system for nursery schools was previewed on December 21, 2022, and a demonstration experiment was conducted on February 24, 2023; the VR training system for the retail industry was demonstrated on February 14 and 17, 2023, with the participation of two companies; and the VR training system for hotels was demonstrated on February 20, 2023. The VR training system for hotels was tested on 2/20/20, 2023. As described above, the completion dates of the VR training systems for three completely different industries were concentrated within a two-week period, and the

development had to be carried out simultaneously. The 3D models and voices were socially outsourced, scenario editing was done by a different person from the developer, and scene creation and system implementation were done by one person.

4.1.1 VR training system for nursery schools

In this VR training system, infants are checked during naptime, and they randomly perform actions such as lying face down, stopping breathing, and getting up (Figure 7, top). The trainee detects and handles infants who need attention such as napping on their stomachs, and if the trainee fails to detect them, the trainee experiences a failure scene. The HMD also has a biosignal sensor attached to the HMD, which enables the trainee to check the stress level during the experience.

4.1.2 VR training system for hotels

In this VR training system, participants can switch between three different scenarios ((1) scenario in which they could handle the situation without any problems, (2) scenario in which the room is different from the one they reserved and a room is available, and (3) scenario in which the room is different from the one they reserved and a room is not available). (1) scenario that was handled without any problems, (2) scenario different from the room reserved, room available, (3) scenario different from the room reserved, room not available). The same way, the staff's subjective viewpoint and the images from the surveillance camera are displayed to allow recording and replaying.

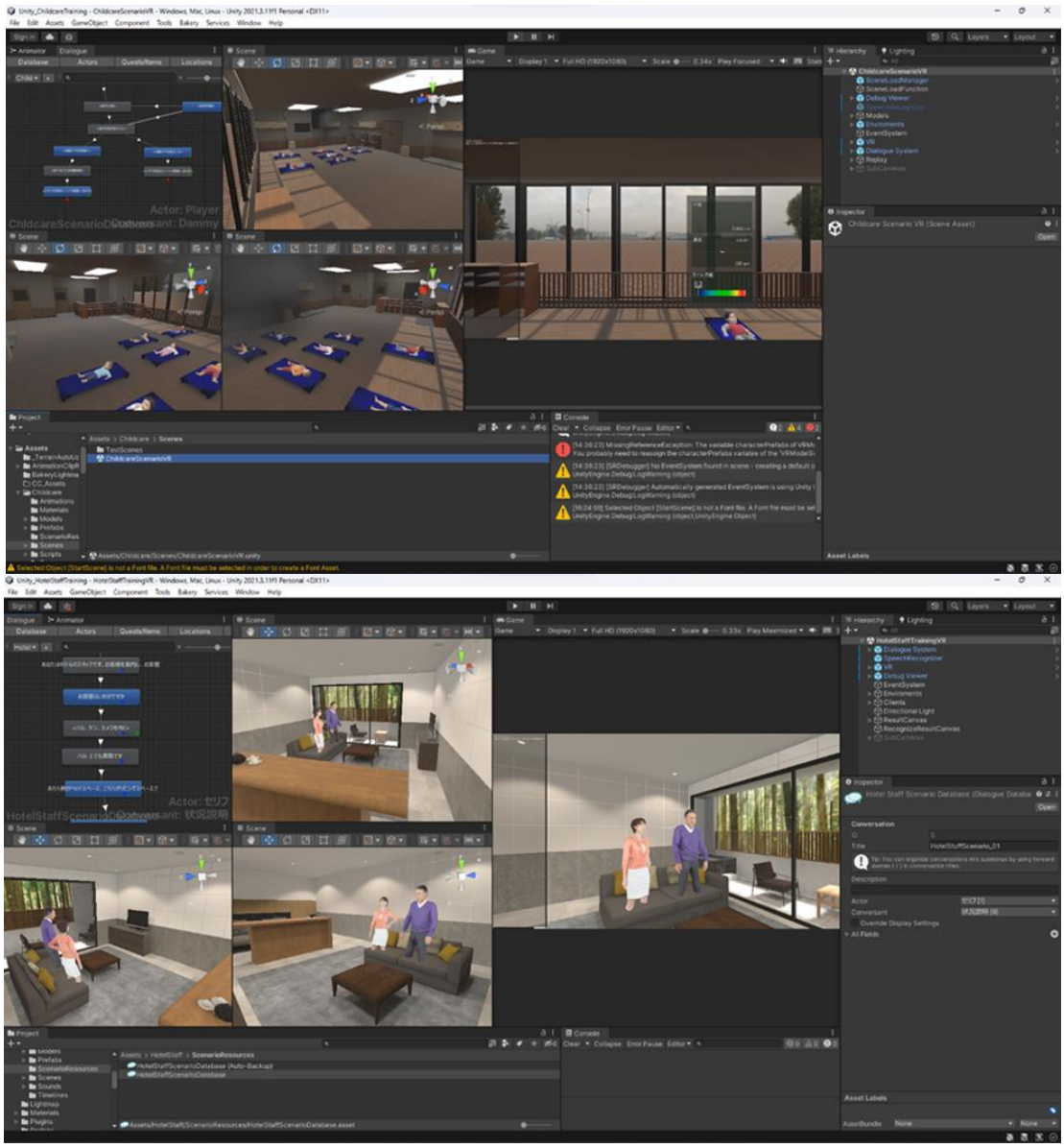
4.1.3 VR Training System for Retail Industry

In this VR training system, participants take on the role of supermarket staff and deal with a problem in which a receipt does not come out of the self-checkout machine (Fig. 7, bottom). The user can switch between three scenarios (1) a scenario in which he/she responds well, (2) a scenario in which he/she is offended by poor language, and (3) a scenario in which he/she responds in the wrong order and is offended by the wrong response).

4.2 Feedback from companies

Two or three frontline staff and managers from each company were interviewed for the experience. The experience was more powerful than expected. Positive feedback was obtained, such as "It is good because there is a big difference between having an experience and not having an experience. These evaluations were the same as those of the VR training system using the low-code development platform and the previous VR training system, and it is considered that there was no decrease in quality due to the use of the proposed platform. In addition, we were able to obtain more specific feedback because we were able to construct a VR training system customized for the industry. In addition, the ability to easily change

scenarios and replace 3D models via GUI was commented as very attractive for actual implementation and operation.



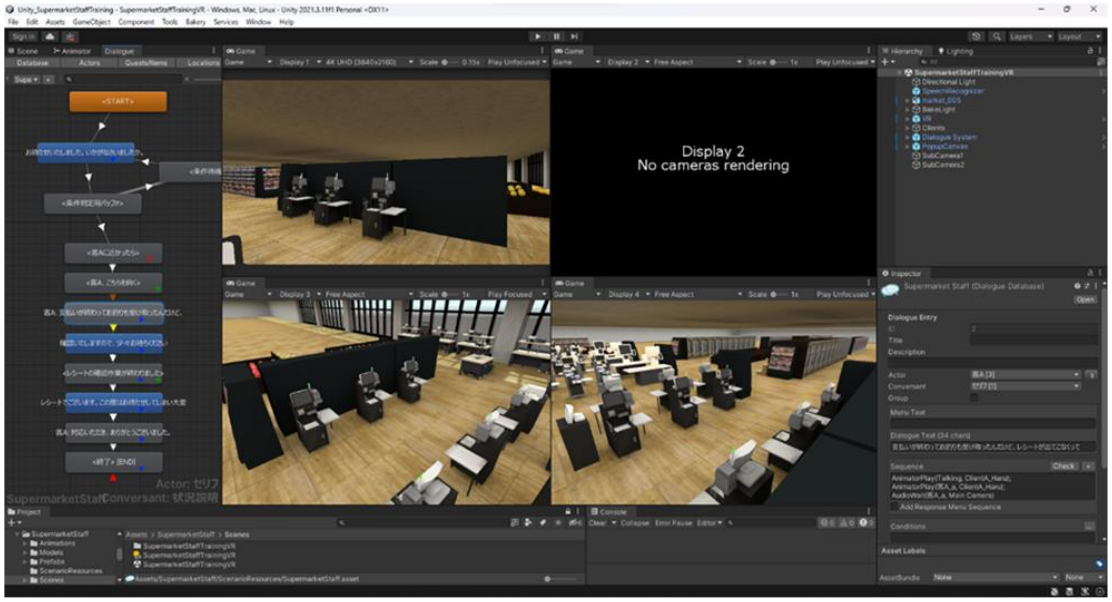


Figure 9: VR training system implementation and execution screens
(top: for a nursery school, middle: for a hotel, bottom: for a supermarket)

5. CONCLUSION

The world's industrial structure is changing, with a shift to service industries as well as manufacturing, and human factors are playing an increasing role in industry, not only in the handling of physical objects. Therefore, VR training systems need to be able to address not only manufacturing-related fields but also service industry fields. Therefore, in this study, we first proposed a VR simulator that can handle various situations involving people and training objectives, and an architecture for a VR system that can realize an autonomous avatar to realize training involving people. Because business training based on communication with people requires a flexible response to a wide variety of situations with a thousand different contents and a wide range of contents to be trained, the respective development costs and the difficulty of operating and customizing the system are barriers to introducing such training. In providing customer service, based on appropriate responses in interpersonal communication, the essential elements necessary for customers to feel safe and comfortable and for their legitimate requests and wishes to be fulfilled are clearly defined, and these are based on XR technology centered on VR, using AI-based training scenario progression and evaluation of training results. The items to be considered when developing the system as a training system based on XR technology with a focus on VR, using AI to facilitate training scenarios and evaluate training outcomes, are presented.

By utilizing the proposed architecture and developing a customer service operations training and support system, we expect that it will lead to higher quality customer service practices, increased motivation and job satisfaction for operations staff, as well as the utilization of a wide range of human resources and increased efficiency and productivity in operations. In addition, the accelerated introduction of economic activities in the metaverse, which is currently

expected to develop, will lead to the creation of a diverse and more convenient living environment. In the future, in addition to face-to-face meetings, there will be a trend toward remote customer service and customer service by avatars and other means that are not bound by the appearance of the metaverse, and further study will be needed on these new forms of communication.

REFERENCES.

Parts of this research was obtained through the "SIP/Big Data and AI-based Cyberspace Infrastructure Technology" (managed Parts of this research was obtained through the "SIP/Big Data and AI-based Cyberspace Infrastructure Technology" (managed by the New Energy and Industrial Technology Development Organization (NEDO)) of the Council for Science, Technology and Innovation, Cabinet Office, Government of Japan. Government of Japan.

REFERENCES.

1. Tecnomatix Plant Simulation Runtime, https://plm.sw.siemens.com/en-US/tecnomatix/products/plant-simulation-software/plant-simulation-runtime/

2. Januszka, Marcin & Panfil, Wawrzyniec. (2015). AUGMENTED REALITY TECHNIQUES FOR VEHICLE MAINTENANCE. PROCEEDINGS OF THE INSTITUTE OF VEHICLES. 2. 37-48.

3. TUMIKISEISAKU, “VR TRAINING+SAFETY EXPERIENCE”, https://tsumikiseisaku.com/safetyvr/

4. van Toll, Wouter & Iv, Atlas & Geraerts, Roland. (2012). “A Navigation Mesh for Dynamic Environments.” Computer Animation and Virtual Worlds. 23. 535-546. 10.1002/cav.1468.

5. Bando, M. and Hasebe, K. and Nakayama, A. and Shibata, A. and Sugiyama, Y. (1995), “Dynamical model of traffic congestion and numerical simulation” Phys. Rev. E, Vol. 51, pp.1035-1042.

6. Tanikawa, T., Ban, Y., Aoyama, K., Shinbori, K., Komatsubara, S., Hirose, M., (2019), “Service VR Training System: VR Simulator of Man-to-Man Service”, Proceedings of IDW '19, pp. 993-994.

7. Tanikawa, T., Shiozaki, K., Ban, Y., Aoyama, K., Hirose, M., (2021), “Semi-automatic Reply Avatar for VR Training System with Adapted Scenario to Trainee’s Status,” Proceedings of HCII 2021.

8. Tanikawa, T., Fukaya, R., Hara, T., Maeda, H., Komatsubara, S., Aoyama, K., Amemiya, T., Hirose, M., (2023), “Case Study of Low-Code VR Platform for Training and Evaluating Employee’s Service Skills,” Proceedings of HCII 2023.

9. Dialogue System, https://www.pixelcrushers.com/dialogue_system/manual2x/html/

10. Web Speech API, https://developer.mozilla.org/en-US/docs/Web/API/Web_Speech_API

THERMAL MANAGEMENT OF A MULTI-FUNCTIONAL BATTERY CASE

İbrahim DİKER, idiker@cu.edu.tr Cukurova University, 01250, Adana, Türkiye

O. Cem GÖKCİLER, ocgokciler@cu.edu.tr Cukurova University, 01250, Adana, Türkiye

Göktürk M. ÖZKAN, gmozkan@cu.edu.tr Cukurova University, 01250, Adana, Türkiye

Durmuş Can ACER, dcacer@cu.edu.tr Cukurova University, 01250, Adana, Türkiye

Ahmet ÇETİN, acetin@adiyaman.edu.tr Adıyaman University, 02040, Adıyaman, Türkiye

Necdet GEREN, gerendr@cu.edu.tr Cukurova University, 01250, Adana, Türkiye

ABSTRACT

The current study aims to optimize the thermal management system of the composite battery case, which is planned to protect and improve the battery's safety and life cycle. The relatively heavier and more complex structure of liquid-cooled thermal management systems will be compensated by a composite battery case produced with a new patent-protected technique. The thermal management system will be studied first numerically to obtain an optimized geometry for the highest heat transfer and minimum pressure loss. Then, measurements will be performed on the manufactured battery case. Maximum surface temperature and pressure losses were compared according to the results of two different analyses with laminar and turbulent flow regimes.

Keywords: Liquid cooling battery thermal management system, Battery casing technology, Response surface methodology

ÖZET

Mevcut çalışma, batarya güvenliğini ve yaşam döngüsünü korumak ve iyileştirmek için planlanan kompozit batarya paketinin termal yönetim sistemini optimize etmeyi amaçlamaktadır. Sıvı soğutmalı termal yönetim sistemlerinin nispeten daha ağır ve karmaşık yapısı, yeni patent korumalı teknikle üretilen kompozit pil paketiyle telafi edilecek. Minimum basınç kaybı ile en yüksek ısı transferi için optimize edilmiş bir geometri elde etmek amacıyla termal yönetim sistemi ilk olarak sayısal olarak incelenecektir. Daha sonra üretilen batarya paketi üzerinde ölçümler yapılacaktır. Laminer ve türbülanslı akış rejimine sahip iki farklı analiz sonuçlarına göre maksimum yüzey sıcaklığı ve basınç kayıpları karşılaştırılmıştır.

Anahtar Kelime: Sıvı soğutmalı batarya termal yönetim sistemi, Batarya muhafaza teknolojisi, Yanıt yüzeyi yöntemi

1. INTRODUCTION

In recent years, the use of electric vehicles (EVs) and hybrid vehicles (HVs) is increasing rapidly [Yang et al. 2022]. The main reason for this uptrend is the environmental concerns such as; global warming and reducing air quality [Zhu et al. 2019]. EVs and HVs most commonly use lithium-ion (Li-ion) batteries because of their high energy density, long service life, reliability, and relatively wide operating temperature range [Senyshyn et al. 2015]. For the best performance, the Li-ion batteries should operate within the suggested operated temperature that has a range of 15 °C–35 °C [Pesaran et al. 2013]. Should the temperature of the batteries surpass this range, it could lead to safety hazards like fire or explosion. Additionally, beyond this temperature range, the efficiency, lifespan, and performance of the batteries decrease [Spitthoff et al. 2021]. Therefore, thermal management of the battery package of an EV/HV becomes an issue. The required thermal management is provided via thermal management systems that are attached to the battery packs. According to their heating/cooling mechanisms, thermal management systems have their advantages and disadvantages in battery packs, and they can be categorized into three distinct groups presented in Table 1 [Ali, 2023].

Various techniques aimed at dissipating heat from the battery pack or pre-heating/heating the batteries have been experimented with and tested by different research groups in recent years. The research that is performed by Mahamud et al. (2013) can be an example of the group of air cooling. Nevertheless, despite the simplicity of structure and lightweight, this approach is not as effective as liquid systems, as heat transfer is generally faster in liquids than in gases [Cengel, et al. 2015]. Thus, it is advisable to utilize liquid-based thermal management systems for more efficient heating/cooling of battery packs. The weight of the existing battery cooling systems is too heavy. A typical battery active cooling system consists of pipes, a water pump, a compressor, an evaporator, a condenser, and an expansion valve that creates additional weight [Kalaf et al. 2021].

The high efficiency of liquid-based thermal management systems has led to an increase in research activity in this area. As an example; A new direct liquid cooling strategy was suggested for large-scale lithium-ion pouch-type cells, aiming to maintain the cells' operating temperature within the optimal range for both performance and safety by Larranaga-Ezeiza

et al. (2022). As another example under this topic; He et al. (2023) designed a double-layered I-shaped liquid cooling plate to optimize the working temperature of a Li-ion battery.

Amongst studies on liquid-based thermal management systems, some focus specifically on the utilization of heating pipes to manage the temperature of the battery pack [Jaguemont and Van Mierlo, 2020]. Because of the benefits of liquid-based thermal management systems, leading companies such as Tesla and General Motors have incorporated these systems into their EVs [Kannan et al. 2021]. A typical liquid-to-liquid cooled active battery thermal management system schematic is shown in Figure 1 [Kalaf et al., 2021]. Although the advantages of liquid-based thermal management systems mentioned above are significant, it's important not to overlook some of their disadvantages. The existence of the piping system creates not only additional weight but also, manufacturing and maintenance costs [Khateeb et al., 2004]. Also, the failure possibility is increased due to the number of additional parts. To address the existing challenges of conventional thermal management systems, we propose a composite battery case with thermal management and self-healing capabilities, utilizing liquid thermal management as its foundation. The problem of the high weight can be overcome with a novel approach provided in this work. Because this battery casing does not contain any additional piping system, it is lighter. The liquid flow is facilitated through channels integrated within the composite layers, eliminating the need for additional piping materials. The thermal management channels are created within the Carbon Fiber Reinforced Polymer (CFRP) laminate by using a novel microvascular channel-creating method based on the patent-protected technique [Geren et al. 2024]. The required patent applications were made in 2022 and 2023 for this novel channel-creating method, for the name of Çukurova University. This approach makes the creation of the thermal management system cheaper, safer, and easier to apply.

Table 1. Comparison between different types of thermal management systems [Ali, 2023]

System Type	**Additional Thermal Power Source**	**Thermal Conductivity**	**Type of Thermal Management**	**System**	**Required Space**	**Cost**
Air Cooling	Exist	Low	Heating/Cooling	Basic	Large	Low
PCM	Non-exist	Low	Cooling	Basic	Small	Low
Liquid Cooling	Exist	High	Heating/Cooling	Complicated	Large	High

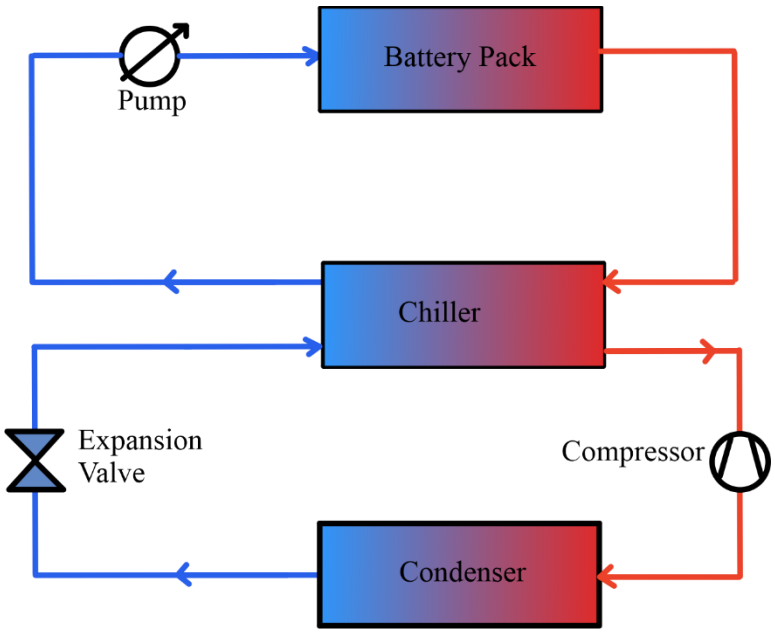


Figure 1. Schematic Representation of Liquid to Liquid Cooled Active Battery Thermal Management System

2. MATERIAL AND METHOD

In the current ongoing work of this project, the novel channel-creating method will be utilized to create the integrated channels with circular cross-section on the surface of the battery case (see in Figure 2). The channels will be located on the top and bottom surfaces of the battery case since the majority of the heat generated due to the internal resistance of battery cells originates from the top edges where connectors are located [Kim et al., 2009]. Four different independent parameters were determined to reduce the maximum surface temperature at the top of the battery pack. Hence the battery case and pack will be kept at an optimum operating temperature of the lithium-ion battery cells. In addition, the aim is also to minimize pressure losses through the piping system. Current work includes both experimental and numerical studies. First, the most suitable configuration for the thermal management system will be determined through numerical studies, and then the optimized configuration will be implemented based on the patent-protected technique [Geren et al. 2024] for experimental measurements.

An optimization study will be carried out to achieve this goal. The response surface methodology is selected for designing experiment runs and optimizing the parameters. Four independent and two dependent parameters are selected by taking into account the relevant studies, see Table 2 for the parameter details.

Table 2. Independent and Dependent Process Parameters

INDEPENDENT PARAMETERS	DEPENDENT PARAMETERS
Number Of Channels, n_c	Surface Temperature of Case, T
Temperature Of Inlet Flow, T_{in}	
Mass Flow Rate, $\dot{m}$	Pressure Loss Between Inlet and Outlet, ΔP
Heat Transfer Coefficient of The Case Material, k	

Response Surface Methodology (RSM) is a collection of statistical and mathematical techniques designed to optimize responses by analysing the independent and interactive effects of variables. RSM provides crucial information for experiments to determine model characteristics. The data generated from RSM are then used to develop a second-order predictive model that links input process parameters to response variables. In this study, the Box-Behnken Design (BBD) will be utilized, enabling the investigation of three input process parameters that influence responses with less time and fewer experimental runs compared to other experimental designs [Ozonoh et al. 2020].

The Bernardi equation (Equation 2.1) given below will be used to calculate the heat production in battery cells [Bernardi et al. 1985].

$$\dot{Q} = (V - V_{ADV})I + IT\frac{dV_{ADV}}{dT} \quad (2.1)$$

Where V is the cell voltage, V_{ADV} is the open circuit voltage, I is the current, and T is the cell temperature. The first term on the right side of the equation represents irreversible heat, while the second term is the reversible heat resulting from the change in entropy.

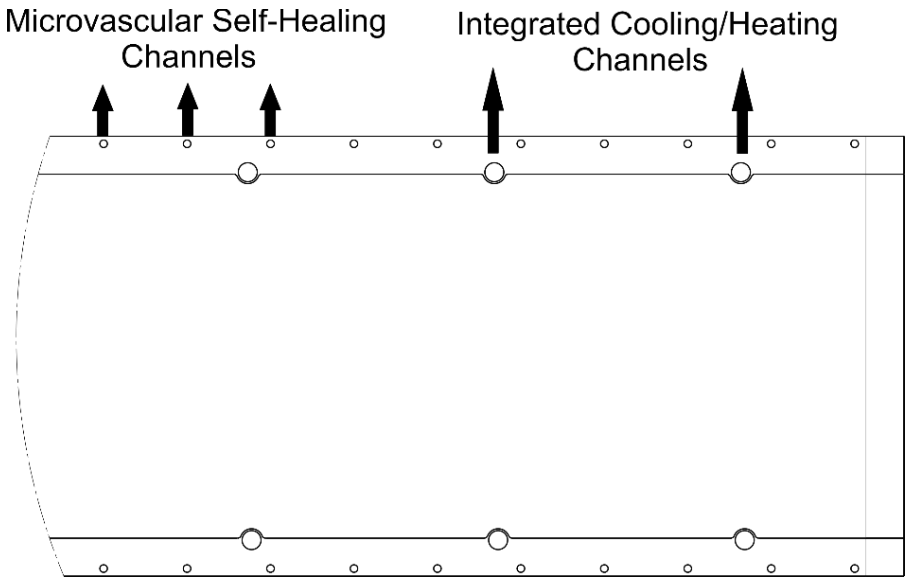


Figure 2. Schematic representation of microvascular self-healing and cooling/heating channels on top surface of battery package

The reversible heat in battery cells is much smaller compared to the irreversible heat, so it can be neglected [Qian et al., 2019]. In this case, equation 2.1 can be simplified as follows:

$$\dot{Q} = I^2 R \tag{2.2}$$

Where R indicates the internal resistance of the relevant battery cell. The cells to be included in the battery pack were chosen as "LG Chem E78" with an internal resistance of 1.48mΩ. With the 96S2P battery configuration obtained by connecting two of ninety-six serially connected battery cells in parallel, the total internal resistance was calculated as 71.04mΩ. The current passing through the battery pack was calculated as 72.3 Ω by dividing the power of the battery, which consumes 25 kW average power, by the nominal voltage value of 345.6V. According to Equation 2, the heat generated from the battery pack was calculated as 371W. When these obtained values are substituted in Equation 2.2, the battery heat released from the package can be calculated as Q̇=371W.

Heat transfer is divided into three groups: conduction, convection, and radiation. Radiative heat transfer in battery packs can be neglected because it is relatively low and difficult to simulate [Qian et al 2019; Zhao et al 2023]. Moreover, these assumptions must be made in order to perform the simulation [Chen et al 2006]: The thermal properties of the material do not change on the surfaces where heat transfer will take place, the specific heat capacity and thermal conductivity of the battery remain constant during charging and with temperature. Furthermore, these assumptions still need to be made: the thermal conductivity of the battery is anisotropic and the internal current is the average value, thus heat production is equal everywhere.

According to Fourier's law, conduction heat transfer occurs due to the internal temperature gradient and can be expressed as follows:

$$Q = -kA\frac{\partial T}{\partial x} \tag{2.3}$$

Where k, A and T are the heat conduction coefficient, surface area and temperature, respectively. The minus sign indicates that the direction of heat transfer is opposite to the temperature gradient. Convective heat transfer occurs between the battery cell at high temperature and the battery pack case at low temperature, thanks to natural convection, and can be expressed by the following equation:

$$Q = hA\Delta T \tag{2.4}$$

The h in the equation represents the convective heat transfer coefficient of the air inside the battery pack. The heat transfer equations in cartesian and cylindrical coordinates are given below with Equation 2.5 and 2.6, respectively:

$$\frac{\partial}{\partial x}\left(k\frac{\partial T}{\partial x}\right)+\frac{\partial}{\partial y}\left(k\frac{\partial T}{\partial y}\right)+\frac{\partial}{\partial z}\left(k\frac{\partial T}{\partial z}\right)+\dot{q}=\rho_c c_p\frac{\partial T}{\partial t} \quad (2.5)$$

$$\frac{1}{r}\frac{\partial}{\partial r}\left(kr\frac{\partial T}{\partial r}\right)+\frac{1}{r^2}\frac{\partial}{\partial \varphi}\left(k\frac{\partial T}{\partial \varphi}\right)+\frac{\partial}{\partial z}\left(k\frac{\partial T}{\partial z}\right)+\dot{q}=\rho c_p\frac{\partial T}{\partial t} \quad (2.6)$$

Where ρ_c, c_p, and $\dot{q}$ express body density, specific heat at constant pressure and volumetric heat flow, respectively.

ANSYS FLUENT 20.0, a computational fluid dynamics commercial package program, will be used to simulate the flow characteristics and thermal behavior. Differences in thermal behavior with laminar and turbulent flow structures with different Reynolds numbers (Re) will be examined. Moreover, the effect of the channel geometry and configuration through which the refrigerant passes on heat transfer will be revealed. The governing equations given below, continuity, momentum, energy, k, and ε respectively, will be discretized by the finite volume method.

$$\frac{\partial \rho}{\partial t}+\nabla\cdot(\rho u)=0 \quad (2.7)$$

where ρ is density, u is mean velocity, t is the time.

$$\frac{\partial(\rho u)}{\partial t}+\nabla\cdot(\rho u u)=-\nabla p+\nabla\cdot(\mu\nabla u)+f \quad (2.8)$$

where p is the pressure, μ is viscosity, f is the body forces.

$$\frac{\partial(\rho E)}{\partial t}+\nabla\cdot(\rho u E)=-\nabla\cdot(up)+\nabla\cdot(\kappa\nabla T)+\Phi \quad (2.9)$$

where E is the total energy (internal and kinetic), T is the temperature, κ is thermal conductivity, Φ is the work done by viscosity.

$$\frac{\partial(\rho k)}{\partial t}+\nabla\cdot(\rho \boldsymbol{u} k)=\nabla\cdot\left[\left(\mu+\frac{\mu_t}{\sigma_k}\right)\nabla k\right]+P_k-\rho\epsilon \quad (2.10)$$

$$\frac{\partial(\rho \epsilon)}{\partial t}+\nabla\cdot(\rho \boldsymbol{u} \epsilon)=\nabla\cdot\left[\left(\mu+\frac{\mu_t}{\sigma_\epsilon}\right)\nabla \epsilon\right]+C_{\epsilon 1}\frac{\epsilon}{k}P_k-C_{\epsilon 2}\epsilon \quad (2.11)$$

Where k is turbulent kinetic energy, ε is dissipation rate, P_k is the turbulent kinetic energy production, μ_t is turbulent viscosity, σ_k and σ_ϵ are Prandtl numbers, and $C_{\epsilon 1}$and $C_{\epsilon 2}$ are model constants.

Details about the CFD analysis setup settings are given in Table 3.

Table 3. CFD Analysis Setup Settings in Ansys Fluent

Solver Type	• Pressure-based
Time Stepping	• Steady
Pressure-Velocity Coupling	• Coupled
Viscous Model	• Laminar and Standard k-epsilon with Standard Wall Function
Energy Equation	• On
Fluid Properties	• Water • Density 1000 kg/m^3 • Dynamic viscosity 0.001 kg/ms • Thermal conductivity 0.6 w/mK • Specific Heat 4182 J/kgK
Solid Properties	• Carbon Fiber Reinforced Polymer • Density 1750 kg/m^3 • Specific Heat 750 J/kgK • Thermal Conductivity 0.7w/mK
Boundary Condition	• Inlet and Outlet mass flow rates are 0.0059 and 0.0196 kg/s. • Reynolds Numbers are 1500 and 5000 • Inlet flow temperature 10°C
Residual Monitors	• Residuals were set to be 1e-06
Initialization	• Standard Initialization

The grid structure utilized in the numerical analysis for our ongoing project is illustrated in Figure 3. The average orthogonal quality and skewness values of the grid structure, which consists of a total of 36.4 million elements, are 0.76 and 0.23, respectively.

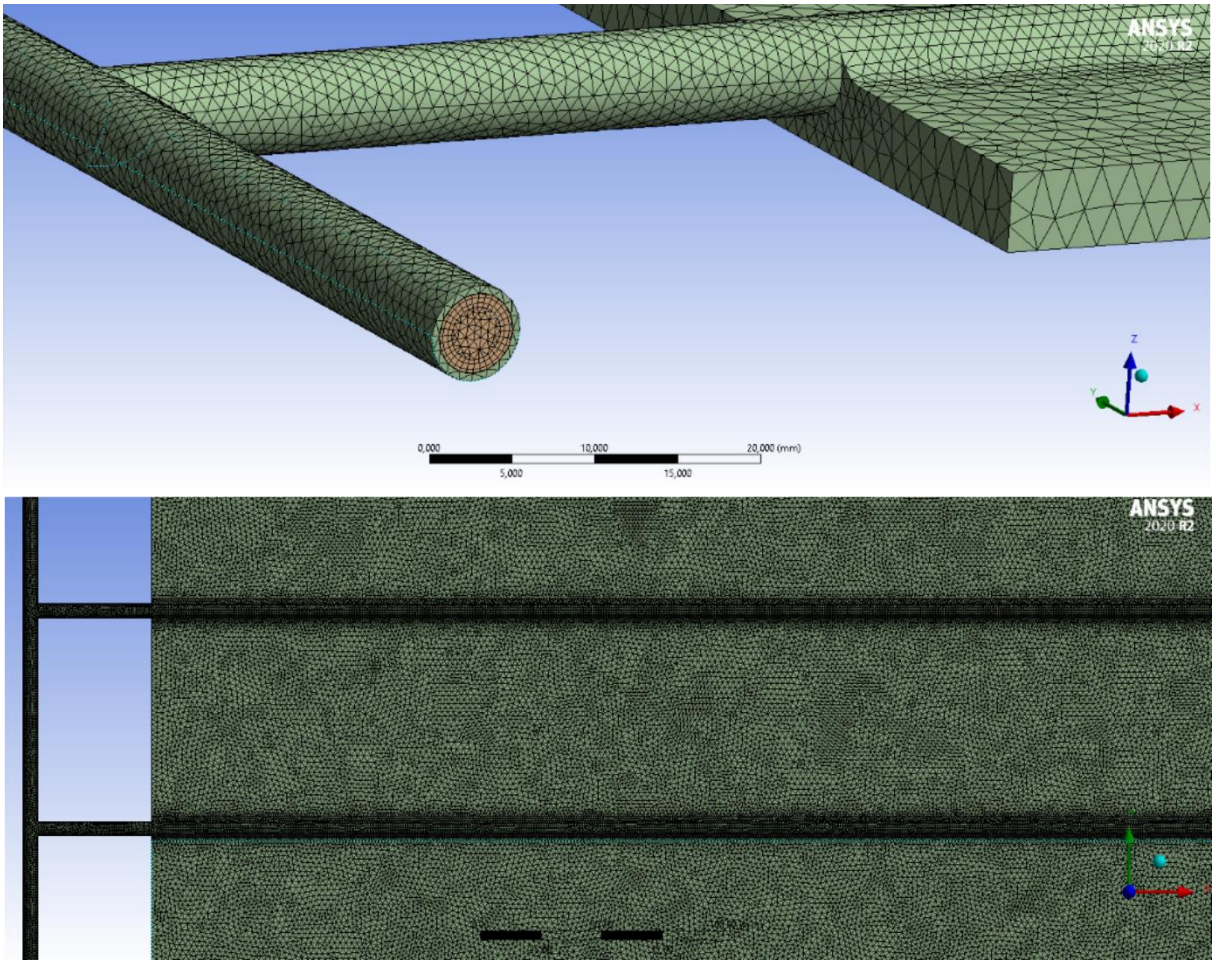


Figure 3. Grid Structure of Battery Case Surface

Flow domain and boundary conditions are defined in Figure 6.

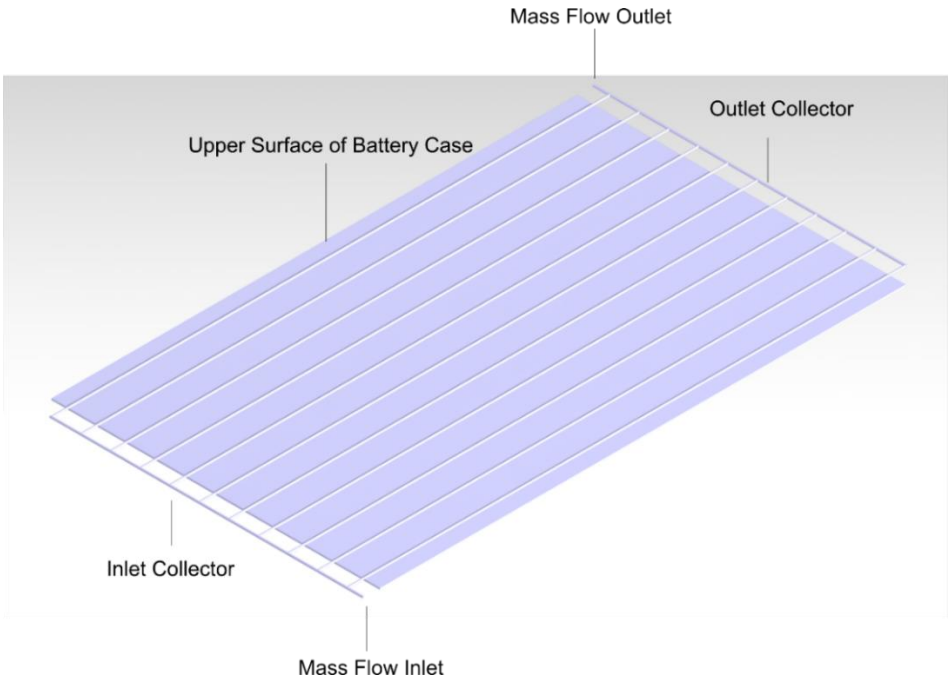


Figure 6. Solid model of the cooling/heating surface of the battery case

3. Preliminary Numerical Analyses

In the CFD model, the Coupled solver scheme was utilized which involves simultaneous solution of momentum continuity and energy equations, ensuring tighter coupling between velocity and pressure fields compared to the other schemes. The standard k-ε model was employed to simulate turbulent fluid flow. In order to obtain more accurate results, the convergence criteria of residuals have been set to 10^{-6}. Initially, the upper cover of the battery case with 11 cooling/heating channels with a heat transfer coefficient of 0.7W/mK was considered, and laminar and turbulent flow regimes were solved. The inlet water temperature was selected as 10 °C and the mass flow rate was determined as 0.0059 and 0.0196 kg/s for laminar and turbulent flow, respectively.

Grid independence analysis was performed to ensure that the analyses performed and to be performed are independent of the grid structure. In Figure 4, the pressure loss differences between the inlet and outlet with five different element numbers are examined.

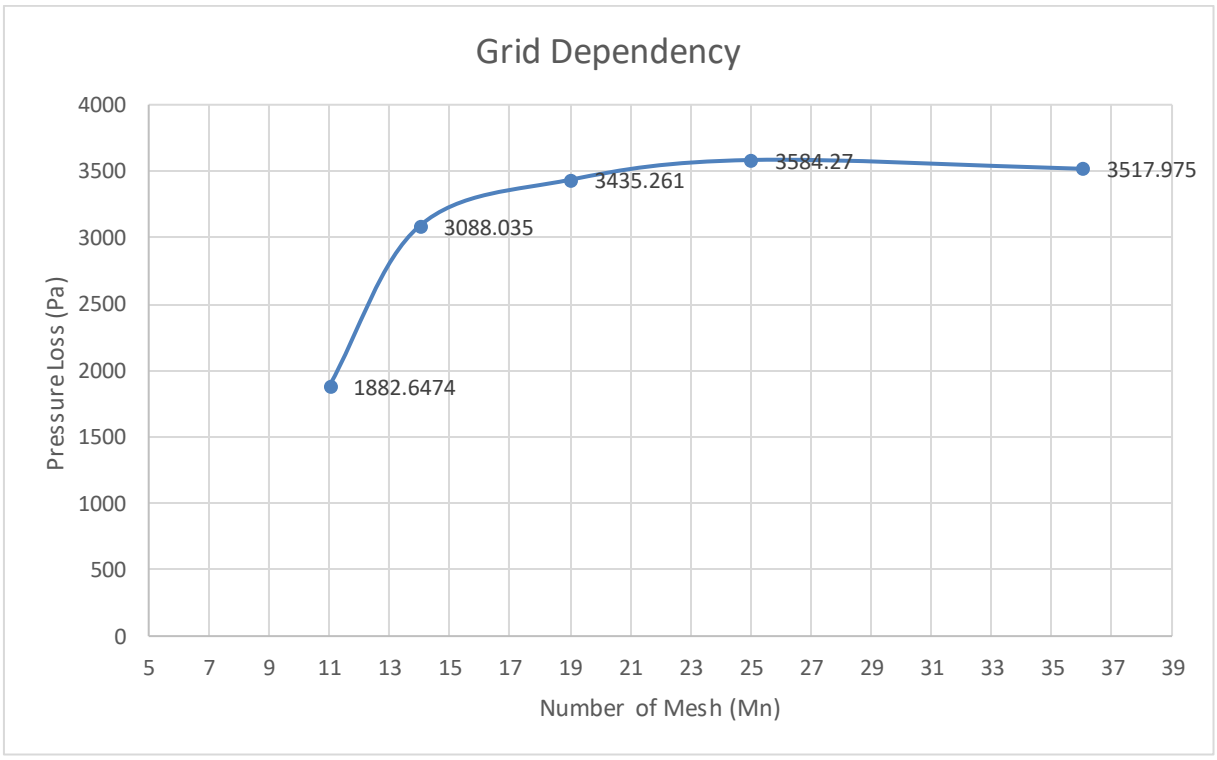
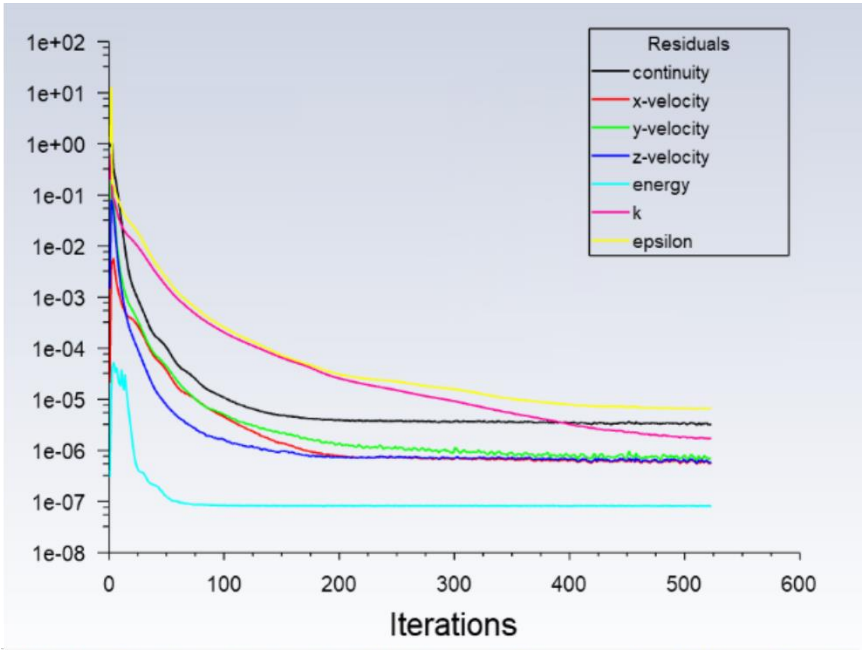


Figure 4. Graph of Grid Dependency Analysis

The residual graph of the numerical analyses performed in Ansys Fluent is presented in Figure 5 to show that the results converge.



iter	continuity	x-velocity	y-velocity	z-velocity	energy	k	epsilon	time/iter	
518	3.3825e-06	6.0212e-07	7.5698e-07	6.2930e-07	8.1761e-08	1.7378e-06	6.5541e-06	3:26:09	246
519	3.4464e-06	6.1672e-07	7.1463e-07	6.4225e-07	8.1969e-08	1.7078e-06	6.5005e-06	3:25:54	245
520	3.2690e-06	5.6852e-07	7.3878e-07	6.1036e-07	8.2284e-08	1.7303e-06	6.5983e-06	3:23:54	244
521	3.1623e-06	5.6101e-07	6.5859e-07	5.9106e-07	8.2295e-08	1.7125e-06	6.6012e-06	3:23:46	243
522	3.2240e-06	5.5851e-07	7.0936e-07	5.7961e-07	8.1733e-08	1.7272e-06	6.5734e-06	3:23:29	242
523	3.2330e-06	5.6261e-07	7.0802e-07	5.6962e-07	8.1276e-08	1.7270e-06	6.6277e-06	3:27:06	241
524	3.4295e-06	6.1463e-07	8.0038e-07	6.5272e-07	8.2117e-08	1.7448e-06	6.6814e-06	3:32:11	240

Done.

Figure 5. Graph of Residual Monitor

Figure 7 shows the temperature and pressure contours for the laminar flow regime at Re=1500. According to the results, the maximum temperature is found to be 105 °C near the exit of channels around the center of plate. Such a temperature is at a level that may degrade the structure of the composite material's resin. Furthermore, the temperature distribution across the plate is highly non-uniform which can damage the battery cell at the down region of the outlet side. Therefore, a laminar flow regime is found to be unsafe for battery life.

The effects of turbulent flow at a Reynolds Number on both heat transfer and pressure loss are illustrated in Figure 8. This figure demonstrates how the presence of turbulence enhances the convective heat transfer as a result of intensified mixing and fluid movement. Additionally, it highlights the corresponding increase in pressure drop, which is a consequence of the higher frictional forces encountered within the turbulent regime. Firstly, much more uniform temperature distribution is obtained on the plate compared to the laminar flow case (Figure 7). Moreover, the maximum surface temperature is decreased to 92 °C at the side regions of the plate, indicating high heat transfer around the channels. However, pressure loss between the inlet and outlet is increased from ΔP=455 Pa to ΔP=3517 Pa

when compared to the laminar flow case. In conclusion, the preliminary numerical analysis showed the favorable and unfavorable characteristics of laminar and turbulent flows i.e. laminar flow provides lower pressure loss but non-uniform temperature distribution through the plate whereas the reverse situation is true for the turbulent flow conditions. The preliminary study results of the cooling and heating system that we will use in our ongoing project coincide with the results of studies with similar configurations in the literature [Fan et al., 2023]. Therefore, more analyses are planned to obtain an optimized case giving the best configuration of channels on the plate. Hence, the upcoming numerical analysis will involve the prescribed independent parameters which are the number of channels (n_c), mass flow rate ($\dot{m}$), inlet water temperature (T_{in}), and heat conduction coefficient (k) to obtain the lowest surface temperature distribution by minimizing the pressure loss.

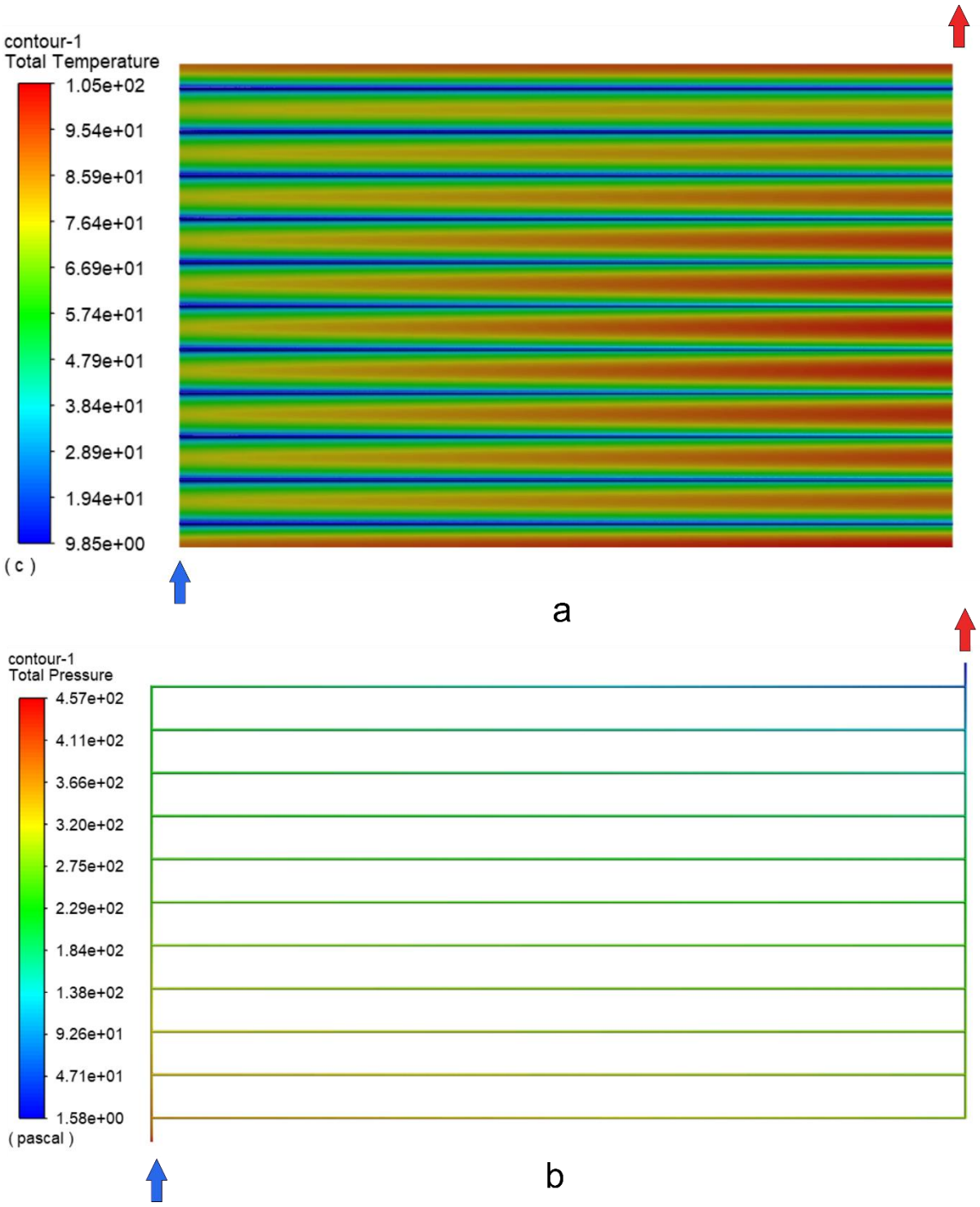


Figure 6. Temperature and Pressure Contours at Re=1500

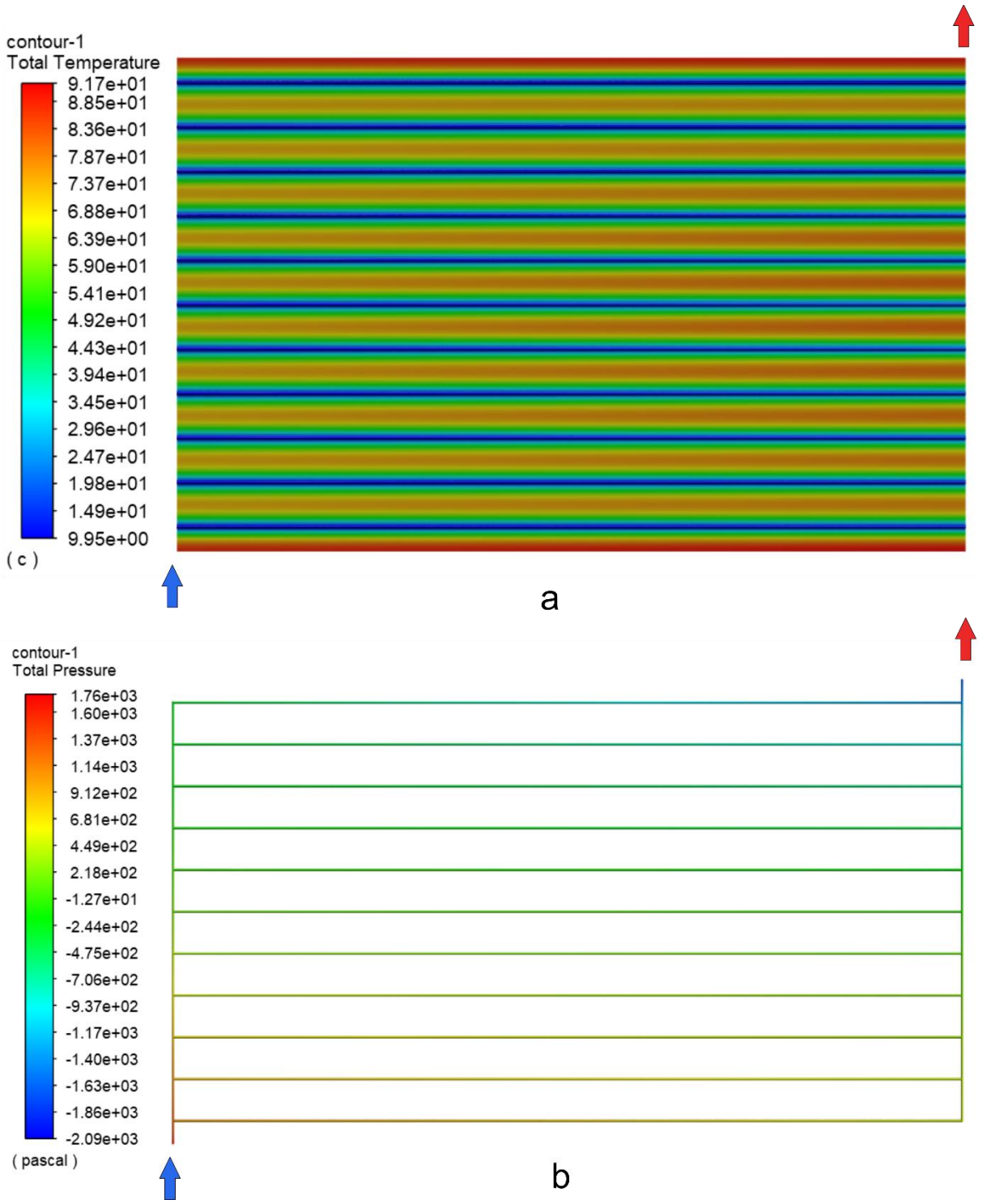


Figure 7. Temperature and Pressure Contour at Re=5000

4. CONCLUSION

In this paper, the thermal optimization characteristics of a novel battery case that has a thermal management system integrated within the CFRP. The required thermal analysis for this patent-protected project [Geren et al., 2024] is performed and proposed in this paper. Initially, the thermal management system will undergo numerical investigation to derive an optimized geometry that maximizes heat transfer while ensuring uniform temperature distribution and minimal pressure loss. After this numerical approach, measurements will be performed on the manufactured battery case.

To sum up, the initial numerical analysis revealed both advantageous and disadvantageous aspects of laminar and turbulent flows. For instance, laminar flow exhibits reduced pressure loss but results in non-uniform temperature distribution across the plate, whereas turbulent flow conditions present the opposite scenario. Consequently, further analyses are scheduled to achieve an optimized scenario determining the ideal configuration of pipes on the plate. Subsequently, the forthcoming numerical analysis will incorporate predetermined independent parameters: the number of pipes (np), mass flow rate ($\dot{m}$), inlet water temperature (Tin), and heat conduction coefficient (k), aiming to minimize pressure loss and achieve the most uniform surface temperature distribution. The preliminary numerical analysis of the thermal management system of this ongoing work is presented in this study. According to the analyses shown in the results section, independence from the number of grids and convergence of iterations, low pressure loss was achieved in the laminar flow regime, while low surface temperature was obtained in the turbulent flow regime.

ACKNOWLEDGEMENTS

The study was supported by the Scientific Research Projects Coordination Unit (BAP) of Cukurova University in Adana, Turkey, under grant No: FBA-2024-16561. Also, this project is supported by ‘Support Programme of Research Universities’ (ADEP).

REFERENCES

1. **Yang, Z., Li, Q., Yan, Y., Shang, W.-L., & Ochieng, W. (2022).** Examining influence factors of Chinese electric vehicle market demand based on online reviews under moderating effect of subsidy policy. Applied Energy, Vol.326, pp 120019.

2. **Zhu, X., Ren, M., Wu, G., Pei, J., & Pardalos, P. M. (2019).** Promoting new energy vehicles consumption: The effect of implementing carbon regulation on automobile industry in China. Computers & Industrial Engineering, Vol.135, pp 211–226.
3. **Senyshyn, A., Mühlbauer, M. J., Dolotko, O., & Ehrenberg, H. (2015).** Low-temperature performance of Li-Ion Batteries: The behavior of lithiated graphite. Journal of Power Sources, Vol.282, pp 235–240.
4. **Pesaran, A., S. Santhanagopalan and G. Kim (2013),** Addressing the impact of temperature extremes on large format li-ion batteries for vehicle applications (presentation), National Renewable Energy Lab.(NREL), Golden, CO (United States).
5. **Spitthoff, L., P. R. Shearing and O. S. Burheim (2021),** "Temperature, ageing and thermal management of lithium-ion batteries." Energies Vol.14, No.5, pp 1248.
6. **Ali, H. M. (2023),** "Thermal management systems for batteries in electric vehicles: A recent review." Energy Reports, Vol.9, pp 5545-5564.
7. **Mahamud, R. and C. Park (2011),** "Reciprocating air flow for Li-ion battery thermal management to improve temperature uniformity." Journal of Power Sources Vol.196, No.13, pp 5685-5696.
8. **Cengel, Y. A., A. J. Ghajar and M. Kanoglu (2015),** "Heat and mass transfer: fundamentals and applications
9. **Kalaf, O., D. Solyali, M. Asmael, Q. Zeeshan, B. Safaei and A. Askir (2021),** "Experimental and simulation study of liquid coolant battery thermal management system for electric vehicles: A review." International journal of energy research 45(5): 6495-6517.
10. **Larrañaga-Ezeiza, M., G. Vertiz, P. Arroiabe, M. Martinez-Agirre and J. Berasategi (2022),** "A novel direct liquid cooling strategy for electric vehicles focused on pouch type battery cells." Applied Thermal Engineering 216: 118869.
11. **He, P., H. Lu, Y. Fan, H. Ruan, C. Wang and Y. Zhu (2023),** "Numerical investigation on a lithium-ion battery thermal management system utilizing a double-layered I-shaped channel liquid cooling plate exchanger." International Journal of Thermal Sciences 187: 108200.
12. **Jaguemont, J. and J. Van Mierlo (2020),** "A comprehensive review of future thermal management systems for battery-electrified vehicles." Journal of Energy Storage 31: 101551.

13. **Kannan, C., Vignesh, R., Karthick, C., and Ashok, B., (2021),** "Critical review towards thermal management systems of lithium-ion batteries in electric vehicle with its electronic control unit and assessment tools." Proceedings of the Institution of Mechanical Engineers, Part D: Journal of Automobile Engineering 235(7): 1783-1807

14. **Khateeb, S. A., Farid, M. M., Selman, J. R., & Al-Hallaj, S. (2004).** Design and simulation of a lithium-ion battery with a phase change material thermal management system for an electric scooter. Journal of Power Sources, Vol.128(2), pp 292–307.

15. **Geren, N., Kostur, E.** Patent Title: Weaving threads forming microvascular channels into fibers in the production of fiber-reinforced polymer composites (Buluş başlığı: fiber takviyeli polimer kompozit üretiminde mikrovasküler kanal oluşturan ipliklerin elyaf içine dokunması), Application Number: PCT/TR2023 051362, Applicants: Cukurova University.

16. **Kim, U. S., Shin, C. B., & Kim, C.-S. (2009),** Modeling for the scale-up of a lithium-ion polymer battery. Journal of Power Sources, 189(1), 841–846.

17. **Ozonoh, M., Oboirien, B. O., & Daramola, M. O. (2020),** Optimization of process variables during torrefaction of coal/biomass/waste tyre blends: Application of Artificial Neural Network & Response Surface Methodology. Biomass and Bioenergy, 143, 105808.

18. **Bernardi, D., Pawlikowski, E., & Newman, J. (1985),** A general energy balance for battery systems. Journal of The Electrochemical Society, 132(1), 5–12.

19. **Qian, X., Xuan, D., Zhao, X., & Shi, Z. (2019),** Heat dissipation optimization of lithium-ion battery pack based on Neural Networks. Applied Thermal Engineering, 162, 114289.

20. **Zhao, L., Li, W., Wang, G., Cheng, W., & Chen, M. (2023),** A novel thermal management system for lithium-ion battery modules combining direct liquid-cooling with forced air-cooling. Applied Thermal Engineering, 232, 120992.

21. **Chen, S.-C., Wang, Y.-Y., & Wan, C.-C. (2006),** Thermal analysis of spirally wound lithium batteries. Journal of The Electrochemical Society, 153(4).

22. **Fan, X., Meng, C., Yang, Y., Lin, J., Li, W., Zhao, Y., Xie, S., & Jiang, C. (2023).** Numerical optimization of the cooling effect of a bionic fishbone channel Liquid Cooling Plate for a large prismatic lithium-ion battery pack with high discharge rate. Journal of Energy Storage, Vol.72, pp 108239.

AN EXPERIMENTAL INVESTIGATION ON THE ENERGY REQUIREMENT OF DIFFERENT MATERIALS MANUFACTURED ON A CNC LATHE

M. Ural ULUER, *uluer@metu.edu.tr* Middle East Technical University, 06800, Ankara, Turkey

Metin AKKÖK, *akkok@metu.edu.tr* Middle East Technical University, 06800, Ankara, Turkey

S. Engin KILIÇ, *engin.kilic@atilim.edu.tr* Atilim University, 06830, Ankara, Turkey

Ulaş YAMAN, *uyaman@metu.edu.tr* Middle East Technical University, 06800, Ankara, Turkey

ABSTRACT

This paper investigates the process energy requirements for machining steel, cast iron and aluminum parts using identical designs. Parts were manufactured on an Anatool TP32 CNC lathe and energy consumption was measured with a Siemens PAC3200 power meter. A measurement methodology was employed to determine and compare the theoretical, variable auxiliary and constant auxiliary energy requirements. This comparison highlights the impact of material properties on different levels of process energy, promoting more sustainable approaches in part design.

Keywords: Energy requirement, CNC lathe, Energy monitoring

1. INTRODUCTION

Electrical energy is an essential resource for manufacturing processes. The total electricity generation in Turkey was 328,379 GWh in 2022 [TEİAŞ, 2022]. The Turkish Ministry of Energy and Natural Resources enacted The Energy Efficiency Law [ETKB, 2007] and the Regulation on Increasing Efficiency in the Use of Energy Sources and Energy [ETKB, 2008] to help decrease energy density (energy consumed per national income) of Turkey. Clauses 8e, 8f, and 8g of the latter regulation detail the responsibilities assigned to the energy management departments within enterprises

- Monitoring and evaluating the energy consumptions and costs, preparing periodical reports.
- Acquiring and installing the necessary meters for tracking energy consumptions.
- Tracking the relation between products and energy consumption and preparing proposals for the reduction of energy intensity of the enterprise.

In line with these points, the purpose of this paper is to monitor and evaluate the energy requirements of various materials manufactured on a CNC lathe (Clause 8e). To achieve this, an energy meter is installed on a CNC lathe (Clause 8f).

Section 2 outlines the energy breakdown structure, categorizing total process energy into three components. Section 3 details the equipment used for the measurement setup. Section 4 explains the methodology for measuring the energy requirement of each component. Section 5 discusses the part design, materials used and measurement results. Finally, Section 6 provides concluding remarks based on the findings.

2. PROCESS ENERGY

Process energy is the total energy requirement for completing the manufacturing process of a part. It is broken down into two components [Rahimifard et al., 2010]:

$$E_{process} = E_{th} + E_{aux} \quad (1)$$

where E_{th} is the theoretical energy which is consumed during the actual metal removal processes and E_{aux} is the energy which is consumed during the operation of the auxiliary equipment such as spindle assembly and cutting fluid system.

Auxiliary energy can also be broken down into variable (E_{aux_var}) and constant (E_{aux_cons}) components.

$$E_{aux} = E_{aux_var} + E_{aux_cons} \quad (2)$$

Variable auxiliary energy is time dependent and can change during the operation of the machine tool. Energy consumed by servo motors, spindle motor or the energy consumed by the turret for each tool change action are examples of variable auxiliary energy.

Constant auxiliary energy is due to the auxiliary components of the machine tools which consume energy even if the machine is in standby mode. Lighting and the embedded computer for the CNC machine tools are two examples for constant auxiliary energy.

3. MEASUREMENT SET-UP

Energy and power consumptions are measured using a SIEMENS SENTRON PAC3200 power meter. Meter is installed on the Anatool TP 32 CNC lathe in the Department of Mechanical Engineering at Middle East Technical University. Specifications of the lathe are given in Table 1 [Anatool, 2009].

Table 1. Technical Specifications of Anatool TP 32 CNC Lathe

Number of Axis	2 (X and Z)
Maximum Turning Diameter	200 mm
Maximum Turning Length	200 mm
Chuck Size	5 inch
Bar Capacity	32 mm
Axis Travel in X-axis	160 mm
Axis Travel in Z-axis	400 mm
Rapid Traverse Rate in X-Z Axes	40000 mm/min
Number of Tools	10
Main Spindle Motor	5.5 kW
Spindle Speed	4500 rpm
Total Nominal/Max. Power	8/15 kW
Nominal/Max. Current	20/40 A
Weight	2100 kg

A 3P4W connection type (Three-phase measuring, four conductors, unbalanced load, without voltage transformers, with three current transformers; Figure 1) is used to collect the necessary parameters from the device.

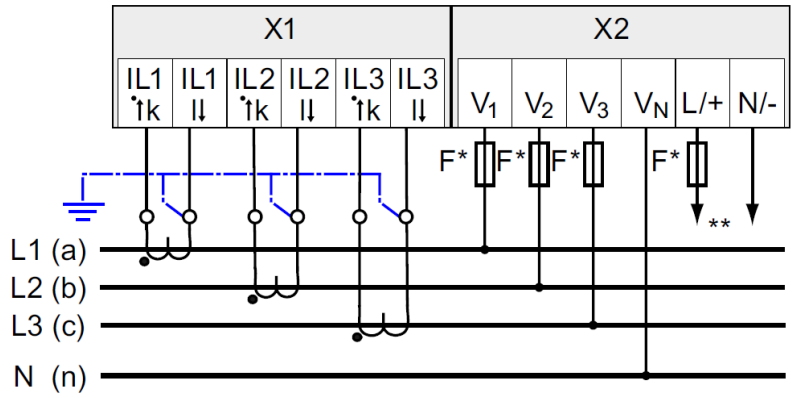


Figure 1. 3P4W connection for PAC3200 [Siemens, 2008]

Parameters measured by PAC3200 are based on voltage and current inputs. Since PAC3200 is designed for measuring current of 1 A or 5 A, three external current transformers with a conversion ratio of 100A/5A are used. PAC3200 is connected to the internet by the RJ45 Ethernet port embedded on the device. Data is accessed with a PC through the OPC Server of MATLAB Simulink (Figure 2). The physical set-up is illustrated in Figure 3.

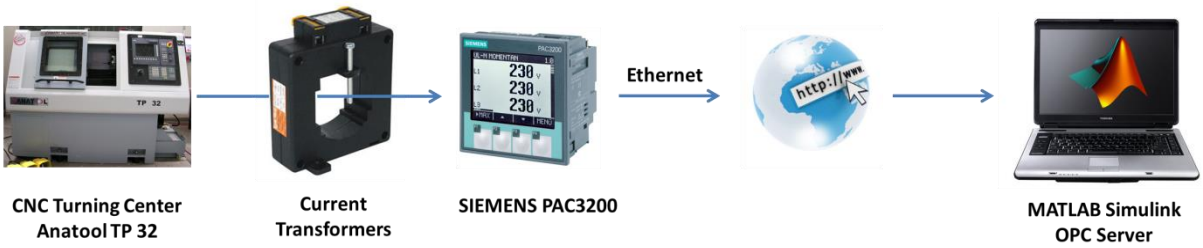
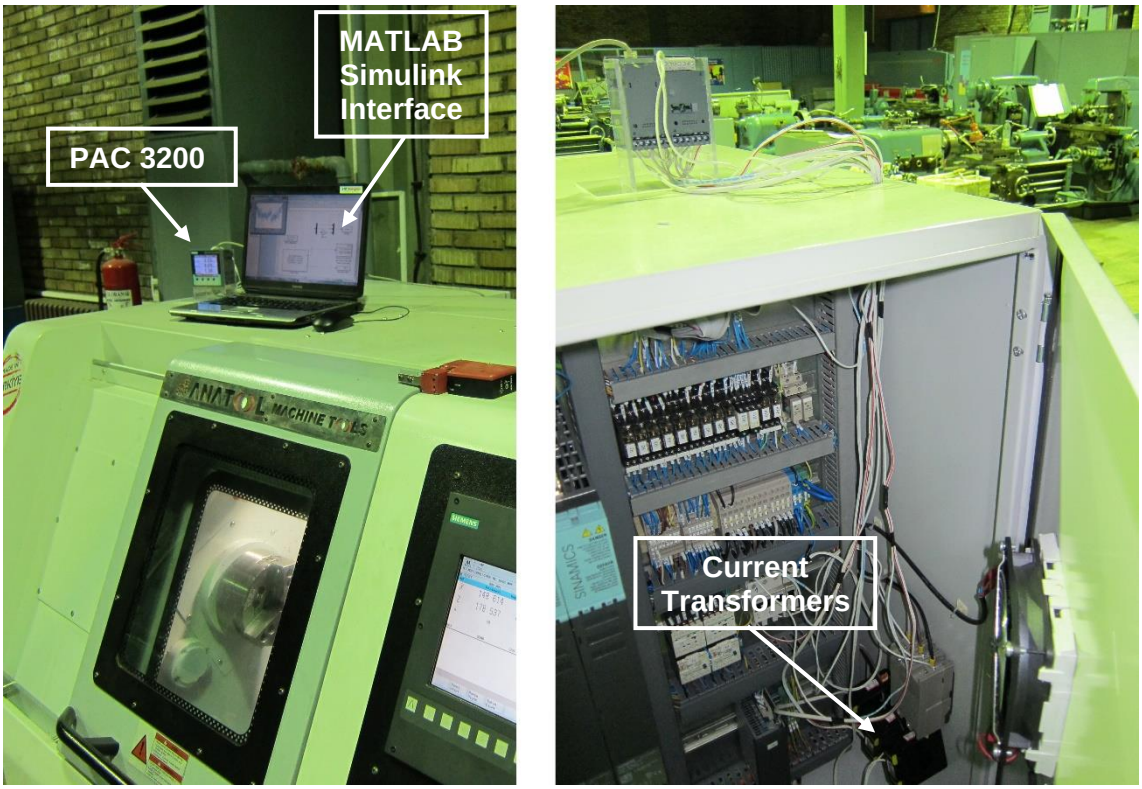


Figure 2. Power Measurement System

Three main parameters are monitored using the Simulink OPC Server. Those are:

- Working Hours Counter (s)
- Total Active Power (W)
- Active Energy Import (Wh)



(a) Front (b) Back

Figure 3. Power Measurement Set-up

4. MEASUREMENT METHODOLOGY

As explained in Section 3, energy data is collected using a Siemens PAC3200 power meter installed on the Anatool TP 32 CNC lathe. Measurement taken during the manufacture of a part provides $E_{process}$ value. A measurement methodology is required to find the process energy components provided in Equations 1 and 2. These two equations can be combined to obtain:

$$E_{process} = E_{th} + E_{aux_var} + E_{aux_cons} \quad (3)$$

To measure the E_{aux_cons} component of processing energy, CNC machine tool is operated at the standby mode. In this mode, since metal is not removed and variable auxiliary energy is not required, only E_{aux_cons} component is measured as $E_{process_standby}$ value:

$$E_{process_standby} = \cancel{E_{th}} + \cancel{E_{aux_var}} + E_{aux_cons} \quad (4)$$

Therefore constant auxiliary energy is:

$$E_{aux_cons} = E_{process_standby} \quad (5)$$

An air cut is performed to find the auxiliary energy requirement (E_{aux}) during machine tool operation. Since material is not removed and only auxiliary equipment is active during an air cut, theoretical energy becomes zero and the measured value ($E_{process}$) becomes equal to the auxiliary energy (E_{aux}).

$$E_{process_air} = \cancel{E_{th}} + E_{aux_var} + E_{aux_cons} \quad (6)$$

Once E_{aux} is measured, variable part of the auxiliary energy ($E_{aux\text{-}var}$) can be calculated by:

$$E_{aux_var} = E_{process_air} - E_{process_standby} \quad (7)$$

A normal cut is performed to find the measured theoretical energy (E_{th}) by subtracting the measured auxiliary energy values from the energy readings of the meter during a normal cut ($E_{process}$) to find the theoretical energy.

$$E_{th} = E_{process_normal} - E_{process_air} \quad (8)$$

5. MEASUREMENTS

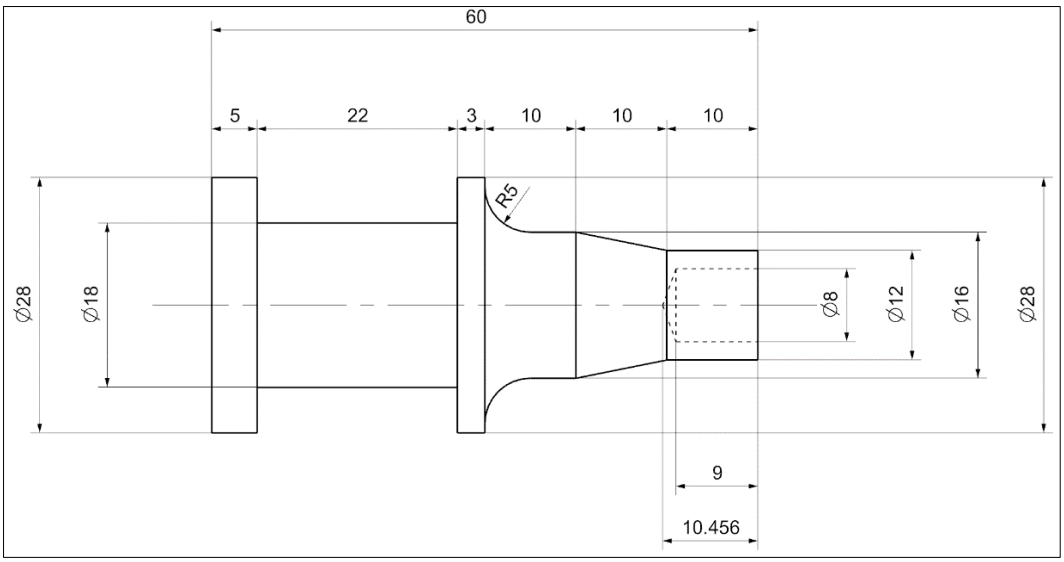


Figure 4. Drawing for the sample part

A sample part is designed for the measurements, with its engineering drawing shown in Figure 4. The part is made from stock with dimensions of ϕ30 mm x 73.5 mm. Three identical parts are machined from 1040 carbon steel, GG25 cast iron, and Aluminum alloy 6013. The manufacturing process for the sample part removes 29,839 mm^3, which is 66.5% of the total volume. Process plans for each material are presented in Table 2 to Table 4.

Table 2. Process Plan for AISI1040

Operation Name	af (mm)	ap (mm)	Cutting Speed (m/min)	Speed (rpm)	Feed (mm/rev)	Feed Rate (mm/min)
Facing	0.1	0.5	180	1910	0.1	191
Turning - Rough	0.2	1.5	162	1720	0.2	344
Turning - Finish	0.1	0.8	180	1910	0.1	191
Drilling	0.1	8	80	3180	0.2	636
Grooving	0.05	3	115	1310	0.05	66
Parting	0.09	3	115	1220	0.09	110

Table 3. Process Plan for GG25

Operation Name	af (mm)	ap (mm)	Cutting Speed (m/min)	Speed (rpm)	Feed (mm/rev)	Feed Rate (mm/min)
Facing	0.1	0.5	170	1800	0.1	180
Turning - Rough	0.2	1.5	153	1620	0.2	324
Turning - Finish	0.1	0.8	170	1800	0.1	180
Drilling	0.11	8	70	2790	0.22	614
Grooving	0.06	3	90	1020	0.06	61
Parting	0.09	3	90	950	0.09	86

Table 4. Process Plan for AL6013

Operation Name	af (mm)	ap (mm)	Cutting Speed (m/min)	Speed (rpm)	Feed (mm/rev)	Feed Rate (mm/min)
Facing	0.15	0.5	250	2650	0.15	398
Turning - Rough	0.3	2	225	2390	0.3	717
Turning - Finish	0.15	1	250	2650	0.15	398
Drilling	0.14	8	120	3500	0.28	980
Grooving	0.05	3	190	2160	0.05	108
Parting	0.09	3	190	2020	0.09	182

The measurement results for the sample parts, obtained using the methodology from Section 4, are shown in Figures 5 to 7 and summarized in Table 5. The figures display power consumption from all three measurements, while the table groups the measured energy results into three categories: theoretical energy, variable auxiliary energy and constant auxiliary energy. Photo of the manufactured sample parts are presented in Figure 8.

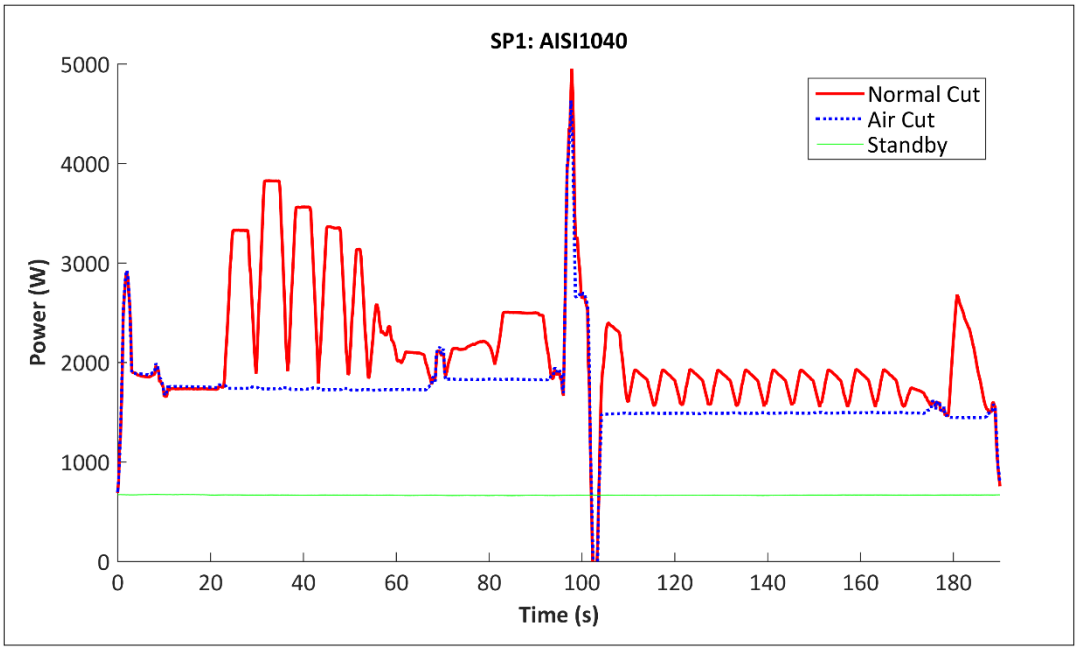


Figure 5. Power consumption measurements for AISI1040

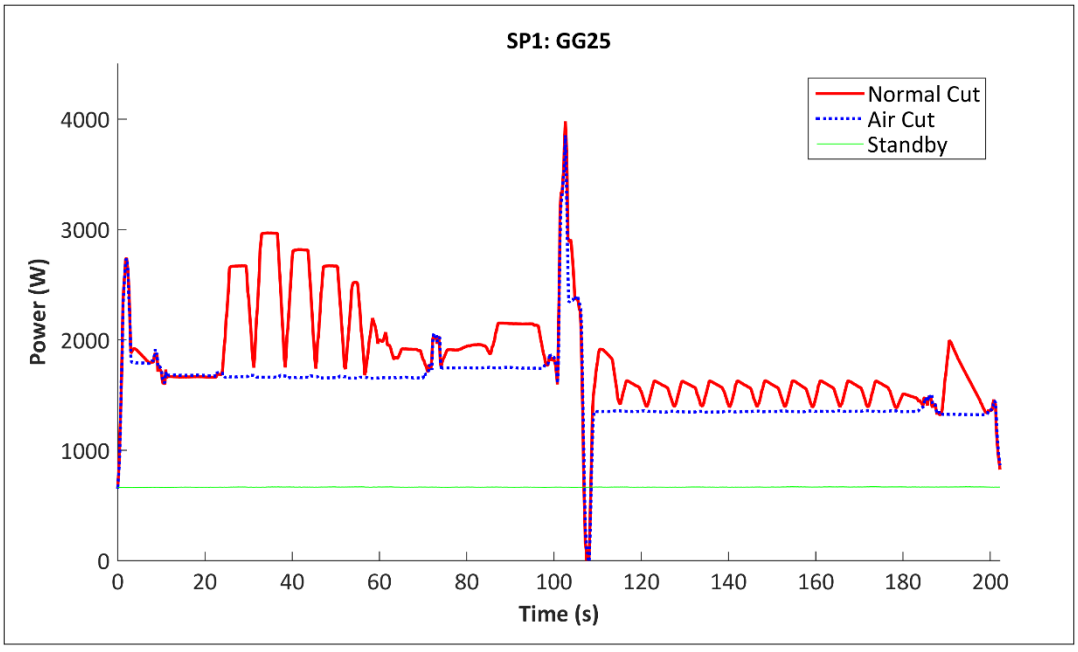


Figure 6. Power consumption measurements for GG25

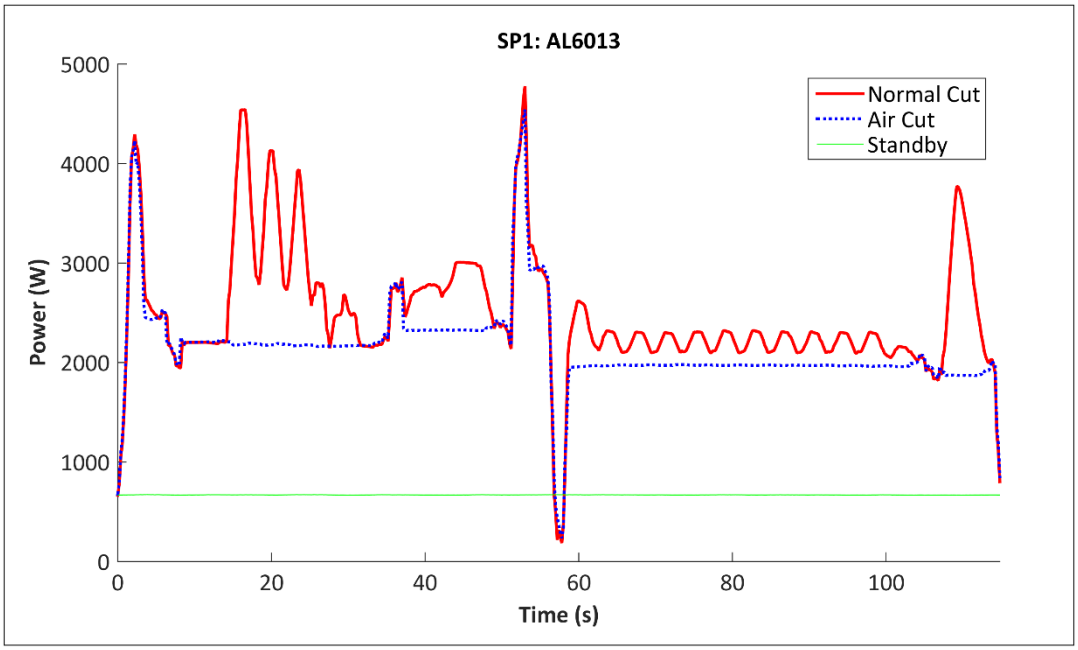


Figure 7. Power consumption measurements for AL6013

Table 5. Energy measurement results for the sample parts

	AISI1040		GG25		AL6013	
Time (s)	189.4		201.6		114.4	
	kJ	**%**	**kJ**	**%**	**kJ**	**%**
E_{th}	84.0	21	56.4	15	39.8	14
E_{aux_var}	191.8	48	180.3	49	169.5	59
E_{aux_cons}	126.4	31	134.4	36	76.6	27
$E_{process}$	**402.2**	**100**	**371.1**	**100**	**285.9**	**100**



Figure 8. Sample parts after manufacturing

6. CONCLUSION

Theoretical energy is independent of time and is determined by the volume removed and the specific cutting energy. Since all sample parts are machined with the same tools, the key factors affecting the specific cutting energy are ps_1, which represents the specific cutting energy for an uncut chip thickness of 1 mm and mc, a material constant. Both of these parameters depend on the hardness of the material being machined. Thus, it can be concluded that theoretical energy increases with the material's hardness. Additionally, as shown in Table 5, theoretical energy accounts for the smallest share (14% - 21%) among the other energy components.

Variable auxiliary energy accounts for the largest share (48% - 59%) of the process energy across all three materials. Previous research [Uluer et al., 2016] has shown that the spindle motor is the primary contributor to variable auxiliary energy, with its power consumption increasing as rotational speed rises. Comparing the rotational speeds for steel and cast iron parts in Tables 2 and 3, it is clear that the steel part is machined at higher speeds, leading to greater variable auxiliary energy. Although the aluminum part operates at the highest rotational speeds (Table 4), its shorter cutting time reduces its overall variable auxiliary energy. In summary, the variable auxiliary energy for different materials is determined by the balance between total cutting time and spindle power consumption.

Constant auxiliary energy is the second-largest contributor (27% - 36%) to total process energy. As discussed in Section 2, this energy represents the base energy required in standby mode, which is independent of material type and depends solely on time and standby power. This explains the higher constant auxiliary energy in the cast iron part and the lower value in the aluminum part.

As a result, process energy for the same design but different materials is influenced by the hardness of the material and cutting parameters. These cutting parameters, in turn, determine the total cutting time and spindle power consumption.

REFERENCES

1. **Anatool Machine Tools, (2009),** "TP 32 CNC Lathe Programming Manual", Ankara, Turkey.

2. **Rahimifard, S., Seow, Y., Childs, T., (2010),** "Minimizing Embodied Product Energy to Support Energy Efficient Manufacturing", CIRP Annals - Manufacturing Technology, Vol. 59, pp. 25-28.

3. **Republic of Turkey, Ministry of Energy and Natural Resources (ETKB), (2007),** “Energy Efficiency Law”, available at: https://www.mevzuat.gov.tr/MevzuatMetin/1.5.5627.pdf

4. **Republic of Turkey, Ministry of Energy and Natural Resources (ETKB), (2008),** “Regulation on Increasing Efficiency in the Use of Energy Sources and Energy”, available at: https://www.mevzuat.gov.tr/MevzuatMetin/yonetmelik/7.5.15437.pdf.

5. **Turkish Electricity Transmission Company (TEİAŞ), (2022),** "Electrical Characteristics by Turkey's Installed Capacity and Gross Generation (1970-2022)".

6. **Uluer, M.U., Ünver, H.Ö., Akkök, M., Kılıç, S.E., (2016),** "An Investigation into Power and Energy Requirements for the Auxiliary Components of a CNC Lathe", Proceedings of the 17th International Conference on Machine Design and Production, 2, 611-628, 12 - 15 July 2016, Bursa, Turkey.

WATER JET GUIDED LASER MICRO DRILLING OF AN AEROSPACE ALLOY

Levent SUBAŞI, *levent.subasi@tei.com.tr* Tusas Engine Industries Inc., 26210, Eskisehir, Turkey

Mustafa İ. GÖKLER, *gokler@metu.edu.tr* Middle East Technical University, 06800, Ankara, Turkey

Ulaş YAMAN, uyaman@*metu.edu.tr* Middle East Technical University, 06800, Ankara, Turkey

ABSTRACT

Micro drilling of aerospace alloys is a challenge considering the material properties, geometrical complexities and the technical requirements. Water Jet Guided Laser (WJGL) machining is a novel process used in several industries. The primary advantage of the process is its combination of precision and cooling, which increase the quality in the machining area. In this study, WJGL technology was adapted for the first time to perform micro drilling of an aerospace alloy. Furthermore, material removal mechanism of the process is investigated, a process model is developed, real-time process monitoring methods are proposed and drilling time and quality optimization was performed.

Keywords: Laser drilling, Process modeling, Process monitoring, Optimization

1. INTRODUCTION

The components used in aero engines work at high temperatures. In order to tolerate the severe conditions, parts are made of nickel-based alloys and micro holes are drilled on them for cooling purpose. Since the materials are hard and the diameter of the holes are small, non-conventional manufacturing methods, such as laser drilling are preferred. Water Jet Guided Laser (WJGL) is a hybrid manufacturing technology that can be used for this purpose as well. In this process, the laser beam is guided through a cylindrical water jet, and the pressurized water provides focusing, cooling, and cleaning on the machining region. Thus, WJGL has the potential to overcome the adverse effects of dry laser drilling.

Research on the WJGL technology is highly limited. Most of the studies are related with dicing [Dushkina, 2003], grooving [Madhukar, 2016], cutting [Bruckert, 2012], and micro machining [Diboine, 2017]. Drilling examples are less and only focus on the quality aspects. In one of the studies, WJGL drilling on steel fuel injector nozzles was performed and surface integrity results with Electrical Discharge Machining (EDM) drilling were compared [Rashed, 2013]. Surface

quality measured from the hole surfaces showed improvement for the WJGL process. It was concluded that WJGL drilling is an alternative to EDM drilling. In another study, WJGL drilling quality results were compared with conventional dry laser and EDM drilling on an aerospace nickel-based alloy [Gurav, 2019]. The drilled holes were evaluated in geometric, surface quality, and metallurgical aspects. Consequently, WJGL drilled holes showed much improved quality.

The material removal mechanism was not properly addressed for the aforementioned studies. Nevertheless, there are some modeling studies dedicated to WJGL grooving and cutting, in which predictions are made for depth of material removal. In one of the studies, a model was presented for WJGL grooving of silicon, in which laser energy, water jet cooling effect, and melting of silicon are taken into account [Li, 2003]. It was found that the maximum depth is reached with the first pulses of the laser and the depth of the groove is not steady especially for higher speeds. In another study, a numerical model was developed estimating the temperature field on the cutting area for WJGL micromachining [Yang, 2009]. It was stated that the temperature field of WJGL is less compared to traditional dry laser machining. The developed model was validated with steel and silicon materials, but it was stated that parameter optimization is needed for different materials. An experimental study on WJGL cutting was done, showing the effect of using different process parameters on the cutting depth for different materials [Adelmann, 2015]. It was found that the cutting depth increases with higher laser power and lower frequency. It was also observed that there is a dimensional depth limit for the WJGL cutting and the material removal rate (MRR) decreases as it gets deeper into the slit, independent of the workpiece material. WJGL pocketing experiments on aerospace nickel-based alloys were performed [Diboine, 2017]. A semi-empirical model was developed using energy balance approximation and 1D thermal diffusion. Prediction of depth per layer was done and validated by further experiments. Accumulation effect of water was reported to adversely affect the material removal as the toolpath got closer to the walls.

As discussed above, a material removal model for WJGL micro hole drilling of nickel-based aerospace alloys has not been encountered in the literature. The physics of the material removal in WJGL is highly complex due to scattering and reflection losses at the surface, with heat diffusion causing phase change, melting, and/or vaporization. The machine parameters, material properties, and hole geometry need to be correlated to the process time and quality. The scope of the study is modeling and process optimization of WJGL micro hole drilling on nickel-based aerospace alloys.

2. WATER JET GUIDED LASER TECHNOLOGY

The working principle of the WJGL technology is shown in Figure 1. In the system, the laser beam is focused on a water jet nozzle so that the laser energy can be carried by total internal reflection within the pressurized jet. The water jet system consists of a high pressure water pump and gas flow controller. In order to stabilize the purified and pressurized water, helium is used as an assist gas. It is possible to adjust the water pressure and gas flow, separately. Water jet nozzles are generally made of diamond or sapphire, and the diameters are ranging between 40 μm to 60 μm for micro drilling purposes. The laser used in the system is a diode-pumped solid state Nd:YAG type, operating at 1064 nm wavelength. A harmonic separator transforms the wavelength to 532 nm green light. This wavelength is specifically chosen for the process since absorption of laser power is very low in water [Porter, 2007] and absorptivity by metals is better [Cabalin, 1998]. A q-switcher transforms the continuous wave to nanosecond pulses. The repetition rate of the laser is in kHz range. Laser power rating is 100 W. The frequency is an adjustable input to the system. However, it is not possible to set the power and pulse width variables directly. The power is indirectly controlled by a command value, which sets the current of the laser diode. Similarly, pulse width can be determined by setting another input called the radio frequency (RF) off time. The RF-off time defines the time during which the Q-switch becomes transparent and let the cavity lasing so that the energy stored in the rod is released. These three major laser parameters interdependently affect the average output power and pulse width. Thus, there is a need to measure the power and pulse width of the produced laser beam using an internal powermeter and oscilloscope. The beam profile in the water is a top-hat profile. Power attenuation is not negligible. There is always loss of power due the optical components (fiber, lenses, glasses, water, etc.) used in the system, as well as non-linear laser interactions in the water jet. Thus, the laser power employed on the workpiece is not directly controllable. It can only be measured using an external waterproof powermeter.

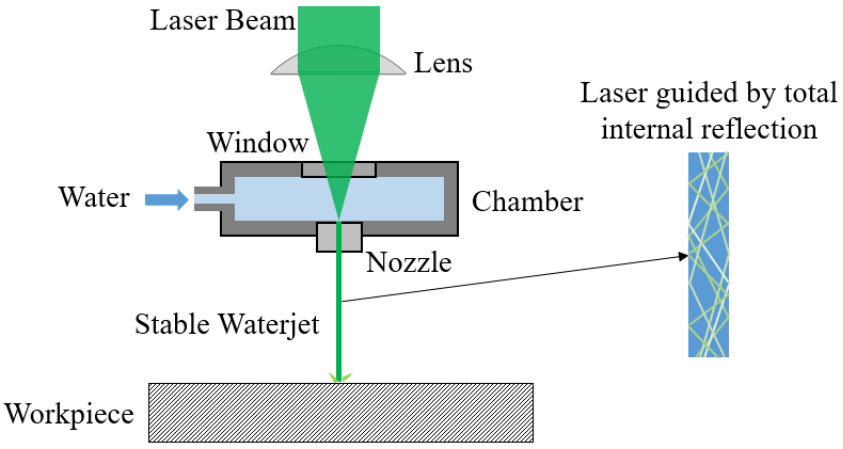


Figure 1. Working Principle of WJGL

The solid range of the adjustable parameters via the machine interface are given in Table 1. The limits are the machine constraints. Similarly, there is a power density constraint for the machine. The damage threshold of the water jet nozzle is approximately 1 GW/cm^2. This limit should not be exceeded. Thus, the laser parameters have to be chosen accordingly, meaning that the process window for the laser parameters are decided by the power density constraint. In order to calculate the power density, I_p, on the nozzle depending on the laser parameters, series of equations shown below can be used [Yeo, 1994].

$$E_p = P/f \tag{1}$$

$$P_p = E_p/\tau_p \tag{2}$$

$$I_p = P_p/A \tag{3}$$

where, E_p is the pulse energy, P is the average laser power, f is the frequency, P_p is the peak power, τ_p is the pulse width, and A is the water jet cross-section area. The area is calculated by using the diameter of the nozzle and multiplying it by a contraction factor, which shows the ratio of the water jet diameter compared to the nozzle diameter. Similarly, the power should be calculated by taking into consideration the transmission loss factor in the optical system until reaching the water jet nozzle. Measurements show that these factors are approximately 0.83 and 0.75, respectively. Using Equations (1-3), taking the nozzle diameter as 50 µm, using the related factors and unit conversions, below equation is obtained for the power density.

$$I_p = \frac{55.475P}{f\tau_p} \tag{4}$$

The power density (or peak intensity) is a compact value including all of the laser parameters. In order to stay below the damage threshold, power should be selected lower or frequency and pulse width should be selected higher.

On the WJGL system, as the laser beam leaves the nozzle, a phenomenon called Raman scattering is observed within the dielectric water jet. The laser beam encapsulated within the jet is visible to some extent and that visible portion is the effective cutting length, as shown in Figure 2. The laser light breaks up and leaves the jet at the end of this length. The laser power decreases gradually along the length due to losses by nonlinear effects [Spiegel, 2004] and

Table 1. Machine Parameters

Command (%)	48.5 – 82.5
RF – off time (µs)	0.02 – 8.00
Frequency (kHz)	6 – 60
Water pressure (bar)	50 – 500
Gas flow (l/min)	0.1 – 2.0

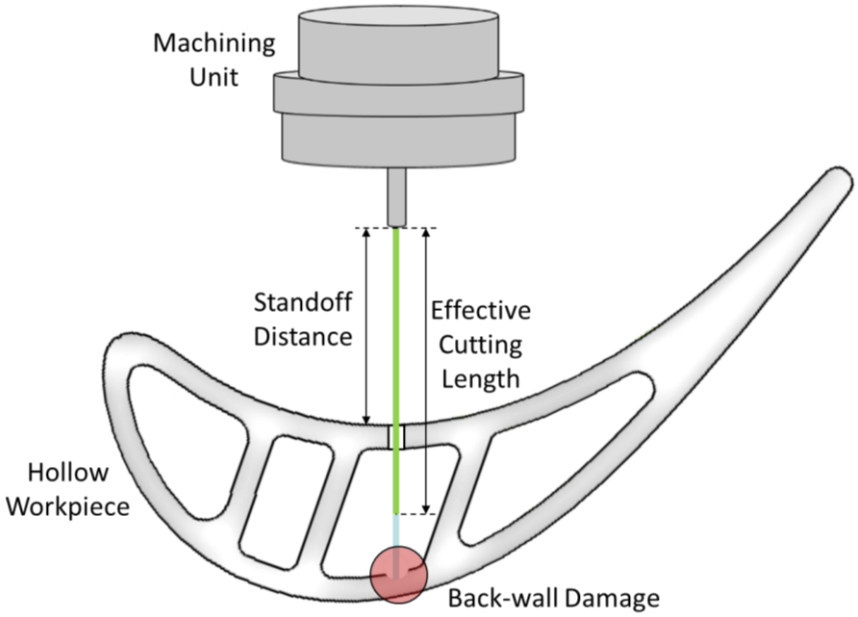


Figure 2. Effective Cutting Length

diminishes drastically at the end, generally below the material removal threshold for most metal alloys. Thus, machining stops beyond the effective cutting length. The effective cutting length can be altered by adjusting laser and water jet parameters. It is important to know about the length before performing drilling so that the standoff distance for the nozzle can be adjusted accordingly. If the standoff distance is too high, there will not be enough laser energy reaching the surface of the workpiece. If it is too low, there will be a risk of back-wall damage on the machined parts, which is a critical issue especially for drilling hollow turbine blades, as can be seen in Figure 2. WJGL, just like other laser systems, cannot prevent the laser beam reaching beyond the other side of the hole after breaking through the material.

On the WJGL system, the water jet splash back from the surface might become an issue while machining. The reflection of pressurized water from the machining area might block the laser beam and decrease the machining efficiency. This is especially more considerable when the diameters of the drilled holes are small, as the water jet is redirected along the walls of the cavity and exits from the hole entry with high velocity. Consequently, the jet entering the cavity needs to penetrate against a counter flow. In practice, this effect is mitigated by using a water jet diameter smaller than the desired hole diameter, and by moving the water jet in spiral motion, as shown in Figure 3. The spiral toolpath removes the material inside the cavity layer by layer, which is useful for avoiding undesirable artifacts on the perimeter of the holes and increasing quality, such as roundness and taper [Jacobs, 2008]. The toolpath works in the X-Y plane, and can be parametrically adjusted by defining the diameter and the size of the spiral step.

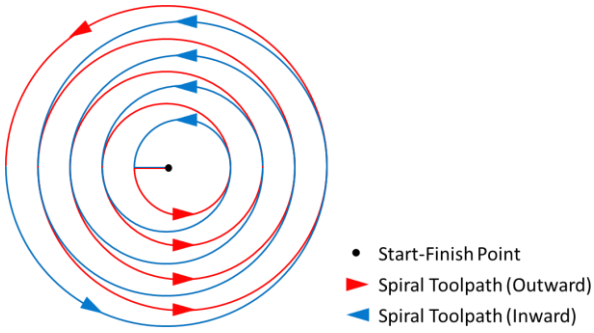


Figure 3. Spiral Toolpath

3. MATERIALS AND METHODS

Within the scope of the study, machinability of different aerospace materials are studied. Process time variations depending on the materials are determined. The power density threshold values for removing volume for each material are studied. Process window of the parameters for efficient drilling are found out. The process limits are determined. Material removal for each laser pulse is calculated. Current theory and formulae for laser-material interactions are used with efficiency factors. The material removal rates are related to the optical and thermophysical properties of the materials. The optimized parameters depending on the material and geometry are found out. Two different real-time measurement methods are proposed based on image and acoustic analysis, respectively.

Different methodologies including machine learning, statistical modeling and mathematical modeling are used, together with data collection and experiments. Taguchi design of experiment is preferred throughout the study since the methodology greatly reduced the number of experiments that are needed. Python, Excel and Minitab software packages are used for data analysis. Image and acoustic sensors are used for data collection for some certain tasks, which are described in the next section. A special ultrasound sensor is used for the purpose. The setup is shown in Figure 4.

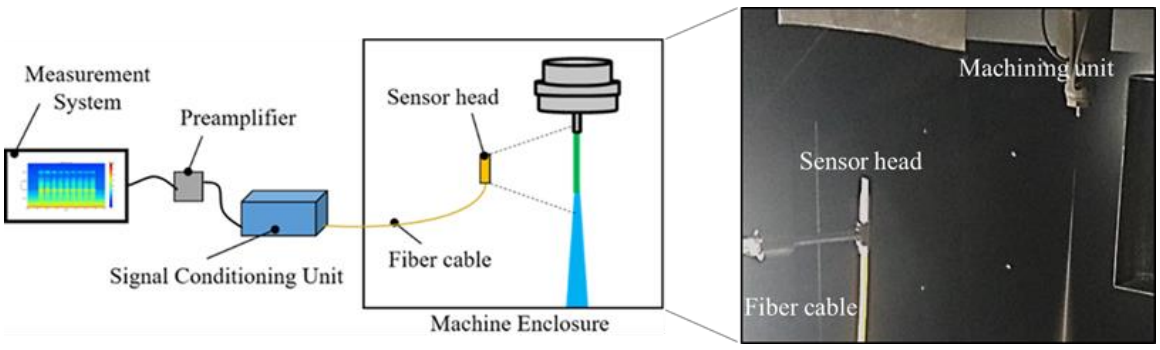


Figure 4. Acoustic Sensor Setup

There are several parameters in WJGL process. For the systematic approach, firstly determining and analyzing of the process parameters are required. For this purpose, a cause-and-effect diagram of the WJGL process has been prepared, as can be seen in Figure 5. At the beginning, the workpiece variables are already known, such as material type, part geometry, hole diameter, etc. The nozzle diameter is almost always chosen as 50 µm, since it is an ideal size by experience for making the required micro hole dimensions. Other process parameters have to be decided based on the previous experiences, best practices and machine constraints. Several types of devices are used for data collection and experiments throughout the study. Table 2 shows these instruments together with measuring and usage purposes.

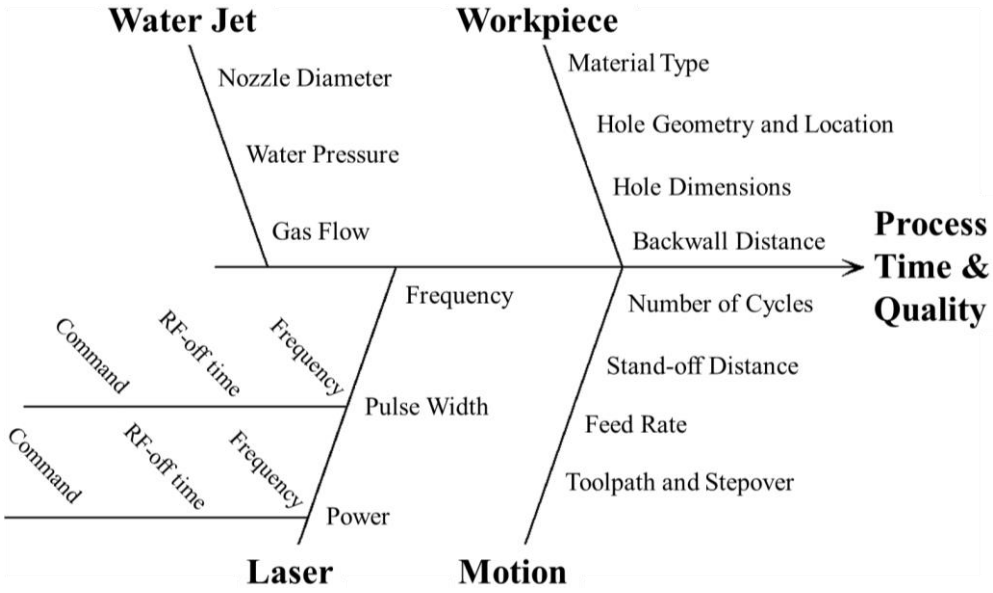


Figure 5. Cause and Effect Diagram of the WJGL Process

Table 2. Types of Measurement Instruments and Their Use

Instrument	For Measuring	Used in
Chronometer	The process time	Experiments on process time and quality
Steel pin gage set	Diameter of the holes	Experiments on process time and quality
Power meter	Laser power	Modeling experiments
Oscilloscope	Pulse width	Modeling experiments
Scale	Weight of the samples	Modeling experiments
Image sensor	Laser length and power	Laser beam characteristic measurements
Acoustic sensor	Laser power, hole depth, machining efficiency, and breakthrough	Laser beam characteristic measurements and studies regarding machining behavior depending on hole geometry
X-ray Computed Tomography (CT) device	Hole depth and morphology	Studies regarding machining behavior depending on hole geometry

4. RESULTS AND DISCUSSION

A simplified holistic material removal model is proposed as seen in Figure 6. The model combines the input parameters in a process flowchart. Each step is considered independently, before moving on to the next step. The methodology is validated with experiments. In order to decide the most important parameters, an experimental study in terms of cycle time and hole quality for hole drilling has been conducted [Subasi, 2020]. An optimization was done, but it was evident that an expanded process window was necessary. Thus, the follow-up study investigated the material removal mechanism of WJGL [Subasi, 2022]. A modeling approach was developed including the necessary parameters for drilling of different aerospace materials. Following that, two different real-time measurement methods related to image processing and acoustic signal processing were proposed, both of which provide instantaneous readings for the laser beam characteristics [Subasi, 2022]. Finally, experiments were conducted with different hole diameters to explore the process limits and find out the machining efficiency depending on the depth [Subasi, 2023]. The experiments showed a correlation between ultrasound emission and material removal depending on the hole geometry in WJGL drilling.

Step 1 – Predict the Laser Output

The laser parameters are highly affected by the construction of the laser unit (variation in properties of the optical components, distance between the components, set temperature, etc.). Each constructed laser is different, so there is no general formula, but the principles are known. There are controllable inputs, so the desired output can be obtained, by adjusting the input parameters. Artificial neural network modeling provides precise predictions, whereas statistical regression modeling shows the important factors and the relations between inputs and outputs. The power density is calculated before moving on to the next step by using a physics based derived formula.

Step 2 – Predict the Effective Cutting Length

The length should be known before drilling, so that the standoff distance can be adjusted accordingly. If the standoff distance is too long, there will not be enough laser energy reaching the surface of the workpiece. If it is too short, there will be a risk of back-wall damage on the machined parts. The effective cutting length can be altered by adjusting laser and waterjet parameters. Artificial neural network modeling provides precise predictions, whereas statistical regression modeling shows the important factors and the relations between inputs and outputs. A real-time measurement method is also proposed based on image analysis, as shown in Figure 7. The length should be checked before moving on to the next step.

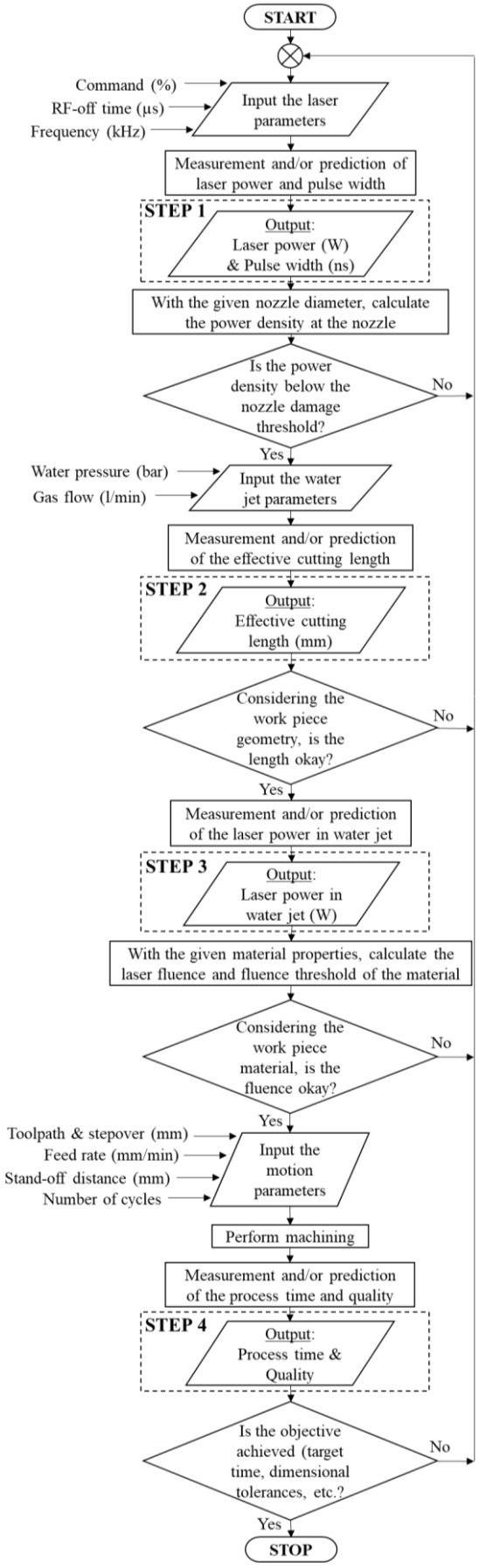


Figure 6. General Flowchart of WJGL Process Modeling

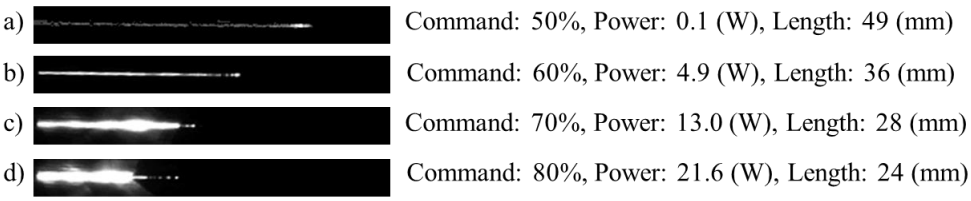


Figure 7. Images for Different Command Values (Water Pressure is 200 bar, Gas Flow is 1 l/min, RF-off Time is 2.00 µs, and Frequency is 10 kHz)

Step 3 – Predict the Laser Attenuation in Water

The laser power decreases gradually along the length due to losses by nonlinear effects. The power for a specified standoff distance can be estimated by using curve fitting method. Two different real-time measurement methods are also proposed based on image and acoustic analysis, respectively. Figure 8 shows the spectrogram of an acoustic measurement. The fluence threshold specific to the material should be calculated and checked before moving on to the next step. A physics based derived formula is used for this purpose.

Step 4 – Predict the Material Removal Rate

Energy balance method is used, which is a physics based derived formula. The material removal model is based on the machining efficiency, so efficiency factors are considered for different cases. A real-time measurement method is also proposed for hole depth and machining efficiency based on acoustic analysis.

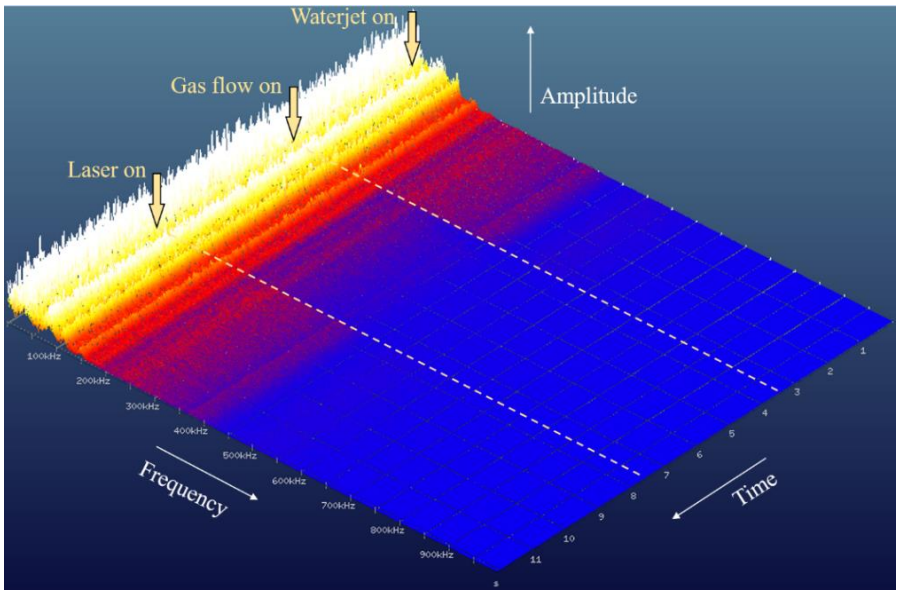


Figure 8. Preliminary Acoustic Measurement (Just the Water Jet is on First-200 bar, Then Gas Flow is Turned on-1 l/min, and Then Laser is Turned on-80%-2.00 µs-10 kHz)

The proposed image and acoustic sensing methods provide some advantages, which are currently missing in the WJGL machine. It is important to know about the laser beam characteristics in the waterjet before the process, in order to adjust the machining parameters accordingly. There is already an external waterproof power meter in the machine for measuring the power level in the water. Although it is possible to use it before starting the process, the measurement takes time, since the nozzle should be moved to a different location in the machine and then stay there at the laser on condition for some time to get the power reading. Regarding the effective cutting length measurement, there is no equipment available on the machine to precisely measure it. The distance from the tip of the nozzle to the tip of the visible laser light is generally measured by eyesight taking a fixed plate as reference. This method may result in repeatability and reproducibility errors. The proposed methods provide a more robust solution and provide instantaneous readings for calculating the exact values of the laser beam characteristics before starting the process.

Additionally, the correlation between ultrasound emission and material removal depending on the hole geometry is revealed. There is currently no depth sensor or any means to monitor the machining process in a WJGL machine. The measured sound signatures are correlated to the hole depth, machining efficiency and hole breakthrough.

5. CONCLUSION

Experimental, optimization, and modeling studies have been conducted to predict the material removal rate for WJGL micro hole drilling. The significant process parameters and their relation to material removal rate and quality are revealed. The physical aspects of material removal mechanisms for WJGL processing have been investigated. The causes of inefficient machining are discussed in light of the theoretical aspects. Laser ablation mechanism, machine process window, processing limits (minimum diameter & maximum depth capability), and related parameters have been studied for the WJGL. Real-time measurement and monitoring of the process both by image processing and acoustic signal processing have been performed. A better understanding of the process is achieved in the end.

The main outcomes of this work are as follows.

1. A methodology has been proposed for simplified and holistic modeling of the WJGL process.

2. It has been presented how the input parameters should be determined for efficient and higher quality micro drilling of nickel-based alloys.
3. It has been shown how image processing with a camera can be used to determine the effective cutting length and the laser power in the water jet.
4. It has been shown how acoustic monitoring with an optical microphone can be used to determine laser power in the water jet, hole depth, machining efficiency, and breakthrough.

The study would create many opportunities for future work. The modeling study can be further extended to cover other materials. The model can be improved to represent the geometrical conditions better. Different tool paths resulting in different geometries may be studied. The physical mechanisms of the inefficiencies related to WJGL micromachining can be studied in more detail so that the model can be developed to give more accurate results. The proposed model can be embedded into a software package so that a digital model of the WJGL machine can be obtained. It is possible to implement intelligent acoustic analysis software into the machine interface so that the acoustic signals would provide feedback to the operator about the machining conditions. Another feedback system can be introduced on the machine, in which the operator inputs the desired length and/or power value in the interface. Machine parameters may change automatically to meet the desired output by using real-time measurement by image/acoustic analysis and active feedback control.

6. ACKNOWLEDGEMENT

This work was supported by The Scientific and Technological Research Council of Turkey (TUBITAK) Directorate of Science Fellowships and Grant Programmes (BIDEB) 2211-A [grant number 1649B031804554]. The authors would also like to thank to Synova SA for their technical support, Tusas Engine Industries (TEI) for their permission to use the facilities and colleagues from TEI who made this study possible.

7. REFERENCES

Dushkina, N.M., Wagner, F.R., Boillat, C., Buchilly, J.M. and Richerzhagen, B., (2003), “Water Jet Guided Laser Versus Saw Dicing”, Photon Processing in Microelectronics and Photonics II, Vol.4977, pp 75-85.

Madhukar, Y.K., Mullick, S. and Nath, A.K., (2016), “A Study on Co-Axial Water-Jet Assisted Fiber Laser Grooving of Silicon”, Journal of Materials Processing Technology, 227:200-15.

Bruckert, F., Pilat, E., Piron, P., Torres, P., Carron, B., Richerzhagen, B., Pirot, M. and Monna, R., (2012), "Tailor Cutting of Crystalline Solar Cells by Laser Micro Jet", High Power Laser Materials Processing: Lasers, Beam Delivery, Diagnostics, and Applications, Vol.8239, pp 191-197.

Diboine, J., Martin, R., Bruckert, F., Diehl, H. and Richerzhagen, B., (2017), "Towards Near-Net Shape Micro-Machining of Aerospace Materials by Means of a Water Jet-Guided Laser Beam", Lasers in Manufacturing Conference, Munich, Germany.

Rashed, C.A., Romoli, L., Tantussi, F., Fuso, F., Burgener, M., Cusanelli, G., Allegrini, M. and Dini, G., (2013), "Water Jet Guided Laser as an Alternative to EDM for Micro-Drilling of Fuel Injector Nozzles: A Comparison of Machined Surfaces", Journal of Manufacturing Processes, 15(4):524-32.

Gurav, M.M., Gupta, U. and Dabade, U.A., (2019), "Quality Evaluation of Precision Micro Holes Drilled Using Pulsed Nd: YAG Laser on Aerospace Nickel-Based Superalloy", Materials Today: Proceedings, 19:575-82.

Li, C.F., Johnson, D.B. and Kovacevic, R., (2003), "Modeling of Waterjet Guided Laser Grooving of Silicon", International Journal of Machine Tools and Manufacture, 43(9):925-36.

Yang, L.J., Wang, M.L., Wang, Y., Tang, J. and Chen, Y.B., (2009), "Numerical and Experimental Research on Water-Jet Guided Laser Micromachining", Materials Science Forum, Vol.626, pp 297-302.

Adelmann, B., Ngo, C. and Hellmann, R., (2015), "High Aspect Ratio Cutting of Metals Using Water Jet Guided Laser", The International Journal of Advanced Manufacturing Technology, 80(9):2053-60.

Porter, J.A., Louhisalmi, Y.A., Karjalainen, J.A. and Füger, S., (2007), "Cutting Thin Sheet Metal With a Water Jet Guided Laser Using Various Cutting Distances, Feed Speeds and Angles of Incidence", The International Journal of Advanced Manufacturing Technology, 33(9):961-7.

Cabalin, L.M. and Laserna, J.J., (1998), "Experimental Determination of Laser Induced Breakdown Thresholds of Metals Under Nanosecond Q-Switched Laser Operation", Spectrochimica Acta Part B: Atomic Spectroscopy, 53(5):723-30.

Yeo, C.Y., Tam, S.C., Jana, S. and Lau, M.W., (1994), "A Technical Review of the Laser Drilling of Aerospace Materials", Journal of Materials Processing Technology, 42(1):15-49.

Spiegel, A., Vago, N. and Wagner, F.R., (2004), "High Efficiency Raman Scattering in Micrometer-Sized Water Jets", Optical Engineering, 43(2):450-4.

Jacobs, P., (2008), “Precision Trepanning With a Fiber Laser”, International Congress on Applications of Lasers & Electro-Optics, Vol.2008, No.1, p 303.

Subasi, L., Gokler, M.I. and Yaman, U., (2020), “Multi Objective Optimization of Water Jet Guided Laser Micro Drilling on Inconel 718 Using Taguchi Method”, Procedia CIRP, 94:505-10.

Subasi, L., Gokler, M.I. and Yaman, U., (2022), “A Process Modeling Approach for Micro Drilling of Aerospace Alloys With a Waterjet Guided Laser System”, Optics & Laser Technology, 148:107682.

Subasi, L., Gokler, M.I. and Yaman, U., (2022), “Real-Time Measurement of Laser Beam Characteristics for a Waterjet Guided Laser Machine”, Int J Adv Manuf Technol.

Subasi, L., Gokler, M.I. and Yaman, U., (2023), “A Comprehensive Study on Water Jet Guided Laser Micro Hole Drilling of an Aerospace Alloy”, Optics & Laser Technology, 164:109514.

INTEGRATION OF 6-AXIS HEXAPOD WITH NANOSECOND LASER FOR MICRO MACHINING

Aykut BAKAN, *aykut.bakan@bilkent.edu.tr* Bilkent University, 06800, Ankara, Turkey

Yiğit KARPAT, *ykarpat@bilkent.edu.tr* Bilkent University, 06800, Ankara, Turkey

ABSTRACT

Manufacturing parts with complex geometries is an everlasting need in the aerospace, automotive, and biomedical industries. Recent developments bring forth the requirements of machining parts with complex geometries. Therefore, machining setups that are flexible and precise are needed to satisfy such requirements. This work presents our findings on machining structured surfaces using a 6-axis hybrid hexapod integrated with a nanosecond fiber laser. In this paper, we provide a detailed description of the inverse kinematic analysis and experimental determination of the workspace of the hexapod, as well as the modeling of the complex surfaces of the parts to be machined. Results indicate the viability of the micromachining setup in advanced manufacturing applications.

Keywords: Complex Geometry, 6-Axis Hybrid Hexapod, Nanosecond Fiber Laser, Workspace, Surface Modelling

1. INTRODUCTION

Machining parts with complex geometries is an ever-increasing need in different areas, such as cooling holes of turbine blades, lubrication holes of bearings and shafts, structured surfaces on biomedical implants, etc. [Michel, 2018]. Moreover, holes themselves can have a complex geometry like converging-diverging nozzles. Such multidimensional holes are utilized in propulsion systems of microsatellites [Louwerse, 2009], fuel injectors, and particle filtration [He, 2019].

Whether it is the part itself or the hole, the primary requirement for processing complex geometries is a high-precision positioning system. There are many examples of robot manipulators being used in manufacturing applications, such as drilling, cutting, milling [Wang, 2023], polishing [Ke, 2023], and grinding [Song, 2023]. Robots may be more suitable for some

applications than CNC machines [Son, 2023]. Robot manipulators can be categorized into serial and parallel manipulators [Kurekova, 2014]. Serial manipulators have an open-loop chain mechanism, while parallel manipulators have a closed-loop mechanism. Due to the accumulation of positional errors at the end effector and their inherently small working volume, serial manipulators are not preferable for high-precision applications. On the contrary, parallel manipulators have a larger working volume than serial manipulators and exhibit better dynamic performance [Dasgupta, 2000]. The combination of serial and parallel manipulators also exists in the literature [Yang, 2018]. Such manipulators are often called “hybrid”.

Computer Aided Manufacturing (CAM) software generates G-codes that generate the locations of the cutter [Xiang, 2016]. Therefore, a typical G-Code program contains commands, and the positioning system moves the tool and the part according to these commands; however, in systems where parallel manipulators are used to position the workpiece. The discrete position inputs are used to create a path for the manipulator through various interpolation methods, and a consistent simulation of the manipulator must be designed and tested on a computer before turning the positions into drive commands. It’s possible to obtain path interpolation using mathematical methods such as B-Spline [Zhang, 2019] and NURBS [Jahanpour, 2016]. The simulation of the position and the orientation of the manipulator can be made via inverse kinematic equations [Li, 2017]. Another critical aspect is analyzing whether the positioning system can execute the generated path. A workspace analysis can be conducted to determine this. The workspace represents the maximum volume that a manipulator can reach. It can be determined experimentally [Desai, 2021] by noting the positions successfully reached by the positioning system or analytically [Ahn, 2007] in a similar manner but using equations instead of experiments. Conducting the workspace analysis provides crucial information on whether a part can be processed before actual machining begins.

After identifying an appropriate positioning system, the secondary requirement is to find a suitable manufacturing tool capable of performing the machining process. Conventionally, cutting tools have been most widely used for machining processes. However, cutting tools are often unsuitable for complex drilling operations or machining parts with complex geometries due to their inherent limitations such as tool wear, spindle speed, and available cutting tool sizes [Karkantonis, 2022]. On the contrary, lasers do not have these disadvantages and offer

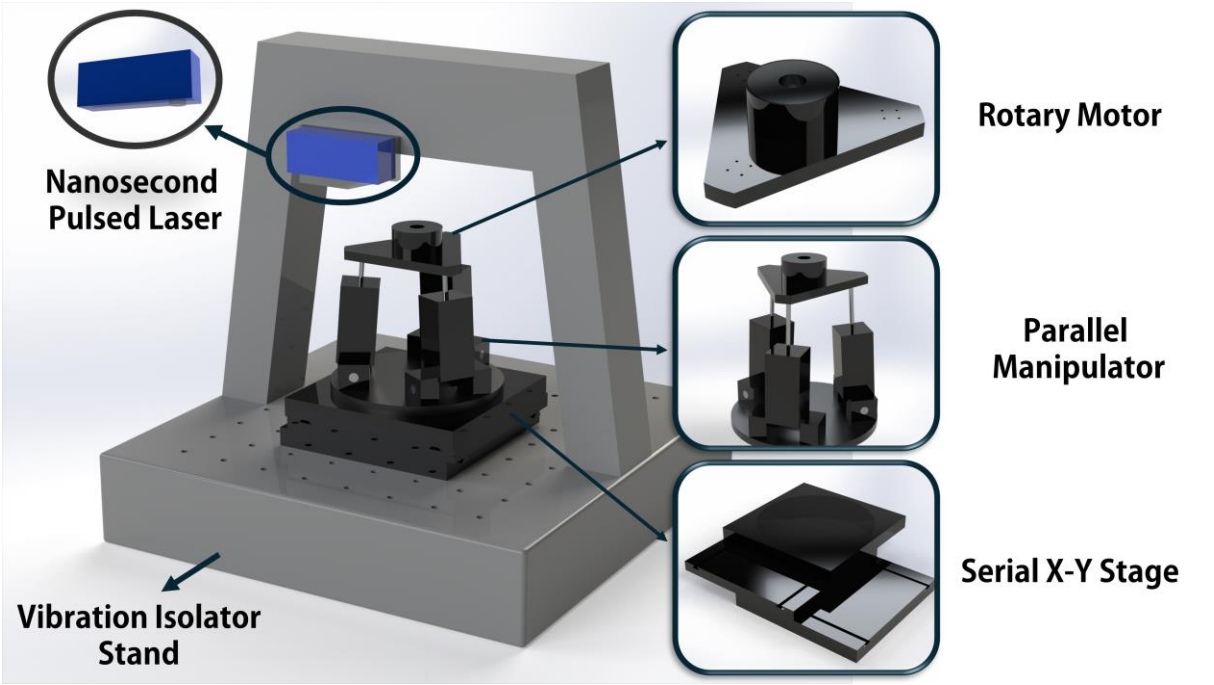


Figure 1. Hexapod-Laser Setup

additional benefits such as non-contact operation, chip-less machining, and the ability to work in very small areas [Popov, 2011]. Laser Micro Machining (LMM) technology offers different kinds of applications in the industry and literature such as drilling [Ashkenasi, 2011], polishing [Manco, 2022], texturing [Wang, 2019]. When combined with a precise positioning system, literature suggests that lasers can perform these types of operations on complex geometries as well [Vidyasagar, 2021].

In this study a 6-DoF hybrid hexapod manipulator is utilized for positioning. The hexapod consists of a 3-RPS (Rotational Prismatic Spherical) parallel manipulator, mounted on a translational X-Y planar serial manipulator, and an independent rotary motor for the rotation around the Z axis standing at the top of the parallel manipulator. The inverse kinematic equations for the parallel 3-RPS part were found to simulate the orientation of the hexapod. Additionally, experimental workspace was analyzed to understand positioning capabilities. Also, a nanosecond Q-switch pulsed laser was assembled on a vibration isolator stage to perform the machining. General configuration of the experimental setup is given in Figure 1. In Section 1, we provide an overview of the approach taken to machine complex geometries or to drill multidimensional holes. In Section 2, we give the inverse kinematic equations and position analysis. Section 3 is about how to model complex geometries in MATLAB environment to ensure accurate positioning of a 6-axis hybrid manipulator including how to divide the surface of the workpiece into grids and determine the normal vectors of each grid to provide appropriate angle inputs to the manipulator. Section 4 explains the experimental

method used for determining the workspace to understand if the hexapod can handle the motion needed to machine the workpiece. On Section 5, we discuss the results obtained for drilling holes on a complex geometry. Lastly, the finalization of the work containing the summaries and conclusions given in Section 6.

2. METHODOLOGY

LMM using a hybrid manipulator is a challenging task from many perspectives, including finding the complex kinematics of the manipulator, modeling the complex geometry, finding the workspace, and trajectory planning. The methodology used in this work can be broken down into six categories as follows: (1) Design a complex geometry using SOLIDWORKS and take the CAD file in IGES format. (2) Read the data using MATLAB IGES Toolbox and extract the NURBS surfaces. There are certain types of entities included in an IGES file. To extract the NURBS surfaces or curves for further analysis, write an external code that searches for them. (3) Model the surface of the complex geometry using MATLAB NURBS Toolbox. This is essential for tiling the surface and finding the normal vectors of the tiles where the holes will be drilled. (4) Find the necessary position inputs by using the normal vectors of the tiles and the kinematic equations. (5) Check if the hexapod can achieve the necessary position inputs from its experimentally found workspace. (6) Write the position inputs in PPMAC (Power – Programmable Multi-Axis Controller) format and give as the input to the hexapod and execute the operation.

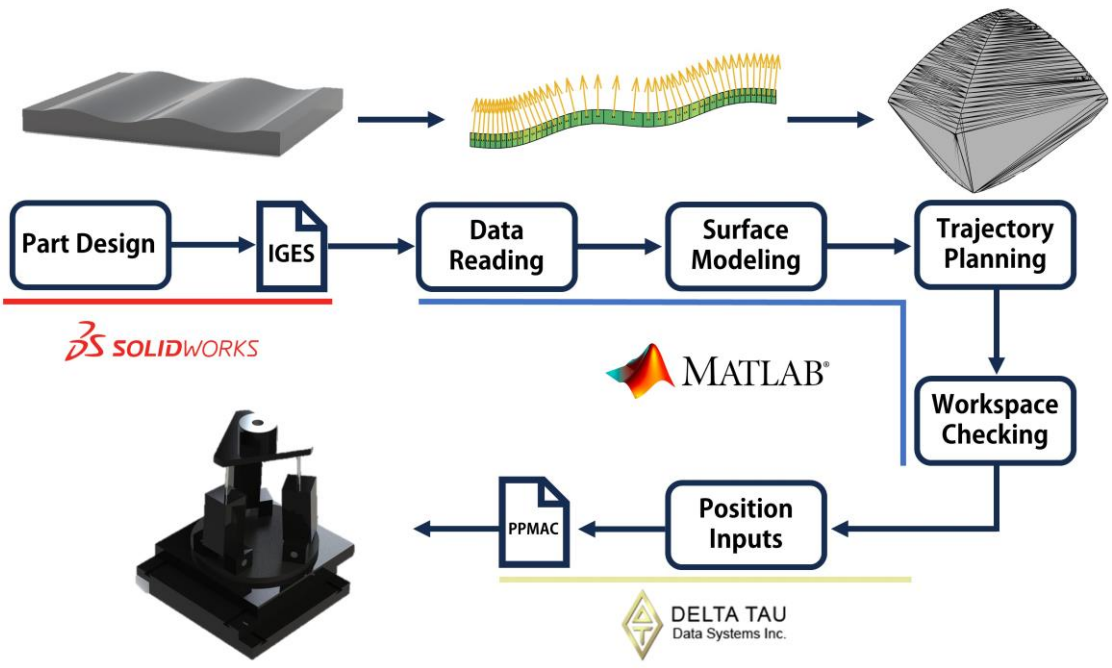


Figure 2. Complex Surface Machining Steps

3. KINEMATICS

In this section, we discuss our method for performing kinematic analysis. The inverse kinematic equations of the hexapod have been derived, and the values that the joints and limbs need to take for a given end-effector position and platform orientation have been determined. These kinematic equations have enabled the identification of independent parameters and allowed for movement based on these parameters when inputting data into the system. Additionally, before processing a part with complex geometry, it has been possible to check in advance the orientations the system will take based on the given angular inputs and verify whether the laser beam and surface normal vectors align. The kinematic equations have been solved in the MATLAB environment.

3.1 Overall Structure of Manipulator and Reference Frames

The type of manipulator that is used in this work is called a hybrid manipulator which has 6 degrees of freedom. A hybrid manipulator is a combination of serial and parallel kinematic structures where the serial part is composed of two sliding stages, which provide a planar movement to the platform. On the other hand, the parallel part is composed of three limbs, which have revolute, prismatic, and spherical joints that provide the setup to move on yaw, pitch, and roll axes to the end-effector and allows it to elevate. A 3-RPS manipulator is composed of 3 revolute, prismatic, and spherical joints. In Figure 3.b., spherical joints are given in blue, prismatic joints are given in red, and revolute joints are given in green.

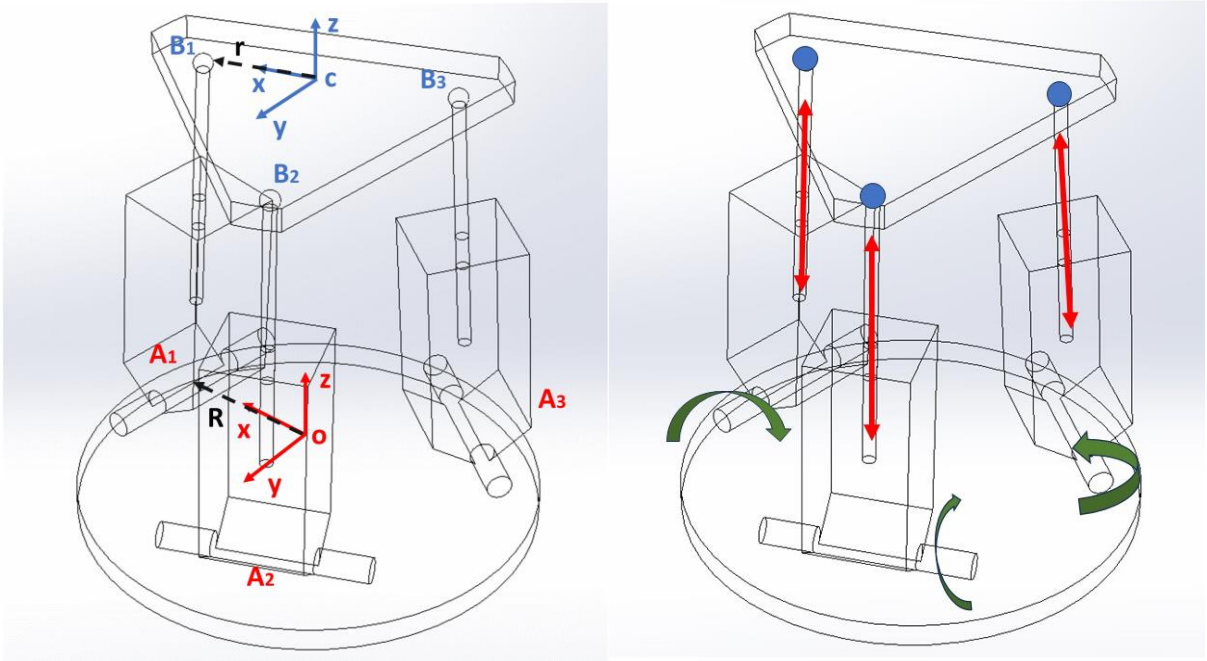


Figure 3. a. Reference Frames o-xyz and c-xyz, b. Joint types indicated in red, green and blue colors for prismatic, rotational, and spherical joints respectively (right).

Two reference frames, one being an inertial reference frame (o-xyz) and the other one is the moving reference frame (c-xyz) in figure 3. In a 3-RPS parallel manipulator, it is assumed that both the points $B_1B_2B_3$ and $A_1A_2A_3$ make equilateral triangles.

3.2 Position Analysis

Positions of points A_1, A_2, A_3 and B_1, B_2, B_3 could be written in their reference frames o-xyz and c-xyz as

$$A_1/o = \begin{bmatrix} R \\ 0 \\ 0 \end{bmatrix}, \qquad B_1/c = \begin{bmatrix} r \\ 0 \\ 0 \end{bmatrix},$$

$$A_2/o = \begin{bmatrix} -\frac{R}{2} \\ -\frac{\sqrt{3}R}{2} \\ 0 \end{bmatrix}, \qquad B_2/c = \begin{bmatrix} -\frac{r}{2} \\ -\frac{\sqrt{3}r}{2} \\ 0 \end{bmatrix}, \qquad (1), (2)$$

$$A_3/o = \begin{bmatrix} -\frac{R}{2} \\ \frac{\sqrt{3}R}{2} \\ 0 \end{bmatrix}, \qquad B_3/c = \begin{bmatrix} -\frac{r}{2} \\ \frac{\sqrt{3}r}{2} \\ 0 \end{bmatrix},$$

where R and r are the distance of the points A_1 and B_1 measured from the origin of the coordinate frames o-xyz, and c-xyz respectively. Ai/o states the position of the joints A_i in the inertial reference frame o-xyz, and B_i/c states the position of the joints B_i in the moving reference frame c-xyz. To find the position of points B_1/c, B_2/c, and B_3/c using their positions in c-xyz reference frame, coordinate transformation could be applied as

$$\begin{bmatrix} B_{ix} \\ B_{iy} \\ B_{iz} \end{bmatrix}_{/o} = Rot \begin{bmatrix} B_{ix} \\ B_{iy} \\ B_{iz} \end{bmatrix}_{/c} + \begin{bmatrix} c_x \\ c_y \\ c_z \end{bmatrix}. \qquad (3)$$

where Rot denotes the rotation matrix given as

$$Rot = \begin{bmatrix} \cos\alpha\cos\beta & \cos\alpha\sin\beta\sin\theta - \sin\alpha\cos\theta & \cos\alpha\sin\beta\cos\theta + \sin\alpha\sin\theta \\ \sin\alpha\cos\beta & \sin\alpha\sin\beta\sin\theta + \cos\alpha\cos\theta & \sin\alpha\sin\beta\cos\theta - \cos\alpha\sin\theta \\ -\sin\beta & \cos\beta\sin\theta & \cos\beta\cos\ \theta \end{bmatrix}. \qquad (4)$$

This matrix is known as Tait-Bryan $Z1Y2X3$ written in α, β, θ angles for the rotations around Z, Y, and X axes respectively.

The revolute joint of the limb A_1B_1 can only rotate around the y axis due to the geometric constraints of the mechanism. Therefore, its position in the y-axis cannot be changed throughout any motion mechanism does. Likewise, the revolute joints of the limbs A_2B_2 and

A_3B_3 can only rotate around the axes y = $\sqrt{3}x$ and y = $-\sqrt{3}x$ respectively. These constraints can be written as

$$B_{1y} = 0, \qquad B_{2y} = \sqrt{3}B_{2x}, \qquad B_{3y} = -\sqrt{3}B_{3x}. \tag{5}$$

Using Equation 4, B_{ix}, B_{iy} and B_{iz} can be found as

$$B_{1x} = c_x + r cos\alpha\, cos\beta, \qquad B_{2x} = c_x - \frac{r cos\alpha\, cos\beta}{2} + \frac{\sqrt{3}r(sin\alpha\, cos\theta - cos\alpha\, sin\beta\, sin\theta)}{2},$$

$$B_{1y} = c_y + r cos\beta\, cos\alpha, \qquad B_{2y} = c_y - \frac{r cos\beta\, sin\alpha}{2} - \frac{\sqrt{3}r(cos\alpha\, cos\theta + sin\alpha\, sin\beta\, sin\theta)}{2},$$

$$B_{1z} = c_z - r sin\beta, \qquad B_{2z} = c_z + \frac{r sin\beta}{2} - \frac{\sqrt{3}r\, cos\beta\, sin\theta}{2}, \tag{6}$$

$$B_{3x} = c_x - \frac{r cos\alpha\, cos\beta}{2} - \frac{\sqrt{3}r(sin\alpha\, cos\theta - cos\alpha\, sin\beta\, sin\theta)}{2},$$

$$B_{3y} = c_y - \frac{r cos\beta\, sin\alpha}{2} + \frac{\sqrt{3}r(cos\alpha\, cos\theta + sin\alpha\, sin\beta\, sin\theta)}{2},$$

$$B_{3z} = c_z + \frac{r sin\beta}{2} + \frac{\sqrt{3}r\, cos\beta\, sin\theta}{2}.$$

Solving Equations 5 and 6 concludes that α, c_x, and c_y are the dependent variables. In other words, it is not possible to give inputs directly to these variables. Therefore, the independent variables are β, c_z, and θ so it is possible to give inputs to roll, pitch, and heave. The equations can be given as

$$\alpha = \text{atan}\left(\frac{sin\beta\, sin\theta}{cos\beta + cos\theta}\right), \tag{7}$$

$$c_x = \frac{r cos\alpha\, cos\beta - r cos\alpha\, cos\theta - r sin\alpha\, sin\beta\, sin\theta}{2}, \tag{8}$$

$$c_y = -r cos\beta\, sin\alpha. \tag{9}$$

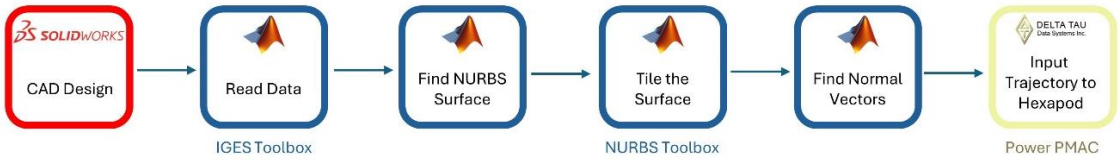


Figure 4. Step-by-step representation from CAD Design to trajectory input.

4. SURFACE MODELING

Surface modelling is key to planning the positions of the hexapod especially when dealing with complex geometries. First, a design could be made in a CAD software, which is SOLIDWORKS in our case. Essentially, SOLIDWORKS utilizes NURBS to create, modify, and visualize complex geometries. Thus, the NURBS data can be extracted by saving the file as .igs and could be found by searching for the entities for NURBS, (for instance Type 128 points out a NURBS surface) the output IGES file from SOLIDWORKS can be transferred into MATLAB by using IGES Toolbox. However, the transferred IGES data is not straightforward most of the time. Thus, a simple search algorithm is used in MATLAB to find and use the NURBS surface. After, the NURBS Library for MATLAB is used to tile the surface to locate the region to be machined and to find the normal vectors of the tiled area. The reason behind finding the normal vector of the tiled region is to give rotation input to the manipulator for keeping the beam incident angle (BIA) perpendicular (0° Angle), i.e., the angle between the laser beam and surface tangent at the incident point, perpendicular. The same tiling methodology could be used for drilling holes, texturing, or surface finishing etc. After tiling the NURBS surface and finding the normal vectors of the tiled areas, a separate MATLAB code utilizes the kinematic equations given in section 2 to find the perpendicular BIA. In the last step, the angles and cartesian positions of the tiles are converted into a PPMAC (Power Programmable Multi-Axis Controller) code and given as input to the hexapod. The overall representation of steps, toolboxes and software used in these steps are given in figure 4.

To find the perpendicular BIA, the position of the laser beam is taken as a unit vector acting downwards. The angle between all the normal vectors of the tiles and the laser beam is found. An example of a tiled complex surface and the normal vectors of the tiles is given in figure 5.

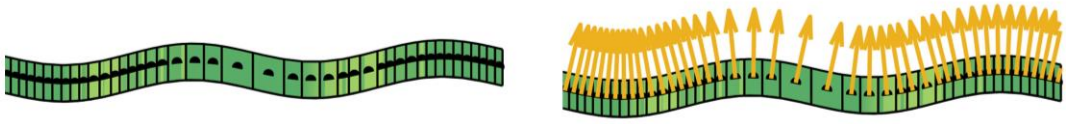


Figure 5. Tiled surface (left), tiled surface with normal vectors (right)

Then, the angle found is used as an input to Equation 4 to recalculate the rotation matrix. The new rotation matrix is used to calculate the new positions of the end-effector, points B1, B2, B3, and the normal vectors of the surface. If the positions are contained in the workspace of the hexapod, they have given to the hexapod are gathered as the output of the MATLAB code and given to the hexapod through PPMAC. The methodology for finding the workspace is given in the following part.

5. WORKSPACE ANALYSIS

Understanding the behavior and the physical limitation of a manipulator is essential especially when used for manufacturing purposes. As mentioned earlier, the hexapod is composed of three parts: parallel (3-RPS) part, serial planar X-Y stage, and independent rotary motor around Z-axis. The parallel part is responsible for rotating the workpiece, with respect to the laser beam. Thus, the workspace analysis of the manipulator is done experimentally for the parallel (3-RPS) part of the hexapod. The experimental workspace is found by giving certain combinations of roll, pitch angles, and Z-axis positions (heave) that are incrementally increasing starting from zero to check if the hexapod can achieve the given inputs. Position data of the limbs when the combinations that are successfully achieved by the hexapod are extracted from the built-in sensors. As the center of the platform (end effector) does not change its position by the rotation of the platform, the workspace of the limbs is found instead of end effector. After, the limb positions are saved and the workspace is represented by convex hull, which is found by a well-known Gift-Wrapping Algorithm [Jarvis, 1973]. The workspace of the limbs essentially gives how much the platform could be rotated at a certain heave input. The representation of workspaces of the limb A_1B_1 and A_2B_2 as a function of heave input are given in figures x y. Obtained workspaces shows that the maximum rotation could be achieved around a heave input of 25 to 30 mm.

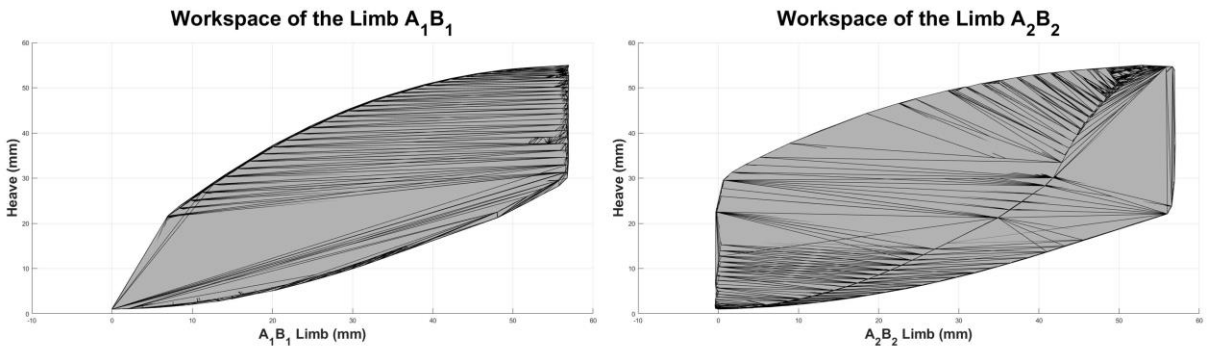


Figure 6. Workspace of the Limbs A_1B_1 and A_2B_2

6. RESULTS & DISCUSSION

Through following the steps mentioned in the previous sections, the results obtained for drilling holes on the normal vectors of a complex surface and angular holes on a flat surface are given in Figure 7 and Figure 8 respectively. A total of 10 holes were drilled on the complex surface and 11 holes were drilled on flat surface to verify the effectiveness of the proposed methodology. The overall results in Figure 7 represent that the holes are successfully drilled in the normal directions of the sinusoidal surface. The parts A and B on Figure 7 zoom in to the regions where the highest angle input is needed for hexapod to rotate. Measurement taken from both parts points out that the holes are very close to be perpendicular to the surface tangents which is another way to verify that the laser beam is in perpendicular incidence with the surface normal. On the other hand, overall results in Figure 8 depict that the holes were drilled with desired angles on the flat surface. Holes number 1 to 5 desired to be drilled with a 15, 12, 9, 6, and 3 degrees to the surface with clockwise rotation respectively, hole number 6 is desired to be perpendicular to the surface, and holes number 7 to 11 desired to be drilled with a 3, 6, 9, 12, 15 degrees to the surface with counterclockwise rotation respectively. The resulting width, height, and angle between the hole and surface normal measurements for the holes in Figure 7 and angle between the hole and surface normal measurements for the holes in Figure 8 are given in Table 1 and Table 2 respectively.

The results indicate that that the proposed methodology is effective in accurately drilling holes using nanosecond pulsed laser on the normal vectors of a complex surface. These findings suggest that the approach proposed in the study can be reliably used in practical applications where precise drilling on complex surfaces or angular drilling on flat surfaces is required.

Hole Number	1	2	3	4	5	6	7	8	9	10
Width (µm)	225.1	225.2	225.3	225.6	225.7	225.4	224.1	225.1	221.1	201.1
Height (µm)	1075.3	833.4	1033.4	1106.2	1192.1	1093	1103.4	1035.5	1058.2	1055.3
Angle (°)	89.9	90.4	90.3	90.8	89.6	90.5	91.5	90.3	90.6	90.4

Table 1. Width, Height, and Angle measurements of the holes drilled on a complex surface

Hole Number	1	2	3	4	5	6	7	8	9	10	11
Desired Angle	15°	12°	9°	6°	3°	0°	3°	6°	9°	12°	15°
Actual Angle	15.04°	12.01°	8.98°	5.89°	2.78°	0.81°	3.2°	6.22°	9.06°	12.05°	15.05°
Difference	0.04°	0.01°	0.02°	0.11°	0.22°	0.19°	0.2°	0.22°	0.06°	0.05°	0.05°

Table 2. Desired Angle and Actual Angle of the holes drilled on a flat surface

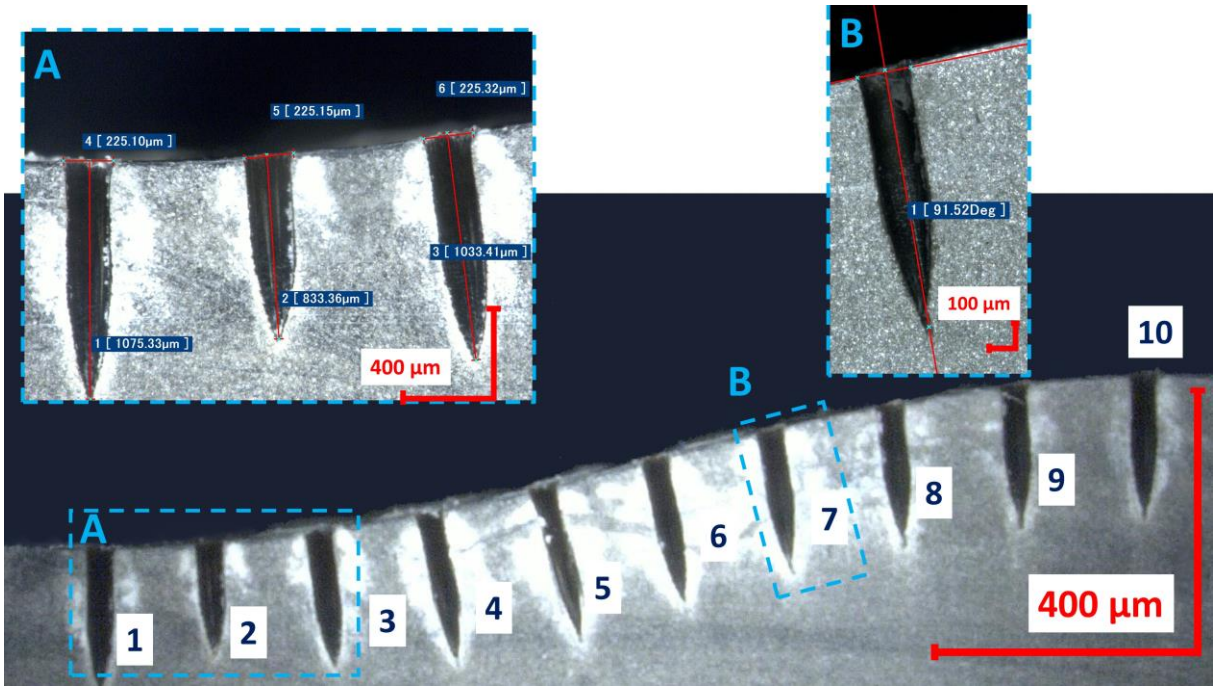


Figure 7. Complex Surface Hole Drilling Results. Box A: Typical width and depth measurement. Box B: Highlighting the outlier hole and its angle measurement.

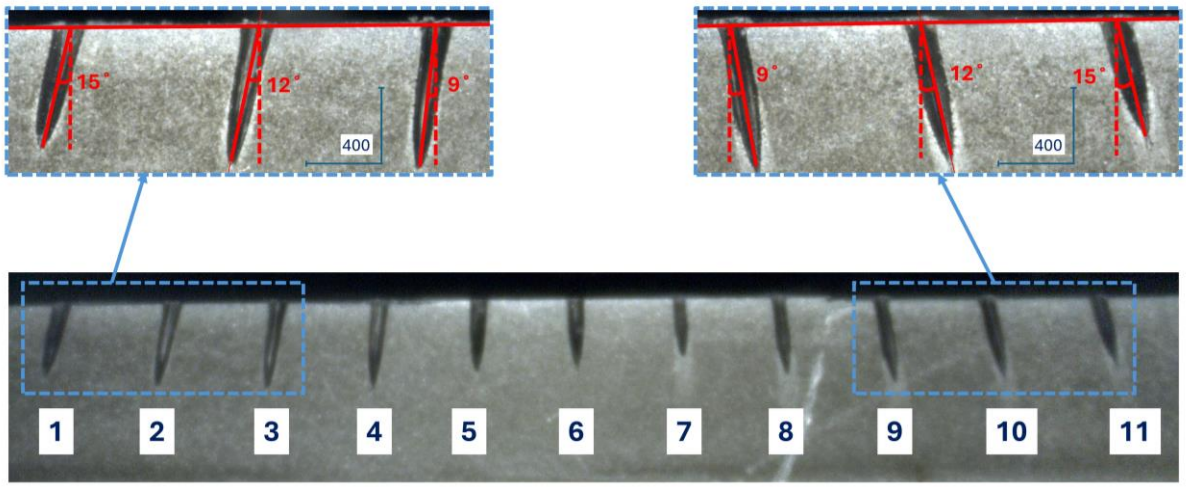


Figure 8. Flat Surface Angular Hole Drilling Results. The scale is in micrometers.

From Table 1 it's observable that the widths of the holes are generally consistent, mostly around 225 µm. The standard deviation for the widths of the holes is 7.21 µm, this indicates that most of the hole widths are close to each other. However, hole number 10 is a notable outlier with 201.1 µm when the standard deviation is considered. Moreover, the average height of the holes and standard deviation of the holes are approximately 1058.6 µm and

86.9 μm respectively, which points out that the standard deviation for the height of the holes is bigger than the width of the holes. On the other hand, hole number 2 is significantly lower than the average height with 833.4 μm meaning that hole number 2 deviates more than 2.6 standard deviations. The most important result for the experiment for drilling holes on a complex surface is the angle between the hole and the normal vector. The results for angles in Table 1 are obtained by measuring the angle between the tangent of the hole entrance and the hole. Thus, when 90 degrees is the perfect result and thereby the results are promising, ranging from 89.6 to 91.5. The biggest outlier is hole number 7, highlighted in box B in Figure 7, which makes 91.5 degrees with the tangent line.

Figure 8 and Table 2 shows the results for the holes drilled with an angle on a flat surface. Boxes with dashed outlines in Figure 8 are for showing how the angular measurements were made. Overall, the actual measured angles of the holes are very close to the desired angles, which reflects that the level of precision is high. Although the difference between the desired holes and the actual holes are very small, it tends to increase as the desired angle approaches 0°. This suggests that achieving a hole with 90° might be more challenging with the proposed setup and may need special attention.

8. CONCLUSION

In this paper, a methodology for laser micromachining using a parallel manipulator has been proposed. The methodology has been verified through experimental studies. The limits of the developed system have been demonstrated via laser micro drilling experiments. The proposed method will be extended to drilling holes with complex geometries.

REFERENCES

1. **Michel, S., Biermann, D., (2018),** "Analysis of the laser drilling process for pilot holes in complex shaped components", Procedia CIRP, 74, 398-402

2. **Louwerse, M. C., Jansen, H. V., Groenendijk, M.N.W, Elwenspoek M.C., (2009),** "Nozzle fabrication for micropropulsion of a microsatellite", J. Micromech. Microeng. 19(4) 045008

3. **He, C., Esch, D., Gillner, A., (2019),** "Adaption of Energy Deposition in Helical Drilling of Multidimensional Micro Holes Using Ultrashort Laser Pulses", JLMN-Journal of Laser Micro/Nanoengineering Vol. 14, No. 2.

4. **Son, J., Kang, H., Kang, S. H., (2023),** "A Review on Robust Control of Robot Manipulators for Future Manufacturing", International Journal of Precision Engineering and Manufacturing 24:1083–1102

5. **Wang, W., Guo, Q., Yang, Z., Jiang, Y., Xu, J. (2023)**, "A state-of-the-art review on robotic milling of complex parts with high efficiency and precision.", Robotics and Computer-Integrated Manufacturing, 79, 102436.

6. **Ke, X., Yu, Y., Li, K., Wang, T., Zhong, B., Wang, Z., Kong, L., Guo, J., Huang, L., Idir, M., Liu, C., Wang, C. (2023),** "Review on robot-assisted polishing: Status and future trends.", Robotics and Computer-Integrated Manufacturing, 80, 102482

7. **Song, K., Xiao, G., Chen, S., Liu, X., Huang, Y. (2023),** "A new force-depth model for robotic abrasive belt grinding and confirmation by grinding of the Inconel 718 alloy.", Robotics and Computer-Integrated Manufacturing, 80, 102483.

8. **Kurekova, E., Halaj, M., Omachelova, M., Martisovits, I. (2014),** "Theoretical Positioning Accuracy for Serial and Parallel Kinematic Structure", Measurement Science Review, Volume 14, No. 5,

9. **Dasgupta, B., Mruthyunjaya, T. S., (2000),** "The Stewart Platform Manipulator: A Review," Mechanism and Machine Theory, vol. 35, no. 1, pp. 15-40

10. **Yang. Z., Zhang., Y., (2018),** "Hybrid Harvester 3-RPS Robotic Parallel Manipulator" IOP Conf. Series: Materials Science and Engineering, 435, 012066

11. **Xiang, S., Altintas, Y., (2016),** "The Stewart Platform Manipulator: A Review", International Journal of Machine Tools & Manufacture 101 (2016) 65–78

12. **Zhang, S., Zhao, M., Ye, P., Zhang, H., (2019),** "A G^4 continuous B-spline transition algorithm for CNC machining with jerk-smooth federate scheduling along linear segments" International Journal of Machine Tools & Manufacture 101, 65–78

13. **Jahanpour, J., Motallebi, M., Porghoveh, M., (2016),** “A Novel Trajectory Planning Scheme for Parallel Machining Robots Enhanced with NURBS Curves” J Intell Robot Syst, 82(2), 257–275.

14. **Li, X., Zhu, D., Mei, Z., Jiang, D., (2017),** “Kinematic Analysis of 3-RPS Parallel Mechanism”, 2nd International Conference on Robotics and Automation Engineering

15. **Desai, R., Muthuswamy, S., (2021),** “A Forward, Inverse Kinematics and Workspace Analysis of 3RPS and 3RPS-R Parallel Manipulators” Iranian Journal of Science and Technology, Transactions of Mechanical Engineering, 45(1), 115–131.

16. **Ahn, C., Seo, T., Kim, J., Kim, T., (2007),** “High-tilt parallel positioning mechanism development and cutter path simulation for laser micro-machining” Computer-Aided Design, 39(3), 218–228.

17. **Karkantonis, T., Penchev, P., Nasrollahi, V., Le, H., See, T. L., Bruneel, D., Ramos-de-Campos, J., Dimov, S., (2022),** “Laser micro-machining of freeform surfaces: Accuracy, repeatability and reproducibility achievable with multi-axis processing strategies”, Precision Engineering 78 233-247

18. **Popov, K., Petkov, P., (2011),** “Layer based micro-machining–New approach for tool-path generation”, CIRP Journal of Manufacturing Science and Technology, 4(4), 370–375.

19. **Ashkenasi, D., Kaszemeikat, T., Mueller, N., Dietrich, R., Eichler, H. J., Illing, G., (2011),** “Laser Trepanning for Industrial Applications” Physics Procedia, 12, 323–331.

20. **Manco, E., Cozzolino, E., Astarita, A., (2022),** “Laser polishing of additively manufactured metal parts: a review”, Surface Engineering, 38:3, 217-233.

21. **Wang, Y., Changjun, K., Wu, T., Zhao, X., Wang, R., (2019),** “Nanosecond laser texturing with hexagonal honeycomb microstructure on Titanium for improved wettability and optical properties”, Optik, 192, 162953.

22. **Vidyasagar, K. E. Ch., Aggarwal, V., Sinha, S. S., Saha, S. K., Kalyanasundaram, D., (2021),** “Laser based micro texturing of freeform surfaces of implants using a Stewart platform” Precision Engineering, 72, 294–303.

23. **Jarvis, R. A. (1973),** "On the identification of the convex hull of a finite set of points in the plane". Information Processing Letters. 2: 18–21

MILLING FORCE ESTIMATION USING ANGULAR DOMAIN HARMONICS WITH CUTTING AND EDGE COEFFICIENTS

Mert İLME, *mert.ilme@metu.edu.tr* Middle East Technical University, 06800, Ankara, Turkey

Hakan ÇALIŞKAN, *chakan@metu.edu.tr* Middle East Technical University, 06800, Ankara, Turkey

ABSTRACT

In line with the industry 4.0 concept, today's milling research focuses more on the control of the cutting process. To identify the cutting forces, this study proposes a novel method. The method requires previous knowledge of the tool and workpiece engagement geometry. It utilizes an improvement of an angular domain convolution model for the forces, which is expressed as explicit functions of cutting parameters and tool/workpiece geometry. The edge cutting coefficients are added to the force model in addition to cutting coefficients to increase the accuracy. The method is validated with experimental data.

Keywords: milling; cutting force calculation; cutting and edge coefficients

INTRODUCTION

In the manufacturing field of production, milling is a common machining method. Current research in milling focuses on controlling the cutting process to achieve benefits such as extended tool life, reduced tool change costs, controlled vibration and noise levels, and health monitoring to minimize maintenance issues. Controlling the cutting process also enhances surface finish quality and optimizes process parameters for efficiency and safety. Understanding the cutting forces, which consist of tangential, radial, and axial components, is essential for achieving these benefits. To control the cutting process, the understanding of cutting forces must be enhanced and an accurate calculation method of force is needed. Measuring the forces with dynamometers or sensors may be another solution but it may not be cost-effective. By utilizing some pre-tests, the necessary parameters can be achieved and using those parameters the cutting forces can be calculated.

For the force model, there exist different assumptions. [Merchant, 1945] found a model by assuming that the shear zone, where the cutter edge and workpiece interact with each other, is a thin layer. [Lee and Shaffer, 1951] and [Palmer and Oxley, 1959] worked on "shear angle

prediction" models using plasticity. [Altıntaş, 2012] explained the mechanics of the cutting process. According to [Wang et al., 1994], [Wang et al., 2003], [Zheng et al., 1998], it is known that the harmonics of the cutting forces occur in the orders of tooth passing frequencies, which is equal to number of tooth multiplied with spindle frequency, in the case of no runout errors. Depending on this fact, in [Wang et al., 1994], [Wang et al., 2003], [Zheng et al., 1998], cutting force models are simplified into cutter geometry, axial and radial depth of cut. In addition, in [Altıntaş, 2012] and [Wang et al., 2003], it is said that the plowing/edge coefficients play an important role for force models. The study focuses on the force calculation methods in which the process parameters are used. The approaches that are used in [Wang et al., 2003], and [Zheng et al., 1998] are combined and an angular domain force calculation method is developed. The edge coefficients will be included in the force calculations in addition to cutting coefficients. At the end, a newly developed force model with four cutting coefficients in angular domain will be acquired. The method is verified with experimental cutting tests. The real cutting and edge coefficients are found with regression method explained in [Altıntaş, 2012]. Using those coefficients, the simulation force is generated and compared with the test data. In addition to this, the necessity of edge parameters is validated from that comparison.

BACKGROUND

In [Altıntaş, 2012], it is determined that the main cutting force model in detail and explained primary, secondary, and tertiary zones in cutter-workpiece interaction. In the tertiary zone, plowing coefficients become important for total cutting force. To have a more accurate force expression, the edge coefficients will be included in addition to cutting coefficients in this study. In the literature, the models are widely based on the nonlinear [Kienzle and Victor, 1957] formula and linear [Altıntaş, 2012] formula. Alternatively, there are time domain calculations as well as frequency domain calculations. In one of the frequency domain force model, [Wang et al., 1994] proposed a simpler way using the cutting process parameters such as the cutter geometry, the axial and radial depth of cut. The basic force model in this study will base on Wang's extended model which is derived from single-tooth to multi-tooth face milling by convolution integration.

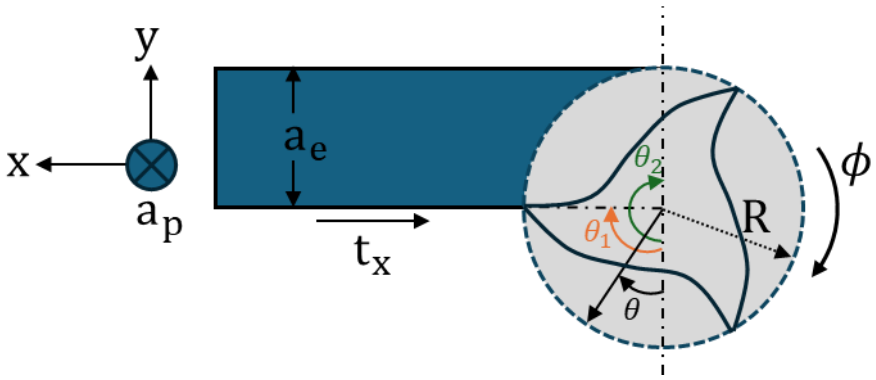


Figure 1. Schematic Representation of a Half Slot Milling

As derived in [5], the total cutting force is expressed with two cutting parameters:

$$\begin{pmatrix} f_x(\phi) \\ f_y(\phi) \end{pmatrix} = \sum_{k=-\infty}^{\infty} \left(\frac{NK_t t_x}{2\pi} CWD(Nk) \begin{bmatrix} 1 & K_r \\ -K_r & 1 \end{bmatrix} \begin{pmatrix} P_1(Nk) \\ P_2(Nk) \end{pmatrix} \right) e^{jNk\phi} \tag{1}$$

CWD is the function of chip width produced by a flute during unit angular rotation of the cutter,

$$CWD(w) = \frac{2R}{tan(\alpha)} \cdot \frac{sin\left(\frac{w}{N/\eta_a}\pi\right)}{w} \cdot e^{-j\cdot\frac{w}{N/\eta_a}\pi} \tag{2}$$

η_a, is the ratio of axial engagement angle to the tooth spacing angle,

$$\eta_a = \frac{Na_p\, tan(\alpha)}{2\pi R} \tag{3}$$

$P(w)'s$ are the elementary cutting functions, which is the unit force occurring in unit cutting area. They are described as,

$$P_1(w) = \frac{1}{2(4-w^2)} \Big[\Big(e^{-jw\theta_1}(jw\, sin(2\theta_1) + 2\, cos(2\theta_1)) - e^{-jw\theta_2}(jw\, sin(2\theta_2) + 2\, cos(2\theta_2)) \Big) \Big] \tag{4}$$

and

$$P_2(w) = \frac{e^{-jw\theta_1} - e^{-jw\theta_2}}{j2w} + \frac{1}{2(4-w^2)} \Big[\Big(e^{-jw\theta_1}(jw\, cos(2\theta_1) - 2\, sin(2\theta_1)) - e^{-jw\theta_2}(jw\, cos(2\theta_2) - 2\, sin(2\theta_2)) \Big) \Big] \tag{5}$$

f_x and f_y are the explicit cutting forces in directions of Figure (1), N is tooth number, t_x is the feed per tooth, a_p depth of cut, a_e the radial depth of cut, ϕ is the spindle angle, θ is the cutter edge angle with -y axis. θ_1 and θ_2 are the entrance and exit angles of cutting edge. K_t and K_r

are tangential cutting coefficient and radial cutting ratio multiplied with elementary cutting functions which are the cutting forces acting on an elemental cutting area of unit chip width with unit feed per tooth. Edge coefficients are not included yet.

In [Wang et al., 2003], Wang et al. added the contribution of edge coefficients to the Eqn. (1). Since edge coefficients are exclusive of feed rate, the derived equation is written in the following form:

$$\begin{pmatrix} f_x(\phi) \\ f_y(\phi) \end{pmatrix} = \sum_{k=-\infty}^{\infty} \left(\frac{N}{2\pi} CWD(Nk) \left\{ \begin{bmatrix} P_1(Nk) & P_2(Nk) \\ P_2(Nk) & -P_1(Nk) \end{bmatrix} \begin{pmatrix} K_t\, t_x \\ K_t K_r\, t_x \end{pmatrix} + \begin{bmatrix} P_3(Nk) & P_4(Nk) \\ P_4(Nk) & -P_3(Nk) \end{bmatrix} \begin{pmatrix} K_{te} \\ K_{te} K_{re} \end{pmatrix} \right\} \right) e^{jNk\phi} \tag{6}$$

$P_3(w)$ and $P_4(w)$ are the elementary cutting functions of edge coefficients. They are described as

$$P_3(w) = -\frac{e^{-jw\theta_2}}{1-w^2}(jw\, cos(\theta_2) - sin(\theta_2)) + \frac{e^{-jw\,\theta_1}}{1-w^2}(jw\, cos(\theta_1) - sin(\theta_1)) \tag{7}$$

and

$$P_4(w) = -\frac{e^{-jw\theta_2}}{1-w^2}(jw\, sin(\theta_2) - cos(\theta_2)) + \frac{e^{-jw\theta_1}}{1-w^2} * (jw\, sin(\theta_1) - cos(\theta_1)) \tag{8}$$

The force model depends on cutter geometry parameters which are tooth number, helix angle, and process parameters such as depth of cut, feed rate, engagement angles, cutting parameters. Using Eqn. (6), the amplitudes of each harmonic of force at the orders of tooth passing frequencies can be calculated. The time domain forces can also be derived with an inverse FFT algorithm.

PROPOSED METHOD

Instead of running an inverse FFT algorithm, [Zheng et al., 1998] developed an angular domain force model which is calculated directly in angular domain using only the cutting coefficients as in Eqn. (9). An analytical force model is given in the cutter angle domain based on finite-series representation. It is beneficial over frequency-based model providing transient characteristics of cutting forces. In this study, the angular domain model developed and rewritten with edge coefficients added. Moreover, the structure of the equation is changed so that all the cutting and edge parameters are collected in a state matrix. Since the scope of this study is only X and Y forces, Z term is not included in for simplicity.

$$\begin{pmatrix} f_x(\phi) \\ f_y(\phi) \end{pmatrix} = k_t t_x b_h K_2 \left\{ \begin{pmatrix} \frac{b_2}{4} \\ \frac{a_0 - a_2}{4} \end{pmatrix} N\beta_0 + \sum_{k=1}^{q} sin\left(\frac{kN\beta_0}{2}\right) \left[\begin{pmatrix} \frac{a_{kN-2} - a_{kN+2}}{2k} \\ \frac{2b_{kN} - b_{kN-2} - b_{kN+2}}{2k} \end{pmatrix} \cdot sin\left(kN\left(\phi - \frac{\beta_0}{2}\right)\right) + \begin{pmatrix} \frac{b_{kN+2} - b_{kN-2}}{2k} \\ \frac{2a_{kN} - a_{kN-2} - a_{kN+2}}{2k} \end{pmatrix} \cdot cos\left(kN\left(\phi - \frac{\beta_0}{2}\right)\right) \right] \right\} \quad (9)$$

where

$$K_2 = \begin{bmatrix} K_t & K_r \\ -K_r & K_t \end{bmatrix} \quad (10)$$

is cutting coefficient/ratio matrix with two parameters, b_h is tool geometry factor,

$$b_h = \frac{R}{tan(\alpha)} \quad (11)$$

found with tool radius and helix angle, β_0 is axial engagement angle,

$$\beta_0 = \frac{a_p\, tan(\alpha)}{R} \quad (12)$$

q is the number of harmonics, a_k's and b_k's are window function coefficients used in [Zheng et al., 1998],

$$a_0 = \frac{\theta_2 - \theta_1}{\pi}, \qquad a_k = \frac{sin(k\theta_2) - sin(k\theta_1)}{k\pi}, b_k = \frac{cos(k\theta_1) - cos(k\theta_2)}{k\pi} \quad (13)$$

describing whether the cutting edge is in interaction with workpiece using the cutter angle.

On the next step, edge coefficients are added into K matrix and the effect of edge coefficients are included in angular domain. As mentioned in [Wang et al., 2003], the edge coefficients affect the elementary cutting functions with:

$$\begin{pmatrix} p_3(\theta) \\ p_4(\theta) \end{pmatrix} = \begin{pmatrix} cos(\theta) \\ sin(\theta) \end{pmatrix} \quad (14)$$

Adding the edge elementary cutting functions to the integration of [Zheng et al., 1998]'s cutting force expression in windowing functions, force equation with two cutting and two edge parameters become as Eqn.(15).

$$\begin{pmatrix} f_x(\phi) \\ f_y(\phi) \end{pmatrix} = b_h K_4 \left\{ \begin{pmatrix} \frac{b_2}{4} \\ \frac{a_0 - a_2}{4} \end{pmatrix} N\beta_0 + \sum_{k=1}^{q} sin\left(\frac{kN\beta_0}{2}\right) \left[t_x \begin{pmatrix} \frac{a_{kN-2} - a_{kN+2}}{2k} \\ \frac{2b_{kN} - b_{kN-2} - b_{kN+2}}{2k} \\ \frac{b_{kN-1} + b_{kN+1}}{k} \\ \frac{a_{kN-1} - a_{kN+1}}{k} \end{pmatrix} \cdot sin\left(kN\left(\phi - \frac{\beta_0}{2}\right)\right) + \begin{pmatrix} \frac{b_{kN+2} - b_{kN-2}}{2k} \\ \frac{2a_{kN} - a_{kN-2} - a_{kN+2}}{2k} \\ \frac{a_{kN+1} + a_{kN-1}}{k} \\ \frac{b_{kN+1} - b_{kN-1}}{k} \end{pmatrix} \cdot cos\left(kN\left(\phi - \frac{\beta_0}{2}\right)\right) \right] \right\} \quad (15)$$

where

$$K_4 = \begin{bmatrix} K_t & K_r & K_{te} & K_{re} \\ -K_r & K_t & -K_{re} & K_{te} \end{bmatrix} \quad (16)$$

with 4 cutting parameters. t_x is not multiplied with edge coefficients, therefore it is taken into the parenthesis to the front of the cutting coefficients.

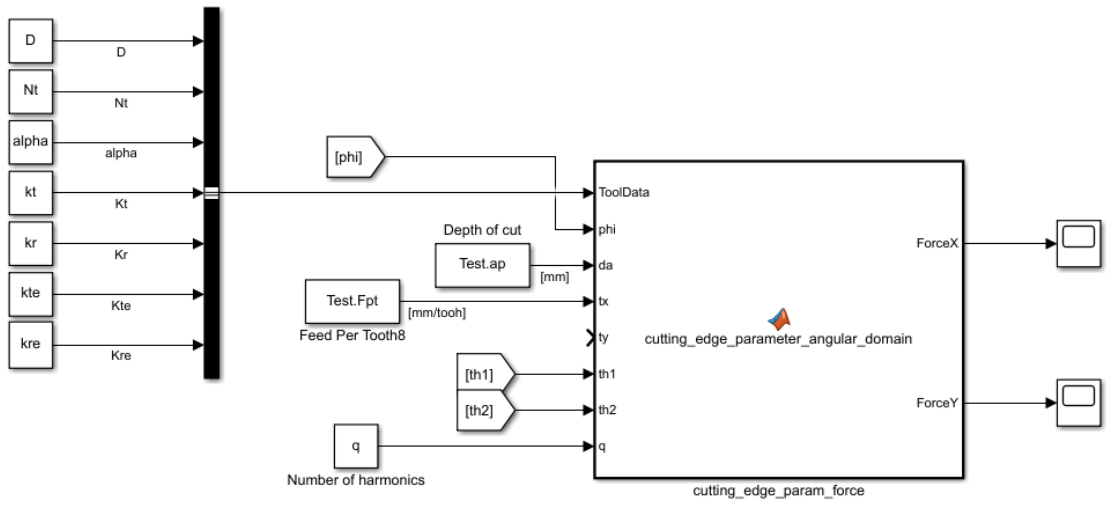


Figure 2. Simulink Diagram for Proposed Method

For the proposed method a Simulink block is developed. Cutting and process parameters are given as an input to the force calculation block. In addition, since the

spindle angle (Φ), is also fed as timeseries, for the changing spindle speed the forces can be calculated, too.

EXPERIMENTAL RESULTS

In order to verify the developed force model, on the other hand to support the accuracy of the four-parameter model rather than the two parameter one, some cutting tests are conducted. The cutting operation is done on a Deckel FP5CC, 5 axis CNC milling machine which uses Beckhoff control system. Cutting tests are done with an AL7075 aluminum alloy block.

The cutting tool has 12 mm diameter and 3 number of tooths with 45° helical angle. Spindle speed is 4500 rpm. The feed rate is 1500 mm/min. Axial depth of cut is 2 mm and radial depth is 6 mm, which is a half slot test. For the force measurement, the dynamometer of KISTLER 9257B and amplifier of 5167A are used. Data acquisition is done through NI 9234 card in 8 kHz.

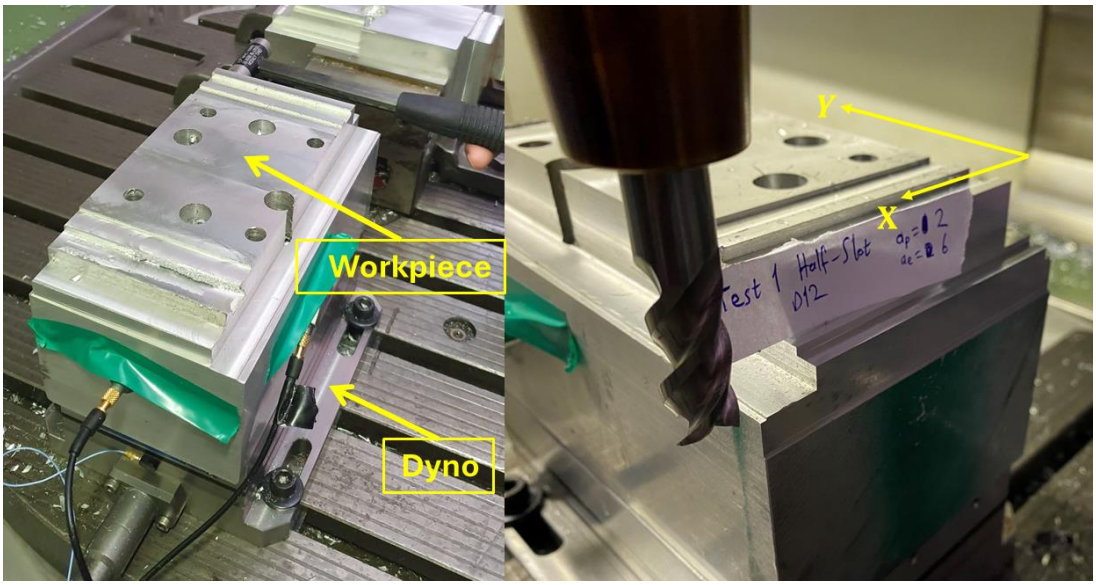


Figure 3. Experimental Setup

Table 1. Cutting Parameters of Experimental Tests

Parameter	Symbol	Value	Unit
Tangential Cutting Coefficient	K_t	272.6	N/mm^2
Radial Cutting Coefficient	K_r	23.09	N/mm^2
Tangential Edge Coefficient	K_{te}	44.06	N/mm
Radial Edge Coefficient	K_{re}	28.4	N/mm
Spindle Speed	ω	4500	rpm
Feed Speed	t_x	0.111	mm/tooth
Cutter Diameter	D	12	mm
Tooth Number	N	3	-

Helix Angle	α	45	deg
Depth of Cut	a_p	2	mm
Radial Depth of Cut	a_e	6	mm

Using the cutting and process parameters in Table (1), force model simulation is run, and the force is generated both with two cutting parameters and four cutting/edge parameters. On the common figure, the test data measured from dynamometer is plotted.

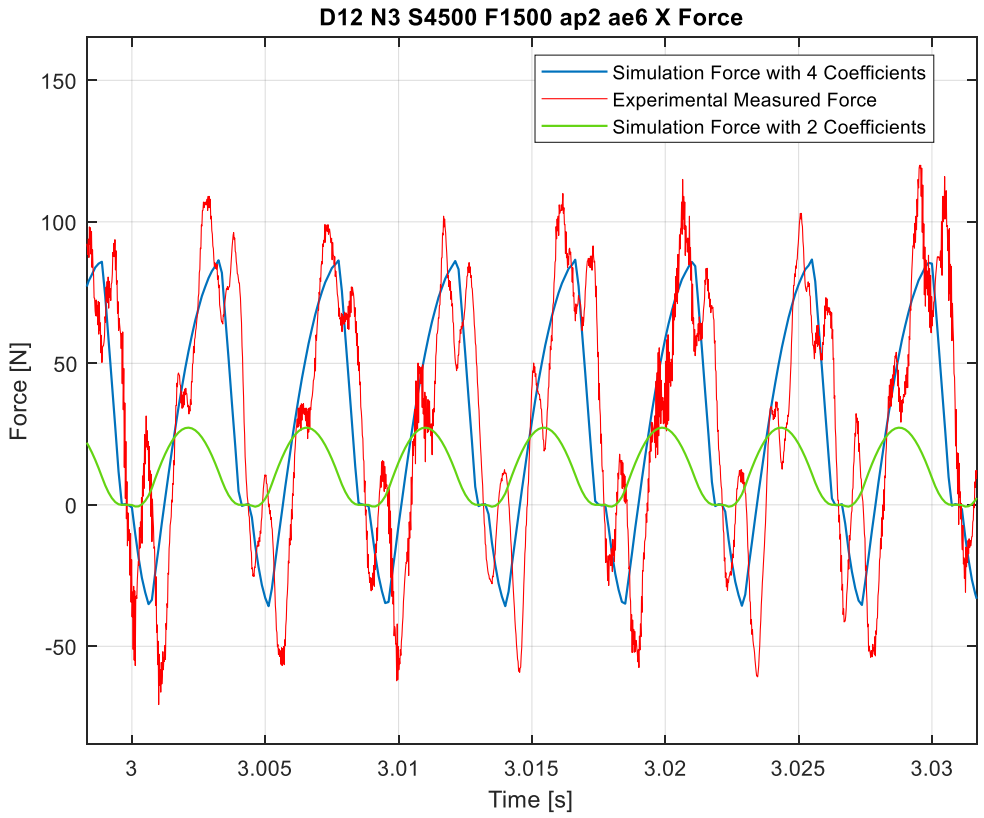


Figure 4. Force Comparison

CONCLUSION

As a conclusion, in the study, an existing force model which was reduced to cutting process parameters, is improved, and used to get more accurate force calculation. The idea of summing up the harmonics in angular domain provides a fast and accurate calculation. Moreover, the study contributed the edge parameters into that model. The proposed method uses the enhanced understanding of milling forces. The main advantage of the proposed method is that with a simple prior knowledge of the process, and less calculation cost, the cutting force can be calculated. The results are supported with experimental data. As the structure of the proposed force model is able to collect the coefficients in a matrix, it is useful

for prediction algorithms, too. The developed force calculation algorithm is proper for real time applications and will be utilized in the future cutting force estimation research.

REFERENCES

1. **Merchant, M.E., (1945)** Mechanics of the metal cutting process. II: Plasticity conditions in orthogonal cutting. Journal of Applied Physics, 16:318–324.

2. **Lee, E.H., and Shaffer, B.W., (1951),** Theory of plasticity applied to the problem of machining. Journal of Applied Mechanics, 18:405–413.

3. **Palmer, W.B. and Oxley, P.L.B., (1959),** Mechanics of orthogonal machining. Proceedings of the Institution of Mechanical Engineers, 173(24):623–654.

4. **Altıntaş, Y., (2012),** Manufacturing Automation: Metal Cutting Mechanics, Machine Tool Vibrations, and CNC Design (2nd ed.). Cambridge University Press.

5. **Wang, Junz, J-J., Liang, S.Y., Book, W.J., (1994),** Convolution Analysis of Milling Force Pulsation. Journal of Engineering for Industry, doi: 10.1115/1.2901804.

6. **Wang, J. J-J., Zheng, C. M., (2003),** Online identification of shearing and plowing constants in end milling. Journal of Manufacturing Science and Engineering-transactions of the ASME, doi: 10.1115/1.1536931.

7. **Zheng, L., Liang, S. Y., Melkote, S. N., (1998),** Angle Domain Analytical Model for End Milling Forces. Journal of Manufacturing Science and Engineering-transactions of the ASME, doi: 10.1115/1.2830121.

8. **Kienzle, O., Victor, H. (1957).** Spezifische Schnittkräfte bei der Metallbearbeitung, Werkstattstechnik und Maschinenbau, vol. 47, no. 5, p. 224-225.

EVALUATION OF DIFFERENT DAMAGE MODELS APPLIED FOR EXTRUDED 6XXX SERIES ALUMINUM

Seda YILDIZ, *seda.yildiz@yesilova.com.tr-yilldizseda@gmail.com* Yeşilova Holding - Bursa Technical University, 16310, Bursa, Turkey

Hüseyin LEKESİZ, *huseyin.lekesiz@btu.edu.tr* Bursa Technical University, 16310, Bursa, Turkey

ABSTRACT

Aluminum alloys are widely used in industry due to their lightweight, machinability, corrosion resistance, and recyclability. Extrusion method makes manufacturing possible for long pieces with specific profiles. However, a comprehensive approach to proper damage modeling is limited in the literature. This study focuses on the material properties and damage parameters of extruded 6xxx series aluminum alloy using Hollomon, Swift, Voce, and Swift & Voce hardening equations. Stress-strain results from analyses were compared with test results. Damage parameters for Johnson Cook and Hosford-Coulomb models were obtained. FE analysis of a crash-box design was evaluated by comparing tensile and compressive behaviors.

Keywords: Aluminum alloy, Extrusion, Hardening curves, Damage model, Crash box

1. INTRODUCTION

Aluminum alloys are widely used in many industries, especially in the automotive, and aerospace sectors, thanks to their advantages such as their lightweight, easy machinability, corrosion resistance, and recyclability. The extrusion method enables materials to be produced in long pieces with a specific cross-sectional profile. In addition, extrusion offers high productivity, low material wastage, easy creation of complex shapes, and excellent surface quality.

To reduce the carbon footprint and decrease fossil fuel consumption, many sectors, especially the automotive industry, have turned to alternative energy sources. In the automotive industry, electric vehicles stand out as a prominent use of alternative energy sources. According to estimates by BloombergNEF, the International Energy Agency (IEA), and the International

Renewable Energy Agency (IRENA), the global stock of electric vehicles is expected to reach between 120 and 250 million by 2030. If the upper limit of this range is reached, the total annual passenger car sales are projected to be around 90 million by 2030 (Saygın, 2019). In line with this projection, aluminum usage in the automotive sector will also increase remarkably. The use of cast, extruded, and sheet aluminum alloys in passenger cars is expected to reach 250 kilograms by 2050. Thanks to the high-tech solutions provided by aluminum materials, it is anticipated that vehicle weight will be significantly reduced without compromising safety, leading to fuel savings throughout the vehicle's lifespan (Dündar, 2002). The widespread use of aluminum material highlights the importance of high-strength aluminum alloys. With the increasing use of aluminum alloys, there is an expectation for the growing importance of design and validation studies. Detailed examination of computer-aided models is necessary for conducting realistic analyses of the material, particularly in cases where shape changes are prevalent. The damage modeling becomes critical in analyses in such instances. Conducting detailed forward-looking computer-aided analysis studies with realistic modeling and reducing prototype production are key topics to be addressed within the framework of sustainability.

There is a lack of an agreed-upon damage model for aluminum profiles produced by extrusion in literature. A crystal plasticity model was proposed that accounts for damage and ductile fracture caused by microcracks or micro voids in single-crystal aluminum alloys produced by extrusion (Frodal et al., 2021). In another study, the crush performance of aluminum extrusions was investigated through analysis based on finite element (FE) simulation including experimental-numerical hybrid ductile damage modeling (Won et al., 2024). The existence of vastly different methods for damage estimation may create difficulties in finding the most appropriate approach. Therefore, it is important to determine which method converges to real test results in the extruded aluminum damage model.

In this study, material properties and damage parameters of extruded 6xxx series aluminum alloy were determined, based on finite element (FE) simulation, by various ductile damage models. Basic parameters of the Hollomon, Swift, Voce and Swift & Voce hardening equations were obtained for defining the material properties. Hardening curves were formed according to these models and FE analyses were performed. The stress-strain results obtained from the analyses were compared with the test results. In this comparison, matching between the test and the analysis results was examined, especially in the plastic region. The damage model parameters were obtained following the hardening fit. With the help of analyses, failure strain and stress triaxiality values were obtained Johnson Cook and Hosford-Coulomb damage parameters were found accordingly based on best fit with experimental results.

Last, the crushing behavior of a representative crash-box design was investigated by using damage models. The analyses were performed in Altair RADIOSS 2022.3 software. The

elastoplastic behavior of the material and the damage model parameters are determined, and the results are evaluated by comparing crush (compressive) and tensile behavior.

2. MATERIALS AND METHODS

Test data is used to create the material and damage model. In this work, damage parameters are calibrated employing an inverse method. To that end, the experimental result of four different specimens is used: tensile, notched tensile, and shear-tension (pure shear, 45° shear) test. The geometries of the specimens are given in Figure 1. The tensile test specimen was produced as a subsize specimen following ASTM E8 standard, while the other specimens were based on the work of Andrade et al.(2016). The thickness of the samples is 2.5 mm.

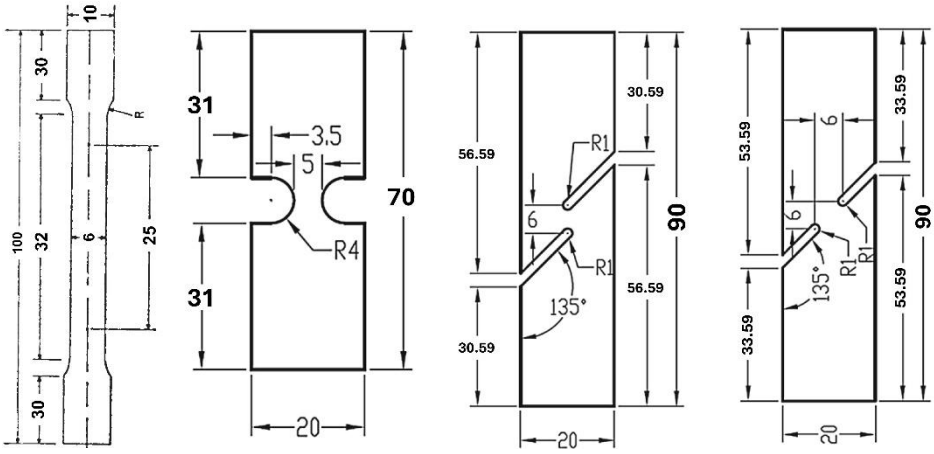


Figure 1. Specimen geometries for the experimental material characterization. Respectively: tensile, notched tensile, shear 0° and shear 45°.

The different experiments provide different triaxiality ranges which help identify the fracture as well as the critical plastic strain curve for the present material. Strain and stress results are taken from tensile tests. Hardening coefficients for the material card are determined using these results. Analyses for the other tests are performed using the model with the most appropriate iteration between the test results and the analyses. In the results of the analyses, stress triaxiality and plastic strain values that occur in case of damage are obtained and the values are used as input in the damage equations and damage coefficients.

2.1. Hardening Laws

The test results of the tensile specimens produced in accordance with ASTM E8 standard were used to determine the hardening curves. The plastic strain and true stress values of the material were obtained from the tensile test results and used to find the coefficients of the hardening equations.

One of the most important empirical equations characterizing hardening curves is the Hollomon equation (Eq. 1). Here ε_p is the plastic strain, K is the strength coefficient, n is the strain hardening exponent (Hertelé et al., 2011). A linearization is applied to obtain parameters.

$$\sigma = K\,\varepsilon_p^n \tag{1}$$

The Hollomon equation is not sufficient to describe the complete behavior of some metals (Swift, 1952) . Swift proposed the equation by adding a parameter (ε_0) which accounts for a possible pre-strain, and the equation is as follows (2):

$$\sigma = K\left(\varepsilon_p + \varepsilon_0\right)^n \tag{2}$$

In this equation, ε_0 represents yield strain. Unlike the Hollomon and Swift equations, the Voce equation describes the hardening curve with an exponential expression (Eq. 3.) (Voce, 1948).

$$\sigma = \sigma_0 + Q\left(1 - e^{-\beta\varepsilon_p}\right) \tag{3}$$

In the Voce equation, σ_0 is the yield stress, Q and β are the material coefficients. The Voce model is based on microstructural considerations and accurately reflects the dynamic recrystallisation given by the flow behavior (Byun et al., 2022).

The Swift–Voce hardening function was used to describe the hardening curves; the expression of this hardening function is as follows Eq. 4. The Swift-Voce combined equation was used as it is repeatedly identified in the literature as one of the most adequate isotropic hardening law to describe large strain hardening behavior of metals (Yang et al., 2020).

$$\sigma = \alpha\left[K\left(\varepsilon_p + \varepsilon_0\right)^n\right] + (1-\alpha)\left[\sigma_0 + Q\left(1 - e^{-\beta\varepsilon_p}\right)\right] \tag{4}$$

In this equation ε_0 is yield strain, Q, K and β are the material coefficients.

2.2. Damage Models

Damage models are fundamental components in the numerical simulation of material damage, particularly at high stress rates. Numerous damage models can be found in the literature (Majzoobi & Rahimi Dehgolan, 2011). A few, such as the Johnson-Cook and Hosford-Coulomb models, have found widespread application in simulations.

In industrial practice, the Johnson–Cook (JC) damage model is widely used in most finite element (FE) tools for metal forming simulations due to its capability to predict model parameters with minimal effort. This damage model offers solutions for product design over a wide range of strain rates and high temperatures to efficiently predict the ductility behavior of the material.

It is undeniable that a well-constructed and reliable proposed flow stress model is highly supportive across a broad range of strain rates and elevated temperatures, making it efficient in predicting material ductility behavior for product design. Although flow stress models are categorized into different types, such as physically based, empirical, and semi-empirical, the primary goal of these models remains the same: to achieve accurate prediction of the material behavior for a specific material. Therefore, developing a proper flow stress model for the design process is crucial to predict material deformation behavior at high strain rates and deformation temperatures. Consequently, considerable research has been conducted considering various materials. Damage model proposed that fracture strain typically depends on the stress triaxiality ratio, the strain rate, and the temperature (Murugesan & Jung, 2019). The JC damage model can be written as follows (Eq. 5).

$$\varepsilon_f = \left[D_1 + D_2 \exp\left(D_3(\eta)\right)\right] + \left[1 + D_4 \ln\left(\dot{\varepsilon}_p^*\right)\right] + \left[1 + D_5 T^*\right] \quad (5)$$

D_1 to D_5 are the damage model constants, η is the stress triaxiality. Stress triaxiality is the ratio of mean stress, and the equivalent stress (Eq. 6). It can be interpreted as a measure of the ratio of the first and second stress tensor invariants (Marcadet et al., 2015). $\dot{\varepsilon}_p^*$ is the plastic deformation rate, T* is the temperature.

$$\eta = \frac{\sigma_m}{\bar{\sigma}} \quad (6)$$

Recent research on ductile fracture has demonstrated that the Lode parameter's effect is as crucial as stress triaxiality. For instance, the significant decrease in metal ductility cannot be explained by traditional stress triaxiality-dependent models like the Johnson-Cook failure model. However, Lode angle-dependent theories, such as the Hosford-Coulomb fracture initiation model (Mohr & Marcadet, 2015), fully account for this phenomenon by considering the increased stability of plastic flow under axisymmetric stress states like equi-biaxial tension compared to generalized shear stress states like plane strain tension (Marcadet et al., 2015).

Lode angle parameter is measured the ratio of the third and second stress tensor invariants, J_3, J_2 (Eq. 7).

$$\bar{\theta} = 1 - \frac{2}{\pi} \arccos\left[\frac{3\sqrt{3}}{2} \frac{J_3}{(J_2)^{3/2}}\right] \quad (7)$$

The ordered principal stresses ($\sigma_I \geq \sigma_{II} \geq \sigma_{III}$) may be constructed as with the Lode angle parameter dependent trigonometric functions (Eq. 8-9).

$$\sigma_i = \bar{\sigma}(\eta + f_i) \quad (8)$$

where

$$f_1(\bar{\theta}) = \frac{2}{3}\cos\left[\frac{\pi}{6}(1-\bar{\theta})\right]; \qquad f_2(\bar{\theta}) = \frac{2}{3}\cos\left[\frac{\pi}{6}(3+\bar{\theta})\right]; \qquad f_3(\bar{\theta}) = -\frac{2}{3}\cos\left[\frac{\pi}{6}(1+\bar{\theta})\right] \quad (9)$$

The onset of ductile fracture is close to the onset of localization. Results from ductile fracture experiments are typically presented in terms of equivalent plastic strain, stress triaxiality and Lode angle parameter (Eq. 10).

$$\bar{\varepsilon}_f^{pr}[\eta, \bar{\theta}\,] = b(1+c)^{\frac{1}{n}}\left(\left\{\frac{1}{2}\left((f_1-f_2)^a + \left((f_2-f_3)\right)^a + \left((f_1-f_3)\right)^a\right)\right\}^{\frac{1}{a}} + c(2\eta + f_1 + f_3)\right)^{-\frac{1}{n}} \quad (10)$$

The Hosford exponent (*a*) controls the influence of the Lode angle parameter, while the friction coefficient (*c*) primarily controls the influence of the stress triaxiality on the strain to fracture. The model parameter is a multiplier that controls the overall magnitude of the stress to fracture; it is defined to be equal to the stress to fracture for uniaxial stress (this is the same as for equiaxial stress). The parameter n = 0.1 is a constant transformation parameter (Marcadet et al., 2015).

2.3. Testing of Specimens

Test specimens were obtained from aluminum profiles in the extrusion direction. Tensile test specimens were manufactured as a subsize specimen in accordance with ASTM E8 standard, while the other specimens were based on the work of Andrade et al.(2016). Experimental data were utilized to create the material card. The tests were carried out on a hydraulic servo-controlled MTS test machine with an axial load capacity of 250 kN. The loading rate of 0.5 mm/min recommended, as recommended by standards, was applied during the experiments (Figure 2). Force and displacement values were obtained from the test device, these data were collected at a frequency of 5 Hz.

In all tests, deformation measurements were performed by Digital Image Correlation (DIC) method. In this method, the test section surfaces of the specimens were first painted white and then point clusters were formed with black spray paint. DIC photographs were taken and analyzed with the GOM ARAMIS 4M DIC system at METUWIND. DIC photographs were taken at a frequency of 1 Hz.

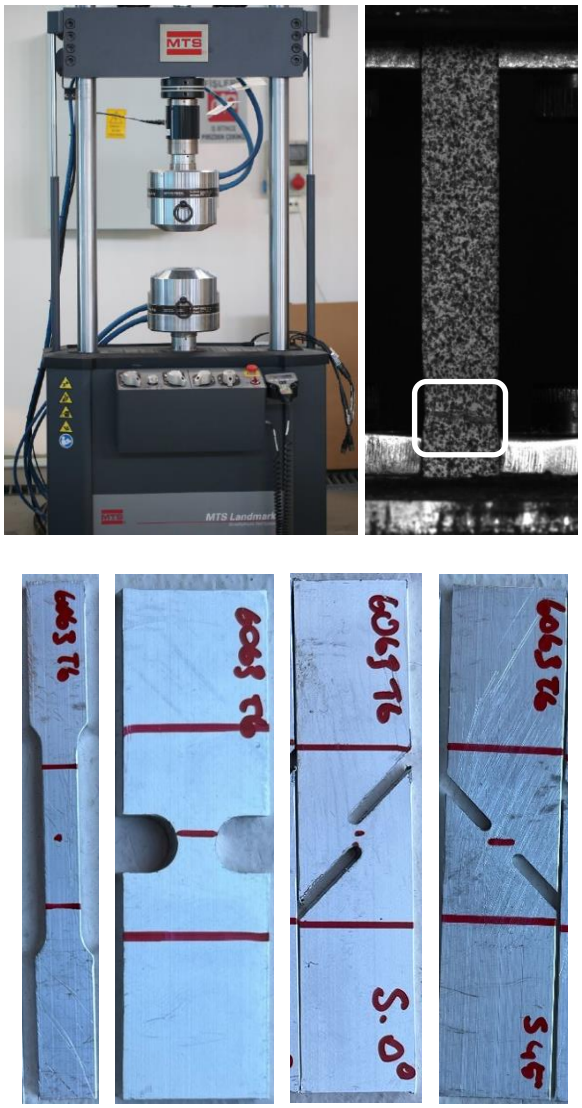


Figure 2. MTS 250 kN load capacity hydraulic servo controlled universal testing machine and tensile, notched tensile, pure shear, and shear 45° specimens, respectively.

2.4. Finite Element Modeling

The analyses were performed using the Altair RADIOSS module with 2D (Figure 3). All of them (notched tensile, pure shear, and shear 45° specimens) were carried out under the analysis conditions specified in the tensile analysis.

The tensile analysis model was created using 2D with a thickness of 2.5 mm. Element type is quad mesh and their size is 0.5 mm. The model was constrained at one end in all degrees of freedom, while the other end was allowed to move in the +x direction. Force and displacement values were obtained from the analysis results.

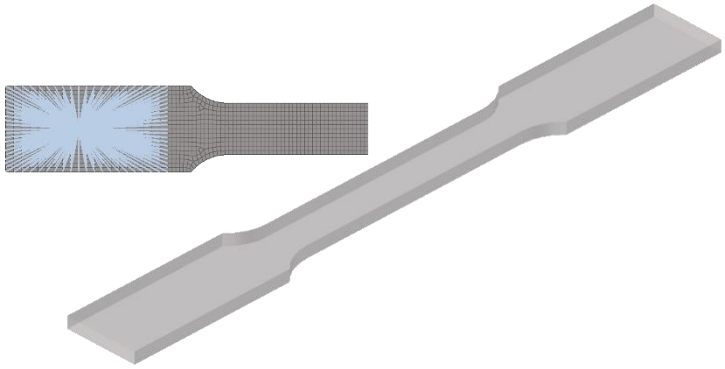


Figure 3. Modelling of tensile specimen.

A representative crash-box with a thickness of 3 mm was modelled in 2D (Figure 4). A quad mesh of 5 mm element size was used. The length of the box is 300 mm, and it is modelled to have a displacement of 200 mm in both tension and crushing (compression). During the analysis, Swift & Voce combined hardening curve was used to create the material card, and Hosford - Coulomb was used as the damage model. Force and displacement values were obtained from the analysis results.

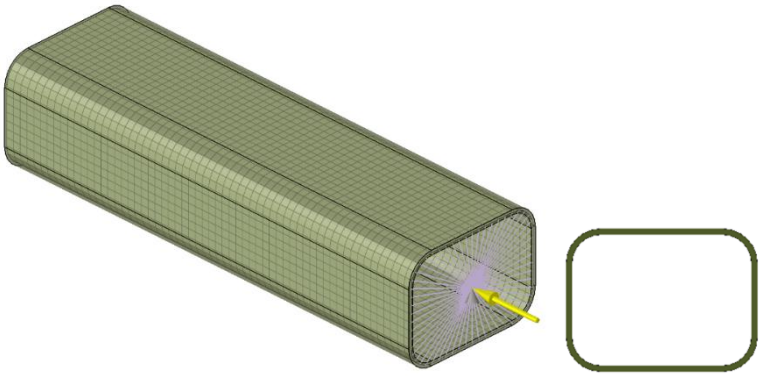


Figure 4. 2D modelling of crash box for crush analysis.

3. RESULTS AND DISCUSSION

Material and damage model used in analyses are crucial for the analysis results to closely match the test results. The hardening coefficients were obtained using the plastic strain and stress values derived from the test data (Table 1).

Table 1. The Hardening Coefficients

Material	Hollomon		Swift		Voce		Swift & Voce			
	n	K	n	K	Q	β	α	K	Q	β
6xxx T6	0.06	307.6	0.08	328.7	57.5	25.1	0.8	335.5	95.9	1190

According to the analysis results, total force, stress, and displacement values were obtained (Figure 5).

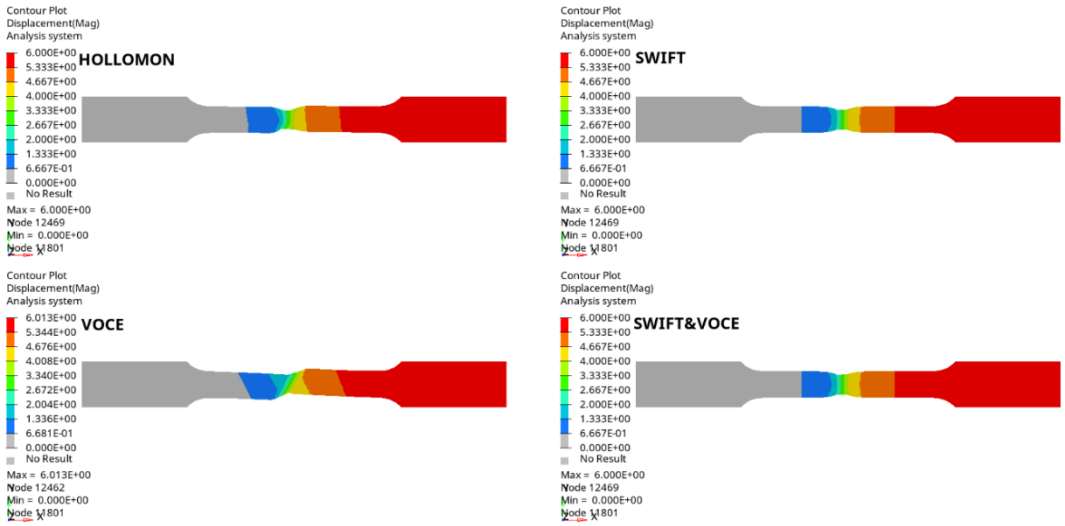


Figure 5. Analysis results created with different hardening curves.

The stress-strain curve obtained from the analysis results is shown in Figure 6. Based on the obtained results, the Swift & Voce combined equation will be used to create the material card in other analyses.

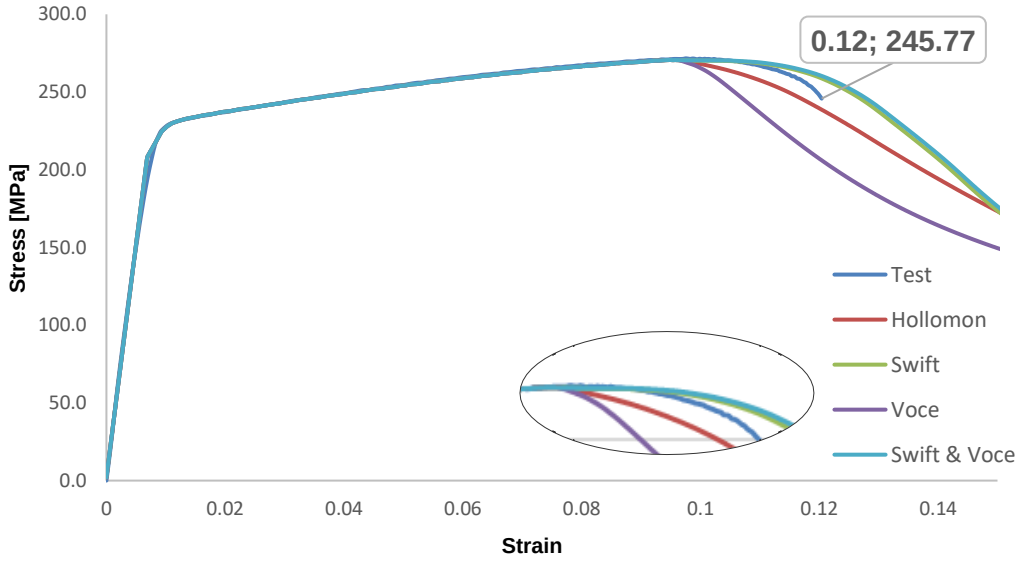


Figure 6. Stress-Strain curve for tensile test results.

After creating the material card, tests and analyses of the samples mentioned in Section 2 (notched tensile, pure shear, and shear 45°) were performed to determine the damage parameters. The tests were conducted with 5 repetitions each. Based on the displacement results obtained from the test results, plastic strain, and stress triaxiality values at those points were derived from the analyses (Table 2). Using the obtained results, the coefficients for the

Johnson-Cook and Hosford-Coulomb damage equations were determined (Table 3). Once the damage parameters were obtained, analyses for the tensile test were conducted using the damage equations.

Table 2. Based on the test results, stress triaxiality and plastic strain values

Test	Stress Triaxiality	Plastic Strain
Pure Shear	0.036	0.36
Tensile	0.33	0.334
Shear 45°	0.42	0.2
Notched	0.5	0.3

Different strain rates and temperatures when determining the parameters of the Johnson-Cook damage model are not involved in the model, therefore the coefficients are $D_4 = D_5 = 0$.

In Altair RADIOSS software, the Hosford-Coulomb damage model is referred to by the Hosford-Coulomb with Domain of Shell-to-Solid Equivalence. It provides a nonlinear strain-based fracture criterion for shells with linear damage accumulation. The DSSE is simply a localized necking criterion for sheet metals subjected to a non-radial (proportional) combined membrane and bending loading. DSSE parameter (d) is the only free material model parameter. In this study, d = 1.57 was taken. The parameter n = 0.1 is a fixed transformation parameter (Keunhwan Pack, 2017) (Marcadet et al., 2015). The analysis images and stress-strain curve results with damage model are shown in Figure 7.

Table 3. Damage parameters for Johnson- Cook and Hosford-Coulomb damage model.

Damage Parameters	Johnson-Cook Damage Model	Damage Parameters	Hosford-Coulomb Damage Model
D_1	0.036	a	3.223
D_2	0.33	b	1.120
D_3	0.42	c	0.082

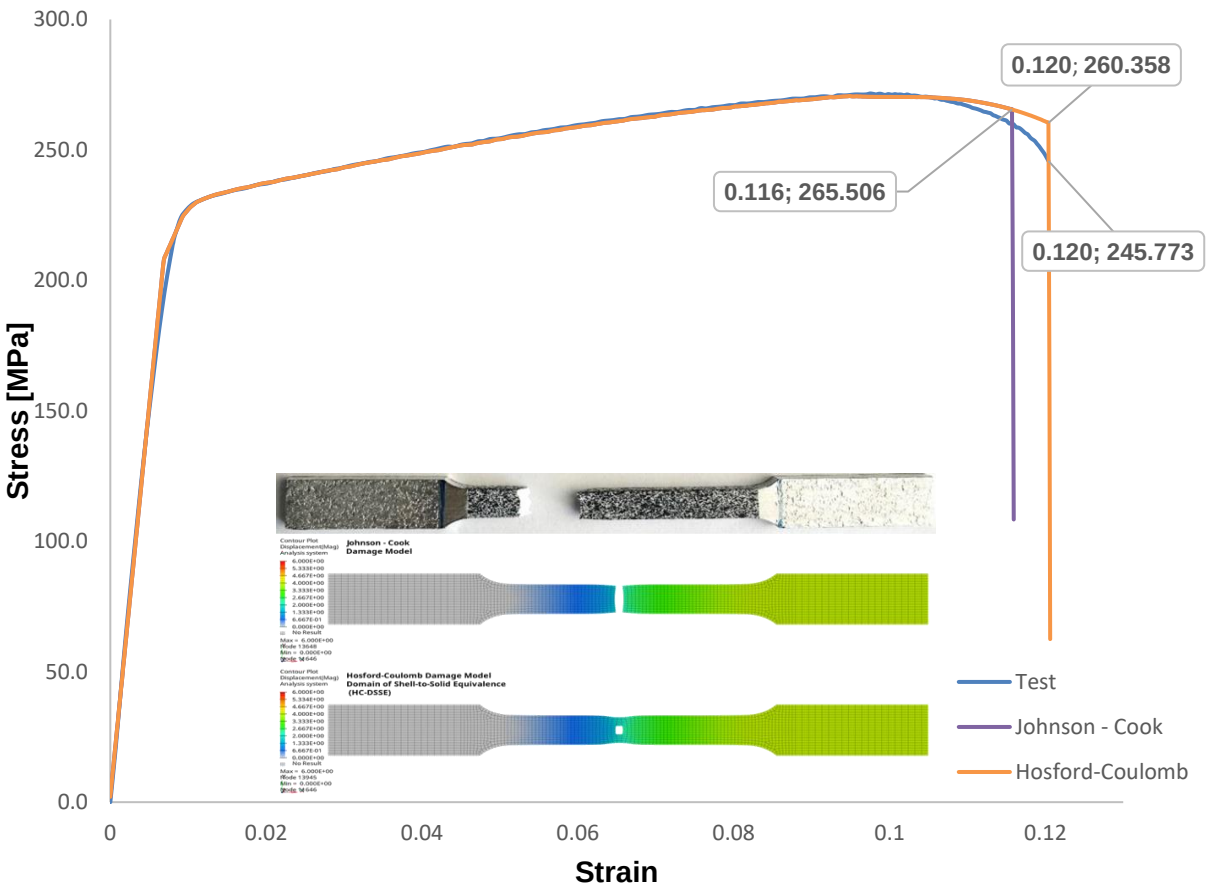


Figure 7. Stress-strain curve with damage model for tensile test result.

Hosford-Coulomb damage model is preferred in crash box analyses. The convergence of fracture behavior and strain value was an important factor in the selection of this model. The force-displacement results of the crush analysis are shown in Figure 8 and the results of the tensile analysis are shown in Figure 9.

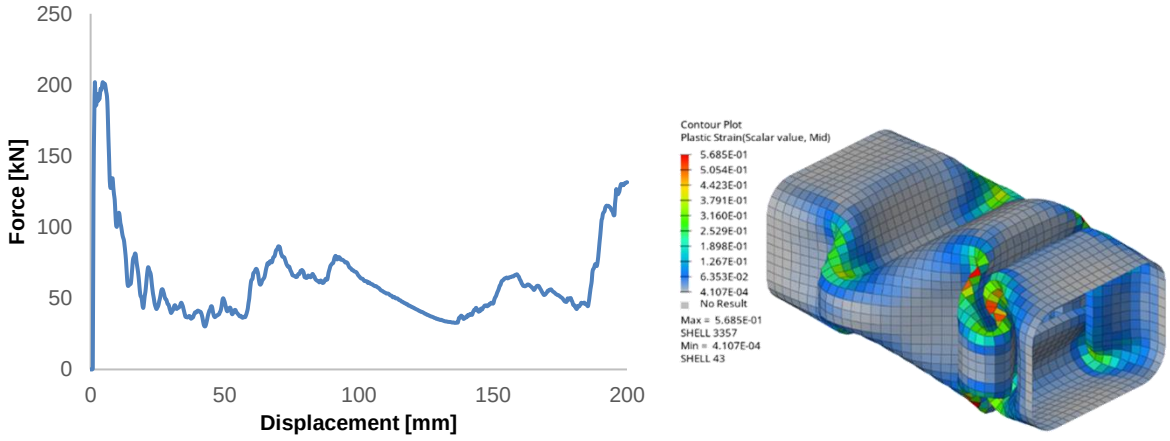


Figure 8. Crush analysis result for crash box.

Due to some restrictions, an actual crash box design of car manufacturers' results is not presented in this study, rather a preliminary design is utilized, and actual crash test data is not available, yet. Wrinkling behavior is anticipated to be the same as in the actual tests which is already verified for actual crash box designs. However, locating crack formation and tearing and capturing the width of the tear remains a challenging task. Red areas represent high plastic strains and tearing is expected to be initiated at these sites. However, stress redistribution following tearing is not captured in this analysis. However, this study offers a more accurate perspective for possible future studies with verified results for different test specimens.

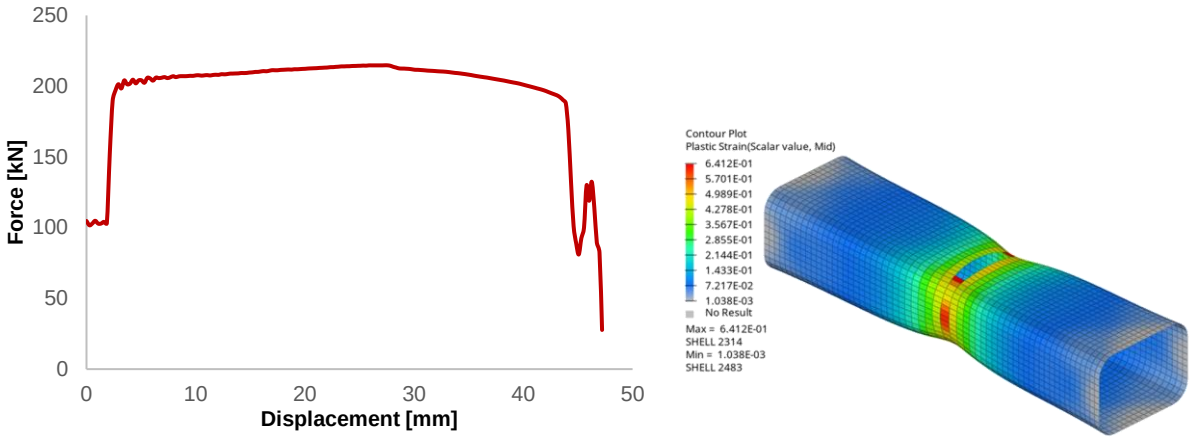


Figure 9. Tensile analysis result for crash box.

4. CONCLUSION

When the Johnson-Cook damage model is used, 3% difference is observed in the strain value in the tensile test results while there is an approximately 8% difference in the stress values. On the other hand, when the Hosford-Coulomb damage model is used, the tensile test results show a 6% difference in stress values while the strain values are approximately the same. In the proposed crash box design, the crashing force reaches a maximum of 200 kN under compression. Plastic deformations occur at the points where the box folds. In the case of crush, the box begins to fold from the point of load application towards the center. In the case of tension, damage occurs right in the middle of the box. In future studies, different crash box sections can be evaluated for more efficient design. The main purpose of this study is to compare the analysis results using the damage model with physical tests.

ACKNOWLEDGEMENT

This work is supported by the TÜBİTAK-2244 project numbered 119C170 in partnership with Yeşilova Holding R&D Center, Bursa Technical University (BTU) and The Scientific and Technological Research Council of Türkiye (TÜBİTAK). Material characterization tests were

carried out at the METU Center for Wind Energy (METUWIND). We thank the relevant institutions for their valuable support.

REFERENCES

1. **Andrade, F. X. C., Feucht, M., Haufe, A., & Neukamm, F. (2016), "**An incremental stress state dependent damage model for ductile failure prediction", International Journal of Fracture.

2. **Byun, J. B., Jee, C. W., Seo, I. D., & Joun, M. S. (2022), "**Characterization of double strain-hardening behavior using a new flow of extremum curvature strain of Voce strain-hardening model", Journal of Mechanical Science and Technology, 36(8), 4115–4126.

3. **Dündar, M., & G. G. (2002), "**Otomotiv Sektöründe Alüminyum Uygulamaları ve Sürekli Döküm Tekniği ile Üretilmiş Alüminyum Levha Alaşımları", Assan Alüminyum.

4. **Frodal, B. H., Thomesen, S., Børvik, T., & Hopperstad, O. S. (2021),** "On the coupling of damage and single crystal plasticity for ductile polycrystalline materials", International Journal of Plasticity, 142.

5. **Hertelé, S., De Waele, W., & Denys, R. (2011), "**A generic stress strain model for metallic materials with two-stage strain hardening behaviour", International Journal of Non-Linear Mechanics, 46(3), 519–531.

6. **Keunhwan Pack. (2017), "**Modeling of sheet metal fracture for shell finite elements with component level validation [Doctoral dissertation]", In M.S. Mechanical Engineering. Massachusetts Institute of Technology.

7. **Majzoobi, G. H., & Rahimi Dehgolan, F. (2011), "**Determination of the constants of damage models", Procedia Engineering, 10, 764–773.

8. **Marcadet, S. J., Roth, C. C., Erice, B., & Mohr, D. (2015), "**A rate-dependent Hosford-Coulomb model for predicting ductile fracture at high strain rates", EPJ Web of Conferences.

9. **Mohr, D., & Marcadet, S. J. (2015),** "Micromechanically motivated phenomenological Hosford-Coulomb model for predicting ductile fracture initiation at low stress triaxialities", International Journal of Solids and Structures, 67–68, 40–55.

10. **Murugesan, M., & Jung, D. W. (2019), "**Johnson Cook material and failure model parameters estimation of AISI-1045 medium carbon steel for metal forming applications", Materials, 12(4).

11. **Saygın, D., Tör, O.B., Teimourzadeh, S., Koç, M., Hildermeier, J., & Kolokathis C. (2019), "**Türkiye ulaştırma sektörünün dönüşümü: Elektrikli araçların Türkiye dağıtım şebekesine etkileri", In SHURA Enerji Dönüşümü Merkezi. Retrieved from www. shura. org. tr.

12. **Swift, H. W. (1952), "**Plastic Instability Under Plane Stress", Journal of the Mechanics and Physics of Solids, 1, 1–18.

13. **Voce, E. (1948), "**The Relationship Between Stress and Strain for Homogeneous Deformation", Journal of the Institute of Metals, 74, 537–562.

14. **Won, J. Y., Kim, C., Hong, S., Yoon, H. S., Park, J. K., & Lee, M. G. (2024),** "Evaluation of crush performance of extruded aluminum alloy tubes based on finite element analysis with ductile fracture modeling", Thin-Walled Structures, 200.

15. **Yang, Y., Vincze, G., Baudouin, C., Chalal, H., & Balan, T. (2021), "**Strain-path dependent hardening models with rigorously identical predictions under monotonic loading", Mechanics Research Communications, 114(103615).

EVALUATING STEEL/ADHESIVE INTERFACIAL FAILURE USING PULL-OFF TESTS

Fatih İBRAHİMOĞLU, *fatih.ibrahimoglu@tedu.edu.tr* TED University, Ankara, Turkey

Ata KHABAZ-AGHDAM, *ata.khabaz@tedu.edu.tr* TED University, Ankara, Turkey

Şehram DİZECİ, *sehram.dizeci@tedu.edu.tr* TED University, Ankara, Turkey

ABSTRACT

This research delves into analyzing the failure mechanisms of the interface layer in Araldite 2011, a toughened epoxy adhesive, when bonded to steel surfaces. The predominant occurrence of interfacial failure in Pull-off testing has prompted the selection of this method to establish a triangular traction-separation (TR) damage model of the adhesive/metal interface, employing 2D cohesive zone modeling (CZM) elements. By scrutinizing failure patterns within the steel interface, a cohesive zone model (CZM) is derived, aligning closely with experimental findings. This comprehensive characterization of interface layer damage not only facilitates the prediction of failure mechanisms in adhesive joints but also enhances the accuracy of mechanical behavior forecasts in scenarios involving adhesive failure.

Keywords: Cohesive zone model, interface failure, pull-off test

1. Introduction

Adhesive bonded joints play a crucial role in various industries, and the accurate prediction of their failure is of utmost importance. The failure of adhesive bonds can have significant implications in terms of structural integrity, safety, and performance [1, 2]. Therefore, understanding and predicting the failure behavior of adhesive bonded joints is vital for design optimization, reliability assessment, and maintenance planning. Advanced techniques such as cohesive zone modeling (CZM) [3], finite element analysis (FEA) [4], and experimental testing are utilized to study the failure mechanisms and predict the failure of adhesive joints [5]. By simulating the behavior of the adhesive material and the interaction between the adherends, these methods enable engineers to assess critical factors such as stress distribution, debonding initiation, propagation, and ultimate failure. Accurate failure prediction of adhesive bonded joints aids in enhancing joint design, selecting appropriate adhesive materials, and improving manufacturing processes, ultimately leading to safer and more reliable products and structures.

Understanding the failure mechanisms in adhesive joints is of paramount importance. Occasionally, adhesive failure at the interface between the adhesive and adherend highlights the necessity of identifying such failure mechanisms in adhesively bonded joints (ABJs). An approach taken to address the interaction of a bi-material medium involves conceptualizing it as a system comprising three distinct materials with two rigid contact surfaces [6, 7], as depicted in Figure 1. Within this framework, material 1 signifies the adhesive layer, material 2 represents the substrate of the adherend, while the interface layer is regarded as an independent material with its own unique properties. This conceptualization is substantiated by the distinctive characteristics of the interface layer compared to each constituent material, owing to the presence of molecular bonds between the adhesive and substrate.

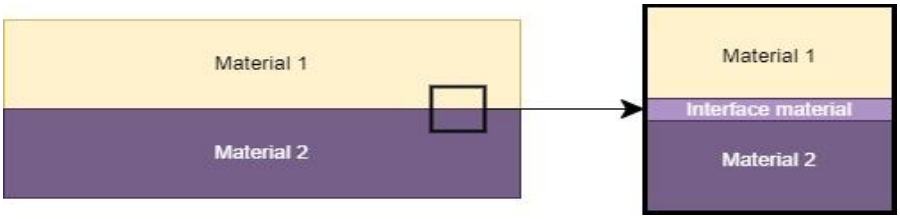


Fig. 1. A bi-material concept with an interfacial area

2. Materials and methods

The investigation employed a two-part epoxy adhesive, Araldite 2011, along with materials including a 2mm steel 304 sheet and a 20 mm diameter steel 304 pulley, to construct the pull-off specimens. To generate adhesive bulk samples, a blend of epoxy resin and hardener was poured into a mold, resulting in ASTM D638 type IV dumbbell-shaped specimens (Figure 2-a) [3]. To prepare the pull-off specimens, the steel sheet underwent sanding with P80 sandpaper followed by cleaning with acetone. Subsequently, adhesive was applied to both surfaces of the sheet and the pulley, after which the pulley was affixed to the sheet. The assembly was then allowed to fully cure at room temperature for 48 hours (see Figure 2-b). A specially designed fixture was utilized for the pull-off test, employing the Zwick/Roell Z 020 tensile testing machine, as illustrated in Figure 2-c. The loading rate for both bulk and pull-off tensile testing was maintained at 2mm/min.

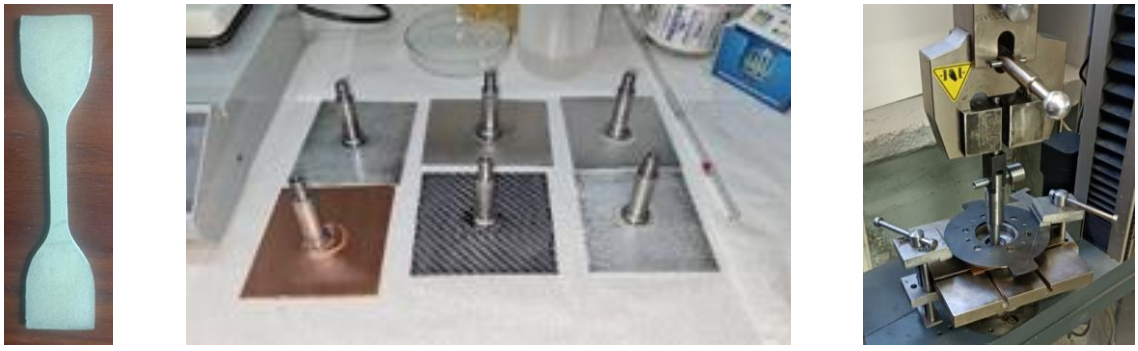


Fig. 2. (a) Araldite 2011 dumbbell-shaped bulk specimen, (b) pull-off specimen, and (c) pull-off testing apparatus

3. Results and decoction

3.1 Tensile test

Figure 2 indicates the stress-strain curve of the epoxy adhesive. Table 1 also presents the mechanical properties of the adhesive and the adherends used in the pull-off specimens. The load displacement diagram of the pull-off specimen under tensile test is indicated on Figure 4.

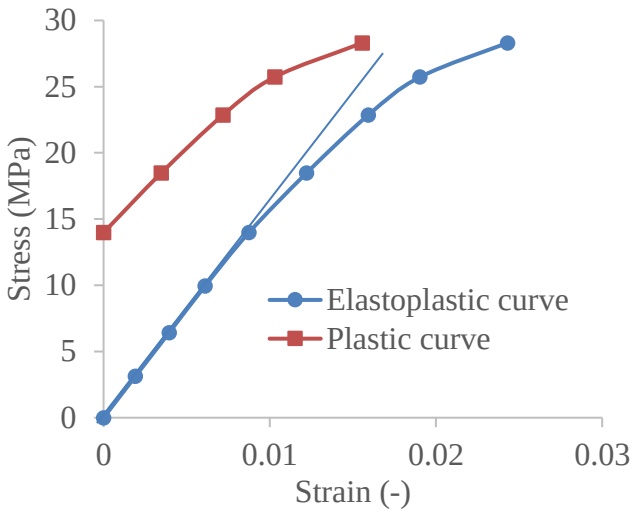


Fig. 3. stress-strain and the plastic curve of Araldite 2011 epoxy adhesive

Table 1. Material properties of the adhesive, steel sheet and the pulley

	E (GPa)	$\sigma_y\ (MPa)$	$\sigma_{Max}\ (MPa)$
Adhesive	1.6	14.6	27.6
SS 304	193	303	709

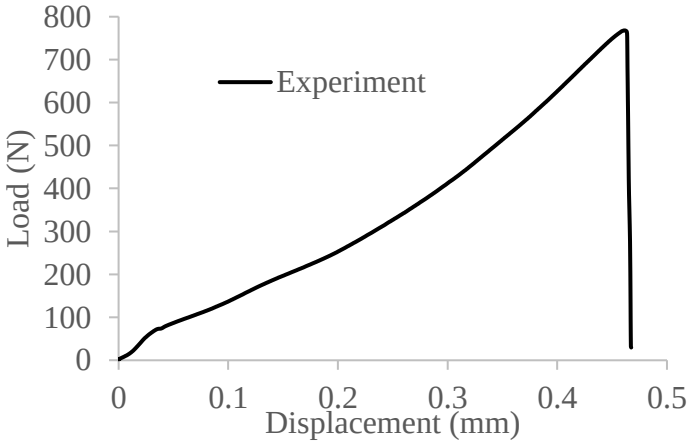


Fig. 4. Load-displacement curve of the pull-off test

3.2 Fracture surface analysis

Figure 5 displays the fracture surfaces of the pull-off specimen. These fracture surfaces reveal a predominant interfacial adhesive rupture within the adhesive/steel interface. This observation

suggests that the load-displacement output of the pull-off test in such cases can accurately represent the mechanical behavior of the interface area.



Fig. 5. steel/adhesive interfacial failure in the fracture surface area in the pull-off tensile test

3.3 Finite element approach

a 2D axisymmetric model is used to simulate the pull-off tensile test. In this model the adhesive layer, with a thickness of 0.3 mm, is divided into two parts: the CZM layer of the adhesive/adherent interface and the other layer with elastoplastic behavior. In this model the interface area is considered to have a thickness of 0.05 mm and the adhesive area to have a thickness of 0.25 mm.

Disregarding the presence of the interfacial CZM layer in the finite element simulation would lead to a notably rigid behavior, as evidenced by the load-displacement curve shown in Figure 6, as an example for the pull-off specimen of P80 surface roughness. Specifically, the stiffness value of the pull-off testing sample obtained from the finite element model, without considering the CZM interface layer, equals 115,635 (N/mm). In contrast, assuming a linear model results in a stiffness value of 1668 (N/mm) derived from the test results, indicating that the interfacial CZM elements should predominantly follow the triangular traction-separation obtained from the load-displacement curve of the tensile test of the pull-off specimens. By attributing the behavior obtained from the load-displacement diagram derived from the test data to the interface layer, a load-displacement diagram is obtained through numerical solution, as depicted in Figure 7 for both the pull-off samples of P80 and P220 surface roughness. The resemblance in shape between the two diagrams is striking, indicating the validity of the assumptions made. Figure 8 further illustrates the von Mises stress distribution of the model before and after separation. It is evident from the figure that the entire layer undergoes sudden brittle rupture, akin to the experimental case, with a short softening displacement of 0.01 mm.

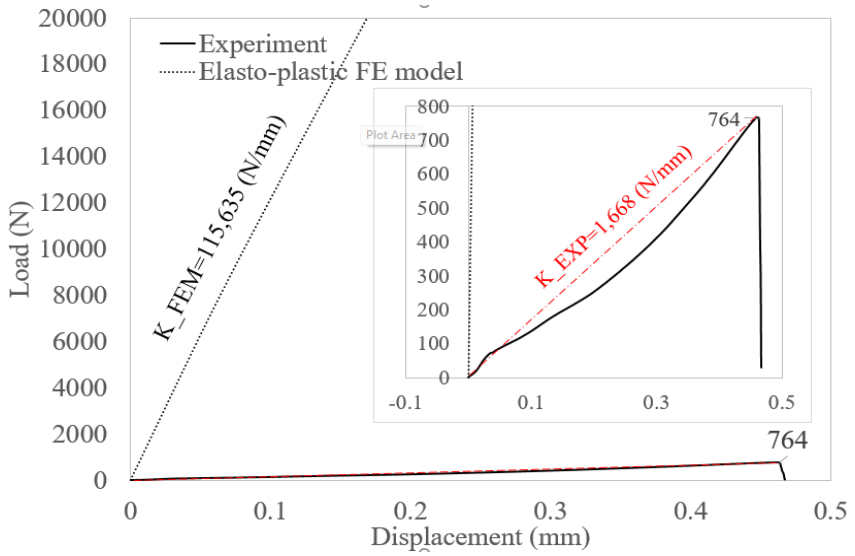


Fig. 6. Load-displacement curve of the pull-off specimens; experimental result, and numerical elasto-plastic simulation with an ideal interface assumption

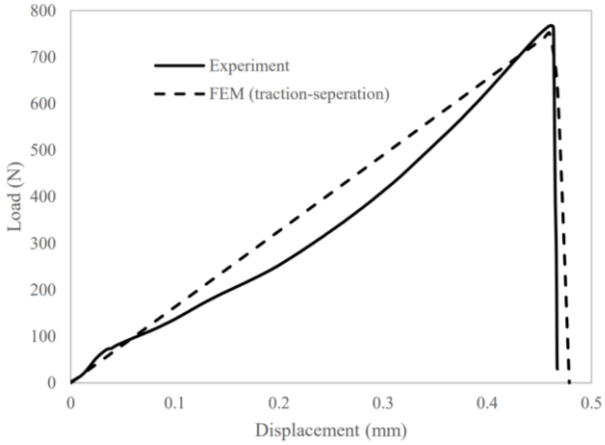


Fig. 8. Load-displacement curve of the pull-off test; experimental and numerical simulation

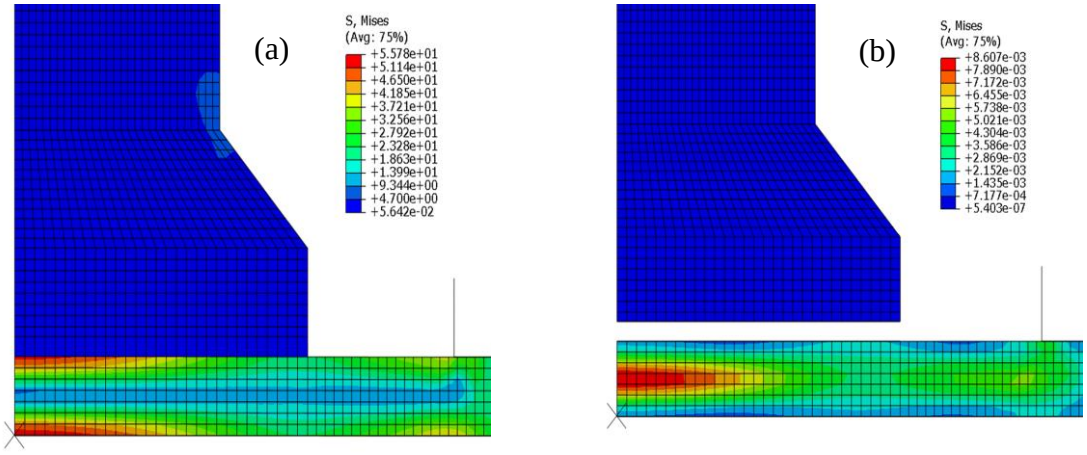


Fig. 9. Von Mises stress distribution of the pull-off test in displacement loading of (a) 0.45 mm, and (b) 0.47 mm.

1. Conclusions

This study investigates interfacial failure between steel and adhesive using pull-off tests and finite element simulations. Cohesive zone modeling (CZM) aligns closely with experimental

findings, revealing predominant interfacial adhesive rupture. Neglecting the CZM layer in simulations results in a rigid behavior inconsistent with experiments. Incorporating experimental data into numerical solutions validates assumptions, showing remarkable similarity in load-displacement diagrams.

4. Accnowledgement

The authors are willing to acknowledge the scientific and technological research council of Türkiye for supporting this research under 221M637 grant number.

References

1. Khabaz-Aghdam A, Behjat B, da Silva LF, Marques EA. A new theoretical creep model of an epoxy-graphene composite based on experimental investigation: effect of graphene content. Journal of Composite Materials. 2020 Aug;54(18):2461-72.
2. Oskui AE, Haddadi E, Ebrahimi M. A technical approach toward pre-crack generation and its effect on the fracture behavior of polymeric materials. Engineering Fracture Mechanics. 2022 Oct 15;274:108780.
3. Paygozar B, Dizaji SA, da Silva LF. Bonding dissimilar materials via adhesively bonded spot-welded joints: cohesive zone model technique. Journal of Adhesion Science and Technology. 2020 Nov 1;34(21):2352-63.
4. Rahmani A, Choupani N. Experimental and numerical analysis of fracture parameters of adhesively bonded joints at low temperatures. Engineering Fracture Mechanics. 2019 Feb 15;207:222-36.
5. Zamani P, da Silva LF, Nejad RM, Moghaddam DG, Soltannia B. Experimental study on mixing ratio effect of hybrid graphene nanoplatelet/nano-silica reinforcement on the static and fatigue life of aluminum-to-GFRP bonded joints under four-point bending. Composite Structures. 2022 Nov 15;300:116108.
6. Roche A, Gaillard F, Romand M, Von Fahnestock M. Metal-adhesive bonded systems: Adhesion measurement using a three point flexure test. Journal of Adhesion Science and Technology. 1987 Jan 1;1(1):145-57.
7. Birro TV, Aufray M, Paroissien E, Lachaud F. Assessment of interface failure behaviour for brittle adhesive using the three-point bending test. International Journal of Adhesion and Adhesives. 2021 Oct 1;110:102891.
8. Khabaz-Aghdam A, Behjat B, Marques EA, Carbas RJ, Silva LF, Roghani-Mamaqani H. Effect of reduced graphene oxide on mechanical behavior of an epoxy adhesive in glassy and rubbery states. Journal of Composite Materials. 2021 Nov;55(26):3839-48.

DAMAGE DETECTION ON BEAM STRUCTURES USING HO-KALMAN IDENTIFICATION METHOD

Ö. Dehan ÖZBOZ, *oozboz@etu.edu.tr,* TOBB ETÜ, 06560, Ankara, Turkey

Özkan ALTAY, *ozaltay@tai.com.tr,* TURKISH AEROSPACE, 06980, Ankara, Turkey

A. Murat ÖZBAYOĞLU, *mozbayoglu@etu.edu.tr,* TOBB ETÜ, 06560, Ankara, Turkey

H. Özgür ÜNVER, *hounver@etu.edu.tr,* TOBB ETÜ, 06560, Ankara, Turkey

ABSTRACT

Due to its non-destructive nature and real time monitoring capabilities, Vibration-Based Structural Health Monitoring Systems have a promising potential for damage assessment. Among possible methods, Sub-Space methods provide state-space model, and modal parameters of the system. Ho-Kalman method forms the backbone of Sub-Space Methods. Using impulse response of the structure, the modal parameters such as natural frequencies, damping ratios, and mode shapes can be captured. By investigating vibration characteristics of intact and damaged specimens, the effect of the damage on the modal parameters of Steel and Carbon Fiber Reinforced Polymer (CFRP) beams has been investigated.

Keywords: Structural Health Monitoring, Sub-Space Identification, Ho-Kalman Method, Model Order Reduction, Damage Detection

ÖZET

Titreşim Esaslı Yapısal Sağlık İzleme Sistemleri, tahribatsız ve gerçek zamanlı inceleme yenetekleri sayesinde hasar tespit sistemleri için gelecek vaad eden bir potansiyele sahiptir. Olası yöntemler arasından Alt-Uzay yöntemleri, sistemin durum-uzayı modelini ve modal parametrelerini belirlemek için kullanılabilmektedir. Ho-Kalman Metodu, Alt-Uzay Metodlarının temelini oluşturmaktadır, yapının darbe etkisine cevabı incelenerek, doğal frekansları, sönümleme oranları ve mod şekilleri gibi modal parametreleri belirlenebilmektedir. Hasarsız ve hasarlı numunelerin titreşim özellikleri incelenerek, hasarın Çelik ve Karbon Fiber Takviyeleri Polimer, CFRP, kirişlerin modal parametreleri üzerindeki etkisi araştırılmıştır.

Anahtar Kelimeler: Yapısal Sağlık İzleme, Alt-Uzay Tanımlama, Ho-Kalman Metodu, Model Boyut İndirgemesi, Hasar Tespiti

1. INTRODUCTION

The development of computer hardware inevitably increases the usage of finite element analyses in the design of engineering structures. The modern structures are pushed to their limit for both economic and performance purposes. Lightweight yet strong structures are the two main goals of these designs. With traditional materials such as steel and aluminum, highly complex structures can be manufactured. Additionally, the development of manufacturing methods of composites drives engineers one step beyond, and tailored material for high strength, lightweight, and thermal needs can be manufactured. As the structural and material designs approach the physical boundaries, the damage evaluation or assessing possible risks on the structural integrity should be executed thoroughly [Chaupal & Rajendran, 2023]. Structural Health Monitoring (SHM) systems are developed to detect discrepancies from the original construction and design.

Assessment of the vibrational characteristics of the structure is one of the methods for SHM. As a result of damage, the stiffness and natural frequencies of the structure change, hence by identifying the dynamical model and extracting modal parameters of the system, observation regarding the health of the structure may be achieved. Identification of the dynamical model can be estimated using non-parametric models such as Frequency Response Function, FRF, parametric models such as autoregressive ARX, ARMAX models [Fritzen, 2005], and sub-space models such as Ho-Kalman, MOESP [Verhaegen & Deprettere, 1991], and N4SID [Van Overschee & De Moor, 1994] methods [Viberg, 1994]. In this study, the focus will be on the sub-space methods, particularly the Ho-Kalman method. In the sub-space methods, the state-space model of the dynamical system is identified using the input-output relationship. In MOESP and N4SID methods, the response of the structure to arbitrary and sufficient excitation can be used for model identification. With known excitation, the state-space model can be extracted deterministically. Furthermore, assuming the excitation is white noise, by observing only the response of the structure, stochastic identification can be achieved with MOESP and N4SID. Ho-Kalman in essence is the basis of the sub-space methods. By analyzing the response of the system to the impulse excitation, the state-space model can be obtained [Juang & Pappa, 1985]. Considering the similarity of the impact test and impulse excitation, modal parameter extraction can be achieved using the Ho-Kalman method. In this study, the response of the structure is measured using a laser vibrometer and 4 piezoelectric sensors. The laser vibrometer measures the velocity of a single point on the structure by the Doppler effect, which is a precise instrument for displacement modal analysis. The piezoelectric sensors generate voltage as their shapes change, by mounting them on the specimen, an output signal proportional to the dynamical strain is measured. On an engineering structure, piezoelectric sensors are cheap and easy-to-use sensors [Piana et al., 2016]. However, the

measurements are in the form of strain, and obtained frequency response is in the strain modal form, also the precision of the piezoelectric sensors is lesser than the laser vibrometer, therefore the performance of the piezoelectric sensors will be validated using laser vibrometer measurement. Additionally, the validation of the laser vibrometer will be done by comparing the identified FRF with theoretical calculations. The study is conducted with a beam structure with fixed-free boundary conditions, and by comparing the natural frequencies and damping ratios of the intact and damaged specimens, the damage's effect on the modal parameters will be held.

2. MATHEMATICAL METHODS

For the global validation of the identification method, theoretical natural frequencies of the structure should be calculated. In the first part of the mathematical methods, theoretical calculations of a transverse vibration of a beam will be discussed. In the second part, the Ho-Kalman Realization algorithm will be discussed, and the technique for utilizing Ho-Kalman with an impact test will be investigated.

Transverse Vibration of Beams

The effect of the damage on the structure has been examined using constant cross-sectioned thin beams under transverse vibration [Rao, 2007]. The representation of the beam and infinitesimal section of the beam are given on the Figure 1.

Calculation of Natural Frequencies: The infinitesimal section is subjected to shear force, *V*, and bending moment, *M*, on the cross-sections. Applying Newton's second law on the infinitesimal part in the z-direction results in the Eq. (1), where the mass is indicated with the density of the material, *ρ*, and the volume of the part, *A dx.* The acceleration term is defined as the second derivative of deflection, *w,* with respect to time.

$$V - (V + dV) + f(x,t)dx = \rho A\, dx \frac{\partial^2 w}{\partial t^2}(x,t) \tag{1}$$

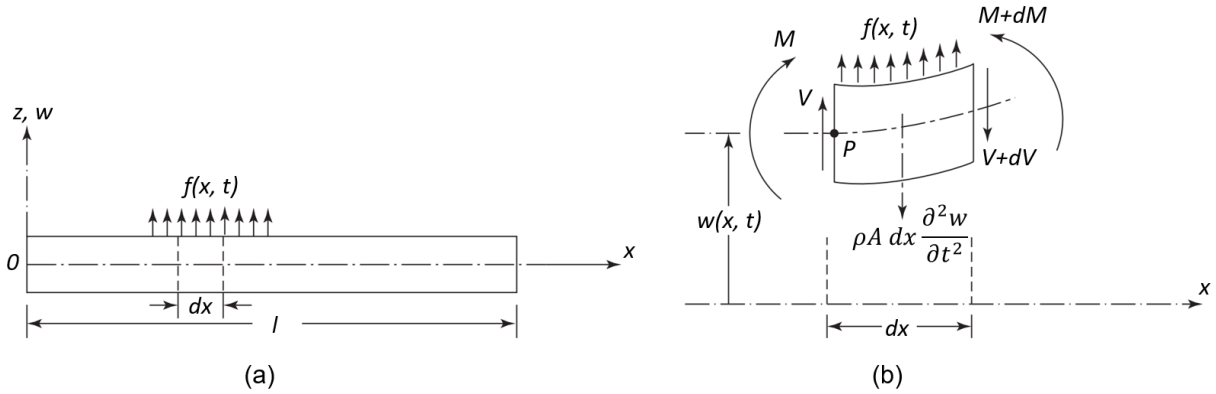


Figure 1. Representation of the Thin Beam (a), Infinitesimal Section of the Beam (b) [Rao, 2007].

Additionally, moment equilibrium around the point *P* results in Eq. (2).

$$(M + dM) - M - (V + dV)dx + f(x,t)dx\frac{dx}{2} = 0 \tag{2}$$

Using equities given in Eq. (3), and considering the second power of *dx* is small compared to other terms, Eqs. (1) and (2) can be written as given on the Eqs. (4) and (5).

$$dV = \frac{\partial V}{\partial x}dx \qquad and \qquad dM = \frac{\partial M}{\partial x}dx \tag{3}$$

Taking the derivative of Eq. (5) with respect to *x*, and inserting Eq. (4) results in Eq. (6).

$$-\frac{\partial V}{\partial x}(x,t) + f(x,t) = \rho A(x)\frac{\partial^2 w}{\partial t^2}(x,t) \tag{4}$$

$$\frac{\partial M}{\partial x}(x,t) - V(x,t) = 0 \tag{5}$$

$$-\frac{\partial^2 M}{\partial x^2}(x,t) + f(x,t) = \rho A(x)\frac{\partial^2 w}{\partial t^2}(x,t) \tag{6}$$

Considering the equity between bending moment and deflection in Eq. (7) from the theory of strength of materials where Young Modulus and Area Moment of Inertia are represented with *E*, and *I* respectively; Eq. (6) can be modified as given in Eq. (8).

$$M(x,t) = EI(x)\frac{\partial^2 w}{\partial x^2}(x,t) \tag{7}$$

$$-\frac{\partial^2}{\partial x^2}\left(EI(x)\frac{\partial^2 w}{\partial x^2}(x,t)\right) + f(x,t) = \rho A(x)\frac{\partial^2 w}{\partial t^2}(x,t) \tag{8}$$

The investigated specimen has a constant cross-section through its length, therefore Eq. (8) can be rewritten as given in Eq. (9).

$$EI\frac{\partial^4 w}{\partial x^4}(x,t) + \rho A\frac{\partial^2 w}{\partial t^2}(x,t) = f(x,t) \tag{9}$$

To calculate the natural frequencies of the beam, a free-vibration form of Eq. (9) is defined in Eq. (10). The equation consists of partial derivative terms with respect to time, and distance.

$$c^2\frac{\partial^4 w}{\partial x^4}(x,t) + \frac{\partial^2 w}{\partial t^2}(x,t) = 0, \qquad where\ c = \sqrt{\frac{EI}{\rho A}} \tag{10}$$

The Separation of Variables Method can be used to define the deflection term where *W(x)* represents the shape of the beam and *T(t)* represents the time-dependent part of the vibration. The time-dependent variable can be assumed as $Ae^{i\omega t}$ as given in Eq. (11).

$$w(x,t) = W(x)T(t) = W(x)Ae^{i\omega t} \tag{11}$$

By inserting the definition of deflection in Eq. (11) into Eq. (10), and eliminating time-dependent part, Eq. (12) can be obtained. It should be noted that if the time-dependent part is assumed to be zero, then there is no vibration.

$$c^2 \frac{d^4W}{dx^4} - \omega^2 W(x) = 0 \tag{12}$$

Collecting constant terms in one variable, Eq. (12) can be rewritten as given in Eq. (13).

$$\frac{d^4W}{dx^4} - \beta^4 W(x) = 0, \qquad where\ \beta^4 = \frac{\omega^2}{c^2} \tag{13}$$

One solution assumption to the differential equation of Eq. (13) is given in Eq. (14).

$$W(x) = Ce^{sx}, \qquad and\ \frac{d^4W}{dx^4} = s^4 Ce^{sx} \tag{14}$$

In Eq. (15), the simplified result of Eq. (13) with the solution assumption of Eq. (14) is given.

$$s^4 - \beta^4 = 0, \qquad where\ s_{1,2} = \pm\beta, \qquad and\ s_{3,4} = \pm i\beta \tag{15}$$

The solution of Eq. (14) given on the Eq. (15) implies that the shape function of the beam is as given on the Eq. (16). Using trigonometric conversions, other forms of shape function with different coefficients can be formed, one example can be seen on the Eq. (17).

$$W(x) = C_1 e^{\beta x} + C_2 e^{-\beta x} + C_3 e^{i\beta x} + C_4 e^{-i\beta x} \tag{16}$$

$$W(x) = A_1 cos(\beta x) + A_2 sin(\beta x) + A_3 cosh(\beta x) + A_4 sinh(\beta x) \tag{17}$$

The obtained shape functions represent the vibrational shapes of the beam. Further investigation requires providing boundary conditions and determining coefficients. For a fixed-free beam, the boundary conditions are specified as zero deflection, and slope at the fixed-end; and zero bending moment, and zero shear force at the free-end as given in Eq. (18).

$$W(x=0) = 0, \qquad \frac{dW}{dx}(x=0) = 0, \qquad \frac{d^2W}{dx^2}(x=l) = 0, \qquad \frac{d^3W}{dx^3}(x=l) = 0 \tag{18}$$

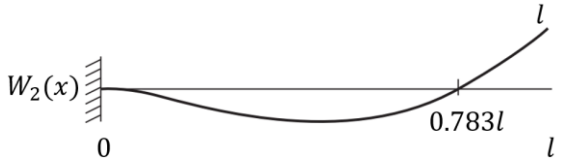
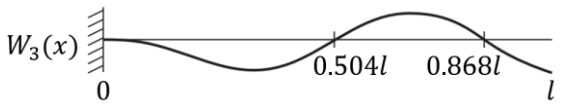
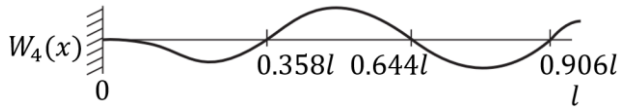
The boundary conditions in Eq. (18) lead to the frequency equation given in Eq. (20). The equation can be solved numerically for βl. The first four numerical solutions and corresponding mode shapes are shown in Table 1.

$$cos(\beta l)cosh(\beta l) + 1 = 0 \tag{19}$$

The definitions of β and c are given on the Eqs. (10) and (13), using the numerical solutions of the Eq. (19) the corresponding natural frequencies can be calculated as given on the Eq. (20).

$$\omega_{n_i} = (\beta_i l)^2 \sqrt{\frac{EI}{\rho A l^4}} \tag{20}$$

Table 1. Numerical Solutions and Mode Shapes of Frequency Equation [Rao, 2007].

Numerical Solutions		Mode Shapes
$\beta_1 l$	1.8751	
$\beta_2 l$	4.6941	
$\beta_3 l$	7.8547	
$\beta_4 l$	10.9956	

Mode shapes become particularly important while selecting measurement points on the beam. For example, a measurement at the point 0.783l away from the fixed end would not have any vibrational amplitude of the second mode, therefore cannot be identified. While selecting measurement points, these nodes should be avoided for laser vibrometer.

Determination of Frequency Response Function: Additional validation of the measurements can be done by comparing the experimental and theoretical FRFs. To investigate the amplification factor corresponding to the excitation frequency, the boundary conditions given in Eq. (18) should be modified for shear force considering the theory of strength of materials as given in Eq. (21) [Schmitz & Smith, 2012]. The beam is excited at the free-end of the beam, and its representation can be seen in Figure 2.

$$W|_{x=0} = 0, \qquad \left.\frac{dW}{dx}\right|_{x=0} = 0, \qquad \left.\frac{d^2W}{dx^2}\right|_{x=l} = 0, \qquad \left.\frac{d^3W}{dx^3}\right|_{x=l} = \frac{V}{EI} = -\frac{F}{EI} \tag{21}$$

Using the boundary conditions given in Eq. (21), on the shape function defined in Eq. (17), the coefficients of the shape function can be obtained.

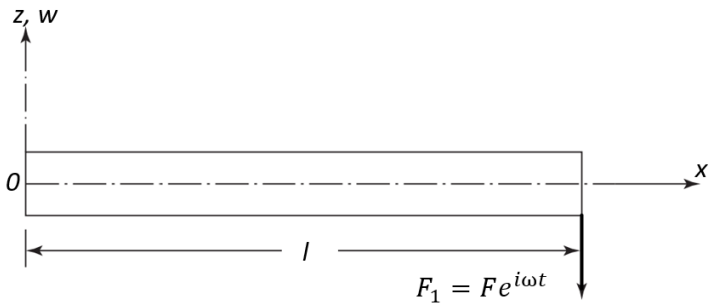


Figure 2. Excitation Condition of the Fixed-Free Beam [Schmitz & Smith, 2012].

The result of the zero deflection and slope at the fixed-end boundary conditions can be seen on the Eqs. (22) and (23). As a result of the equations, the relations between the coefficients can be seen in Eq. (24).

$$W(x=0) = A_1 cos(0) + A_2 sin(0) + A_3 cosh(0) + A_4 sinh(0) = 0 \tag{22}$$

$$\frac{dW}{dx}(x=0) = \beta(-A_1 sin(0) + A_2 cos(0) + A_3 sinh(0) + A_4 cosh(0)) = 0 \tag{23}$$

$$A_1 + A_3 = 0, \qquad A_2 + A_4 = 0 \tag{24}$$

The results of the boundary conditions of the bending moment and the shear force at the free-end of the beam are given in Eqs. (25) and (26).

$$\frac{d^2W}{dx^2}(x=l) = \beta^2(-A_1 cos(\beta l) - A_2 sin(\beta l) + A_3 cosh(\beta l) + A_4 sinh(\beta l)) = 0 \tag{25}$$

$$\frac{d^3W}{dx^3}(x=l) = \beta^3\big(A_1 sin(\beta l) - A_2 cos(\beta l) + A_3 sinh(\beta l) + A_4 cosh(\beta l)\big) = -\frac{F}{EI} \tag{26}$$

The obtained coefficient relations in Eq. (24) can be used to reorganize Eqs. (25) and (*26*), and as a result Eqs. (27) and (28) are obtained.

$$A_3\big(cos(\beta l) + cosh(\beta l)\big) + A_4\big(sin(\beta l) + sinh(\beta l)\big) = 0 \tag{27}$$

$$A_3\big(-sin(\beta l) + sinh(\beta l)) + A_4(cos(\beta l) + cosh(\beta l)\big) = -\frac{F}{\beta^3 EI} \tag{28}$$

Eqs. (27) and (28) consist of two unknown coefficients, the solution to the system of the equations is given in Eqs. (29) and (30).

$$A_3 = \frac{F}{\beta^3 EI}\left(\frac{sin(\beta l) + sinh(\beta l)}{2(1 + cos(\beta l) cosh(\beta l))}\right) \tag{29}$$

$$A_4 = -\frac{F}{\beta^3 EI}\left(\frac{cos(\beta l) + cosh(\beta l)}{2(1 + cos(\beta l) cosh(\beta l))}\right) \tag{30}$$

The rearranged form of the shape function given in Eq. (17) with the acquired coefficients defined in Eqs. (24), (29), and (30) lead to the theoretical FRF in Eq. (31). Obtained FRF is the magnification factor for the displacement of any point on the beam as a response to the excitation at the free-end of the beam. Additionally, the frequency equation obtained on the Eq. (19) is also obtained at the denominator of the FRF. The solution for *βl* to Eq. (19) results in high magnification factor at the corresponding frequency, namely natural frequency.

$$\begin{aligned}\frac{W(x)}{F} = \frac{1}{2\beta^3 EI}\Bigg[&\left(\frac{sin(\beta l) + sinh(\beta l)}{(1 + cos(\beta l)\, cosh(\beta l))}\right)\big(-cos(\beta x) + cosh(\beta x)\big) \\ &- \left(\frac{cos(\beta l) + cosh(\beta l)}{(1 + cos(\beta l)\, cosh(\beta l))}\right)\big(-sin(\beta x) + sinh(\beta x)\big)\Bigg]\end{aligned} \tag{31}$$

On the theoretical FRF, the effect of the damping is not included. Damping effects occur due to the internal energy dissipation of the material within the beam.

Solid Damping: The solid damping model can be defined as *complex elastic modulus* as given in Eq. (32) by unitless solid damping factor, *η.* By incorporating solid damping factor into elastic modulus, the damping is defined as a function that is dependent on the geometric features of the beam such as the second moment of area of the cross-section, and the length of the beam, therefore the stiffness of the beam [Schmitz & Smith, 2012].

$$E_s = E(1 + i\eta) \tag{32}$$

However, the viscous damping factor and the solid damping factor are not equivalent to each other, and further investigation is needed to define the relationship. In Eq. (33), single degree of freedom (sDOF) dynamic equation with viscous damping model can be seen.

$$m\ddot{x} + c\dot{x} + kx = Fe^{i\omega t} \tag{33}$$

The solution assumption of $x(t) = X\mathrm{e}^{\mathrm{i}\omega\mathrm{t}}$ results in FRF defined in Eq. (34).

$$\frac{X}{F}(\omega) = \frac{1}{-\omega^2 m + i\omega c + k} = \frac{1}{k}\left(\frac{1}{\left(1 - \left(\frac{\omega}{\omega_n}\right)^2\right) + i2\zeta\left(\frac{\omega}{\omega_n}\right)}\right) \tag{34}$$

In order to define the relationship between viscous damping, and solid damping factors, the natural frequency can be used, therefore same magnification factor can be achieved at the most important frequency. In Eq. (35), the result for the viscous damping can be seen.

$$\frac{X}{F}(\omega_n) = \frac{1}{i2k\zeta} \tag{35}$$

In Eq. (36), a dynamical model of a sDOF system with the solid damping model can be seen.

$$m\ddot{x} + k(1 + i\eta)x = Fe^{i\omega t} \tag{36}$$

The solution assumption of $x(t) = X\mathrm{e}^{\mathrm{i}\omega\mathrm{t}}$ results in FRF defined in Eq. (37).

$$\frac{X}{F}(\omega) = \frac{1}{-\omega^2 m + k(1 + i\eta)} \tag{37}$$

The magnification factor of the solid damping model at the natural frequency can be calculated as given in Eq. (38).

$$\frac{X}{F}(\omega_n) = \frac{1}{ik\eta} \tag{38}$$

By equating Eqs. (35) and (38) into each other, the relationship given in Eq. (39) is obtained. The measured experimental viscous damping factor, ζ, can be converted to solid damping factor, η, and by incorporating Eq. (32) into FRF in Eq. (31), the theoretical FRF can be modeled.

$$\eta = 2\zeta \tag{39}$$

Ho-Kalman's Realization Method

Ho-Kalman method is a sub-space method and determines the discrete state-space model of a dynamical system by analyzing the response to the impulse excitation. A discrete state space representation of a dynamical system can be formulated as given in Eq. (40). In the formulation, x ∈ $\mathcal{R}^{r\times1}$ represents the State Vector of the system, y ∈ $\mathcal{R}^{p\times1}$ represents the Output Vector, *u* ∈ $\mathcal{R}^{m\times1}$ represents the Input Vector. *A, B, C,* and *D* represent State Matrix, Input Matrix, Output Matrix, and Feedthrough Matrix respectively [Katayama, 2005].

$$\begin{aligned} x(t+1) &= Ax(t) + Bu(t) \\ y(t) &= Cx(t) + Du(t) \end{aligned} \tag{40}$$

Using the state-space formulation, the impulse response of the system can be evaluated where the system is stationary and the states of the system are zero at the beginning, then at the time zero, an impulse input is applied to the system as formulated in Eq. (41).

$$x(t=0) = 0, \qquad x(t\neq 0) \neq 0, \qquad u(t=0) \neq 0, \qquad u(t\neq 0) = 0 \tag{41}$$

Using Eq. (41), in the state-representation given in Eq. (40), the output of the dynamical system can be formulated as given in Eq. (42)

$$y(t) = \begin{cases} Du(0), & t = 0 \\ CA^{t-1}Bu(0), & t \neq 0 \end{cases} \tag{42}$$

The finite Impulse Response of a system can also be represented with response coefficients as given in Eq. (43).

$$y(t) = \sum_{k=0}^{\infty} G_k u(t-k), \qquad y(t) = G_k u(0) \tag{43}$$

Before further development of the Ho-Kalman methodology; Observability and Controllability matrices of the state space system should be defined. Observability matrix can be defined as the criteria whether the system's states can be observed from the output, and the Controllability Matrix can be defined as the criteria whether the system can be excited from an initial state to any desired state. If Observability and Controllability Matrices' ranks are equal to the order of the system, the system is said to be Observable and Controllable. However, it should be noted that the equations in Eq. (44) are Extended Observability Matrix, $\mathcal{O}_{\mathrm{k}}$, and Extended Controllability Matrix, $\mathcal{C}_{\mathrm{n}}$.

$$\mathcal{O}_k = \begin{bmatrix} C \\ CA \\ \vdots \\ CA^{k-1} \end{bmatrix} \qquad \mathcal{C}_n = [B \quad AB \quad \dots \quad A^{n-1}B] \tag{44}$$

For system realization, the system's response to impulse input should be organized in the following format as shown in Eq. (45), which is called Hankel Matrix.

$$H = \begin{bmatrix} G_1 & G_2 & \dots & G_n \\ G_2 & G_3 & \dots & G_{n+1} \\ \vdots & \vdots & \ddots & \vdots \\ G_k & G_{k+1} & \dots & G_{n+k-1} \end{bmatrix} = \begin{bmatrix} CB & CAB & \dots & CA^{n-1}B \\ CAB & CA^2B & \dots & CA^nB \\ \vdots & \vdots & \ddots & \vdots \\ CA^{k-1}B & CA^kB & \dots & CA^{n+k-2}B \end{bmatrix} \in \mathcal{R}^{kp \times nm} \quad (45)$$

Further investigation of the constructed Hankel Matrix shows that Hankel Matrix can be decomposed as matrix multiplication of the Extended Observability and the Extended Controllability Matrix as shown in Eq. (46).

$$H = \begin{bmatrix} CB & CAB & \dots & CA^{n-1}B \\ CAB & CA^2B & \dots & CA^nB \\ \vdots & \vdots & \ddots & \vdots \\ CA^{k-1}B & CA^kB & \dots & CA^{n+k-2}B \end{bmatrix} = \begin{bmatrix} C \\ CA \\ \vdots \\ CA^{k-1} \end{bmatrix} [B \quad AB \quad \dots \quad A^{n-1}B] = \mathcal{O}_k \mathcal{C}_n \quad (46)$$

The Hankel Matrix can also be decomposed using Singular Value Decomposition (SVD). As shown in Eq. (47), where *U* is a matrix containing left singular vectors and *V* is a matrix containing right singular vectors. ∑ is the diagonal matrix containing the singular values in descending order. By taking only the most important singular values, the Hankel Matrix can be represented with reduced order.

$$H = U \sum V^T = [U_1 \quad U_2] \begin{bmatrix} \sum_1 & 0 \\ 0 & 0 \end{bmatrix} \begin{bmatrix} {V_1}^T \\ {V_2}^T \end{bmatrix} = U_1 \sum_1 {V_1}^T \quad (47)$$

One property of the singular value decomposition is the right and left vectors are orthonormal. Which means that the vectors are orthogonal to each other, and the magnitudes of the vectors are unity. To achieve balanced decomposition, the singular value matrix can be further decomposed as shown in Eq. (48).

$$\sum_1 = \begin{bmatrix} \lambda_1 & 0 & 0 \\ 0 & \ddots & \vdots \\ 0 & \dots & \lambda_n \end{bmatrix} = \begin{bmatrix} \sqrt{\lambda_1} & 0 & 0 \\ 0 & \ddots & \vdots \\ 0 & \dots & \sqrt{\lambda_n} \end{bmatrix} \begin{bmatrix} \sqrt{\lambda_1} & 0 & 0 \\ 0 & \ddots & \vdots \\ 0 & \dots & \sqrt{\lambda_n} \end{bmatrix} = \sqrt{\sum_1} \sqrt{\sum_1} \quad (48)$$

Provided decompositions suggest that Hankel Matrix can be formulated with Singular Value Decomposition (SVD), and multiplication of the Extended Observability Matrix and the Extended Controllability Matrix, therefore the relationship between SVD matrices and Observability and Controllability Matrices can be formed as shown in Eq. (49).

$$\begin{aligned} H &= \mathcal{O}_k \mathcal{C}_n = U_1 \sqrt{\sum_1} \sqrt{\sum_1} {V_1}^T = U_1 \sqrt{\sum_1} T T^{-1} \sqrt{\sum_1} {V_1}^T \\ \mathcal{O}_{\mathrm{k}} &= \mathrm{U}_1 \sqrt{\sum_1}\, T \\ \mathcal{C}_{\mathrm{n}} &= \mathrm{T}^{-1} \sqrt{\sum_1} {\mathrm{V}_1}^{\mathrm{T}} \end{aligned} \quad (49)$$

Here it should be noted that there are different state-space matrices that represent the same dynamical system. Which suggests that obtained Observability and Controllability Matrices are not unique, therefore a non-singular matrix, *T*, and its inverse can be used to represent different Observability and Controllability Matrices.

Using the definitions given in Eq. (44), B and C matrices can be obtained directly from Observability and Controllability Matrices that are formed with SVD as given in Eq. (50).

$$C = \mathcal{O}_k(1{:}p,:) \in \mathcal{R}^{p \times r}$$
$$B = \mathcal{C}_{\mathrm{n}}(:,1{:}m) \in \mathcal{R}^{\mathrm{r} \times \mathrm{m}} \tag{50}$$

In order to extract A matrix, parts of the Observability Matrix can be used as given in Eq. (51). In the formulation superscript # operator is the pseudo inverse.

$$\mathcal{O}_{k_1} = \begin{bmatrix} C \\ CA \\ \vdots \\ CA^{k-2} \end{bmatrix} \qquad \mathcal{O}_{k_2} = \begin{bmatrix} CA \\ CA^2 \\ \vdots \\ CA^{k-1} \end{bmatrix} \tag{51}$$

$$\mathcal{O}_{\mathrm{k}_1} A = \mathcal{O}_{\mathrm{k}_2}$$
$$A = {\mathcal{O}_{\mathrm{k}_1}}^{\#} \mathcal{O}_{\mathrm{k}_2} \in \mathcal{R}^{\mathrm{r} \times \mathrm{r}}$$

Considering the formulations given in Eqs. (*42*) and (*43*), D matrix can be obtained from G_0 of the response coefficients.

Ho-Kalman Method and Impact Test Similarity

In mathematics, impulse function can be defined as an infinitely large excitation for an infinitely small duration that has an integral of one. However, in the Ho-Kalman methodology, impulse excitation is assumed to have a unit amplitude as magnitude at time zero, *u(0)*. Additionally, since collected data is discrete and the assumed function is zero except at time zero. Depending on the sampling frequency, the time integral of the assumed impulse excitation function should be Δt -sampling interval-. However, an impact for a single sampling instant cannot be achieved, therefore time integral of the impact data should be calculated. Assuming linearity between input and output, normalization should be applied to the measured data. In Figure 3, normalized experimental impact data and assumed impulse data are represented.

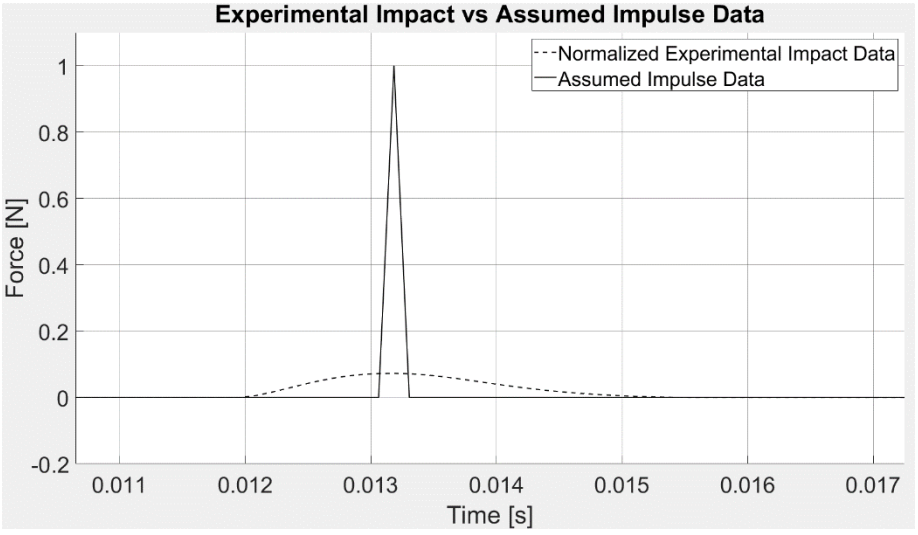


Figure 3. Normalized Experimental Impact vs Assumed Impulse Data.

Frequency Response Assurance Criterion (FRAC)

The State-Space representation of the vibration characteristics of the system can be obtained using the Ho-Kalman method. Although the result of the Ho-Kalman method can be compared graphically with the FRF, using the Bode-Plot of the State-Space representation; Frequency Response Assurance Criterion, FRAC, provides numerical results whether the identified Bode-Plot thus the State-Space representation is in accordance with the FRF result of the system. In Eq. (*52*), the method for the calculation of FRAC is given. H_A *and* H_B represent two complex frequency domain results that are compared, and asterisk, *, represents the conjugate of the complex values. FRAC calculation results in a numerical value between 0 and 1, where 1 means a perfect match between frequency domain results [Manring et al., 2022].

$$FRAC = \frac{\left|\sum_{\omega=\omega_1}^{\omega_2} H_A(\omega) {H_B}^*(\omega)\right|^2}{\sum_{\omega=\omega_1}^{\omega_2} H_A(\omega) {H_A}^*(\omega) \sum_{\omega=\omega_1}^{\omega_2} H_B(\omega) {H_B}^*(\omega)} \tag{52}$$

3. EXPERIMENTAL SETUP

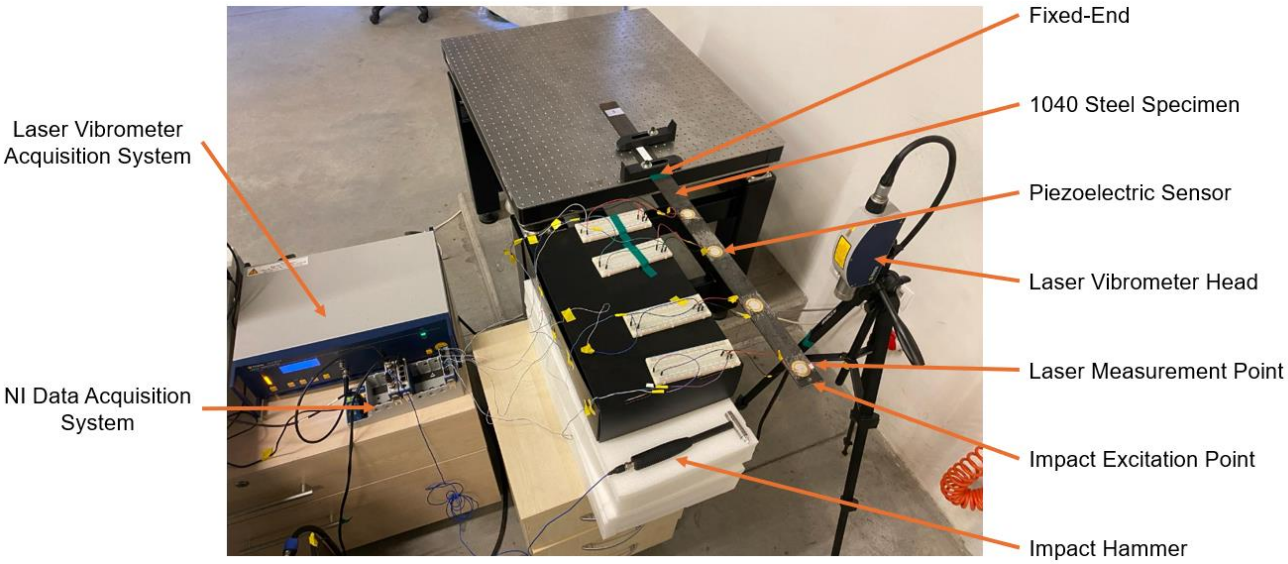


Figure 4. Experimental Setup.

Vibration measurements have been conducted using 1040 Steel and CFRP materials, and the physical properties of the specimens and material properties are given in Table 2. An example experimental setup for 1040 Steel is shown in Figure 4, and the representations of the setups are given in Figure 5. Experiments have been conducted on the intact materials first, then damage is induced to the material, and experiments have been repeated. For each experiment 5 samples have been collected. The data has been collected with a 10240 Hz sampling rate. Controlled damages have a length of 10 mm and a width of 2 mm as shown in Figure 6. The details of the sensor locations and the damage locations are given in Table 3.

Table 2. Specimen Properties.

	Material Properties		Physical Properties		
	Elastic Modulus	**Density**	**Length**	**Width**	**Thickness**
	GPa	kg/m^3	m	m	m
1040 Steel	200	7845	0.65	0.05	0.005
CFRP	35	1140	0.39	0.05	0.003

Table 3. Sensor and Damage Locations.

		1040 Steel	CFRP
Piezoelectric Gauge Locations	**1st**	0.25 L	0.1 L
	2nd	0.45 L	0.5 L
	3rd	0.70 L	0.90 L
	4th	0.95 L	-
Laser Measurement Location		0.95 L	0.85 L
Damage Location		259 mm (≈0.40 L)	155 mm (≈0.40 L)

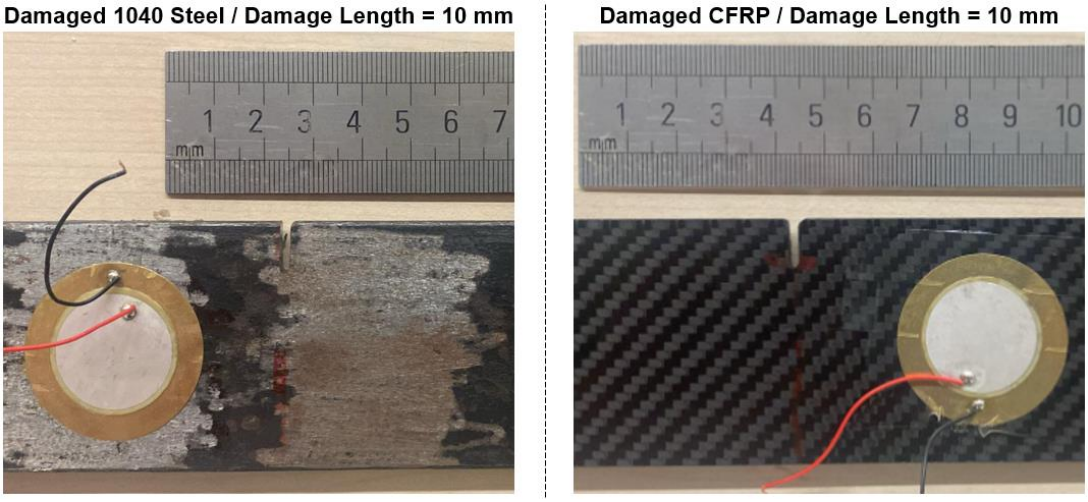


Figure 6. Damaged Samples.

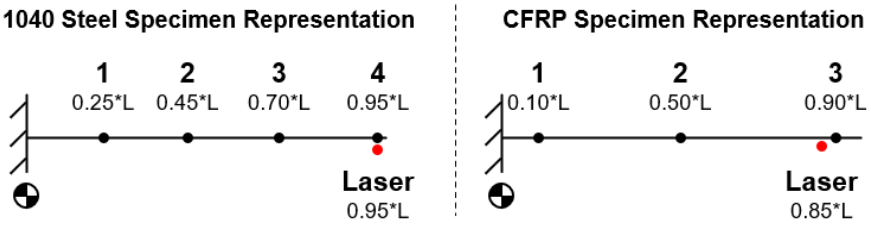


Figure 5. 1040 Steel and CFRP Experimental Setup Representations.

4. RESULTS

1040 Steel Results

The frequency domain results of the experiments of 1040 Steel are given in Figure 7. In the figure, theoretical FRF, experimental FRF results, and the bode plot of the identified state-space model can be seen. 5 bode plots of the intact experimental data have FRAC of 0.9806±0.0064 and bode plots of the damaged experimental data have FRAC of 0.9708±0.0101 with corresponding FRF results. An additional mode that is not obtained with the theoretical transverse vibration calculation can be seen around 250 Hz. In order to identify the first 4 transverse vibration modes that correspond to 8 orders, the Ho-Kalman identification method is used with 12 number of orders. Chosen first 4 transverse vibration modes' natural frequencies and the damping ratios are given in Table 4. In order to compare the modal parameter results of the laser vibrometer and the piezoelectric sensor, output measurements are identified separately. In the table and the FRAC calculations, ± corresponds to the standard deviation of the 5 experimental measurement data. The first 3 modes' natural frequencies decreased by 0.174, 0.296, and 0.141 percent with small standard deviations. However, the 4th mode's modal result has a high standard deviation with respect to the mean, and significant observation is not seen.

Table 4. 1040 Steel Specimen Numerical Results.

		1040 Steel							
		1st Mode		2nd Mode		3rd Mode		4th Mode	
		f_{n_1} Hz	ζ_1 %	f_{n_2} Hz	ζ_2 %	f_{n_3} Hz	ζ_3 %	f_{n_4} Hz	ζ_4 %
	Theor.	9.6525	-	60.492	-	169.38	-	331.92	-
Laser	Intact	9.3509	0.2080	59.566	0.1941	164.85	0.0978	331.72	0.5340
		±0.0011	±0.0052	±0.006	±0.0046	±0.01	±0.0018	±0.20	±0.0269
	Damaged	9.3346	0.1809	59.389	0.2169	164.61	0.0934	330.48	0.8992
		±0.0014	±0.0026	±0.007	±0.0027	±0.02	±0.0009	±2.67	±0.2422
	Diff (%)	**-0.174**	-12.97	**-0.296**	11.85	**-0.141**	-4.396	**-0.374**	71.11
		±0.026	±3.42	**±0.022**	±4.08	**±0.020**	±2.712	**±0.864**	±53.98
Piezoelectric Sensors	Intact	9.3507	0.1979	59.564	0.1968	164.85	0.1022	332.15	0.6546
		±0.0011	±0.0123	±0.006	±0.0058	±0.01	±0.0054	±0.49	±0.1349
	Damaged	9.3347	0.1650	59.388	0.2214	164.62	0.0984	333.82	0.9844
		±0.0013	±0.0180	±0.007	±0.0058	±0.02	±0.0056	±3.74	±0.0959
	Diff (%)	**-0.171**	-15.72	**-0.296**	12.71	**-0.140**	-3.100	**0.505**	60.20
		±0.026	±14.33	**±0.023**	±6.28	**±0.019**	±10.65	**±1.273**	±47.67

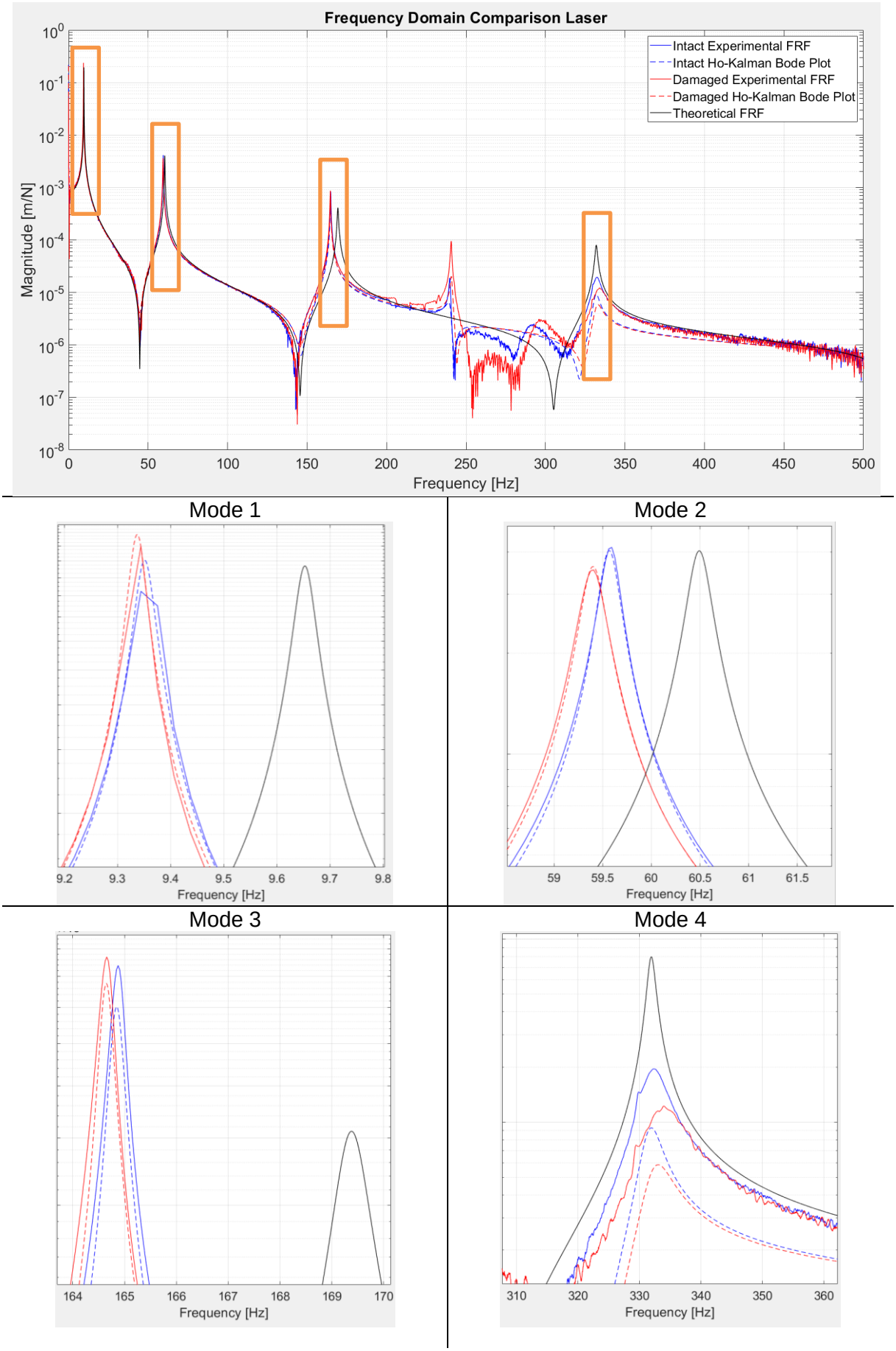


Figure 7. 1040 Steel Specimen Frequency Domain Results.

CFRP Results

Frequency domain results of the experiments of CFRP specimen are given in Figure 8. On the figure, theoretical FRF, experimental FRF results and the bode plot of the identified state-space model can be seen. 5 bode plots of the intact experimental data have FRAC of 0.9914±0.0009 and bode plots of the damaged experimental data have FRAC of 0.9960±0.0008 with corresponding FRF results. In order to identify first 4 transverse vibration modes which corresponds to 8 orders, Ho-Kalman identification method is used with 12 number of orders. Chosen first 4 transverse vibration modes' natural frequency and the damping ratios are given in Table 5. In order to compare the modal parameter results of laser vibrometer and piezoelectric sensor, output measurements are identified separately. On the table and the FRAC calculations, ± corresponds to standard deviation of the 5 experimental measurement data. The first 4 modes' natural frequencies decreased by 0.801, 0.897, 0.542, and 0.400 percent with small standard deviations. Additionally, the laser vibrometer's and the piezoelectric sensors' identification results are in accordance with each other in terms of the first two modes' damping ratios, as a result, due to the induced damage, the first two mode's damping ratios decrease by 57, and 48 percent, respectively. Similar observations are not obtained with the 3rd and 4th modes' damping ratios.

Table 5. CFRP Specimen Results

		CFRP							
		1st Mode		2nd Mode		3rd Mode		4th Mode	
		f_{n_1} Hz	ζ_1 %	f_{n_2} Hz	ζ_2 %	f_{n_3} Hz	ζ_3 %	f_{n_4} Hz	ζ_4 %
	Theor.	17.654	-	110.64	-	309.79	-	607.07	-
Laser	Intact	17.217	1.0717	107.45	0.3754	300.55	0.1456	589.29	0.2115
		±0.010	±0.0656	±0.02	±0.0245	±0.01	±0.0060	±0.03	±0.0085
	Damaged	17.079	0.4547	106.49	0.1919	298.93	0.1430	586.93	0.2019
		±0.002	±0.0285	±0.00	±0.0017	±0.01	±0.0021	±0.02	±0.0041
	Diff (%)	**-0.801**	-57.24	**-0.897**	-48.63	**-0.542**	-1.547	**-0.400**	-4.290
		±0.068	±5.28	**±0.022**	±3.79	**±0.004**	±5.439	**±0.007**	±5.782
Piezoelectric Sensors	Intact	17.206	1.0157	107.45	0.3923	300.55	0.1344	589.23	0.1986
		±0.013	±0.0816	±0.02	±0.0281	±0.01	±0.0125	±0.07	±0.0145
	Damaged	17.079	0.4566	106.49	0.2002	298.91	0.1308	586.85	0.1966
		±0.002	±0.0308	±0.00	±0.0093	±0.01	±0.0137	±0.09	±0.0061
	Diff (%)	**-0.741**	-54.51	**-0.895**	-48.54	**-0.544**	-0.919	**-0.403**	-0.242
		±0.085	±6.69	**±0.020**	±6.05	**±0.007**	±19.441	**±0.026**	±10.346

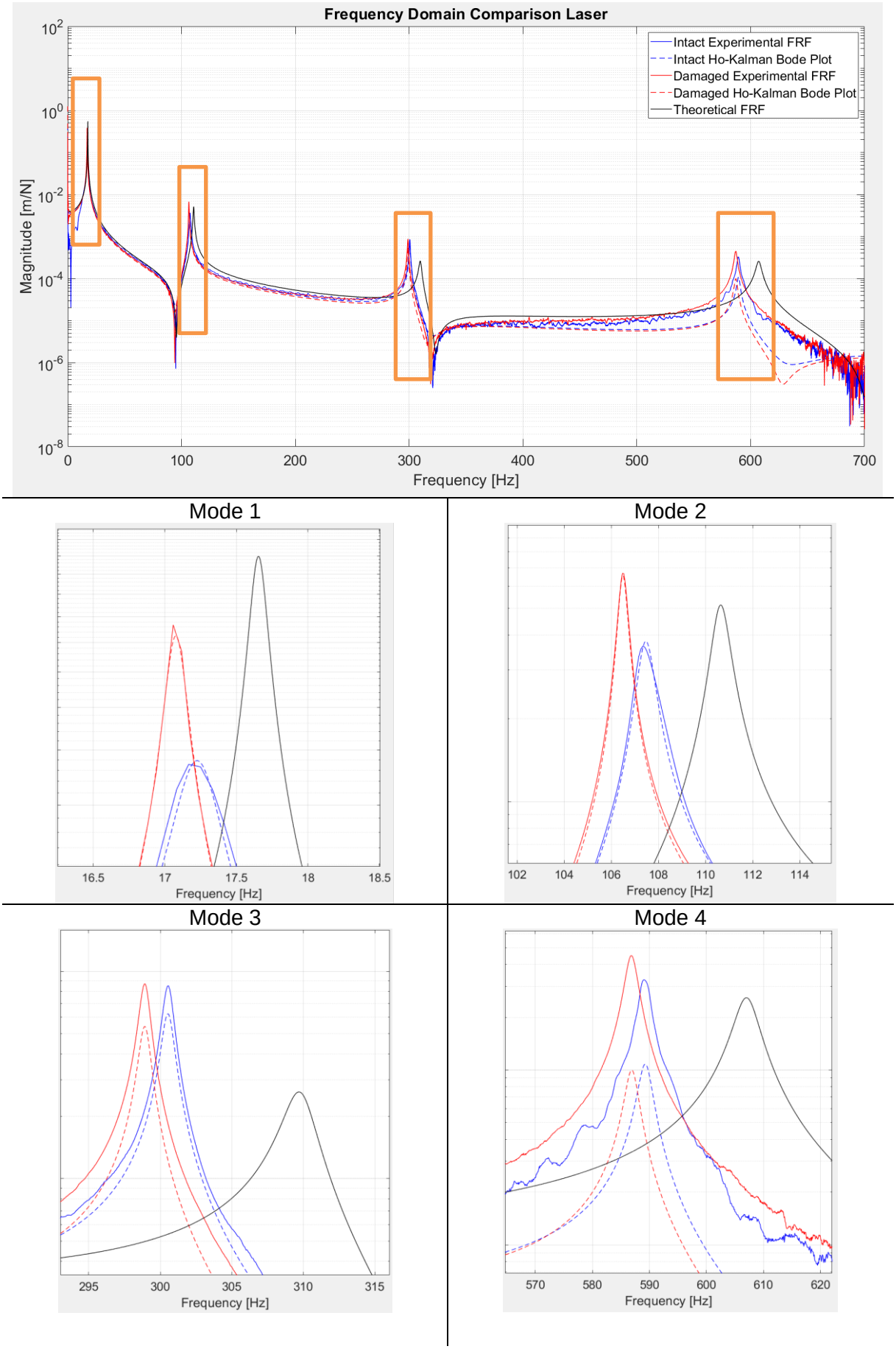


Figure 8. CFRP Specimen Frequency Domain Results.

5. CONCLUSION AND FUTURE WORK

As a result of the damage applied to the specimens, the rigidness of the structures decreased which caused the natural frequencies of the specimens to also decrease. With the Ho-Kalman method, the change of the natural frequencies has been observed for the first 4 modes of the CFRP, and the first 3 modes of the 1040 Steel. On the fourth mode of the 1040 Steel, a clear result is not observed. Additionally, the effect of damage on the first two modes' damping ratios are observed for the CFRP specimen.

Although the Ho-Kalman method showed potential for damage detection systems, for operational modal analysis other Sub-Space methods such as MOESP and N4SID which use arbitrary excitation as input should be used. With deterministic Sub-Space methods, by capturing arbitrary excitation, or with stochastic Sub-Space methods, by assuming excitation as white noise, operational modal analysis and therefore damage detection can be achieved. For future work, MOESP and N4SID methods will be investigated with progressively increasing damage size, and the effect of damage on the modal parameters will be operationally investigated.

ACKNOWLEDGEMENTS

This study is funded by TUBITAK (The Scientific and Technological Research Council of Turkey) through project grant no 123M891.

REFERENCES

1. **Chaupal, P., & Rajendran, P. (2023).** A review on recent developments in vibration-based damage identification methods for laminated composite structures: 2010–2022. Composite Structures, 311, 116809.
2. **Fritzen, C. P. (2005).** Vibration-Based Structural Health Monitoring-Concepts and Applications. Key Engineering Materials, 293, 3-20.
3. **Verhaegen, M., & Deprettere, E. (1991).** A fast, recursive MIMO state space model identification algorithm. In [1991] Proceedings of the 30th IEEE Conference on Decision and Control (pp. 1349-1354). IEEE.
4. **Van Overschee, P., & De Moor, B. (1994).** N4SID: Subspace algorithms for the identification of combined deterministic-stochastic systems. Automatica, 30(1), 75-93.
5. **Viberg, M. (1994).** Subspace Methods in System Identification, IFAC Proceedings Volumes, 27(8), 1-12.
6. **Juang, J. N., & Pappa, R. S. (1985).** An Eigensystem Realization Algorithms (ERA) for Modal Parameter Identification and Model Reduction. In NASAIJPL Workshop on Identification and Control of Flexible Space Structures, J. of Guidance, Control and Dynamics (Vol. 8, No. 5, p. 620).
7. **Piana, G., Lofrano, E., Carpinteri, A., Paolone, A., & Ruta, G. (2016).** Experimental modal analysis of straight and curved slender beams by piezoelectric transducers. Meccanica, 51, 2797-2811.
8. **Rao, S. S. (2007),** "Vibration of Continuous Systems", John Wiley & Sons, New Jersey.
9. **Schmitz, T. L. & Smith, K. S. (2012).** Mechanical Vibrations Modeling and Measurement, Springer Science, New York.
10. **Katayama, T. (2005).** Subspace Methods For System Identification, Springer Science, London.
11. **Manring, L. H., Schultze, J. F., Zimmerman, S. J., & Mann, B. P. (2022).** Improving Magnitude and Phase Comparison Metrics for Frequency Response Functions Using Cross-Correlation and Log-Frequency Shifting. Journal of Sound and Vibration, 539, 117255.

THE ADDITIVE MANUFACTURING PROCESS AND ITS CHALLENGES IN HUMAN PROSTHESIS DEVELOPMENT: PRELIMINARY STUDIES

Carla ANFLOR, *anflor@unb.br* GMEC/University of Brasilia, Brasilia, Brazil

Euclides SANTANNA, *euclidesunb@gmail.com* GMEC/University of Brasilia, Brasilia, Brazil

Karla SARTIN, *ksartin@udf.edu.br* GMEC/University of Brasilia, Brasilia, Brazil

ABSTRACT

This study examines the methodologies employed in computational modeling of the mandible and their effects on research outcomes. It reviews prior research that modeled the mandible with different material properties, treating it as a single unit, in pairs, or as multiple sub-regions. By utilizing sliced tomographic images, a finite element model of an intact mandible was constructed to investigate the dispersion of stress fields based on various bone material properties reported in the literature. The study elaborates on the methods used for mandible model development, approaches to achieve high precision, and the impact of mechanical properties. Significant variations in stress field outcomes were identified, with differences ranging from 4.4% to 67.4% in the symphysis region, evaluated using RMSE to determine model similarity.

Keywords: mandible, finite element method, computational modeling, orthotropic material, bi-material

1. INTRODUCTION

Mandible fractures have been extensively researched over the past few decades, with significant contributions from studies by Van Den Bergh et al. (2012) and Chen et al. (2020). These studies show that the mandible is a common site for fractures due to its prominent position in the cranial skeleton, with a prevalence ranging from 36% to 70%. To reduce surgical risks and durations, advanced computational modeling techniques have been utilized. These models simulate the structural analysis of fractures in the mandibular region, aiding in the stabilization process using titanium plates and screws. The main challenge is optimizing the positioning and design of these components to achieve optimal biomechanical stability. Modeling bone structures with mechanical components is complex due to the nonlinearity of contact problems, which involves frictional coefficients at the interfaces between screws, bone,

and plates. This leads to computationally intensive analyses. CAD drawings, derived from tomographic images, require detailed preparation for numerical analysis. Despite the high geometric detail provided by tomographic scans, many simplifications are often made, such as modeling screws as cylinders, ignoring alveolar process cavities, treating teeth as a single unit, neglecting orthotropic properties, and combining trabecular and cortical tissues. The Finite Element Method (FEM) is employed to evaluate displacement, strain, and stress fields, with its accuracy heavily dependent on mesh quality. However, much of the existing literature on mandible modeling often overlooks mesh metrics, which are crucial for accurate numerical integration. Only a few studies, such as Caraveo et al. (2008), account for contact boundary conditions at the fracture site, which are essential for accurately modeling nonlinearities. Vajgel et al. (2013) used FEM to evaluate fixation locking plates in Class III atrophic mandibular fractures, but they simplified the nonlinear contact by assuming a gap at the fracture site. Arora et al. (2020) modeled the mandible as a bi-material structure with elastic and isotropic properties, treating teeth as a single reinforcing unit and considering the contact problem linearly. Pałka et al. (2020) introduced a new plate topology for fracture stabilization, modeling the mandible with isotropic cortical and trabecular tissues and treating the contact linearly, excluding screws. The literature review indicates that while many studies address complex problems, they often include significant simplifications and lack mesh metrics. Additionally, the use of different mechanical properties in bone modeling results in varied stress-strain field outcomes. This study revisited major research on mandible modeling, highlighting the variability in stress results. It underscored the absence of comprehensive 3D modeling that considers all engineering aspects and provides comparisons with previous works. The study focused on the accuracy of stress field calculations using various mechanical approaches from the literature. An intact mandible finite element model, based on tomographic images, was developed to assess stress distribution caused by different bone material properties. The methodology and strategies for achieving high precision and incorporating mechanical properties present an innovative approach, ensuring accurate results. By adopting sound modeling practices and including mesh metric studies, a precise representation is achieved, facilitating the consideration of complex issues such as nonlinear contact problems and topology optimization.

2. MATERIAL AND METHODS

2.1 The mechanical properties of bone

In recent years, researchers have developed computational models to analyze the mandible with various material properties, as shown in Table 2.1. This study uses a realistic, healthy mandible model with material properties derived from specialized literature (Arora et al., 2020;

Caraveo et al., 2008, 2021; Fernández et al., 2003; S. T. Lovald et al., 2006; Vajgel et al., 2013). The objective is to compare stress distribution across different material property sets using a finite element model of the mandible. Both isotropic and orthotropic materials will be considered, and multiple modeling approaches will be explored, such as treating the mandible as a single entity or dividing it into multiple subregions. The evaluated models are categorized based on their isotropic/orthotropic behavior and the mandible regions considered, resulting in isotropic bimaterial (IsoBi), isotropic monomaterial (IsoMono), isotropic bimaterial 2 (IsoBi_2), and orthotropic material with subregions (OrthoSubreg). IsoBi models assign different isotropic mechanical properties to cortical and trabecular tissues, while IsoMono models treat the mandible as a single isotropic material. The OrthoSubreg model uses orthotropic properties that vary for each anatomical region, distinguishing between trabecular and cortical tissues.

Table 2.1 Mandible Material properties

Material properties								
Isotropic models	IsoBi	Fernandez (2003), Lovald (2006) and Arora (2020) Models						
			Cortical bone	Trabecular bone				
		E_x	13700	7930				
		ν	0,3	0,3				
	IsoMono	Lovald (2010) Model						
			Cortical bone	Trabecular bone				
		E_x	20000	20000				
		ν	0,3	0,3				
	IsoBi_2	Palka (2020) Model						
			Cortical bone	Trabecular bone				
		E_x	14800	1850				
		ν	0,3	0,3				
Orthotropic models	OrthoSubreg	Caraveo (2008), Caraveo (2021), Vajgel (2013) *in Caraveo 2021 Gxy=Gyz=Gxz = 3050) Models						
			Cortical bone					Trabecular bone
			Symphysis	Body	Angle	Ramus	Condyle	Coronoide	
		E_x	20492	21728	23793	24607	23500	28000	1500
		E_y	12092	12700	12757	12971	12650	14000	1500
		E_z	16350	17828	19014	18357	17850	17500	1500
		ν_{xy}	0.43	0.45	0.41	0.38	0.32	0.28	0.3
		ν_{yz}	0.22	0.2	0.22	0.23	0.25	0.28	0.3
		ν_{xz}	0.34	0.34	0.3	0.28	0.24	0.23	0.3
		G_{xy}	5317	5533	5493	5386	5500	5750	-
		G_{yz}	4825	5083	4986	5014	5150	5300	-
		G_{xz}	6908	7450	7579	7407	7150	7150	-

** E_{ij} (MPa) and G_{ij} (MPa), i,j = 1:3*
Abbreviations: E, Young's modulus; ν, Poisson's ratio; G, shear modulus.

2.2 The boundary conditions and loads

A pressure of 0.5MPa was applied laterally to two opposite areas of the mandible, each area (surface patches) with a size of 10mm x 10mm. The pressures were of equal magnitude and direction but in opposite senses, and the condylar areas were assumed to be fixed. (1) stated that this type of impact can cause an indirect fracture in the symphysis region. The boundary conditions are depicted according Figure 2.1.

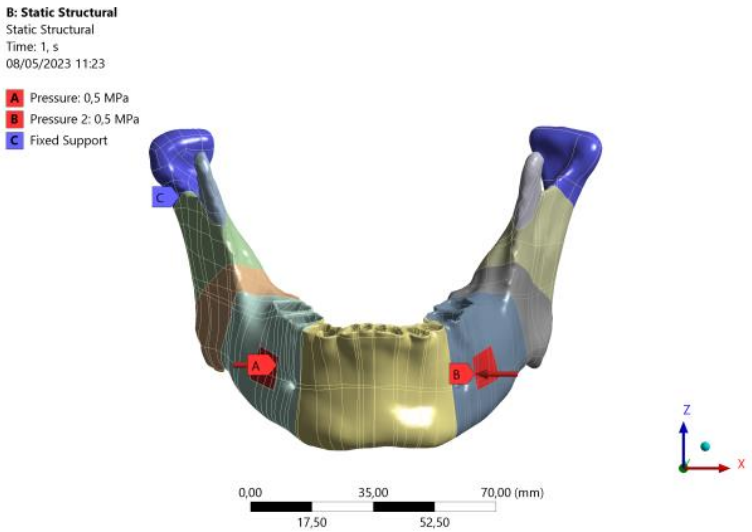
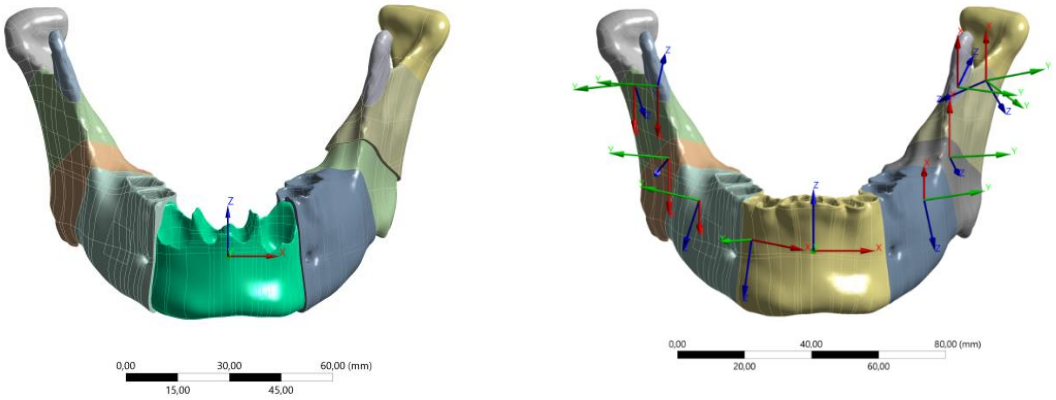


Figure 2.1. Boundary conditions applied to the healthy mandible.

2.3 Mandible subregions and orthotropic orientation

Figure 2.2(a) illustrates the sub-regions of the mandible model (ramus, condylar process, symphysis, angle) and provides a detailed view of the trabecular tissue subdivision in the symphysis and ramus. This model supports both isotropic and orthotropic materials, with bone tissue mechanical properties varying by region and tissue type (see Figure 2.2(b)). By incorporating mandible sub-regions, the model assigns appropriate mechanical properties to each area, enhancing the accuracy of numerical results and improving the evaluation of trauma behavior in specific regions.



(a) (b)

Figure 2.2. Mandible model: a) sub-regions and b Material orientation.

Figure 2.3 presents a schematic diagram outlining the steps for generating a 3D mandible model, adhering to sound engineering practices. The steps are as follows:

- Step 1 - Tomographic Image Acquisition in STL: Acquire tomographic images and save them as STL files. Verify the STL file for issues like split edges, extra edges, duplicated faces, self-intersections, over-connected edges/vertices, and openings. Use additional software to fix these problems if necessary.

- Step 2 - Cleaning: Remove structures like the mandibular, inferior alveolar, and lingual nerves captured during imaging, as they do not contribute to structural strength.
- Step 3 -Convert to Solid: Transform the mandible into a shell faceted structure and then create the width of this structure before converting it into a solid model.
- Step 4 - Defining Subregions: Define subregions according to the mandible's anatomy, considering all anatomical regions. This allows for a customizable model that can be adapted for more complex considerations.
- Step 5 - Defining Mechanical Properties: Assign mechanical properties to the subregions based on selected models (isomono, isobi, or orthotropic).
- Step 6 - Defining Boundary Conditions: Set boundary conditions, which can include representative masticatory forces or other loads as required.
- Step 7 - Checking the Mesh Metric: Verify the mesh metric, with the option to use additional mesh metrics.
- Step 8 - Perform Finite Element Analysis: Conduct the finite element analysis to assess the model.

These steps ensure the development of a precise and reliable 3D mandible model suitable for various computational analyses.

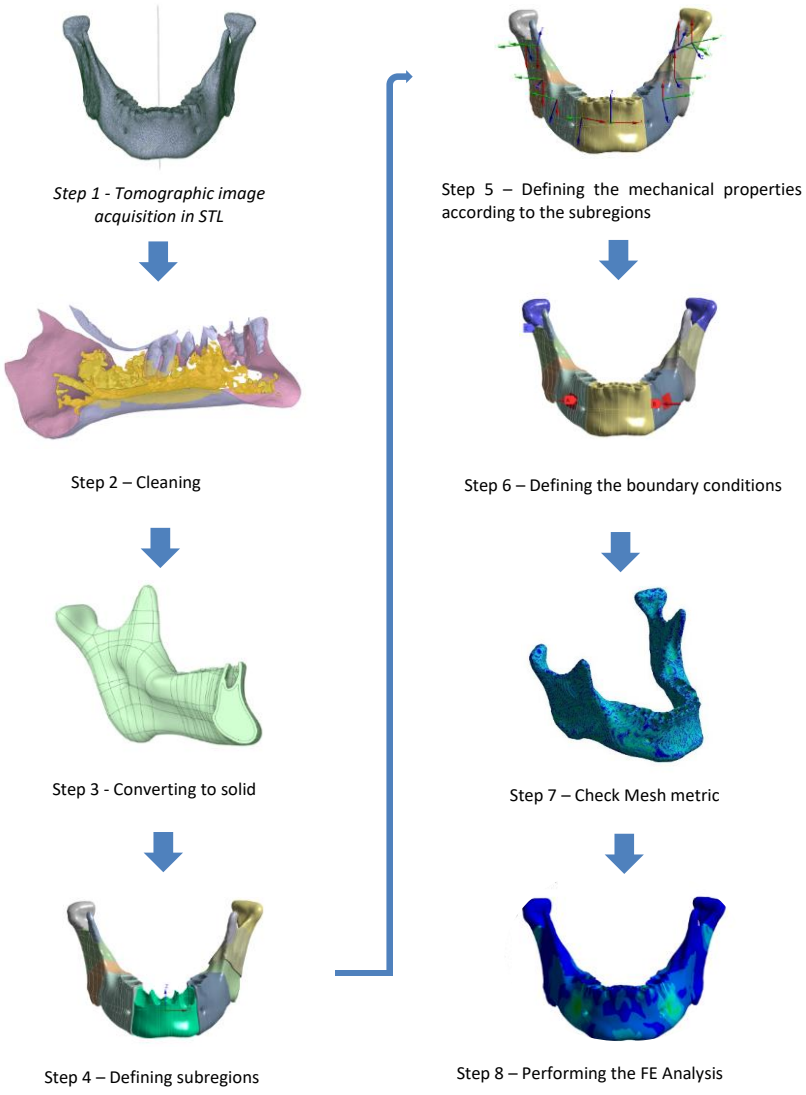
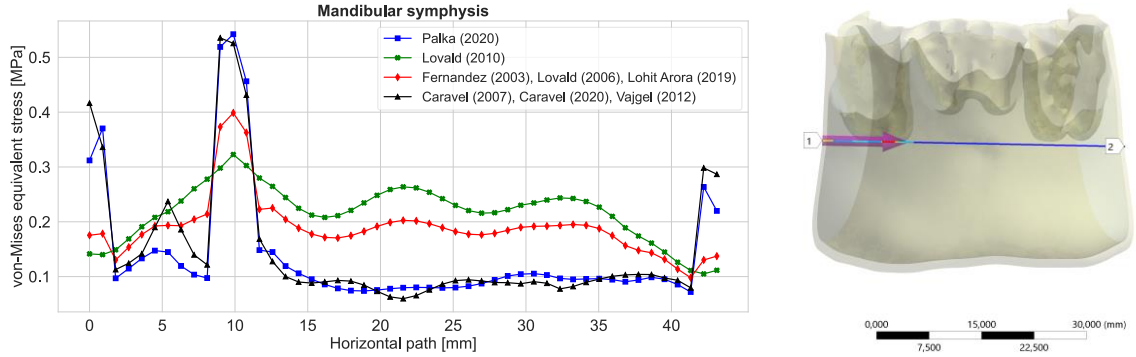


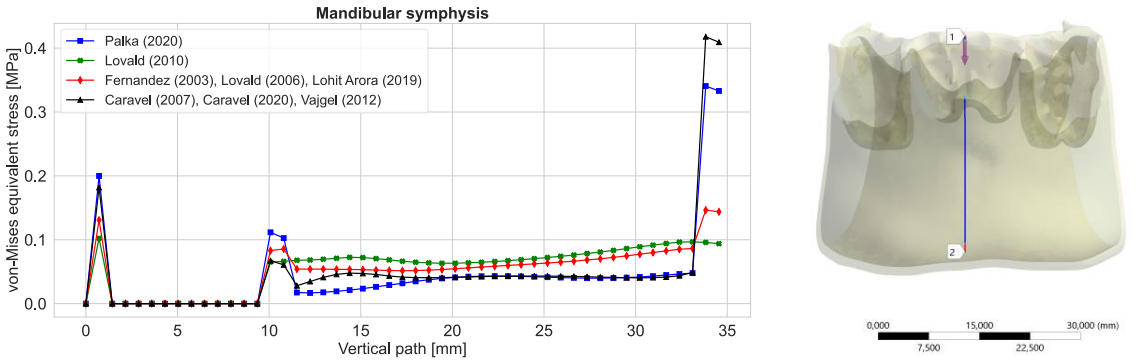
Figure 2.3 Mandible modeling scheme – Main steps.

3. NUMERICAL RESULTS

This section compares the numerical results of the proposed mandible models, focusing on orthotropic and isotropic (bimaterial and monomaterial) properties. The mesh quality was assessed using the element quality metric, which is crucial for achieving accurate and convergent numerical integration results. The mandible model utilized a mesh with 495,427 quadratic tetrahedral elements, each having ten degrees of freedom. To analyze the forces in the symphysis region, a line path was created to track the stress field horizontally and vertically, as shown in Figure 3.1. This analysis allows for comparing stress distribution in the symphysis region based on various models' mechanical properties. Figure 3.1 reveals that the Caraveo et al. (2021) and Palka (2020) models show similar stress distribution along the horizontal line. The peak stress occurs between 0 and 10mm, due to stress concentration near the alveolar process floor. From 15 to 40mm, stress distribution becomes more uniform, influenced by cortical tissue and distant from the alveolar processes. In contrast, simpler isotropic models by Fernández et al. (2003) and S. Lovald et al. (2010) show more dispersion and offset results. Vertical stress distribution in the symphysis region, illustrated in Figure 3.1(b), shows higher stress amplitudes at 0-1mm and 10-12mm in the thinner alveolar process region, which should be disregarded. Due to the 0.5MPa compressive load (see Figure 2.2), the highest stress is observed near the mandible base, between 42 and 44mm.



(a)



(b)

Figure 3.1 Line path to track the stress field: a) Horizontal path x von Mises stresses b) Vertical path x von Mises stresses.

Figure 3.1 shows the peak and average von Mises stresses for all analyzed models. The Fernandez and Lovald models exhibited maximum stress amplitudes that were 37.8% and 67.4% higher, respectively, than those in the Caraveo (2008) model. This significant difference highlights the potential underestimation of internal forces in simpler models, which is crucial when calculating safety coefficients for bone fixation plates. The Palka and Caraveo models had very similar maximum stress values, with a difference of less than 5% between them.

Table 3.1 Peak and average von Mises stresses

Models	***average***	***peak***	***% Difference average***	***% Difference peaks***
Fernandez (2003), Lovald (2006) and Arora (2020)	0,12192	1,9094	12,90%	37,8%
Lovald (2010)	0,12136	1,5027	13,30%	67,4%
Palka (2020)	0,13334	2,9342	4,74%	4,4%
Caraveo 2008 (orthotropic)	0,13997	3,0701	Reference	Reference

4. ADVANCES AND PERSPECTIVES

The complete results of this work can be found in Anflor et al. (2024), where constitutive models for bone tissues and numerical precision control were thoroughly discussed and evaluated. As a continuation of the research, several studies based on the methodology developed by Anflor (2024) are already underway. The next challenges for this research group include obtaining optimal topologies for nonlinear contact problems, considering auxetic and lattice structures. Additionally, modeling the manufacturing process, focusing on the control of input design variables and evaluating defects in the printed part, such as warping, are also areas of interest.

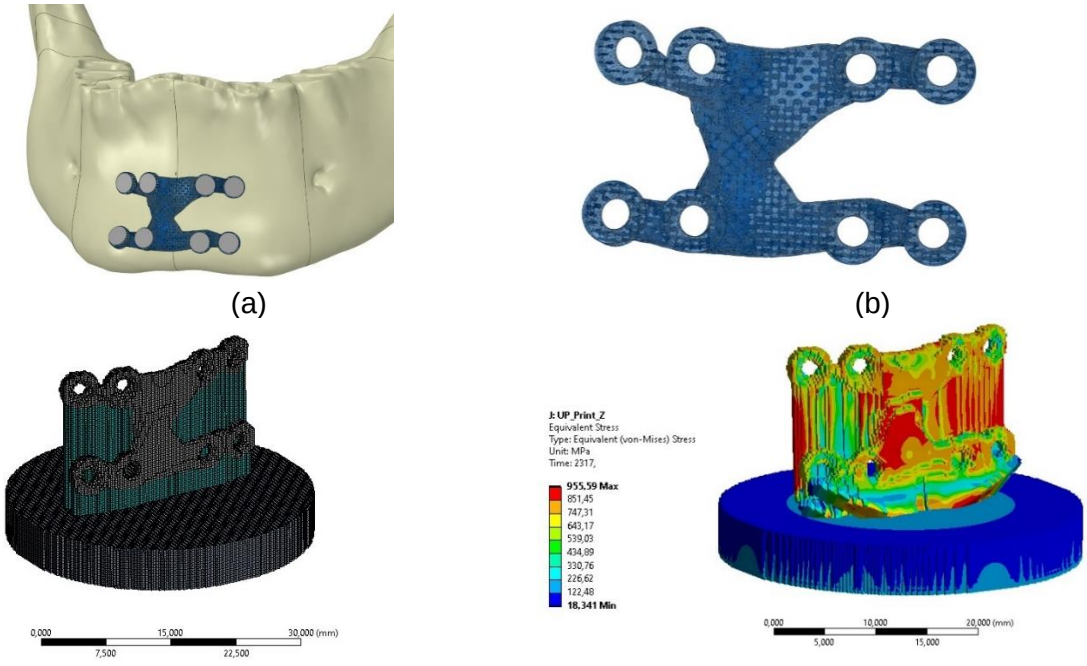


Table 4.1 Advances: (a) complete model, (b) optimized plate, (c) MA numerical model, (d) Warping.

5. FINAL CONCLUSIONS

The main objective of this study was to evaluate the mechanical properties of key mandible models from existing literature, considering mono, bi-material, and/or multi-region modeling approaches, and assessing their impact on the accuracy of stress field calculations. Notably, there is a lack of comparative studies in the literature that comprehensively address these issues. We extensively discussed the process of image processing from tomography-derived data (*.stl) to facilitate CAD (Computer-Aided Design) reconstruction for fellow researchers. Additionally, rigorous verification of mesh quality was conducted to ensure precise numerical results regarding stress fields. During our evaluation of models proposed by other authors, we observed significant dispersion, with stress field discrepancies ranging from 4.4% to 67.4% at the symphysis region. RMSE served as an estimator to assess similarity between models, revealing that the Caraveo (2008) and Palka (2020) models exhibited good convergence in predicting stress fields at the symphysis region. Although both models provided satisfactory predictions, employing Caraveo's mechanical properties resulted in more precise numerical outcomes, especially under various loads from masticatory forces, which induce internal bending and shear forces. Moving forward, our future research aims to expand upon the calibrated model presented here by exploring issues such as symphysis fractures, bone loss due to tumors, and developing corresponding solutions. This will include integrating the modelling of the additive manufacturing process, controlling warping, and heat treatment, beyond considering nonlinear contact mandible models that incorporate screws and optimized plates, as aforementioned in section 4.

REFERENCES

1. **Arora, L., Bhardwaj, S., Hashmi, G. S., Anwar, S. F., & Rahman, S. A. (2020)**, Finite Element Analysis (FEA) of Perpendicular Plating Versus Conventional Plating in Mandibular Symphysis Fracture. Journal of Maxillofacial and Oral Surgery, 19(1), 143–148. https://doi.org/10.1007/s12663-019-01244-7

2. **Caraveo, V., Lovald, S., & Khraishi, T. (2021)**, A Study of the Mechanical Characteristics of a Mandibular Parasymphyseal Fracture with Internal Fixation Device Subject to Variable Bite Forces: Finite Element Analysis. Journal of Biosciences and Medicines, 09(04), 158–178. https://doi.org/10.4236/jbm.2021.94014

3. **Caraveo, V., Lovald, S., Khraishi, T., Wagner, J., & Baack, B. (2008)**, The effects of frictionless/frictional contact boundary conditions in finite element modeling of mandibular fractures. Multidiscipline Modeling in Materials and Structures, 4(3), 227–236. https://doi.org/10.1163/157361108784890714

4. **Chen, Y. T., Chiu, Y. W., Chang, Y. C., & Lin, C. W. (2020),** Ten-year retrospective study on mandibular fractures in central Taiwan. Journal of International Medical Research, 48(7). https://doi.org/10.1177/0300060520915059

5. **Fernández, J. R., Gallas, M., Burguera, M., & Viaño, J. M. (2003)**, A three-dimensional numerical simulation of mandible fracture reduction with screwed miniplates. Journal of Biomechanics, 36(3), 329–337. https://doi.org/10.1016/S0021-9290(02)00416-5

6. **Lovald, S., Baack, B., Gaball, C., Olson, G., & Hoard, A. (2010)**, Biomechanical optimization of bone plates used in rigid fixation of mandibular symphysis fractures. Journal of Oral and Maxillofacial Surgery, 68(8), 1833–1841. https://doi.org/10.1016/j.joms.2009.09.108

7. **Lovald, S. T., Khraishi, T., Wagner, J., Baack, B., Kelly, J., & Wood, J. (2006)**, Comparison of plate-screw systems used in mandibular fracture reduction: Finite element analysis. In Journal of Biomechanical Engineering (Vol. 128, Issue 5). https://doi.org/10.1115/1.2244575

8. **Pałka, Kuryło, P., Klekiel, T., & Pruszyński, P. (2020)**, A mechanical study of novel additive manufactured modular mandible fracture fixation plates - Preliminary Study with finite element analysis.☆. Injury, 51(7), 1527–1535. https://doi.org/10.1016/j.injury.2020.03.057

9. **Vajgel, A., Camargo, I. B., Willmersdorf, R. B., De Melo, T. M., Filho, J. R. L., & De Holanda Vasconcellos, R. J. (2013)**, Comparative finite element analysis of the biomechanical stability of 2.0 fixation plates in atrophic mandibular fractures. Journal of Oral and Maxillofacial Surgery, 71(2), 335–342. https://doi.org/10.1016/j.joms.2012.09.019

10. **Van Den Bergh, B., Heymans, M. W., Duvekot, F., & Forouzanfar, T. (2012)**, Treatment and complications of mandibular fractures: A 10-year analysis. Journal of Cranio-Maxillofacial Surgery, 40(4), e108–e111. https://doi.org/10.1016/j.jcms.2011.05.015

11. **Anflor, C. T. M., Santanna, E. D. M., Nascimento, F. F. A. O., & Goulart, J. N. V. (2024)**, Isotropic and orthotropic mechanical properties of in vivo mandible model: Assessment of computational modelling. International Journal of Solids and Structures, 298, 112875. https://doi.org/10.1016/j.ijsolstr.2024.112875

METHODOLOGY FOR THE OPTIMIZED ARRANGEMENT OF MICROELECTRONIC COMPONENTS ON THE PRINTED CIRCUIT BOARD FROM A MECHANICAL PERSPECTIVE

Fahri Berk BİLBAY, *bilbayberk@gmail.com* Marelli Mako Turkey, 16220, Bursa, Turkey

Mustafa Cemal CAKIR, *cemal@uludag.edu.tr* Uludag University, 16059, Bursa, Turkey

ABSTRACT

Printed circuit boards (PCBs) may vary in terms of the electronic components (transistor, capacitor, resistor, integrated circuit, etc.) and their layout on the circuit boards depending on the use. These specific loading circumstances greatly complicate the process of defining the design idea for the PCBs. Vibrational loadings can result in damage to both the PCBs and the electronic components. When developing and verifying PCBs in the automotive lighting business, it is crucial to consider certain dynamic test circumstances.

The goal of this work is to consider road conditions when designing PCBs for automotive lighting systems and strategically place the components in suitable locations using experimental (DoE) techniques. The research constructed a finite element model of the PCB, including all its components, and compared it to physical testing. The dynamic test scenario often employed in the industry was utilized for this purpose. The positions of the components on the PCB were established as the design parameters, while the stresses and fatigue damage acquired from random vibration studies were used as the response functions in the DoE approach. Consequently, an interface has been developed that allows the PCB designer to select component positions on the board using test standards and confirmed analyses, rather than relying on human experience. This interface also enables the designer to do a pass/fail assessment of the PCB for fatigue damage and acquire the most favorable component positions.

Keywords: Printed Circuit Board; Sine Sweep Analysis; Random Vibration Analysis; Thermal-Mechanical Analysis; PCB Reliability; Thermal Map; Sherlock; Optislang; Optimization; Automotive Lighting; LEDs.

1. INTRODUCTION

Considering the anisotropic material structure of PCBs, the presence of various electronic components (such as transistors, resistors, diodes, and integrated circuits), the challenging test conditions, and the vulnerability of electronic components to vibration-induced damage, it is crucial to incorporate these factors into the concept design of the PCB.

PCBs, extensively utilized in the automotive sector, can encounter diverse dynamic loads and vibrations of varying frequencies during their operational lifespan. Electronic cards can experience vibration loads during transit, handling, manufacture, and customer usage. Hence, the assessment of the structural dependability of the circuit board in electronic packaging, which is prone to vibrations, has emerged as a crucial concern in the industry. Furthermore, the temperature produced by the operation of the light emitting diode (LED) components on the PCBs utilized in the automotive lighting sector, along with the vibration experienced in challenging settings, have a cumulative impact. Therefore, it is essential to consider both scenarios while doing virtual analysis or physical testing of the PCBs.

PCBs possess a sandwich configuration, including an insulating composite layer sandwiched between two conducting copper layers. The printed circuit board's material property cannot be classified as isotropic because of its unique structure. It's also hard to make and test the finite element (FE) model for the PCB because there are so many variables, such as the different types of components on the board, the properties of the material, the types of solder leads, and the thickness of the sandwich structure [Maia et al. 2010]. Cracks may form on the core layer or solder leads of the PCB if the design is unable to endure the stresses during testing in the design process, rendering the board inoperable.

The literature contains studies that concentrate on extraction of natural frequencies and reliability for PCBs by using finite element analysis and experimental modal analysis methodologies. [Zhang et al. 2016] performed a modal study of the PCB in a simulated environment to confirm its dynamic characteristics. They successfully determined the shape and numerical values of the first four modal modes and performed an impact test with a hammer under identical conditions and compared the frequencies of the first four modes. [Somashekar et al. 2016] employed the Finite Element Method (FEM) to determine the natural frequencies and Frequency Response Functions (FRF) of PCBs. This approach was used to analyze the dynamic characteristics of PCBs and minimize the need for several physical tests, which were then conducted to validate the obtained results. [Che et al. 2015] developed a finite element model of PCB and successfully handled the random vibration scenario within the frequency range of 20 to 2000 Hz. The model provided extensive

information on the solder lead that connects the integrated circuit and the PCB. The fissures in the physical examination were also observed at the solder connections. [García et al. 2018] employed a finite element model of a PCB to replicate the vibrational forces experienced by space rockets during takeoff. He conducted a stochastic vibration study to investigate the solder leads' fatigue life. Consequently, it was determined that the damage in the physical fatigue test occurred at the solder leads, as anticipated by the finite element analysis (FEA) result, which showed a strong connection. [Verma et al. 2020] conducted modal and random vibration analyses for the PCB. Various stochastic vibration scenarios were employed to forecast its fatigue lifespan. The random vibration analysis revealed that the solder lead portions of the components experienced the highest levels of stress. [Aoues et al. 2012] investigated several design factors and analyzed their impact on the fatigue life of solder leads. The design factors were selected as parameters, including temperature, soldering lead length and thickness, and component thickness. The investigation focused on examining the impact of design factors on PCB fatigue damage.

Some research involves conducting optimization and experimental design studies to investigate different design variables and responses related to PCBs. [Gao et al. 2021] conducted modal and fatigue analyses using the finite element method and simplified the modeling of electronic components on the PCB. The electronic components on the PCB were distributed over three distinct places and assessed for their dependability. Consequently, it was shown that the placement of the electronic components on the PCB had a significant impact on the distribution of stress and the lifespan of the PCB. [Bilbay et al. 2023] developed a finite element model for the PCB that was validated by physical testing. While the LED light was turned on, three strain gauges were positioned in the regions corresponding to the transistors, and real-time strain measurements were obtained and documented. The PCB underwent finite element analysis by including the temperature distribution with the LED light turned on while maintaining consistent boundary conditions. This facilitated the determination of strain values at the corresponding locations. [Kalyani et al. 2020] conducted a modal analysis on a PCB using both isotropic and anisotropic material properties in order to investigate the PCB's material properties. Consequently, it was said that the impact of the elasticity modules in the X and Y directions on the analysis is significantly more influential than that of the Z direction. [Xu et al. 2016] performed modal and fatigue analyses using the FEM to find the most appropriate model for the PCB They also identified certain design factors, such as the material characteristics of the anisotropic PCB, and derived the corresponding response functions.

The objective of this work is to consider the road conditions while designing PCBs for automotive lighting systems and to strategically place the components in suitable locations

using the DoE technique. Understanding the loads exerted on the PCB under vehicle road conditions poses a significant challenge. Consequently, the industry relies on the utilization of random vibration analyses to address this complexity. A finite element model of the PCB, including all its components, was constructed in the research and compared to physical testing. The dynamic test scenario often employed in the industry was utilized for this purpose. The positions of the components on the PCB were established as the design parameters, while the stresses and fatigue damage acquired from random vibration studies were used as the response functions in the DoE approach. Consequently, an interface has been developed that allows the PCB designer to select component positions on the board using test standards and confirmed analyses, rather than relying on human experience. This interface also enables the designer to conduct a pass/fail assessment of the PCB for fatigue damage and determine the most optimal component locations.

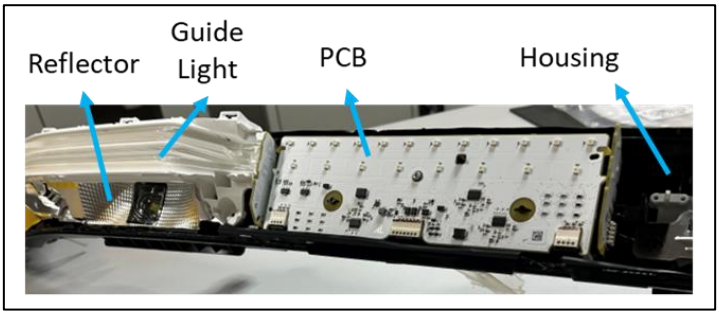


Figure 1. Internal structure of rear lamp

The research includes a depiction of the PCB utilized in the automotive rear illumination system, shown in Figure 1, together with the accompanying environmental components.

2. MATERIAL & METHODS

The study involved conducting a uniaxial tensile test on FR4 samples to determine the anisotropic characteristics of the FR4 material, which is often used in the core layer of PCBs. The objective was to accurately specify these features in the finite element model. The plates measuring 160 x 400 mm underwent Experimental Modal Analysis (EMA) to assess the accuracy of their modal shapes using the Modal Assurance Criterion (MAC). The modes and geometries of FR4 plates were determined using the finite element model under identical circumstances. The results of both EMA and FEM analyses were evaluated and the characteristics of FR4 material were confirmed. The PCB was modeled using the Sherlock program. The model incorporated the types, locations, and materials of the components on the PCB, as well as the connecting leads. When considering the running state of LEDs, it is crucial to incorporate pre-stresses into the model of PCBs in vehicle lighting. The temperature distribution was acquired by the utilization of a thermal camera and subsequently applied to the PCB model. The PCB model was subjected to finite element

analysis under the sine sweep loading condition, with the LEDs in an open state. Tests on a shaker conducted with identical boundary conditions and loading conditions to validate the finite element model of the PCB. Consequently, the obtained results were compared. Ultimately, the design factors and response functions were identified in order to construct a Design of Experiments (DoE) model for the PCB. The samples of DoE were analyzed and the impacts of each parameter were explored. Regression analysis was conducted using the experimental design data, resulting in the derivation of equations that describe the relationship between the design parameters and each response function. Figure 2 provides a concise summary of the procedure.

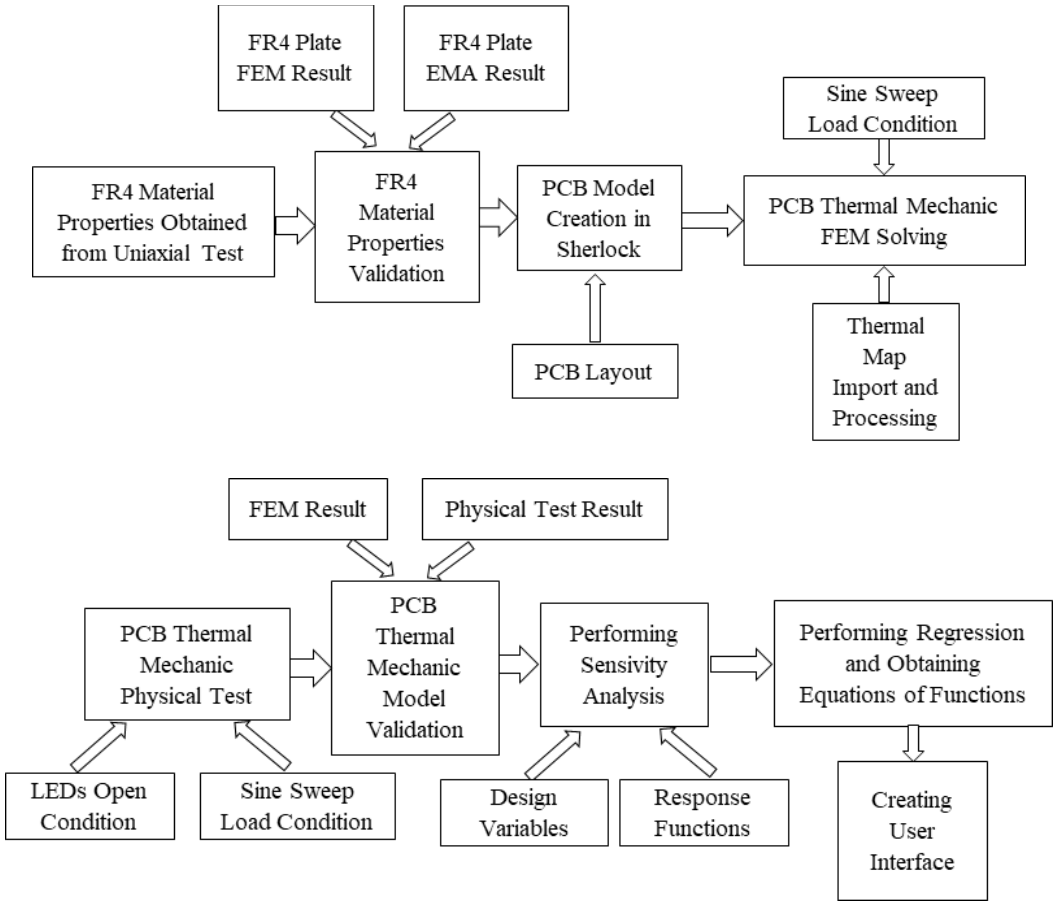


Figure 2. Workflow of the PCB model

2.1. Obtaining FR-4 Material Properties

The investigation involved preparing several samples in both the X and Y directions to determine the elastic modulus of the tensile test samples. Tensile tests were conducted in two separate directions to determine the anisotropic characteristics of the material. FR-4 samples were produced following the ISO 527-4 standard for uniaxial tensile testing. The INSTRON brand 34TM-50 model testing equipment was utilized. A test was conducted using

10 samples for both the X and Y axes at a speed of 2 mm/min. The machine software calculated the elastic modulus of each sample, and the average value was determined in the FE program.

2.2. Material Property Validation of FR-4 Plate

Experimental Modal Analysis (EMA): Vibration has a significant impact on several structures, necessitating thorough investigation and control measures to mitigate its effects. It is necessary to measure the dynamic qualities of the structures in order to conduct this research. Figure 3 illustrates that the structure is subjected to a force exerted by a hammer. The fundamental structure of the EMA process is shown in Figure 3.

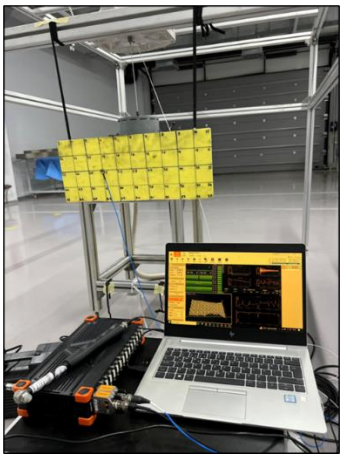


Figure 3. EMA test setup of FR-4 plate

FEM Modal Analysis: The FR-4 plate in the finite element model was specified as a rectangular plate of 160 x 400 mm with a thickness of 1.5 mm. The model utilized second-order brick elements (C3D20), and the modal analysis was solved at room temperature (23 °C) with free-boundary conditions.

2.3. Validation of Printed Circuit Board

LED lights in automotive lighting systems exert stress on the PCB due to their electrical components, including transistors, and the heat they emit. Therefore, it is crucial to thoroughly analyze and include these thermal-induced pre-stresses into the model. The FLIR SC 620 thermal camera was utilized to gauge the temperature on the surface of the PCB under the operating circumstances of LED lights. The PCB was linked to a 13.5 Volt power source, and the LED lights were lit up for a duration of 30 minutes to establish a stable temperature distribution. Subsequently, thermal measurements were conducted using a thermal camera, and the resulting data was integrated and shown on the finite element mesh structure.

Sine Sweep Test Setup of PCB: Sine sweep analysis involves the application of a sinusoidal oscillation to a system, such as a mechanical component. During a sine sweep, the components exhibit a high degree of sensitivity to resonance frequencies. Resonance has the potential to cause damage or destruction to components within a PCB or other devices, leading to malfunction. The investigation involved conducting a sine sweep test using the "Dongling ES-20-320" type shaker test machine, as seen in Figure 4 (a). The purpose was to determine the modal frequencies and the FRF curve of the PCB. The numbers correspond to the components utilized in the sine sweep test. Figure 4 (b) depicts three components: 1 symbolizes the plate that is linked to the ground, 2 represents the fixture that connects the PCB to the plate, and 3 represents the PCB itself. The boundary condition was also depicted in Figure 4 (b). The test was conducted under ambient temperature conditions with the LED lights activated.

The sine sweep test is characterized by the following parameters:

• The system's driving amplitude value was set at 1g.

• The initial frequency of the test was set at 5 Hz, while the final frequency was set at 500 Hz.

• The sweep rate was precisely defined as 1 Hz per second and followed a linear pattern. The test duration was precisely 8 minutes and 15 seconds.

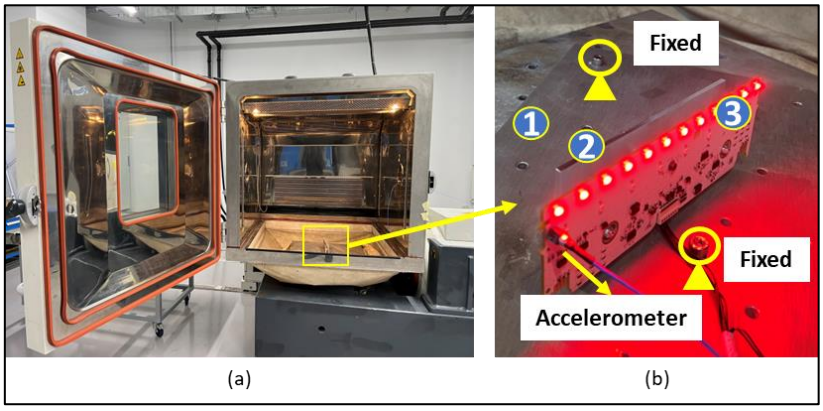


Figure 4. (a) Shaker test machine (b) Sine sweep test setup

FEA Model Creation of PCB: The complexity of modeling using conventional FE software is exacerbated by the numerous components on the PCB and their diverse positions. The Sherlock module streamlines labor and saves time with its library, which includes a diverse selection of components and materials for electronic board design [Bilbay et al. 2023]. To establish the sine sweep test in a virtual setting, a finite element model was utilized to design the fixture and test plate of the PCB, as seen in Figure 5. The numbers correspond to the components utilized in the sine sweep analysis. Figure 5 illustrates the components of the system: 1 represents the plate, which is connected to the ground. 2 represents the fixture

that connects the PCB to the plate. 3 represents the PCB itself. The temperature distribution acquired by the thermal camera was projected onto the finite element analysis mesh. The model used the temperature distribution on the PCB as the load condition. In this way, the effects of the temperature difference were included in the model.

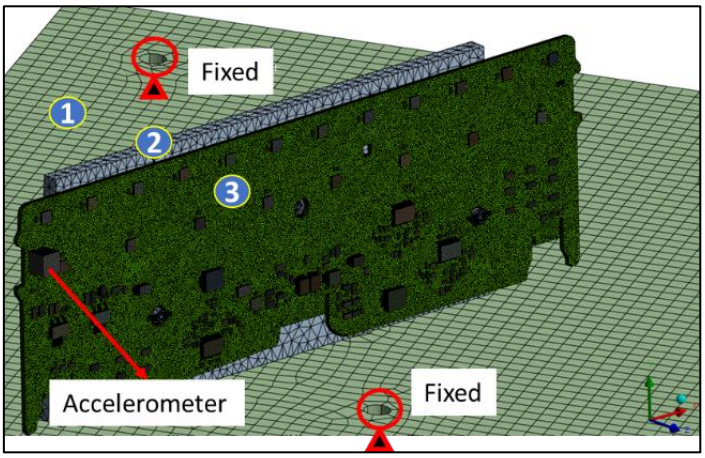


Figure 5. FEA model of PCB

FEA was conducted as same boundary conditions as the sine sweep test. For the purpose of conducting sine sweep analysis, a total of 495 solution intervals were obtained within the frequency range of 5 Hz to 500 Hz. The system experienced an acceleration of 1g in the positive Z direction, and a damping ratio of 0.003 was determined using the EMA test. A linear sine sweep was utilized to generate a response from the accelerometer in Figure 5, specifically measuring the amplitude and resonance frequencies in the Z direction.

DoE Model Creation of PCB: The Advanced Latin Hypercube Sampling Method is considered one of the most effective small sampling methods. Latin Hypercube sampling constructs a strongly correlated joint probability density function for the random variables in the problem, enabling precise estimation of the response parameters with a limited number of samples [Bilbay et al. 2023]. This study utilized DoE to investigate the variations in PCB components based on their location. The design variable for determining the placement of each PCB component was established. Based on the findings of literature research [Maia et al. 2010, Che et al. 2015, Garcia et al. 2018, Verma et al. 2020], it has been shown that the leads that link electronic components to the copper layer are the most crucial component when subjected to a load. Therefore, the highest stress at the leads derived from random vibration analysis, namely at the 3σ level, was selected as the response function. Figure 6 illustrates the definition of six distinct zones, each representing a different combination of factors for the positions of three types of components: transistors, diodes, and integrated circuits. Figure 6 provides the geographical range for each region. DoE was conducted for each component in these locations, resulting in the acquisition of response surfaces.

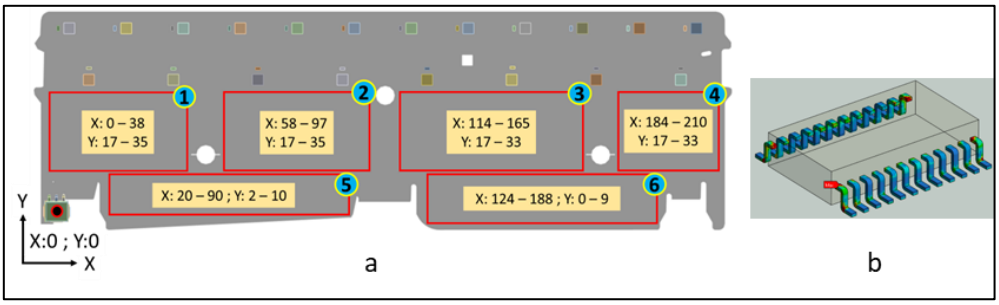


Figure 6. (a) Design space of PCB (b) An illustration of a crucial lead as response

The study employed the three-band technique, utilizing Miner's Cumulative Damage Ratio, to quantify the fatigue damage accumulated on the critical leads identified as the response function in the DoE. The PSD profile was calculated over duration of 28800 seconds (8 hours). The sampling method employed in the DoE was Latin Hyper Cube. A total of 100 samples were generated and solved for each DoE. The DoE methodology involved solving case problems using Ansys Mechanical and collecting the results using Ansys Optislang. A polynomial metamodel was utilized to perform regression, and the obtained data were analyzed using statistical tools. The study yielded equations of response functions that are dependent on design factors for each component type and location using regression analysis. The provided equations determine the 3σ stresses on leads based on the X and Y coordinates of the components. The fatigue damage at the leads was determined by utilizing the 3σ stresses. The data was collected using Excel, software and an interface was developed to enable users to rapidly evaluate the safety of leads based on their preferred locations. When damage develops on a component's leads, the "Solver" tool with an "Evolutionary Algorithm" can be used in Excel to optimize the design parameters and minimize fatigue damage.

3. RESULTS & DISCUSSION

3.1. Verification of FR-4 Material Property

The natural frequency modes and modal shapes acquired from the experimental modal analysis (EMA) test of the FR-4 plate, which served as the core material in the PCB, were compared with the findings obtained from finite element analysis (FEA). This comparison helped to validate the material characteristics of the FR-4 plate. The results derived from the physical test (EMA) and the virtual analysis (FEA) are shown in Table 1. An analysis revealed a maximum discrepancy of 5% between the EMA and the FEA.

Table 1. Comparison of the EMA and the FEA for the natural frequencies of the FR-4 Plate

	Mode 1	Mode 2	Mode 3	Mode 4
EMA	33,5 Hz	98,4 Hz	192 Hz	223 Hz

FEA	33,3 Hz	93,4 Hz	189,7 Hz	225,8 Hz
Error	0,5%	5%	1%	1%

The similarity between the modal shapes derived from the EMA test and the FEA was assessed using the modal assurance criteria (MAC), which were judged to be 99%, 96%, 89%, and 86%, respectively. The EMA and FEA modal shapes exhibited a similarity of over 85%.

3.2. Verification of Printed Circuit Board

The transmissibility-frequency curve was acquired as outputs from both the sine sweep test and the sine sweep FEA. Transmissibility is the quantitative relationship between the amplitude of the output and the amplitude of the input in a system. Figure 7 provided the names of the PCB resonances as a, b, and c. From the figure, it was observed that the additional peaks with low transmissibility values originated from the test plate and the fixture. Consequently, these resonances were eliminated. The Figure 8 displays the shapes of the three natural frequency modes generated from the PCB sine sweep FEA.

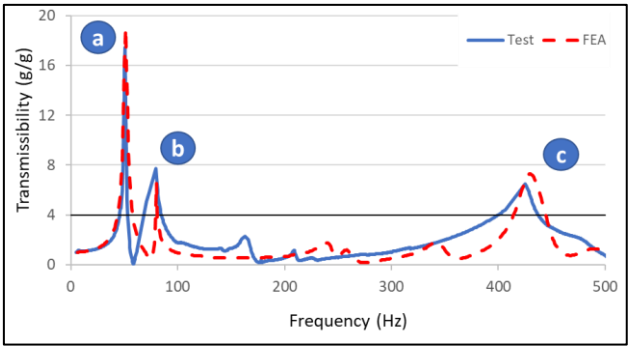


Figure 7. Sine sweep test and FEA curve

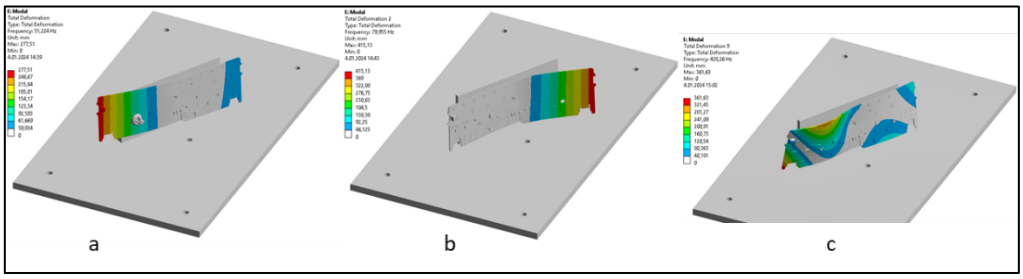


Figure 8. PCB natural frequency modes (a) First mode (b) Second mode (c) Third mode

Upon examination of the sine sweep results, it was determined that there was a maximum difference of 3.8% in frequency between the FEA, and the actual test. A smaller degree of deviation was observed in comparison to previous research [Zhang et al. 2016, Somashekar et al. 2016], resulting in the successful acquisition of a validated PCB model using the Finite Element Method.

3.3. Result of DoE and Creating User Interface

According to the DoE, changing the location of components on the PCB has no effect on the overall PCB's natural frequency. Figure 9 illustrates that there is a correlation between the responses and the design parameters, but only for components of the same type. These red boxes indicate the Coefficient of Prognosis (CoP), which indicates the accuracy of the regression model. The analysis determined that the regression accuracy for the transistor in the second region was 90.7%, while for the rest of the transistors, it exceeded 95%.

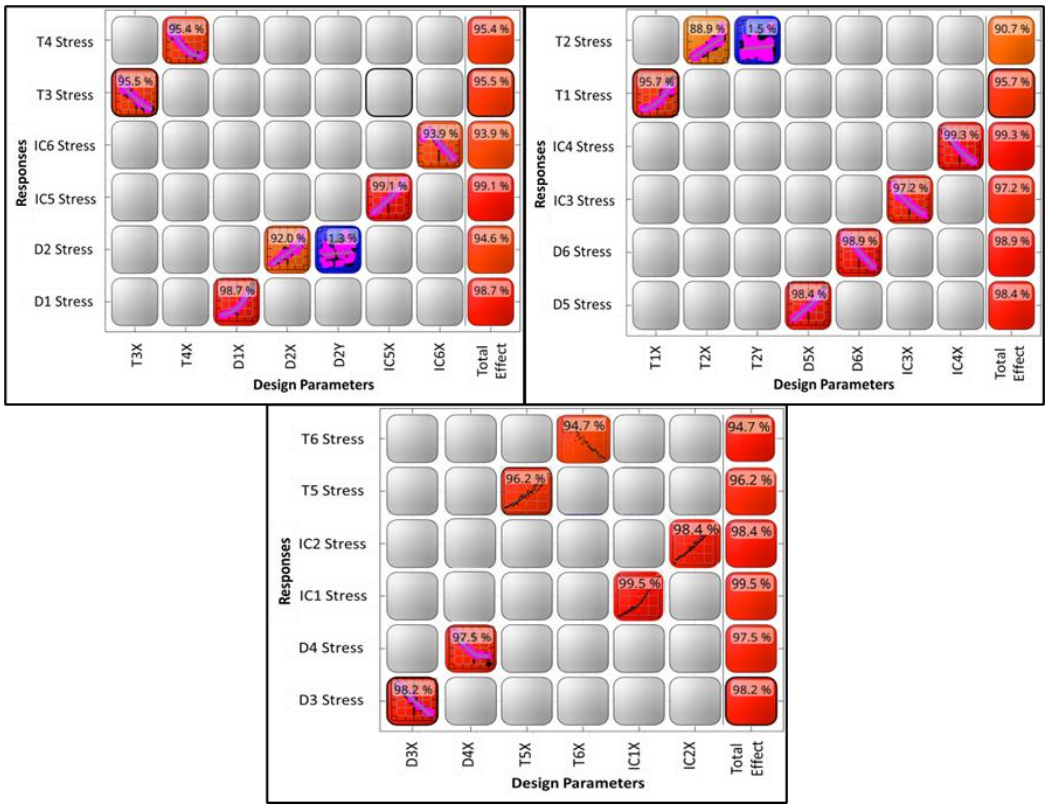
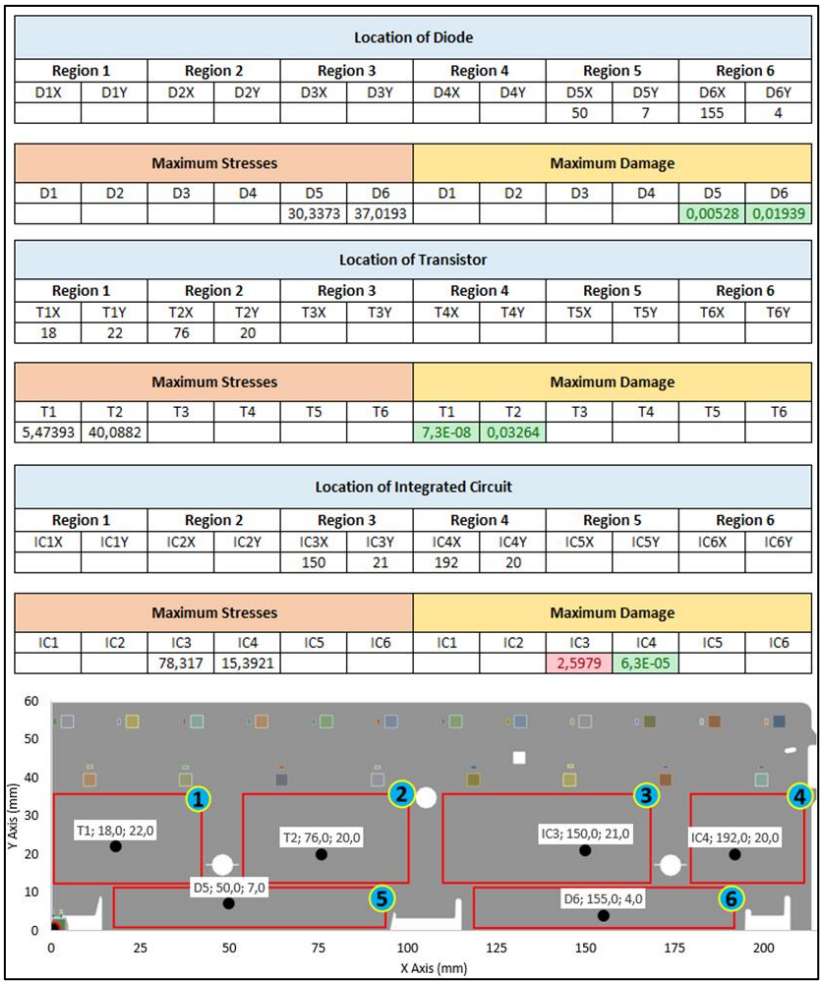


Figure 9. Interactions between responses and design parameters

Figure 9 displays the component types using abbreviations: D for diode, IC for integrated circuit, and T for transistor. The second number in the abbreviations corresponds to the specific location indicated in Figure 6. The design parameters consist of three parts: the first part represents the type of component, the second represents the region of its position, and the third part represents the axes of the locations. The PCB design was created by arbitrarily selecting locations from Figure 10 as an illustrative example. Based on this design example, the integrated circuit in the third region fails to meet the fatigue scenario, resulting in the failure of the PCB. The user has the ability to manually adjust the position of the defective integrated circuit within specified limits until it reaches a safe state.



Location of Diode											
Region 1		Region 2		Region 3		Region 4		Region 5		Region 6	
D1X	D1Y	D2X	D2Y	D3X	D3Y	D4X	D4Y	D5X	D5Y	D6X	D6Y
								50	7	155	4

Maximum Stresses						Maximum Damage					
D1	D2	D3	D4	D5	D6	D1	D2	D3	D4	D5	D6
				30,3373	37,0193					0,00528	0,01939

Location of Transistor											
Region 1		Region 2		Region 3		Region 4		Region 5		Region 6	
T1X	T1Y	T2X	T2Y	T3X	T3Y	T4X	T4Y	T5X	T5Y	T6X	T6Y
18	22	76	20								

Maximum Stresses						Maximum Damage					
T1	T2	T3	T4	T5	T6	T1	T2	T3	T4	T5	T6
5,47393	40,0882					7,3E-08	0,03264				

Location of Integrated Circuit											
Region 1		Region 2		Region 3		Region 4		Region 5		Region 6	
IC1X	IC1Y	IC2X	IC2Y	IC3X	IC3Y	IC4X	IC4Y	IC5X	IC5Y	IC6X	IC6Y
				150	21	192	20				

Maximum Stresses						Maximum Damage					
IC1	IC2	IC3	IC4	IC5	IC6	IC1	IC2	IC3	IC4	IC5	IC6
		78,317	15,3921					2,5979	6,3E-05		

Figure 10. Example of PCB design in the interface

An alternative approach involves utilizing Excel's "Solver" optimization approach, where the maximum damage is set as the objective and the locations on the X and Y axes are designated as design parameters. By establishing limits on the location of each component, one may identify the optimal placements for all components in various locations.

In this example, the objective of minimizing damage was achieved by selecting the maximum damage of IC3. Additionally, the design parameters for D5, D6, T1, T2, IC3, and IC4 were set by specifying their X and Y coordinates. An evolutionary algorithm was employed for the purpose of optimization. Constraints were established for all design parameters, specifying limit range values. Additionally, constraints were set between 0 and 1 for all maximum damages to assure the PCB's safety. The optimization process yielded the optimal design parameters based on the specified aim, which are presented in Figure 11. The interface improved the component placement of the PCB design in the given example, resulting in a reduction of maximum damage from 2.59 to 0.43, thereby making the PCB safe. Moreover, the user has successfully accomplished one of the most exceptional PCB designs by utilizing data that has been validated by testing and finite element analysis.

The optimal model was determined by real-time finite element analysis, and the maximum stresses of each lead were compared in Table 2. A maximum discrepancy of 7% between the projected outcome and the actual result was identified.

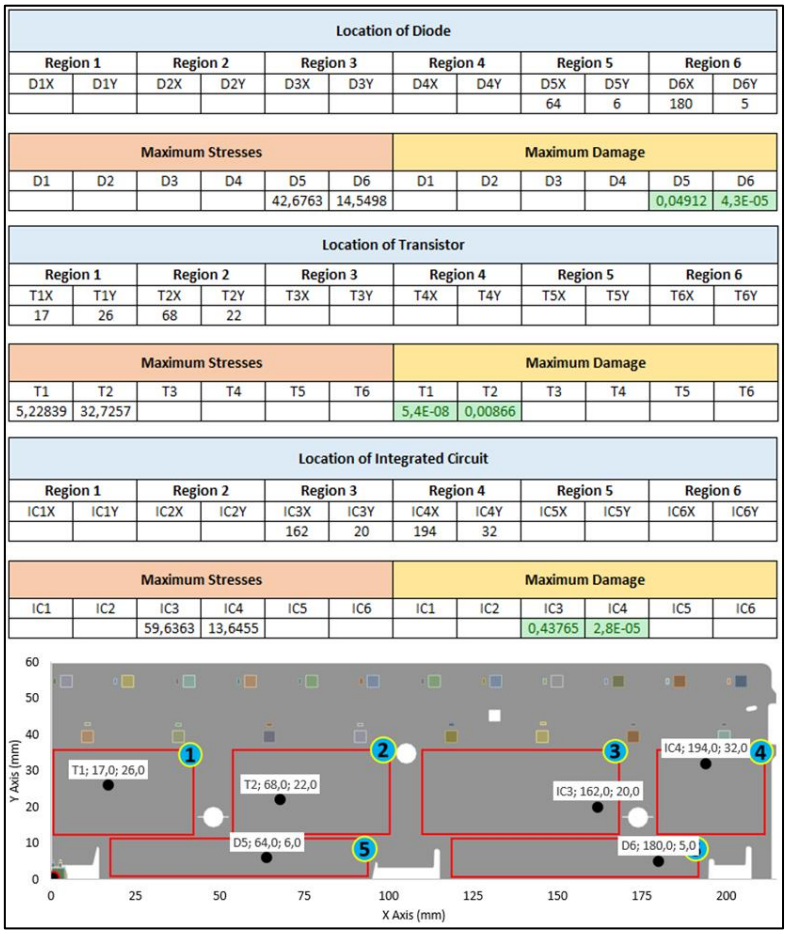


Figure 11. Optimum example of PCB design in the interface

Table 2. Comparison of Maximum Stresses Between Predicted Design and Real-Run

	D5	D6	T1	T2	IC3	IC4
Predicted Max Stress (MPa)	42,6763	14,5498	5,22839	32,7257	59,6363	13,6455
Real-Run Max Stress (MPa)	39,87	14,65	4,98	31,36	56,91	12,93
Deviation %	7%	1%	5%	4%	5%	6%

4. CONCLUSION

A finite element model of the PCB, including all its components, was constructed in the research and compared to physical testing. The dynamic test scenario often employed in the industry was adopted for this purpose. The locations of the components on the PCB were established as the design parameters, while the stresses and fatigue damage acquired from random vibration studies were used as the response functions in the DoE approach. Consequently, an interface has been developed that allows the PCB designer to select

component locations on the board using test standards and confirmed analyses, rather than relying on human experience. This interface also enables the designer to conduct a pass/fail assessment of the PCB for fatigue damage and determine the most optimal component locations. The results have been summarized below:

• The frequency divergence between the EMA and FEA findings of the FR-4 plate was found to be a maximum of 5%. Additionally, there was a minimum of 85% similarity in the mode shapes.

• On a frequency basis, the sine sweep findings revealed a maximum variation of 3.8% between the FEA and the physical test.

• The sensitivity analysis revealed that the accuracy of the regression was 90.7% for the transistor in the second area and over 95% for the other answers.

• A highly accurate user interface was developed by utilizing DoE and regression analysis. This allowed for the optimal placement of components on the PCB, which was confirmed by physical testing and FEA.

• The optimal design model generated by the optimization process was compared to the results of a real-run finite element analysis. The comparison revealed a maximum error rate of 7%.

REFERENCES

1. **Maia Filho, W. C., Brizoux, M., & Grivon, A., (2010),** Optimization of PCB build-up layer configuration for electronic assemblies with active embedded components in the board. In 2010 11th International Thermal, Mechanical & Multi-Physics Simulation, and Experiments in Microelectronics and Microsystems (EuroSimE) (pp. 1-5). IEEE.

2. **Zhang, W., Li, Y., & Qian, R. (2016).** Optimization Design of Printed Circuit Board Structure Based on Modal Analysis. In 2016 4th International Conference on Electrical & Electronics Engineering and Computer Science (ICEEECS 2016) (pp. 1118-1123).

3. **Somashekar, V. N., Harikrishnan, S., Ahmed, P. A., & Kamesh, D. (2016).** Vibration response prediction of the printed circuit boards using experimentally validated finite element model. Procedia Engineering, 144, 576-583.

4. **Che, F. X., & Pang, J. H. (2015).** Study on reliability of PQFP assembly with lead free solder joints under random vibration test. Microelectronics Reliability, 55(12), 2769-2776.

5. **Garcia, A., Sorribes-Palmer, F., & Alonso, G. (2018).** Application of Steinberg vibration fatigue model for structural verification of space instruments. In AIP Conference Proceedings (Vol. 1922, No. 1, p. 100003).

6. **Verma, S. K. V. K., Saravanan, S., & Sathiyaseelan, V. P. A. K. (2020).** Dynamic Response Characteristics and Fatigue Life Prediction of Printed Circuit Boards for Random Vibration Environments (Vol. 20, p. 920–929)

7. **Aoues, Y., Makhloufi, A., Pougnet, P., & El Hami, A. (2012).** Probabilistic assessment of thermal fatigue of solder joints in mechatronic packaging. Proceedings of the 1st International Symposium on Uncertainty Quantification and Stochastic Modeling, Maresias, Brazil.

8. **Gao, Y., Wang, F., Ding, S., Yang, B., Liu, L., & Salmani, M. (2021).** Device architecture optimization of solder ball joints fatigue lifetime under random vibration frequencies. Soldering & Surface Mount Technology, 33(1), 1-7.

9. **Bilbay F.B., Arslan E., Ediz B., Çakır M.C. (2023).** Investigation of the effect and optimization of material properties on the printed circuit board. Composites and Advanced Materials. 2023;32.

10. **Kalyani, U. H., & Wylie, M. (2020).** Modal finite element analysis of PCBs and the role of material anisotropy. Vibroengineering Procedia, 32, 75-80.

11. **Xu, F., Li, C. R., Jiang, T. M., & Zhang, D. P. (2016).** Fatigue life prediction for PBGA under random vibration using updated finite element models. Experimental Techniques, 40(5), 1421-1435.

12. **Schwarz, B. J., Richardson, M. H. (1999).** Experimental modal analysis. Vibrant Technology Inc., Jamestown, California, (pp. 12).

13. **Samavatian, V., Masoumian, A., Mafi, M., Lakzaei, M., & Ghaderi, D. (2018).** Influence of directional random vibration on the fatigue life of solder joints in a power module. IEEE Transactions on Components, Packaging and Manufacturing Technology, 9(2), 262-268.

THE INFLUENCE OF METAL FORMING ON CRASHWORTHINESS

Murat BÜYÜK, *murat.buyuk@atilim.edu.tr* Atilim University, 06830, Ankara, Turkey

V. Emre SAVAŞ, *veli.savas@metu.edu.tr* Middle East Technical University, 06800, Ankara, Turkey

ABSTRACT

In this study, the effects of metal forming on the Numisheet'96 [1] S-Rail model are considered to evaluate the overall crashworthiness behavior. S-Rail manufacturing simulations are performed through a metal stamping operation followed by a spring-back stage. These stages are compared and validated with the experimental results. Then, a mapping algorithm is developed to transfer the residual effects of metal forming including deformed geometry, thicknesses, strains and stresses from metal stamping model to the crashworthiness model, which can significantly be different in terms of mesh sizes. A sensitivity study for different mesh sizes is conducted to observe the mesh dependency while mapping residual data from metal forming simulation into the crashworthiness model and overall effects during the crushing. Both metal forming and crushing simulations are conducted by using a 3-D non-linear, explicit dynamics numerical solver, LS-DYNA [2]. It is found that the residual effects of metal forming have more significant effects on the energy absorption capability of parts under crash loads than the effects of mesh size dependency.

Keywords: Metal Forming, Crashworthiness, Residual Stress and Strain

1. INTRODUCTION

The process of metal forming on a crash part leaves material history with residual stresses and strains during the forming process. However, during the crashworthiness analysis, it is often a common practice not to include the deformed geometry, thicknesses of the manufactured part and ignore the material history such that the residual stresses and strains from the metal forming processes are not transmitted to the impact stage of the analysis.

It is shown that during the development of a recent vehicle model, incorporating the effects of deep drawing simulations with high strength steel results led to a much different structural behavior than regular models when pristine material properties are used for crash stage [3].

In this study, the metal forming process of Numisheet'96 S-Rail problem is simulated to be able to include the effects of deformed geometry, thicknesses, residual stresses and strains in the crashworthiness calculations. During the crashworthiness simulation, the amount of energy absorbed by the part with and without metal forming effects are addressed as the criteria for comparison. The thicknesses, residual stresses and strains from the sheet metal forming simulation model, which has a much finer mesh density, is mapped to the crash simulation model with different mesh densities by using an averaging algorithm over numerical integration points. Additionally, the effects of using different mesh sizes within the models are also considered as a secondary factor for comparison since the element sizes used for metal forming and crashworthiness can significantly be different. The most dominant factor is obtained at the end by comparing the internal energies of the deformed part that is subjected to crushing.

2. METHODOLOGY

In this study, the effects of metal forming on a representative part that absorbs most of the crash energy on vehicles during a frontal impact is investigated. A S-Shaped geometry is studied extensively in literature for its manufacturability and the first part of the methodology depends on the validation of this part during deep drawing and spring-back stages. The second part of the study depend on the fact that the numerical models for manufacturing and crash simulations can dramatically be different in terms of the element density and may not be used directly before a mapping operation. Therefore, S-Shaped geometries are modelled with different element sizes to reflect the influence of mesh sensitivity on the results. The last stage of the study is a comparison between the models, where the structure is subjected to crushing and the internal energies are calculated during the deformation. The outline of the methodology is illustrated in Figure 1.

3. METAL FORMING SIMULATIONS

The metal forming simulations for the Numisheet'96 S-Rail problem are performed in two stages. In the first stage a metal drawing operation is performed and in the second stage the model is subjected to a free-free spring-back operation.

Deep Drawing and Sequential Spring-Back Operations

The 3D CAD and finite element mesh of the punch, die, blank and the binders can be seen in Figure 2 for the forming operation. The punch movement is controlled at a constant velocity of 1000 mm/s as illustrated in Figure 3. Three different choices are given in the Numisheet'96 problem for blank holder force.

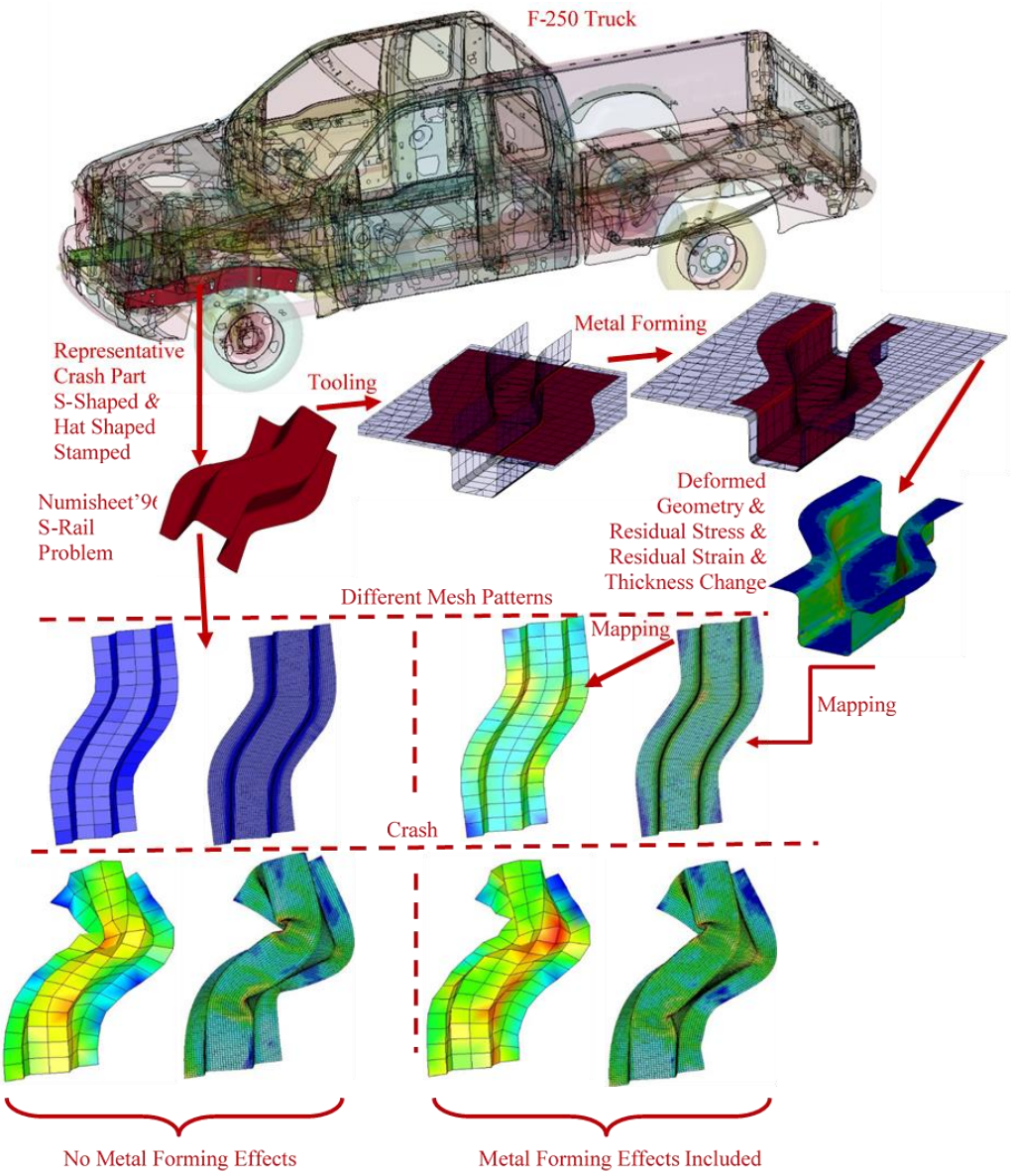


Figure 1. Methodology.

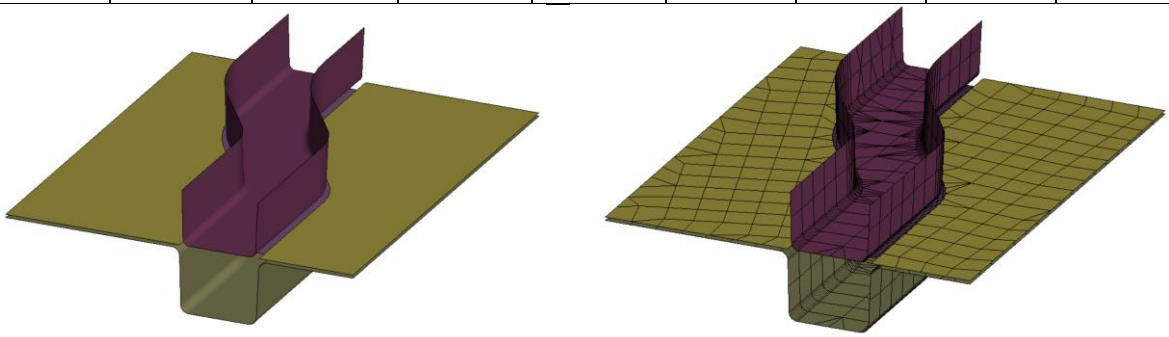
In this study, A 10 kN force is applied through the blank holder as shown in Figure 4. In both cases, a CONTACT_ONE_WAY_SURFACE_TO_SURFACE algorithm is utilized between the punch, binder and blank with a contact friction coefficient of 0.125. Three different material choices are given in the Numisheet'96 problem for the blank. A draw quality mild steel (IF) is selected with the anisotropic material properties that are listed in Table 1 and modeled by

utilizing MAT_036_MAT_3-PARAMETER_BARLAT material model. The flow curves of the material handled by the relation in Equation 1.

$$\sigma = K\varepsilon^n \dot{\varepsilon}^m \quad (1)$$

Table 1. Numisheet'96 S-Rail Material Properties.

Density [ton/mm^3]	Young's Modulus [MPa]	Poisson's Ratio	K [MPa]	n	r_0	r_{45}	r_{90}	m
7.83x10^{-9}	206000	0.3	648	0.223	1.87	1.27	2.17	0.015



(a) (b)

Figure 2. Numisheet'96 S-Rail Model: (a) 3D CAD Geometries of Punch, Die, Binders and Blank, (b) Finite Element Model of the Corresponding Parts.

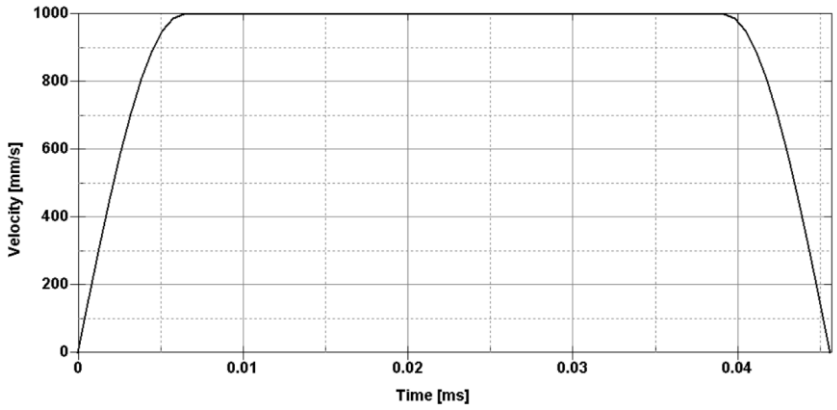


Figure 3. Velocity Profile of the Punch.

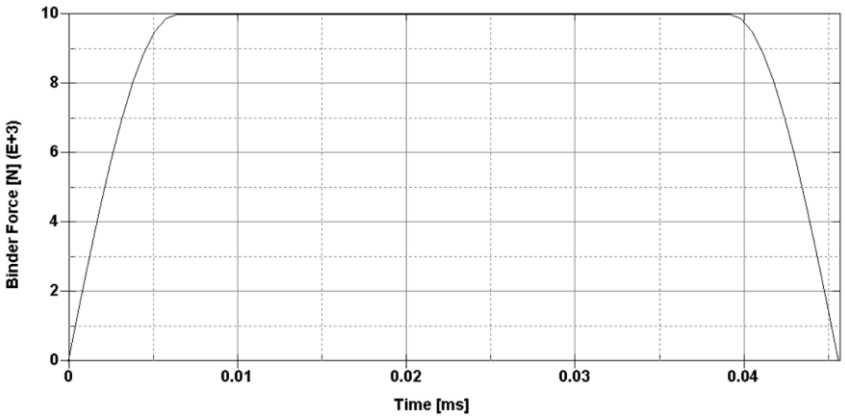
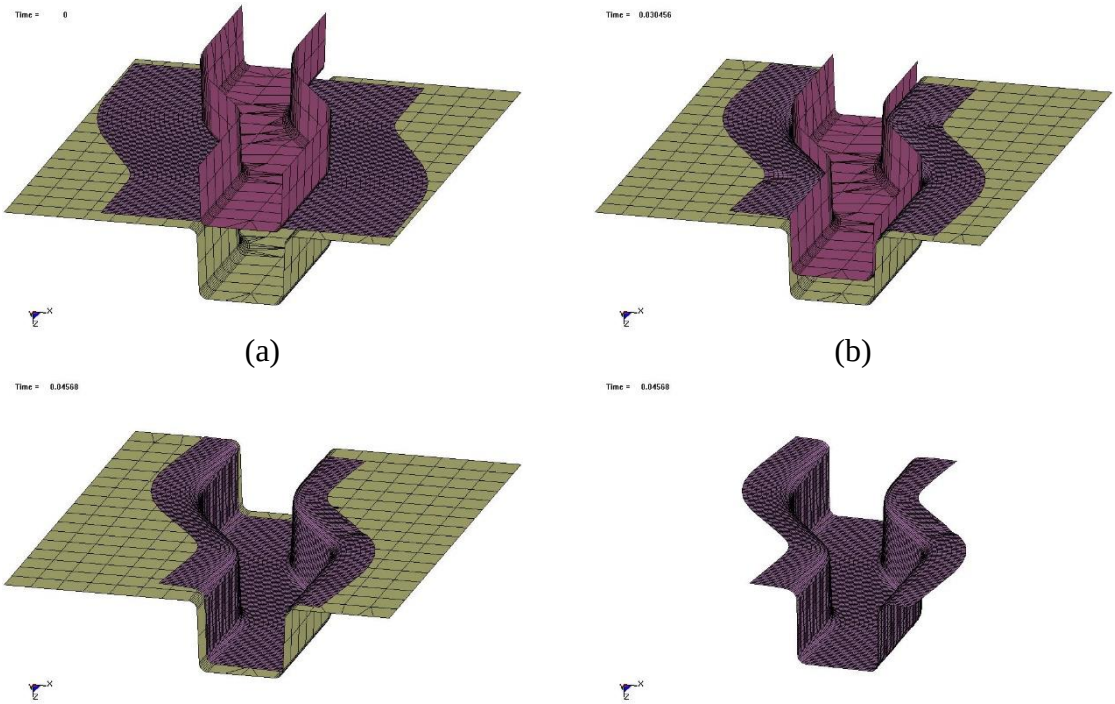


Figure 4. Blank Holder Force Profile.

The metal forming operation stages are illustrated in Figure 5 including the point where free-free spring-back stage begins sequentially after deep drawing.

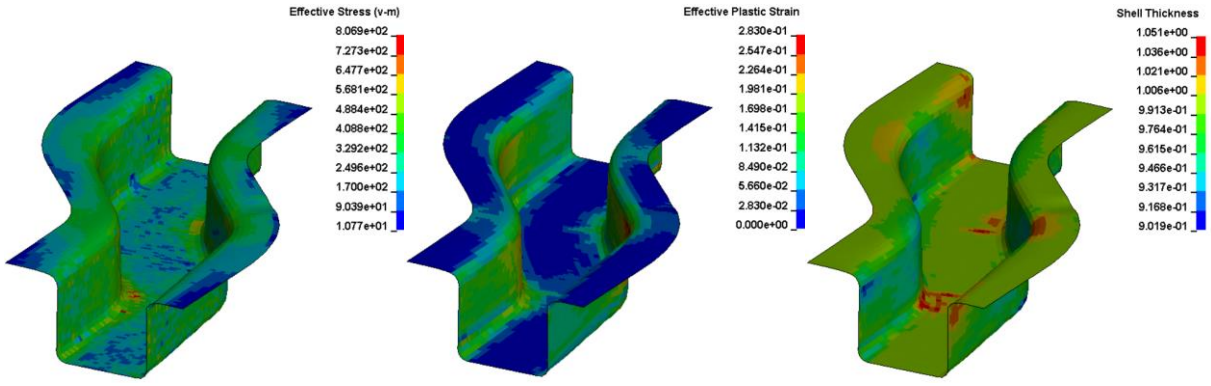


(a) (b)

(c) (d)

Figure 5. Metal Forming Simulation Stages of Numisheet'96 S-Rail; (a) Initial Positioning, (b) Blank Holder and Punch is in Progress, (c) Deep Drawing Stage and (d) Final Sequential Operation with Free-Free Spring-Back Stage.

The residual effects from the metal forming operations are illustrated in Figure 6 for the deformed geometry. The blank geometry is structurally meshed with a very dense and fine pattern to be able to obtain a detailed calculation for metal forming. The two edges of the blank are meshed with 64x128 elements, respectively.



(a) (b) (c)

Figure 6. Residual Effects of Metal Forming Simulation; (a) Equivalent Stress, (b) Plastic Strain and (c) Thickness Distribution.

The formability of the part is verified through a FLD as illustrated in Figure 7 and it is seen that the part can be manufactured within the given parameters. It is utmost important to verify the manufacturability of the part before and crashworthiness stage since the part should be validated first.

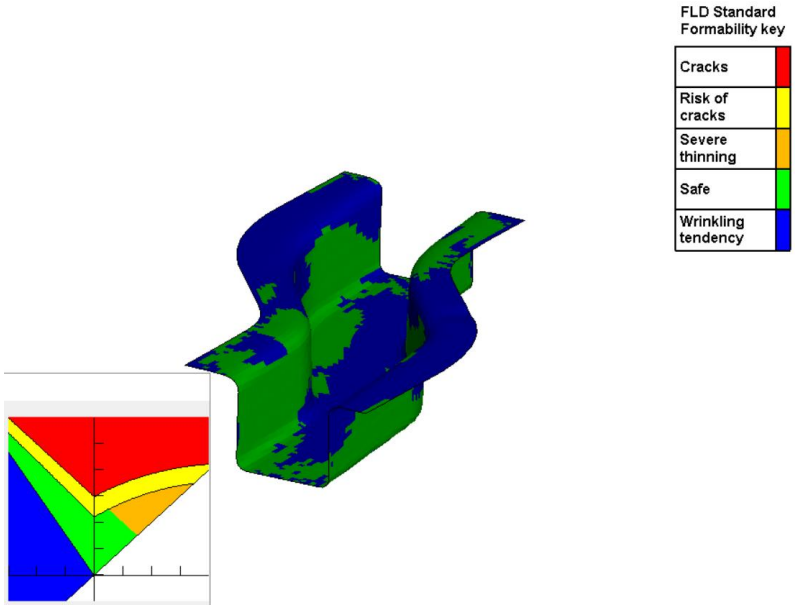


Figure 7. Manufacturability of the Part by Using a FLD.

4. MAPPING

The final geometry of the S-Rail is meshed with different mesh sizes for crash simulations because crash simulations are usually computationally more expensive and it may not always be possible to use the mesh density that is preferred during the metal forming stage. Consequently, it is expected that the models with different mesh sizes give different results for a given crash problem. In addition, the effects of metal forming should also be incorporated considering the changes in mesh size. A direct interpolation function and method is utilized to map the results found after metal forming through the integration points of the hat shaped part with different mesh densities as illustrated in Figure 8. The mesh pattern and corresponding minimum mesh sizes are listed in Table 2.

Table 2. Mesh Sizes for the Corresponding Models.

	Number of Mesh Along the Edges

	64x128	32x64	16x32	8x16
Minimum Mesh Size [mm]	2.04	4.08	8.15	16.3

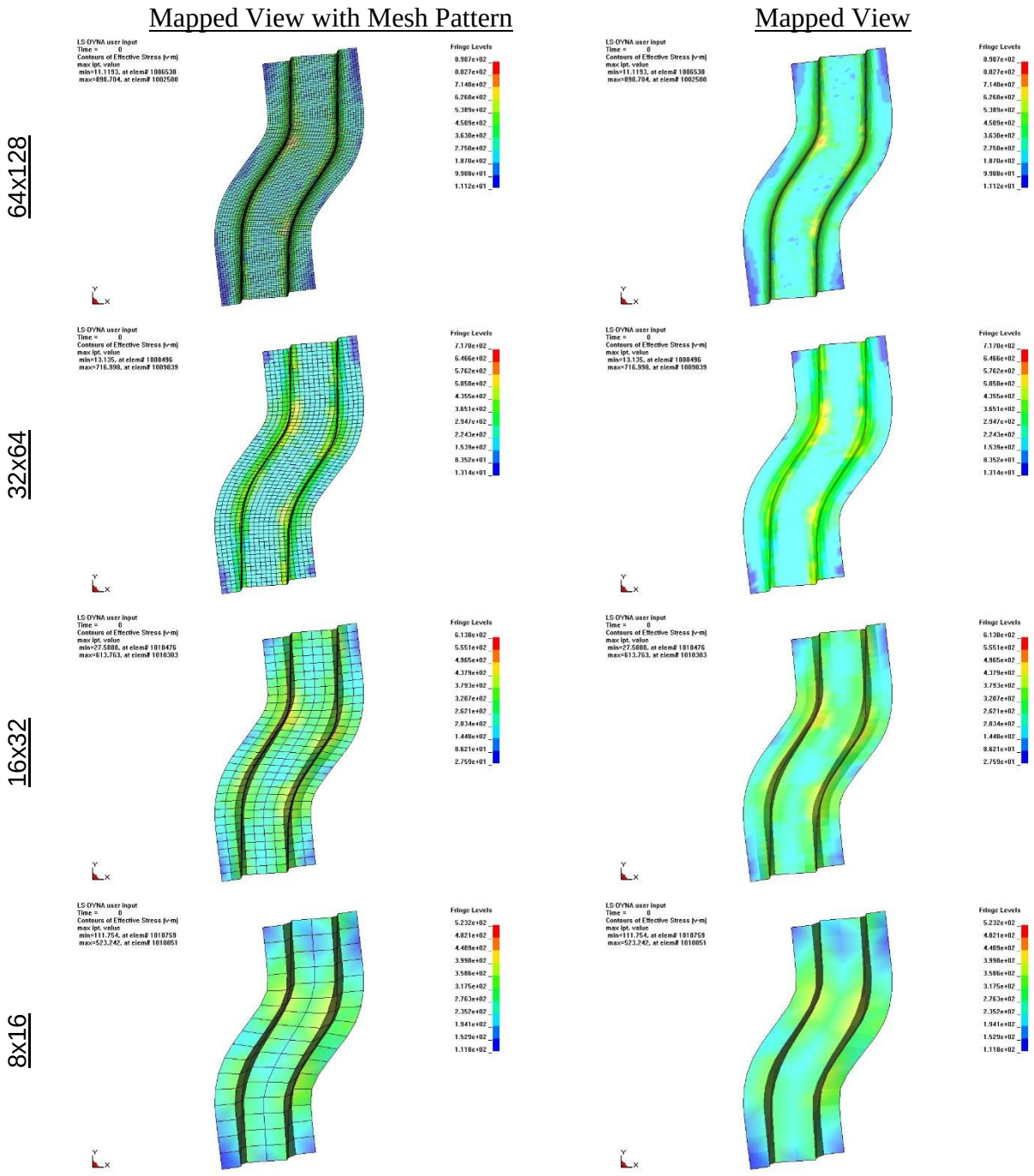


Figure 8. Mapping Residual Effects of Metal Forming Simulation for the Corresponding Crash Models with Different Mesh Distribution.

5. CRUSHING SIMULATIONS

To test the crashworthiness of the part, the S-Rail subjected to an axial loading in the direction of a possible crash scenario, where a progressive buckling response is desired. The simulations are performed for both unmapped and mapped models with different mesh sizes to qualitatively compare the effects as illustrated in Figure 9 for without metal forming effects and in Figure 10 with metal forming effects, successively.

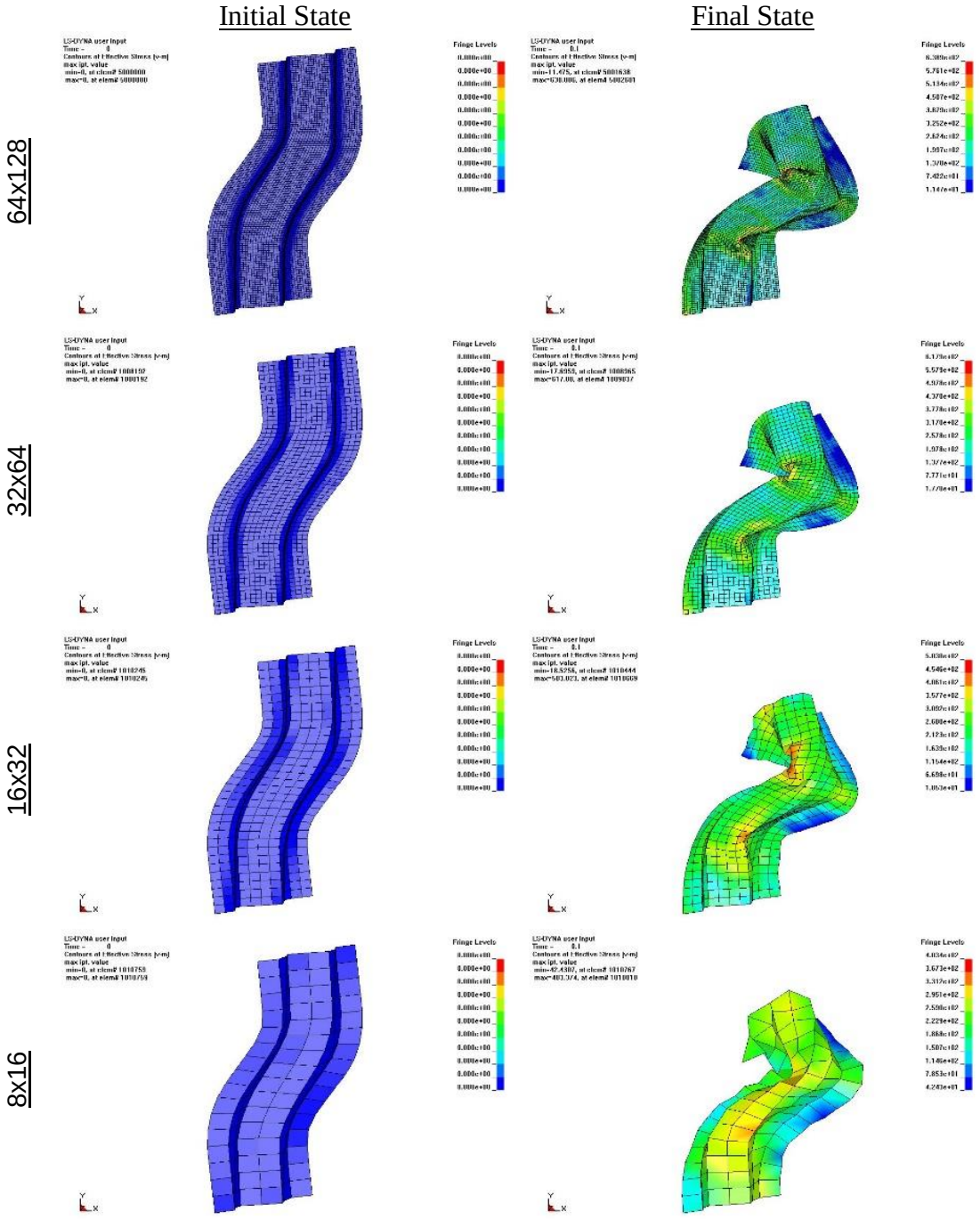


Figure 9. Crush Results without Metal Forming Effects.

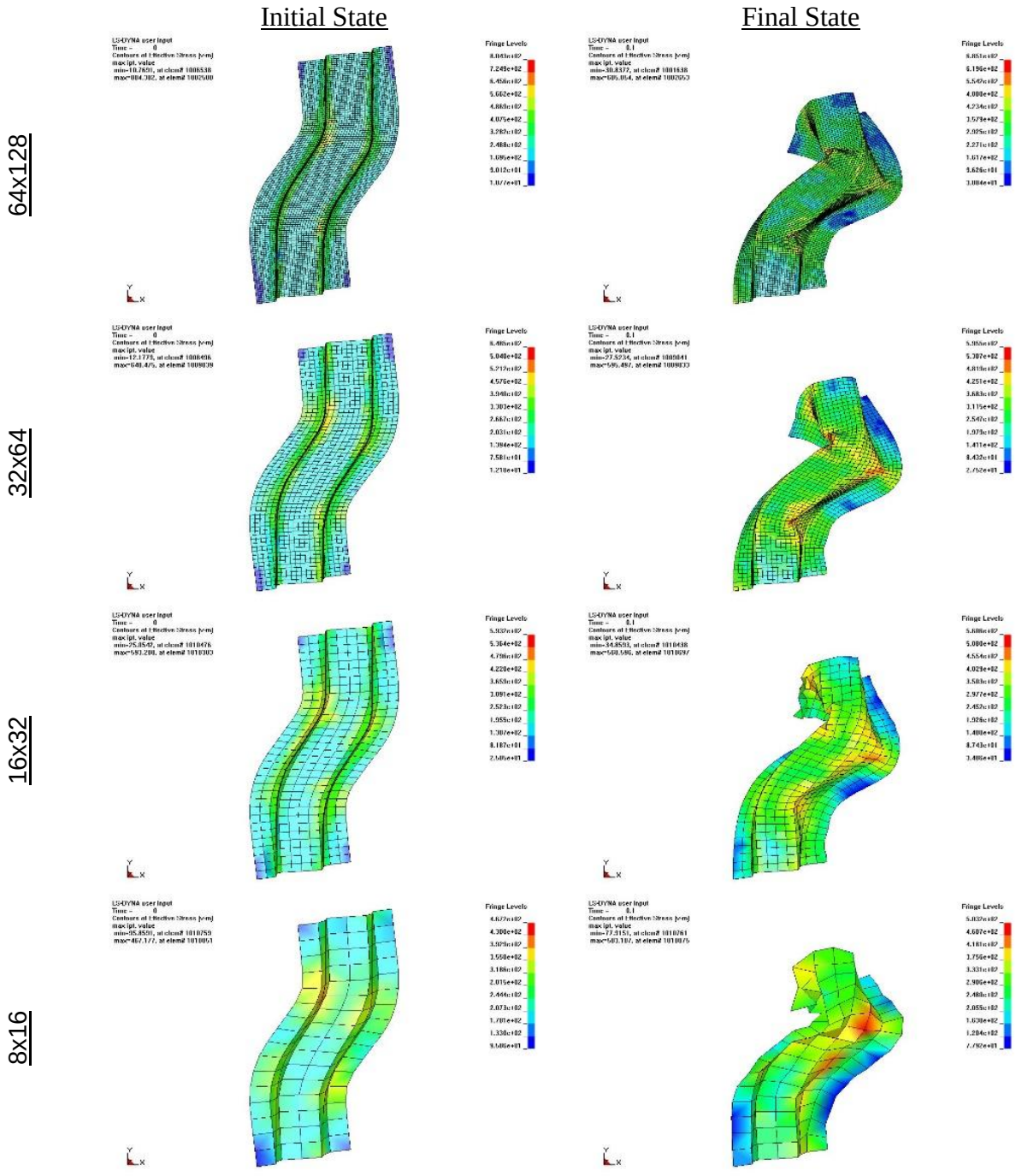


Figure 10. Crush Results with Metal Forming Effects.

6. RESULTS

Crash analyses of the Numisheet'96 S-Rail are performed to evaluate the influence of metal forming on crashworthiness. Internal energies of the S-Shaped rails are calculated for a

quantitative analysis. It is shown in Figure 11 that both mesh density and metal forming effects have an influence on the crashworthiness or the amount of energy absorbed. However, it is shown that the effects of metal forming have a more significant and dominant effect on the final response.

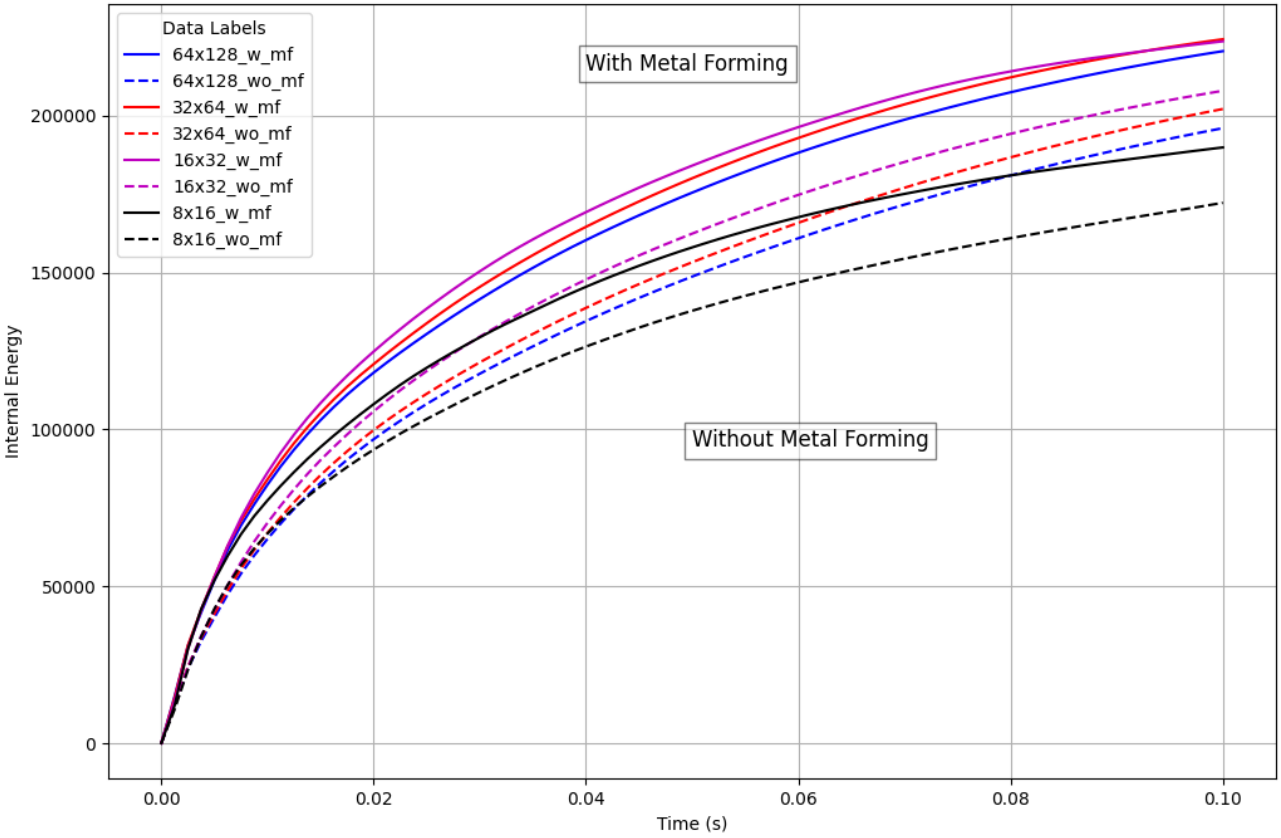


Figure 11. Material Internal Energy.

The parts which include the metal forming effects have absorbed more energy compared to the parts which do not include the metal forming effects. It is also observed that as the mesh size gets bigger, the absorbed energy becomes lower. This is due to the artificial plastic hinge effects on bigger elements that cause more bending type of deformation than progressive buckling, where less amount of energy can be absorbed. It is seen that smaller mesh sizes allowed to predict buckling modes more successfully. It is concluded that after mapping the deformed geometry, inhomogeneous thickness distribution, residual stress and strain as a material history, the material in not pristine anymore and points of imperfection behave like a crash initiator to progressive buckling. The work hardened material properties also contributed to the amount of energy absorption. Therefore, it is concluded that the metal forming effects should be considered for crashworthiness calculation with the adequate mesh size.

7. REFERENCES

1. **Lee, K.J., Kinzel, G.L., (1996),** Wagoner R.H. (Eds.), Numisheet‘96, Michigan.

2. **Hallquist, J. O., (1998),** LS-DYNA User’s Manual, Livermore Software Technology Corporation.

3. **Böttcher, C-S., Frik, S., (2003),** “Consideration of Manufacturing Effects to Improve Crash Simulation Accuracy”, 4th European LS-DYNA Users Conference,

IMPLEMENTATION OF THE KANBAN SYSTEM ON A MACHINE ASSEMBLY LINE

Hafize DURMAZ, *hafizedurmaz@yilmazmachine.com.tr* Yılmaz Makine, R&D Department, 41455, Kocaeli, Türkiye

Hasan ÇAKIR, *hasancakir@yilmazmachine.com.tr* Yılmaz Makine, R&D Department, 41455, Kocaeli, Türkiye

Alper YETER, *alperyeter@yilmazmachine.com.tr* Yılmaz Makine, R&D Department, 41455, Kocaeli, Türkiye

Mustafa BAKKAL, *bakkalmu@itu.edu.tr* Istanbul Technical University, 34367, İstanbul,Türkiye.

ABSTRACT

In this paper, the discussion is going to be about Lean Manufacturing (LM) and how it aims to optimize efficiency in industrial operations. However, assembly lines in the machine industry often face challenges such as production delays and operational inefficiencies. This study indicates these issues by implementing Failure Mode and Effects Analysis (FMEA) and Kanban systems in Yilmaz Machine company. By identifying potential failures through FMEA and improving workflow management with Kanban, the research demonstrates significant growth in production effectiveness. This approach not only reduces risks but also arranges processes, resulting in reduced lead times and improved overall efficiency in manufacturing operations.

Keywords: Lean Manufacturing, Kanban.

1. INTRODUCTION

Due to the exponential growth in the machine industry, many companies are competing to stay on top. However, they face many obstacles, such as increasing production speed and minimizing time wastage during working hours. To outline these challenges, Yilmaz Machine, one of the leading companies in the machine sector that provides its services to small and large Door and Window manufacturers both in Turkey and abroad, used PVC and Aluminum

Profile Machines in its production as well as to furniture manufacturers using Wood Cutting Machines in its production, has decided to implement Lean Manufacturing strategies that can help to identify and eliminate non-value-added resources. FMEA technique is applied to analyze the possible failures, to raise the safety factor and consequently customer satisfaction. It is one of the most effective methods for improving production efficiency and preventing time waste. To ensure the effectiveness of this study, we went through few different studies related to this case.

Lean Manufacturing Case Study with Kanban System Implementation. A qualitative research design was adopted for this research. This case study was carried out on one purposively selected Malaysian manufacturing company that has implemented lean manufacturing system deploying the Kanban practices Three managers were purposively selected as respondents for the study and interviews were conducted in their respective offices. Analysis found that all three managers reiterated the same factors supporting the needs for Kanban system and with good production practices. The study suggested that inventory management, vendor and supplier participation, quality improvement and quality control, employee and top management commitment were the factors that lead to successful implementation of the Kanban system in this organization. At the manufacturing company, the Kanban system begins with the A-Man, a production worker, who retrieves Kanban cards from child posts along the production line as inventory is used. These cards are then brought to a central point called the mother post by the A-Man. At the mother post, the B-Man collects and sends the cards to a Kanban sorter room where they are sorted using a Kanban sorter machine. Information about used raw materials is logged into an E-SIMS database during this sorting process, which is accessible to vendors by a web-based system. Once sorted, Kanban cards are placed in labeled shopping bags and stored on logistics racks. Different bags are used for different suppliers. Finally, the C-Man places the bags onto a mini truck for delivery to suppliers at the loading bay. Delays by A-Man, B-Man, or C-Man in collecting or delivering cards can disrupt the production process, which operates on a cycle time of 38 minutes per cycle [1]. The other study is An Application of Lean Manufacturing Techniques in Paint Manufacturing Company. Due to the economic downturn in Saudi Arabia, manufacturing companies have begun to focus on reducing operational costs and increasing productivity through lean manufacturing principles. This study aims to enhance the productivity of a paint manufacturing company by implementing various lean manufacturing techniques. Initially, a value stream mapping analysis was conducted across the manufacturing process, identifying improvement areas using a fishbone diagram. Subsequently, techniques such as Workplace Organization (5S), Single Minute Exchange of Dies (SMED), Work Standardization, and Kanban were selected to address specific

challenges within these areas. Each technique was systematically implemented to evaluate its impact on productivity. Results showed that applying 5S and SMED techniques in the filling process reduced changeover times by 59% and increased daily productivity. Work standardization in the charging process, as recommended by Pareto chart analysis, decreased defect batches by 57%. Implementing a Kanban system resolved semi-finished product shortages and increased output in pre-weighing batches by 57%. Moreover, overtime hours were reduced by 77%, and handling of non-hazardous and hazardous waste decreased by 85% and 53%, respectively. Understanding the manufacturing process deeply is a vital to track the bottlenecks and then the area of improvements. Lean manufacturing principles proofs its ability to increase the productivity without the need to spend much money [2]. The aim of this study is to improve the understanding on how Kanban impacts on software project work. Boddy and Macbeth address four practices explaining successful implementation of projects: goals, resources, structures, and controls. Moreover, Addison and Vallabh identify that two of the most frequent risk factors in software projects are unrealistic schedules and budgets, and continuous requirement changes. The investigation indicated considerable benefits of the Kanban process model including motivation and control over the project activities. These, on their parts, benefit software project management. This is an advantage for practitioners: by being aware of the nine aspects of work suggested in the study, management can use them as lenses to concretize the basically abstract environment of the software development process [3]. In this study, a methodology to adopt cellular layout for LM is discussed for a manufacturing-based case study. First, an existing and familiar cell formation technique based on binary machine-part incidence matrix was applied to identify machine cells for the given set of part types. Depending on individual part's operation sequence and processing, material handling time, etc., the original cell layout is analyzed to reduce the several wastages in the form of non-value adding activities. A generalized group technology (problem with alternative process plans) approach can identify more efficient lean cells. The benefits from lean layout design are evident from the production output and may open more research issues regarding cell design for lean implementation. The results of the studies above underscore the valuable relevance of lean manufacturing strategies, including Kanban, which can be similarly beneficial for Yilmaz Machine company [4].

Lean manufacturing aims to eliminate waste and minimize defects by eliminating non-value-added activities. It optimizes processes, cuts costs, boosts efficiency, and reduces time through two main strategies: zero defects and waste elimination [5].

1.1. Key Approaches of Lean Manufacturing

There are two approaches of LM the first one is 5S Technique, which Eliminates waste through sorting, setting in order, shining, standardizing, and sustaining. And the second one is Pull System Technique, which Improves workflow by having downstream processes pull from upstream or storage.

FMEA was first widely used by the US Military at the end of the 1940s. The military developed the technique to reduce sources of variation and corresponding potential failures in the production of munitions – and it proved a highly effective tool. FMEA stands for Failure Mode and Effects Analysis; it's a step-by-step way to identify how a product's design or production process may fail or not work as intended. Many organizations use FMEA to anticipate things that may go wrong in the design or build of a product, predict how those things may impact the business, and evaluate ways to avoid them [6].

Failure Modes and Effect Analysis (FMEA) predicts potential failures by defining, evaluating, prioritizing, and acting on risks. FMEA can be applied to new designs, modifications, customer demands, warranty returns, and improvement efforts. There are four types of FMEA: system FMEA balances operational and economic factors, design FMEA focuses on design-related failures before production, process FMEA analyzes manufacturing and assembly processes, and service FMEA **a**nalyzes services before reaching customers.

To be able to use FMEA, we should implement the following factors:

- Occurrence is a ranking number associated with the likelihood that the failure mode and its associated cause will be present in the item being analyzed. For System and Design FMEAs, the occurrence ranking considers the likelihood of occurrence.

- Severity is a ranking number associated with the most serious effect for a given failure mode, based on the criteria from a severity scale. It is a relative ranking within the scope of specific FMEA and is determined without regard to the likelihood of occurrence or detection.

- Detection is a ranking number associated with the best control from the list of detection-type controls, based on the criteria from the detection scale. The detection ranking considers the likelihood of detection of the failure mode/cause, according to defined criteria.

After that, we implement the Risk Priority Number (RPN) by multiplying all occurrence, severity, and detection with each other. Therefore, the most critical parameters for the scoring system can be identified, ensuring a more effective production.

This project's goal is to ensure fair worker compensation based on performance. Although a 75% raise was given to all workers, it is not equitable as some perform better than others. To address this, data will be collected from the machine assembly line, and a scoring system will be developed. This system will help track performance and minimize errors by displaying common mistakes before tasks begin [7] [9].

1.2. Two-Card Kanban System

Two-card Kanban is a system used for managing large items without flow racks. It combines Kanban card racks and a Kanban board, using two types of cards: one for Production Order Kanban (POK) and the other for Withdrawal Kanban (WK). When items are produced or received, two cards are filled out; one stays with the item and the other goes into a FIFO box. When an item is needed, a material handler retrieves it using the card from the FIFO box, which then signals the need for restocking or production. This system ensures efficient flow and product rotation.

It can be seen in the figure below that, when the boxes are full, their Kanban card should be located on the side of them. On the other hand, when they are empty, they should be put on the floor and their Kanban cards should be put in the blue box attached to the shelf. Integrating the two-card Kanban system into the lean manufacturing approach helps manage inventory effectively, ensuring that production is aligned with actual demand and minimizing waste [8].

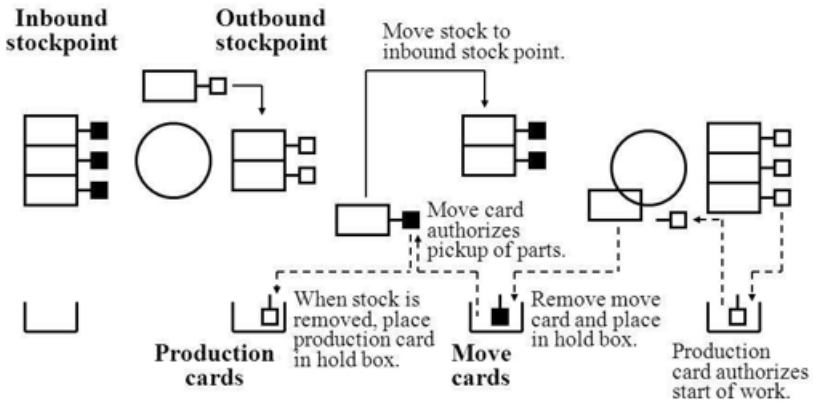


Figure 1. Kanban Card Location



Figure 2. Machine Assembly Line



Figure 3. Two Card Kanban System in Yilmaz Machine Factory

Also, the machine assembly line is illustrated in the figure below.

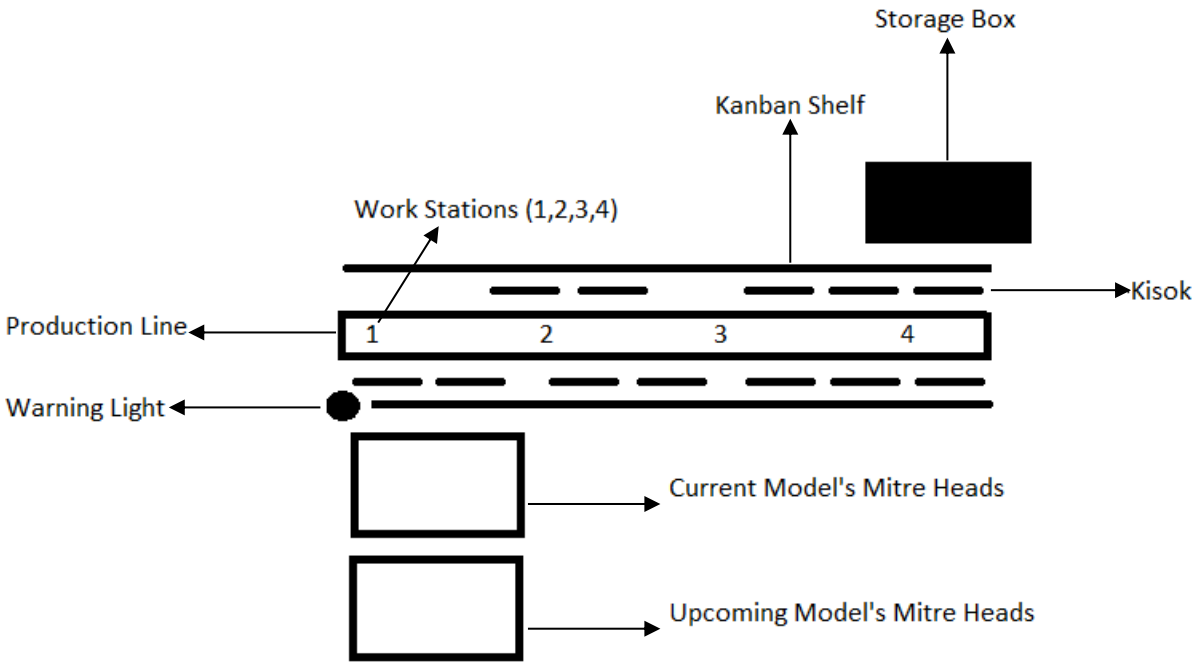


Figure 4. Machine Assembly Line

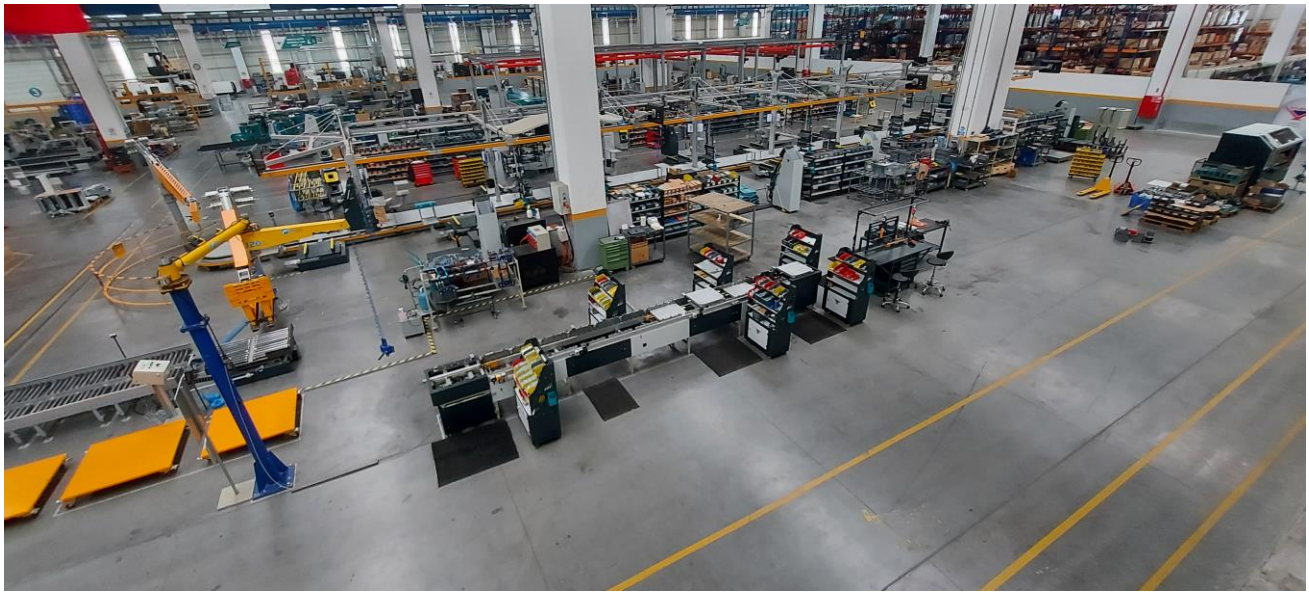


Figure 5. Machine Assembly Department

It can be observed on the assembly machine line that when the boxes are full, their Kanban cards should be located on the side of them. On the other hand, when they are empty, they should be put on the floor and their Kanban cards should be put in a blue box attached to the shelf.

2. APPLICATION

The application is going to be applied on the machine assembly line and the purpose of it is to prevent inequality among workers and minimize errors before they start. The machine assembly line at Yilmaz Machine consists of seven employees: four operators, one line manager, and two sub-assembly operators. Five employees have been with the company for 5 to 15 years and are considered experienced, while the remaining two have been employed for six months. Employee rotation is practiced on the assembly line, allowing each worker to learn the job by working at every station. All employees have provided competency certificates for their roles. There are no additional rewards for employees, and year-end salary increases are based on their performance throughout the year.

The qualifications for workers include certifications, participation in company-held trainings and seminars, and ongoing self-improvement. Competence is measured by the occurrence and reporting of defects and failures, maintaining an organized workspace, providing suggestions for improvement, time taken to complete tasks, workplace tidiness, adherence to safety rules, cleanliness of work clothing, work quality, and seniority. Absenteeism considers whether off days are planned and by whom, tardiness, and breaks for smoking or coffee. Adaptability is assessed by how well an employee adjusts to different models assembled, the assembly line, and coworkers. Other factors include job satisfaction, the number of employees trained by the operator, and the employee's place of residence.

Determined parameters will be matched with points with plus or minus signs, and employees will have a grade in the scoring system that will be evaluated according to these parameters in certain periods.

The application will be done by the following methodologies to help in reaching the aim of the application:

Forced ranking employees are scored by their managers at the end of the year. Employees who enter the top 20% are rewarded for being successful. The 70% remaining in the middle class is considered normal. The worst 10% are laid off.

Failure Modes and Effect Analysis (FMEA) Risk evaluation can be applied to the process or product by using the equation below.

Risk Priority Number:

$$RPN = SEVERITY * OCCURRENCE * DETECTION \quad (1)$$

Overall Labor Effectiveness (OLE) Measures the following:

- Availability: The percentage of time employees spend making effective contributions.
- Performance: The amount of product delivered per unit time.
- Quality: The percentage of perfect or saleable product produced.

Employee Performance Management (EPM)

- Evaluates the performance of employees and identifies their development needs.

- Components of the EPM System include:
- Employee Self-Appraisal
- Goal-Based Performance
- Rating Skills & Competencies
- Employee Development Needs
- Overall Grade, Relative Rating & Pen-picture

These methodologies ensure a structured and fair evaluation of employees, aiming to foster an equitable work environment and enhance overall productivity on the machine assembly line at Yilmaz Machine [7] [10].

2.1. Rating Criteria

To determine the importance of the parameters, FMEA analysis has been conducted and it is listed in the table below by using the following parameters and finding the RPN.
Taking these into account FMEA table of parameters is created and listed from higher RPN to lower RPN.

Table 1. Initial FMEA Table

Parameters	Occurrence	Severity	Detection	RPN
Quality of the work	6	9	7	378
Occurrence of detects and failures	7	8	6	336
Obeying the rules of safety of work	6	9	5	270
Job satisfaction	6	5	7	210
Reporting defects and failures	7	6	4	168
Number of employees that is trained by the operator	7	6	4	168
Adaptability to model assembled	6	5	5	150
Adaptability to assembly line	5	6	4	120
Smoking/coffee breaks	6	5	4	120
Providing improving suggestions about the work	7	4	4	112
Whether or not the employee continues self-improvement	4	4	6	96
Keeping an organized	6	5	3	90

workspace				
Adaptability to coworkers	4	3	6	72
Elapsed time to complete a work	5	7	2	70
Are the off days planned - by whom?	5	7	2	70
Tidiness of the workplace	5	6	2	60
Certifications	4	3	3	36
Tardiness	5	7	1	35
Image (Cleanliness of the work clothing etc.)	5	3	2	30
Participation to trainings/seminars held within the company	5	5	1	25
Seniority	4	5	1	20
Residence	2	2	1	4

After applying Kanban method on the assembly machine line as it is mentioned above, it can be observed that all the occurrence, severity, and detection decreased which makes the production more effective. A new table set from higher RPN to lower RPN, later a comparison will be done to see the effectiveness of the method:

Table 2. Final FMEA Table

Parameters	Occurrence	Severity	Detection	RPN
Quality of the work	5	8	6	240
Occurrence of detects and failures	6	7	5	210
Obeying the rules of safety of work	5	8	4	160
Job satisfaction	6	5	4	120
Reporting defects and failures	6	5	4	120
Number of employees that is trained by the operator	6	5	4	120
Adaptability to model assembled	5	5	4	100
Adaptability to assembly line	4	5	4	80

Smoking/coffee breaks	6	3	4	72
Providing improving suggestions about the work	5	3	4	60
Whether or not the employee continues self-improvement	4	3	5	60
Keeping an organized workspace	7	2	4	56
Adaptability to coworkers	6	2	4	48
Elapsed time to complete a work	5	3	3	45
Are the off days planned - by whom?	2	3	7	42
Tidiness of the workplace	4	2	5	40
Certifications	8	2	2	32
Tardiness	4	7	1	28
Image (Cleanliness of the work clothing etc.)	4	3	2	24
Parameters	Occurrence	Severity	Detection	RPN
Participation to trainings/seminars held within the company	3	2	3	18
Seniority	2	2	3	12
Residence	1	2	1	2

3. CONCLUSION

Comparing the two tables on assembly times reveals a wide overview of the improvements made in the production process, highlighting both risk reduction and efficiency gains. The initial and improved Risk Priority Numbers (RPNs) indicate the successful reduction of risks through targeted changes in occurrence, severity, and detection. Significant reductions in RPNs for parameters such as the quality of work (from 378 to 240), occurrence of defects and failures (from 336 to 210), and adherence to safety rules (from 270 to 160) improve control and management, making production safer and more efficient.

Table 3. Assembly Time

Old Assembly	New	Takt (minute)	Difference	Difference	Monthly

Time (minute)	Assembly Time (minute)		(minute)	Percentage (%)	Time Saved (minute)
100	66	11	34	34	680
240	180	30	60	25	720
190	108	18	82	43.15	1230
120	96	16	24	20	600
70	60	10	10	14.28	100

The table above for assembly times provides a clear picture of the practical outcomes of these improvements. For example, the old assembly time of 100 minutes was reduced to 66 minutes, saving 34 minutes per assembly, and resulting in a monthly time saving of 680 minutes. Similar reductions for other assembly times, such as from 240 to 180 minutes (saving 720 minutes monthly) and from 190 to 108 minutes (saving 1230 minutes monthly).

As a result, the comprehensive approach to improving the production process through both risk mitigation and efficiency enhancements has led to substantial time savings and increased productivity. The combination of reduced RPNs and decreased assembly times highlights the effectiveness of the changes implemented, resulting in a more productive manufacturing operation.

ACKNOWLEDGEMENT

Thanks to each of Utku Özdil, İrem F. Aytaç, Aycan Yumrukçal, H. Kübra Ünlü, and Demet Çil, for conducting this study. It's a highly effective method to improve production at Yilmaz Machine Company.

REFERENCES

1. **Abdul Rahman , N.A., Sharif, S.M., Esa, M.M.,(2013),**“Lean Manufacturing Case Study with Kanban System Implementation”, research. International Journal of Operations & Production Management. Vol. 15, No. 1, p.38 – 49.] Surendra, M.G.,Yousef, A.Y., Ronal, F.P. 1999. Flexible Kanban system. International Journal of Operations and Production Management. Vol. 19, No. 10, p.1065-1093.

2. **Badeeb, A.M., Abdulaal, R.M.S., Bafail, A.O. (2019),** “ An Application of Lean Manufacturing Techniques in Paint Manufacturing Company: A Case Study“, JKAU: Eng. Sci., Vol. 28 No. 2, pp: 51 – 73 (1438 A.H./ 2017 A.D.) Doi: 10.4197/Eng. 28-2.5.

3. **Ikonen, M., Pirinen, E., Fagerholm, F., Kettunen, P., Abrahamsson, P., (2011),** “ On the Impact of Kanban on Software Project Work An Empirical Case Study Investigation“.

4. **Sharma, B.P., Pattanaik, L.N., (2008),** “ Implementing lean manufacturing with cellular layout: a case study“, Springer-Verlag London Limited.

5. **Ohno, T. (1988),** “Toyota production system: beyond large-scale production. Productiv-ity Press”.

6. **Ćatić, D., Arsovski, S., Jeremić, B., Glišović, J., (2011),** “ FMEA IN PRODUCT DEVELOPMENT PHASE“, Center for Quality, Faculty of Mechanical Engineering, University of Kragujevac.

7. **Lipol, A.S., Haq, J., (2011),** “Risk analysis method: FMEA/FMECA in the organizations”, International Journal of Basic & Applied Sciences IJBAS-IJENS Vol: 11 No: 05.

8**. Latest Quality, 26 07 2018.** [Online].Available: https://www.latestquality.com/two-card-kanban-system/ [Accessed 03 06 2024]

9. **Accendo Reliability, Carlson, C.S.,** [Online]. Available: https://accendoreliability.com/understanding-fmea-severity-part-1/#:~:text=What%20is%20the%20definition%20of,criteria%20from%20a%20severity%20scale. [Accessed 21 05 2024]

10. **Wikipedia,** [Online]. Available: https://en.wikipedia.org/wiki/Overall_labor_effectiveness. [Accessed 26 05 2024].

DESIGN, ANALYSIS AND VERIFICATION OF EMC WITH VARIOUS BALL AND TRAPEZOIDAL DRIVES

Berk KURT, *berk.kurt@hktm.com.tr*, Hidropar Hareket Kontrol Teknolojileri Merkezi A.Ş. (HKTM), 41400, Gebze, Kocaeli

Ö. Faruk UYSAL, *omer.uysal@hktm.com.tr,* Hidropar Hareket Kontrol Teknolojileri Merkezi A.Ş. (HKTM), 41400, Gebze, Kocaeli

Tolga CANKURT, *tolga.cankurt@hktm.com.tr,* Hidropar Hareket Kontrol Teknolojileri Merkezi A.Ş. (HKTM), 41400, Gebze, Kocaeli

ÖZET

Bu yayımda lineer hareket sistemlerinden olan elektromekanik silindir sistemi incelenmiştir. Elektromekanik silindir sistemi yüksek hassasiyet ile kontrol edilebilen, nispeten yüksek kuvvet çıktısı verebilen dinamik bir sistem bütünüdür. Elektromekanik silindirin çalışma mantığı ile genel tasarımda kısıtlayan parça tasarımlarının üstüne farklı tipte eyleyicilerde entegre edilip tasarım kısıtları incelenmiştir. Yapılan tasarımsal incelemelerin ardından tasarımın tamamlanması ile birlikte farklı yükler ve hızlar ile sistemin verdiği cevaplar incelenmiştir. Bu incelemeler ile birlikte teorik ile pratik sonuçlar karşılaştırılmıştır. Bu karşılaştırmalar ve testler ile birlikte sistemin ömür testleri yapılmıştır

Anahtar Kelimeler: Elektromekanik Silindir, Vidalı Mil, Trapez Mil

ABSTRACT

This paper examines electromechanical cylinder system, one of the linear motion systems. The electromechanical cylinder system is a dynamic system that can be controlled with high precision and can provide relatively high force output. The operating logic of an electromechanical cylinder and the design constraints were studied by integrating different types of actuators in addition to the restrictive part designs in the general design. Following the design investigations, once the design was complete, the response of the system at different loads and speeds was investigated. These investigations were used to compare theoretical and practical results. Along with these comparisons and tests, durability tests of the system were also carried out.

Keywords: Electro-mechanical Cylinder, Ball Screw, Trapezoidal Screw

1. INTRODUCTION

An electromechanical cylinder (EMC) system converts the circular motion of electric motors into linear motion with a highest efficient using machine elements such as screws and nuts. With no air or oil leaks compared to hydraulic and pneumatic systems, it provides cleaner working conditions for the user and offers great design flexibility by eliminating the need for an oil tank and compressor. Thanks to its lubrication channels, it operates smoothly for a long time with low maintenance costs [Parr, 1991].

In terms of machine dynamics, the EMC works as an active prismatic joint. Active prismatic joints traditionally thought of as hydraulic and pneumatic linear actuators. However, these systems are inadequate compared to EMC in terms of operating sensitivity, response speed and controllability. In addition, the output force that can be applied is relatively high. Although it cannot achieve the high forces of a hydraulic cylinder, it can achieve much higher forces than pneumatic cylinders.

Table 1: The comparison between electromechanical, hydraulic and pneumatic systems [Parr, 1991]

Number	Criteria	Electromechanical System	Hydraulic System	Pneumatic System
1	Force Capability	Light to moderate force capability	High force capability	Light to moderate force capability
2	Precision	Highest	Medium	Lowest
3	Controllability	Easy to Control	Complex Control System	Easy to control
4	Efficiency	Highest	Medium	Lowest
5	Speed	Moderate to High	Lowest	Highest
6	Initial Cost	Moderate to High	Highest	Moderate to High
7	Maintenance Cost	Lowest	Highest	Medium

As shown in Table 1, electromechanical systems are ideal for high precision and controllability, higher initial cost, efficient and low maintenance operation. These systems exist as a single system with the motor connected to the end of the actuator, rather than adding additional compressor or pump areas as with hydraulic or pneumatic systems. This makes them ideal for low-volume applications.

This paper discusses the electromechanical cylinder system. This system is not only a linear actuator, but also a system with its motor.

2. TYPES OF ELECTROMECHANICAL CYLINDERS

Depending on the motor connection, EMC systems are divided into parallel or straight systems, but the main difference is the type of drive. This difference varies according to the sensitivity of the system, its efficiency, the load it can carry and price differences. Two different EMC series developed by HKTM will be examined here [HKTM, n.d.]. The first is the model developed with a ball screw and nut. In addition to being faster than the other EMC type, this EMC type is a more efficient, retractable, cost-effective and sensitive system. The other type is the model developed using a trapezoidal screw and nut. The main advantage of this model over the other is that it is not retractable, in addition to its lower cost. A comparison of the two types of EMC can be seen in Table 2 [Rexroth (EMC), n.d.].

Table 2: Comparison between EMC with ball screw and EMC with trapezoidal screw

Number	Criteria	EMC with ball screw and nut	EMC with trapezoidal screw and nut
1	Force Capability	Higher	Lower
2	Velocity	Higher	Lower
3	Efficiency	Higher	Lower
4	Precision	Higher	Lower
5	Retractable	Yes	No
6	The Cost	Higher	Lower

3. GENERAL EMC DESIGN

When designing EMC, there are certain standards to keep the external dimensions constant for each manufacturer. Considering the places where EMC systems are used, this standard is ISO-15552-2018, which is the standard, used in the design of pneumatic cylinders. Taking into account this standard, certain dimensions have been defined. For this reason, some dimensions of the main designed parts are determined. Once these have been determined, other parts are designed and the loads they can mechanically withstand are determined according to the design [ISO 15552, 2018]. When we look at the standard, the products that comply with this standard are defined within the ISO 3320 standard according to their bore sizes. This standard covers products with bore sizes 32, 40, 50, 63, 80, 100, 125, 160, 200, 250 and 320 [ISO 15552, 2018].

The first product is designed by selecting based on the bore size and force output we require. Here the choice was made by studying equivalent products and the load capacity of ball screws. The bore size 63 product developed by Bosch Rexroth achieves a force of 15900N using the 25x5 ball screw nut duo. As these values can be tested at the beginning of the design and are also producible, the EMC with bore size 63 is developed [Rexroth (EMC), n.d.].

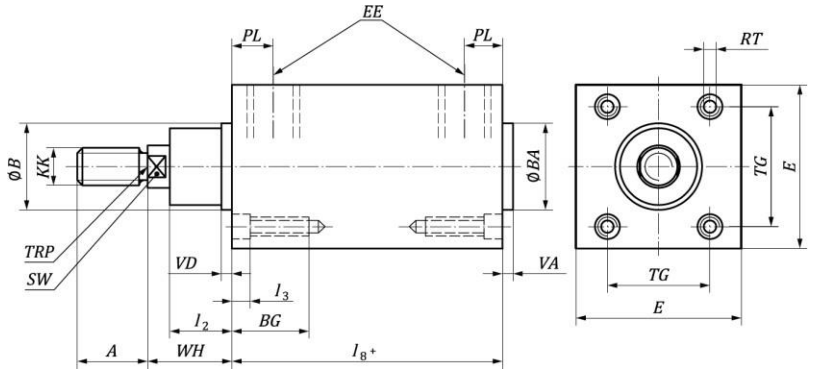


Figure 1: The basic dimension of a single rod cylinder according to ISO-15552-2018 [ISO 15552, 2018]

After selecting the type to be designed, the working mechanism must be designed. As the working mechanism, slides are added to the bed supporting the nut, and it is moved back and forth by the nut and screw. A piece of pipe is added to the end of this system, which allows the back-and-forth movement by passing a screw through it and is used as a rod. As shown in Figure 2, the back-and-forth movement of the bar is provided by the glide pads added to the profile.

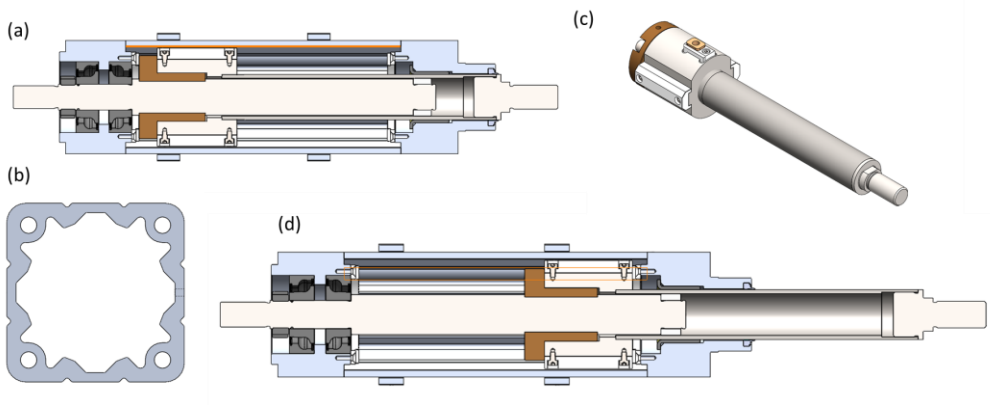


Figure 2: (a) The closed form of EMC, (b) The profile of EMC, (c) The nut, rod and sleight bed of EMC, (d) The open form of EMC

There are parts other than nuts and bolts that determine the load that can be lifted. The first of these is the pipe part used as the rod. Given that this piece of pipe is working vertically, two types of deformation should be considered. The first is compression and the second is buckling.

3.1 Rod Design

A 25x5 mm ball screw is used in 63-bore size EMC. Since the outer diameter of the screw shaft used is less than 25 mm, the inner diameter of the rod was taken as 25 mm. The outer diameter was taken as a reference to the outer diameter of the equivalent products studied. This is 30 mm. At the same time, the material chosen for the rod is also of great importance

[Rexroth (EMC), n.d.]. As the rod is a pipe, the pipe must be a seamless. 316 stainless steel was chosen because of its high strength and resistance to rust. After production, the surface is hard chrome plated to prolong the service life [316 (1.4401) stainless steel, n.d.].

To model the buckling, a model with one side fixed and the other free was used. Figure 3 shows the model used. Using this model, a mathematical model was obtained using the parabolic equation (Johnson-Euler equation) together with the Euler buckling model [Hibbeler, 2017].

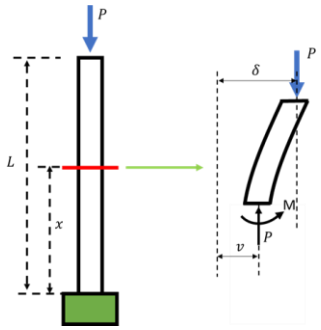


Figure 3: Column with one end fixed and one end free and force diagram

The critical load and stress can be found using the model in Figure 3. The critical load and stress can be found from equations 1 and 2.

$$P_{cr} = \frac{\pi^2 EI}{4L^2} \tag{1}$$

$$\sigma_{cr} = \frac{\pi^2 E}{4\left(\frac{L}{r}\right)^2} \tag{2}$$

Above formulation, E is the modulus of elasticity, I is the moment of inertia, L is the free length of the bar and r is the radius of gyration. Using these values, the following two buckling analysis graphs (Figures 4) were obtained. The first of these graphs is the stress vs slenderness ratio, which is the ratio of the free length to the radius of gyration. This ratio gives us a unit less value. Therefore, with the graph of these two, we can obtain a relationship between length and diameter.

In buckling deformation, the loads are not only on the central axis but also mostly off this axis. The second graph shows possible eccentric loads and the load curves that they can handle. This graph has been modeled under different eccentric loads by finding the length determined by the load capacity of the Bosch Rexroth model 63, which is an equivalent product. The load capacity of the equivalent product is 15900 N [Rexroth (EMC), n.d.]. If the critical load is targeted at 15900 N, the maximum rod (stroke) unit is 1600 mm. At this load capacity, the rod will buckle after a 1600 mm stroke.

As a result, if we take into account the force that can be obtained from the rod design compared to the equivalent product and take the inner diameter as 25 mm and the outer diameter as 30 mm, a cylinder with a maximum size of 1600 mm can be produced under these force conditions.

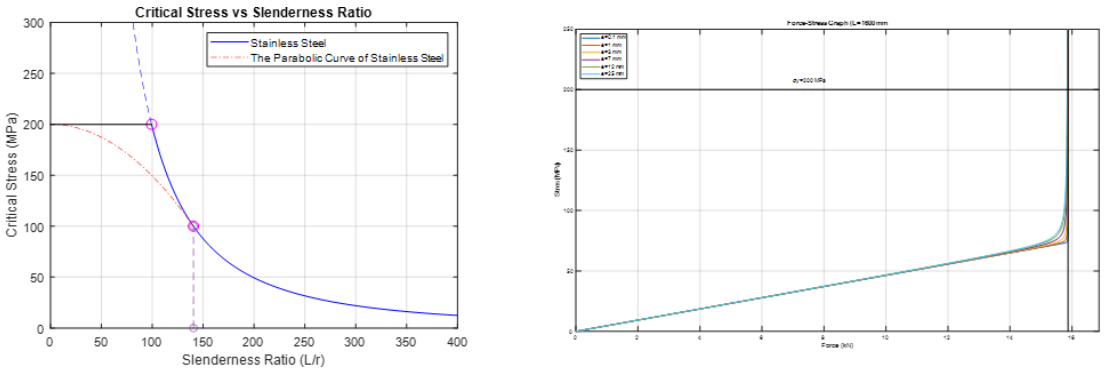


Figure 4: (a) Critical Stress vs Slenderness Ratio of Rod **(b)** The Force vs Stress Graph (L=1600 mm)

4. DESIGN OF EMC WITH BALL SCREW AND NUTS

Ball screws and nuts are generally preferred for EMC systems due to their high sensitivity and efficiency (%90). For this reason, the ball screw and nut were preferred in the first EMC product developed. Ball screws and nuts are manufactured by major companies in the market, and from Bosch Rexroth component, R151221012 ZEM-E-S 25x5Rx3.5-4 ball screw and R151121700 - 25X5RX3 (T7) ball screw were preferred in the EMC developed. The table below shows the values of the products we obtained from the manufacturer's catalog [Rexroth Ball Screw, n.d.] [Rexroth (EMC), n.d.].

Table 3: Ball nut characteristics [Rexroth Ball Screw, n.d.]

The Name of Nut	Part Number	Load Ratings		Linear Speed (m/min)
		Dynamic (N)	Static (N)	
25 x 5R x 3 - 4	R1512 210 12	19100	27200	30

The product we looked at as an equivalent product in the previous section had a load capacity of 15900 N [Rexroth (EMC), n.d.]. The dynamic load capacity of the product we have selected and used is 19100 N. Therefore, the products we have selected and added to the design can mechanically exert a force of 15900 N. Again, as the length of the system can vary depending on the stroke, the part that limits the design and the load capacity is buckling. When modelling the buckling here, we model one side as fixed and the other as hinged.

Table 4: Buckling and Contact Stress Check of Ball Screw

Number	Description	Symbol	Value			Unit
1	Length of Screw	Ls	150			mm
2	Density	ro	7850			kg/m^3
3	Modulus of elasticity in tension	E	206000			MPa
4	Yield Strength (0.2)	Rp (0.2)	320			MPa
6	Limit Slenderness Ration (short/intermediate)	SRcs	17.94088			
7	Limit Slenderness Ration (intermediate/long)	SRc	112.7258			
12	Ineffective length	elc	50			mm
13	Effective length	Leff	100			mm
14	Profile Area	A	268.8025			mm^2
15	Moment of inertia of screw	Ix	5749.854			mm^4
16	Mass of Screw	m	0.427492			kg
17	Radius of Gyration	rx	4.625			mm
18	Maximum distance of fibre	y	9.25			mm
19	Slenderness Ratio	SR	21.62162			
20	Eccentricity Ratio	u	0.1			
21	Eccentricity	e	0.23125			mm
22	Stress in the extreme fibre of the screw core	s	65.16701			MPa
23	Critical Stress	sc	320			MPa
24	Critical Force	ncr	86016.81			N
25	Safety Coefficient	SF	4.500227	A	0	
				B	1	1.817957
				C	0	

The short stroke system provides a system with a high safety factor. As can be seen in table 4, screws are classified as short, medium, and long. Here the minimum SF required for the short screw is 1.75. For long screws, this value is set at 3.5. In the intermediate range, the value is found as an interpolation of these two values. As the screw grows, the possibility of buckling increases, and since the safety factor in the design is adjusted according to the elongation class, an attempt has been made to prevent the system from failing [MitCalc, n.d.].

As a result, in the designed EMC system, the stresses caused by the equivalent stress do not limit the system. This is because the preferred products remain above this stress level. However, the potential for the rod and screw to buckle increases as the system lengthens. Therefore, the buckling problem is the criterion that limits the actual load limit. In this problem, as the system lengthens, the load capacity is determined by a safety factor by limiting the rod and screw as short, intermediate, and long. Here, according to the 1000 mm stroke capacity, the safety factor remains above 3.5 and it can handle 15900 N force [Rexroth (EMC), n.d.]. If this value is exceeded, the force should be reduced as much as the buckling analysis and the safety factor allow.

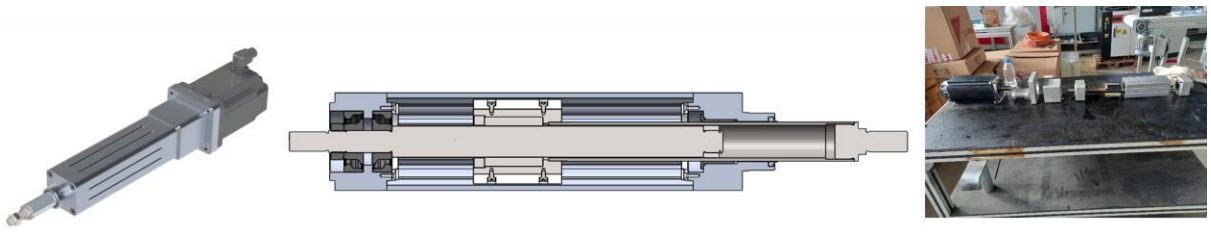


Figure 5: EMC 63 with ball screw and nut

5. DESIGN OF EMC WITH TRAPEZOIDAL SCREW AND NUTS

Compared with the trapezoidal screw and ball screw, there are no balls to facilitate movement between the nut and screw, and the force is transmitted directly by mechanical contact between the nut and screw. For this reason, it is difficult to reverse, as more than half of the force transmitted is reaction force. At the same time, since it is a low-efficiency system, it is used to activate the system and stay there by using the feature of not being able to be driven back, rather than fast working conditions. Therefore, reaction forces and their outputs should be considered in the design part [Rexroth (EMC), n.d.] [Budynas & Nisbett, 1972].

If we look at the EMC 63 product here, we also get identical products if we do not change the rod design, but only update the trapezoidal nut bedding in the design, and only the plain nut differs. For this reason, the screw-nut duo should be selected, taking into account the rod's internal diameter of 25 mm [Rexroth (EMC), n.d.].

The Tr24x5 was the closest product developed and commercially released by TEZPAR. However, as TEZPAR's nut would cause lubrication problems in a closed system such as EMC in continuous use, the design was completed by making some changes to the standard product. These changes are the grease channels as shown in Figure 7 [TEZPAR, n.d.].

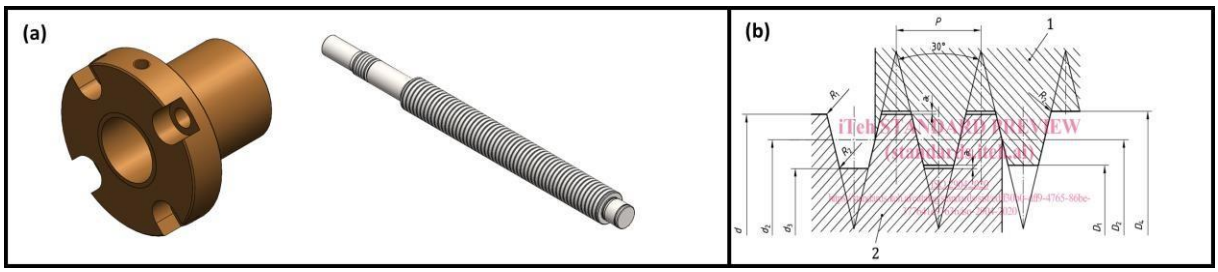


Figure 6: (a) Trapezoidal nut and screw design (b) IS0 2904:1977 Trapezoidal Screw [IS0 2904, 1977]

Depending on the trapezoidal thread selected, and taking into account the IS0 2904:1977 standard, the dimensions shown in Figure 6b are given in Table 3 [IS0 2904, 1977].

Table 5: The Tr24x5 screw dimensions

Number	Description	Metric Trapezoidal Screw 30º (IS0 2904:1977)		
		Symbol	Value	Unit
1	Thread Size	Tr	24	mm
2	Pitch	P	5	mm
3	Outer Diameter of the screw thread	d	24	mm
4	Inner Diameter of the nut thread	d1	19	mm
5	Pitch Diameter	d2	21.5	mm
6	Clearance of Major and minor diameters	ac	0.25	mm
7	Inner Diameter of the screw thread	d3	18.5	mm
8	Outer Diameter of the nut thread	d4	24.5	mm
9	Number of the thread start	ns	1	Single Start
10	Thread Pitch	L	5	mm
11	Pitch Angle	Y	4.23363	deg
12	Thread Angle 1	a1	15	deg
13	Thread Angle 1	a1	15	deg

The first product designed using the EMC with a bore size 63 trapezoidal screw has a stroke length of 100 mm. Therefore, the calculations have been made for a 100 mm stroke. At the same time, since we are trying to make an equivalent product from Bosch Rexroth, we set our target strength at 15900 N.

Table 6 shows the operating speed and yield strength as a function of the load, the design criteria, and the material of the screw and nut [Ugural, 2011] [MitCalc, n.d.].

Table 6: The design criteria's of system

Number	Description	Symbol	Value	Unit
1	Material of Screw	Hardened Steel		
2	Tensile Strength	Rm	580	MPa
3	Allowable Torsion Stress	Rt	192	MPa
4	Yield Strength (0.2)	Rp (0.2)	320	MPa
5	Material of Nut	Bronze		
6	Tensile Strength	Rm	200	MPa
7	Yield Strength (0.2)	Rp (0.2)	110	MPa
8	Force	Q	15900	N
9	Feed Speed	v	50	mm/s
10	Friction Coefficient in threads	f	0.08	

Having defined our design criteria and our screw and nut, we can find the torque, angular speed and power requirements to operate this system. Since we know the geometry of the screw (Figure 7), we can also determine the efficiency of the system as a function of the load and its angle.

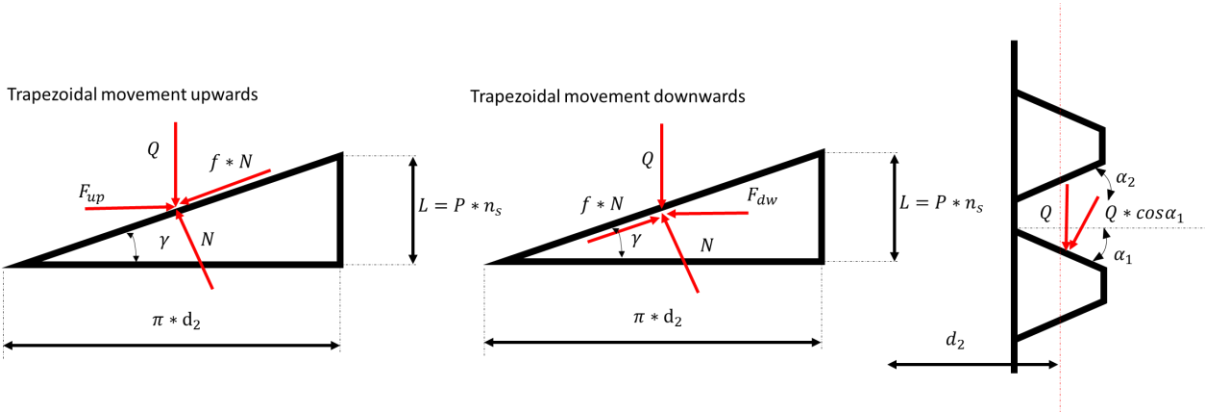


Figure 7: The free body diagram on the teeth

Table 7: Operating requirements and efficiency

Number	Description	Symbol	Value		Unit
1	Coefficient of friction of the bearing	fj	0.005		
2	Mean bearing diameter	dj	17		mm
3	Pin friction Torque	Mkj	1.3515		Nm
4	Lifting Torque	Mkup	28.32606		Nm
5	Lowering Torque	Mkdw	2.845887		Nm
6	Overall Efficiency	eff	0.446685	44.67%	%
7	Angular Velocity	n	600		rpm
8	Drive Power	Pmin	1.779779		kW

The efficiency of the system is lower than that of the ball screw and nut system. Therefore, it is not suitable for high-speed applications. At the same time, thanks to the aforementioned oil channel, grease oil can reach the entire contact surface of the nut and screw through these channels during maintenance [Ugural, 2011] [MitCalc, n.d.].

Table 8: Stress and Safety Factor Check [Ugural, 2011]

Number	Description	Symbol	Value			Unit
1	Length of Screw	Ls	100			mm
2	Density	ro	7850			kg/m^3
3	Modulus of elasticity in tension of screw	E	206000			MPa
4	Yield Strength of screw (0.2)	Rp (0.2)	320			MPa
5	Permissible mean pressure in the thread	pD	22.5			MPa
6	Limit Slenderness Ration (short/intermediate)	SRcs	17.94088			
7	Limit Slenderness Ration (intermediate/long)	SRc	112.7258			
8	Torsional Stress	t	22.78459	<	192	MPa
9	Tensile/Compressive Stress in the direction	s	59.15123	<	320	MPa
10	Equivalent Stress	sred	71.10753	<	320	MPa
11	Safety Coefficient	SF	4.500227	>	2	

As can be seen in Table 8, when the equivalent stress is compared with the yield strength of the material, the safety factor becomes 4.5. In general, the safety factor we want to achieve here is 2. This means that it can handle a load much higher than 15900 N. If we want to achieve the safety factor 2, we see that the safety factor 2 under these conditions is 35 kN load.

However, in such linear actuators, the other value to check under load is the buckling deformation. This is because the risk of buckling increases as the length of the screw increases according to the stroke value of the system. The buckling values are examined in Table 9.

Table 9:Buckling and Contact Stress Check of Trapezoidal Screw

Number	Description	Symbol	Value			Unit
1	Ineffective length	elc	50			mm
2	Effective length	Leff	50			mm
3	Profile Area	A	268.8025			mm^2
4	Moment of inertia of screw	Ix	5749.854			mm^4
5	Mass of Screw	m	0.284994			kg
6	Radius of Gyration	rx	4.625			mm
7	Maximum distance of fibre	y	9.25			mm
8	Slenderness Ratio	SR	10.81081			
9	Eccentricity Ratio	u	0.1			
10	Eccentricity	e	0.23125			mm
11	Stress in the extreme fibre of the screw core	s	65.09125			MPa
12	Critical Stress	sc	320			MPa
13	Critical Force	ncr	86016.81			N
14	Safety Coefficient of buckling	SF	4.500227	Short	1	1.75
				Intermediate	0	
				Long	0	
15	Factor according to mounting method	l	1.875			
16	Permissible Rotational Speed by the critical Speed	N	254527.3			rpm
17	Permissible Rotational Speed by the critical Speed	N	1272.637			m/min
18	Nut height	h	46			mm
19	Number of threads in the nut	nz	9.2			
20	Number of active threads in the nut	nzmax	8	<	8	
21	Thread Pressure	p	11.77006	<	22.5	MPa
22	Safety Coefficient Thread Pressure	SF	1.911629	>	1.25	

As a result, in the designed EMC system, the stresses caused by the equivalent stress do not limit the system. However, the potential for the rod and screw to buckle increases as the system lengthens. Therefore, the buckling problem is the criterion that limits the actual load limit. In this problem, as the system lengthens, the load capacity is determined by a safety

factor by limiting the rod and screw as short, intermediate, and long. Here, according to the 1000 mm stroke capacity, the safety factor remains above 3.5 and it can handle 15900 N force. If this value is exceeded, the force should be reduced as much as the buckling analysis and the safety factor allow.

6. EMC TEST SETUP

A test bench has been developed to test and verify the developed EMC system. This device has the capacity to test strokes up to 2 meters. Thanks to the pneumatic cylinders connected to the back, it will be possible to test the EMC by checking the position under load. If we add the force exerted by the pneumatic cylinders and the weight of the system, we obtain a system test set-up with a force of 10 kN. This shows us the shortcomings of the cylinder we have developed with this system. At the same time, the tester can also be used for durability testing. Figure 8 shows photographs of the test setup. Table 10 shows the unloaded weight of the system, the properties of the pneumatic cylinders, and the loads generally applied to the EMC.

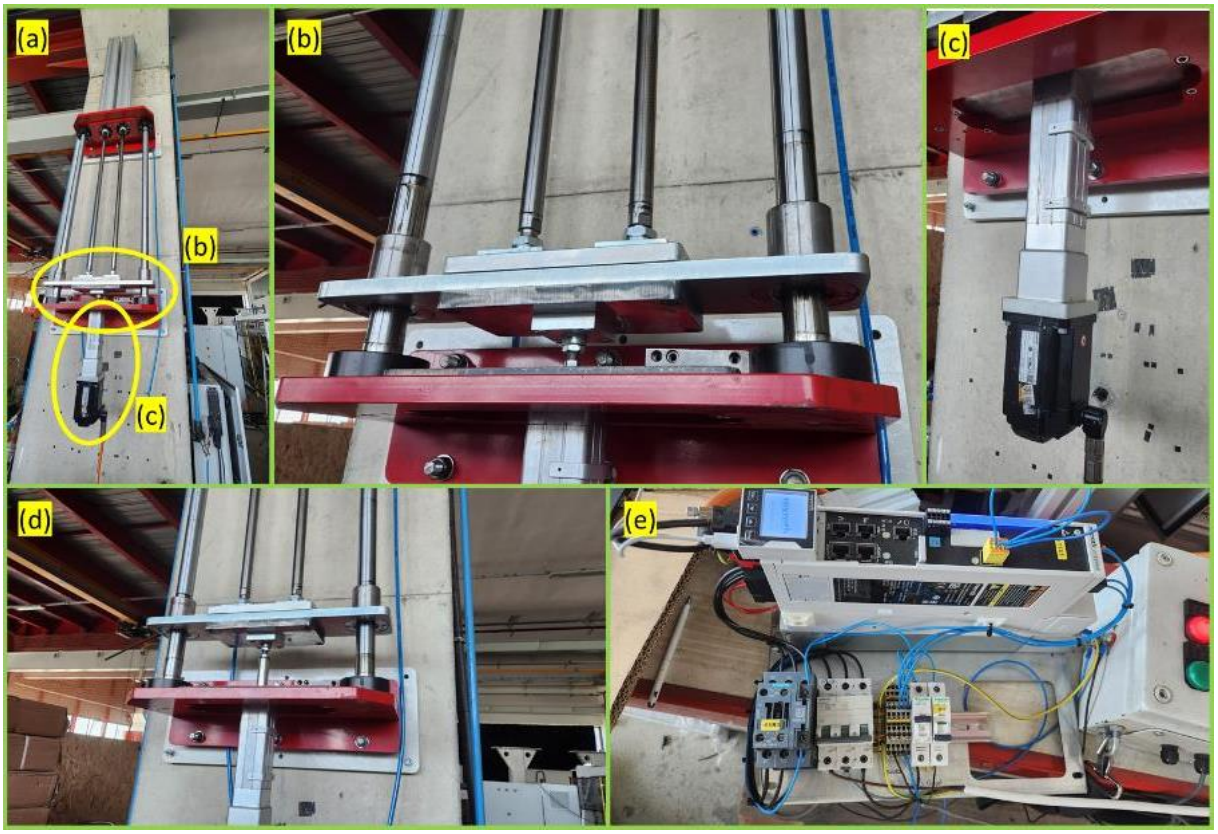


Figure 8:(a) (b) (c) (d) Mechanical side of the test set-up (e) Electrical side of the test set-up

Table 10: Characteristics of the test setup and force outputs

Number	Description	Symbol	Value	Unit
1	Idle operating mass of the system	msys	50	kg
2	Idle operating force on the EMC	Nsys	490.5	N
3	Pneumatic Cylinder Piston Diameter	Dp	125	mm
4	Force applied to EMC at 1 bar pressure	F_1bar	2943.625	N
5	Force applied to EMC at 1.5 bar pressure	F_1.5bar	4170.188	N
6	Force applied to EMC at 2 bar pressure	F_2bar	5396.75	N
7	Force applied to EMC at 3 bar pressure	F_3bar	7849.875	N
8	Force applied to EMC at 6 bar pressure	F_6bar	15209.25	N

7. RESULTS AND DISCUSSION

7.1. EMC with ball screw and nut

A total of 231,109 cycles were run with the pneumatic force against the direction of movement of the system. 183,704 cycles of this study were completed without failure. Failures occur after 183,704 cycles. The system completed a total of 41,467 cycles at a speed of 3000 mm/min and a total of 189,345 cycles at a speed of 5000 mm/min. It ran for 18,496 cycles without pressure effect. 27,010 cycles were performed at 1 bar pressure, 24,957 cycles at 1.2 bar pressure, 45,029 cycles at 1.5 bar pressure, and 115,617 cycles at 2 bar pressure. The effects of pressure and speed changes on the system can be understood from the motor's torque/force and temperature values. It can be seen that there is a 2.5% increase in the motor % torque/force value as the speed increases. As the pressure increases there is a 44% increase in the torque/force value. With both speed and pressure increase, there is a 68% increase in torque/force. As the speed and load change, the force required by the motor to move the system increases, causing the motor to heat up. 2 bar pressure and 5000 mm/min speed are the most demanding conditions for the system. Under these conditions, the maximum motor temperature was 63.1°C and the maximum torque/force was 94%.



Figure 9: After EMC test with ball screw

The product resulting from the EMC project has been tested and the reactions of the system under the influence of pressure and speed changes have been observed. The system has been tested for about 6 months, although it was unclear before. The endurance test was carried out under a varying load of 0-2 bar and a lack of lubrication of the electromechanical cylinder internal mechanics was observed. For this reason, it was thought that there was wear in the internal mechanical structure.

7.2. EMC with trapezoidal screw and nut

Due to the lack of oil in the ball screw EMC system and the wear on the ball screw, the oil channels of the trapezoidal screw EMC system are more compact. This is because the efficiency of the trapezoidal system is much lower than that of the ball screw system.

The EMC with trapezoidal screw is currently connected to the test rig and undergoing testing. To date, it has completed 41000 cycles. These tests will continue with 30000 cycles without pressure effect at 1000 mm/min speed and 11000 cycles with 3 bar pressure effect at 2000 mm/min speed. Even taking into account the improvement in the design of the lubrication system and its trapezoidal nature, there has been an improvement in the heating problem of the EMC.

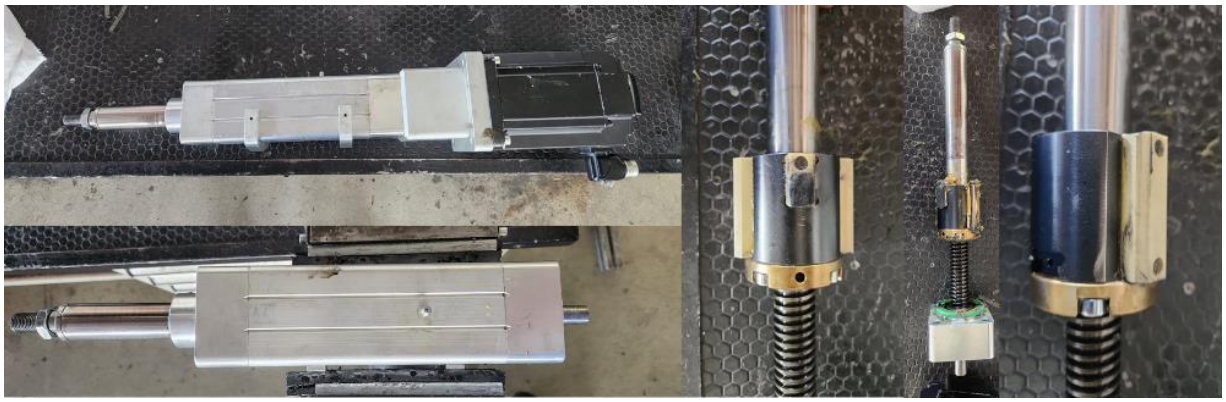


Figure 10: After EMC test with trapezoidal screw

8. CONCLUSION

As a result, the aim is to develop high-precision systems by designing, manufacturing and testing the developed EMC systems with different actuator types such as ball screw nut and trapezoidal screw nut.

The future goal is to achieve 1 million cycles by improving the lubrication mechanism of the internal mechanism of the ball screw type EMC and restarting the test. Similarly, if the design of the EMC trapezoidal screw needs to be revised based on the test results, it will be revised and put into mass production after achieving at least 1 million cycles.

REFERENCES

1. **316 (1.4401).4401) stainless steel. (n.d.).** https://bircelik.com/en/category/316-1-4401-

2. **BOSCH REXROTH (EMC), (n.d.),** Electromechanical Cylinders EMC catalogue

3. **BOSCH REXROTH SCREW ASSEMBLİES., (n.d.),** Ball screw assemblies BASA/Planetary screw assemblies PLSA

4. **Budynas, R. G., & Nisbett, J. K. (1972).** Shigley's Mechanical Engineering design. http://ci.nii.ac.jp/ncid/BA79780428

5. **HİDROPAR HAREKET KONTROL TEKNOLOJİLERİ MERKEZİ SANAYİ VE TİCARET ANONİM ŞİRKETİ , info@hktm.com.tr. (n.d.).** Elektrikli silindirler. https://www.hktm.com.tr/elektrikli-silindirler

6. **Hibbeler, R. C. (2017).** Mechanics of materials in SI units. Chapter 13.

7. **ISO 15552-2018 International Standard., (2018),** Pneumatic fluid power — Cylinders with detachable mountings, 1 000 kPa (10 bar) series, bores from 32 mm to 320 mm — Basic, mounting and accessories dimensions

8. **IS0 2904:1977 International Standard., (1977),** ISO metric trapezoidal screw threads

9. **MITCalc. (n.d.).** MITcalc - Power screws, design, calculation and check. https://www.mitcalc.com/doc/powerscrew/help/en/PowerScrew.htm

10. **Parr, A., (1991),** "Hydraulics and pneumatics: a technician's and engineer's guide". Choice/Choice Reviews, 29(01), 29–0334. https://doi.org/10.5860/choice.29-0334

11. **Tezpar Takım Tezgahları inşaat Otomotiv San. Tic. Ltd. Şti. (2024, January 23).** Tezpar - Trapez Vida imalatı. TEZPAR - Trapez Vida Imalatı. https://tezpar.com.tr/

12. **Ugural, A. C., & Fenster, S. K. (2011).** Advanced mechanics of materials and applied elasticity. Pearson Education.

THE DESIGN OF A ROTATING MODULAR UPPER LIMB PROSTHETIC WRIST UNIT

A. Ali GÜRLER, aykut.guler@proted.com.tr Proted Prosthetic & Orthotics INC, 06378, Ankara, Turkey

E. İlhan KONUKSEVEN, *konuk@metu.edu.tr* Middle East Technical University, 06800, Ankara, Turkey

ABSTRACT

This design study investigates a Prosthetic Wrist Unit for upper limb amputations using the Design Thinking methodology. It covers Problem Definition, Information Gathering, Concept Generation and Evaluation, Product Architecture, Configuration Design, Parametric Design, Detail Design, and Production. The study aims to create a small prosthetic wrist unit (50 mm diameter, 50 mm length, less than 125 gr), provides 360° rotation, connects easily with prosthetic hands, enables electric and data transfer, and is controllable via EMG sensors. This research contributes to prosthetic product design, enhancing the quality of life for amputees.

ÖZET

Bu tasarım çalışması, Üst Ekstremite Amputasyonları için Protez Bilek Ünitesini araştırmaktadır ve Tasarım Odaklı Düşünme metodolojisini kullanmaktadır. Problem Tanımı, Bilgi Toplama, Kavram Oluşturma ve Değerlendirme, Ürün Mimarisi, Konfigürasyon Tasarımı, Parametrik Tasarım, Detay Tasarımı ve Üretim adımlarını kapsamaktadır. Çalışma, küçük (50 mm çap, 50 mm uzunluk, 150 gr'dan az), 360° dönebilen, protez ellere kolayca bağlanabilen, elektrik ve veri transferi yapabilen, EMG sensörleri sayesinde kas hareketleriyle kontrol edilebilen bir protez bilek ünitesi yaratmayı amaçlamaktadır. Bu araştırma, ampütelerin yaşam kalitesini artırarak protez ürün tasarımına katkıda bulunmaktadır.

Keywords: Prosthetics, Wrist Unit, Amputation

INTRODUCTION

Prosthetic hands without wrist rotation struggle to mimic natural hand movements, hindering tasks that need precise hand and object orientation. This limitation affects the prosthetic's usefulness and can frustrate users. The project incorporates a motor-controlled wrist unit in

the prosthetic hand to address this, allowing for finer hand direction control and more intuitive item handling. The project aims to enhance the adaptability and functionality of prosthetic hands through wrist rotation, improving users' quality of life.

Key goals include ensuring the wrist unit can rotate fully and continuously, carry weight, withstand moment and rotational inertia, and remain compact and energy-efficient under various conditions. Additionally, the unit must lock securely, rotate precisely, and integrate with existing prosthetic hand. The report will cover market and patent search, literature review, problem definition, project planning, conceptual design, and selection of the best concept based on evaluation criteria. The final design stage will detail the properties, calculations, software analysis, manufacturing, and testing plans. The report concludes with a summary of achievements and future improvement suggestions.

PROBLEM DEFINITION

Prosthetic hands without wrist rotation struggle to replicate natural movements and gestures, limiting tasks requiring precise positioning. This deficiency hampers adaptability and functionality, causing user frustration. To address this, the project integrates a motor-controlled wrist unit into prosthetic hands, enabling fine hand orientation adjustments for a more natural grip. The goals include ensuring the wrist unit allows full, continuous rotation, locks securely, operates quietly, and is compact, rigid, lightweight, smooth, and affordable. It must be suitable for men, women, and children, allow electricity and data transfer, consume low energy, and handle daily activities. It should withstand various forces and thermal conditions without lubricant leakage. Commercial product information that helps identify wrist unit needs is given below.

Goals	Requirement
Full Continues Rotation	360 Degree Endless Rotation
Quiet Operation	< 45 dB
Compact	Diameter < 50 mm, Length < 50 mm
Lightweight	< 150 gr
Fast Working	< 5 s Full Rotation Time
Low Energy Consumption	< 5 W
Axial Carriage	> 30 kg
Moment Carriage	> 2 Nm
Torque Capacity	> 2 Nm

TABLE 1: GOALS AND REQUIREMENTS

STATE OF ART-INFORMATION GATHERING

Commercial Products

Three main prosthetic wrist rotators are easily accessible: Ottobock Electric Wrist Rotator, Fillauer MC ProWrist Rotator, and Ossur i-Limb Powered Wrist Rotator. These products have similar specifications and features with minor differences.

Ottobock Electric Wrist Rotator: The most well-known product due to the company's reputation. Specific details on its working principle, systems, and design are unavailable, but some specifications are known.

Fillauer MC ProWrist Rotator: An alternative to Ottobock, with limited information on its working principle and systems, but some specifications are known.

Ossur i-Limb Powered Wrist Rotator: Another alternative, which has been removed from the company's site, indicating potential discontinuation. Limited specifications are available, without details on its working principle or systems.

Comparison

Due to limited documentation, we could only compare some specifications of the three products, which are similar overall. Fillauer: Faster than the other two, but the speed of the others is sufficient. Ottobock: Approximately 2/3 lighter than the other two, though their weights are also acceptable. Other comparisons are not possible due to limited information. Key specifications include noise level (38.5 dB), operating temperature range (0-40°C), and dimensions. Price information, crucial for affordability, is unavailable. Specifications and product images are shown below.

Specifications-Products	Ottobock	Fillauer	Ossur
Weight	96 g	168 g	150 g
Speed	17 rpm	28 rpm	15 rpm
Voltage	7.2 V	7.2 V	6-8.4 V
Current	1 A	?	6 A
Length	? mm	70 mm	56 mm
Diameter	? mm	47 mm	? mm
Torque	? in-lb	15 in-lb	? in-lb
Static Load	? kg	22.7 kg (from all ways)	90 kg (axially)
Temperature	? degree C	0-44 degree C	0-40 degree C
Decibel	? dB	38.5 dB (1 m)	? dB
Price	?	?	?

FIGURE 1: COMMERCIAL PRODUCT INFORMATION

State-of-the-Art on Related Technologies

In this section, detailed information related to the literature survey is provided. The goal is to offer a comprehensive understanding of various aspects of the project topic. The state of the art on related technologies and mechanisms is examined. The intricacies of different driving and locking mechanisms, as well as the electric transfer mechanism, are explored to highlight their unique characteristics and operational details.

Locking-Transmission Subsystem:

- Gear Mechanisms:

1. Kapelevich et al.: Developed self-locking gears that don't rely on clutch or brake systems, with higher efficiency and less heat generation than worm gears. However, they are costly to manufacture due to specialized tools and new gear profiles.
2. Takayama and Hisamatsu: Created a system using small vibrations to reduce friction in worm gears, enhancing back drivability with minimal force.
3. Popper and Wessen: Designed a meshing system for worm gears allowing almost any reduction ratio, where the driver gear can drive in both directions but not be back driven.

- Brake Systems:

1. Electro-Mechanical Brake Systems: Despite many patents and designs, no marketed EMB systems exist. They save space and are faster than hydraulic brakes but require a DC motor, making them complex and less favorable.
2. Mechanical Brake Systems: These brakes don't need an actuator but are manually activated, like hand tools. A similar locking mechanism is noted in the patents section.
3. Hydraulic Brake Systems: Unsuitable for our design due to maintenance needs and weight issues.

- Pin Lock Mechanism:

1. Designed by Cappello et al., this mechanism uses a cylindrical pin and a step motor to lock the wrist in the pronation/supination axis, adaptable to our design.

- Ball Lock Mechanism:

1. Utilized in micro-switching valves, this system uses steel balls to lock components precisely. However, it requires additional space for solenoids and can cause heating issues, limiting rotation options.

- Multi-Function Myoelectric Hand:

1. A novel self-locking mechanism using a cam-ball clutch, enabling unidirectional power transmission and stability, with four distinct operating modes for driving and locking.

Turning Subsystem:

- Transmission System I: Gill [12] describes a single-degree-of-freedom wrist unit with an actuator module that rotates various components and transmits rotation to the prosthetic hand. The module includes a motor, gears, and bearings, with a planet gear system to minimize backlash.
- Transmission System II: Lorenzo et al. [3] detail a prosthetic wrist with a drive motor and a two-stage cycloidal reduction mechanism. The first stage involves satellite wheels and a central wheel with a reduction ratio of 8:1. The second stage has a cycloidal mechanism with a reduction ratio of 33:1, resulting in a total reduction ratio of 264:1.

Actuator Types: According to Binda (2018)[7], the key criteria for choosing an actuator for a prosthetic wrist are torque, size, and weight. The three main motor types are:

- DC Motors: High RPM, small size, easy to control, high torque at low speeds, and available in brushed (low cost) and brushless (quiet, efficient) variants.
- Step Motors: Low RPM, high torque, precise positioning, but noisy and less efficient than DC motors.
- Servo Motors: High RPM, high torque, larger and heavier, complex control.

Based on the literature and commercial products, brushless DC motors are recommended, but all motor types will be considered as the project progresses.

Electrical Transfer Technologies:

Various electrical transfer technologies for rotating interfaces include cable-wrap, goose-neck, twist capsule, slip ring, and rolling contact connector (RCC).

- Cable-wrap and Twist Capsule: Compatible with twisted shielded pairs and have high angular ranges, but they cannot rotate continuously.
- Goose-necks: Can rotate more than 360° but are not suitable due to angular limitations. Detailed information and images are in [18].
- Slip Rings: Widely used for continuous rotation without restrictions, consisting of brush blocks, rotor, and stator. MOFLON’s MFS Series is an example of a waterproof slip ring. Slip rings require precise alignment and lubrication to reduce friction and wear.

- Rolling Contact Connector (RCC): Also known as a brushless slip ring, transfers electrical signals across a rolling contact interface, composed of an inner ring, flexible planets, and an outer ring.

Housing & Shielding:

For protection, the wrist unit should have durable, customizable, lightweight housing, ideally made from carbon fiber, which is light yet strong. Epoxy-impregnated carbon fiber sheets allow for customization to meet the different needs of amputees. For moisture protection, the contacts on the wrist coupler should be internally located and shielded by a plastic casing

CONCEPT GENERATION

This section covers the conceptual design processes, including concept development and evaluation. We reviewed literature, patents, academic papers, and commercial products to identify suitable concepts. This investigation expanded our state of art, with findings shared here. Concepts were then evaluated against project requirements using decision matrices. Ultimately, the best concept is presented based on these evaluations.

Concept Development and Presentation

In this section, the project is split into subfunctions, and concepts are developed for each subfunction. The functional decomposition method is used for this purpose. Various concepts are created according to functional decomposition. Then, a morphological chart is created with these concepts. Explanations for each concept are also provided.

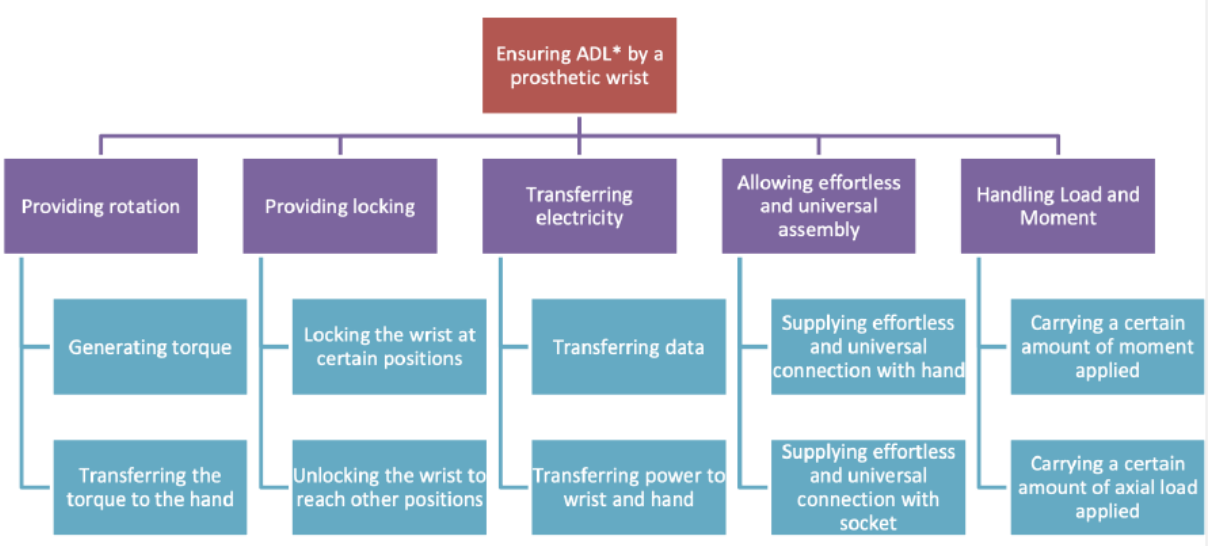


FIGURE 2: FUNCTIONAL DECOMPOSITION

Explanation of Concepts

Providing Rotation:

- Internal Gear Mechanism: Internal gears have teeth cut into their inner surfaces, engaging with external gears to transmit motion and power. They feature a self-locking mechanism that resists motion under external forces, making them suitable for applications requiring fixed positions and efficient rotational motion.
- Planetary Gear System: This system includes fixed outer and sun gears with multiple planetary gears rotating freely. Motion from the sun gear transfers through the planetary gears and coupling mechanism, providing versatile motion transmission.
- Planetary Gear System with Ball Bearing: Incorporates fixed planetary gears and a stationary sun gear, with a ball bearing in the outer part facilitating rotational motion. This system includes a self-locking mechanism, enhancing stability without additional components.
- Harmonic Drive System with Ball Bearings: Utilizes an elliptical rotating gear and a circular outer gear to create a rotational drive. Ball bearings rotate to sustain the motion of the elliptical gear, providing efficient and self-locking operation.
- Harmonic Drive System with Frictional Contact: Rotational energy from the motor transfers to an elliptical gear through frictional contact. This system features a harmonic drive between the elliptical and circular gears, offering self-locking capabilities.
- Cycloidal Drive: Composed of an input shaft, eccentric bearing, two cycloidal disks, and a housing with pins and rollers. Eccentric motion drives the cycloidal disks, producing reverse rotation at reduced speeds. It includes a self-locking mechanism for stability.
- BLDC Motor: Brushless DC motors are commonly used for their high efficiency and precise control in prosthetic applications.
- Servo Motor: Servo motors are favored for position control due to their accuracy and ability to maintain set positions.

These mechanisms vary in design and application, offering different advantages for achieving rotational motion and stability in prosthetic designs.

Locking Mechanisms:

- Ball Locking Mechanism: This mechanism uses balls and holes in a rigid body. When the motor rotates, the balls move into place within the rotating part, locking the system. Solenoids and springs control the ball motion: the solenoid helps balls enter holes during rotation, and the spring locks them in place afterward. Disadvantages include

increased energy consumption and potential damage to components due to solenoid heat.

- Pin Locking Mechanism: This system employs a pin-to-lock gear mechanism controlled by a solenoid. The pin disengages from the gear gap when the solenoid activates, allowing easy rotation. After rotation, the solenoid deactivates, and the pin locks the mechanism in place. Compared to ball locking, it offers more precise locking locations but shares the drawbacks of energy consumption and solenoid heating.
- Worm Gear Lock Mechanism: Worm gears prevent back driving, enabling them to lock when external force is applied. Positioning the worm gear perpendicular to the turning table can complicate design due to space requirements, while positioning it parallel resolve some issues but may necessitate specially manufactured components.
- Harmonic Drive Lock Mechanism: Harmonic drives transmit torque through a pure couple, allowing for torque sensor integration without radial force interference. This feature enables back-drivability for compliant movements in robotic applications, though high-ratio harmonic drives lack back drivability.
- Pad Brake Lock Mechanism: Like car disk brakes, a pad brake can be applied to the turning table or gears. This requires an actuator and significant space. To conserve energy, it should only be released when turning the wrist, posing design challenges.

These mechanisms offer various locking solutions with specific advantages and challenges in prosthetic applications.

Transferring Electricity:

- Slip Ring: A slip ring facilitates continuous rotation in machinery by transmitting power and signals between stationary and rotating parts. It comprises a rotor (rotates with the machinery) and a stator (stationary structure), forming band-pass circuits for independent electrical transmission. Key components like connectors ensure reliable operation.
- Capsulated: Protects wires by enclosing them, preventing damage—a common method for wire protection.
- Pancake Slip Rings: Organizes conductors in concentric rings on a flat disc aligned with the shaft, compact but prone to wear and debris accumulation along its axis.
- Through Bore: Features a central opening allowing cables to pass through, ideal for applications needing uninterrupted 360-degree rotation, ensuring low electrical noise and reliable connections.
- Mercury-Wetted: Uses liquid mercury for stable, low-resistance connections, though safety concerns due to toxicity require careful handling.

- Rotating Contact Connector (RCC): Utilizes rolling contact for electrical signal transmission, reducing parasitic torque and ensuring stable operation with low inter-contact resistance. Materials like beryllium copper and aluminum alloys optimize endurance and conductivity.
- Cable Wrap: Clock-spring configuration compatible with twisted pairs, offering a significant angular range (100°-700°) for rotational applications.

These technologies offer diverse solutions for continuous rotational applications, each with specific advantages and considerations.

Allowing Effortless and Universal Assembly:

- Commercial and Magno Flex Connectors: Commercial products typically use standard modules for wrist-to-hand connection, involving a push and small turn for coupling. Magnetic locks automatically connect by aligning the wrist tip with a conical shape using magnetic fields, suitable mainly for lower body prosthetics due to space requirements.
- Rotary-Pin Type Connection: This mechanism employs a spring plunger lock housed in a cylindrical body. It ensures secure locking with a spring-loaded plunger that can be easily engaged or disengaged, offering simplicity and functionality for securing components in wrist and hand applications.
- Push-and-Turn Locking Mechanism: Like those on medication containers, this mechanism requires downward pressure and simultaneous rotation to open. It provides secure access while incorporating child-resistant features, suitable for ensuring safe and easy assembly in wrist systems.

CONCEPT EVALUATION

In this section, evaluation criteria and weighting factors are created according to the problem definition and project requirements. More specific criteria for each subfunction are also established. Four decision matrices for each subfunction are made based on these criteria, and unsatisfactory solutions are eliminated. With the satisfactory solutions, complete design concepts are created. The best concept is then chosen from these according to the decision matrix.

Evaluation Criteria

Design Criteria for General Concept:

- Locking Capability: Essential for daily activities like handling objects such as glasses, forks, or spoons.

- Full Rotation: Overcomes the limitation of typical prosthetic arms by providing complete wrist rotation.
- Rotation Time Limit: Rotation speed must be optimal for practical use.
- Energy Consumption: Must be efficient to ensure suitable battery life without adding excessive weight.
- Noiseless Running: Operation should be quiet to avoid disturbing the user.
- Load Carriage: Capable of handling up to 30 kg, meeting user needs and requirements.
- Ease of Assembly: Easy to assemble and disassemble, ensuring user-friendly application.
- Operating Under Different Thermal Conditions: Should function reliably in various climates and temperatures.
- Cost: Affordable pricing to make the product accessible.
- Manufacturing: Production should be straightforward and align with company capabilities.
- Angular Precision: Stops accurately in desired positions during rotation.
- Compact and Lightweight Design: Must be lightweight and compact for user comfort and practicality.
- Lifetime: Expected to be durable, with a minimum operational lifespan of 2 years.
- Rigidity: Ensures structural integrity throughout its lifespan.

Design Criteria for Sub-Functions:

- Turning Sub-Function Criteria:

1. Angular Precision: Ensure precise positioning capability for daily life activities.
2. Rotation Time Limit: Rotation speed should be efficient for practical use.
3. Full Rotation: Provide unrestricted rotation like a human arm.
4. Ease of Production and Cost: Ensure cost-effective and easy manufacturing.
5. Noiseless Running: Operation should be within acceptable noise limits.
6. Providing Enough Torque: Capable of handling tasks like turning while holding objects.
7. Compact and Lightweight: Design should meet size and weight restrictions.

- Locking Sub-Function Criteria:

1. Locking Time Limit: Ensure quick and efficient locking/unlocking.
2. Noiseless Locking: Operation should be quiet to meet noise limits.
3. Need for More Actuator: Minimize additional space and weight for extra mechanisms.

4. Self-Locking Capability: Provide reliable self-locking without additional components.
5. Compact and Lightweight Design: Ensure the design meets size and weight constraints.
6. Ease of Production and Cost: Focus on easy production and affordability.
7. Angular Precision: Precise locking for user convenience.

- Electric and Data Transfer Sub-Function Criteria:

1. Continuous Full Rotation: Ensure cables and transfer elements allow unrestricted movement.
2. Transferring Data and Electricity: Enable seamless transfer of power and data to prosthetic hand components.
3. Assembly: Facilitate convenient assembly of electrical and mechanical components.
4. Cost: Ensure affordability of electronic components for commercial viability.
5. Compact: Design should be compact to fit limited space requirements.

- Assembly Sub-Function Criteria:

1. Universal: Compatible with various prosthetic hand brands without modification.
2. Ease of Assembly: Designed for easy assembly to accommodate users with disabilities.

Best Concept

The decision of the best concept is chosen by the given below method. According to the created sub-function design criteria, the best sub-function mechanisms are decided. Then, with these chosen sub-function mechanisms, 12 concepts are created. According to the created concept design criteria, the best concept is decided. The decided mechanisms and concepts given below. The assembly mechanism has 2 different mechanisms. The decided assembly mechanism is a standard commercial mechanism, however, to achieve a unique mechanism, a second assembly mechanism was created inspired by a quick hydraulic coupling mechanism.

Hypocycloid Mechanism: The design enables a 360-degree rotation through an elliptical object in the center engaging with internal gears, which push against stationary external gears. This interaction provides a natural and comprehensive range of motion, ensuring seamless and precise control.

Self-Locking Gear Ratio: The gear ratio ensures the prosthetic wrist locks securely in position without external mechanisms, enhancing precision, safety, and stability.

Pancake Slip Ring Mechanism: A flat, disk-shaped pancake slip ring enables continuous electrical power and data transfer between stationary and moving parts, ensuring uninterrupted flow of electrical signals and data for the prosthetic's components.

Commercial Assembly Mechanism: To enhance durability and user-friendliness, a commercially available assembly mechanism is combined with the self-locking hypocycloid mechanism, minimizing wear and tear and ensuring long-term reliability.

Renewed Assembly Mechanism: A mechanism inspired by the hydraulic quick connect (HQC) system has been designed with a key difference: the balls are located inside the mechanism, unlike the external placement in traditional HQC systems. This mechanism operates by pushing the balls through a channel that restricts their axial movement. The balls secure hand unit and wrist unit in place, ensuring a stable connection.

PRODUCT ARCHITECTURE-CONFIGURATION DESIGN-PARAMETRIC DESIGN-DETAIL DESIGN

After the concept decision, the product design details are determined. Then, according to determined architecture, configurations and parameters, detailed design is made. Initially, the physical elements are arranged to carry out the intended functions, forming the architectural design. Following this, the first complete design is created, known as the configuration design. Subsequently, final dimensions, materials, and tolerances are determined during the parametric design phase. Finally, detailed drawings and specifications are produced in the detail design stage. Each phase builds on the previous one, refining the product design until it is ready for production.

Properties of Designed System

To start with, the product features a unique and innovative coupling design. This concept was adopted from hydraulic systems known for their high safety factors. It is believed that a similar approach could be implemented in this design. Additionally, a different drive system for the wrist unit was utilized, specifically a hypocycloidal drive system, unlike the commonly used harmonic drive in other products on the market. The hypocycloidal drive system offers potential advantages in terms of backlash level and lifespan. Furthermore, a different method for electric and data transfer was implemented using a pancake slip ring. These changes were necessary due to the design layout in the casing. The combination of these sub-mechanisms can be seen in the figures below.

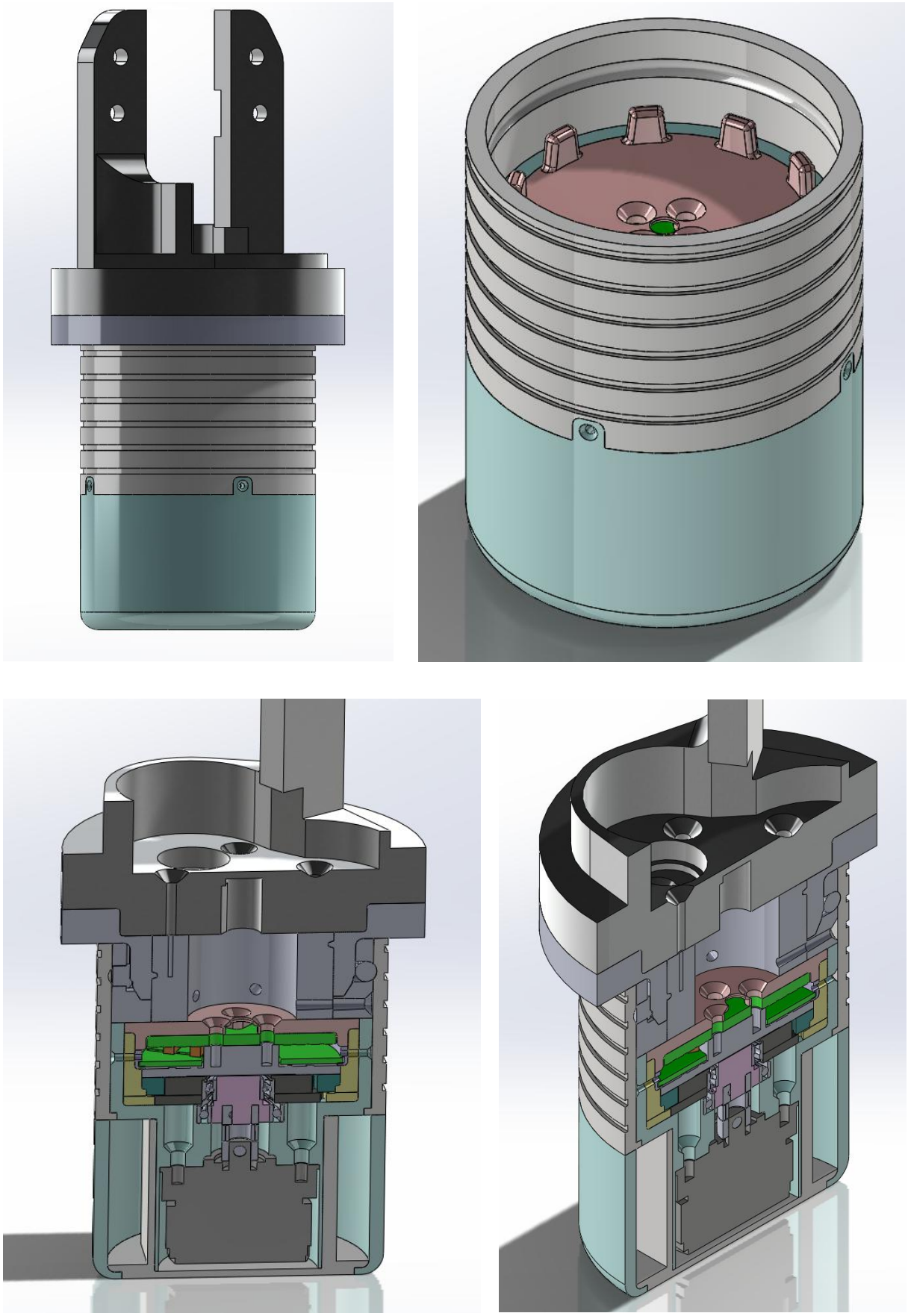


FIGURE 3: MODEL VIEWS

Engineering Calculations

The detailed design of the system is completed before starting the manufacturing of the prototype system. In the engineering calculation, weight and dimension of the system; used as optimization criteria. The optimization process is realized, according to BLDC motor parameters, to achieve the necessary speed, torque, angular precision and energy consumption values, needed reduction ratio is determined; also, this optimization process consists of the determination of the gear mechanism's gear teeth values to achieve this reduction ratio. According to calculations, the necessary reduction ratio comes around 300. Thanks to hypocycloidal gear mechanism, in the place of 35 mm diameter and 6 mm height, design achieved this reduction ratio. This gear mechanism's 4 gears have around 30 teeth per gear, according to optimization and working principle, some has a little mor some have a little less tooth.

Analysis Results

To validate the design, some analyses are conducted. These analyses are made for force and momentum carriages, and capacity of torque that the wrist unit can apply, strength of the gear mechanism and gear tooths. Also, some tests are conducted which are made for turning speed, energy consumption values, noise decibel values, etc. According to results of these analyses and tests, future works are determined. Most of the results are satisfactory, but since this product is a prototype, some of the design parameters must be improved. These are decibel values, energy consumption values and torque capacity. The result can be seen in the Discussion-Conclusion Part, Table 2.

PRODUCTION

The final system has nearly 50 parts. Most of these parts can be produced by machining operations. Some of these parts need to be metal and some others plastic. According to system criteria Aluminum 7075 T5 was chosen as metal material, and POM-C was chosen as plastic. Another material is used for slider bearing and the material is iglidur. With machining of these materials, most of the parts produced thanks to facilities of Proted Prosthetics & Orthotics INC. Some other parts like bearings, screws, pancake PCB, pancake connectors, BLDC motor, etc. purchased. Also, some parts are manufactured by 3D printing with the use of TPU 85A, PLA, etc. One of the most important aspects of the production Is that the hypocycloidal gears are produced by wire erosion with Titanium.

DISCUSSION-CONCLUSION

As a result of the studies conducted, a prototype at the product level has been developed. While the prototype meets most of the expected requirements, some deficiencies have been identified. The most critical issues affecting the system's functionality are the insufficient torque transmitted to the hand unit and the high noise and vibration occurring when the wrist unit is operating. To address these critical issues, special lubrication preferences, gear material preferences, mechanism tolerance preferences, mechanism dimension preferences, and some design preferences will be modified. You can see the outputs obtained in the table below.

Goals	Requirement	Output
Full Continues Rotation	360 Degree Endless Rotation	360 Degree Endless Rotation
Quiet Operation	< 45 dB	Unknown but not satisfied
Compact	Diameter < 50 mm Length < 50 mm	Diameter = 40mm Length = 37 mm
Lightweight	< 150 gr	Around 100 gr
Fast Working	< 5 s Full Rotation Time	2-4 s
Low Energy Consumption	< 5 W	Around 4 W
Axial Carriage	> 30 kg	> 45 kg
Moment Carriage	> 2 Nm	Around 4 Nm
Torque Capacity	> 2 Nm	Unknown but not satisfied

TABLE 2: OUTPUT

ACKNOWLEDGEMENT

This study was supported by Tübitak-Teydeb-“Döner Modüler Üst Ekstremite Bilek Tasarımı”, Proted Prosthetics & Orthotics project.

REFERENCES

[1] url: https://www.faulhaber.com/fileadmin/Import/Media/EN_TI_DC-MOTORS.pdf.

[2] url: https://www.steepergroup.com/prosthetics/upper-limb-prosthetics/espire%E2%84%A2-elbow/system-components/espire-power-options/.

[3] Fondazione Si Italiano Tecnologia [It]; Istituto Naz Per Iassicurazione Contro Gli Infortuni Sul Lavoro [It] Lince Andrea [It]; Traverso Simone [It]; Gruppioni Emanuele [It]; Laffranchi Matteo [It]; De Michieli Lorenzo [It]. Prosthetic Wrist Unit. URL: https://patents.google.com/patent/US20210259856A1/en?oq=US2021259856A1. Aug. 2021.

[4] Edmund Biden Arthur Zinck Oyvind Stavdahl and Peter Kyberd. “Design of a Compact, Reconfigurable, Prosthetic Wrist”. In: Applied Bionics and Biomechanics 9 (2012). doi: 10.3233/ABB-2011-0043. url: https://doi.org/10.3233/ABB-2011-0043.

[5] Furkan Aydo˘gan et al. “R1-Literature Survey”. In: (Oct. 2023).

[6] Furkan Aydo˘gan et al. “R2-Problem Definition and Design Specifications”. In: (Nov. 2023).

[7] Jasper Binda. “Multiple degrees of freedom wrist prostheses: Design of an electrically powered two DoF wrist prosthesis”. In: (2018).

[8] Issam Bourai et al. “Prosthetic Gripper with a Powered Wrist”. In: (2020).

[9] Leonardo Cappello et al. “A 2-Degree-of-Freedom Quasi-Passive Prosthetic Wrist With Two Levels of Compliance”. In: IEEE Robotics and Automation Letters 8.3 (2022). doi: 10.1109/lra.2022.3208692. url: https://doi.org/10.1109%2Flra.2022.3208692.

[10] Jun-Uk Chu, Dong-Hyun Jung, and Yun-Jung Lee. “Design and control of a multifunction myoelectric hand with new adaptive grasping and self-locking mechanisms”. In: 2008 IEEE International conference on robotics and automation. IEEE. 2008, pp. 743–748.

[11] SAHIL VIKAS DANGE. DESIGN OF A WORKING MODEL OF AN UPPER LIMB PROSTHESIS: WRIST MECHANISM. 2017.

[12] Hugh Gill. System for Control of a Prosthetic Device. URL: https://patents.google.com/patent/US10369024B2/en. Aug. 2019.

[13] Tadahiro Hasegawa et al. “Multi-directional micro-switching valve chip with rotary mechanism”. In: Sensors and Actuators A: Physical 143.2 (2008), pp. 390–398.

[14] ISO. ISO - International Organization for Standardization. ISO, Jan. 2019. url: https://www.iso.org/home.html.

[15] Alexander L Kapelevich and Elias Taye. “Self-locking gears: Design and potential applications”. In: American Gear Manufacturers Association Fall Technical Meeting. 2010, pp. 212–219.

[16] Congcong Li et al. “A Review of Electro-Mechanical Brake (EMB) System: Structure, Control and Application”. In: Sustainability 15 (Mar. 2023), p. 4514. doi: 0.3390/su15054514.

[17] Lois Liow, Angus B Clark, and Nicolas Rojas. “Olympic: A modular, tendon-driven prosthetic hand with novel finger and wrist coupling mechanisms”. In: IEEE Robotics and Automation Letters 5.2 (2019), pp. 299–306.

[18] P-A M¨ausli, G Feusier, and V Gass. “Rotating electrical joints with continuous metallic connections”. In: 10th European Space Mechanisms and Tribology Symposium. Vol. 524. 2003, pp. 33–38.

[19] Inc MOFLON TECHNOLOGY. MOFLON: Provide High Performance 360° Rotary Solutions for Worldwide. https://www.moflon.com/ [Accessed: 21/10/2023].

[20] Sanghwa Park. “Fundamental development of hypocycloidal gear transmissions”. PhD thesis. University of Texas at Austin, 2005. url: https://api.semanticscholar.org/CorpusID:109131227.

[21] B. Popper and D. W. Pessen. “The Twinworm Drive: A Self-Locking Worm-Gear Transmission of High Efficiency”. In: Journal of Engineering for Industry 82.3 (Aug. 1960), pp. 191–198. issn: 0022-0817. doi: 10.1115/1.3663030. eprint: https://asmedigitalcollection.asme.org/manufacturingscience/article-pdf/82/3/191/6494453/191_1.pdf. url: https://doi.org/10.1115/1.3663030.

[22] LUCZAK ADAM RAJEWSKI BARTOSZ. Active Prosthetic Wrist. URL: https://worldwide.espacenet.com/patent/search/family/069315488/publication/EP3695813A1. Aug. 2020.

[23] Manuel Reyes. Prosthetic Wrist. URL: https://patents.google.com/patent/US2021330479A1. Nov. 2021.

[24] robocraze. “What is the Difference Between Servo Motor vs DC Motor”. In: (). url: https://robocraze.com/blogs/post/what-is-the-difference-between-servo-motor-vs-dc-motor.

[25] Chris Santoro, Ron Hayes, and Jason Herman. “Brushless Slip Ring for High Power Transmission”. In: (Sept. 2009). doi: 10.2514/6.2009-6673.

[26] Joseph Edward Shigley et al. Shigley’s Mechanical Engineering Design: Richard G. Budynas, J. KeithNisbett. McGraw-Hill Higher Education, 2008.

DEVELOPMENT OF A ROLL OVER PREVENTION CONTROL STRATEGY FOR AN ARTICULATED BUS EQUIPPED WITH ON-BOARD ELECTRIC MOTORS

Kerem Bayar, kerem.bayar@man.eu, Saracalar Mahallesi, Özal Bulvarı, No 212, 06750, Akyurt Ankara

ABSTRACT

Articulated buses equipped with electric drivetrain provide high degrees of freedom in terms of actuators for vehicle stability control algorithms. Through coordination of individual wheel braking/acceleration and articulation joint damping moment, the existing algorithms can be improved. With this background, this work focuses on developing a roll-over prevention control algorithm for an articulated bus equipped with on-board electric motors at middle and rear axles. The desired yaw and roll rates are tracked by utilization of the control allocation algorithm, based on the load transfer ratio, such that the possibility of roll over prevention is mitigated.

Keywords: roll over prevention, articulated bus, control allocation, yaw rate, roll angle, articulation angle, vehicle sideslip angle, on board electric motor

1. INTRODUCTION

Vehicle stability control for articulated buses is an area with research potential. The reason of this is the fact that the damping moment associated with the articulation joint provides an additional degree of freedom for generating additional / counter yaw moment for the rear and front compartments of the bus. The key question though, is how to incorporate the articulation damping moment control into the brake actuated vehicle stability control algorithm.

Moreover, considering an articulated bus equipped with on-board electric motors [DeNovellis et al. 2015] at the middle and rear axles, the yaw/roll moment control problem further becomes the subject of a control allocation problem [Bayar 2024], with individual front wheel braking, individual middle and rear wheel braking/acceleration, and the articulation damping moment, providing the actuation degrees of freedom.

In [Huang et al. 2023], active articulation steering is coordinated with wheel torque control through a model predictive control approach. However, it is not stated clearly in this work, how the coordination works; the control input vector consists of the wheel torques only.

In [Yang et al. 2022], a wheel torque control based skid steering control system is developed for a distributed drive articulated heavy vehicle. The developed control system is proposed to be the sole power source during steering, replacing the conventional hydraulic steering system of the vehicle.

In [Bayar 2024], the coordination of the articulation damping moment with individual wheel torque control is established within a control allocation algorithm with the purpose of yaw control of an electric articulated bus on low μ. The results show that the developed yaw controller outperforms the conventional articulation damping moment based algorithm, in terms of tracking the desired yaw rates and stabilizing the vehicle.

In [Xu et al. 2020] a 16 dof non-linear vehicle dynamics model is developed for analysing rollover dynamics of articulated vehicles. Results show that the roll stability decreases with the increase in vehicle speed, centroid height, and lateral slope angle, as expected.

The brief literature survey given above, sheds light onto the research need for focusing on the articulation damping moment – individual wheel torque control coordination, for better performing vehicle stability control algorithms developed for articulated buses. With this background, this work aims at developing a roll over prevention – direct yaw moment control algorithm for an articulated bus equipped with on-board electric motors. In other words, this work is an extension of [Bayar 2024], which concentrated on direct yaw moment control only, considering low μ. This one has the objective of roll control on high μ, as well. The organization of the paper is as follows: Section 2 outlines the vehicle dynamics model, used for testing the developed control algorithm. Section 3 explains the control algorithms for preventing roll motion and tracking desired yaw rate. Section 4 gives simulation results, and the work is concluded with Section 5.

2. THE VEHICLE DYNAMICS MODEL

The vehicle dynamics model used for simulations, is shown in Figure 1a and Figure 1b.

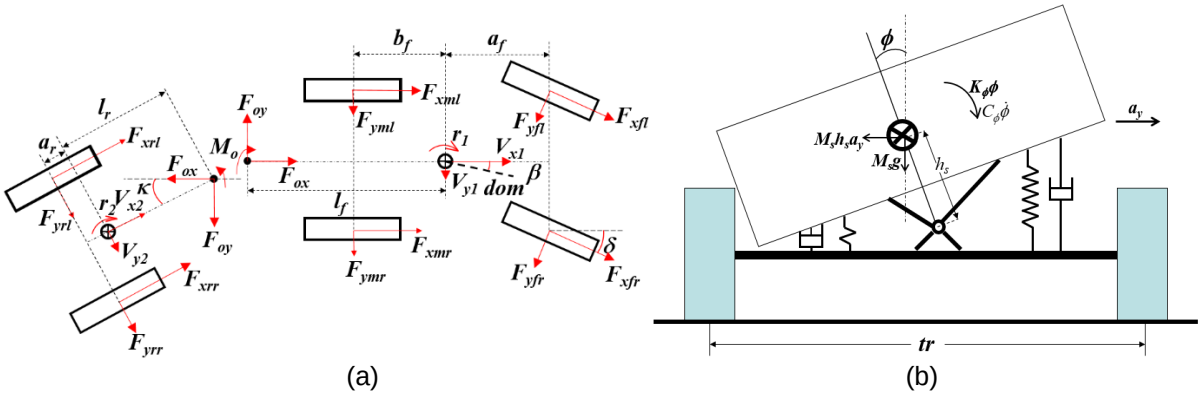


Figure 1 (a) The planar degrees of freedom, and (b) the roll model (for both front and rear compartments of the vehicle) used for simulations

where F_x and F_y represent the longitudinal and lateral tire forces, with *fl*, *fr*, *ml*, *mr*, *rl*, *rr* standing for front left, front right, middle left, middle right, rear left and rear right. V_{x1}, V_{x2}, V_{y1}, V_{y2}, r_1, r_2 represent the longitudinal and lateral speeds, and yaw rate of the front and rear compartments of the vehicle, respectively. β is the vehicle sideslip angle, κ is the articulation angle, δ is the steering angle, whereas "*dom*" stands for direction of motion.

For modelling the force / moment interaction between the front and rear compartments through the articulation joint, the forces F_{ox} and F_{oy} are used, along with the moment M_o. Regarding the roll motion, M_s is the sprung mass, h_s represents the distance between height of center of gravity and the roll center, ϕ is the roll degree of freedom, K_f and C_f are the overall roll stiffness and roll damping of the vehicle.

The equations of motion regarding Figure 1a for the front and rear compartments can be derived as follows (the derivation is not given here for brevity; they can be found in [Bayar 2024] or [Lei et al. 2021]):

$$\begin{aligned}&(M_1+M_2)(\dot{V}_{x1}-V_{y1}r_1)=M_2l_r\dot{r}_2\sin(\kappa)-M_2l_fr_1^2-M_2l_rr_2^2\cos(\kappa)+(F_{xfl}+F_{xfr})\cos(\delta)\\&-(F_{yfl}+F_{yfr})\sin(\delta)+F_{xml}+F_{xmr}+(F_{xrl}+F_{xrr})\cos(\kappa)+(F_{yml}+F_{ymr})\sin(\kappa)\end{aligned} \tag{1}$$

$$\begin{aligned}&(M_1+M_2)(\dot{V}_{y1}+V_{x1}r_1)=M_2l_r\dot{r}_2\cos(\kappa)+M_2l_f\dot{r}_1+M_2l_rr_2^2\sin(\kappa)+(F_{xfl}+F_{xfr})\sin(\delta)\\&+(F_{yfl}+F_{yfr})\cos(\delta)+F_{yml}+F_{ymr}-(F_{xrl}+F_{xrr})\sin(\kappa)+(F_{yrl}+F_{yrr})\cos(\kappa)\end{aligned} \tag{2}$$

$$\begin{aligned}&I_1\dot{r}_1=M_o+(F_{xfl}-F_{xfr})\cos(\delta)\frac{tr}{2}+(F_{xfl}+F_{xfr})\sin(\delta)a_f+(F_{yfl}+F_{yfr})\cos(\delta)a_f+(-F_{yfl}+F_{yfr})\sin(\delta)\frac{tr}{2}\\&+(F_{xml}-F_{xmr})\frac{tr}{2}-(F_{yfl}+F_{yfr})b_f+l_f\left(-M_1(\dot{V}_{y1}+V_{x1}r_1)+(F_{yfl}+F_{yfr})\cos(\delta)+(F_{xfl}+F_{xfr})\sin(\delta)+F_{yml}+F_{ymr}\right)\end{aligned} \tag{3}$$

$$\begin{aligned}&I_2\dot{r}_2=-M_o+(F_{xrl}-F_{xrr})\frac{tr}{2}-(F_{yrl}+F_{yrr})a_r\\&+\left(\begin{pmatrix}-M_1(\dot{V}_{y1}+V_{x1}r_1)+(F_{yfl}+F_{yfr})\cos(\delta)\\+(F_{xfl}+F_{xfr})\sin(\delta)+F_{yml}+F_{ymr}\end{pmatrix}\cos(\kappa)-\begin{pmatrix}M_1(\dot{V}_{x1}-V_{y1}r_1)-(F_{xfl}+F_{xfr})\cos(\delta)\\+(F_{yfl}+F_{yfr})\sin(\delta)-F_{xml}-F_{xmr}\end{pmatrix}\sin(\kappa)\right)l_r\end{aligned} \tag{4}$$

Regarding roll motion of the front and rear chassis compartments, the following equations of motion can be written:

$$I_{xx1}\dot{p}_1=M_{s1}h_{s1}(\dot{V}_{y1}+V_{x1}r_1)\cos(\phi_1)+M_{s1}h_{s1}g\sin(\phi_1)-C_{\phi1}p_1-K_{\phi1}\phi_1-K_{\phi art}(\phi_1-\phi_2) \tag{5}$$

$$I_{xx2}\dot{p}_2=M_{s2}h_{s2}(\dot{V}_{y2}+V_{x2}r_2)\cos(\phi_2)+M_{s2}h_{s2}g\sin(\phi_2)-C_{\phi2}p_2-K_{\phi2}\phi_2+K_{\phi art}(\phi_1-\phi_2) \tag{6}$$

where p is roll speed, I_{xx1} and I_{xx2} are the front and rear roll moment of inertia, and $K_{\phi art}$ represents the roll stiffness of the articulation joint.

Wheel dynamics can be written by:

$$\dot{\omega}_i = \frac{T_{hs} - T_b - rF_x}{I_\omega} \tag{7}$$

where T_b is the brake torque, I_ω is the wheel inertia. T_{hs} represents the half shaft torque, which is the electric motor torque amplified by the gear ratio. For half shaft and gear backlash models, the reader is referred to [Bayar 2023], they are not given here for brevity. The electric motor torque as a function of electric motor speed is given in Figure 2 [ZF website url].

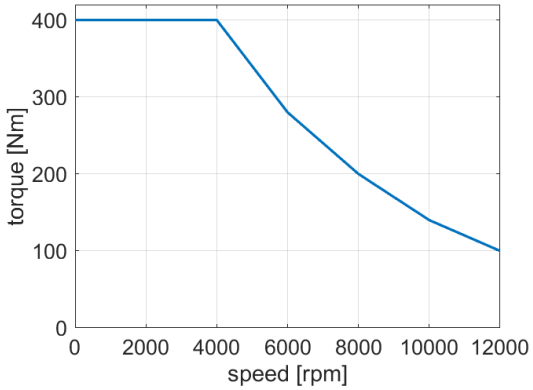


Figure 2 The torque vs speed curve of the on board motor. The total gear ratio between the motor and the wheel is 21,5.

The tire forces F_x and F_y are modelled using the Pacajka tire model for combined slip [Pacejka 2012].

For the articulation joint, the model given in Figure 3 is used:

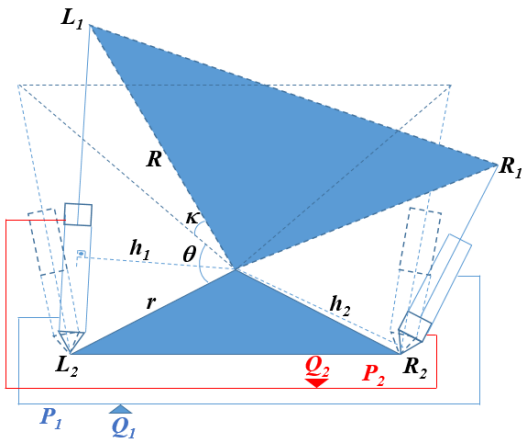


Figure 3 Model of the articulation joint

The equations of motion representing the articulation damping moment can be found in [Bayar 2024] or [Lei et al. 2021], they are not given here for brevity.

Simulator parameters are given in Table 1.

Table 1. Vehicle simulator parameters.

Mass of front compartment, M_1 [kg]	11600
Mass of rear compartment, M_2 [kg]	10300
Front axle static load, F_{zf0} [N]	46107
Middle axle static load, F_{zm0} [N]	64746
Rear axle static load, F_{zr0} [N]	101043
distance between front axle and front compartment centre of gravity, a_f [m]	3.12
distance between middle axle and front compartment centre of gravity, b_f [m]	2.08
distance between front compartment centre of gravity and articulation joint, l_f [m]	3.28
distance between rear axle and rear compartment centre of gravity, a_r [m]	0.16
distance between rear compartment centre of gravity and articulation joint, l_r [m]	5.32
distance between overall centre of gravity and front axle, g_f [m]	7.23
Wheel track, tr [m]	2.08
Front compartment yaw moment of inertia, I_1 [kg.m^2]	86736
Rear compartment yaw moment of inertia, I_2 [kg.m^2]	50863
Front compartment roll moment of inertia, I_{xx1} [kg.m^2]	64269
Rear compartment roll moment of inertia, I_{xx2} [kg.m^2]	57489
Tire rolling radius, r [m]	0.56
Wheel rotational inertia, I_ω [kg.m^2]	25
Articulation joint, link 1 length, R [m]	0.45
Articulation joint, link 2 length, r [m]	0.55
Piston cylinder cross-sectional area, A [cm^2]	28.26
Volume of the fluid in the initial position, V_0 [cm^3]	1500
Hydraulic bulk modulus, K_c [MPa]	700
Cornering stiffness of rear axle, at μ = 0.9 and static loading, C_r, [N/deg]	-16049
Cornering stiffness of middle axle, at μ = 0.9 and static loading, C_m, [N/deg]	-11765
Cornering stiffness of front axle, at μ = 0.9 and static loading, C_f, [N/deg]	-8759
Roll stiffness of each compartment, $K_{\phi 1/2}$ [Nm/deg]	5533
Roll damping of each compartment, $C_{\phi 1/2}$ [Nm/(deg/s)]	349
Articulation joint roll stiffness, $K_{\phi art}$ [Nm/deg]	873

Figure 4 illustrates the response of the simulator during a sinusoidal steering input at an initial speed of 53 km/hr on asphalt compared to the actual vehicle response. It can be observed that despite minor errors in magnitudes of yaw rate and articulation angle, the simulator exhibits a good performance in terms of capturing vehicle response during the manoeuvre. Sample validation result obtained on low μ can be found in [Bayar 2024].

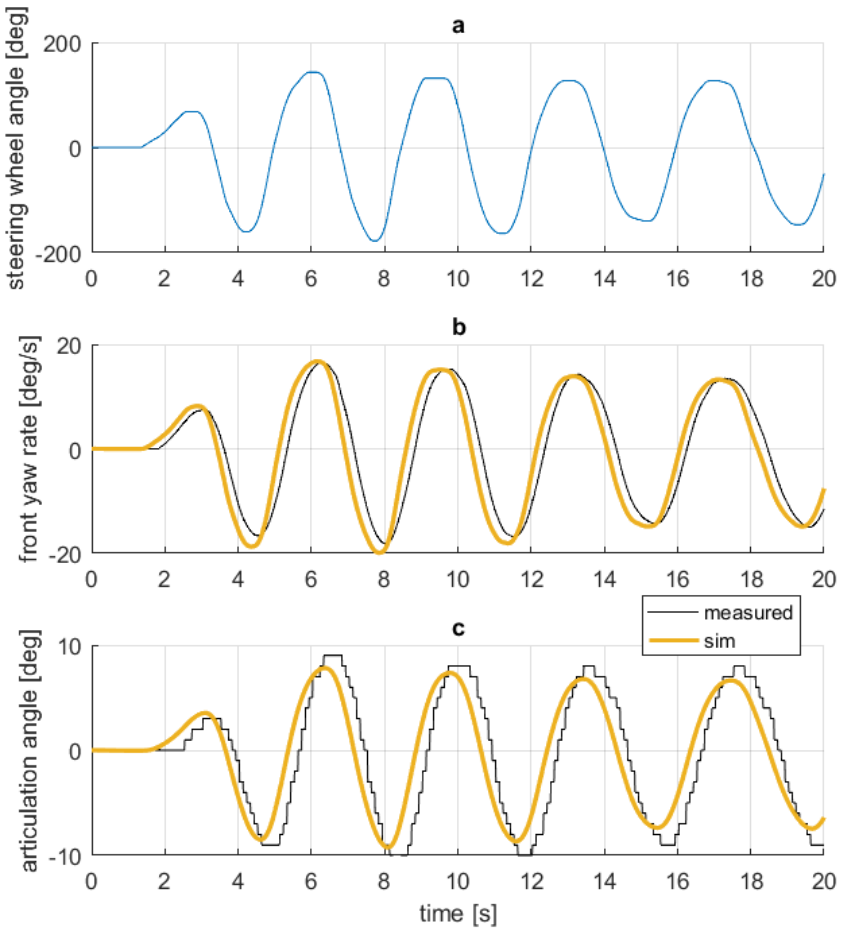


Figure 4 Vehicle model validation results for (b) yaw rate and (c) articulation angle for (a) handwheel angle input

3. CONTROL STRATEGY DEVELOPMENT

The overall scheme of the controller with each subsection is shown in Figure 5. The new feature of this controller with respect to the one in [Bayar 2024] is additional roll control, as stated in the Introduction section.

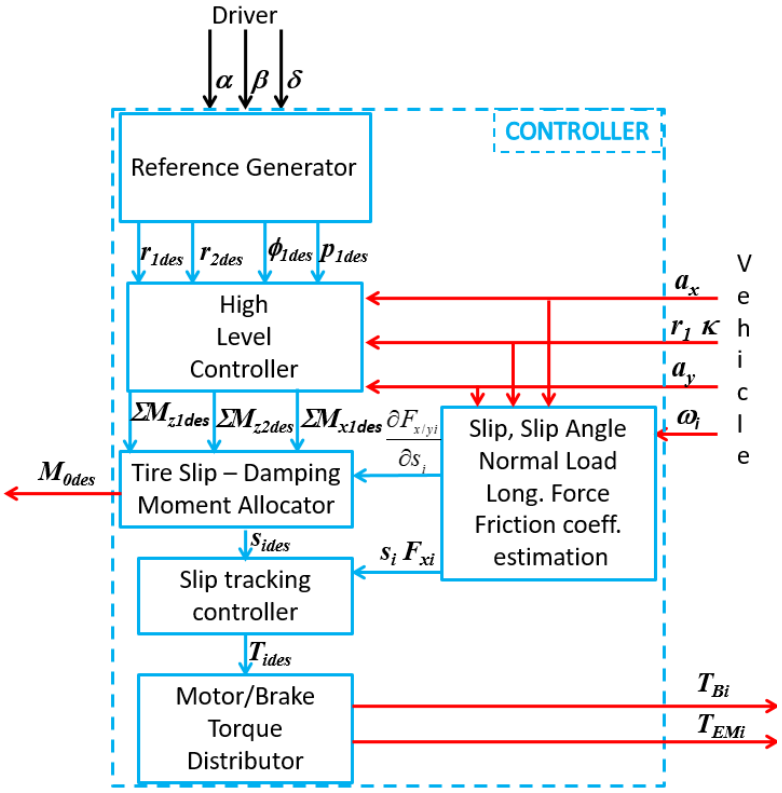


Figure 5 Controller model. The reference generator taking the driver inputs, α, β and δ, accelerator and brake pedal positions and steering wheel angle, generating the desired front and rear yaw rates, front roll rate and angle. High level controller generates the desired yaw/roll moments for the given desired yaw rates. Tire slip – damping moment allocator distributes the control action onto tire slips and articulation moment. Slip tracking controller generates the net wheel torque for tracking the desired tire slips. Finally, motor brake torque distributor distributes the net wheel torque onto friction brakes and electric motor torques.

Assuming steering angle and articulation angle are small enough for simplifying sine and cosine expressions, ignoring M_o and eliminating non-linear terms, the following set of linear state space equations can be derived:

$$\begin{Bmatrix} \dot{\beta} \\ \dot{r}_1 \\ \dot{r}_2 \\ \dot{\kappa} \\ \dot{\phi}_1 \\ \dot{p}_1 \\ \dot{\phi}_2 \\ \dot{p}_2 \end{Bmatrix} = \begin{bmatrix} A_{11} & A_{12} & A_{13} & A_{14} & 0 & 0 & 0 & 0 \\ A_{21} & A_{22} & A_{23} & A_{24} & 0 & 0 & 0 & 0 \\ A_{31} & A_{32} & A_{33} & A_{34} & 0 & 0 & 0 & 0 \\ 0 & 1 & -1 & 0 & 0 & 0 & 0 & 0 \\ 0 & 0 & 0 & 0 & 0 & 1 & 0 & 0 \\ A_{61} & A_{62} & A_{63} & A_{64} & A_{65} & A_{66} & A_{67} & 0 \\ 0 & 0 & 0 & 0 & 0 & 0 & 0 & 1 \\ A_{81} & A_{82} & A_{83} & A_{84} & A_{85} & 0 & A_{87} & A_{88} \end{bmatrix} \begin{Bmatrix} \beta \\ r_1 \\ r_2 \\ \kappa \\ \phi_1 \\ p_1 \\ \phi_2 \\ p_2 \end{Bmatrix} + \begin{bmatrix} b_1 \\ b_2 \\ b_3 \\ 0 \\ 0 \\ b_6 \\ 0 \\ b_8 \end{bmatrix} \delta \tag{8}$$

The elements of the matrix A_{ij} and b_i are given in *Appendix A*. All Eigenvalues are negative considering an operational speed range, indicating stability. Equation 8 is utilized for computing

the desired yaw/roll rate and angle. The desired yaw rates are saturated based on the tyre road adhesion coefficient as [Rajamani 2012]:

$$r_{1/2\max} = 0.85\frac{\mu g}{V_{x1/2}} \tag{9}$$

3.1 High Level Controller

The high level controller, receives the desired yaw and roll rates, and generates the desired yaw & roll moments to be allocated onto tire slips and articulation damping moment in order to yield these desired values. Equations 1-4 can be decoupled in terms of $\dot{V}_{x1}$, $\dot{V}_{y1}$, $\dot{\omega}_1$, $\dot{\omega}_2$. This is needed especially for the next section of the controller; the tire slip – articulation damping moment allocator, where the desired yaw moments should be expressed in terms of individual tire forces, and the damping moment due to articulation.

$$\begin{aligned}
\dot{r}_1 &= a_{xfl}F_{xfl} + a_{yfl}F_{yfl} + a_{xfr}F_{xfr} + a_{yfr}F_{yfr} + a_{xml}F_{xml} + a_{yml}F_{yml} + a_{xmr}F_{xmr} + a_{ymr}F_{ymr} + a_{xrl}F_{xrl} + a_{yrl}F_{yrl} + a_{xrr}F_{xrr} + a_{yrr}F_{yrr} \\
&+ \left(\frac{I_2 + \frac{M_1M_2l_r^2}{M_1+M_2}}{I_1I_2 + \frac{M_1M_2\left(I_1l_r^2 + I_2l_f^2\right)}{M_1+M_2} + \frac{M_1^2M_2^2l_f^2l_r^2\sin^2(\kappa)}{\left(M_1+M_2\right)^2}} + \frac{\frac{M_1M_2l_fl_r\cos(\kappa)}{M_1+M_2}}{I_1I_2 + \frac{M_1M_2\left(I_1l_r^2 + I_2l_f^2\right)}{M_1+M_2} + \frac{M_1^2M_2^2l_f^2l_r^2\sin^2(\kappa)}{\left(M_1+M_2\right)^2}} \right) M_0 \\
&+ \frac{I_2 + \frac{M_1M_2l_r^2}{M_1+M_2}}{I_1I_2 + \frac{M_1M_2\left(I_1l_r^2 + I_2l_f^2\right)}{M_1+M_2} + \frac{M_1^2M_2^2l_f^2l_r^2\sin^2(\kappa)}{\left(M_1+M_2\right)^2}} \frac{-M_1M_2l_fl_rr_2^2\sin(\kappa)}{M_1+M_2} \\
&- \frac{\frac{M_1M_2l_fl_r\cos(\kappa)}{M_1+M_2}}{I_1I_2 + \frac{M_1M_2\left(I_1l_r^2 + I_2l_f^2\right)}{M_1+M_2} + \frac{M_1^2M_2^2l_f^2l_r^2\sin^2(\kappa)}{\left(M_1+M_2\right)^2}} \frac{M_1M_2l_fl_rr_1^2\sin(\kappa)}{M_1+M_2} \\
\dot{r}_2 &= b_{xfl}F_{xfl} + b_{yfl}F_{yfl} + b_{xfr}F_{xfr} + b_{yfr}F_{yfr} + b_{xml}F_{xml} + b_{yml}F_{yml} + b_{xmr}F_{xmr} + b_{ymr}F_{ymr} + b_{xrl}F_{xrl} + b_{yrl}F_{yrl} + b_{xrr}F_{xrr} + b_{yrr}F_{yrr} \\
&- \left(\frac{\frac{M_1M_2l_fl_r\cos(\kappa)}{M_1+M_2}}{I_1I_2 + \frac{M_1M_2\left(I_1l_r^2 + I_2l_f^2\right)}{M_1+M_2} + \frac{M_1^2M_2^2l_f^2l_r^2\sin^2(\kappa)}{\left(M_1+M_2\right)^2}} + \frac{I_1 + \frac{M_1M_2l_f^2}{M_1+M_2}}{I_1I_2 + \frac{M_1M_2\left(I_1l_r^2 + I_2l_f^2\right)}{M_1+M_2} + \frac{M_1^2M_2^2l_f^2l_r^2\sin^2(\kappa)}{\left(M_1+M_2\right)^2}} \right) M_0 \\
&- \frac{\frac{M_1M_2l_fl_r\cos(\kappa)}{M_1+M_2}}{I_1I_2 + \frac{M_1M_2\left(I_1l_r^2 + I_2l_f^2\right)}{M_1+M_2} + \frac{M_1^2M_2^2l_f^2l_r^2\sin^2(\kappa)}{\left(M_1+M_2\right)^2}} \frac{-M_1M_2l_fl_rr_2^2\sin(\kappa)}{M_1+M_2} \\
&+ \frac{I_1 + \frac{M_1M_2l_f^2}{M_1+M_2}}{I_1I_2 + \frac{M_1M_2\left(I_1l_r^2 + I_2l_f^2\right)}{M_1+M_2} + \frac{M_1^2M_2^2l_f^2l_r^2\sin^2(\kappa)}{\left(M_1+M_2\right)^2}} \frac{M_1M_2l_fl_rr_1^2\sin(\kappa)}{M_1+M_2}
\end{aligned} \tag{10}$$

where the tire force coefficients a_{xi}, a_{yi}, b_{xi}, b_{yi} can be found in [Bayar 2024].

The desired yaw moment generated by the high level controller can be expressed as:

$$\left(\sum M_1\right)_{des} = \frac{I_2 + \frac{M_1 M_2 l_r^2}{M_1 + M_2}}{I_1 I_2 + \frac{M_1 M_2 \left(I_1 l_r^2 + I_2 l_f^2\right)}{M_1 + M_2} + \frac{M_1^2 M_2^2 l_f^2 l_r^2 \sin^2\left(\hat{\kappa}\right)}{\left(M_1 + M_2\right)^2}} \frac{M_1 M_2 l_f l_r \hat{r}_2^2 \sin\left(\hat{\kappa}\right)}{M_1 + M_2}$$
$$+ \frac{\frac{M_1 M_2 l_f l_r \cos\left(\hat{\kappa}\right)}{M_1 + M_2}}{I_1 I_2 + \frac{M_1 M_2 \left(I_1 l_r^2 + I_2 l_f^2\right)}{M_1 + M_2} + \frac{M_1^2 M_2^2 l_f^2 l_r^2 \sin^2\left(\hat{\kappa}\right)}{\left(M_1 + M_2\right)^2}} \frac{M_1 M_2 l_f l_r \hat{r}_1^2 \sin\left(\hat{\kappa}\right)}{M_1 + M_2}$$
$$+ k_{1p}\left(r_{1des} - \hat{r}_1\right) + k_{1I}\int\left(r_{1des} - \hat{r}_1\right)dt + k_{1d}\left(\dot{r}_{1des} - \dot{\hat{r}}_1\right) \tag{11}$$

$$\left(\sum M_2\right)_{des} = -\frac{\frac{M_1 M_2 l_f l_r \cos\left(\hat{\kappa}\right)}{M_1 + M_2}}{I_1 I_2 + \frac{M_1 M_2 \left(I_1 l_r^2 + I_2 l_f^2\right)}{M_1 + M_2} + \frac{M_1^2 M_2^2 l_f^2 l_r^2 \sin^2\left(\hat{\kappa}\right)}{\left(M_1 + M_2\right)^2}} \frac{M_1 M_2 l_f l_r \hat{r}_2^2 \sin\left(\hat{\kappa}\right)}{M_1 + M_2}$$
$$- \frac{I_1 + \frac{M_1 M_2 l_f^2}{M_1 + M_2}}{I_1 I_2 + \frac{M_1 M_2 \left(I_1 l_r^2 + I_2 l_f^2\right)}{M_1 + M_2} + \frac{M_1^2 M_2^2 l_f^2 l_r^2 \sin^2\left(\hat{\kappa}\right)}{\left(M_1 + M_2\right)^2}} \frac{M_1 M_2 l_f l_r \hat{r}_1^2 \sin\left(\hat{\kappa}\right)}{M_1 + M_2}$$
$$+ k_{2p}\left(r_{2des} - \hat{r}_2\right) + k_{2I}\int\left(r_{2des} - \hat{r}_2\right)dt + k_{2d}\left(\dot{r}_{2des} - \dot{\hat{r}}_2\right) \tag{12}$$

where $\hat{r}_1$, $\hat{r}_2$, $\hat{\kappa}$ are filtered front and rear compartment yaw rates, and filtered articulation angle, based on measured front compartment yaw rate and articulation angle. For deriving the desired roll moment that would be distributed onto individual tire slips and articulation damping moment, Equation 5 is revisited with a small angle assumption:

$$\dot{p}_1 = \frac{M_{s1} h_{s1}}{I_{xx1}} \dot{V}_{y1} + \frac{M_{s1} h_{s1}}{I_{xx1}} V_{x1} r_1 + \frac{M_{s1} h_{s1} g \phi_1}{I_{xx1}} - \frac{C_{\phi 1}}{I_{xx1}} p_1 - \frac{K_{\phi 1}}{I_{xx1}} \phi_1 - \frac{K_{\phi art}}{I_{xx1}} \left(\phi_1 - \phi_2\right) \tag{13}$$

$\dot{V}_{y1}$ can be obtained as a function of individual tire forces and damping moment by decoupling Equations 1-4:

$$\dot{V}_{y1} = c_{xfl} F_{xfl} + c_{yfl} F_{yfl} + c_{xfr} F_{xfr} + c_{yfr} F_{yfr} + c_{xml} F_{xml} + c_{yml} F_{yml} + c_{xmr} F_{xmr} + c_{ymr} F_{ymr} + c_{xrl} F_{xrl} + c_{yrl} F_{yrl} + c_{xrr} F_{xrr}$$
$$+ c_{yrr} F_{yrr} + c_m M_o + a_{12}\left(-M_2 l_f r_1^2 - M_2 l_r r_2^2 \cos\left(\kappa\right)\right) + a_{22} M_2 l_r r_2^2 \sin\left(\kappa\right) - r_1 V_{x1} \tag{14}$$

where c_{xi}, c_{yi}, c_m, a_{12}, a_{22} can be found in *Appendix B*.

Substituting Equation 14 into Equation 13 yields:

$$\dot{p}_1 = \frac{M_{s1}h_{s1}}{I_{xx1}}\left(\sum M_{roll}\right)_{des} + \frac{M_{s1}h_{s1}}{I_{xx1}}a_{12}\left(-M_2 l_f r_1^2 - M_2 l_r r_2^2\cos(\kappa)\right) + \frac{M_{s1}h_{s1}}{I_{xx1}}a_{22}M_2 l_r r_2^2\sin(\kappa) + \frac{M_{s1}h_{s1}g\phi_1}{I_{xx1}} - \frac{C_{\phi 1}}{I_{xx1}}p_1 - \frac{K_{\phi 1}}{I_{xx1}}\phi_1 - \frac{K_{\phi art}}{I_{xx1}}(\phi_1 - \phi_2) \tag{15}$$

where

$$\left(\sum M_{roll}\right)_{des} = c_{xfl}F_{xfl} + c_{yfl}F_{yfl} + c_{xfr}F_{xfr} + c_{yfr}F_{yfr} + c_{xml}F_{xml} + c_{yml}F_{yml} + c_{xmr}F_{xmr} + c_{ymr}F_{ymr} + c_{xrl}F_{xrl} + c_{yrl}F_{yrl} + c_{xrr}F_{xrr} + c_{yrr}F_{yrr} + c_m M_o \tag{16}$$

Defining the following states:

$x_1 = f_1 - f_{1des}$ (17)

$x_2 = p_1 - p_{1des}$ (18)

and structuring the control vector $\left(\sum M_{roll}\right)_{des}$ as

$$\left(\sum M_{roll}\right)_{des} = v - a_{12}\left(-M_2 l_f r_1^2 - M_2 l_r r_2^2\cos(\kappa)\right) - a_{22}M_2 l_r r_2^2\sin(\kappa) - \frac{K_{\phi art}}{M_{s1}h_{s1}}\phi_2 - \frac{I_{xx1}}{M_{s1}h_{s1}}\left(\frac{M_{s1}h_{s1}g}{I_{xx1}} - \frac{K_{\phi 1}}{I_{xx1}} - \frac{K_{\phi art}}{I_{xx1}}\right)\phi_{1des} + \frac{I_{xx1}}{M_{s1}h_{s1}}\frac{C_{\phi 1}}{I_{xx1}}p_{1des} + \frac{I_{xx1}}{M_{s1}h_{s1}}\dot{p}_{1des} \tag{19}$$

yields

$$\begin{Bmatrix}\dot{x}_1\\ \dot{x}_2\end{Bmatrix} = \begin{bmatrix}0 & 1\\ \dfrac{M_{s1}h_{s1}g - K_{\phi 1} - K_{\phi art}}{I_{xx1}} & -\dfrac{C_{\phi 1}}{I_{xx1}}\end{bmatrix}\begin{Bmatrix}x_1\\ x_2\end{Bmatrix} + \begin{bmatrix}0\\ \dfrac{M_{s1}h_{s1}}{I_{xx1}}\end{bmatrix}v \tag{20}$$

The system is controllable; Eigenvalues can be placed as desired, such that the error states for roll speed and angle converge to zero as fast as desired.

3.2 Control Allocation

As seen in Figure 5, the desired yaw moments are distributed onto articulation damping moment and tire slips, through the control effectiveness matrix, within a quadratic optimization problem:

$$J = \arg\min_{U} = \frac{1}{2}\left(B_{3x7}u_{7x1} - \begin{Bmatrix} (\sum M_1)_{des} \\ (\sum M_2)_{des} \\ (\sum M_{roll})_{des} \end{Bmatrix} \right)^T \begin{bmatrix} w_{r1} & 0 & 0 \\ 0 & w_{r2} & 0 \\ 0 & 0 & w_{\phi 1} \end{bmatrix} \left(B_{3x7}u_{7x1} - \begin{Bmatrix} (\sum M_1)_{des} \\ (\sum M_2)_{des} \\ (\sum M_{roll})_{des} \end{Bmatrix} \right) + \frac{1}{2}U^T \begin{bmatrix} w_s & 0 & 0 & 0 & 0 & 0 & 0 \\ 0 & w_s & 0 & 0 & 0 & 0 & 0 \\ 0 & 0 & w_s & 0 & 0 & 0 & 0 \\ 0 & 0 & 0 & w_s & 0 & 0 & 0 \\ 0 & 0 & 0 & 0 & w_s & 0 & 0 \\ 0 & 0 & 0 & 0 & 0 & w_s & 0 \\ 0 & 0 & 0 & 0 & 0 & 0 & w_{M0} \end{bmatrix} U \tag{21}$$

where

$$U = \begin{bmatrix} s_{fl} & s_{fr} & s_{ml} & s_{mr} & s_{rl} & s_{rr} & M_0 \end{bmatrix}^T \tag{22}$$

Subject to

$$-0.1 < s_i < 0.1 \text{ and } M_0 < M_{0max} \tag{23}$$

and the elements of the control effectiveness matrix equal to

$$\begin{aligned} b_{11} &= a_{xfl}\frac{dF_{xfl}}{d_{sfl}} + a_{yfl}\frac{dF_{yfl}}{d_{sfl}} \quad b_{12} = a_{xfr}\frac{dF_{xfr}}{d_{sfr}} + a_{yfr}\frac{dF_{yfr}}{d_{sfr}} \quad b_{13} = a_{xml}\frac{dF_{xml}}{d_{sml}} + a_{yml}\frac{dF_{yml}}{d_{sml}} \\ b_{14} &= a_{xmr}\frac{dF_{xmr}}{d_{smr}} + a_{ymr}\frac{dF_{ymr}}{d_{smr}} \quad b_{15} = a_{xrl}\frac{dF_{xrl}}{d_{srl}} + a_{yrl}\frac{dF_{yrl}}{d_{srl}} \quad b_{16} = a_{xrr}\frac{dF_{xrr}}{d_{srr}} + a_{yrr}\frac{dF_{yrr}}{d_{srr}} \\ b_{17} &= \frac{I_2 + \frac{M_1M_2l_r^2}{M_1+M_2}}{I_1I_2 + \frac{M_1M_2\left(I_1l_r^2 + I_2l_f^2\right)}{M_1+M_2} + \frac{M_1^2M_2^2l_f^2l_r^2\sin^2(\kappa)}{\left(M_1+M_2\right)^2}} + \frac{\frac{M_1M_2l_fl_r\cos(\kappa)}{M_1+M_2}}{I_1I_2 + \frac{M_1M_2\left(I_1l_r^2 + I_2l_f^2\right)}{M_1+M_2} + \frac{M_1^2M_2^2l_f^2l_r^2\sin^2(\kappa)}{\left(M_1+M_2\right)^2}} \end{aligned} \tag{24}$$

$$\begin{aligned} b_{21} &= b_{xfl}\frac{dF_{xfl}}{d_{sfl}} + b_{yfl}\frac{dF_{yfl}}{d_{sfl}} \quad b_{22} = b_{xfr}\frac{dF_{xfr}}{d_{sfr}} + b_{yfr}\frac{dF_{yfr}}{d_{sfr}} \quad b_{23} = b_{xml}\frac{dF_{xml}}{d_{sml}} + b_{yml}\frac{dF_{yml}}{d_{sml}} \\ b_{24} &= b_{xmr}\frac{dF_{xmr}}{d_{smr}} + b_{ymr}\frac{dF_{ymr}}{d_{smr}} \quad b_{25} = b_{xrl}\frac{dF_{xrl}}{d_{srl}} + b_{yrl}\frac{dF_{yrl}}{d_{srl}} \quad b_{26} = b_{xrr}\frac{dF_{xrr}}{d_{srr}} + b_{yrr}\frac{dF_{yrr}}{d_{srr}} \\ b_{27} &= -\frac{\frac{M_1M_2l_fl_r\cos(\kappa)}{M_1+M_2}}{I_1I_2 + \frac{M_1M_2\left(I_1l_r^2 + I_2l_f^2\right)}{M_1+M_2} + \frac{M_1^2M_2^2l_f^2l_r^2\sin^2(\kappa)}{\left(M_1+M_2\right)^2}} - \frac{I_1 + \frac{M_1M_2l_f^2}{M_1+M_2}}{I_1I_2 + \frac{M_1M_2\left(I_1l_r^2 + I_2l_f^2\right)}{M_1+M_2} + \frac{M_1^2M_2^2l_f^2l_r^2\sin^2(\kappa)}{\left(M_1+M_2\right)^2}} \end{aligned} \tag{25}$$

$$\begin{aligned} b_{31} &= c_{xfl}\frac{dF_{xfl}}{d_{sfl}} + c_{yfl}\frac{dF_{yfl}}{d_{sfl}} \quad b_{32} = c_{xfr}\frac{dF_{xfr}}{d_{sfr}} + c_{yfr}\frac{dF_{yfr}}{d_{sfr}} \quad b_{33} = c_{xml}\frac{dF_{xml}}{d_{sml}} + c_{yml}\frac{dF_{yml}}{d_{sml}} \\ b_{34} &= c_{xmr}\frac{dF_{xmr}}{d_{smr}} + c_{ymr}\frac{dF_{ymr}}{d_{smr}} \quad b_{35} = c_{xrl}\frac{dF_{xrl}}{d_{srl}} + c_{yrl}\frac{dF_{yrl}}{d_{srl}} \quad b_{36} = c_{xrr}\frac{dF_{xrr}}{d_{srr}} + c_{yrr}\frac{dF_{yrr}}{d_{srr}} \quad b_{37} = c_m \end{aligned} \tag{26}$$

The derivative of longitudinal and lateral forces with respect to tire slip is not given here for brevity; they can be found in [Bayar et al. 2012].

For the on board motor at middle and rear axle bus configuration, for which this controller is developed, the tire slip thresholds are given as in Equation 23, whereas for the front axle, only brake slip can be commanded.

The next stage of the controller is the tire slip control. Sliding mode control method is chosen for tracking the desired yaw rate. The controller can be found in [Bayar et al. 2012], as well; it is not given here for brevity, since it is not the main focus of this work.

Finally, the net wheel torque for achieving the desired tire slip is split between the hub motor torque, and the pneumatic brake torque. This is done through simple heuristic methods; the positive torque is satisfied entirely with the on board motors, whereas the brake torque is satisfied as much as the electric motors can provide, with the remaining part satisfied by the electro-pneumatic friction brakes.

4. SIMULATIONS

The first simulated maneuver is lane change on asphalt, with an average road surface adhesion coefficient of 0.9, at an initial speed of 70 km/hr. In order to assess the yaw + roll control strategy summarized in Section 3, the simulation results for yaw control only are provided in Figure 6, as well.

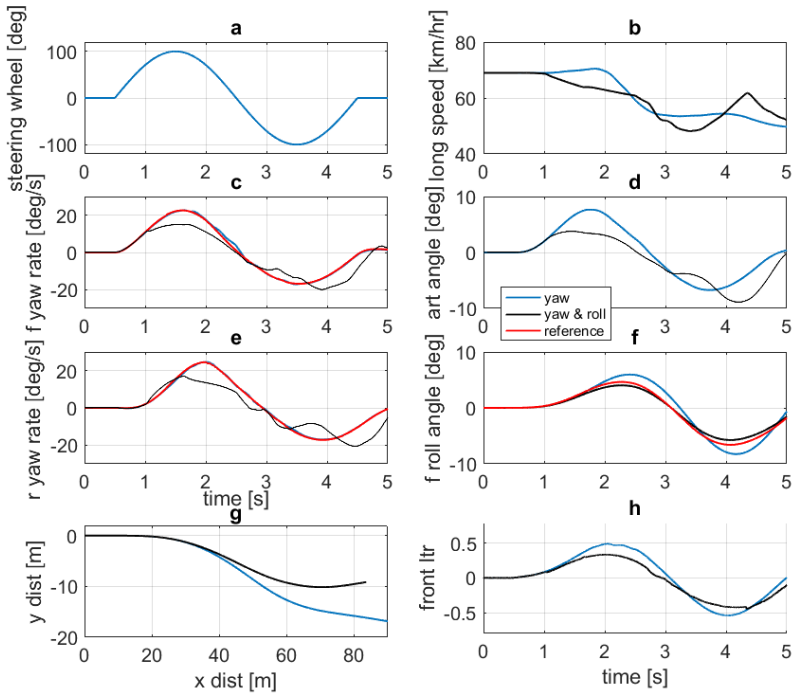


Figure 6 (a) Steering wheel angle (b) Longitudinal speed (c) Front compartment yaw rate (d) Articulation angle (e) Rear compartment yaw rate (f) Front compartment roll angle (g) Vehicle trajectory (h) Front

compartment load transfer ratio (ltr), for yaw control only (blue), yaw & roll control (black) results, together with the reference (red) curves.

It can be clearly seen from Figure 6c and Figure 6e, that with yaw control only, the reference yaw rates are tracked perfect (blue and red curves coincide), whereas with yaw + roll control, there are deviations from the reference curve. This causes the result in Figure 6g; the vehicle controlled with the yaw & roll controller is not able to perform the lane change as wide as the one equipped with the yaw control only. However, the gain is tracking the desired roll angle much better with the yaw + roll control, as shown in Figure 6f. This achievement is shown in Figure 6h, as well: The load transfer ratio (ltr), which is a performance metric in roll control strategies [Feng et al. 2022] formulated by Equation 27, shows that with yaw + roll controller, the maximum ltr is brought down from 0.55 to 0.42.

$$ltr_f = \frac{F_{zfl} + F_{zml} - F_{zfr} - F_{zmr}}{F_{zfl} + F_{zml} + F_{zfr} + F_{zmr}} \tag{27}$$

Figure 7 shows the difference in tire slip trends and articulation damping moment, between each strategy.

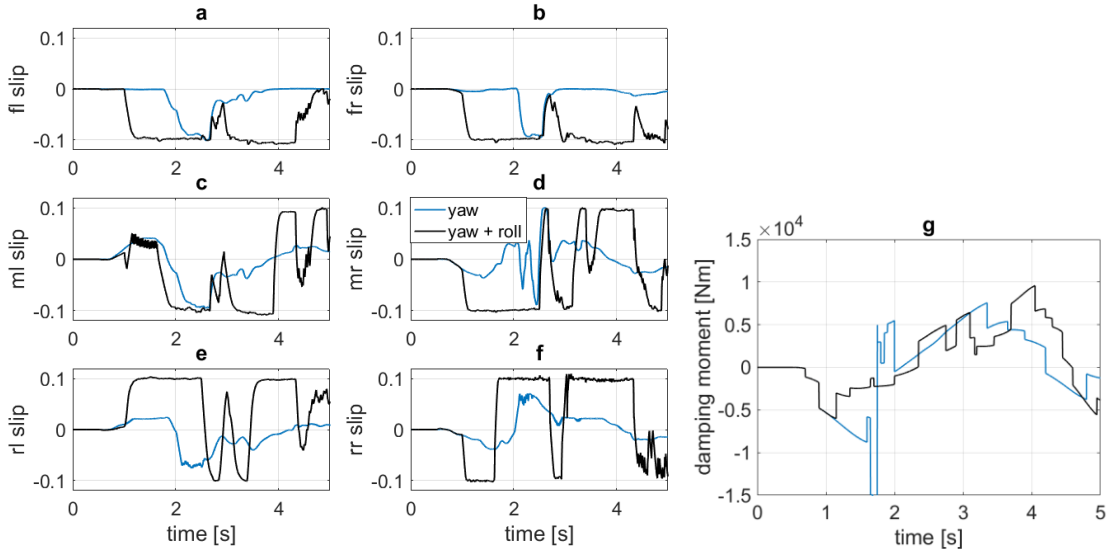


Figure 7 Tire slip and articulation damping moment trends for each control strategy

It can be seen from Figure 7a-d, that the roll control dominates yaw control as intended; the vehicle is braked quicker and for a longer period of time (in order to lower speed and lateral acceleration), with the yaw & roll control vehicle, compared to the yaw control vehicle, with the objective of avoiding a roll angle increase. In other words, tracking the reference yaw rates is not the primary control objective (this is achieved through the weighting factors of Equation 21). The effect of this action, can be seen in Figure 7b, as well. The speed reduction with the

yaw & roll control is higher compared to the yaw only control, until almost end of the manoeuvre at around t = 4 s.

Similar comments can be made for the rear tire slip trends; Figure 7e-f, in relationship to Figures 6e-f. The sole purpose of the yaw controlled vehicle is tracking the reference yaw rate, whereas the yaw & roll controlled vehicle sacrifices this objective for mitigating roll.

Figure 7g shows that the control allocation algorithm applies a more aggressive articulation damping moment trend with the yaw control only, compared to yaw & roll controlled vehicle.

These results show that the weighting factors of Equation 21 should be optimized depending on the manoeuvre. The load transfer ratio is picked as the decisive parameter: The roll control weighting parameter w_{f1} is increased if the ltr increases. For estimating the ltr in real time, Equation 28 is used [Tsourapas et al. 2009]:

$$ltr = \frac{2h_s}{tr}\left(\frac{a_y}{g} + \sin(\phi)\right) \tag{28}$$

Figure 8 shows the application of this strategy, for an extended sine with dwell manoeuvre, at an initial vehicle speed of 50 km/hr on asphalt, with an average road surface adhesion coefficient of 0.9.

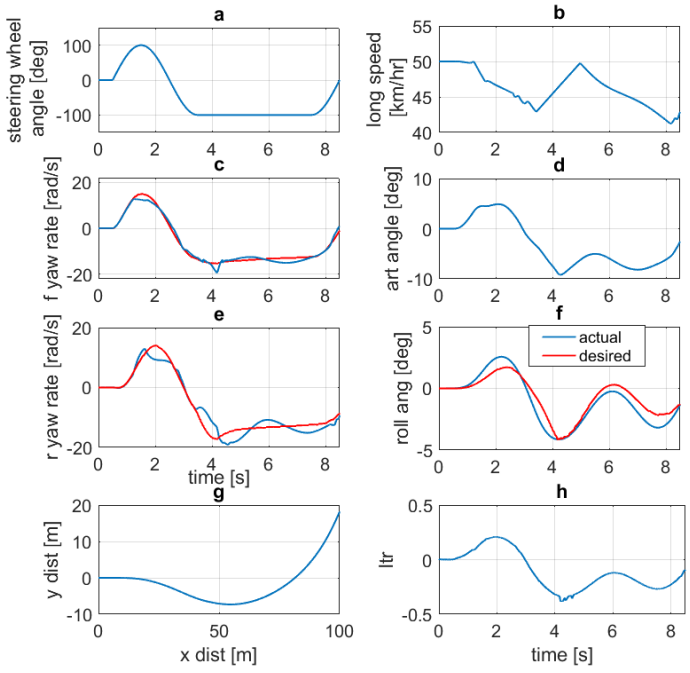


Figure 8 (a) Steering wheel angle (b) Longitudinal speed (c) Front compartment yaw rate (d) Articulation angle (e) Rear compartment yaw rate (f) Front compartment roll angle (g) Vehicle trajectory (h) Front compartment load transfer ratio (ltr), for the ltr based yaw & roll control strategy.

It can be seen that by increasing w_{f1} as the ltr shows an increasing trend around t = 2 and t=4 sec (Figure 8h), desired roll angle can be tracked well (Figure 8f), with a maximum ltr of 0.38

during the manoeuvre. The cost is slight deviations in tracking the reference yaw rates, shown in Figure 8c and Figure 8e, which is tolerable considering the gain in mitigating roll angle.

5. CONCLUSIONS

A roll-over prevention control strategy is developed in this work for an articulated bus equipped with on-board electric motors at middle and rear axles. Using the control allocation method, the pro/counter yaw and roll moments are distributed onto individual wheel braking/acceleration and articulation damping moment. This work is an extension of the previous work by the author [Bayar et al. 2024], which was on yaw control on low μ for the same bus configuration; current work focuses on both yaw and roll control as the latter is more critical on high μ.

Lane change manoeuvre on asphalt simulation results show that there is a trade-off between yaw and roll control; tracking the desired yaw rate perfect causes sacrifices from roll rate, and vice versa. Therefore, in order to mitigate the possibility of roll over, the control strategy is designed such that the weighting of roll control within the control allocation scheme is adjusted based on the load transfer ratio. The sine with dwell simulation results show the success of the adjusted control strategy; the desired roll angle is tracked quite satisfactorily without sacrificing yaw rate tracking.

REFERENCES

[1] DeNovellis, L., Sorniotti, A., Gruber, P., Orus, J., Fortun, J-M R., Theunissen, J. and De Smet, J. 2015 “Direct yaw moment control actuated through electric drivetrains and friction brakes: Theoretical design and experimental assesment”, Mechatronics, 26, 1-15, DOI:

http://dx.doi.org/10.1016/j.mechatronics.2014.12.003.

[2] Bayar, K. 2024 “Development of a Direct Yaw Moment Control Strategy for an Articulated Bus Equipped with onboard Electric Motors”, International Journal of Heavy Vehicle Systems, in press.

[3] Huang, B., Yuan, Z., Peng, D., Wei, X. and Wang, Y. 2023 “Coordination Control of Active Steering and Direct Yaw Control for the Articulated Steering Vehicle”, Shock and Vibration, Vol. 2023, Article ID 5577119, pp.1–16, DOI: https://doi.org/10.1155/2023/5577119.

[4] Yang, F., Cao, X., Xu, T. and Ji, X. 2022 “A Skid-Steering Method for Path-Following Control of Distibuted-Drive Articulated Heavy Vehicles”, IEEE Access, Vol. 10, pp.31538–31547, DOI:

10.1109/ACCESS.2022.3159333.

[5] Xu, X., Ai, X., Chen, R., Jiang, G. and Hua, X. 2020 “Research on roll stability of articulated engineering vehicles based on dynamic lateral transfer load”, Proceedings of the Institution of Mechanical Engineers, Part D Journal of Automobile Engineering, Vol 234, Issue 9, pp 2364 – 2376, DOI: 10.1177/0954407020909242.

[6] Bayar, K. 2023 “Active motor damping strategy for driveline vibrations of a hybrid electric vehicle during ABS operation”, Proceedings of the Institution of Mechanical Engineers, Part D: Journal of Automobile Engineering. DOI: 10.1177/09544070221114678, Vol 237, Issue 10-11, 2499 – 2510.

[7] Website url: https://www.youtube.com/watch?v=23-i0niqDP4

[8] Pacejka, H.B. (2012) Tyre and Vehicle Dynamics, Butterworth-Heinemann, ISBN: 978-0-08-097016-5.

[9] Lei, T., Wang, J. and Yao, Z. (2021) ‘Modelling and stability analysis of articulated vehicles’, Applied Sciences, Vol. 11, p.3663, https://doi.org/10.3390/app.11083663.

[10] Rajamani, R. 2012 “Vehicle Dynamics and Control”, Springer, ISBN 978-1-4614-1432-2.

[11] Bayar, K., Wang, J. and Rizzoni, G. 2012 “Development of a vehicle stability control strategy for a hybrid electric vehicle equipped with axle motors”, Proceedings of the Institution of Mechanical Engineers, Part D: Journal of Automobile Engineering, Vol 226, Issue 6, pp 795-814, DOI: 10.1177/0954407011433396.

[12] Xiao, F., Hu, J., Zhu, P. and Deng, C. 2022 “Chassis coordinated control based on ideal roll angle to improve vehicle stability”, Vehicle System Dynamics, Vol 61, Issue 8, pp. 2074 – 2102, DOI: 10.1080/00423114.2022.2101479.

[13] Tsourapas, V., Piyabongkarn, D. Williams, A. and Rajamani, R. 2009 “New Method of Identifying Real-Time Predictive Lateral Load Transfer Ratio for Rollover Prevention Systems”, American Control Conference, St Louis.

APPENDIX A

$$A_{11}=\frac{x}{V_{x1}}\left[C_f\left(\frac{a_f b_f M_2}{I_1}+\frac{b_f^2 M_2}{I_1}+\frac{l_r^2 M_2}{I_2}+1\right)+C_m\left(\frac{-M_2 b_f l_f}{I_1}+\frac{M_2 l_f^2}{I_1}+\frac{l_r^2 M_2}{I_2}+1\right)+C_r\left(\frac{-M_2 a_r l_r}{I_2}+1\right)\right]$$

$$A_{12}=\frac{x}{V_{x1}}\left[\begin{array}{l} C_f\frac{a_f}{V_{x1}}\left(\frac{a_f b_f M_2}{I_1}+\frac{b_f^2 M_2}{I_1}+\frac{l_r^2 M_2}{I_2}+1\right)-C_m\frac{b_f}{V_{x1}}\left(\frac{-M_2 b_f l_f}{I_1}+\frac{M_2 l_f^2}{I_1}+\frac{l_r^2 M_2}{I_2}+1\right) \\ -C_r\frac{b_f}{V_{x1}}\left(\frac{-M_2 a_r l_r}{I_2}+1\right) \end{array}\right]-1$$

$$A_{13}=\frac{x}{V_{x1}}\left(-C_r\frac{a_r+l_r}{V_{x1}}+1\right)\left(\frac{-M_2 a_r l_r}{I_2}+1\right)\quad A_{14}=\frac{x}{V_{x1}}.C_r\left(\frac{-M_2 a_r l_r}{I_2}+1\right)$$

where

$$x=\frac{I_1I_2\left(M_1+M_2\right)}{\left(I_2b_f^2M_1^2M_2+I_2b_f^2M_2^2M_1+I_1l_r^2M_1^2M_2+I_1l_r^2M_2^2M_1+I_1I_2M_1^2+2I_1I_2M_1M_2+I_1I_2M_2^2\right)}$$

$$A_{21}=C_1a_fC_f+\frac{I_2}{I_1I_2+\frac{M_1M_2\left(I_1l_r^2+I_2l_f^2\right)}{M_1+M_2}}\left(l_f-\frac{M_1l_f}{M_1+M_2}\right)C_f-C_1b_fC_m$$

$$-\frac{I_2}{I_1I_2+\frac{M_1M_2\left(I_1l_r^2+I_2l_f^2\right)}{M_1+M_2}}\left(l_f-\frac{M_1l_f}{M_1+M_2}\right)C_m-C_2a_rC_r-\frac{C_rI_2M_1l_f}{I_1I_2\left(M_1+M_2\right)+M_1M_2\left(I_1l_r^2+I_2l_f^2\right)}$$

$$A_{22}=\frac{C_1a_f^2C_f}{V_{x1}}+\frac{I_2}{I_1I_2+\frac{M_1M_2\left(I_1l_r^2+I_2l_f^2\right)}{M_1+M_2}}\left(l_f-\frac{M_1l_f}{M_1+M_2}\right)\frac{C_fa_f}{V_{x1}}+\frac{C_1b_f^2C_m}{V_{x1}}$$

$$+\frac{I_2}{I_1I_2+\frac{M_1M_2\left(I_1l_r^2+I_2l_f^2\right)}{M_1+M_2}}\left(l_f-\frac{M_1l_f}{M_1+M_2}\right)\frac{C_mb_f}{V_{x1}}+\frac{C_2a_rC_rb_f}{V_{x1}}+\frac{C_rI_2M_1l_f}{I_1I_2\left(M_1+M_2\right)+M_1M_2\left(I_1l_r^2+I_2l_f^2\right)}\frac{b_f}{V_{x1}}$$

$$A_{23}=\frac{C_rC_2a_r\left(l_r+a_r\right)}{V_{x1}}+\frac{C_rI_2M_1l_f}{I_1I_2\left(M_1+M_2\right)+M_1M_2\left(I_1l_r^2+I_2l_f^2\right)}\frac{l_r+a_r}{V_{x1}}\quad A_{24}=-C_rC_2a_r-\frac{C_rI_2M_1l_f}{I_1I_2\left(M_1+M_2\right)+M_1M_2\left(I_1l_r^2+I_2l_f^2\right)}$$

where

$$C_1=\frac{I_2+\frac{M_1M_2l_r^2}{M_1+M_2}}{I_1I_2+\frac{M_1M_2\left(I_1l_r^2+I_2l_f^2\right)}{M_1+M_2}}\qquad C_2=-\frac{\frac{M_1M_2l_fl_r}{M_1+M_2}}{I_1I_2+\frac{M_1M_2\left(I_1l_r^2+I_2l_f^2\right)}{M_1+M_2}}$$

$$A_{31}=C_2a_fC_f+\frac{I_1}{I_1I_2+\frac{M_1M_2\left(I_1l_r^2+I_2l_f^2\right)}{M_1+M_2}}\left(l_r-\frac{M_1l_r}{M_1+M_2}\right)C_f-C_2b_fC_m$$

$$+\frac{I_1}{I_1I_2+\frac{M_1M_2\left(I_1l_r^2+I_2l_f^2\right)}{M_1+M_2}}\left(l_r-\frac{M_1l_r}{M_1+M_2}\right)C_m-C_4a_rC_r-\frac{C_rI_1M_1l_r}{I_1I_2\left(M_1+M_2\right)+M_1M_2\left(I_1l_r^2+I_2l_f^2\right)}$$

$$A_{32}=\frac{C_2a_f^2C_f}{V_{x1}}+\frac{I_1}{I_1I_2+\frac{M_1M_2\left(I_1l_r^2+I_2l_f^2\right)}{M_1+M_2}}\left(l_r-\frac{M_1l_r}{M_1+M_2}\right)\frac{C_fa_f}{V_{x1}}+\frac{C_2b_f^2C_m}{V_{x1}}$$

$$-\frac{I_1}{I_1I_2+\frac{M_1M_2\left(I_1l_r^2+I_2l_f^2\right)}{M_1+M_2}}\left(l_r-\frac{M_1l_r}{M_1+M_2}\right)\frac{C_mb_f}{V_{x1}}+\frac{C_4a_rC_rb_f}{V_{x1}}+\frac{C_rI_1M_1l_r}{I_1I_2\left(M_1+M_2\right)+M_1M_2\left(I_1l_r^2+I_2l_f^2\right)}\frac{b_f}{V_{x1}}$$

$$A_{33}=\frac{C_rC_4a_r\left(l_r+a_r\right)}{V_{x1}}+\frac{C_rI_1M_1l_r}{I_1I_2\left(M_1+M_2\right)+M_1M_2\left(I_1l_r^2+I_2l_f^2\right)}\frac{l_r+a_r}{V_{x1}}$$

$$A_{34}=-C_rC_4a_r+\frac{-C_rI_1M_1l_r}{I_1I_2\left(M_1+M_2\right)+M_1M_2\left(I_1l_r^2+I_2l_f^2\right)}$$

where

$$C_4 = \frac{I_1 + \frac{M_1 M_2 l_f^2}{M_1 + M_2}}{I_1 I_2 + \frac{M_1 M_2 \left(I_1 l_r^2 + I_2 l_f^2\right)}{M_1 + M_2}}$$

$$A_{61} = \frac{M_{s1} h_{s1}}{I_{xx1}} V_{x1} A_{11} \quad A_{62} = \frac{M_{s1} h_{s1}}{I_{xx1}} V_{x1} A_{12} + \frac{M_{s1} h_{s1}}{I_{xx1}} V_{x1} \quad A_{63} = \frac{M_{s1} h_{s1}}{I_{xx1}} V_{x1} A_{13} \quad A_{64} = \frac{M_{s1} h_{s1}}{I_{xx1}} V_{x1} A_{14}$$

$$A_{65} = \frac{M_{s1} h_{s1} g - K_{\phi 1} - K_{\phi art}}{I_{xx1}} \quad A_{66} = \frac{-C_{\phi 1}}{I_{xx1}} \quad A_{67} = \frac{K_{\phi art}}{I_{xx1}} \quad A_{81} = \frac{M_{s2} h_{s2}}{I_{xx2}} V_{x1} A_{11} - \frac{l_f M_{s2} h_{s2}}{I_{xx2}} A_{21} - \frac{l_r M_{s2} h_{s2}}{I_{xx2}} A_{31}$$

$$A_{82} = \frac{M_{s2} h_{s2}}{I_{xx2}} V_{x1} A_{12} - \frac{l_f M_{s2} h_{s2}}{I_{xx2}} A_{22} + \frac{M_{s2} h_{s2}}{I_{xx2}} V_{x1} - \frac{l_r M_{s2} h_{s2}}{I_{xx2}} A_{32}$$

$$A_{83} = \frac{M_{s2} h_{s2}}{I_{xx2}} V_{x1} A_{13} - \frac{l_f M_{s2} h_{s2}}{I_{xx2}} A_{23} - \frac{l_r M_{s2} h_{s2}}{I_{xx2}} A_{33} \quad A_{84} = \frac{M_{s2} h_{s2}}{I_{xx2}} V_{x1} A_{14} - \frac{l_f M_{s2} h_{s2}}{I_{xx2}} A_{24} - \frac{l_r M_{s2} h_{s2}}{I_{xx2}} A_{34}$$

$$A_{85} = \frac{K_{\phi art}}{I_{xx2}} \quad A_{87} = \frac{M_{s2} h_{s2} g - K_{\phi 2} - K_{\phi art}}{I_{xx2}} \quad A_{88} = \frac{-C_{\phi 2}}{I_{xx2}}$$

and

$$b_1 = -\frac{x}{V_{x1}} C_f \left(\frac{a_f b_f M_2}{I_1} + \frac{b_f^2 M_2}{I_1} + \frac{l_r^2 M_2}{I_2} + 1 \right)$$

$$b_2 = -C_1 a_f C_f - \frac{I_2}{I_1 I_2 + \frac{M_1 M_2 \left(I_1 l_r^2 + I_2 l_f^2\right)}{M_1 + M_2}} \left(l_f - \frac{M_1 l_f}{M_1 + M_2} \right) C_f$$

$$b_3 = -C_2 a_f C_f - \frac{I_1}{I_1 I_2 + \frac{M_1 M_2 \left(I_1 l_r^2 + I_2 l_f^2\right)}{M_1 + M_2}} \left(l_r - \frac{M_1 l_r}{M_1 + M_2} \right) C_f$$

$$b_6 = \frac{M_{s1} h_{s1} V_{x1} b_1}{I_{xx1}} \quad b_8 = \frac{M_{s2} h_{s2} V_{x1} b_1}{I_{xx2}} - \frac{l_f M_{s2} h_{s2} b_2}{I_{xx2}} - \frac{l_r M_{s2} h_{s2} b_3}{I_{xx2}}$$

APPENDIX B

$$a_{12} = \frac{-I_1 l_r^2 M_1 M_2 \sin(\kappa)\cos(\kappa)}{l_f^2 l_r^2 M_1^2 M_2^2 \sin^2(\kappa) + I_2 l_f^2 M_1^2 M_2 + I_2 l_f^2 M_2^2 M_1 + I_1 l_r^2 M_1^2 M_2 + I_1 l_r^2 M_2^2 M_1 + I_1 I_2 M_1^2 + 2 I_1 I_2 M_1 M_2 + I_1 I_2 M_2^2}$$

$$a_{22} = \frac{I_1 \left(M_1 M_2 l_r^2 \sin^2(\kappa) + I_2 \left(M_1 + M_2 \right) \right)}{l_f^2 l_r^2 M_1^2 M_2^2 \sin^2(\kappa) + I_2 l_f^2 M_1^2 M_2 + I_2 l_f^2 M_2^2 M_1 + I_1 l_r^2 M_1^2 M_2 + I_1 l_r^2 M_2^2 M_1 + I_1 I_2 M_1^2 + 2 I_1 I_2 M_1 M_2 + I_1 I_2 M_2^2}$$

$$c_{xfl} = a_{12} \left(\frac{M_2 l_r^2 \sin(\kappa)\cos(\kappa)\sin(\delta)}{I_2} + \frac{M_2 l_r^2 \sin^2(\kappa)\cos(\delta)}{I_2} + \cos(\delta) \right)$$

$$+ a_{22} \left(\frac{M_2 l_f \cos(\delta) tr}{2 I_1} + \frac{a_f l_f M_2 \sin(\delta)}{I_1} + \frac{M_2 l_f^2 \sin(\delta)}{I_1} + \frac{M_2 l_r^2 \cos^2(\kappa)\sin(\delta)}{I_2} + \frac{M_2 l_r^2 \sin(\kappa)\cos(\kappa)\cos(\delta)}{I_2} + \sin(\delta) \right)$$

$$c_{yfl} = a_{12}\left(\frac{M_2 l_r^2 \sin(\kappa)\cos(\kappa)\cos(\delta)}{I_2} - \frac{M_2 l_r^2 \sin^2(\kappa)\sin(\delta)}{I_2} - \sin(\delta)\right)$$

$$+a_{22}\left(\begin{array}{l}\frac{a_f l_f M_2 \cos(\delta)}{I_1} - \frac{M_2 l_f \sin(\delta) tr}{2I_1} + \frac{M_2 l_f^2 \cos(\delta)}{I_1} \\ + \frac{M_2 l_r^2 \cos^2(\kappa)\cos(\delta)}{I_2} - \frac{M_2 l_r^2 \sin(\kappa)\cos(\kappa)\sin(\delta)}{I_2} + \cos(\delta)\end{array}\right)$$

$$c_{xfr} = a_{12}\left(\frac{M_2 l_r^2 \sin(\kappa)\cos(\kappa)\sin(\delta)}{I_2} + \frac{M_2 l_r^2 \sin^2(\kappa)\cos(\delta)}{I_2} + \cos(\delta)\right)$$

$$+a_{22}\left(\begin{array}{l}-\frac{M_2 l_f \cos(\delta) tr}{2I_1} + \frac{a_f l_f M_2 \sin(\delta)}{I_1} + \frac{M_2 l_f^2 \sin(\delta)}{I_1} \\ + \frac{M_2 l_r^2 \cos^2(\kappa)\sin(\delta)}{I_2} + \frac{M_2 l_r^2 \sin(\kappa)\cos(\kappa)\cos(\delta)}{I_2} + \sin(\delta)\end{array}\right)$$

$$c_{yfr} = a_{12}\left(\frac{M_2 l_r^2 \sin(\kappa)\cos(\kappa)\cos(\delta)}{I_2} - \frac{M_2 l_r^2 \sin^2(\kappa)\sin(\delta)}{I_2} - \sin(\delta)\right)$$

$$+a_{22}\left(\begin{array}{l}\frac{a_f l_f M_2 \cos(\delta)}{I_1} + \frac{M_2 l_f \sin(\delta) tr}{2I_1} + \frac{M_2 l_f^2 \cos(\delta)}{I_1} \\ + \frac{M_2 l_r^2 \cos^2(\kappa)\cos(\delta)}{I_2} - \frac{M_2 l_r^2 \sin(\kappa)\cos(\kappa)\sin(\delta)}{I_2} + \cos(\delta)\end{array}\right)$$

$$c_{xml} = a_{12}\left(\frac{M_2 l_r^2 \sin^2(\kappa)}{I_2} + 1\right) + a_{22}\left(\frac{M_2 l_f tr}{2I_1} + \frac{M_2 l_r^2 \sin(\kappa)\cos(\kappa)}{I_2}\right)$$

$$c_{yml} = a_{12}\frac{M_2 l_r^2 \sin(\kappa)\cos(\kappa)}{I_2} + a_{22}\left(\frac{-b_f M_2 l_f}{I_1} + \frac{M_2 l_f^2}{I_1} + \frac{M_2 l_r^2 \cos^2(\kappa)}{I_2} + 1\right)$$

$$c_{xmr} = a_{12}\left(\frac{M_2 l_r^2 \sin^2(\kappa)}{I_2} + 1\right) + a_{22}\left(-\frac{M_2 l_f tr}{2I_1} + \frac{M_2 l_r^2 \sin(\kappa)\cos(\kappa)}{I_2}\right)$$

$$c_{ymr} = a_{12}\frac{M_2 l_r^2 \sin(\kappa)\cos(\kappa)}{I_2} + a_{22}\left(\frac{-b_f M_2 l_f}{I_1} + \frac{M_2 l_f^2}{I_1} + \frac{M_2 l_r^2 \cos^2(\kappa)}{I_2} + 1\right)$$

$$c_{xrl} = a_{12}\left(\frac{M_2 l_r \sin(\kappa) tr}{2I_2} + \cos(\kappa)\right) + a_{22}\left(\frac{M_2 l_r \cos(\kappa) tr}{2I_2} - \sin(\kappa)\right)$$

$$c_{yrl} = a_{12}\left(\frac{-M_2 a_r l_r \sin(\kappa)}{I_2} + \sin(\kappa)\right) + a_{22}\left(\frac{-M_2 a_r l_r \cos(\kappa)}{I_2} + \cos(\kappa)\right)$$

$$c_{xrr} = a_{12}\left(\frac{-M_2 l_r \sin(\kappa) tr}{2I_2} + \cos(\kappa)\right) + a_{22}\left(\frac{-M_2 l_r \cos(\kappa) tr}{2I_2} - \sin(\kappa)\right)$$

$$c_{yrr} = a_{12}\left(\frac{-M_2 a_r l_r \sin(\kappa)}{I_2} + \sin(\kappa)\right) + a_{22}\left(\frac{-M_2 a_r l_r \cos(\kappa)}{I_2} + \cos(\kappa)\right)$$

$$c_m = a_{12}\frac{-M_2 l_r \sin(\kappa)}{I_2} + a_{22}\left(\frac{M_2 l_f}{I_1} - \frac{M_2 l_r \cos(\kappa)}{I_2}\right)$$

PLANETARY GEARBOX DESIGN FOR HYBRIDIZATION OF A PROTOTYPE POWERTRAIN

Özgür AKDENİZ, *ozgur.akdeniz@atilim.edu.tr* Atilim University, 06830, Ankara, Turkey

Ali EMİN, *ali.amini@atilim.edu.tr* Atilim University, 06830, Ankara, Turkey

ABSTRACT

This paper aims to design a planetary gearbox design that can be used to hybridize an existing internal combustion engine in a cost-effective way. A planetary gearbox system allows mechanical coupling between two different power sources with speed summation properties. Another important factor of the planetary gearset is the high efficiency and the potential for a high gear reduction, allowing two different power units with different operating ranges to work together flawlessly. A mathematical model was created using Goodman Criterion and the resultant parameters were used to design and manufacture a planetary gearbox system. The resultant gearbox aims to offer a highly efficient mechanical coupling system for hybridization.

Keywords: Planetary Gearset, Powertrain Coupling Systems, Electrification, Hybrid, Hybridization, Fuel Consumption

INTRODUCTION

Internal combustion engines are the main choice for powering land vehicles since they are inexpensive and easy to manufacture. However, their high running costs and their polluting nature make their viability and sustainability uncertain. Electric vehicles are the hot topic of the moment in automotive sector since they promise lower operating costs compared to their ICEV equivalents along with zero tailpipe emissions. However, there are a few important issues that

can more than offset the advantages related to a reduction in operating costs. The main issue lies with battery packs, the fact that they are very expensive to produce is the main culprit. Comparing a modern ICEV with a BEV equivalent shows that the BEV equivalent costs at least 10,000 $ more (A United States-Based Comprehensive Assessment, n.d.). For this reason, hybridizing existing vehicles to reduce their fuel consumption seems to be the more economical option. A theoretical study shows that by hybridizing existing vehicles, a fuel consumption reduction of over 15% can be achieved (Liu et al., 2021). Another benefit would be a reduction in emissions, since hybridized vehicles won't have the production emissions related with BEVs. In fact, a study conducted by (Burton et al., 2022) showed that for the average US customer, choosing a FHEV rather than a BEV was actually more ecological and more economical, which would also be a huge benefit. To achieve this goal, a mechanical coupling system is required in parallel HEV design. It needs to be compact, durable, and offer 2 inputs and 1 output port (Ehsani et al., n.d.).

All these requirements can be satisfied with a planetary gearset system, since it allows a 2 input, 1 output coupling system without requiring the synchromesh on gears or clutch packs, along with a gear reduction in the form of gear ratios between ring gear, planet gears and sun gear (De Carlo & Mantriota, 2020). Research conducted shows that one of the most common hybrid coupling systems use a planetary gearset system to act as a coupler between power sources and the transmission.

In this study, a planetary gearset system was chosen for the coupler design. First, a mathematical model was constructed of the powertrain components. Second, the outputs, along with their RPM range, for both the ICE and the EM, are added to the mathematical model to determine the gear ratios required for the sun, planet, and ring gears. Then the forces and moments acting upon each of the components were determined. Third, with this information along with the safety factor of 3, a 3D model of the gearbox is created using CAD software. Next, the technical drawings of the parts are created. The parts are mostly manufactured. The next step is to finish the assembly of the gearbox to make sure it works as intended. It is

expected to see a minimum of 15-20% reduction in fuel consumption according to the mathematical model calculations and research conducted.

METHODOLOGY

A mechanical coupling system using a planetary gearset was determined. It was designed with space, cost, manufacturability and modularity points in mind. A mathematical model was created using MATLAB software and Goodman Criterion. Other criterions such as S-N curve was considered; but the Goodman Criterion was determined to be used for our calculations since it fulfilled all our requirements for our calculations. (Budynas et al., 2011) This mathematical model was cross checked and validated. Several different materials were checked with a market and literature search and their engineering data were determined. Using our mathematical model and input values from our power units, along with material data found from research, specifications of each component of the gearbox were determined. These specifications were then entered into another software to double check the validity of our specifications for our application. After validating the specifications, with the help of CAD software, each part of the gearbox assembly was modeled and put in an assembly in order to check for compatibility. After validating the compatibility, it was decided to produce the resultant gearbox assembly to test for a prototype powertrain. Then, technical drawings for each component were created. After creating the technical drawings, the parts were manufactured. The assembly of the parts are currently in progress.

MATERIAL

Grade 2, carburized and hardened steel was used for the gears and its properties are taken from (Silva & Perera, 2012). AISI 4140 steel was used for the shafts, whose properties are taken from (Silva & Perera, 2012). Al 6061-T6 was used for the ring connector and arm that connects carrier gears with the hollow shaft and its properties are taken from (Shi et al., 2013).

Al 7075-T6 was used for the bearing housings and the floor of the gearbox and its properties are taken from (Bałon et al., 2018). Material properties for the gears and shafts are given in the table 1 and for the aluminum parts are given in the table 2.

Table 1: Properties of materials used on construction of the gears and shafts

	Grade 2, carburized and hardened steel (Gears)	**AISI 4140 steel (Shafts)**
Young's Modulus (MPa)	71000	200000
Poisson's Ratio	0.33	0.3
Allowable Bending Stress Number (kPsi)	65	22
Allowable Contact Stress Number (kPsi)	225	145

Table 2: Properties of materials used on construction of aluminum parts

	Aluminum 6061-T6	**Aluminum 7075-T6**
Young's Modulus (MPa)	71000	71700
Poisson's Ratio	0.33	0.33
Tensile Yield Strength (kPsi)	26	75
Tensile Ultimate Strength (kPsi)	35	81

MATHEMATICAL MODEL

To define the requirements for the for the coupling system, a mathematical model was constructed, and a CAD model was constructed according to the results.

Before constructing a CAD model, a mathematical model was constructed using MATLAB. Its validity was confirmed using the example gearbox design found in Shigley's engineering design book (Budynas et al., 2011), cross checked with the results. Goodman Criterion was used. Gear and shaft dimensions are shown below in Table 3.

Table 3: Gear and Shaft Dimensions from book and model

Gear	Diameter from model (in)	Diameter from book (in)	Width from model (in)	Width from book (in)
2	2.67	2.67	1.5	1.5
3	12	12	1.5	1.5
4	2.67	2.67	2	2
5	12	12	2	2

After conducting these tests, the mathematical model was verified for this application. Part of the mathematical model can be seen in figure 1.

Figure 1: Part of the mathematical model for the example gearbox

```
clc
clear all
%
%Input parameters and requirements
%
wi=1750; %Input speed in rpm
wo=85; %Output speed should be BTW 82 and 88 rpm, 85 is middle of 82-88 rpm --> good starting point
N(2)=16; % the minimum number of teeth from Eq. (13–11), p. 686, is 16.
N(4)=N(2); % the minimum number of teeth from Eq. (13–11), p. 686, is 16.
H=20; %Power rating in HP
phi=20 %pressure angle in degrees
%Shaft minimum safety factor is 1.5
%
%Gear 4 Calculations
%
w(5)=wo;
w(2)=wi;
e=w(5)/w(2) % total gear ratio
N2_N3=sqrt(e)
N(3)=N(2)/(N2_N3) %Try rounding down to check if w(5) is between limits.
N(3)=floor(N(3))
N(5)=floor(N(3))
w(5)=(1750*N(2)*N(4))/(N(3)*N(5)) %w5=86.42 rpm is between 82-88 rpm, so it is acceptable.
w(3)=(N(2)*1750)/(N(3))
w(4)=(N(4)*1750)/(N(5))
T(2)=(H/w(2))*(550*60)/(2*pi) %Converting Eq. (18-1) to determine torque values. Unit conversion to lbf.ft made.
T(3)=(T(2)*w(2))/(w(3))
T(5)=(T(2)*w(2))/(w(5))
Pmin=(N(3)+(N(2)/2)+(N(5)/2))/(22-1.5) %Unit is teeth/in. Allow 1.5 in for clearances and wall thicknesses.
P(1)=6 %5.66 rounded up to 6. Start with P=6 teeth/in.
d(2)=N(2)/P(1) %unit is inch
d(4)=N(4)/P(1) %unit is inch
d(3)=N(3)/P(1) %unit is inch
d(5)=N(5)/P(1) %unit is inch
V23=(pi*d(2)*w(2))/(12) %Eq. (13–34), p. 707
V45=(pi*d(5)*w(5))/(12) %Eq. (13–34), p. 707
Wt23=(33000*H)/(V23) %Eq. (13–35), p. 707
Wr23=Wt23*tand(phi) % Eq. (13-38), p. 709
Wt45=(33000*H)/(V45) %Eq. (13–35), p. 707
Wr45=Wt45*tand(phi) % Eq. (13-38), p. 709

I(4)=(((cosd(phi))*(sind(phi))*4.5)/(2*1*(4.5+1))) %Eq. (14–23), p. 755
Qv(4)=7 %Assumption for Kv(4), Eq. (14-29), p. 756
B(4)=0.731 %Assumption for Kv(4), Eq. (14-29), p. 756
A(4)=65.1 %Assumption for Kv(4), Eq. (14-29), p. 756
Kv(4)=((A(4)+sqrt(V45))/(A(4)))^(B(4))
F(4)=((4*pi)/P(1)) %On www.globalspec.com, entering P = 6 teeth/in and d = 2.67 in, stock spur gears from several
sources have face widths of 1.5 in or 2.0 in.
F(4)=2.0 %These are also available for the meshing gear 5 with d = 12 in. Choose F = 2.0 in.
Cpf(4)=((F(4)/(10*d(4)))-(0.0375)+((0.0125*F(4))))%Eq. (14–32), p. 760
Cmc(4)=1 %Uncrowned teeth, Eq. (14–31), p. 760
Cpm(4)=1 %Straddle-mounted pinion, S1/S<0.175, Check Figure 14-10, p.760 for values, Eq. (14–33), p. 760
Acma(4)=0.127 %Commercial, enclosed units, Table 14-9, p. 760
Bcma(4)=0.0158 %Commercial, enclosed units, Table 14-9, p. 760
Ccma(4)=-0.930*(10^-4) %Commercial, enclosed units, Table 14-9, p. 760
Cma(4)=Acma(4)+(Bcma(4)*F(4))+(Ccma(4)*(F(4)^2)) %Eq. (14–34), p. 760
Ce(4)=1 %For any combination other than gearing adjusted at assembly, or compatibility is improved by lapping, or
both, Eq. (14–35), p. 760
Km(4)=1+Cmc(4)*((Cpf(4)*Cpm(4))+(Cma(4)*Ce(4))) %Eq. (14–30), p. 759
Cp(4)=2300 %Pinion and Gear Materials are Steel, value from Table 14-8, p.757
Ko(4)=1
Ks(4)=Ko(4)
Cf(4)=Ko(4)
STNWc(4)=Cp(4)*(sqrt((Wt45*Ko(4)*Kv(4)*Ks(4)*Km(4)*Cf(4))/(d(4)*F(4)*I(4)))) %STN=σ since σ is invalid, U.S
customary units equation used, Eq. (14-16), p. 746
L(4)=12000*60*389 % Use 12000h as lifetime, unit conversion to rev
ZN(4)=0.9 %Fig. 14-15, p. 750
Kr(4)=1
Kt(4)=1
Ch(4)=1
SH=1.2 %Taken as 1.2 as per design ratio. SH is the AGMA factor of safety, a stress ratio. p. 750
Sc(4)=(SH*STNWc(4))/(ZN(4)) %From Table 14–6, p. 751, this strength is achievable with Grade 2 carburized and
hardened with Sc = 225 000 psi.
Sc(4)=225000 %Grade 2 carburized and hardened with Sc = 225 000 psi.
nc(4)=(Sc(4)*ZN(4))/(STNWc(4)) %To find the achieved factor of safety, nc = σc,all/σc with SH = 1.
J(4)=0.27 %16 teeth, Fig. 14-6, p.753
KH(4)=1
STNB(4)=(Wt45*Kv(4)*P(1)*Km(4))/(F(4)*(J(4)))
YN(4)=0.9 %Fig. 14–14, p. 763
StB(4)= 65000 %Using Grade 2 carburized and hardened, same as chosen for wear, find St = 65 000 psi (Table 14–3,
p. 748).
STNBall(4)=(StB(4)*YN(4))
nb(4)=STNBall(4)/ STNB(4)
```

The mathematical model was modified to work with a planetary gearbox system. The input values for the application of the gearbox were applied. Input values are given in table 4.

Table 4: Input values for the gearbox

Parameters	Values
Gear Module (ig)	3
Input Speed (wi)	4000 RPM
Output Speed (wo)	Same as wi
Number of Teeth of Carrier Gears (N(3))	27
Number of Teeth of Sun Gear (N(2))	26
Number of Teeth of Internal Ring Gear (N(5))	78
Electric Motor (EM) Power rating (H1)	3 HP
Internal Combustion Engine (ICE) Power rating (H2)	20 HP
Gear pressure angle (phi)	20 °
mG	3
mN	1
SH	2
Sc	225 000 Psi for all gears
StB	65 000 Psi for all gears
Operation life (L(2-5))	12000 h

CALCULATIONS

This section explains the calculations for the planetary gearset system. The requirements for the mechanical parts are a minimum operation life of 12000 hours with the inputs provided. All calculations were mentioned in (Budynas et al., 2011).

Speed, torque, transmitted loads

First, the amount of torque that will be transferred on the gears were determined:

$$T_i = \frac{H}{w_i} \cdot 33000 \quad \text{.....(1)}$$

$$T_o = \frac{H}{w_o} \cdot 33000 \quad \text{.....(2)}$$

The values for the gearbox were determined according to the requirements of the prototype powertrain setup. The power inputs are 3 HP for the EM and 20 HP for the ICE. The input and output speeds are determined as 4000 RPM:

$$H_1 = 3 \text{ HP} \quad \text{.....(3)}$$

$$H_2 = 20 \text{ HP} \quad \text{.....(4)}$$

$$w_i = w_o = 4000 \text{ RPM} \quad \text{.....(5)}$$

The transferred torque can be determined as:

$$T_{(3)} = \frac{H_1}{w_3} \cdot 33000 = \frac{3\ HP}{4000 * 2 * \pi\ rad/min} \cdot 33000 \cong 4.0 \text{ lbf. ft} \quad \text{.....(6)}$$

$$T_{(5)} = \frac{H_2}{w_5} \cdot 33000 = \frac{20\ HP}{4000 * 2 * \pi\ rad/min} \cdot 33000 \cong 26.3 \text{ lbf. ft} \quad \text{.....(7)}$$

These calculations show that the ring gear needs to transfer 26.3 lbf.ft of torque, which is the higher value of the two. Second, the pitch line velocities and transmitted loads were calculated for use in calculations later:

$$V = \pi \cdot \mathrm{d} \cdot n \div 12 \quad \text{(8)}$$

$$d = \mathrm{N} \div P \quad \text{(9)}$$

$$W_t = 33000 \cdot \frac{H}{V} \quad \text{(10)}$$

$$W_r = W_t \cdot \tan(phi) \quad \text{(11)}$$

The values for the application were once again determined according to the requirements of the prototype powertrain setup, using the determined input values given above:

$$V12 = \pi \cdot 2.89\mathrm{in} \cdot 4000RPM \div 12 \cong 3.02 \cdot 10^3\ ft/min \quad \text{(12)}$$

$$V34 = \pi \cdot 3.00\mathrm{in} \cdot 4000RPM \div 12 \cong 3.14 \cdot 10^3\ ft/min \quad \text{(13)}$$

$$V45 = \pi \cdot 8.67\mathrm{in} \cdot 4000RPM \div 12 \cong 9.07 \cdot 10^3\ ft/min \quad \text{(14)}$$

$$W_{t12} = 33000 \cdot \frac{23HP}{3.02 \cdot 10^3\ ft/min} \cong 250.89\mathrm{lbf} \quad \text{(15)}$$

$$W_{r12} = 250.89\mathrm{lbf} \cdot \tan(20°) \cong 91.32\mathrm{lbf} \quad \text{(16)}$$

$$W_{t34} = 33000 \cdot \frac{3HP}{3.14 \cdot 10^3\ ft/min} \cong 31.51\mathrm{lbf} \quad \text{(17)}$$

$$W_{r34} = 250.89\mathrm{lbf} \cdot \tan(20°) \cong 11.47\mathrm{lbf} \quad \text{(18)}$$

$$W_{t45} = 33000 \cdot \frac{20HP}{9.07 \cdot 10^3\ ft/min} \cong 72.72\mathrm{lbf} \quad \text{(19)}$$

$$W_{r45} = 250.89\mathrm{lbf} \cdot \tan(20°) \cong 26.47\mathrm{lbf} \quad \text{(20)}$$

With the pitch line velocities and transmitted loads determined, gear and shaft calculations can be carried out.

Gears

For the gear wear and bending calculations, gear number 2, which is any one of the carrier gears, will be used for our example calculations. These calculations will be applied to every gear. You can find the constants and the formulas below:

$I_n = \cos(\text{phi}) \cdot \sin(\text{phi}) \cdot \text{mG} \,/\, (2 \cdot \text{mN} \cdot (\text{mG} + 1))$ ……(21)

$Qv_n = 3 - 7$ for commercial applications ……(22)

$B_n = 0.25 \cdot (12 - Qv_n)^{2/3}$ ……(23)

$A_n = 50 + (56 \cdot (1 - B_n))$ ……(24)

$Kv_n = (A_n + \sqrt{V_n})/{A_n}^{B_n}$ ……(25)

$C_{pfn} = F_n / ((10 \cdot d_n) - 0.025$ ……(26)

$C_{mc} = 1$ for uncrowned teeth ……(27)

$C_{pm} = 1$ for straddle − mounted pinion……(28)

$A_{cma} = 0.127$ for commertial, enclosed units ……(29)

$B_{cma} = 0.016$ for commertial, enclosed units ……(30)

$C_{cma} = -0.93 \cdot 10^{-4}$ for commertial, enclosed units ……(31)

$C_{ma} = A_{cma} + (B_{cma} \cdot F_n) + (C_{cma} \cdot {F_n}^2)$ ……(32)

$C_e = 1$ for most combinations……(33)

$K_m = 1 + (C_{mc} \cdot C_{pm}) + (C_{ma} \cdot C_e)$ ……(34)

$C_p = 2300$ for steel pinion and gears ……(35)

$C_f = K_o = K_s = 1$……(36)

$F_n = (4 \cdot)\pi / P_n$……(37)

$\sigma_c = C_p \cdot \left(\sqrt{\left(\frac{W_t \cdot K_o \cdot K_v \cdot K_s \cdot K_m \cdot C_f}{\text{d} \cdot F_n \cdot I_n}\right)}\right)$ ……(38)

$L_n = 12000 \cdot 60 / w_n \; for \; 12000 \; hour \; lifetime, unit \; convertion \; to \; rev$……(39)

$ZN_n = 2.466 \cdot {L_n}^{-0.056}$ ……(40)

$C_h = K_t = K_r = 1$……(41)

$S_H = 1.2$ ……(42)

$S_c = (S_H \cdot \sigma_c)/\ ZN_n$ ……(43)

$S_c =$

225000 Psi for $Grade\ 2, carburized\ and\ hardened\ steel$ ……(44)

$n_c = (S_c \cdot \mathrm{ZN}_n)/\ \sigma_c$ ……(45)

$J_n = 0.32$……(46)

$KH_n = 1$ ……(47)

$\sigma_b = W_t \cdot K_v \cdot P_n \cdot K_m \cdot C_f / F_n \cdot J_n$ ……(48)

$S_t =$

65000 Psi for $Grade\ 2, carburized\ and\ hardened\ steel$……(49)

$\mathrm{YN}_n = 1.4488 \cdot {L_n}^{-0.023}$ ……(50)

$\sigma_{ball} = \sigma_b \cdot YN_n$ ……(51)

$n_b = \sigma_{ball}/\ \sigma_b$ ……(52)

Insert the input values to obtain the following results:

$I_2 = \cos(20°) \cdot \sin(20°) \cdot 3\ /\ (2 \cdot 1 \cdot (3+1)\ \cong 0.12$ ……(53)

$B_2 = 0.25 \cdot (12-7)^{2/3} \cong 0.73$ ……(54)

$A_2 = 50 + \big(56 \cdot (1-0.73)\big) \cong 65.06$ ……(55)

$Kv_2 = (65.06 + \sqrt{3.02 \cdot 10^3})/65.06^{0.73} \cong 1.57$ ……(56)

$F_2 = 30/25.4 \cong 1.18$ in ……(57)

$C_{pf2} = 1.18/\ ((10 \cdot 2.89) \cong 0.02$ ……(58)

$C_{ma}2 = 0.127 + (0.016 \cdot 1.18) + ((-0.93 \cdot 10^{-4}) \cdot 1.18^2) \cong 0.15$ ……(59)

$K_{m2} = 1 + (1 \cdot 1) + (0.15 \cdot 1) \cong 1.16$ ……(60)

$\sigma_{c2} = 2300 \cdot (\sqrt{\left(\frac{250.89 \cdot 1 \cdot 1.57 \cdot 1 \cdot 1.16 \cdot 1}{2.89 \cdot 1.18 \cdot 0.12}\right)}) \cong 7.66 \cdot 10^4\ Psi$ ……(61)

$L_2 = 12000 \cdot 60/\ 4000\ \cong 2.88 \cdot 10^9\ rev$……(62)

$ZN_2 = 2.466 \cdot (2.88 \cdot 10^9)^{-0.056} \cong 0.73$ ……(63)

$n_{c2} = (225000 \cdot 0.73)/\ (7.66 \cdot 10^4) \cong 2.14$ ……(64)

$\sigma_{b2} = 250.89 \cdot 1.57 \cdot 9 \cdot 1.16 \cdot 1/1.18 \cdot 0.32 \cong 1.09 \cdot 10^4\ Psi$ ……(65)

$\mathrm{YN}_2 = 1.4488 \cdot (2.88 \cdot 10^9)^{-0.023} \cong 0.88$……(66)

$\sigma_{ball2} = 65000 \cdot 0.88 \cong 5.71 \cdot 10^4\ Psi$. ……(67)

$n_{b2} = 5.71 \cdot 10^4/\ 1.09 \cdot 10^4 \cong 5.26$ ……(68)

These results show that for our carrier gears, wear safety factor of 2.14 and bending safety factor of 5.26 was achieved, which is above the minimum requirements, therefore concluding that this design is safe for our application. When these calculations are adjusted for every gear, a safety factor of 2 or above is always obtained, with the results given below:

$n_{c3} = (225000 \cdot 0.73)/\ (4.63 \cdot 10^4) \cong 3.54$ ……(69)

$n_{c4} = (225000 \cdot 0.70)/\ (4.95 \cdot 10^4) \cong 3.18$ ……(70)

$n_{c5} = (225000 \cdot 0.73)/\ (2.89 \cdot 10^4) \cong 5.67$ ……(71)

$n_{b3} = 5.71 \cdot 10^4/\ 1.09 \cdot 10^4 \cong 13.88$ ……(72)

$n_{b4} = 5.61 \cdot 10^4/\ 4.54 \cdot 10^3 \cong 12.37$ ……(73)

$n_{b5} = 5.71 \cdot 10^4/\ 7.07 \cdot 10^3 \cong 8.07$ ……(74)

According to these results, every gear that will be used on this gearbox meets the safety requirements for our application.

Shafts

For the shaft calculations, shaft number 4 will be used as an example. These calculations will be integrated to the other shafts. First, a free body diagram of the shaft is drawn, which can be found in the figure 2 below. Second, the forces acting on the shaft is calculated:

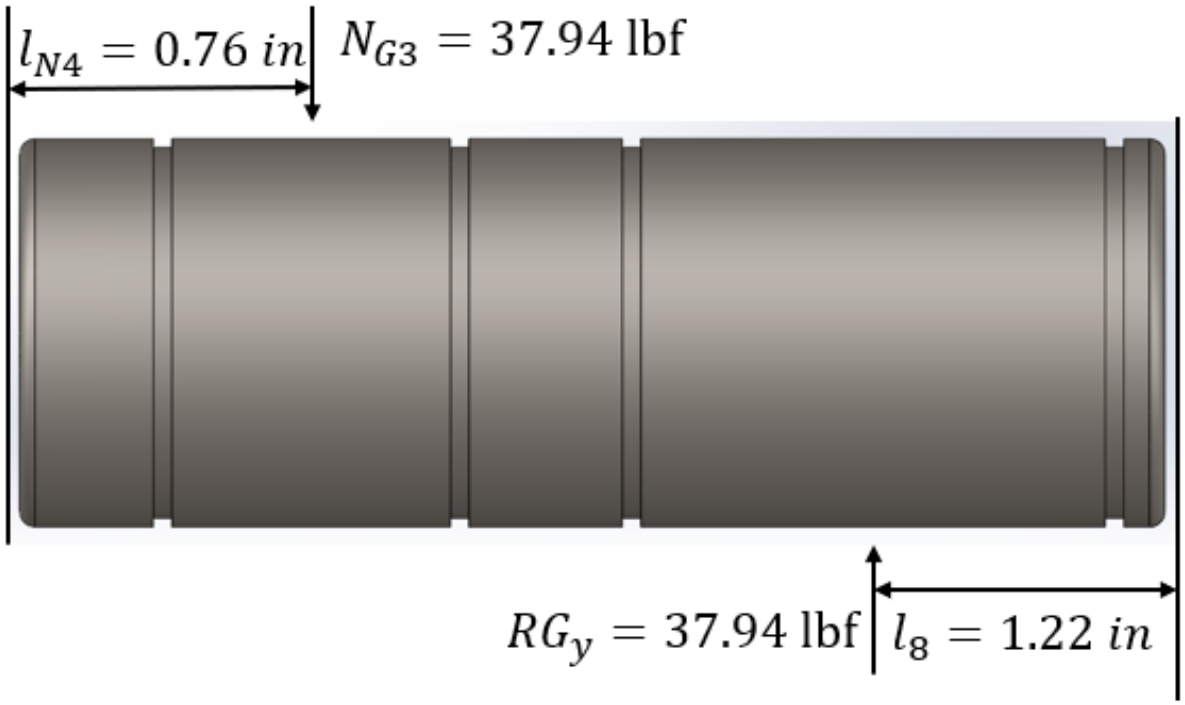


Figure 2: FBD of Shaft 4

$$RG_{y4} = w_{r34} + w_{r45} \cong 37.94 \text{ lbf} \quad \text{(75)}$$

$$l_8 = 1.22\ in \quad \text{(76)}$$

Third, using these information, the torques and moments acting on the shaft are calculated.

$$TS_4 = T_{m4} = (w_{r34} + w_{r45}) \cdot (d_4/2) \cong 37.94 \text{ lbf} \quad \text{(77)}$$

$$M_{ay4} = (w_{r34} + w_{r45}) \cdot l_8 \cong 46.30 \text{ lbf} \quad \text{(78)}$$

$$M_{az4} = M_{m4} = T_{a4} = 0 \quad \text{(79)}$$

$$M_{a4} = \sqrt{({M_{ay4}}^2 + {M_{az4}}^2)} \cong 46.30 \text{ lbf} \quad \text{(80)}$$

Then, with the torque and moments known, critical points on the shaft are checked.

$K_{tL} = K_{fL} = 1.7$ ……(81)

$K_{tsL} = K_{fsL} = 1.5$ ……(82)

$d_{s4} \cong 0.59\ in$ ……(83)

$S_{utL} = 75\ kPsi$ ……(84)

$a_L = 2.7$ ……(85)

$b_L = -0.265$ ……(86)

$ka_L = a_L \cdot {S_{utL}}^{b_L} \cong 0.86$ ……(87)

$kb_L = (d_{s4}/0.3)^{-0.107} \cong 0.93$ ……(88)

$kc_L = 1$ ……(89)

$kd_L = 1.02$ ……(90)

$ke_L = 0.868$ ……(91)

$S_{e1L} = 0.5 \cdot S_{utL} = 37.5\ kPsi$ ……(92)

$S_{eL} = ka_L \cdot kb_L \cdot kc_L \cdot kd \cdot ke \cdot S_{e1L} \cong 26.55\ kPsi$ ……(93)

$$d_4 = \sqrt[3]{(16 \cdot n_{b4}/\pi) \cdot (((2 \cdot K_{fL} \cdot M_{a4})/(S_{eL} \cdot 1000)) + ((\sqrt{3} \cdot K_{fsL} \cdot T_{m4})/(S_{utL} \cdot 1000)))}$$ …(94)

$d_4 \cong 1.63$ in. …….(94a)

$\sigma_{a4} = (32 \cdot K_{fL} \cdot M_{a4})/(\pi \cdot {d_4}^3) \cong 1.14 \cdot 10^3\ Psi$ .....(95)

$$\sigma_{m4} = \sqrt{3 \cdot (((16 \cdot K_{fsL} \cdot T_{m4})/(\pi \cdot {d_4}^3))^2} \cong 2.84 \cdot 10^3\ Psi$$ .....(96)

$n_{f4} = 1/\left((\sigma_{a4}/S_{eL} \cdot 1000)\right) + (\sigma_{a4}/S_{utL} \cdot 1000))) \cong 12.37$ ……(97)

These results show that for carrier gear shaft, safety factor of 12.37 was achieved, which is above the minimum requirements, therefore concluding that this design is safe for our application. When these calculations are adjusted for every shaft, a safety factor of 2 or above is always obtained, with the results given below:

$n_{f1} = 1/\left((\sigma_{a1}/S_{eI} \cdot 1000)\right) + (\sigma_{a1}/S_{utI} \cdot 1000))) \cong 5.25$ .....(98)

$$n_{f2} = 1/\left(\left(\sigma_{a2}/S_{eJ} \cdot 1000\right)\right) + \left(\sigma_{a2}/S_{utJ} \cdot 1000\right))) \cong 5.25 \quad \text{.....(99)}$$

$$n_{f3} = 1/\left(\left(\sigma_{a3}/S_{eK} \cdot 1000\right)\right) + \left(\sigma_{a3}/S_{utK} \cdot 1000\right))) \cong 12.37 \quad \text{.....(100)}$$

$$n_{f5} = 1/\left(\left(\sigma_{a1}/S_{eM} \cdot 1000\right)\right) + \left(\sigma_{a1}/S_{utM} \cdot 1000\right))) \cong 29.04 \quad \text{.....(101)}$$

According to these results, every gear that will be used on this gearbox meets the safety requirements for our application.

MODEL

After verifying the specifications of the mechanical parts of the gearbox, a 3D CAD model was constructed using a CAD software. Then, an assembly model was created on the CAD software to verify functionality and compatibility of every part of the gearbox. A 3D CAD model of the gearbox can be found below in figure 3.

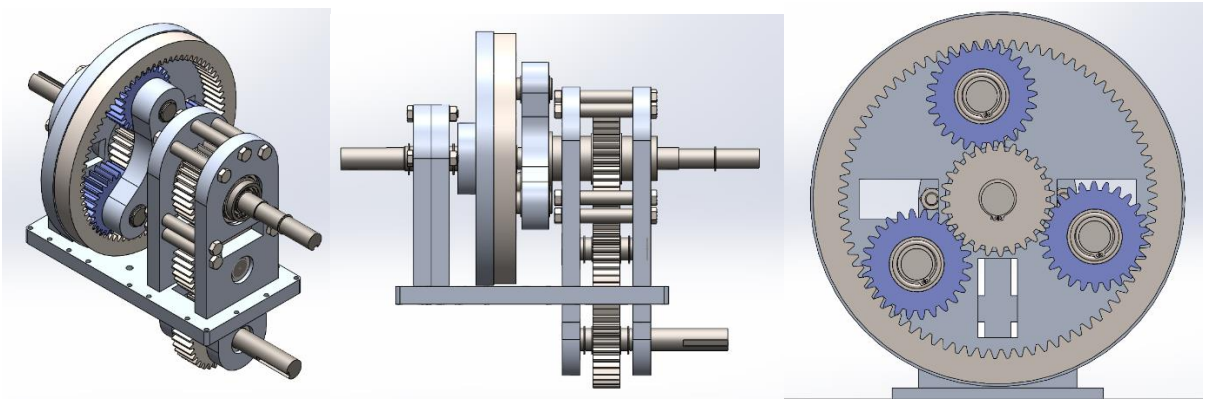


Figure 3: Isometric, side and front cutaway views of 3D CAD model

Next, technical drawings of each one of the parts were created. After creating the technical drawings, parts were bought or manufactured according to the specifications. Some of the produced parts can be found below in figure 4. Production of the parts is mostly complete and the assembly of the gearbox is in progress.



Figure 4: Some of the produced parts for the gearbox.

CONCLUSION

A mathematical model was constructed using an example gearbox design with Goodman Criterion. After it was validated, it was modified to fit our purposes. The aim was to determine the wear and bending safety factors for the gears and the safety factors on the critical points on the shafts. In conclusion, the parts were designed to meet our safety criteria using a custom mathematical model, which sped up the calculation process as it was made possible to make small alterations on the design and validate the safety of the parts very easy. First, a mathematical model was created using an example gearbox design and its validity was double checked. Second, it was modified to be compatible with a planetary gearbox system which would be used in hybridization of an existing ICE powertrain. With this model, a new planetary gearbox was constructed and properties of each mechanical part was determined. With the results, it was made possible to create an accurate 3D CAD model for the gearbox which could satisfy our requirements. Then, technical drawings were created and the production phase began. The parts are mostly finished and the assembly of the gearbox is in progress.

REFERENCES

A United States-Based Comprehensive Assessment. (n.d.).

Bałon, P., Rejman, E., Smusz, R., Szostak, J., & Kiełbasa, B. (2018). Implementation of high speed machining in thin-walled aircraft integral elements. *Open Engineering*, *8*(1), 162–169. https://doi.org/10.1515/eng-2018-0021

Budynas, R. G. (Richard G., Nisbett, J. Keith., & Shigley, J. Edward. (2011). *Shigley's mechanical engineering design*. McGraw-Hill.

Burton, T., Powers, S., Burns, C., Conway, G., Leach, F., & Senecal, K. (2022). A Data-Driven Greenhouse Gas Emission Rate Analysis for Vehicle Comparisons. *SAE International Journal of Electrified Vehicles*, *12*(1). https://doi.org/10.4271/14-12-01-0006

De Carlo, M., & Mantriota, G. (2020). Electric vehicles with two motors combined via planetary gear train. *Mechanism and Machine Theory*, *148*. https://doi.org/10.1016/j.mechmachtheory.2020.103789

Ehsani, M., Gao, Y., Longo, S., & Ebrahimi, K. M. (n.d.). *Modern Electric, Hybrid Electric, and Fuel Cell Vehicles, Third Edition*.

Liu, Y., Liao, Y. G., & Lai, M. C. (2021). Fuel economy improvement and emission reduction of 48 V mild hybrid electric vehicles with P0, P1, and P2 architectures with lithium battery cell experimental data. *Advances in Mechanical Engineering*, *13*(10). https://doi.org/10.1177/16878140211036022

Shi, G., Ban, H., Bai, Y., Wang, Y., Luo, C., & Shi, Y. (2013). A novel cast aluminum joint for reticulated shell structures: Experimental study and modeling. *Advances in Structural Engineering*, *16*(6), 1047–1060. https://doi.org/10.1260/1369-4332.16.6.1047

Silva, G. I. P. De, & Perera, W. C. (2012). *Improvement of the Mechanical Properties of Aluminum 6063 T5 Extrudates By Varying the Aging Condition Cost-Effectively*. *July 2020*, 62–64.

A LIGHTWEIGHT MULTIFUNCTIONAL BATTERY CASE

Necdet GEREN, *gerendr@cu.edu.tr* Cukurova University, 01250, Adana, Türkiye

O. Cem GÖKCİLER, *ocgokciler@cu.edu.tr* Cukurova University, 01250, Adana, Türkiye

M. Burak İBEKCİ, *mbibekci@cu.edu.tr* Cukurova University, 01250, Adana, Türkiye

Çağrı UZAY, *cagriuzay@ksu.edu.tr* Kahramanmaras Sutcu Imam University, 46050, Kahramanmaras, Türkiye

Melih BAYRAMOĞLU, *bayramog@cu.edu.tr* Cukurova University, 01250, Adana, Türkiye

ABSTRACT

In this paper, a battery casing that incorporates an active cooling system is invented and introduced. The case has features of light weight, ability to absorb impact loads and self-healing. Carbon-fiber reinforced polymer composite with micro-vascular channels of different diameters will be produced and used as the case material. Active cooling is achieved by circulating coolant in the larger diameter channels and the smaller diameter channels are responsible for self-healing ability. Thus, this innovative energy storage device will have the potential to be used in electric/hybrid vehicles with its self-healing ability, without the need for additional piping system.

Keywords: battery casing technology, energy storage, thermal management, self-healing, micro-vascular composites

ÖZET

Bu bildiride, aktif soğutma sistemi içeren, hafif, darbe yüklerini absorbe etme ve kendi kendini iyileştirme yeteneğine sahip, yenilikçi bir batarya muhafaza kutusu tasarım esasları tanıtılmıştır. Karbon elyaf takviyeli polimer kompozitler, farklı çaplarda mikro vasküler kanallara sahip olacak şekilde üretilecektir. Daha büyük çaplı kanallar, içinde dolaşacak akışkan ile termal yönetim sağlarken, daha küçük çaplı kanallar olası bir hasar durumunda kendi kendini iyileştirme yeteneğinden sorumlu olacaktır. Böylece hafif ve yenilikçi enerji depolama cihazı, harici termal yönetim sistemine, dolayısıyla fazladan ağırlık yaratacak borulama sistemine, ihtiyaç duymadan, kendi kendini iyileştirme özelliğiyle elektrikli ve hibrit araçlarda kullanılabilecek potansiyele sahip olacaktır.

Anahtar Kelimeler: batarya paket teknolojisi, enerji depolama, termal yönetim, kendi-kendini iyileştirme, mikro vasküler kanallar

1. INTRODUCTION

The usage of electric vehicles (EVs) and hybrid vehicles (HVs) is increasing day by day, due to economic and environmental reasons. Looking at the world in general, it is predicted that in the next 20-30 years, restrictions will be gradually imposed on the sale and use of gasoline and diesel engine vehicles, and then it is expected that, they will be completely banned. For example, Ireland has decided to ban the use of gasoline and diesel engine vehicles by 2030 to reduce carbon emissions and protect the environment. Also, the UK bans the sale of fossil fuel vehicles by 2040 and it aims to use zero-emission vehicles by 2050. Likewise, France has stated that they will allow the sale of vehicles that use clean energy sources by 2040. In Türkiye, in the 12th Development Plan which is prepared by the Strategy and Budget Directorate of the Presidency of the Republic of Türkiye, policies prepared for both reducing the impact of climate change and energy conversion processes were emphasized and it was aimed to reach net zero emission targets in 2053. Considering all these facts, the electric vehicle market is growing and most of the investments are shifting to this area. Thus, the studies on the EVs and their battery packages gain importance.

The most important part of an electric vehicle (EV) and hybrid vehicle (HV) is its battery package since it is the power supplier of the entire system. Therefore, the researchers have concentrated on increasing the battery pack efficiency and performance with different approaches. A typical battery casing of the existing EVs is very heavy and occupies a lot of space. Therefore, the excess weight of the EV and HV creates several problems such as; low driving range, low baggage carrying capacity, and high power consumption. One way to overcome these problems is to make the vehicle's components as light as possible without compromising their mechanical strength. When all these mechanical requirements are considered an ideal battery casing for an EV/HV must be strong and stiff enough to protect the batteries. Also, it must resist sudden loads such as impacts and crashes that may come from the outside of the vehicle and prevent batteries from being damaged [Pety et al., 2017]. Any impact on a battery cell within the package can result in electrolyte leakage, potentially leading to an explosion of the battery assembly [Han et al., 2022]. For an ideal battery casing design, a material that can offer as low density as possible while providing sufficient stiffness and strength, must be used. Recently, in order to overcome these conflicting objectives, carbon-fiber-reinforced polymer (CFRP) composites have begun to be used as the main material for the battery boxes of EVs.

Thus, it is very proper to use CFRP composites as the main material of the battery case of the EV, for a strong and lightweight design. As an industrial application, BMW has used CFRP composites as the battery casing's main material for the BMW i3 EV [Pety et al., 2017]. The supplier of this battery package, SGL, says carbon fiber construction can provide

a 40% weight savings over aluminium and high-strength steel in battery cases [Gardner, 2020]. Also, the usage of CFRP composites in battery case of the EVs offers several other advantages, such as; excellent electromagnetic interference (EMI) shielding [Luo and Chung, 1999] and superior performance in terms of thermal runaway [E-mobility, 2024]. Since the battery pack of an EV is located under the vehicle (Figure 1), electromagnetic waves become an issue for the driver and the passengers. This issue can be overcome by using CFRP composites for the battery case, due to the excellent EMI shielding of the CFRP composites.

Another dangerous issue for the batteries of the EVs/HVs is named as the danger of the thermal runaway. The result of this latent and slow temperature rise can be catastrophic. Due to these reasons, the material of the battery box should have superior EMI and thermal runaway properties that can be provided by CFRP composites. A produced carbon-fiber battery case is present in the Figure 2.

The most commonly used battery type for EVs is the lithium-ion (Li-ion) battery, due to its high energy density, long service life, reliability, and relatively wide operating temperature range. Currently, the mass-energy density value of the Li-ion batteries varies between 265– 280 Wh/kg and volumetric-energy density varies between 200-400 Wh/L [Khan et al., 2023]. Also, according to the United States Advanced Battery Consortium LLC (USABC), as a long- term goal; the mass-energy density value of the Li-ion batteries will reach 350 Wh/kg and the volumetric-energy density will reach up to 750 Wh/L [LLC, 2021].

An energy density comparison between Li-ion batteries and other alternatives is given in Figure 3, which emphasizes why Li-ion batteries are the most commonly used battery type in EVs. For this reason, it would be more proper to use Li-ion batteries as a basis when making designs and studies of the battery packaging.

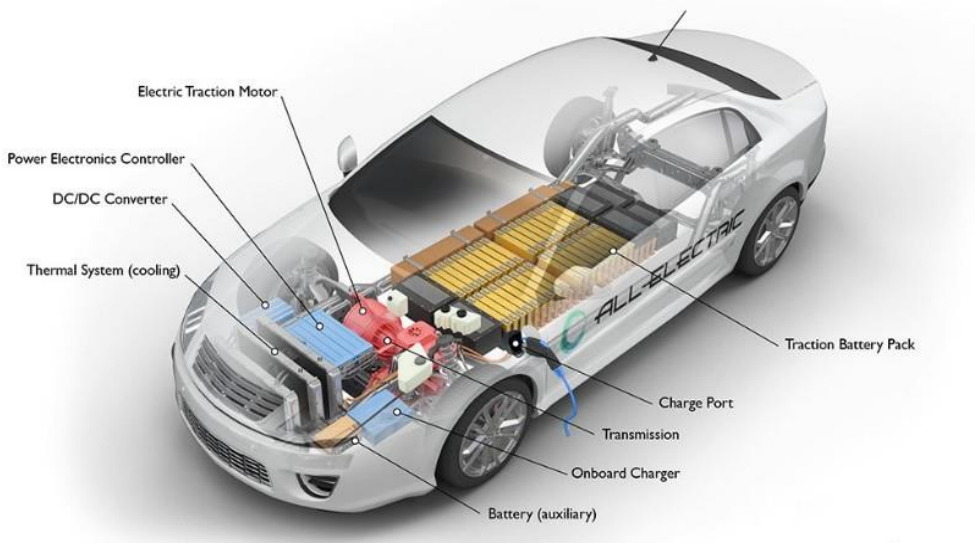


Figure 1. Schematic view of an EV [AFDC, 2018]

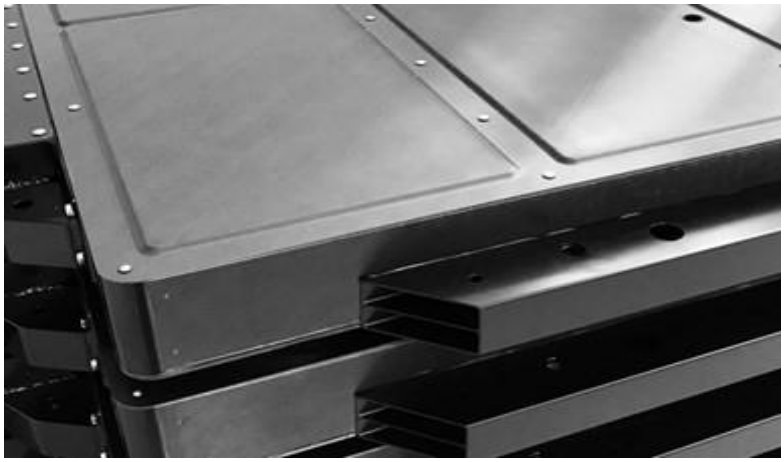


Figure 2. Carbon fiber battery case of BMW i3 battery case, produced by SGL [Gardner, 2020]

A Li-ion battery package system requires thermal management. Because, the performance and the efficiency of the batteries decrease, significantly, at the outside of the optimum operation temperature range. The existing thermal management systems of the battery packs are too heavy and contain piping systems that cause extra weight and extra cost.

As the objective of this study; in order to overcome all the current problems that are mentioned above, a battery casing structural system, that contains its own thermal management system, is lightweight, reliable, with high capability to absorb collision energy, and capable of self-repairing instantly in the event of potential damage from external impact loads is introduced, and the main design features are given for the ongoing work.

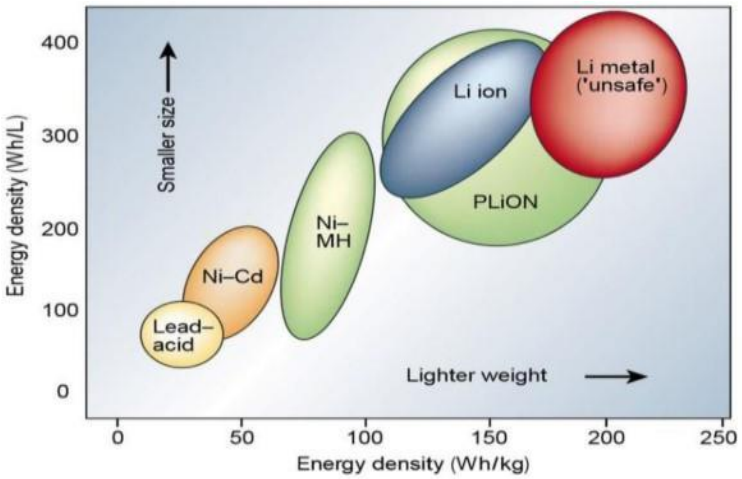


Figure 3. Current volumetric and mass-energy density values of battery types [Khan et al., 2023]

2. THERMAL MANAGEMENT SYSTEMS IN BATTERY PACKS

One of the most commonly used battery types in EVs are the Li-ion battery type as mentioned before, due to its reliability, high energy density, long service life, and relatively large operating temperature. Because of these advantages, the Li-ion battery has been considered to be one of the most promising long-term advanced battery technologies by the U.S. Advanced Battery Consortium [Pesaran, 2007]. However, the temperature range that the Li-ion batteries are able to operate is −20 °C ~ 60 °C [Ji et al., 2013]. Furthermore, the recommended operating temperature range, that the batteries can operate safely and efficiently, is even narrower. For example, a research has shown that commercial Li-ion battery cells achieve optimum performance near room temperature (25 °C) [Basu et al., 2016]. Another research showed that the optimal operation temperature range of Li-ion batteries is 15 °C–35 °C [Pesaran et al., 2013]. Once the temperature of the batteries exceeds this range some safety problems, that can include fire and explosion, emerge. Also, outside of this temperature range, the efficiency, lifetime, and performance of the batteries are decreased [Spitthoff et al., 2021].

Since the batteries generate heat while operating, the battery pack needs continuous cooling in hot and warm environments. On the other hand, in cold places such as Russia, Canada, and Greenland Island the batteries must be pre-heated before the usage to obtain the optimum performance. Because, the outdoor temperatures of these places, in winter, are much lower than 0 °C [Jaguemont et al., 2016]. These kinds of low temperatures, affect the performance, efficiency, and life of Li-ion batteries that are used in EVs and HVs. Another extremely cold environment in which Li-ion batteries are used is outer space. In recent years, Li-ion batteries have quickly become the most common energy storage solution for space missions [Bugga et al., 2007]. In such a case, the battery package requires continuous heating rather than continuous cooling.

These heating and cooling requirements are provided via thermal management systems that are attached to the battery packs. Thermal management systems in battery packs can be classified into three different groups according to the heating/cooling mechanisms [Li et al., 2023]. These are; air cooling [Lu et al., 2018], phase change material (PCM) [Youssef et al., 2023], and liquid cooling [Malik et al., 2018] systems. The advantages and disadvantages of these systems against each other are presented in Table 1.

In recent years, several techniques that aim to remove heat from the battery pack or aim to pre-heat/heat the batteries, have been tried and tested by different research groups. As the simplest and most cost-effective way, blowing air from a fan is the first candidate that comes to mind to manage the battery thermally [Mahamud and Park, 2011]. The amount of heat

removed from the battery is increased as the speed of the blown air is increased. However, even with the extremely high-speed air, this approach is not as effective as the liquid systems, since the heat transfer is generally faster in liquids than in gases [Cengel et al., 2015]. Also, the poor thermal conductivity of the air, which is about $2.623 - 6.763 \times 10^{-2}$ W/m K between 300 and 900 K (27 °C and 627 °C) [Kadoya et al., 1985], makes it hard to cool a battery pack, especially in the hot environments. Therefore it is better to use liquid-based thermal management systems for more efficient heating/cooling of the battery packs.

Compared to air-based thermal management systems liquid-based systems are more efficient because they provide a better heat exchange. However, an active liquid-cooled thermal management system consists of pipes, a water pump, a compressor, an evaporator, a condenser, and an expansion valve, which means extra weight and extra cost [Kalaf et al., 2021]. Due to the efficiency of liquid-based thermal management systems, the number of research in this area is increasing. For example; Larrañaga-Ezeiza et al. [2022] proposed a novel direct liquid cooling strategy for a large-scale lithium-ion pouch-type cell to control the cell working temperature within the optimum range of performance and safety. He et al. [2023] designed a double-layered I-shaped liquid cooling plate to optimize the working temperature of a Li-ion battery. Some studies of liquid-based thermal management systems can be sub-grouped as studies that use heating pipes for thermal management of the battery pack [Jaguemont and Van Mierlo, 2020].

As an example for this sub-group; Smith et al. [2018] proposed a safe, simple heat pipe- based thermal management system for high-powered Li-ion batteries. Liang et al. [2018] investigated the thermal performance of heat pipe-based thermal management systems and reported that the reduction in the coolant temperature can enhance the thermal performance of heat pipe-based thermal management systems. Also according to the reports in the same study, when ambient temperature is lower than 25 °C, the thermal performance of heat pipe-

Table 1. Comparison between different types of thermal management systems [Ali, 2023]

System Type	Additional Thermal Power Source	Thermal Conductivity	Type of the Thermal Management	System	Size	Cost
Air Cooling	Exist	Low	Heating/Cooling	Basic	Large	Low
PCM	Non-exist	Low	Cooling	Basic	Small	Low
Liquid Cooling	Exist	High	Heating/Cooling	Complicated	Large	High

based thermal management systems improves slightly as ambient temperature decreases. In another research; Huang et al. [2018] designed a thermal management system by using a heating pipe and PCM together. They reported that the liquid-assisted PCM shows great control over the temperature rise of the battery pack.

Due to the advantages of liquid-based thermal management systems some leading firms like Tesla and General Motors integrated this type of systems in their EVs [Kannan et al., 2021]. The schematic view of Tesla S model battery cooling system is given in Figure 4, where BTMS is the abbreviation of battery thermal management system.

Besides the advantages of the liquid-based thermal management systems that are mentioned above, some disadvantages cannot be ignored. The existence of the piping system creates not only additional weight but also, manufacturing and maintenance costs. Also, the failure possibility is increased due to the number of additional parts.

To overcome all the current problems of the conventional thermal management systems, we propose a composite battery case with thermal management and self-healing ability which is based on liquid thermal management. Since, the designed battery box that is proposed in this paper, does not contain any piping system the disadvantages of the current solutions that are mentioned above, can be overcome. The liquid flow is provided via channels that are integrated within the composite layers without using any additional piping material. The thermal management channels are created within the CFRP laminate by using a novel microvascular channel-creating method based on the patent-protected technique [Geren et al., 2023]. The required patent applications were made in 2022 and 2023 for this novel channel-creating method, for the name of TAI and Cukurova University. This approach makes the creation of the thermal management system cheaper, safer, and easier to apply.

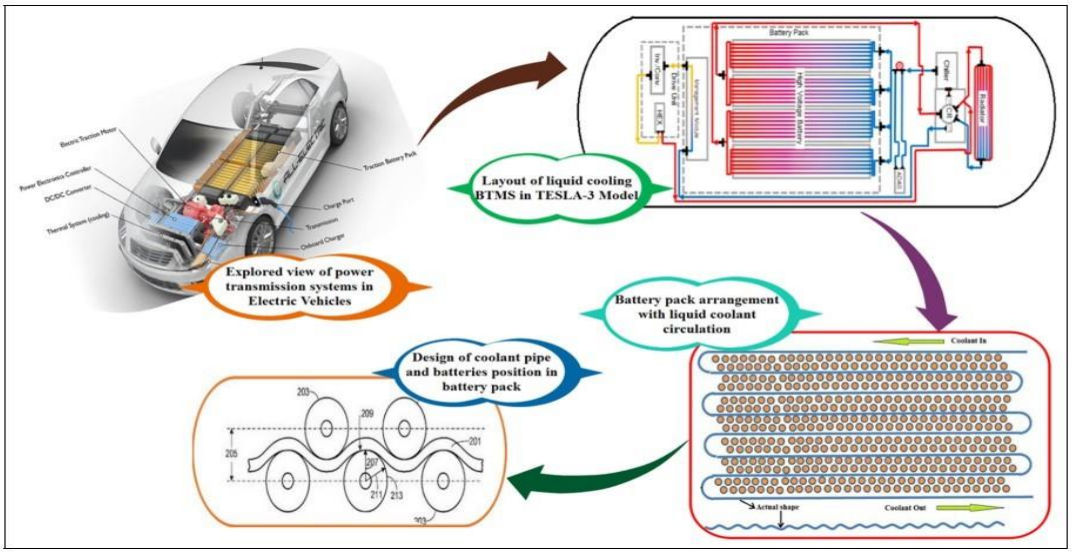


Figure 4. The schematic view of the Tesla S model battery cooling [Kannan et al., 2021]

3. INTEGRATED MICROVASCULAR CHANNELS AND SELF HEALING

The battery packs of the EVs and HVs are subjected to sudden and impact loads since the packs are located underneath the vehicle's chassis frame. These types of damage factors cause microcracks in the surface of the structure, which leads to sudden rupture and catastrophic failures. In the case of damage in the service, usually, it is not possible to repair the structure during the operation. Therefore, to overcome this issue of composites, self-healing fiber-reinforced polymer (FRP) composites are fabricated to heal cracks and damages if there be any to restrict failure and enhance the longevity of structures [Kanu et al., 2019].

Currently, self-healing mechanisms can be classified broadly into three groups: capsule-based, vascular, and intrinsic [Blaiszik et al., 2010]. The differences between these three self-healing mechanisms are shown in Figure 5. As the focus of this study, the vascular-type self-healing mechanism will be used as the self-healing mechanism. This is because continuous and repeated healing with an interconnected network is possible contrary to the capsule-based approach, and the intrinsic mechanism is based on reversible chemical bonding. In order to achieve this purpose an innovative micro-vascular channel system was built within the composites structure.

Vascular-type self-healing composites are inspired by healing by the vascular and circulation systems in animals and humans. In case of damage, the filler materials fill the damaged area and prevent any catastrophic failure. Healing agents are located and filled within the micro-channels and the catalyst is mixed into the matrix material. Once the damage occurs, the healing agents fill the crack and create bonding with the catalyst. This creates a healing part that acts as a patch. As the major advantage of the vascular-type self-healing systems, healing agents can be refilled, providing the potential for continuous healing agent delivery and flow control [Wang, 2017].

There are several methods available in the literature, to produce micro-vascular channel systems in the composite. Such as; sacrificial fibers [Lewis and Gratson, 2004], electrostatic discharge method [Huang et al., 2009], and embedding hollow fibers method [Dry, 1996]. However, none of these existing methods are either not applicable to CFRP or not suitable, as in the case of hollow fiber, embedding since overall strength is reduced.

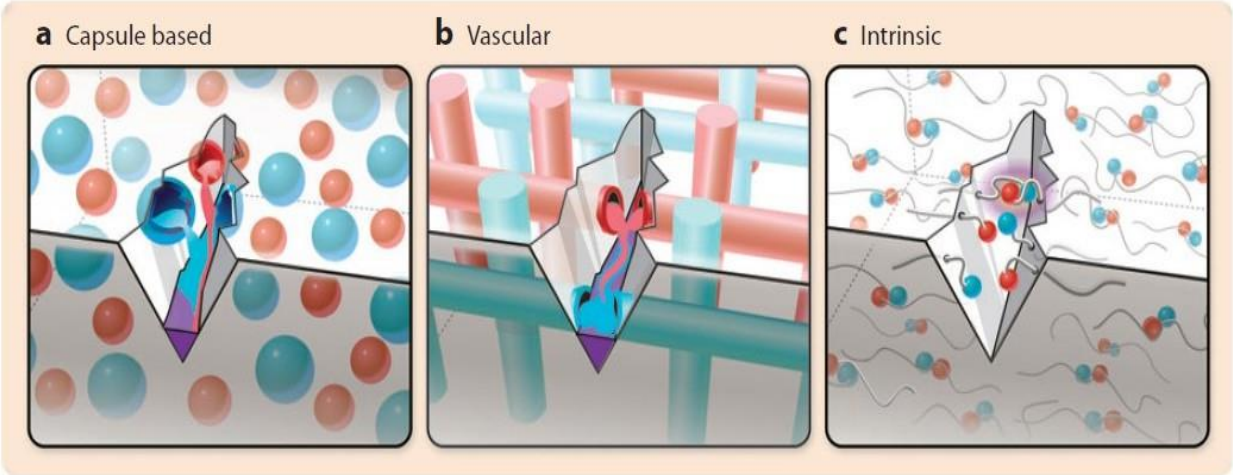


Figure 5. Self-healing mechanisms: a) capsule-based, b) microvascular-based, c) intrinsic-based [Blaiszik et al., 2010]

On the other hand, the novel micro-vascular channel-creating method, which is presented in the patent-protected technique [Geren et al., 2023], offers a method that can be put into commercial and industrial applications.

4. DESIGN METHODOLOGY OF THE BATTERY CASING

A battery casing of an EV must have some properties in order to provide safety, reliability, maximum performance, and efficiency. A battery case must be stiff and strong enough to protect the batteries against the sudden impact loads that may be applied to the battery pack from the outside. Besides these features, a battery casing must be as light as possible and should be thermally managed in order to obtain maximum performance and driving range. The reasons for these reductions have been mentioned in the previous sections. When all these limitations and criteria are considered it is necessary to design a battery casing that has all these features in the same structure.

Firstly, to provide high stiffness and high strength with light-weight CFRP composites will be used as the main material of the structure. Because of the high specific strength (σ_f/ρ) and high specific modulus (E/ρ) properties of the CFRP composites as can be seen in the material selection chart that is provided by Ashby [2011], in Figure 6.

The required thermal management system is integrated via micro-vascular channels that are located within the composite layers, as mentioned in section 2. Through this system, the extra weight of the pipes will no longer be a problem since the cooling/heating fluid can flow within the micro-vascular channels.

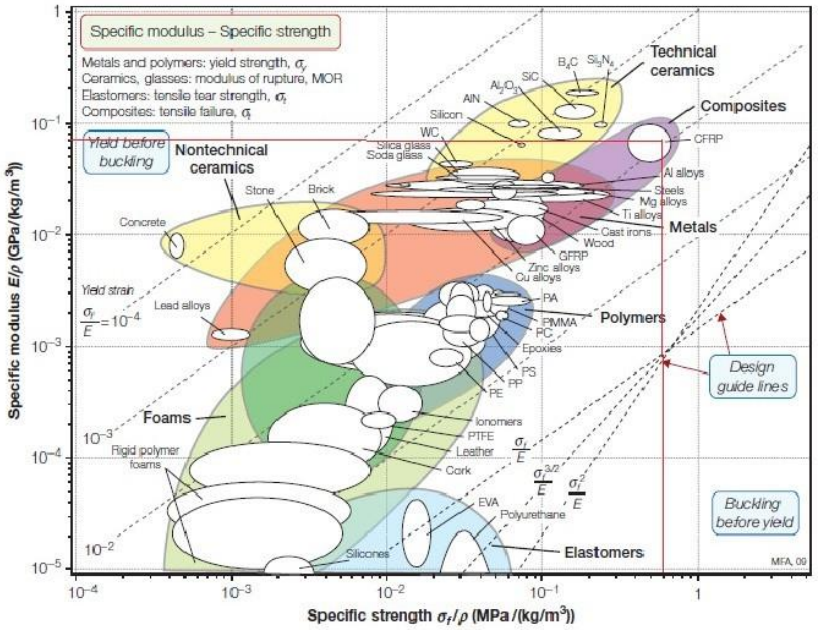


Figure 6. The graph of specific modulus E/ρ against specific strength σf /ρ [Ashby, 2011]

Another important property of our novel battery casing is its self-healing ability. Since the battery package is located under the EV, it is open to take damage and fail. In case of failure, usually, it is not possible to repair the damage, while the EV is operating. Thus, the result can be catastrophic.

Therefore, the casing has the self-healing ability to repair any damage under operation. The mechanism of the self-healing, for the designed battery case is given in section 3.

Thus; a novel battery casing system for an EV and HV is being designed, developed, and will be produced. The fact that this battery casing contains all these features in one structure makes this design original and unique. A schematic view of our design is given in Figure 7. The channels with the larger diameters in Figure 7 are the thermal management channels, in which the cooling/heating fluid is flowing and the smaller sized channels are the self-healing channels, which contain the self-healing agents. All the channels will be created by using the patent-protected novel microvascular channel-creating method [Geren et al., 2023a, 2023b].

5. CONCLUSION

A novel battery casing that is stiff, strong, and lightweight, featuring its own thermal management system and has self-healing ability is being designed, developed, and

proposed in this paper. The main material will be CFRP composite due to its unique advantages. All the micro-vascular channels, that aim to provide thermal management and self-healing, will be created by using a novel patent-protected microvascular channel- creating method [Geren et al., 2023a, 2023b]. The aim of this paper is to propose a unique battery casing design, as a patent protective innovation [Geren et al., 2024]. Carbon fiber-reinforced polymer composites are designed to have microvascular channels of different diameters. While the channels with larger diameters provide thermal management, smaller diameter channels contain healing agents to provide the self-healing ability in case of possible damage. This project aims to provide a battery casing that is reliable, light, unique, and applicable to all battery types; so it can be a good candidate to replace the current solutions, in the developing electric vehicle and composite market. The schematic view of the battery case design with integrated thermal management and self-healing microvascular channels can be seen in Figure 7 where number 1 shows larger channels for thermal management and number 2 shows the smaller channels for self-healing.

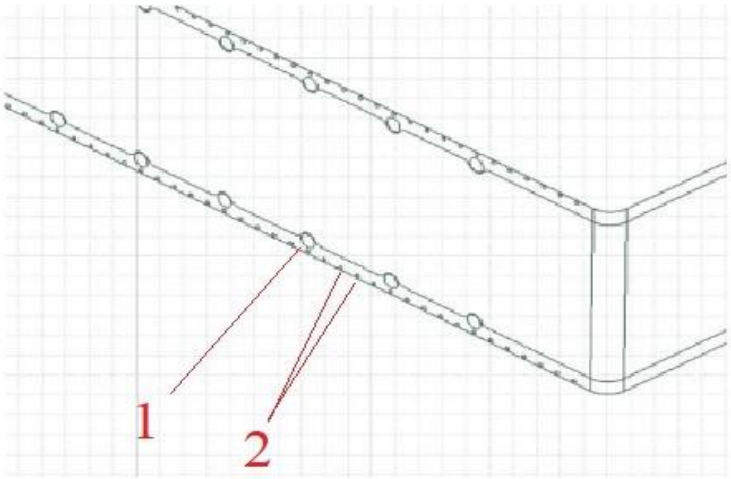


Figure 7. Schematic view of the battery case design with integrated thermal management and self-healing microvascular channels

ACKNOWLEDGEMENTS

The study was supported by the Scientific Research Projects Coordination Unit (BAP) of Cukurova University in Adana, Turkey, under grant No: FBA-2024-16561. Also, this project is supported by 'Support Programme of Research Universities' (ADEP).

REFERENCES

1. **Pety, S. J., Chia, P. X., Carrington, S. M., and White, S. R., (2017),** "Active cooling of microvascular composites for battery packaging." Smart Materials and Structures 26(10): 105004.
2. **Han, Q., Sheng, Y., Liu, X., Zhang, X., Chen, X., Li, B., and Han, Z., (2022),** "Carbon fiber reinforced epoxy composite combining superior electrochemical energy storage and mechanical performance." Chemical Engineering Journal 437: 135228.
3. **Gardner, (2020),** "https://www.gardnerweb.com/news/sgl-to-supply-bmw-hybrid-with-carbon-fiber-battery-case".
4. **Luo, X., and Chung, D., (1999),** "Electromagnetic interference shielding using continuous carbon-fiber carbon-matrix and polymer-matrix composites." Composites Part B: Engineering 30(3): 227-231.
5. **E-mobility, (2024),** " https://www.emobility-engineering.com/battery-case-materials".
6. **AFDC Energy, (2018),** "https://afdc.energy.gov/vehicles/how-do-all-electric-cars- work" .
7. **Khan, F. N. U., Rasul, M. G., Sayem, A., and Mandal, N., (2023),** "Maximizing energy density of lithium-ion batteries for electric vehicles: A critical review." Energy Reports 9: 11-21.
8. **LLC, U. S. A. B. C., (2021),** "Advanced Anode Prelithiation Development For Electric Vehicle Cell Technology"
9. **Pesaran, A., (2007),** "Battery Requirements for Plug-In Hybrid Electric Vehicles: Analysis and Rationale (Presentation), National Renewable Energy Lab.(NREL), Golden, CO (United States) "
10. **Ji, Y., Zhang, Y., and Wang, C. Y., (2013),** "Li-ion cell operation at low temperatures." Journal of The Electrochemical Society 160(4): A636
11. **Basu, S., Hariharan, K. S., Kolake, S. M., Song, T., Sohn, D. K., and Yeo, T., (2016),** "Coupled electrochemical thermal modelling of a novel Li-ion battery pack thermal management system." Applied Energy 181: 1-13.
12. **Pesaran, A., Santhanagopalan, S., and Kim, G., (2013),** "Addressing the impact of temperature extremes on large format li-ion batteries for vehicle applications" (presentation), National Renewable Energy Lab.(NREL), Golden, CO (United States).
13. **Spitthoff, L., Shearing, P. R., and Burheim, O. S., (2021),** "Temperature, ageing and thermal management of lithium-ion batteries." Energies 14(5): 1248.

14. **Jaguemont, J., Boulon, L., and Dubé, Y., (2016),** "A comprehensive review of lithium-ion batteries used in hybrid and electric vehicles at cold temperatures." Applied Energy 164: 99-114.
15. **Bugga, R., Smart, M., Whitacre, J., and West, W., (2007),** "Lithium ion batteries for space applications". 2007 IEEE Aerospace Conference, IEEE.
16. **Li, R., Gan, Y., Luo, Q., Yan, Y., and Li, Y., (2023),** "Research progress on efficient thermal management system for electric vehicle batteries based on two-phase transformation." Applied Thermal Engineering: 121270.
17. **Lu, Z., Yu, X., Wei, L., Qiu, Y., Zhang, L., Meng, X., and Jin, L., (2018),** "Parametric study of forced air cooling strategy for lithium-ion battery pack with staggered arrangement." Applied Thermal Engineering 136: 28-40.
18. **Youssef, R., Kalogiannis, T., Behi, H., Pirooz, A., Van Mierlo, J., and Berecibar, M., (2023),** "A comprehensive review of novel cooling techniques and heat transfer coolant mediums investigated for battery thermal management systems in electric vehicles." Energy Reports 10: 1041-1068.
19. **Malik, M., Dincer, I., Rosen, M. A., Mathew, M., and Fowler, M., (2018),** "Thermal and electrical performance evaluations of series connected Li-ion batteries in a pack with liquid cooling." Applied Thermal Engineering 129: 472-481.
20. **Mahamud, R., and Park, C., (2011),** "Reciprocating air flow for Li-ion battery thermal management to improve temperature uniformity." Journal of Power Sources 196(13): 5685-5696.
21. **Cengel, Y. A., Ghajar, A. J., and Kanoglu, M. (2015),** "Heat and mass transfer: fundamentals and applications."
22. **Kadoya, K., Matsunaga, N., and Nagashima, A., (1985),** "Viscosity and thermal conductivity of dry air in the gaseous phase." Journal of physical and chemical reference data 14(4): 947-970.
23. **Kalaf, O., Solyali,D., Asmael, M., Zeeshan, Q., Safaei, B., and Askir, A., (2021),** "Experimental and simulation study of liquid coolant battery thermal management system for electric vehicles: A review." International journal of energy research 45(5): 6495-6517.
24. **Larrañaga-Ezeiza, M., Vertiz, G., Arroiabe, P., Martinez-Agirre, M., and Berasategi, J. (2022),** "A novel direct liquid cooling strategy for electric vehicles focused on pouch type battery cells." Applied Thermal Engineering 216: 118869.

25. **He, P., Lu, H., Fan, Y., Ruan, H., Wang, C. and Zhu, Y., (2023),** "Numerical investigation on a lithium-ion battery thermal management system utilizing a double- layered I-shaped channel liquid cooling plate exchanger." International Journal of Thermal Sciences 187: 108200.

26. **Jaguemont, J. and Van Mierlo, J., (2020),** "A comprehensive review of future thermal management systems for battery-electrified vehicles." Journal of Energy Storage 31: 101551.

27. **Ali, H. M.,(2023),** "Thermal management systems for batteries in electric vehicles: A recent review." Energy Reports 9: 5545-5564.

28. **Smith, J., Singh, R., Hinterberger, M., and Mochizuki, M., (2018),** "Battery thermal management system for electric vehicle using heat pipes." International Journal of Thermal Sciences 134: 517-529.

29. **Liang, J., Gan, Y., and Li Y., (2018),** "Investigation on the thermal performance of a battery thermal management system using heat pipe under different ambient temperatures." Energy conversion and management 155: 1-9.

30. **Huang, Q., Li, X., Zhang, G., Zhang, J., He, F., and Li, Y., (2018),** "Experimental investigation of the thermal performance of heat pipe assisted phase change material for battery thermal management system." Applied Thermal Engineering 141: 1092- 1100.

31. **Kannan, C., Vignesh, R., Karthick, C., and Ashok, B., (2021),** "Critical review towards thermal management systems of lithium-ion batteries in electric vehicle with its electronic control unit and assessment tools." Proceedings of the Institution of Mechanical Engineers, Part D: Journal of Automobile Engineering 235(7): 1783-1807.

32. **Geren, N., Kostur, E. Demirel, M., Ö., (2023),** Patent Title: A composite production system (Buluş başlığı: Bir kompozit üretim sistemi), Application Number: 2023/000772, Applicants: Turkish Aerospace Industry (TAI). (According to the contact).

33. **Kanu, N. J., Gupta, E., Vates, U. K. and Singh, G. K., (2019),** "Self-healing composites: A state-of-the-art review." Composites Part A: Applied Science and Manufacturing 121: 474-486.

34. **Blaiszik, B. J., Kramer, S. L., Olugebefola, S. C., Moore, J. S., Sottos, N. R., and White, S. R., (2010),** "Self-healing polymers and composites." Annual review of materials research 40: 179-211.

35. **Wang, Y., (2017),** Sustainable self-healing structural composites, University of Birmingham.
36. **Lewis, J. A. and Gratson, G. M., (2004),** "Direct writing in three dimensions." Materials today 7(7-8): 32-39.
37. **Huang, J. H., Kim, J., Agrawal, N., Sudarsan, A. P., Maxim, J. E., Jayaraman, A., and Ugaz, V. M., (2009),** "Rapid fabrication of bio-inspired 3D microfluidic vascular networks." Advanced Materials 21(35): 3567-3571.
38. **Dry, C. (1996),** "Procedures developed for self-repair of polymer matrix composite materials." Composite structures 35(3): 263-269.
39. **Ashby, M. F., (2011),** "Materials Selection in Mechanical Design Fourth Edition.
40. **Geren, N., Kostur, E., (2023),** Patent Title: Weaving threads forming microvascular channels into fibers in the production of fiber-reinforced polymer composites (Buluş başlığı: fiber takviyeli polimer kompozit üretiminde mikrovasküler kanal oluşturan ipliklerin elyaf içine dokunması), Application Number: PCT/TR2023 051362, Applicants: Cukurova University.
41. **Geren, N., Bayramoğlu, M., Özkan, G., M., Uzay, Ç., Çetin, A., Acer, D., C., Diker, İ., İbekçi, M., B.,** Patent Title: Composite battery enclosure with thermal management and self-healing (repairing) features ((Buluş başlığı: Termal yönetim ve kendini iyileştirme (tamir etme) özellikli kompozit batarya kutusu), (Application Number: PCT/TR2024/050872, Applicants: Cukurova University.

DESIGN AND ANALYSIS OF SUSPENSION AND STEERING SYSTEM FOR AN ELECTRIC VEHICLE

Umut B. HAKTANIR, *ubhaktanir@gmail.com* Atilim University, 06830, Ankara, Turkey

Emre ÇELİKCAN, *emrecelikcangs@gmail.com* Atilim University, 06830, Ankara, Turkey

Umut NAZLIER, *umutnazlier1@gmail.com* Atilim University, 06830, Ankara, Turkey

Berkay KANDEMİR, *kndberkay@gmail.com* Atilim University, 06830, Ankara, Turkey

Özgür AKDENİZ, ozgur.akdeniz@atilim.edu.tr Atilim University, 06830, Ankara, Turkey

Ali EMİN, ali.amini@atilim.edu.tr Atilim University, 06830, Ankara, Turkey

ABSTRACT

This paper aims to design a new suspension and steering system, including an electronic differential system and electric-powered steering for an electric vehicle. The main goal is to design the new systems to be strong, durable to forces from the road and car itself, lightweight, and efficient. The electronic differential system for the vehicle will be created and optimized for better driving dynamics and efficiency. The electrically assisted steering pump and motor will be optimized by integrating them into the system.

Keywords: Steering System, Suspension System, Electric Powered Steering, Electronic Differential System, Knuckle, Double Wishbone, Electric Vehicle

INTRODUCTION

The automotive industry has transformed significantly over the past century. Steering and suspension systems are two essential parts that have undergone tremendous advancement.

These are critical in maintaining handling, stability, and, most importantly, comfort as a driver. This system controls the vehicle's direction by transforming the driver's input into wheel rotation. Nowadays, powered steering systems have eliminated conventional mechanical linkages, increased maneuverability and reducing driver effort. At the same time, progress has been made in suspension technology aimed at improving ride quality and safety. Such systems bear the car's weight while absorbing road bumps, thus making it smooth and comfortable to drive (Gillespie, Thomas. 1992).

The car's steering is operated through a powered or power steering system, a technological marvel that significantly reduces the physical inputs necessary, especially during slow-moving turns and parking. Whether hydraulic or electrical, this system has revolutionized driving comfort. The introduction of electrically powered steering (EPS) has further elevated this, providing speed-sensitive variable assist plus better integration with electronic stability control systems for improved responsiveness in driving.

The suspension system, a crucial vehicle component, plays a pivotal role in maintaining control and comfort. Comprising various elements such as shock absorbers, control arms, and springs, the suspension system ensures that the tires maintain contact with the ground, providing good grip and control over the car. However, it is not just about control. Modern suspension technologies, such as adaptive and active suspensions, allow for real-time adjustments in spring rate and damping, enhancing performance and ensuring a comfortable driving experience.

The electronic differential system (EDS) is among the most remarkable progressions in automotive technology. Instead of traditional mechanical differentials, this system distributes power to individual wheels using electronic controls. It dramatically improves handling, traction, and stability, especially in challenging road conditions. The vehicle does not require heavy-duty mechanical components like a differential box, shaft, or gearbox. This method allows the electric vehicle to travel further on a single battery and weigh less. With this system, the tasks

of the removed mechanical parts are determined and done by the hub motors in the rear two wheels with EDS.(ÇELİK & SONUGUR, 2022)

In summary, integrating sophisticated steering and suspension systems, such as powered steering and electronic differentials, has significantly advanced automotive engineering. These developments improve vehicle performance and driving comfort while bolstering modern cars' general safety and dependability. Further developments in these systems are expected as technology progresses, offering even more significant enhancements to the driving experience.

METHODOLOGY

The suspension and steering system designed to be strong, durable, light, easy to integrate and easy to manufacture. All parts related to suspension system and steering system was sketched and assembled in CAD program. All parts are assembled by their own systems and the assemblies were mounted to the chassis of the electric vehicle. More robust structural integrity was achieved with the changes made to the steering column for the newly added electrical support to the steering system. The code written for the added electronic differential system ensured integrated operation with the engine drives. Thanks to the electronic differential system prepared by making use of Ackerman geometry, the speed of the inner and outer wheels is ensured to operate optimally in bends. In contrast, the vehicle provides efficiency, speed, and comfort. Thanks to the designs, the suspension system has become adaptive, making it easier to adjust the vehicle's height, camber, and caster. A new knuckle has been designed to make the connections safer for the hub motors to be used in the vehicle. Thanks to the design and material changes, safety, lightness, and durability have been increased. As a result of the market and literature research for knuckle production, it was decided to use AL 7075-T6, which has high strength and whose processing and part prices are low. Analysis of the parts to be produced showed that they met the required strengths and were suitable for use.

MATERIAL

Aluminum 7075-T6 was used for the knuckle and its properties taken from (Sunar et al., 2020). Structural steel was used for the wishbones and their properties taken from (Yao & Wang, 2022).

Table 1: Properties of materials used on knuckle and wishbones

Materials	Structural Steel	AL 7075-T6
Density $[kg * m^{-3}]$	7850	2810
Young's Modulus [MPa]	200000	71700
Poisson's Ratio	0,3	0,33
Tensile Yield Strength [MPa]	406	493.2
Tensile Ultimate Strength [MPa]	585	548.6

ANALYSIS

Some analysis was done to see the durability of the Knuckles, the wishbone, and the designed parts. The forces obtained from the calculations were used to analyze the parts used in the suspension system. In the steering system, the analysis was completed using the general weight and the maximum force the driver can apply to the steering wheel. Analysis was made using the Ansys program and adding the obtained material data to the material library. Mesh independence testing was performed before applying the tests to define the security of the designs. It was performed with mesh sizes ranging from 1.5 to 3 mm to eliminate negative situations that may occur due to different mesh sizes. Ansys static structural analysis was used.

Table 2: Mesh Values

Mesh Size (mm)	Element Number	Node Number	Stress (MPa)
1.5	876453	1231700	72.481
2	373539	533975	59,597
2.5	192353	279680	59,104
3	113820	168520	58,497

After applying the test, the 1.5 mm mesh size was chosen for our application since it was determined it would give consistent results. The applied static analysis consisted of 11 steps with load changes of 0.1 seconds. The analysis results are shown in Figure 1.

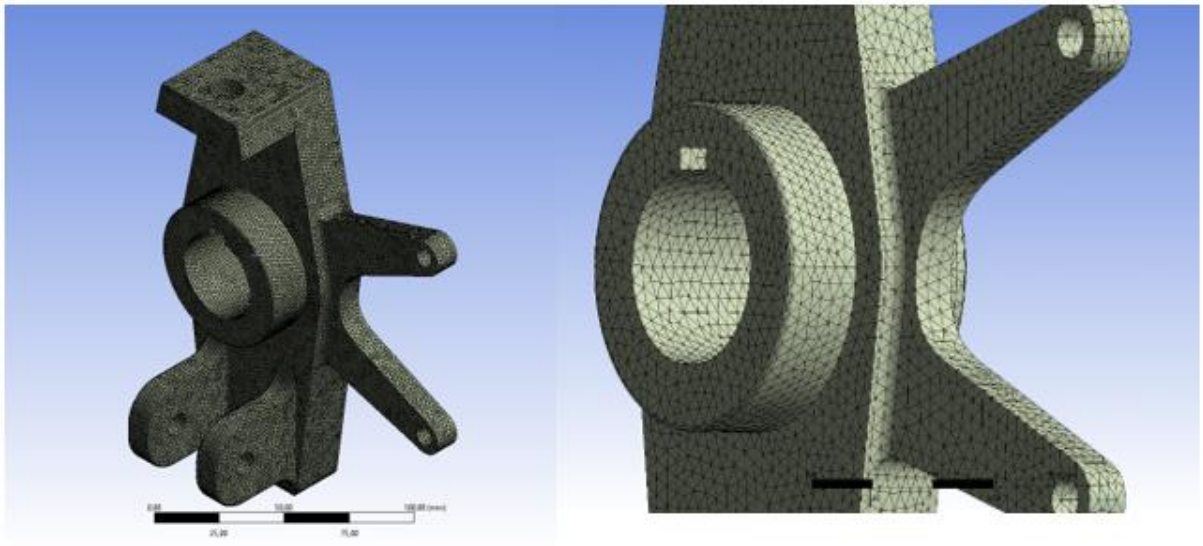


Figure 1: Mesh structure

The analysis was made because it would provide a more difficult condition than a constant load analysis, and the given forces represent instantaneous forces that may occur in real life. The forces of this analysis appear in table 3.

Table 3: The forces and moment on analysis

Step	Time	Force X(N)	Force Y(N)	Force Z(N)	Moment Z(N*mm)
1	0	-500	2250	1500	1000
2	0,1	-500	2250	1500	1000
3	0,2	-500	2250	1500	1000
4	0,3	-500	2250	1500	1000
5	0,4	-1000	4500	3000	1000
6	0,5	1000	-4500	-3000	1000
7	0,6	-500	2250	1500	1000
8	0,7	-500	2250	1500	1000
9	0,8	-1000	4500	3000	1000
10	0,9	1000	-4500	-3000	1000
11	1	-500	2250	1500	1000

STEERING SYSTEM

Designing the steering system for an electric car demands precision, innovation, and a thorough understanding of both automotive engineering principles and the unique demands of

the event for which we are preparing the car. This process involves several crucial steps, each contributing to the vehicle's overall performance and safety. The search for electric-supported steering systems started after the market and literature research. The research showed that the electric power steering system used in the Hyundai i20s met the desired conditions (size, weight, compatibility with the vehicle, price) and that the product was supplied. The work started modeling the electrically powered pump, motor, and other steering system parts and assembled them to ensure optimal fit and functionality. This virtual representation serves as the blueprint for the physical integration of the steering system with the chassis. We did not need to design a new rack, as it meets the current driving geometry and requirements.

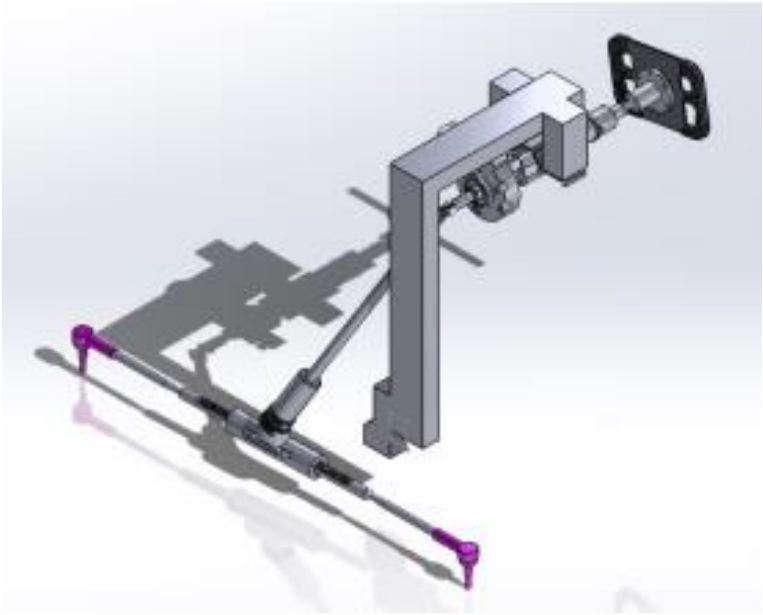


Figure 2: Steering system assembly

Electronic Differential System

The electronic differential system adjusts the torque distribution using electronic controls and sensors and independently adjusts the speed of the inner and outer wheels (Y. E. Zhao, J. W. Zhang, 2009). The vehicle's torque control ensures that the required wheel turns more, and the corner is taken better. As a result of the research carried out for integrating the electronic differential system into the electric vehicle, the main calculations (Jazar, n.d.)emerged due to the specific constraints such as the vehicle's weight distribution, powertrain capabilities, and

desired performance. These constraints were addressed with the help of a series of calculations, and the mathematical model was created using MATLAB software. The vehicle's data (track width, wheel center distance, speed, and steering angles) were defined in the resulting mathematical model, and the model was fully prepared.

Track Width $w = 1.25$ m ……(1)

Wheelbase $l = 2.15$ m ……(2)

Velocity $V = 0:5:80$ (0 km/h steps 5 km/h to 80 km/h) ……(3)

Steering Angle $a = 0:2:40$ (2° steps 0° to 40°) ……(4)

This mathematical model defined the speeds of the inner and outer wheels, turning angles, yaw velocity, and vehicle turning angle. The code shows the vehicle at a 0 to 80 km/h limit for every 5 km/h acceleration step and every 2 degrees of steering angle between 0 and 40 degrees. The data obtained calculates all steering degrees at each speed step.

Yaw Velocity $r = \frac{R}{V}$……(5)

Inner Angular Velocity $V_{ri} = (R_1 - \frac{w}{2}) * r = R_w * w_{ri}$……(6)

Outer Angular Velocity $V_{ro} = (R_1 + \frac{w}{2}) * r = R_w * w_{ro}$……(7)

Turning Radius $R = \frac{w}{\tan(a)}$……(8)

Thanks to the card to be produced, this data will be transferred to the motor drivers, and the hub motors can operate at independent speeds.

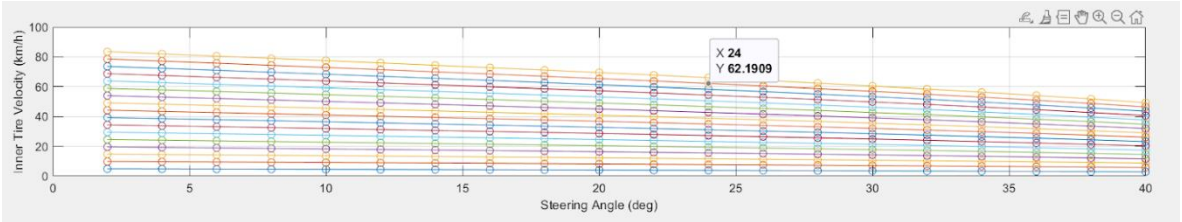


Figure 3: Inner tire velocity and steering angle graph

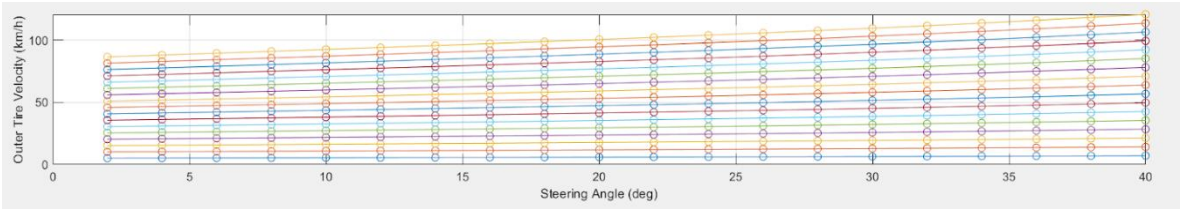


Figure 4: Outer tire velocity and steering angle graph

Another code is the specific value code. While the first code calculates all speeds and angles for each step by specifying the desired step in all speed ranges, the second code is more straightforward. It can produce the desired results at specific speed and steering angle values. The formulas used in all codes are the same.

Electric Powered Steering

Electric Power Steering is undoubtedly one of the most exciting developments in steering systems since the introduction of power steering. The electric power steering provides a more comfortable ride with less effort for the driver. With the addition of this project, it is planned to provide a more comfortable ride for the driver. After the motor and pump of the electric power steering system arrived, solid models of the parts were first created and integrated into the chassis. After the integration was completed, the necessary changes were implemented.



Figure 5: Electric powered steering pump and motor

SUSPENSION SYSTEM

Suspension Systems contribute to road safety (road-holding, cornering performance), vehicle stabilization, and driving comfort. Vehicles can use many different systems depending on their type(Lim B and Lim H 2017). These systems are used in vehicles for various reasons, such as carrying loads or comfort. Double wishbone system used in the vehicle (Pecht, N. 2004). The shock absorber used to carry the load, positioning it at an angle and transmitting the loads from the wheel hub to the shock absorber from the bottom and top with the help of knuckles ensured optimum protection in terms of driving safety and comfort both at the moment of bending and on the straight road.

Shock Absorber

After the market research, we found 12 shock absorbers that we compared based on price, durability, and size. Due to high prices, shock absorber height and weight, and shipping reasons, most of the selected shock absorbers were removed from the options. The chosen shock absorber is a unique find from the market studies. Despite its weight of 3046 grams, it stood out for its innovative features, including a hardness adjustment and an open length of 31.5 cm from center to center, making it easy to position in the vehicle. This shock absorber is used in Pulsar RS200 motorcycles. After the shock absorber was delivered, it was made ready for use by solid modeling to assemble the vehicle model.



Figure 6: Shock absorber

Shock Absorber Tests

Since the manufacturer could not obtain the data on the shock absorber to be used in the vehicle, these data had to be determined. Specific tests have been and will be performed to obtain this data. Since the first test did not provide the necessary data and had deficiencies, it needed to meet the requirements and be more suitable.



Figure 7: Failed shock absorber test mechanism

The new test will be obtained using a more capable dynamometer machine, which is used specifically for shock absorbers and can provide detailed data. With the help of these tests, we obtained some constants (Damping force, Elongation "**Δ**X", "c", Spring constant "k") of the shock absorber.



Figure 8: Machine to be used in new tests

Knuckle And Wishbones

Knuckles and wishbones, which are the most important parts, are the main supporting parts of the vehicle. The double wishbone system was used in the vehicle to benefit from its affordable prices, high load carrying capacity and easy to adaptation.(Ahmed M., Mehahoob M., 2018) Since the load on the wheels will increase due to the hub motors that will be added, the knuckle design was designed from scratch, and it was aimed to be safe and strong. In order to be suitable for the engines to be used, first trial designs were made and the deficiencies in the design were highlighted.

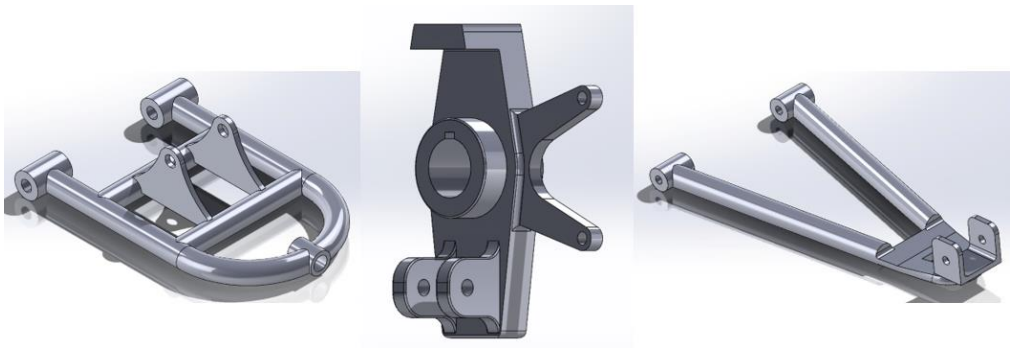


Figure 9: Rear upper wishbone, knuckle and lower wishbone

Thanks to the updates made based on these deficiencies, the strength of the designed part was simultaneously increased and lightened as a result of topology optimizations.

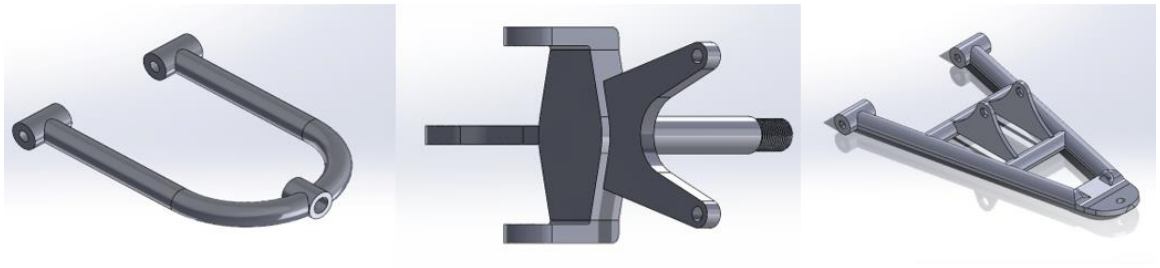


Figure 10: Front upper wishbone, knuckle and lower wishbone

While the parts used and produced in previous years were made of structural steel, providing strength gains, it was concluded that they were not efficient because they were heavy. For this reason, it was decided to produce the newly designed knuckles with aluminum 7075-T6, reducing production and part costs and creating a more durable part compared to the old design.

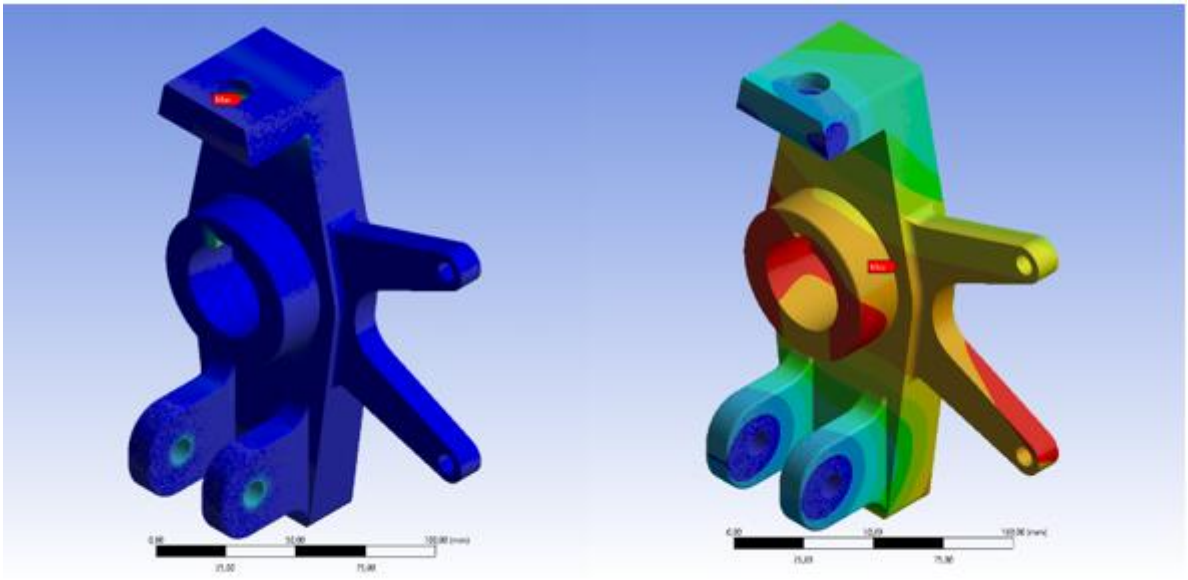


Figure 11: Static structural analysis of knuckle

CONCLUSION

While the work to operate the electric power steering system continues, the necessary preparations for the shock absorber test are being made. The production and planning of the parts required for the steering system and shock absorber testing will be completed as soon as possible. While all of the parts to be used in the electric vehicle are produced with the chassis production, the remaining parts of the steering system will be planned and allocated together with the manufacturer. The prepared electronic differential system card is awaiting production as integrated with other electronic cards. We deemed it appropriate that all of the parts designed and produced reached the desired strength and lightness and that the work carried out was by the requirements and could be used in the vehicle. As a result of the drawings, analysis, and calculations we made, we tried to leave sustainable and permanent work by completing the parts missing in the steering and suspension systems.

REFERENCES

1. **Reza N. Jazar (2017)** “Vehicle Dynamics: Theory and Application”

2. **Pecht, N. (Hrsg) (2004)** Fahrwerktechnik für PKW – Grundlagen, Konzepte, Prozesse und Trends. Landsberg: Verlag Moderne Industrie

3. **Gillespie, Thomas. (1992)** Fundamentals of Vehicle Dynamics. Warrendale, PA: Society of Automotive Engineers

4. **Reimpell, Jörnsen, Helmut Stoll, and Jürgen W. Betzler (2001)** The Automotive Chassis: Engineering Principles Chassis and Vehicle Overall, Wheel Suspensions and Types of Drive, Axle Kinematics and Elastokinematics, Steering, Springing, Tyres, Construction and Calculations Advice. 2nd ed. Oxford: Butterworth Heinemann

5. **Y. E. Zhao, J. W. Zhang, and X. Q. Guan, (2009)** "Modelling and simulation of the electronic differential system for an electric vehicle with two-motor-wheel drive", International Journal of Vehicle Systems Modelling and Testing, vol. 4, no. 1-2, pp. 1209-1214

6. **Çelik İ. and Sonugür G., (2022)** "The test of electric vehicle with electronic differential system in different road conditions", Journal of Polytechnic, 25(3): 1021-1030

7. **Sunar T. And Tuncay T., (2020)** "Investigation of Mechanical Properties of AA7075 Alloys Aged by Various Heat Treatments", Physics of Metals and Metallography, 2020, Vol. 121, No. 14, pp. 1440–1446

8. **Yao, Z., & Wang, W. (2022**). Full-range strain-hardening behavior of structural steels: Experimental identification and numerical simulation. Journal of Constructional Steel Research, 194.

9. **Ahmed, M. A., Mehaboob, M., Mujavar, H., Professor, A., Akbar, M. M., Mohammed, M., & Dakhani, S. (n.d.). (2018)** Design and Analysis of Double Wishbone Suspension System using Fea and Matlab.

10. **Lim, B. S., Lim, H. E., Mitchell, J., Readman, M., Ling, N. K., & Yong, Y. K. (2017)** FORMULA SAE-SUSPENSION SYSTEM.

IMPROVEMENTS ON THE LIGHTWEIGHT SHELL OF AN ELECTRIC VEHICLE

Mustafa EROL, *mustafaerol99@gmail.com,* Atilim University, 06830, Ankara, Turkey

Cemal Emre HOKKAÖMEROĞLU, *cemalemre14@gmail.com,* Atilim University, 06830, Ankara, Turkey

Özgür AKDENİZ, *ozgur.akdeniz@atilim.edu.tr,* Atilim University, 06830, Ankara, Turkey

ABSTRACT

The purpose of this study is to achieve a 75% weight reduction in the shell of an electric racing vehicle using composite materials. Factors considered in the design of the composite shell include maintaining aerodynamic functionality under required flow loads without deformation, and achieving a lightweight structure that forms a three-part system for quick and easy access to the vehicle's interior when needed. All analyses were performed using ANSYS-Student software. For aerodynamic load analysis, a one way fluid-structure interaction model was used. For defining composite materials from scratch, a material designer tool was employed, a composite prep and post-processing tool was utilized for composite layup method and application, and a mechanical analysis tool was used to easily view these results. After the designed shell system was produced, an 80% weight reduction was achieved, meeting the necessary factors.

Keywords: Composite Vehicle Body, Electric Vehicle, Composite Analysis Methods

INTRODUCTION

Electric vehicles are are recently gaining attention because they offer a promising solution for greenhouse gas emissions. They have the potential to have zero emissions during operation, depending on whether the electricity source is zero emissions or not. This is an important

consideration since climate change is a recurring issue of this century, greenhouse gas emissions being one of the main culprits (Breuer et al., 2021). One of the leading sectors for greenhouse gas emissions is the transportation sector behind only of food production sector (Alimujiang & Jiang, 2020). Electric vehicles, specifically Battery Electric Vehicles (BEVs), only create emissions during production and recycling and can operate with zero local emissions, resulting with lower lifetime emissions compared to their internal engine powered equivalents (Hoekstra, 2019). Another advantage they provide is the reduced overall complexity since they don't need a complicated Internal Combustion Engine (ICE) or transmission system, instead requiring a simpler electric motor or motors, depending on application. Their efficiency is regarded as the solution for a sustainable transportation solution for the future.

A significant problem with BEVs is that they are generally about 400-500 kg heavier than their ICE powered counterparts. For example, a 2013 Renault Zoe, which is a supermini (B segment) has a kerb weight of 1468 kg while an equivalent 2013 Renault Clio 1.2 has a kerb weight of 980 kg. In fact, a 2012 Renault Latitude, which is 2 segments above Clio and Zoe (compact executive or D segment), has a kerb weight of 1425 kg. This is a significant issue since increased weight can accelerate wear on components or infrastructure along with increasing the energy consumption, increasing stress on the infrastructure. A second issue is the cost of BEV compared to their ICE equivalents. A study conducted by (Brennan & Barder, 2016) found out that over a 20 year life span, in compact segment vehicles (C segment) BEVs cost 20% more than ICEs in overall operating costs while in mid-size segment vehicles (D segment) BEVs cost 44% more than ICEs in overall operating costs. Another important detail for energy consumption on a vehicle in motion is aerodynamics, specifically the drag forces it must overcome. That is why an aerodynamic body can reduce energy consumption, especially on higher speeds.

One of the main areas of a vehicle where weight reduction can be applied is the body panels or shell. Several materials were studied and it was determined that fiberglass or carbon fiber

could be used to reduce the weight of the body shell (Wilson, 2017). When looked at both materials, carbon fiber offered the highest potential for weight reduction, up to 50% when compared to steel, however it also came with a huge cost being 5.7 times more expensive than steel. Fiberglass on the other hand offered very similar weight reduction potentials while costing 5-10 times less than carbon fiber, potentially costing less than steel (Patel et al., 2008). For these reasons, S-Glass fiberglass was determined as the optimal solution owing to its high strength, low weight and low cost. When looked at the literature, it was discovered that a fiberglass structure with predetermined layers weren't studied before.

The body shell designed here aims to meet these criteria. By using S-Glass fiberglass, a low drag body shell, and comprehensive analysis including a custom defined fiberglass structure with each layer predetermined for optimization, CFD and FEA analysis. This study undertaken by the automotive engineering students at Atilim University aims to design and produce an optimum body shell for an electric racing car named ATEV regarding weight, cost and strength

METHODOLOGY

The vehicle shell was designed to be lightweight and easy to manufacture. After discussing where the shell, made from an Medium Density Fiberboard (MDF) male model, could be divided into three parts, an analysis was conducted using the mechanical analysis tool of ANSYS Student. Based on the analysis results, the division points of the vehicle were determined, and the flange section for the molds to be used in the lay-up was adjusted, and the production of the female mold commenced. Since the desired fiber structure was not available in the material library, a sample measuring 30x30 was produced and tested by the Metal Forming Center of Excellence at Atilim University, and a report was provided. Based on the report from the Metal Forming Center of Excellence, the values of the product were manually entered into the material library, and the material was defined. After the definition, using the data obtained with a material designer tool, the twill composite material was virtually produced initially as yarn, then as UD, and finally in a woven form. The produced fabric was

redefined as a material in the system, and its lay-up on the vehicle shell geometry was virtually performed using a composite prep and post-processing tool. The flow loads were included in this system via a fluid-structure interaction system and conveyed to the results section from this system. The data obtained from all systems were finally transferred to the mechanical analysis tool, and analysis results for each ply were obtained. As a result of the analyses, the vehicle shell system successfully passed the necessary analyses and was ready for production. During the production of the body shell, the glass fiber layers were applied in the same way that they were applied during the analyses for a total of 3 layers and reinforcements as needed. The result was a body shell that was significantly lighter than the previous body shell, so the results were satisfactory.

MATERIAL PROPERTIES

S-Glass Fiber was used for the body shell, whose properties, along with the epoxy used for bonding the fibers, are taken from the study conducted by (Gotsis et al., 2009). Material properties used are given in Table 1.

Table 1: Properties of materials used on construction of the chassis

	S-Glass Fiber	**Epoxy Matrix**
Normal Modulus (GPa)	85500	3394
Poisson's Ratio	0.20	0.35
Shear Modulus (MPa)	35670	-
Tensile Ultimate Strength (MPa)	2482	103.41

ANALYSIS

A couple of tests were performed to ensure the integrity of the shell under air pressure when the vehicle is driven at 80 km/h, such as CFD and static structural analyses.

Before applying the tests to define the integrity of the shell, mesh independency test was conducted with mesh sizes ranging from 1 to 5 mm, with and without large deflection. The aim of this test was to get rid of any potential discrepancies which could be caused by mesh sizes. Mesh sizes and its corresponding attributes as well as stress values from the analysis results are shown below in Table 2 without large deflection and Table 3 with large deflection.

Table 2: Mesh values without large deflection

Mesh Size (mm)	Element Number	Deformation (mm)	Stress (MPa)
1	564000	2.3010	139.12
1.5	168084	2.3010	119.93
3	21376	2.3006	92.85
5	8684	2.3006	81.58

Table 3: Mesh values with large deflection

Mesh Size (mm)	Element Number	Deformation (mm)	Stress (MPa)
1	564000	2.3016	139.12
1.5	168084	2.3015	119.94
3	21376	2.3013	82.85
5	8684	2.3011	81.59

After conducting these tests, 3 mm mesh was chosen for its consistent behavior. The mesh types used and the distribution of cells on the body shell are shown in Figure 1.

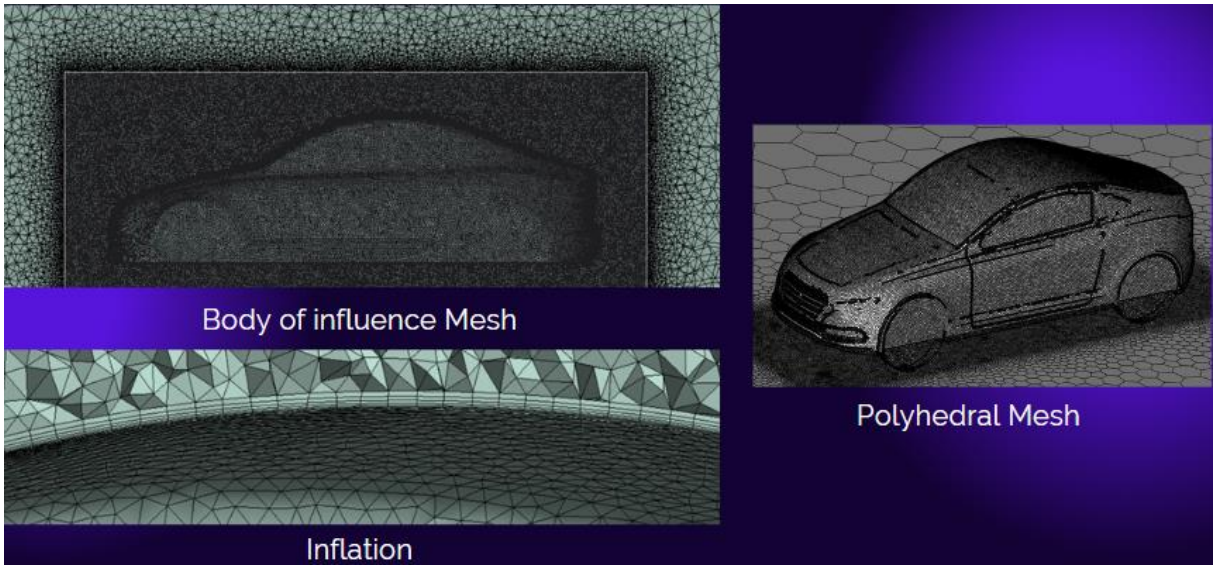


Figure 1: The type of meshes used

After determining the mesh settings, the next step was to define the fiberglass structure. The weight of the shell could be minimized by only adding or removing layers and adjusting the adhesive density. It was observed that the most optimized result was achieved using three layers of fiber, with the twill structure fabrics laid at 0, +45, and -45 degrees relative to the plane for each layer for extra strength. The adhesive density was adjusted, and the final product thickness was determined to be 1 mm. Using these values, a realistic fiberglass structure was created and used throughout the analysis processes. The fiberglass layout for a layer is written in Table 4. The fiberglass twill construction can be seen in Figure 2.

Table 4: Fiberglass layout for one layer

Fiberglass Layer	Twill angle (°)	Twill thickness
1	0	0.11
2	+45	0.11
3	-45	0.11



Figure 2: Fiberglass twill layer sample

Then, a CFD analysis was made on the body, finding a drag coefficient value of 0.23, and the analysis results were imported to be used on the static structural FEA on the body. Analysis results showed that these factors lead to a 2.4 mm deformation and 2 MPa equivalent stress. Analysis details, along with the fiberglass structure, can be seen in Figure 3.

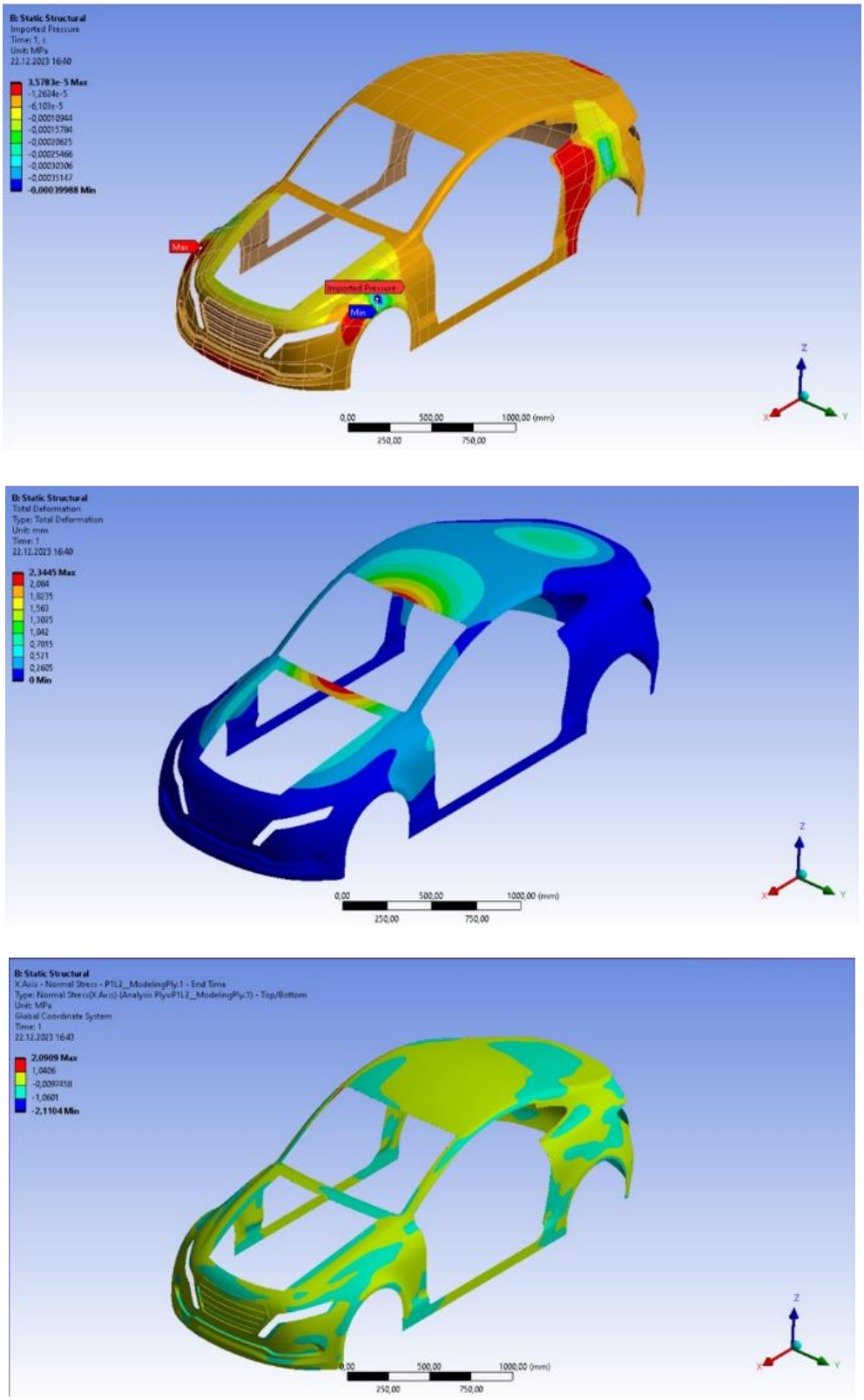


Figure 3 (From top to bottom): CFD pressure distribution, FEA total deformation and FEA nominal stress distribution of body shell

PRODUCTION

In this part of the article, the body shell was produced according to the test results. Female molds, produced using a Medium Density Fiberboard (MDF) male mold, were separated by flanges to divide the vehicle into three parts. After completing the flanges, all surfaces were thoroughly cleaned, and mold release was applied to ensure easy separation from the male mold once the mold was produced. The mold production was carried out by applying a gelcoat and fiber with the necessary chemical mixture. After the molds were removed from the male mold, metal parts were added to give them structural integrity. The stages of this process are illustrated in Figure 4.



Figure 4: Production of the female mold

At the beginning of the production of our composite vehicle shell, a gelcoat with black pigment was applied inside these molds using a spray for safety purposes. Once the gelcoat dried, sealing tape was applied around the molds to define the boundaries. During these processes, the chemicals and fabrics to be used were prepared in specific sizes, and the lay-up processes commenced. As in the analysis, the fabrics were laid at certain angles and combined with the chemical mixture. This process was repeated for three layers, with the adhesive density being weighed and calculated as demonstrated in Figure 5.



Figure 5: Fiber glass preparation for part of the body shell

The sealing tapes initially applied around the mold were then used to attach the vacuum infusion bag. After the bag was laid out properly and ensured to be airtight, a compressor was connected to the vacuum lines to completely evacuate the air inside. This process lasted for three days with the compressor running continuously. At the end of the three days, the compressor and vacuum bag were removed from the mold as illustrated in Figure 6. As a result of this process, a body shell meeting our requirements weighing a total of 16 kilograms was obtained as shown in Figure 7.

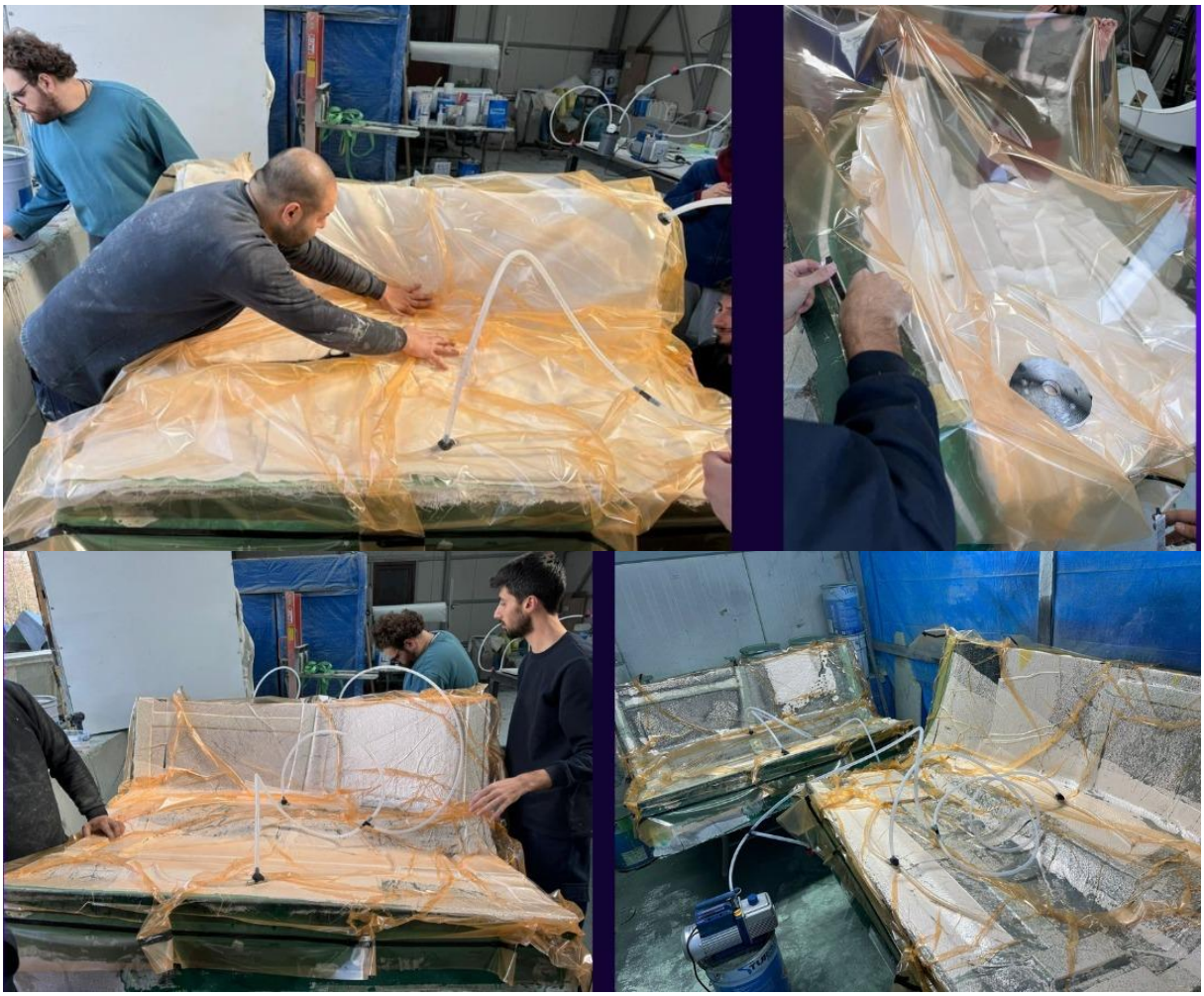


Figure 6: Production of part of the body



Figure 7: Produced body shell

The next step planned is to integrate the body shell to the chassis of the vehicle and to integrate flanges to the body shells to easily connect and disconnect them with each other for easy access to the various parts of the vehicle in the future.

CONCLUSION

Since the material of our composite shell was not available in the material library, we produced a sample of the desired material and took it to the Metal Forming Center of Excellence to obtain a report on its properties. Using the information from this report, we defined the material from scratch in the analysis software and, using a material designer tool, created a fabric and performed its lay-ups via a composite prep and post-processing tool. With the loads from our fluid-structure interaction system, we processed our results in the mechanical analysis tool and optimized them as needed. It was observed that our composite vehicle shell successfully passed the virtual tests, and we concluded that we could comfortably proceed with its production.

ACKNOWLEDGMENTS

This study was performed as a part of a student project named ATEV at Atilim University. We would like to express our thanks and gratitude to all of our advisors and fellow students who provided us technical support during the project. Special thanks go to our department chair Prof. Dr. Hasan U. Akay for his guidance and encouragement throughout all phases of our work. The financial support and encouragement provided by our university administration is greatly appreciated.

REFERENCES

Alimujiang, A., & Jiang, P. (2020). Synergy and co-benefits of reducing CO2 and air pollutant emissions by promoting electric vehicles—A case of Shanghai. Energy for Sustainable Development, 55, 181–189. https://doi.org/10.1016/j.esd.2020.02.005

Brennan, J. W., & Barder, T. E. (2016). Battery Electric Vehicles vs. Internal Combustion Engine Vehicles - A United States-Based Comprehensive Assessment.

Breuer, J. L., Samsun, R. C., Stolten, D., & Peters, R. (2021). How to reduce the greenhouse gas emissions and air pollution caused by light and heavy duty vehicles with battery-electric, fuel cell-electric and catenary trucks. Environment International, 152. https://doi.org/10.1016/j.envint.2021.106474

Gotsis, P. K., Chamis, C. C., David, K., & Abdi, F. (2009). Progressive fracture of laminated composite stiffened plate. Theoretical and Applied Fracture Mechanics, 51(2), 144–147. https://doi.org/10.1016/j.tafmec.2009.04.008

Hoekstra, A. (2019). The Underestimated Potential of Battery Electric Vehicles to Reduce Emissions. In Joule (Vol. 3, Issue 6, pp. 1412–1414). Cell Press. https://doi.org/10.1016/j.joule.2019.06.002

Patel, M., Pardhi, B., Chopara, S., & Pal, M. (2008). Lightweight Composite Materials for Automotive-A Review. International Research Journal of Engineering and Technology, 41. www.irjet.net

Wilson, A. (2017). Vehicle weight is the key driver for automotive composites. Reinforced Plastics, 61(2), 100–102. https://doi.org/10.1016/j.repl.2015.10.002

Dynamic Height Adjustment and Obstacle Climbing Capabilities of a 6x6 Unmanned Ground Vehicle with Advanced Hydropneumatic Suspension Systems

Meliksah BESIR, *mbesir@hidroan.com.tr* Hidroan Ankara Hidrolik Mak. San. Tic. Ltd. Şti., 06800, Ankara, Turkey

Eren DOYMUS, *eren.doymus@hidroan.com.tr* Hidroan Ankara Hidrolik Mak. San. Tic. Ltd. Şti., 06800, Ankara, Turkey

I. Melih CANBOLAT, *melih.canbolat@hidroan.com.tr* Hidroan Ankara Hidrolik Mak. San. Tic. Ltd. Şti. & Middle East Technical University, 06800, Ankara, Turkey

E. Ilhan KONUKSEVEN, *konuk@metu.edu.tr* Middle East Technical University, 06800, Ankara, Turkey

1. ABSTRACT

This study presents the design and development of a 6x6 unmanned ground vehicle (UGV) equipped with advanced hydropneumatic suspension systems. These systems allow dynamic height adjustment of each wheel, enhancing stability and traction for obstacle climbing. Using a LIDAR sensor and RANSAC algorithm, the UGV detects and measures obstacles, adjusting its suspension to navigate challenging terrains. The Webots simulation platform and test vehicle validated the system's performance, demonstrating the UGV's ability to autonomously climb various obstacles with stability. This research highlights significant advancements in UGV mobility and obstacle negotiation capabilities.

Keywords: Unmanned ground vehicle, 6x6 UGV, hydropneumatic suspension, obstacle climbing, LIDAR sensor, RANSAC algorithm, Webots simulation

2. INTRODUCTION

Our study employs a 6x6 unmanned ground vehicle (UGV) equipped with advanced hydropneumatics suspensions. This design offers exceptional terrain adaptability and obstacle negotiation, making it suitable for demanding applications such as search and rescue missions, military reconnaissance, and autonomous exploration. The hydropneumatics suspension system is particularly critical, as it allows the vehicle to dynamically adjust the height of each wheel, ensuring stability and traction, which are essential for climbing obstacles effectively.

There are some unmanned ground vehicles that have inspired vehicle design. The Rook, developed by Elbit Systems and Roboteam, is a military-standard 6x6 UGV with a modular design that can navigate pre-programmed routes and avoid obstacles using advanced sensors and a communication system (Elbit Systems, 2021). Another example is the Valkyrie developed by SASCorp (SASCorp, 2021). It is an amphibious 6x6 UGV with high mobility

and carrying capacity that can overcome vertical obstacles up to 0.7 meters. Another example, the Sharp Claw 2, is a 6x6 UGV designed for reconnaissance and transportation, and has a high obstacle-climbing capability thanks to its adaptable wheel configurations (Army Recognition, 2021). Furthermore, research on a portable six-wheeled mobile robot with a self-reconfigurable body highlights the benefits of self-adaptive obstacle-climbing mechanisms (Song et al., 2022).

Many researchers have conducted studies on new 6x6 wheel-track unmanned ground platforms with six independently driven wheel-track mechanisms due to the low capability of multi-wheeled vehicles in harsh terrain conditions. In these studies, the vehicles are designed for harsh terrain structures and adaptive control methods have been studied for 6X6 slip-type UGVs with six in-wheel motors to improve the control performance of the vehicles (Zhang, J., & He, X. 2021) (Shin, J., & Joo, S. 2014).

It has also been observed that multi-wheeled systems such as 6x6 have better mobility in difficult terrain conditions compared to other systems. The geometric suspension systems of 6x6 unmanned ground vehicles increase their ability to overcome obstacles (Miki et al., 2019) (Noh et al., 2006). Another important development is the obstacle clearance algorithm developed for the 8x8 unmanned ground vehicle to overcome obstacles by climbing. With this algorithm, a hydraulic motor was used, and it was observed that the vehicle easily overcame an obstacle with a height of 950 mm (Miaolei et al., 2020). With this approach, it has been observed that the vehicle can maintain its stability during obstacle climbing and make a safe climb. Apart from these approaches, artificial intelligence methods such as ANN are also used to improve the control performance of unmanned ground vehicles (Shin, J., & Joo, S. 2014), and in addition, studies have been conducted on 6-wheeled mobile robots with different types of configurations and climbing mechanisms that allow the body to adjust itself (Song et al., 2022).

The focus of this paper is to develop a 6x6 unmanned ground vehicle with obstacle-climbing capability. The process of developing this capability includes the design of the vehicle, the use of sensors such as LIDAR for obstacle detection and the development of algorithms, the calculations required for obstacle climbing, and the development of control algorithms that guide the vehicle for the climbing process. Other methods proposed to increase the mobility of UGVs include advanced suspension systems and obstacle avoidance algorithms (Masood et al., 2017) (Yoon et al., 2009).

The tool processes the obstacle data received by LiDAR, i.e. it performs masking operations to detect obstacles and performs ground segmentation using the RANSAC algorithm

(Tarsha-Kurdi et al., 2007) (Su et al., 2021) (Narksri et al., 2018). After this data processing process, the data of the detected obstacles are sent to the control algorithms. If the obstacle height is suitable for climbing, the control algorithm performs the climbing process by adjusting the arm angles according to the obstacle height. If the obstacle height is not suitable for climbing, the vehicle stops and prevents safety and damage.

One of the major problems in multi-wheeled unmanned ground vehicles such as 6x6 is to ensure vehicle dynamics and stability. Especially when these vehicles are traveling in harsh terrain conditions, it is very important to ensure the stability and safety of the vehicle. For this situation, while designing the 6x6 vehicle, an independent hydropneumatics suspension system was used for each wheel (Besir et al., 2024). Thus, while the vehicle is climbing, the wheels move independently of each other thanks to the independent suspension system, and driving safety is ensured by maintaining the vehicle dynamics in difficult terrain conditions and especially during the climbing process.

3. METHODOLOGY

The methodology section details the development and implementation of an obstacle-climbing mechanism for a 6x6 unmanned ground vehicle (UGV). This includes the use of the Webots simulation platform and the test vehicle to validate the system, integration of various sensors and algorithms, and the decision-making process for climbing obstacles.

Development Environment

The Webots simulation platform was chosen for its versatility and comprehensive support for robotic systems. This environment allowed for the detailed modeling of the UGV, integration of sensors, and testing of the obstacle-climbing algorithms in a controlled, repeatable manner.

System Components

- UGV Model: The UGV is a 6x6 wheeled vehicle equipped with hydropneumatic suspension systems for each wheel. This setup allows for independent control of each wheel's height, essential for maintaining stability while climbing obstacles.
- Sensors: The UGV uses a LIDAR sensor for obstacle detection and measurement. The LIDAR data is processed using the RANSAC algorithm to filter out ground points and identify potential obstacles accurately.
- Control Algorithms: The core of the climbing mechanism is the "HeightController" class, which governs the adjustment of the vehicle's arms. This class ensures that the

UGV adjusts its suspension in a sequence that maintains stability while climbing over obstacles.

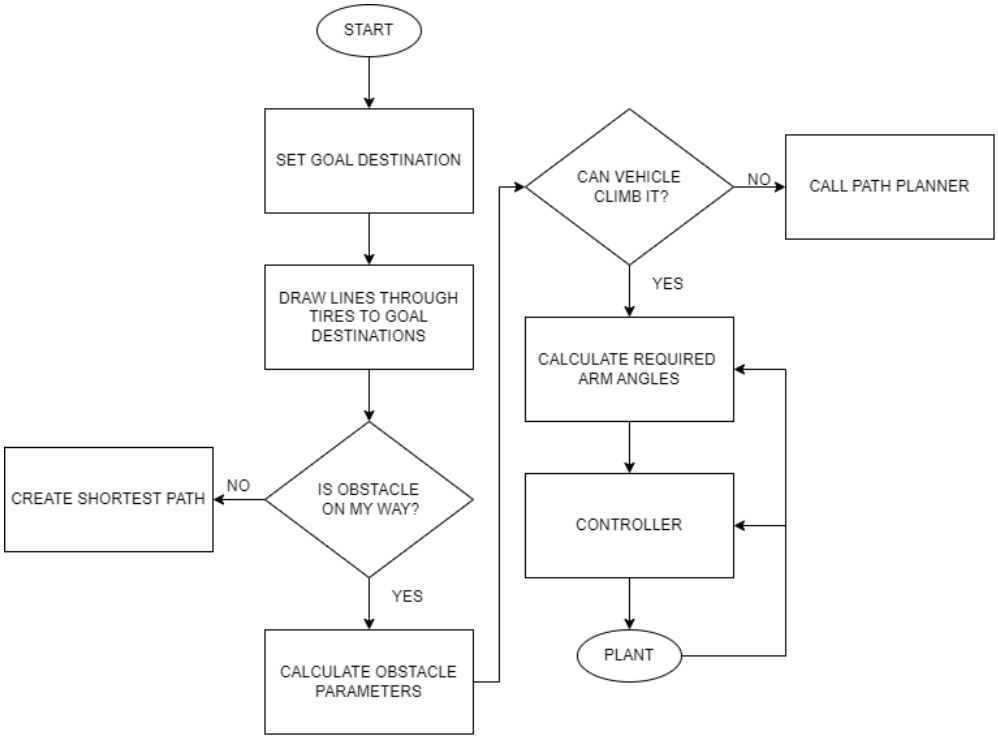


Figure 1 Flowchart of the Algorithm

The flowchart given in Figure 1 outlines the decision-making process for the UGV as it navigates towards its goal, encountering and addressing obstacles along the way. The process begins with the UGV's navigation system, followed by identifying and setting its target destination. The system then draws direct lines from the vehicle's current position to the goal, plotting an initial path. The path is analyzed for any obstacles, and if none are detected, the UGV proceeds along the planned path. If an obstacle is detected, its parameters, such as height and position, are calculated using LIDAR data and the RANSAC algorithm. The system assesses whether the obstacle is climbable based on the UGV's capabilities, a decision crucial for determining the subsequent actions. If the obstacle is deemed climbable, the necessary adjustments for the suspension arms are calculated, involving determining the optimal angles for each arm to ensure a stable climb. The “HeightController” class then executes the calculated adjustments, modifying the suspension arms accordingly to climb the obstacle. If the obstacle is not climbable, the system triggers the path planner to generate an alternative route that bypasses the obstacle. The UGV either proceeds with climbing the obstacle or follows the new path to continue towards its goal. This flowchart illustrates the comprehensive decision-making framework that ensures the UGV can navigate complex environments autonomously, with the ability to dynamically adjust its

path or suspension based on real-time obstacle detection and analysis being crucial for effective operation in varied and unpredictable terrains.

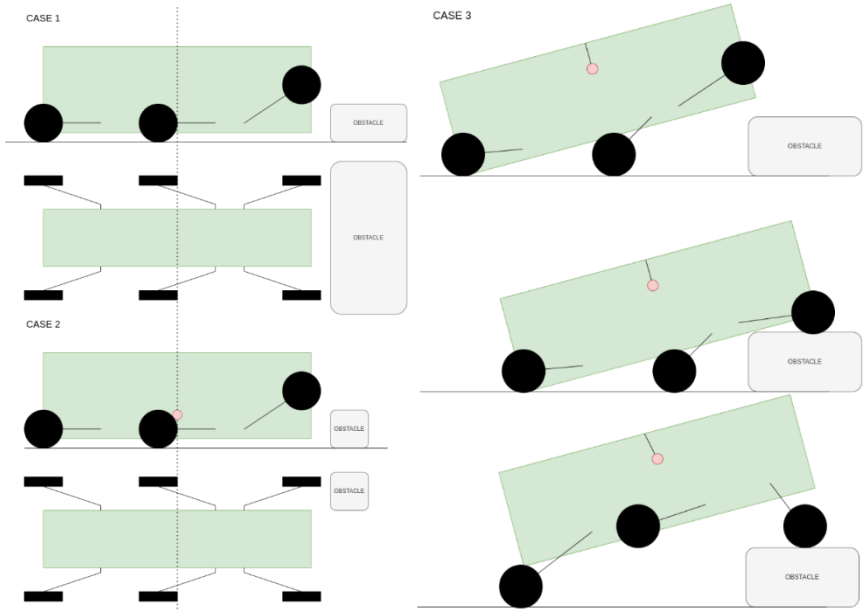


Figure 2 Some of the Cases Vehicle Encounters

In the first case given in Figure 2, the UGV encounters a small obstacle that affects all arms of the vehicle. As the obstacle is small, it does not significantly disrupt the vehicle's balance or require complex adjustments. The UGV responds by making uniform adjustments to all its arms, slightly raising each to ensure the wheels can climb over the obstacle while maintaining stability. The pink circle represents the Center of Gravity (CoG), which remains relatively centered, indicating that the vehicle's balance is well-maintained as it negotiates the small obstacle. The second case involves an obstacle that affects only one side of the UGV. This obstacle can vary in size, being either large or small. If the obstacle is small, the UGV only adjusts the arms on the side of the vehicle encountering the obstacle, raising them to climb over while keeping the other side stable. For larger obstacles, the vehicle raises the arms on the affected side while simultaneously lowering the arms on the opposite side. This differential adjustment helps in maintaining the CoG within an optimal range, ensuring the vehicle's stability as it navigates the obstacle. The CoG, indicated by the pink circle, shifts slightly towards the unaffected side, balancing the vehicle effectively. In the third case, the UGV faces a large obstacle that impacts all arms. This scenario requires the most significant adjustments as the vehicle needs to ensure all wheels can climb over the obstacle without compromising stability. The UGV raises all arms significantly, with more pronounced adjustments to ensure each wheel can grip and ascend the obstacle. The CoG, depicted by the pink circle, shifts upward, but remains centrally aligned to prevent tipping. The vehicle's

suspension system works uniformly across all arms, allowing it to overcome the large obstacle while maintaining a balanced and stable posture. This comprehensive adjustment ensures the vehicle's integrity and continued operation after navigating the large obstacle.

Obstacle Detection and Distance Measurement

Accurate obstacle detection and measurement are foundational to the UGV's performance. The system utilizes LIDAR sensors for high-precision distance measurements and 3D mapping. The process begins with the LIDAR sensor continuously collecting point cloud data that represents the surrounding environment. This data includes detailed information about the distance and position of nearby objects. The raw data is then filtered to remove noise and transformed into the vehicle’s base frame. Using the RANSAC algorithm, we segment the ground plane from the LIDAR data, effectively isolating obstacles from ground points. This segmentation is crucial for accurately detecting and measuring the height, width, and depth of obstacles. After segmentation, bounding boxes of detected obstacles are extracted, providing comprehensive information about their dimensions, which helps in determining whether an obstacle is climbable based on the vehicle's capabilities.

Obstacle Detection and Segmentation using LIDAR and RANSAC Algorithm

The developed algorithm includes the detection of obstacles by filtering the data from the LIDAR sensor with the necessary transformation processes and separating the point clouds representing the obstacles in front of the sensor from the ground point clouds. With this application, the obstacles detected by the sensor are separated from the ground utilizing the RANSAC algorithm and after the necessary filtering processes, the bounding boxes (width, depth, height, etc.) of these obstacles are extracted and published in detection3DArray message type for use in other algorithms.

The reason why the LIDAR sensor is preferred for this algorithm is that it is resistant to physical environment components such as light and temperature, in short, the efficiency of the sensor decreases less compared to other sensors in various and extreme environmental conditions. This algorithm can also be developed with other devices such as the Intel RealSense camera, however, it was observed that the Intel RealSense camera is not resistant to physical environment conditions and therefore incorrect results are obtained in the developed algorithm.

Transformation of LIDAR Data

Point cloud of the obstacles were generated by the lidar sensor and then transformed to the vehicle's base frame using these data and the quaternion data in the IMU data. In addition, the noise in the IMU data affects the performance of the developed algorithms, so it was

decided to use a Kalman filter to prevent this situation and a ROS package was developed to use this filter. In this way, accurate data is obtained from the lidar sensor.

Ground Segmentation

After the transform operations, the RANSAC method was used to determine and segment the ground plane from the LIDAR data. This step is critical to isolate obstacles from ground points and to process obstacle data with high accuracy.

Plane Fitting Using RANSAC: With RANSAC, a random subset of points is selected (In this method, this value is chosen as 3. In other words, 3 points are selected from the point cloud set.), a plane model is fitted with the help of the least squares method. The plane model (1) and the least squares method (2) are respectively represented as follows:

$$ax + by + cz + d = 0 \tag{1}$$

$$min_{n,d} \sum_{i=1}^{N} (ax_i + by_i + cz_i + d)^2 \tag{2}$$

n is the normal vector of the plane.

Plane Model Definition: The plane model consists of 2 main components, the center and the normal vector. The center of the plane model is the center of the sample points, and the normal vector is generated using Singular Value Decomposition (SVD).

Distance Calculation and Masking: After the plane model was created, the distance of each point cloud from the sensor to this plane was calculated. The distance of a point (x_i, y_i, z_i) to the level is calculated as follows:

$$distance = \frac{|ax_i + by_i + cz_i + d|}{\sqrt{a^2+b^2+c^2}} \tag{3}$$

The point clouds outside the threshold value determined after the distance calculation were accepted as external points and as a result, the point clouds below this threshold value were filtered and the ground segmentation process was completed.

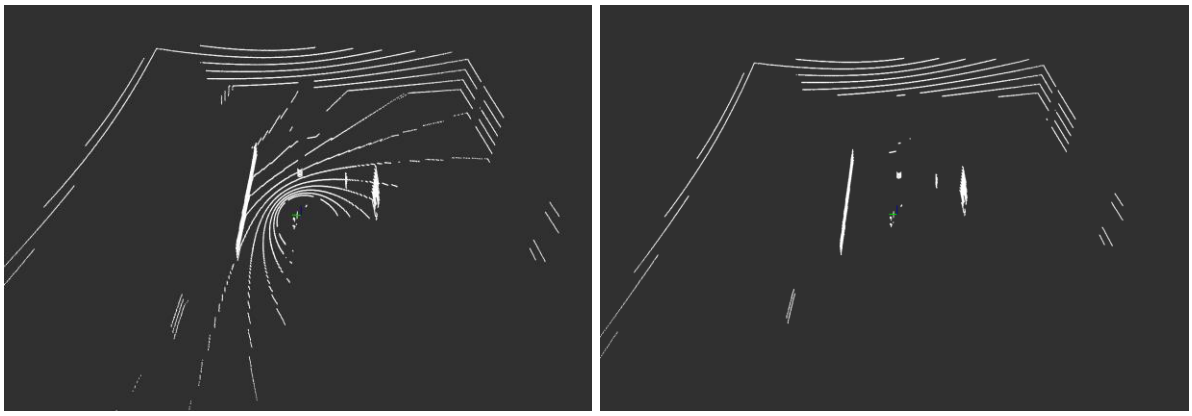


Figure 3 Lidar Data Without RANSAC Algorithm and with RANSAC Algorithm

Filtering

After the ground points were segmented using RANSAC, some filtering was performed to eliminate some problems such as only the data of the obstacles in the desired direction and the unnecessary point clouds slowing down the developed algorithm. As a result, this helped to isolate the obstacle points.

Decision-Making Process for Obstacle Climbing

Once an obstacle is detected, the system calculates its height using the processed LIDAR data. The decision to climb or avoid the obstacle is based on a predefined threshold, derived from the vehicle's mechanical design constraints and the hydropneumatic suspension's maximum extension and retraction capabilities. The maximum height the vehicle can climb is calculated using the formula:

$$H_{max} = sin(\theta) * l - R \tag{4}$$

where θ is the lowest angle of the suspension, l is the length of the suspension arm, and R is the tire radius. This calculation provides the maximum obstacle height the vehicle can surmount. For our vehicle θ is 38, l is 0.45 m and the R is 0.3 m.

Climbing Mechanism

The climbing mechanism involves a precise and coordinated adjustment of the vehicle's hydropneumatic suspensions, orchestrated by the control algorithm implemented in the "HeightController" class. Initially, the system evaluates the obstacle's height to determine if it falls within the vehicle's climbing capability. If the obstacle is deemed climbable, the vehicle calculates the necessary suspension adjustments. These adjustments are made sequentially for the front, middle, and rear arms or right and left arms to prioritize stability and ensure a smooth transition over the obstacle.

Based on the obstacle position, the code determines which arms should move. For example, if the obstacle only affects the right arms which are decided by obstacle position and width coming from LIDAR data, the code just adjusts the right arms. Also, for larger objects, it lowers the left arms and raises the right arms in the same situation. The front left (FL) and front right (FR) arms are adjusted first. The required angle for each arm is computed based on the obstacle height and current arm angles, ensuring the vehicle maintains an appropriate distance from the obstacle. Next, the middle left (ML) and middle right (MR) arms are adjusted with similar calculations to ensure these arms can clear the obstacle without compromising stability. Finally, the rear left (RL) and rear right (RR) arms are adjusted. For larger obstacles, the rear arms are lowered first to create a stable base, followed by the front and middle arms. During the climbing process, the system continuously monitors the pressure in each hydropneumatic arm. Low pressure in any arm indicates that the arm is not under load, prompting the system to lower the arm to engage with the terrain. This real-time pressure check ensures all arms effectively contribute to the climbing effort. Using trigonometric functions, the required angles are calculated to ensure precise adjustments. The calculated angles are communicated to the cmd_arms topic, which controls the hydraulic actuators to adjust the arm positions accordingly. The system continuously monitors the vehicle's position and obstacle height, making real-time adjustments as necessary. Throughout the climbing process, feedback from the LIDAR and odometry data is used to dynamically adjust the arm angles, maintaining stability and traction.

Path Planning and Real-Time Operation

Our system integrates closely with a path planner for real-time operation. When an obstacle is detected and assessed for climbability, the system communicates with the path planner. The path planner then generates a path based on the vehicle's current position, the obstacle data, and the vehicle’s capabilities. This real-time path planning allows the vehicle to navigate complex terrains autonomously, efficiently, and safely.

Validation and Testing

To validate the proposed climbing mechanism, extensive testing was conducted using the Webots simulation platform, which provides a controlled virtual environment for comprehensive evaluation, and a test vehicle. The tests included scenarios with low and high obstacles. For low obstacles, the vehicle successfully climbed by sequentially adjusting the front, middle, and rear arms, demonstrating precise control over the suspension arms and ensuring smooth, stable transitions. For larger obstacles, the vehicle first lowered the rear arms to provide a stable base, followed by adjustments to the front and middle arms, maintaining stability and traction throughout the climb. The simulation also tested the

pressure monitoring mechanism, effectively detecting low-pressure conditions in the arms and adjusting them accordingly to ensure proper load distribution and stability during the climb. The results from the Webots simulation and the test vehicle confirmed that the vehicle could accurately and efficiently climb obstacles within its design limits, with the control algorithm effectively adjusting the suspension arms, providing stability, and maintaining traction throughout the climbing process.

This methodology ensures that the UGV can autonomously navigate challenging terrains by dynamically adjusting its suspension system to overcome obstacles, enhancing its operational capability in diverse environments.

4. RESULTS and DISCUSSION

The results from our extensive testing in the Webots simulation platform and the test vehicle confirmed the effectiveness and reliability of our obstacle climbing mechanism for the 6x6 unmanned ground vehicle (UGV). The system's performance was evaluated based on its ability to accurately detect obstacles, decide on climbability, adjust the suspension arms, and navigate complex terrains autonomously.

The LIDAR sensor integrated with the RANSAC algorithm provided high-precision obstacle detection and measurement. The filtering and transformation processes effectively isolated obstacles from ground points, and the bounding boxes generated offered accurate dimensions of the obstacles. The decision-making process, which considers the vehicle's mechanical design constraints, proved efficient in determining climbable obstacles.

The climbing mechanism, orchestrated by the control algorithm in the "HeightController" class, demonstrated precise and coordinated adjustments of the vehicle’s hydropneumatic suspensions. The simulation tests included scenarios with both low and high obstacles, where the vehicle successfully climbed by sequentially adjusting the front, middle, and rear arms. This sequential adjustment ensured smooth and stable transitions over the obstacles.

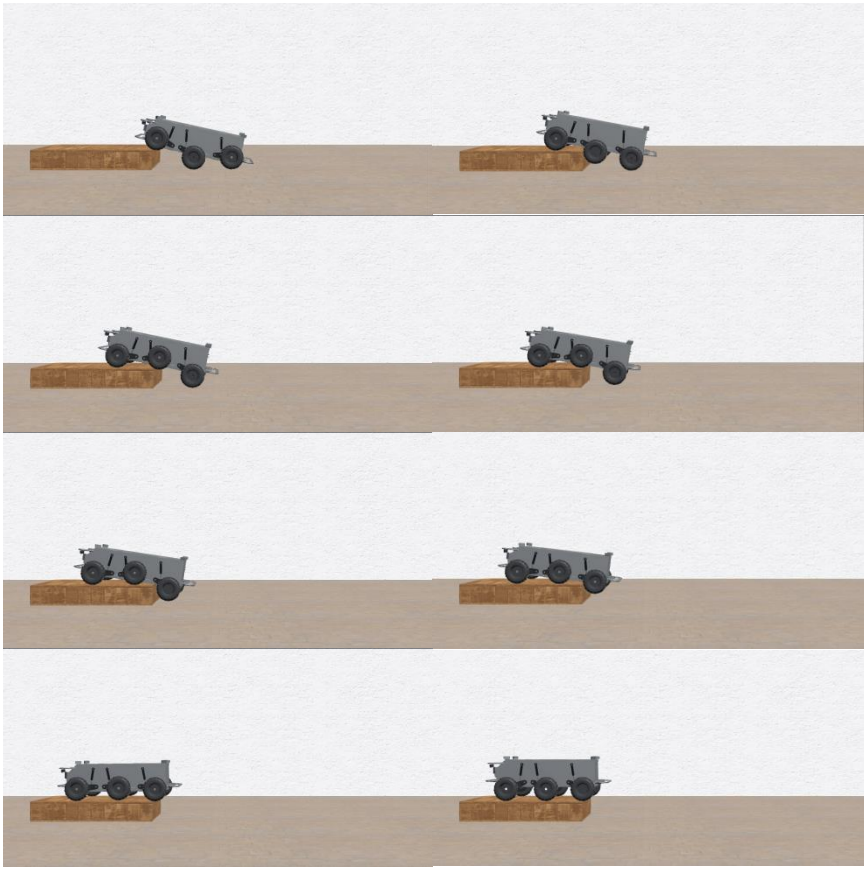


Figure 4 Climbing Large Object Which Affects Both Side of Arms in Webots Simulation

In Figure 4, vehicle performance is evaluated with a large object that affects both arms. The algorithm first analyzes the climbable situation and then based on the obstacle height and position, the algorithm adjusts the arm angles. If the vehicle is too close obstacle algorithm gives feedback to the user vehicle is too close and cannot adjust the arm without crashing the obstacle or if the obstacle is too high to climb algorithm communicates with the path planning algorithm and path generation starts. In this scenario the vehicle approaches a large object within the vehicle limits. The vehicle first lowers the rear arms, then adjusts the middle arms and finally raise the front arms according to the obstacle height. When the front arms climb the obstacle rear and front arms adjust the vehicle's chassis height and the middle arm raises. After the middle arm climbing the obstacle middle and front arm lowered for rear arms climbing to the obstacle. After climbing the obstacle based on arm angles and pressures algorithm communicates with the leveling and balancing algorithm (Besir et al., 2024) to balance itself.

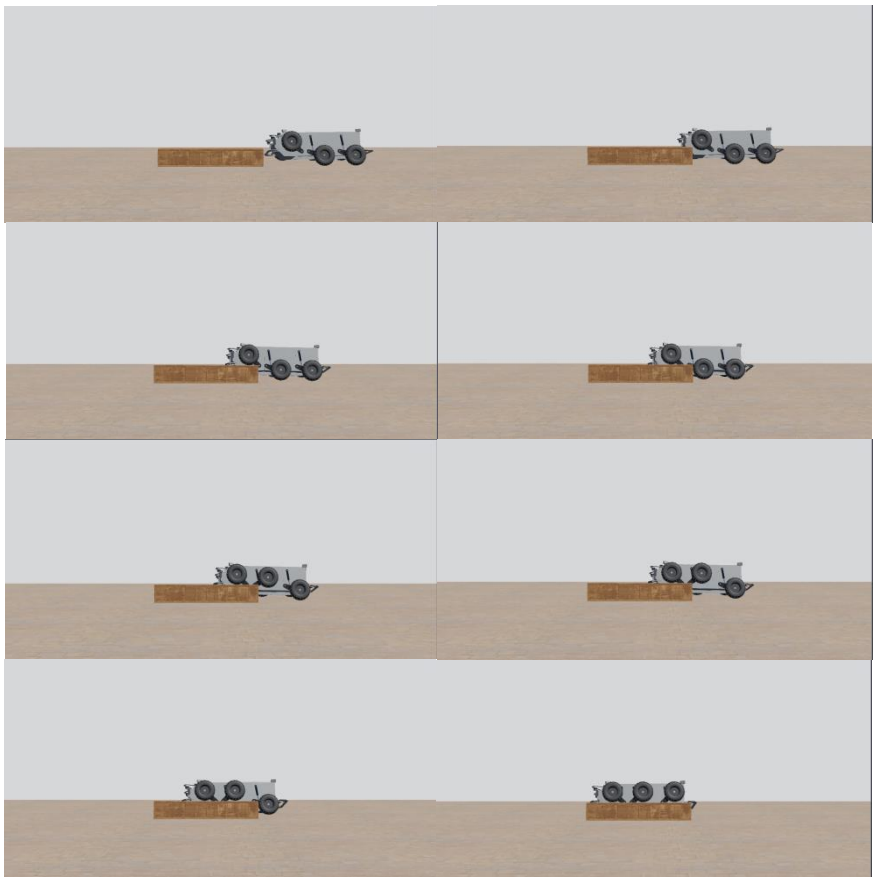


Figure 5 Climbing Large Object Which Affects Only Left Arms in Webots Simulation

In Figure 5, vehicle performance is evaluated with the large object which affects only the left arms. Algorithm firstly analyzes climbable situation and then based on the obstacle height it adjusts the arm angles. In this scenario vehicle approaches a large object within the vehicle limits. Vehicle firstly lowers the right arms, then raise the front arms according to the obstacle height and position. If the vehicle is too close obstacle algorithm gives feedback to the user vehicle is too close and cannot adjust the arm without crashing the obstacle. When the front left arm climbs the obstacle, the middle left arm raises. After the middle arm climbs the obstacle rear left arm climbs to the obstacle. After climbing the obstacle based on arm angles and pressures algorithm communicates with a leveling and balancing algorithm to balance (Besir et al., 2024) itself.

For low obstacles, the vehicle's control algorithm effectively adjusted the arms to climb the obstacles without compromising stability. In the case of larger obstacles, the algorithm prioritized stability by first lowering the rear arms to create a stable base before adjusting the front and middle arms. This strategy-maintained traction and stability throughout the climbing process. During the climbing process, real-time pressure monitoring in each hydropneumatics arm ensured proper load distribution. Low-pressure conditions in any arm were detected promptly, allowing the system to lower the arm to engage with the terrain. This

mechanism was critical in maintaining stability and ensuring all arms contributed effectively to the climbing effort.



Figure 4 Obstacle Climbing Tests on the Test Vehicle

In Figure 4, algorithm performance is evaluated on the test platform. Vehicle successfully climbs and comes down slowly after climbing the obstacle. Crane is waits for the vehicle as a safety option if the vehicle rolls down or cannot climb the obstacle.

The integration with the path planner for real-time operation was seamless. When an obstacle was detected, the system communicated with the path planner, which generated a

path based on the vehicle's current position, obstacle data, and capabilities. This real-time path planning allowed the vehicle to navigate complex terrains autonomously, efficiently, and safely. The feedback loop from the LIDAR and odometry data enabled dynamic adjustments of the arm angles during the climbing process. The continuous monitoring and real-time adjustments ensured that the vehicle-maintained stability and traction, effectively climbing obstacles within its design limits.

The results of the Webots simulation and the test vehicle validate the proposed climbing mechanism and its control algorithm. The ability to accurately detect and measure obstacles, decide on climbability, and make precise adjustments to the suspension arms demonstrates the system's potential for real-world applications. The integration with real-time path planning further enhances the vehicle's operational capability, making it suitable for search and rescue missions, military reconnaissance, and autonomous exploration in diverse environments. Here are some bullet points of this work:

- Enhanced Autonomy: The ability to autonomously detect, evaluate, and navigate over obstacles significantly enhances the operational capabilities of the UGV. This autonomy is crucial for missions where human intervention is limited or dangerous, such as disaster response or military reconnaissance.
- Improved Adaptability: The integration of advanced hydropneumatic suspensions and real-time pressure monitoring allows the UGV to adapt to a wide range of terrains and obstacles. This adaptability is vital for UGVs operating in unpredictable environments where terrain conditions can vary significantly.
- Increased Safety and Efficiency: By dynamically adjusting the suspension system and continuously monitoring the vehicle's position and obstacle height, the UGV can maintain stability and traction. This capability reduces the risk of vehicle overturning or becoming stuck, ensuring mission success and increasing overall efficiency.
- Versatility in Applications: The developed system's ability to handle diverse terrains and obstacles makes it suitable for various applications beyond search and rescue and military operations. It can be employed in agricultural monitoring, environmental surveys, and infrastructure inspections, where navigating complex terrains is often required.
- Technical Advancements: This work contributes to the technical advancement of UGVs by integrating state-of-the-art sensors, algorithms, and control mechanisms. The use of LIDAR and the RANSAC algorithm for obstacle detection and segmentation sets a high standard for precision and reliability in robotic perception systems.

- Future Research and Development: The findings and methodologies presented in this work lay the groundwork for future research and development. By demonstrating the effectiveness of the proposed mechanisms and control algorithms, this study encourages further exploration and enhancement of autonomous navigation systems for UGVs.

In conclusion, the developed system shows a high level of robustness and adaptability, capable of overcoming various obstacles with stability and efficiency. Future work will focus on further refining the control algorithms, enhancing the real-time decision-making process, and testing the system in real-world scenarios to validate its performance in dynamic and unpredictable environments. This ongoing development is essential to fully realize the potential of UGVs in various critical applications.

5. FUTURE WORKS

Building on the successful implementation and validation of the obstacle climbing mechanism for the 6x6 unmanned ground vehicle (UGV), future work will focus on further enhancing the system's capabilities and performance. One of the primary areas of development will be the integration of a reinforcement learning (RL) system for the climbing mechanism. This approach aims to improve the decision-making process and adaptability of the UGV in various and unpredictable environments.

The integration of reinforcement learning will involve the following key aspects:

- Adaptive Learning: Reinforcement learning will enable the UGV to learn from its interactions with the environment, improving its climbing strategy over time. The RL system will be trained to optimize the adjustment of the suspension arms based on different obstacle characteristics and terrain conditions.
- Dynamic Decision-Making: Unlike predefined algorithms, an RL-based system can make real-time decisions that consider the current state of the environment and the vehicle. This dynamic decision-making process will enhance the UGV's ability to handle unexpected obstacles and changes in terrain.
- Simulation and Real-World Testing: The initial training and testing of the RL system will be conducted in the Webots simulation platform. This controlled environment allows for extensive experimentation and fine-tuning of the RL algorithms. Once the system demonstrates reliable performance in simulation, it will be tested in test vehicle to validate its effectiveness and robustness.

- Performance Metrics: To evaluate the performance of the RL system, various metrics such as the success rate of obstacle climbing, stability, efficiency, and adaptability will be monitored. These metrics will help in continuously refining the RL algorithms to achieve optimal performance.
- Integration with Existing Systems: The RL system will be integrated with the existing path planner and control algorithms. This seamless integration will ensure that the UGV can autonomously navigate complex terrains by leveraging both the deterministic path planning and the adaptive learning capabilities of the RL system.

In addition to the development of the RL system, future work will explore expanding the application scenarios of the UGV. This includes testing the vehicle in more diverse and challenging environments to ensure its versatility and reliability in various operational contexts.

The integration of a reinforcement learning system represents a significant step forward in the development of autonomous UGVs. By enabling adaptive learning and dynamic decision-making, the UGV will be better equipped to handle complex and unpredictable environments. This advancement will not only improve the vehicle's performance and reliability but also expand its potential applications in critical missions. The ongoing research and development efforts will ensure that the UGV remains at the forefront of technological innovation, capable of meeting the challenges of the future.

6. ACKNOWLEDGEMENTS

We would like to thank Hidroan Ankara Hidrolik Mak. San. Tic. Ltd. Şti. and its employees who built the test vehicle with the company's resources. This study was supported by Tübitak-Teydeb “Yüksekliği Ayarlanabilen 6x6 Taktik Tekerlekli Ve Hidrolik Tahrikli Modüler Kara Taşıtının Tasarımı Ve Geliştirilmesi” Hidroan Ankara Hidrolik Mak. San. Tic. Ltd. Şti. project.

7. REFERENCES

1. **Song, Z., Luo, Z., Wei, G., & Shang, J. (2022).** A portable six-wheeled mobile robot with reconfigurable body and self-adaptable obstacle-climbing mechanisms. Journal of Mechanisms and Robotics, 14(5), 051010.

2. **Zhang, J., & He, X. (2021).** Design and Obstacle-surmounting Analysis of a Novel 6× 6 Wheel-tracked Unmanned Ground Platform. In Proceedings of the 7th International Conference on Robotics and Artificial Intelligence (pp. 46-51).

3. **Shin, J., & Joo, S. (2014).** NN-based Adaptive Control for a Skid-type Autonomous Unmanned Ground Vehicle. Journal of Institute of Control, Robotics and Systems, 20(12), 1278-1283.

4. **Miki, T., Khrapchenkov, P., & Hori, K. (2019).** UAV/UGV autonomous cooperation: UAV assists UGV to climb a cliff by attaching a tether. In 2019 International Conference on Robotics and Automation (ICRA) (pp. 8041-8047). IEEE.

5. **Noh, T. B., Yoo, W. S., Kim, M. H., Noh, H. W., Kim, H. W., Huh, N., ... & Park, S. J. (2006).** Analysis and design of a multi-wheeled vehicle with variable geometry suspension. In Sensors, and Command, Control, Communications, and Intelligence (C3I) Technologies for Homeland Security and Homeland Defense V (Vol. 6201, pp. 274-280). SPIE.

6. **Miaolei, H. E., He, J., Ren, C., & He, Q. (2020).** A horse inspired eight-wheel unmanned ground vehicle with four-swing arms. In 2020 IEEE/RSJ International Conference on Intelligent Robots and Systems (IROS) (pp. 7723-7728). IEEE.

7. **Masood, M. U., Sami, M. A., Sohail, H., Mujtaba, M., Siddique, M. A., Akram, H., Iqbal, J. (2017).** Design and development of a semi-autonomous stair climbing robotic platform for rough terrains. In 2017 17th International Conference on Control, Automation and Systems (ICCAS) (pp. 212-217). IEEE.

8. **Yoon, Y., Shin, J., Kim, H. J., Park, Y., & Sastry, S. (2009).** Model-predictive active steering and obstacle avoidance for autonomous ground vehicles. Control Engineering Practice, 17(7), 741-750.

9. **Tarsha-Kurdi, F., Landes, T., & Grussenmeyer, P. (2007).** Hough-transform and extended ransac algorithms for automatic detection of 3d building roof planes from lidar data. In ISPRS Workshop on Laser Scanning 2007 and SilviLaser 2007 (Vol. 36, pp. 407-412).

10. **Su, Z., Gao, Z., Zhou, G., Li, S., Song, L., Lu, X., & Kang, N. (2021).** Building plane segmentation based on point clouds. Remote Sensing, 14(1), 95.

11. **Narksri, P., Takeuchi, E., Ninomiya, Y., Morales, Y., Akai, N., & Kawaguchi, N. (2018).** A slope-robust cascaded ground segmentation in 3D point cloud for autonomous vehicles. In 2018 21st International Conference on intelligent transportation systems (ITSC) (pp. 497-504). IEEE.

12. **M. Besir, K. B. Ulusoy, A. Alkan and E. I. Konukseven (2024),** "Design and Implementation of Leveling and Balancing Algorithm for 6x6 Electric Unmanned Ground Vehicle with Active Hydro-Pneumatic Suspension System," 3rd International Conference on Innovations and Development of Information Technologies and Robotics (IDITR), IEEE.

20. ULUSLARARASI MAKİNA TASARIM VE İMALAT KONGRESİ

BİLDİRİ KİTABI

Editörler

M. Cemal ÇAKIR
Barış ÇETİN
S. Engin KILIÇ
E. İlhan KONUKSEVEN
Bahram LOTFİ
Ramazan H. NAMLU
Ali ORAL
İ. Etem SAKLAKOĞLU
Ulvi ŞEKER
Damla TOPALLI
Hakkı Özgür ÜNVER
Volkan ESAT
Selcuk HIMMETOĞLU

umtik 2024

14-17 Ağustos 2024

ANKARA- TURKİYE

MATİMAREN
MAKİNA MÜHENDİSLİĞİ BÖLÜMÜ
ORTA DOĞU TEKNİK ÜNİVERSİTESİ
ANKARA-TÜRKİYE

Bu bildiri kıtabın yayın hakkı Orta Doğu Teknik Üniversitesi'nindir. Bu Kitapta yayımlanan bildirilerin aynen yayımlanması, yazarlardan ve editörlerden yazılı izin almak koşulu ile mümkündür.
Alıntı için kaynak göstermek yeterlidir.

Bu Bildiri Kitabı

UMTIK
Mechanical Engineering Department
Middle East Technical University
06800 Ankara- Turkey

Manufacturing Engineering Department
ATILIM University
06830 Ankara- Turkey

Adreslerinden sağlanabilir.

Kapak Baskı:

ODTÜ- Ankara

Baskı ve Cilt:

ODTÜ- Ankara

Matbaa Adı:

ODTÜ- Ankara

ISBN

TÜRKÇE BİLDİRİLER

PAPERS IN TURKISH

AĞIR TİCARİ ARAÇLARDA KARDAN MİLİ U-SACININ GÜÇLENDİRİLMESİ

Umut Can GÖLBAŞI, *u.golbasi@tirsankardan.com.tr* Tirsan Kardan, 45030, Manisa
Murat ÖZBAKIŞ, *m.ozbakis@tirsankardan.com.tr* Tirsan Kardan, 45030, Manisa
Onur ŞEN, *o.sen@tirsankardan.com.tr* Tirsan Kardan, 45030, Manisa

ÖZET

Kardan milinin önemli bir parçası olan askı, barındırdığı kauçuk parça ile oluşan titreşimleri sönümlerken bir diğer parçası U-sacı ile kardan milinin araç ile bağlantısını sağlamaktadır. Dolayısıyla U-sacının tasarımı kardan milin ömür ve performansı üzerinde önemli bir etkiye sahiptir. Bu durum göz önünde bulundurularak ortaya koyulan çalışmada, yol dışı ve ağır ticari araçlarda U-sacına yönelik geliştirmeler konu edinilmiştir. Bu kapsamda literatür araştırması yapılmış, U-sacında mukavemet ve rijitliği artırmaya yönelik tasarım çalışmaları gerçekleştirilmiştir. Sonlu elemanlar analiz sonuçlarına göre, maksimum gerilme ve deformasyon miktarında sırası ile %33,2 ve %9,1 iyileşme sağlandığı görülmüştür.

Anahtar Kelimeler: FEA, Kardan Mili, Askı, U-sacı

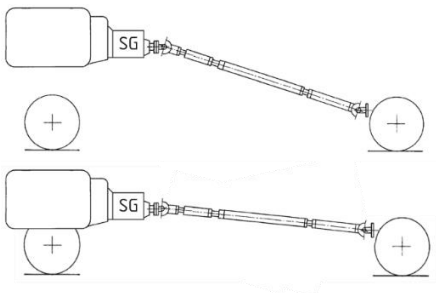
ABSTRACT

The center bearing, an important part of the propeller shaft, absorbs vibrations with its rubber part, while the U-support provides the connection between motor vehicle and driveshaft. Therefore, the design of the U-support has a significant impact on the life and performance of the driveshaft. By considering this situation, the study focused on developments for the U-support in off-road and heavy commercial vehicles. Design studies were conducted to increase the strength and rigidity on the U-support. According to the finite element analysis, it was observed that improvement of 33,2% and 9,1%, was achieved for the stress and deformation, respectively.

Keywords: FEA, Driveshaft, Center Bearing, U-support

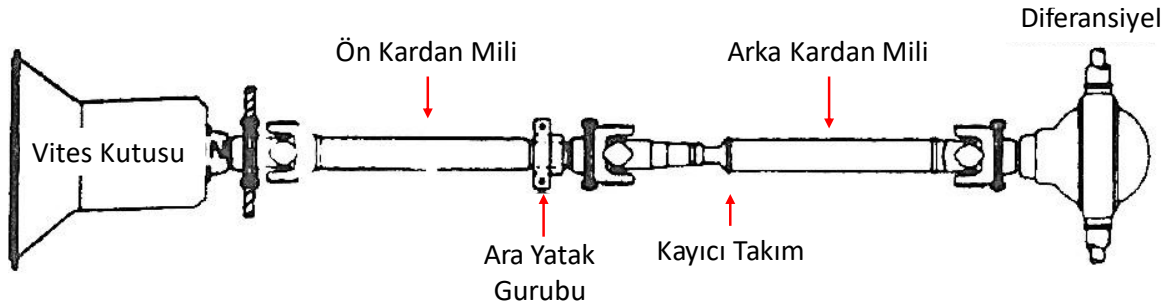
GİRİŞ

Kardan mili, araçlarda motor çıkışındaki gücü tekerleklere iletmek için kullanılan kritik bir güç aktarma organıdır. Dişli kutusu veya transfer kutusu çıkış milini diferansiyele bağlayarak iki ünite arasındaki güç ve devir aktarımını sağlar [SAE International, 1991]. Kardan mili, doğrusal bir şekilde hizalanmamış olan iki güç aktarma organı arasındaki açı farkını telafi ederek tork ve devir aktarımını mümkün kılar. Aracın yol koşullarında ilerlemesi sırasında, süspansiyon hareketiyle iki ayrı güç aktarma organı arasında açı ve mesafe farkı oluşur, bu durum Şekil 1'de gösterilmektedir. Bu farklar kardan mili üzerinde, açı değişimi için üniversal mafsallar, mesafe değişimi için kayıcı takım tarafından karşılanmaktadır.



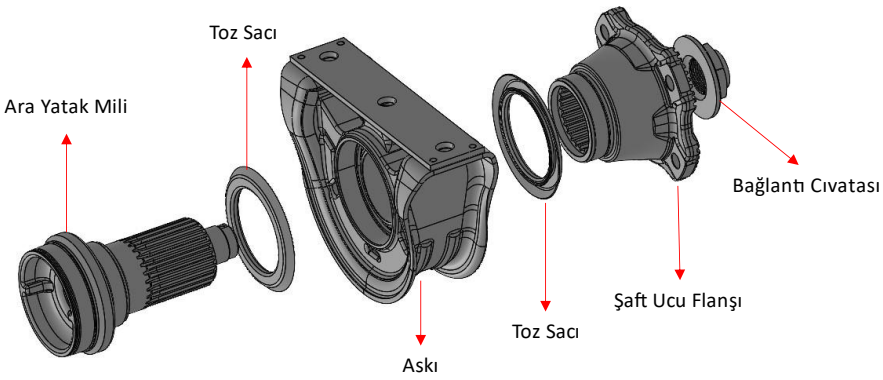
Şekil 1 Kardan Milinin Yol Koşullarında Ortaya Çıkan Farklı Diferansiyel Pozisyonlarına Göre Konumu [Thoss, ve diğerleri, 2006].

Kardan milleri araç yerleşimi ve teknik özelliklerine bağlı olarak, ön kardan mili ve kayıcı özelliğe sahip arka kardan mili olarak adlandırılır. Bir ön ve bir arka kardan milinden oluşan çift parçalı bir kardan mili Şekil 2 üzerinde örnek olarak verilmiştir.



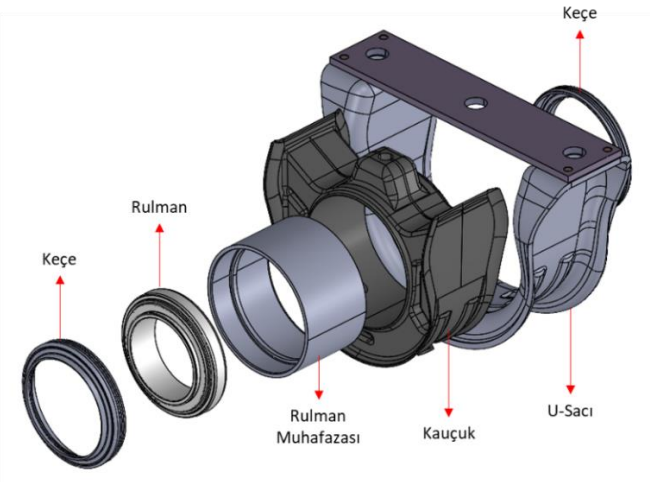
Şekil 2 Çift Parçalı Bir Kardan Milinin Araç Altı Konumu [SAE International, 1991].

Ön kardan millerinde, kardan mili ile araç şasi bağlantısı ara yatak grubu ile sağlanmaktadır. Ara yatak gurubu güç aktarımının sağlandığı, aynı zamanda içerdiği elastomer malzemeli eleman ile titreşimlerin bir miktar sönümlendiği ara mesnet noktası olarak tanımlanabilir. Ara yatak gurubu Şekil 3'te görüldüğü gibi bir askı, askıyı kardan mili üzerinde tutan ara yatak mili, şaft ucu flanşı ve bağlantı cıvatası, askı rulmanını dış etkenlerden koruyan toz saclarından oluşur.



Şekil 3 Ara Yatak Gurubu.

Askı ise Şekil 4'te ifade edildiği gibi kauçuk bir eleman, rulman ve rulmana yataklık yapan rulman muhafazası, sızdırmazlık amacı ile kullanılan keçe, tüm bu elemanları üzerinde toplayarak gövde görevi gören ve aynı zamanda kardan milinin araç şasisine bağlanmasını sağlayan U-sacından oluşur. Askı tasarımlarında kullanılan tekil parçalarda ve montaj yapılanmalarında farklılar görülebilir, üzerinde çalışma gerçekleştirilen U-sacı tarafımızca 2023/013218 numarası ile patentlenmiştir.



Şekil 4 Askıyı Oluşturan Elemanların Demonte Görüntüsü.

Askının araç şasisi ile bağlantısı, U-sacı üzerinde bulunan iki boşaltma kullanılarak, Şekil 5'te verildiği gibi cıvata ve somun ile yapılmaktadır.



Şekil 5 Askının Araç Şasisi ile Bağlantısı.

Yol dışı ve ağır ticari araç uygulamalarında askının üzerine gelen yükler diğer uygulamalar ile kıyaslandığında ağır çalışma koşullarından dolayı nispeten fazladır. Dolayısıyla kardan milinin ömür ve performansı üzerinde direkt ve daha belirleyici bir etkiye sahiptir.

U-sacı yol koşullarında ortaya çıkan titreşim ve eksenel kuvvetlerin etkisi altında kalmaktadır. Eksenel kuvvetlere ek olarak kardan mili montaj işleminde oluşan cıvata ön yüklemeleri ve kardan milinin ağırlığından kaynaklı ön yüklemeleri U-sacı üzerine etki etmektedir. Söz konusu kuvvetlerin etkisi altında çalışan U-sacında, aracın kapasitesinin üzerinde yüklenmesi gibi çok zorlu çalışma koşullarında deformasyonlar görülebilmektedir. Şekil 6'de verildiği gibi, olması gerekenden çok zorlu çalışma durumların yaşanabileceği göz önüne alınarak, ağır ticari araçlarda kullanılan U-sacının tasarımına yönelik geliştirmeler bu çalışmaya konu edinilmiştir.



Şekil 6 U-sacı Çalışma Koşulları

Yapılan literatür incelemeleri değerlendirildiğinde, Rayeen ve ark. bükerek şekillendirilmiş araç şasi braketinde kalınlık-mukavemet optimizasyonu konusunda bir çalışma gerçekleştirildiği görülmüştür. İki farklı tasarım ve üç farklı malzeme ile oluşturdukları deney guruplarını sonlu elemanlar yöntemi ile analiz etmişlerdir. Güçlendirilmiş tasarımda mevcut tasarıma göre kenar bükümüne ezme formu eklenmiştir. Güçlendirilmiş forma sahip olan braketin mevcut tasarıma göre, kuvvet altındaki deplasman ve gerilme değerlerinin daha iyi olduğunu belirterek, kenar büküm bölgesine ezme prosesinin eklenmesinin parçanın dayanımını ve rijitliğini arttırdığını aktarmışlardır [Rayeen, ve diğerleri, 2019].

Gillberg ve ark. ise otobüslerde kullanılan sac metal bileşenlerin imalat sırasında, bükme ve ezme tekniklerini incelemişlerdir. Çalışmada, yük taşıyan bileşenlerin daha hafif hale getirilmesi için ezme yönteminin avantajlarına odaklanılmıştır. Bu bağlamda dört farklı geometriye sahip parçaya ekstra bükümler ve ezme prosesleri ekelenerek parçaların güçlendirilmesi amaçlanmıştır. Ezme yöntemi ile güçlendirilen parçalar sonlu elemanlar yöntemi ile analiz edilerek karşılaştırılmıştır. Ezme yöntemi ile üretilen parçalarda hafiflik ve mukavemet avantajı sağlanırken kaynak gibi proseslerin ezme yöntemi ile kaldırılabileceği belirtilerek sac parçalarda ezme tekniklerinin kullanımı önerilmiştir [Gillberg, ve diğerleri, 2017].

Bir diğer çalışmada, Gunjawate ve ark. araçlarda yaprak yay tutucu braket için optimizasyon çalışması yürütmüştür. Braket üzerine üçgen, daire, vb. farklı formlarda yapılan boşaltmaların braket üzerindeki gerilme değerlerine etkisi araştırılmıştır. Bilgisayar destekli analiz sonucunda parça üzerine dairesel formda bir boşaltma yapılarak ve gerilim görülmeyen kıvrımlar çıkartılarak bir optimizasyon çalışması yürütülmüştür. Optimizasyon çalışması sonrasında gerilim değerlerinde azalmayla birlikte rijitlikte artış görülmüştür [Gunjawate, ve diğerleri, 2020].

Jeyaseelan ve ark. ise, bir damperli kamyonun hidrolik tankı için montaj braketinin dayanıklılığını ve güvenliğini sağlamak amacıyla sonlu elemanlar yöntemi ile analiz çalışması gerçekleştirmişlerdir. Maksimum gerilme, eşdeğer gerilme, kayma gerilmesi ve deformasyon miktarları yorumlanarak, montaj braketlerinin aşırı güvenli tasarlandığı (over-design) ve üzerinde optimizasyon yapılabileceği öne sürülmüştür [Jeyaseelan, ve diğerleri, 2022].

Farklı bir çalışmada ise Liao ve ark. mini-van bir araçta braket optimizasyon çalışması yapmışlardır. İlgili çalışmada bir U formundaki braketin optimizasyonu için bir denklem önermişlerdir. Sonlu elemanlar yöntemi ile yapmış oldukları analizler sonrası elde ettikleri verileri, oluşturmuş oldukları denklem içerisinde kullanarak sac parçanın kalınlığını optimize etmişleridir. Optimize ettikleri sac parçayı tekrar analiz ederek verileri karşılaştırmışlardır. Yapılan çalışmalar sonucunda yaklaşık %37 ağırlık avantajı elde edilmiştir [Liao, ve diğerleri, 2012].

Khalid ve ark. otomotiv endüstrisinde kullanılan bir sac metal parçanın ANSYS yazılımı ile optimizasyonunu gerçekleştirmiştir. Çalışmanın amacı, parçanın kütlesini minimize ederken belirli bir emniyet faktörünü korumaktır. Başlangıçta yapılan sonlu elemanlar analizi sonucunda elde edilen veriler kullanılarak optimizasyon süreci başlatılmıştır. Çalışma sac kalınlığı ve delik çapı gibi parametreleri değiştirerek optimum çözümü bulmayı hedeflemiştir. Optimizasyon süreci sonunda parçanın kütlesinde %23 oranında azalma sağlanmış ve optimize edilen tasarımın stres değerlerinin orijinal tasarıma yakın olduğu belirtilmiştir [KHALID, ve diğerleri, 2020].

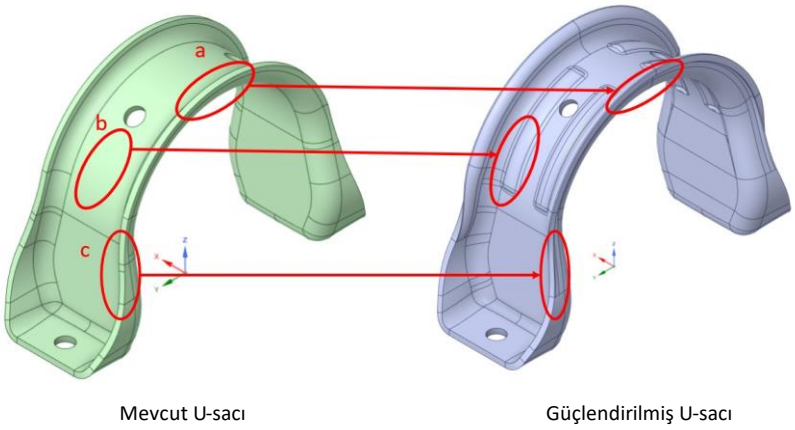
Netsanet yapmış olduğu bir çalışmada, Altair Inspire yazılımını kullanarak otomotiv sac metal parçasının topoloji optimizasyonuna odaklanmıştır. Tasarımın kavramsal aşamasında optimum geometriyi belirlemek amacıyla bilgisayar destekli analizler gerçekleştirilmiştir. Burada sac metal parçanın kütlesinin %65,9 oranında azaltılması ve mukavemetin artırılması hedeflenmiştir. Von-Mises gerilme analizi, yer değiştirme ve farklı yük durumlarıyla yapılan karşılaştırmalar sonucunda, optimize edilen tasarımın daha düşük maliyet ve ürün geliştirme süresi, malzeme tüketimi ve dolayısıyla ürün ağırlığında avantaj sağladığı görülmüştür [Ferede, 2020].

Literatür araştırmasında görüldüğü üzere, sac parçalar üzerinde yapılan optimizasyon çalışmalarında söz konusu parçaları güçlendirmek için çoğunlukla kalınlık arttırma ve bükülmüş kenarlarda ek ezme metotları sıkça kullanılmıştır. Ancak sac kalınlığının arttırılması tekil parçayı ağırlaştırırken malzeme ve işleme maliyetlerini de arttırmaktadır. Bu nedenle, mukavemet ve yorulma dayanımını artırmak için kalınlık arttırma yöntemi genellikle tercih edilmemektedir. Buna Gunjawate ve ark, Gillberg ve ark. çalışmalarında tekil parçalarda rijitliği ve mukavemeti arttırmak için uyguladıkları ezme prosesleri örnek olarak verilebilir.

Bu çalışmada, U-sacının rijitlik ve mukavemet bakımından iyileştirilmesi konu edinilmiştir. Bu kapsamda mevcut U-sacına ek büküm ve ezme formları eklenerek güçlendirilmesi amaçlanmıştır. Sonlu elemanlar analiz yöntemi kullanılarak elde edilen güçlendirilmiş U-sacının mevcut U-sacı ile karşılaştırılması yapılmış, diğer makalelerden farklı olarak vulkanize kauçuk içeren U-sacının geliştirilmesi ele alınmıştır. Yapılan analizlerde araç montajı sırasında kardan mili ağırlığı nedeniyle oluşan ön gerilmeler ve cıvata ön gerilmeleri de dikkate alınmıştır.

MATERYAL VE METOT

Sürekli olarak bileşke kuvvetlerin etkisi altında çalışan U-sacının güçlendirme çalışması, Şekil 7.a'da verilen U-sacının çeperlerinin uzatılarak dışarı kıvrılmasını, Şekil 7.b'de verilen üst bölgesine ezme formunun eklenmesini ve Şekil 7.c'de verilen cıvata bölgesinde çeper ovalliğinin arttırılmasını içermektedir. Burada, güçlendirilmiş yapının mukavemetinin ve rijitliğinin mevcut U-sacına göre daha iyi seviyeye getirilmesi amaçlanmıştır.

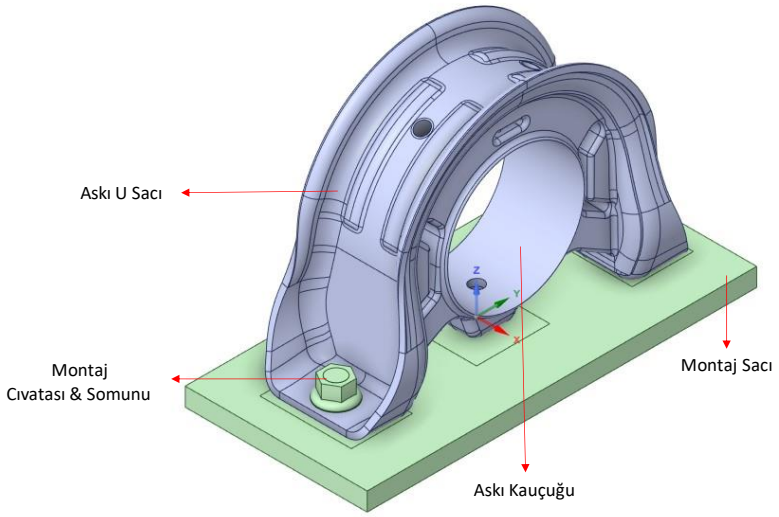


Şekil 7 U-Sacında Yapılan Geliştirmeler: a) Üst Bölgedeki Çeperleri Uzatılması, b) Üst Bölgeye Yeni Ezme Formunun Eklenmesi, c) Cıvata Bölgesinde Çeper Ovalliğinin Arttırılması.

U-sacında yapılan geliştirmelerin incelenmesi ve yorumlanması için bilgisayar destekli sonlu elemanlar yöntemi kullanılmıştır. Bilgisayar destekli analiz ANSYS 23.1 programı ile gerçekleştirilmiştir. Mevcut ve güçlendirilmiş U-sacları aynı sınır koşulları ve kontak tanımlamaları ile analiz edilmiştir. Yapılan analizler sonucunda, U-sacları üzerinde oluşan eşdeğer gerilmeler ve deformasyon miktarları değerlendirilmiştir.

Analiz için Üç Boyutlu Modelin Hazırlanması

Basitleştirmek amacıyla analiz içerisinde kullanılan model sadece U-sacı, askı kauçuğu, montaj plakası (montaj yapılan yüzey), montaj cıvatası ve somunu içermektedir. Her iki U-sacı için aynı montaj plakası, cıvata ve somun kullanılmıştır. Modeli basitleştirmek ve çözüm sürelerini azaltmak amacı ile cıvata ve somunun dişleri modellenmemiştir. Cıvata ve somunun boyutsal ölçüleri teknik resimlere uygun olarak cıvatanın diş üstü çapında modellenmiştir. Güçlendirilmiş U-sacı için hazırlanan bilgisayar destekli tasarım Şekil 8'de görülmektedir.

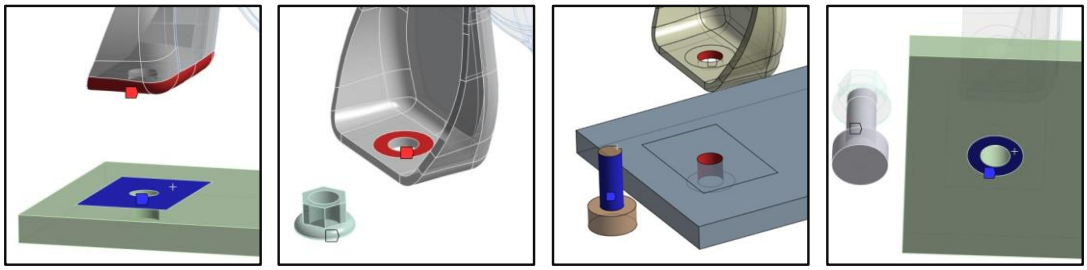


Şekil 8 Analiz için Hazırlanmış Güçlendirilmiş U-sacı Modeli.

Sonlu Elemanlar Modelinde Kontakların Tanımlanması

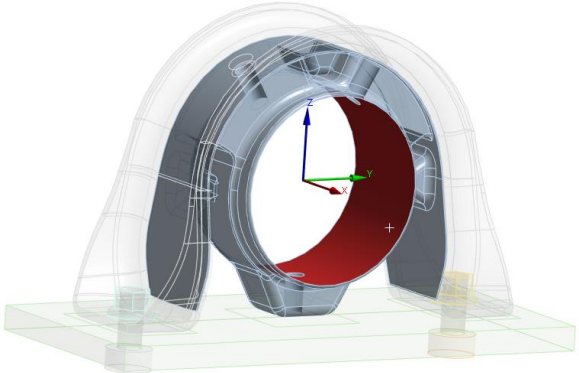
Sonlu elemanlar yönteminde, Şekil 8'de tanımlı olan her bir tekil parça modeli arasındaki kuvvet aktarımları, tanımlanan kontaklar ile sağlanmaktadır. Askı kauçuğu, U-sacına vulkanize olarak üretilmektedir. Bu nedenle U-sacı ve kauçuk arasına "bounded" kontağı ataması yapılmıştır. Benzer şekilde cıvata ile somun arasında dişlerin temas ettiği bölgeye "bounded" kontağı atanarak cıvata ve somun temas bölgesi tanımlanmıştır. Belirtilen bölgeler dışında cıvata, somun, U-sacı, montaj plakası arasında oluşan temas yüzeylerinin tamamına 0,2 sürtünme katsayısına sahip "frictional" kontak ataması yapılmıştır. İlgili kontak yüzeyleri Şekil 9'de verilmiştir.

Kontak tanımlaması için "contact" ve "target" olarak iki yüzey seçilmektedir. Sac parça üzerinden değer okunacağı için kontak tanımlamalarında "contact" yüzeyleri sac parçadan seçilmiştir. Kontak yüzeylerinde ortaya çıkan yüklerin doğru aktarılması için kontak yüzeyindeki eleman boyutu mümkün oldukça küçük tutulmalıdır. Küçük boyutlarda eleman kullanımı eleman sayısını arttıracağı için çözüm süresini uzatmaktadır. Bu nedenle, Şekil 9'de verildiği gibi "contact" ve "target" yüzeyleri için bir sınır belirlenmiş, ve bu sınır içerisindeki eleman boyutları küçük ve çok sayıda kurulmuştur. Bu sayede temas bölgelerine kullanılan elemanların boyutları lokal olarak küçültülerek analizin hesaplama süresi kısaltılmıştır.



Şekil 9 Kontak Tanımlamaları; a) U-Sacı İle Montaj Plakası b) Somun Alın Yüzeyi İle U-Sacı c) Cıvata Silindirik Yüzeyi İle U-Sacı Ve Montaj Plakası d) Cıvata Alın Yüzeyi İle Montaj Plakası.

Analizde model basitleştirme amacı ile rulman muhafazası modellenmemiştir. Dolayısıyla U-sacı kauçuğu dışarıdan sararken iç yüzeyde kauçuğun desteklenmesini sağlayan bir eleman (rulman muhafazası) bulunmamakta, bu ise kauçuk daireselliğini bozmaktadır. Bunu engellemek adına kauçuk malzemenin iç yüzeyine rijit joint atanabilir. Bu durumda ise, U-sacı ekseni ile kauçuk ekseni arasındaki paralellik bozulmaktadır. Bu nedenle ilgili joint atamasına Şekil 10'da belirtilen x, y ve z eksenlerinde dönme hareketine kısıtlama getirilmiştir.



Şekil 10 Rijit Joint Atamasının Yapıldığı Kauçuk İç Yüzeyi.

Sonlu Elemanlar Modelinde Kauçuk Malzeme Tanımlanması

Kauçuk malzemelerin modellenmesinde farklı yöntemler kullanılmaktadır. Bu yöntemlerden biri olan Mooney-Rivlin modeli, elastomerik malzemelerin gerilme-deformasyon ilişkisini matematiksel olarak ifade etmektedir. Huri ve ark. tarafından yapılan çalışmada Mooney-Rivlin ve Yeoh malzeme modelleri sonlu elemanlar yöntemi kullanılarak analiz edilmiş ve sonuçlar test verileri ile karşılaştırılmıştır. Mooney-Rivlin modelinin Yeoh modeline göre test verilerine daha yakın olduğu aktarılmıştır [Huri, ve diğerleri, 2018].

Ortaya koyduğumuz çalışmada 2 değişkenli (C_1 ve C_{10}) Mooney-rivlin malzeme modeli kullanılmıştır. Kauçuk modelinde, gerilme-deformasyon ilişkisinin tanımlanmasında kauçuk tedarikçisinden alınan değerler kullanılmış olup Tablo 1'de verilmiştir.

Tablo 1 Analizde Kullanılan Mooney-Rivlin Katsayıları.

Mooney-Rivlin Katsayıları	Mevcut Tasarım	Yeni Tasarım
C_1	0,333578	0,128365
C_{10}	0,460473	0,560555

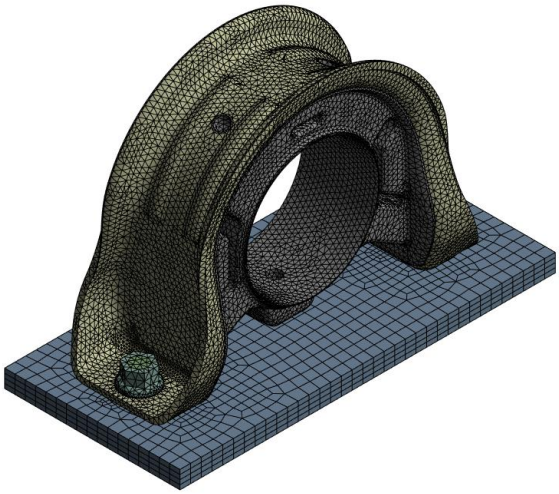
Sonlu Elemanlar Modelinde U-sacı Malzeme Tanımlanması

U-sacı EN 10149-2 S355MC malzemeden üretilmektedir. Yürütülen analizde askıya tanımlanan kuvvetler düşük olduğu için U-sacı lineer bölgede çalışmaktadır. Bu nedenle U-sacı, montaj plakası, cıvata ve somunlar için 200 GPa elastisite modülüne ve 0,3 poisson oranına sahip lineer malzeme tanımlanmıştır.

Sonlu Elemanlar Modelinde Ağ Yapısının Kurulması

Sonlu eleman yapısı oluşturulurken yüksek gerilme görülen bölgelerde daha küçük elemanlar kullanılmıştır. Kauçuk ve U-sacı ağ yapısında modellerin karmaşıklığından dolayı ikinci derece tetrahedral elemanlar kullanılmıştır. U-sacı ve kauçuk arasındaki kuvvet aktarımının doğru şekilde gerçekleştirilmesi için kauçuk ve U-sacı temas bölgelerinde oluşturulan tetrahedral elemanların düğüm noktaları karşılıklı konumlandırılmıştır.

Montaj plakası ağ yapısında hexahedral elemanlar kullanılarak "sweep" metodu uygulanmıştır. Kontak tanımlamalarının yapıldığı yüzeylerde oluşan mesh yapısını düzenlemesi amacı ile "Face Meshing" metodu uygulanmıştır. U-sacı, askı kauçuğu, montaj plakası, cıvata ve somun geometrilerinin birbiri ile temas ettiği bölgelerde oluşturulan sonlu elemanların boyutları kuvvet aktarımının daha doğru şekilde sağlanması için küçültülmüştür. Bu işlemlerden sonra güçlendirilmiş U-sacı üzerinde elde edilen ağ yapısı Şekil 11'da görülmekte olup aynı işlemler mevcut U-sacı için de gerçekleştirilmiştir.



Şekil 11 Güçlendirilmiş U-sacı Sonlu Elemanlar Analiz Modeli Ağ Yapısı.

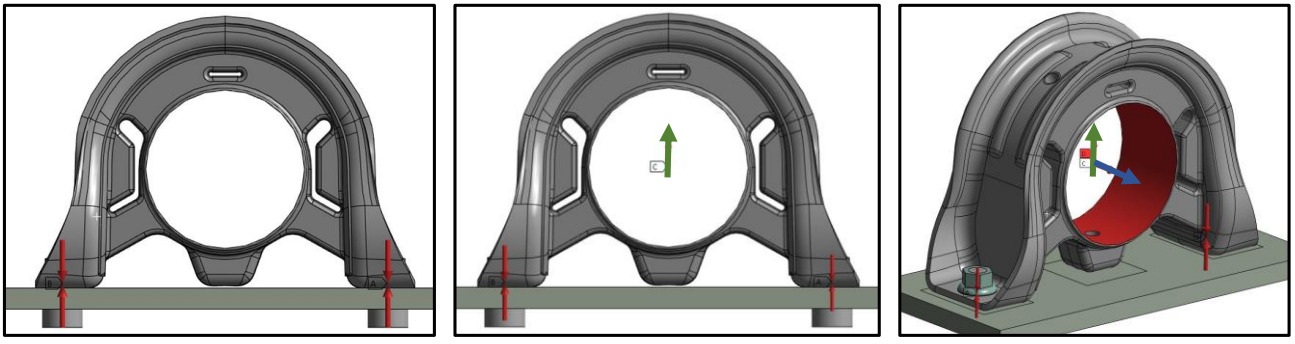
Her iki modelde oluşturulan ağ yapısına ait çarpıklık (skewness) ve ortalama eleman kalitesi değerleri Tablo 2'de verilmiştir.

Tablo 2 Her İki Analiz Modeli İçin Sonlu Eleman Kaliteleri.

U-Sacı	Sonlu Eleman Kalite Ölçütleri	Değer
Mevcut	Ortalama Eleman Kalitesi	0,78
	Çarpıklık (Skewness)	0,30
Güçlendirilmiş	Ortalama Eleman Kalitesi	0,78
	Çarpıklık (Skewness)	0,29

Sonlu Elemanlar Modelinde Sınır Koşullarının Tanımlanması

Montaj sırasında U-sacı üzerinde oluşacak ön gerilmelerin analize dahil edilebilmesi için analiz birden fazla adımda gerçekleştirilmiştir. Sırasıyla birinci adımda cıvata ön yüklemesi, ikinci adımda kardan mili ağırlığının radyal ön yüklemesi ve üçüncü adımda eksenel yükleme gerçekleştirilmiştir. Analiz adımlarında uygulanan kuvvetler ve ilgili yüzeyler Şekil 12'de verilmiştir. Montaj sacı dört yan yüzeyden "fixed support" ile sabitlenmiştir.



1. Adım 2. Adım 3. Adım

Şekil 12 Analizde Uygulanan Kuvvetler.

Uygulanan cıvata ön yükleme kuvvetinin belirlenebilmesi Denklem 1 [Güneş, 2012] kullanılarak hesaplama yapılmıştır. Hesaplanan cıvata ön gerilme değeri analizde cıvata üzerine ilk adımda yüklenmiştir.

$$F_M = \frac{M_A}{0{,}16 \times p \times 0{,}58 \times d_2 \times \mu_v \times \mu_K \times \left(\frac{d_w + d_h}{4}\right)} \quad (1)$$

U-sacı, araca M14 cıvata üzerine 175 N.m sıkma torku uygulanarak montajlanmaktadır. Hesaplamada kullanılan değerler Tablo 3'de verilmiştir. İlgili değerler Denklem 1 içerisinde kullanılarak hesaplama yapılmıştır.

Tablo 3 Cıvata Ön Gerilme Kuvvetinin Bulunmasında Kullanılan Değerler.

Sembol	Birim	Açıklama	Değer
p	mm	Vida Adımı	2
M_A	N.m	Cıvata Sıkma Torku	175.000
d_2	mm	Profil Çapı (Bölüm Dairesi Çapı)	12,95
μ_v	-	Cıvata Dişi Sürtünme Katsayısı	0,15
μ_K	-	Cıvata Başı Sürtünme Katsayısı	0,15
d_w	mm	Yataklama Yüzeyi Çapı	28,60
d_h	mm	Delik Çapı	15,10
r_k	mm	Cıvata Sürtünme Kuvveti Eksen Mesafesi	6,80

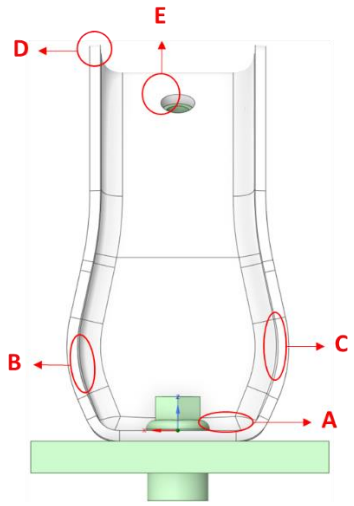
Yapılan hesaplama sonucunda 71.390 N cıvata ön gerilme kuvveti hesaplanmıştır. Hesaplanan bu değer analizin birinci adımında uygulanmıştır. Analizin ikinci adımında kauçuğa 1.000 N büyüklüğünde radyal yükleme yapılırken üçüncü adımında 1.000 N eksenel yükleme yapılmıştır. Bu yükler araç üreticisi tarafından belirlenmektedir. Yükleme değerleri ve analiz adımları Tablo 4'de verilmiştir.

Tablo 4 Yükleme Değerleri ve Uygulandığı Analiz Adımı.

Kuvvet	Birinci Adım	İkinci Adım	Üçüncü Adım
Cıvata Ön Yükleme	71.390 N	71.390 N	71.390 N
Radyal yükleme	0 N	1.000 N	1.000 N
Eksenel Yükleme	0 N	0 N	1.000 N

SONUÇ

U-sacı analizi sonuçlarında yüksek gerilme görülen bölgeler göz önüne alınarak Şekil 13 üzerinde tanımlanmış olan 5 bölge incelenmiştir. Söz konusu 5 bölgede görülen en yüksek gerilme değerleri her iki U-sacı için karşılaştırılmıştır. Belirlenen bölgelere ek olarak U-sacı üzerinde görülen maksimum deformasyon miktarları da karşılaştırılmıştır.



Şekil 13 Gerilmelerin Karşılaştırılması İçin Seçilen Bölgeler.

Mevcut ve güçlendirilmiş U-sacı analiz sonuçlarının yüzdesel farkları Tablo 5'de detaylı olarak verilmiştir. Tablo üzerindeki negatif değerler güçlendirilmiş U-sacı sonuçlarının mevcut U-sacına göre düşük olduğunu ifade etmektedir.

Tablo 5 Mevcut ve Güçlendirilmiş U-Sacı Analiz Sonuçlarının Yüzdesel Farkları

U-sacı	A Bölgesi	B Bölgesi	C Bölgesi	D Bölgesi	E Bölgesi	Maksimum Def.
% Fark	-3,69	-13,57	-15,63	-33,19	-11,28	-9,12

Ortaya koyulan çalışma sonucunda;

1. Güçlendirilmiş U-sacında görülen gerilme değerlerinin mevcut U-sacına göre en az %3,69; en fazla %33,2 daha düşük olduğu görülmüştür.
2. Aynı zamanda güçlendirilmiş U-sacının, mevcut U-sacına göre %9,1 daha az deforme olduğu tespit edilmiştir.
3. Tasarım esnasında güçlendirme amaçlı uygulanan aşağıdaki çalışmaların U-sacı üzerinde olumlu sonuç verdiği görülmüştür.
   - Çeperlerin (Şekil 7.a bölgesi) uzatılarak dışarı kıvrılması
   - Üst bölgede (Şekil 7.b bölgesi) ezme formunun eklenmesi
   - Cıvata bölgesinde (Şekil 7.c bölgesi) çeper ovalliğinin arttırılması

KAYNAKÇA

1. **SAE International (1991),** "Universal Joints and Driveshafts Design Manual AE-07", The Society of Outomative Engineers, Warrendale.

2. **Seherr-Thoss, H. C., Schmelz, F. and Aucktor, E. (2006),** "Universal Joints and Driveshafts: Analysis, Design, Applications", 2nd ed., Springer-Verlag, Berlin Heidelberg.

3. **Rayeen, M. F. and Patel, A. S. (2019),** "Design and Study of Automotive Chassis Bracket", International Research Journal of Engineering & Applied Sciences, Vol. 7, No. 4.

4. **Gillberg, L. and Sandberg, C. (2017),** "Developing Design Guidelines for Load Carrying Sheet Metal Components with Regards to Manufacturing Method", Master of Science Thesis, Department of Production Engineering, Royal Institute of Technology, Stockholm.

5. **Khalid, U., Mustafa, O., Naeem, M. A., Alkhateeb, M. and Awad, B. (2020),** "Direct Optimization of an Automotive Sheet Metal Part Using ANSYS", International Journal of Engineering and Management Sciences (IJEMS), Vol. 5, No. 3, Debrecen.OK

6. **Liao, S. and Chuansheng, C. (2012),** "Finite Element Analysis and Optimization Research of Mounting Bracket of a Mini Van", Applied Mechanics and Materials, Vols. 121-126, pp. 4811-4815.

7. **Jeyaseelan, A. S. and Sivakumar, M. (2022),** "Modeling and Finite Element Analysis of Hydraulic Tank Mounting Bracket Structure for A Dump Truck", International Journal of Advances in Engineering and Management (IJAEM), Vol. 1, No. 1, pp. 802-808.

8. **Gunjawate, S. R. and Solapur, S. B. (2020),** "Structural Analysis and Topology Optimization of Leaf Spring Bracket", International Journal of Engineering Research & Technology (IJERT), Vol. 9, No. 7, Pune.

9. **Netsanet, F. (2020),** "Topology Optimization of Automotive Sheet Metal Part using Altair Inspire", International Journal of Engineering and Management Sciences (IJEMS), Vol. 5, No. 3, Debrecen.

10. **Tayfun, G. (2012),** "Cıvatalı Bağlantılarda Emniyetli Tork Değerinin Teorik ve Deneysel Olarak Belirlenmesi", Yüksek Lisans Tezi, Aksaray Üniversitesi Makine Mühendisliği Anabilim Dalı, Aksaray.

11. **Huri, D. and Mankovits, T. (2018),** "Comparison of the Material Models in Rubber Finite Element Analysis", IOP Conference Series: Materials Science and Engineering, Debrecen.

ABKANT PRESLERDE DİNAMİK BOMBELEME SİSTEMİNİN TASARIM KRİTERLERİ VE AVANTAJLARI

Abdullah ÖZKAN, *abdullah.ozkan@karatay.edu.tr* KTO Karatay Üniversitesi, 42020, Konya

Mustafa GÜLTEKİN, *arge@mvdinan.com* MVD Makina San. A.Ş., 42050, Konya

ÖZET

Bu bildiri, metal şekillendirme sektöründe kullanılan abkant preslerde kullanılan hidrolik dinamik bombeleme sistemlerinin tasarımı ve endüstriyel avantajlarını incelemektedir. Geleneksel mekanik sistemlerden farklı olarak, hidrolik dinamik bombeleme daha yüksek hassasiyet, esneklik ve verimlilik sağlar. Geleneksel sistemlerde kamalı tertibat sistemi yüksek tonaj altında anlık bombeleme miktarı değiştirilemezken, hidrolik bombeleme sistemi tasarımında üç tabla kullanarak bu sorunu çözer ve presleme anında bombeleme miktarı ayarlanabilir. Yapısal sonlu elemanlar analizleri, sistemin farklı malzeme uzunluklarında gerekli performansı gösterdiğini doğrulamaktadır. Sonuç olarak, bu teknoloji üretim süreçlerini iyileştirir ve rekabet avantajı sunar.

Anahtar Kelimeler: Hidrolik Bombeleme, Abkant Pres, Metal Şekillendirme

ABSTRACT

This paper examines the design and industrial advantages of hydraulic dynamic crowning systems used in press brakes within the metal forming industry. Unlike traditional mechanical systems, hydraulic dynamic crowning offers higher precision, flexibility, and efficiency. In traditional systems, wedge mechanisms do not allow for instantaneous adjustment of the crowning amount under high tonnage, whereas the hydraulic crowning system resolves this issue by using a three-table design, enabling crowning adjustment during pressing. Structural finite element analyses confirm that the system achieves the required performance for different material lengths. Consequently, this technology improves production processes and offers a competitive advantage.

Keywords: Hydraulic Crowning, Press Brake, Metal forming

1. GİRİŞ

Pres makineleri hemen hemen her imalat sektöründe uzun yıllardır kullanılan temel makinelerdir. Mekanik biliminin uygulama alanlarından olan metal şekillendirme makineleri ve presler, endüstrinin birçok kolunda yüksek kaliteli ve seri üretim yapılmasına olanak sağlamaktadır. Yeni malzemeler, ürünler ve yeni imalat süreçleri de presler için yeni uygulama alanlarının ortaya çıkmasına yol açmaktadır[Özkan, 2020].

Abkant presler, metal levha işleme endüstrisinde yaygın olarak kullanılan önemli araçlardır. Bu presler, metal levhaları bükme işlemi için kullanılır ve genellikle karmaşık geometriler oluşturmak için kullanılan temel araçlardan biridir. Abkant preslerin etkinliği ve hassasiyeti, üzerinde çalışılan malzemenin mekanik özellikleri ve işleme sürecinde kullanılan teknikler ile doğrudan ilişkilidir. Özellikle, bombeleme sistemleri abkant preslerin işlevselliğini ve üretim kalitesini önemli ölçüde etkileyen unsurlardan biridir.

Abkant Preslerin en önemli fonksiyonel özelliklerinden biri olan bombeleme sisteminde genelde bükülen malzemenin ortasında meydana gelen açı farklığının önüne geçilmesi için gövde ortasına ek bir basınç uygulamak gerekir[Sarıer, 2004].

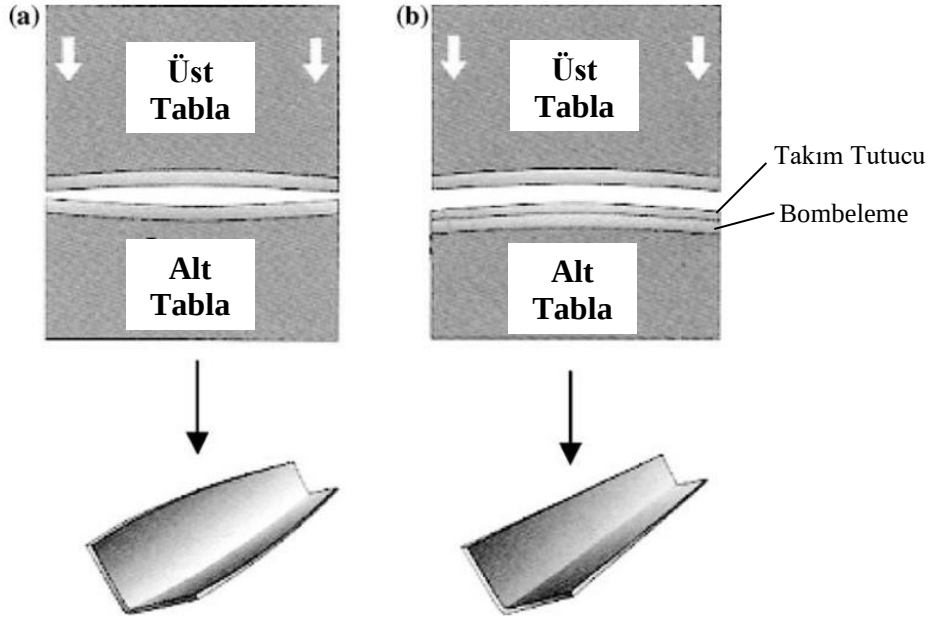
Bilinen mekanik bombeleme sistemlerinde, kamalı bir tertibat manuel veya bir eyleyici yardımıyla tahrik edilerek bombeleme sağlanırken, kamaların şeklinden dolayı bir bombe oluşabilmektedir. Hidrolik bombeleme sisteminde bilinen tek alt tabla yerine üç tane tabla kullanılacak ve orta tabla kısa stroklu özel hidrolik silindirler tarafından bombelenmektedir. Burada, orta tablayı yukarı yönde zorlayan silindirler, dıştaki tablaları etki-tepki sebebiyle aşağı yönde esnetmektedir.

Bu çalışmada, abkant preslerde kullanılan hidrolik dinamik bombeleme sistemlerinin tasarımı, geliştirilmesi ve endüstriyel avantajlarını ele almaktadır. Geleneksel sistemlere kıyasla, hidrolik dinamik bombeleme teknolojisi daha yüksek hassasiyet, esneklik ve verimlilik sağlamaktadır. Geleneksel yöntemde yaygın olarak kullanılan mekanik bombeleme sistemlerinde kamalı bir tertibat manuel veya bir eyleyici yardımıyla tahrik edilerek bombeleme sağlanır. Burada kamaların formundan dolayı bir bombe oluşabilmektedir. Bu yapı yüksek tonaj altında çalışmaya imkan vermemektedir, bununla beraber baskı altında anlık bombeleme miktarı değiştirilememektedir. Hidrodinamik sistemde ise bilindik tek alt tabla yerine üç tane tabla kullanılır ve orta tabla kısa stroklu özel hidrolik silindirler tarafından bombeleme işlemi yapılır. Bu sistemde orta tablayı yukarı yönde zorlayan silindirler, dıştaki tablaları da etki-tepki prensibi gereği aşağı yönde esnetmektedir. Tasarım yüksek tonajlı preslere uyarlanabilmektedir ve gerekli bombeleme miktarı sağlanabilmektedir. Başka bir avantaj olarak presleme anında bombeleme miktarı kontrolcüden alınan veriye göre değiştirilebilmektedir. Hidrolik dinamik bombeleme sisteminin farklı sınır şartları altında yapılan yapısal sonlu elemanlar analizleri,

sistemin farklı uzunluklarda malzeme bükümü esnasında istenilen performansı gösterdiğini ortaya koymaktadır. Sonuç olarak, hidrolik dinamik bombeleme sisteminin abkant preslerde kullanımı, üretim süreçlerinde önemli iyileştirmeler sağlamakta ve rekabet avantajı sunmaktadır. Bu bildiri, yenilikçi metal şekillendirme teknolojinin potansiyelini, avantajlarını özetlemektedir.

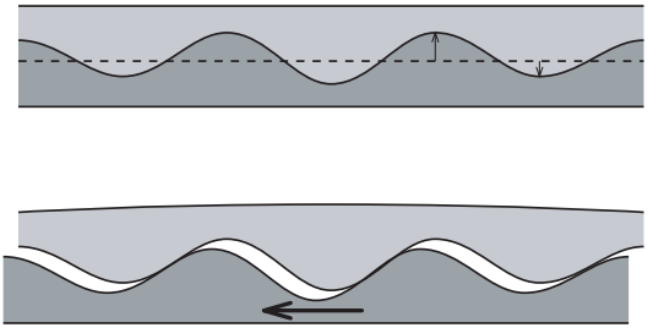
2. ABKANT PRES BOMBELEME SİSTEMİ

Abkant preslerde büküm kuvveti genellikle iki hidrolik silindir aracılığıyla sağlandığından dolayı büküm çizgisi boyunca eşit yayılı kuvvet elde edilememektedir. Şekil 1'de bu durumun etkisi gösterilmektedir.



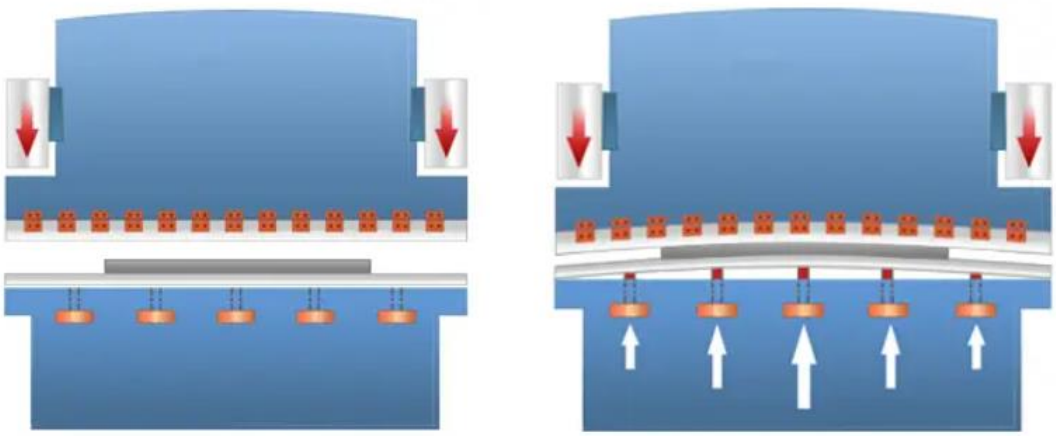
Şekil 1. Koç ve tabla sapmasının iş parçasının açısal hassasiyeti üzerindeki etkisi. (a) 'Tekne göbeği' etkisi. (b) Tekdüze bükme açısı. [Coelho,2005]

Yaygın olarak kullanılan mekanik bombeleme sistemlerinde, kamalı bir tertibat manuel veya bir eyleyici yardımıyla tahrik edilerek bombeleme sağlanır ve şekil 2'de bir görünümü verilmiştir. Burada kamaların formundan dolayı belirli bir sabit bombe oluşabilmektedir.



Şekil 2. Mekanik bombeleme sistemi kızağı [Simons, 2006]

Hidrodinamik sistemde ise bilindik tek alt tabla yerine üç tane tabla kullanılır ve orta tabla kısa stroklu özel hidrolik silindirler tarafından bombelenir. Bu sistemde orta tablayı yukarı yönde zorlayan silindirler, dıştaki tablaları da etki-tepki prensibi gereği aşağı yönde esnetmektedir, işlemin bir örnek görünümü şekil 3'te verilmiştir.



Şekil 3. Mekanik bombeleme sistemi kızağı [Simons, 2006]

3. ABKANT PRES HİDROLİK BOMBELEME SİSTEMİ TASARIMI

Büküm esnasında üst ve alt tablalar arasında paralellik elde etmek için eğriliklerin eşit olması gerekmektedir. Hidrolik bombeleme sisteminde büküm işleminde paralelliği sağlamak ve büküm işlemini iyileştirmek için alt tablada deformasyon sönümleme silindirleri kullanılır. Burada yan duvarlarda ölçülen kuvvetlerle, alt tablayı büyük ölçüde düz tutmak için uygulanabilir basınç arasında iletişim sağlayan bir kontrolcü kullanılır. Büküm operasyonu boyunca, kontrolcü sensörlerden alınan deplasman ve gerinim değerlerini, yan duvarlardan ölçülen kuvvetlere göre sönümleme silindirlerine uygular. Üst tabla ve yan duvarların deformasyonu, iş parçasının kalınlığı ve uzunluğu ve yaylanma etkisi hesaba katılarak bir alt ölü nokta yeniden hesaplanır.

Alt ölü nokta hesaplamasında parçanın uzun ya da kısa olması durumu dikkate alınmalıdır. Uzun parça durumu için 3200mm bir abkant presin tam kapasite büküm yapılması, kısa parça durumu için ise yarısı veya daha küçük parçaların büküm yapılması durumu olarak belirlenmiştir. İş parçasının uzunluğu, yan duvar arası mesafeye yaklaşık eşitse parça uzun kabul edilir. Duvarlar arası mesafenin üçte birini geçmeyen uzunluktaki parça ise kısa kabul edilir. Aşağıda parça uzunluğuna göre alt ölü noktanın bulunabileceği denklem verilmiştir [Hibbeler, R. C. , 1989]:

Kısa parçalar için (Büküm uzunluğunun yarısından daha kısa) bombeleme eğrisi:

$$\Delta f_{max} = (F.{l_a}^2.{l_b}^2)/(3.E.I.L) \quad (1)$$

Burada;

F : Parça üzerindeki yük, [N]

L : Yan duvarlar arası mesafe, [mm]

l_a, l_b: Parça merkezinden duvarlara olan uzaklık,

E : Elastisite modülü, [N/mm^2]

I : Alt tablanın atalet momenti, [mm^4]

Uzun parçalar için (Büküm uzunluğunun yarısından daha uzun) bombeleme eğrisi:

$$\Delta f_{max} = (5.Q.I^4)/(384000.E.I) \quad (2)$$

Burada;

Q : İş parçasının birim uzunluğu başına düşen yükü belirtir. [N/m]

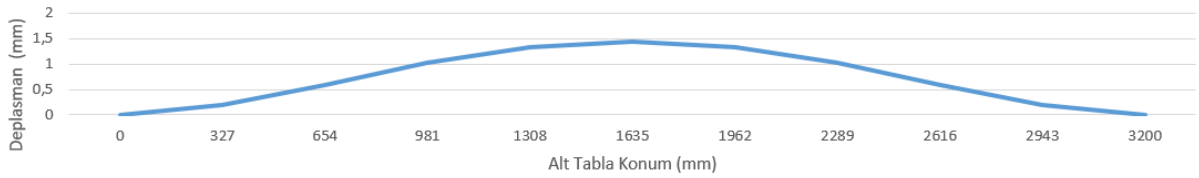
4. ANALİZ SONUÇLARI

Denklem (1) ve Denklem (2)'ye göre hesaplanan 3200mm büküm uzunluğuna sahip bir pres için işlemler yapılmış, bombeleme deplasmanları ve bu deplasmanların oluşması gereken alt konumları belirlenmiştir. Tablo 1'de alt tabla uzunluğu 10 noktaya ayrılarak bombeleme deplasmanları belirlenmiştir.

Tablo 1. Kısa ve Uzun parçaların bükümü esnasında bombeleme deplasmanları

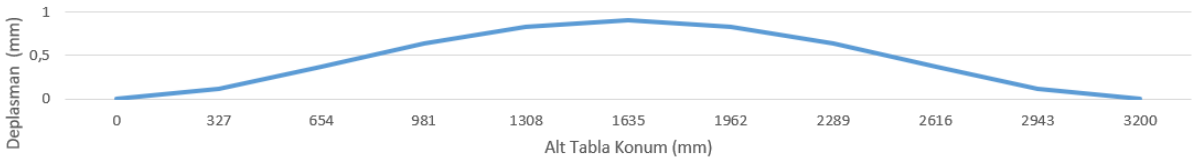
		0	1	2	3	4	5	6	7	8	9	10
Alt Tabla Konumu	X (mm)	0	327	654	981	1308	1635	1962	2289	2616	2943	3200
Büküm uzunluğunun yarısından daha kısa parçalar	Δf (mm)	0	0,187	0,591	1,018	1,329	1,442	1,329	1,018	0,591	0,187	0
Büküm uzunluğunun yarısından daha uzun parçalar	Δf (mm)	0	0,116	0,369	0,636	0,830	0,901	0,830	0,636	0,369	0,116	0

Büküm uzunluğunun yarısından daha kısa parçaların bükümü esnasında oluşan bombeleme eğrisi şekil 4'te verilmiştir.



Şekil 4. Kısa parçalar için (Büküm uzunluğunun yarısından daha kısa) bombeleme eğrisi

Büküm uzunluğunun yarısından daha uzun parçaların bükümü esanasında oluşan bombeleme eğrisi şekil 5'te verilmiştir.



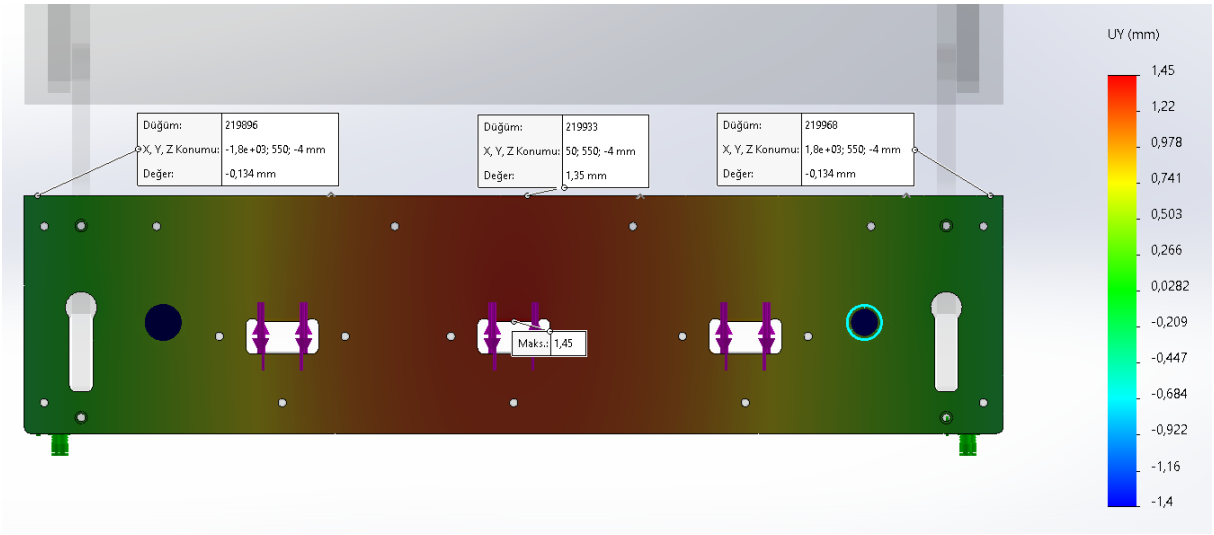
Şekil 5. Uzun parçalar için (Büküm uzunluğunun yarısından daha uzun) bombeleme eğrisi

Belirlenen bombeleme eğrilerinin elde edilmesi için 3200mm uzunluğundaki alt tablaya üç silindir konumlandırılması ön görülmüştür. Bu silindirlerin konumları ve tonajlarını belirlemek , tasarım kriterlerini oluşturmak için iki parametrenin belirlenmesi gerekmektedir. Bunlardan biri sağ-sol silindirlerin orta eksenden yatay uzaklığı iken diğeri ise üç silindirin tonajlarıdır. Silindirlerin konumları ve tonajlarını belirlemek üzere iteratif tasarım çalışması yapılmıştır. Tasarım etüdünde 3200mm alt tablanın orta ekseninde belirlenecek tonajında bir silindir, orta ekseninden belirlenecek kadar uzaklıkta ise belirlenecek tonajında yan silindirler olacak şekilde iteratif tasarım tablosu hazırlanmıştır. Tablo 2'de verilen iteratif tasarım kriterleri aralığında yapılan analizlerin karşılaştırılması sonucunda belirlenen eğriyi elde edebilmek için optimum konum ve tonajlar belirlenmiştir.

Tablo 2. Kısa ve Uzun parçaların bombeleme eğrisi eldesi için silindir tasarım parametreleri

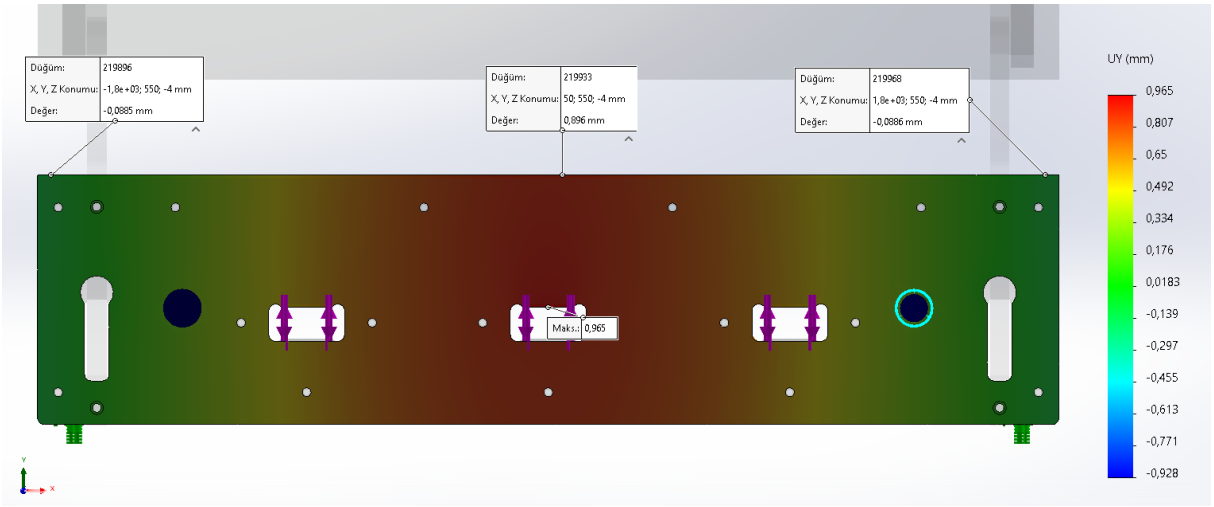
		Sol Silindir	Orta Silindir	Sağ Silindir
Büküm uzunluğunun yarısından daha kısa parçalar	Orta eksenden yatay uzaklık İteratif Aralık	500-1000mm	0	500-1000mm
	Orta eksenden yatay uzaklık	**782.5mm**	**0**	**782.5mm**
	Tonaj – İteratif Aralık	5-100 Ton	50-100 Ton	5-100 Ton
	Tonaj	**10 Ton**	**90 Ton**	**10 Ton**
	Orta eksenden yatay uzaklık İteratif Aralık	500-1000mm	0	500-1000mm
Büküm uzunluğunun yarısından daha uzun parçalar	**Orta eksenden yatay uzaklık**	**782.5mm**	**0**	**782.5mm**
	Tonaj – İteratif Aralık	5-150 Ton	50-150 Ton	5-150 Ton
	Tonaj	**17.5 Ton**	**130 Ton**	**17.5 Ton**

Kısa parçaların bükümü için belirlenen bombeleme eğrisinin tasarım kriterlerine göre sonlu elemanlar programıyla analiz edilerek sağlanması şekil 6'da gösterilmektedir.



Şekil 6. Kısa parçalar için (Büküm uzunluğunun yarısından daha kısa) bombeleme eğrisinin elde edilmesini sağlayan hidrolik bombeleme silindirlerinin konumlandırılması ve tonajı

Uzun parçaların bükümü için belirlenen bombeleme eğrisinin tasarım kriterlerine göre sonlu elemanlar programıyla analiz edilerek sağlanması şekil 7'de gösterilmektedir.



Şekil 7. Uzun parçalar için (Büküm uzunluğunun yarısından daha uzun) bombeleme eğrisinin elde edilmesini sağlayan hidrolik bombeleme silindirlerinin konumlandırılması ve tonajı

Belirlenen bombeleme eğrilerinin hidrolik silindirlerin tasarımda konumlandırılmasından sonra sonlu elemanlar yazılımıyla deplasmanlar elde edilmiştir. Farklı durumlar için gerekli eğrilerin silindir tonajlarının ve konumlarının değiştirilmesiyle hidrolik bombeleme sistemi kullanılarak tasarlanmasına olanak vermektedir. Alt tablaya konumlandırılmış hidrolik silindirlerin kullanılmasıyla istenilen bombeleme eğrisi elde edilebilmektedir.

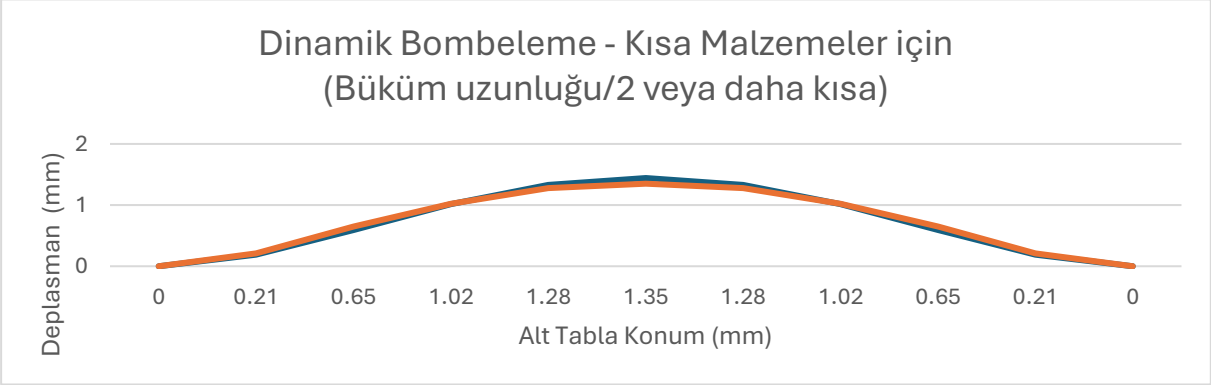
5. SONUÇLAR

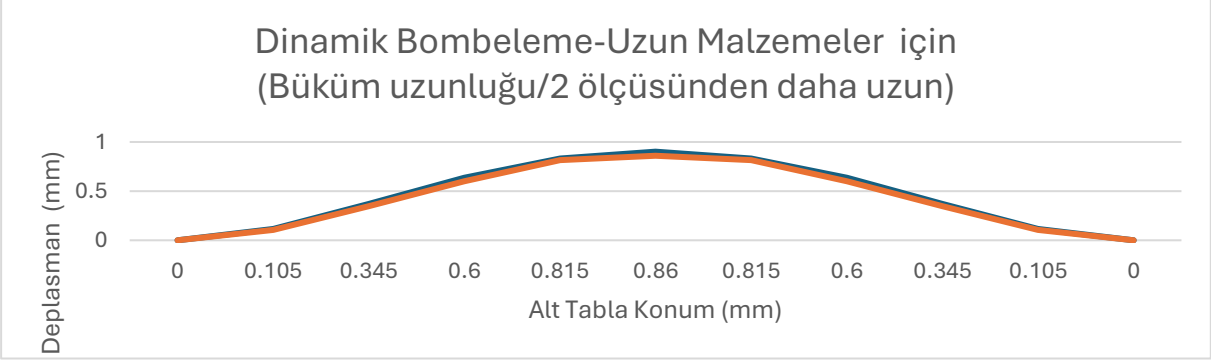
Bu çalışmada, abkant preslerde kullanılan hidrolik bombeleme sistemlerinin performansları, belirlenen bombeleme eğrisinin yapısal olarak elde edilmesi sonlu elemanlar analizi (FEA) yöntemiyle iteratif parametrik tasarım kriterleri belirlemek amacıyla incelenmiştir. Tablo 3'te verilen karşılaştırmalı analiz sonuçları, hidrolik bombeleme sistemlerinin, belirlenen bombeleme eğrisini elde edebildiği sonuçlarını ortaya koymaktadır. Hidrolik bombeleme sistemleri, kamalı mekanik sistemlere kıyasla belirgin avantajlar ortaya sunmaktadır. Hidrolik sistemler, yapısal dayanımı sebebiyle bilinen kamalı mekanik bombeleme sistemlerine göre daha ağır tonajlı preslerde kullanılabilmektedir. Ayrıca, hidrolik bombeleme, yük altındayken bombeleme miktarının ayarlanabilmesi ve hassasiyeti sayesinde farklı uzunluklarda, kalınlıklarda ve malzemelerde daha geniş bir uygulama yelpazesi sunmaktadır.

Tablo 3. Δf:Analitik beklenen eğri, Δf':Nümerik tasarımla hesaplanan eğri

Malzeme uzunluğunun büküm uzunluğunun yarısından daha kısa işlemler için					Malzeme uzunluğunun büküm uzunluğunun yarısından daha uzun işlemler için				
	x	Δf	Δf'	%Fark		x	Δf	Δf'	%Fark
0	0	0	0	0	0	0	0	0	0
1	327	0,187	0,21	-12,30	1	327	0,1165	0,105	9,87
2	654	0,591	0,65	-9,98	2	654	0,369	0,345	6,50
3	981	1,0181	1,02	-0,19	3	981	0,636	0,6	5,66
4	1308	1,3298	1,28	3,74	4	1308	0,8305	0,815	1,87
5	1635	1,4429	1,35	6,44	5	1635	0,9015	0,86	4,60
6	1962	1,3298	1,28	3,74	6	1962	0,8305	0,815	1,87
7	2289	1,0181	1,02	-0,19	7	2289	0,636	0,6	5,66
8	2616	0,591	0,65	-9,98	8	2616	0,369	0,345	6,50
9	2943	0,187	0,21	-12,30	9	2943	0,1165	0,105	9,87
10	3200	0	0	0	10	3200	0	0	0

Δf:Analitik beklenen eğrinin ve Δf':Nümerik tasarımla hesaplanan eğrinin karşılaştırması şekil 8'de verilmiştir.





Şekil 6. Δf:Analitik beklenen eğrinin ve Δf':Nümerik tasarımla hesaplanan eğrinin karşılaştırması

Özetle, bu çalışmanın bulguları, hidrolik bombeleme sistemlerinin abkant pres uygulamalarında mekanik kamalı sistemlere kıyasla daha kullanışlı olmasıyla beraber dinamik parametre ayarı ve dayanımı sayesinde daha üstün performans sergilediğini ve metal işleme endüstrisinde kalite ve verimlilik açısından önemli avantajlar sunduğunu göstermektedir. Gelecekteki çalışmalar, bu bulguların farklı malzeme ve kalınlıklarla genişletilerek daha kapsamlı sonuçlar elde edilmesine yönelik olmalıdır.

TEŞEKKÜR

Bu çalışma, MVD Makina San. A.Ş. Ar-Ge Merkezinde, Türkiye Bilimsel ve Teknolojik Araştırma Kurumu (TÜBİTAK) tarafından desteklenen 3231711 numaralı TÜBİTAK-1501 projesi kapsamında yapılmıştır. İlgili kurumlara değerli desteklerinden dolayı teşekkür ederiz.

KAYNAKÇA

1. Özkan, A. (2020). *Mekanik Pres Eksantrik Sisteminin Dinamik Analizler Ile Optimum Tasarımı* (Master's thesis, Necmettin Erbakan University (Turkey)).

2. Sarıer, H. (2004). *Saç işleme Makinelerinin Incelenmesi Ve Ürün Maliyetlerinin Analizi* (Master's thesis, Marmara Universitesi (Turkey)).

3. Simons, J. (2006). Redesign of a press brake. *Master's thesis, Technische Universiteit Eindhoven, The Netherlands. Available at http://www. kelue. edu/repository [accessed 19 July 2012]*.

4. Coelho, P. G., Faria, L. O., & Cardoso, J. B. (2005). Structural analysis and optimisation of press brakes. *International Journal of Machine Tools and Manufacture*, *45*(12-13), 1451-1460.

5. Hibbeler, R. C. (1989). Statics. Macmillan.

3B YAZICI İLE ÜRETİLEN PARÇALARIN FARKLI BASKI YÖNLERİNDEKİ DAYANIMININ DENEYSEL VE NÜMERİK İNCELENMESİ

Emre Can HASKİLİT, *haskilitemrecan@mail.com* Niğde Ömer Halisdemir Üniversitesi, 51240, Niğde

Habip Gökay KORKMAZ, *hkorkmaz@ohu.edu.tr Niğde* Ömer Halisdemir Üniversitesi, 51240, Niğde

Remzi Ecmel ECE, *reece@tai.com.tr* Türk Havacılık Uzay Sanayii A.Ş. 06980, Ankara

Serkan TOROS, *serkantoros@ohu.edu.tr* Niğde Ömer Halisdemir Üniversitesi, 51240, Niğde

Fahrettin ÖZTÜRK, *fahrettin71@gmail.com* Türk Havacılık Uzay Sanayii, A.Ş., 06980, Ankara, Ankara Yıldırım Beyazıt Üniversitesi, Etlik, 06010, Keçiören, Ankara

ÖZET

Bu çalışmada, Ultem 9085 malzemesi kullanılarak 3 boyutlu (3B) yazıcı ile belirli standartlarda üretilmiş deney numunelerinde farklı baskı yönlerinin mekanik dayanım üzerindeki etkisi deneysel ve sayısal olarak incelenmiştir. Sayısal analizler ANSYS yazılımı kullanılarak yapılmış olup, analiz sonuçları deneysel sonuçlarla karşılaştırılmıştır. Ayrıca, baskı kalitesi kırılma yüzeylerinin mikroskop altında incelenmesiyle değerlendirilmiştir. Sonuç olarak çekme deneyinde kuvvetin, numunelerin baskı yönünde kullanılan katmanların yönü ile aynı olması durumunda yüksek bir dayanım sergilerken, kuvvete dik baskı yönlerinde yapılan deneylerde gerilme katmanlar arası yapışma yüzeylerinde meydana geldiği için daha düşük gerilme ve birim deformasyon değerlerinde malzeme kopmaktadırlar. Aynı durum 3 nokta eğme testin de de gözlemlenmiştir.

Anahtar Kelimeler: 3 Boyutlu Yazıcı, Eklemeli İmalat, Ultem 9085, Sonlu Elemanlar Analizi

ABSTRACT

In this study, the effect of different printing directions on the mechanical strength of test specimens produced in specific standards with a 3D printer using Ultem 9085 material was investigated experimentally and numerically. Numerical analyses were performed using ANSYS software and the results were compared with the experimental results. In addition, the stress quality was assessed by examining the fracture surfaces under a microscope. As a result, in the tensile test, if the force is the same as the direction of the layers used in the printing direction of the specimens, the material breaks at lower stress and unit deformation values since the stress occurs on the adhesion surfaces between the layers in the experiments performed in the printing directions perpendicular to the force. The same situation was also observed in the 3-point bending test.

Keywords: 3D Printer, Additive Manufacturing, Ultem 9085, Finite Element Analysis

1. GİRİŞ

Günümüzde eklemeli imalat teknolojilerinin gelişmesi ile birçok parçanın tasarım ve üretim süreçleri değişmiştir. En zor parçalar kolayca üretilmekte ve maliyet açısından da ciddi kazançlar sağlanmaktadır. Eklemeli imalat yaygın olarak tıp, havacılık ve uzay, kalıpçılık, otomotiv, dişçilik, askeri donanım, mimari, kişisel araç gereç, heykelcilik, kuyumculuk ve eğitim alanlarında kullanılmaktadır [Sönmez, 2018]. 3B yazıcılar kullanılarak gerçekleştirilen bu imalat yöntemi, geleneksel yöntemler gibi malzeme azaltmaya değil katman katman malzeme eklemeye dayalı oldukları için sarfiyatın da önüne geçmektedir. Baskı sonucu yekpare bir parça çıkartabilme kabiliyeti bazı montajlı veya çok parçadan oluşan karmaşık yapıların üretiminde de kolaylık sağlamaktadır. Çok karmaşık parçalar kolayca üretilebilmektedir. Kullanılan malzemelerin çeşidine ve baskı türüne göre farklılık gösteren 3B yazıcılar ilgili sektöre ve kullanılacak alana göre seçilirler. Eklemeli imalat işlemleri bilgisayar destekli tasarım (Computer Aided Design, CAD) dosyasından alınan ve daha sonra bir STL uzantılı dosyaya dönüştürülen bilgiyi kullanmaktadır. Bu süreçte, CAD yazılımında yapılan çizim üçgenlere yaklaştırılır ve her bir katmanın basılacak olan bilgisini içeren dilimlenmiş bir dosya oluşturulur [Wong ve ark., 2012]. Polimerik 3B baskılı parçaların imalatında yaygın olarak kullanılan Erimiş Biriktirme Modellemesi (Fused Deposition Modelling, FDM), bir filamentin ısıtılmış bir nozuldan çıkarılması ve istenen şekli oluşturmak için yarı erimiş bir durumda biriktirilmesi ile meydana gelmektedir. Yapı, bu katmanlı birikimlerin ardışık olarak

oluşturulmasıyla imal edilmekte, her yeni katman, zaten birikmiş olan malzemeyle birleşerek kaynaşmaktadır [Zaldivar ve ark., 2016]. Bu kaynaşmanın sağlıklı olabilmesi için kullanılan filamentin gerektirdiği nozul sıcaklığı ve baskı tablası sıcaklığı sağlanmalıdır. 3B baskı ile üretilmiş parçalarda mekanik özellikleri etkileyen birçok faktör vardır. Dayanım söz konusu olduğunda baskı hızı, yapı yönelimi, dolgu miktarı, katman yüksekliği, soğuma süresi bu parametrelerden başlıcalarıdır [Naik ve ark., 2022]. Üretim sürecinde oldukça kazanç sağlayan eklemeli imalat yöntemi, üretilen parçanın işletme şartlarına dayanabilmesini de sağlamalıdır. Bundan dolayı yukarıda belirtilen faktörler belirlenirken malzemenin bulunduğu ortam ve üzerine gelecek yükler kritik öneme sahiptir. Malzeme üzerine gelen yükün büyüklüğü, yönü, ısıl yükler ve istenilen malzeme ömrüne göre üretim parametreleri belirlenmelidir. Her ne kadar malzemenin çalışma şartları öngörülebilse de bu şartlar altındaki dayanım cevabını hesaplamak her zaman kolay olmayabilir. Bu tür karmaşık geometrilerde veya büyük montajlı yapılarda bilgisayar destekli mühendislik (Computer Aided Engineering, CAE) yazılımları doğru sonuçlar verecektir. Bu yazılımlarda çoğunlukla bir nümerik çözüm yöntemi olan sonlu elemanlar analizi (Finite Element Analysis, FEA) yöntemini kullanılmaktadır. Sonlu Elemanlar Analizi (SEA), Turner ve ark. tarafından (1956) tanıtılan ve süreklilik şartlarında fiziksel modeli sonlu sayıda elemana bölerek her elemanın bağlandığı düğüm noktaları için gerekli fizik denklemlerini çözümlemektedir. Böylelikle geometrik model matematiksel modele dönüştürülür ve her bir düğümdeki bilinmeyen değerler hesaplanabilir [Madenci ve ark., 2015]. Katı cisimler mekaniğinde sonlu elemanlar analizi hareket denklemlerini kullanmaktadır ve bu denklemler malzemenin cinsine bağlı olan rijitlik, sönümleme gibi etkileri de içerir. Bir analizin sonucunun gerçeğe yakın olması için ilk adım malzemenin tanımlanmasıdır. Aksi halde deneysel verilerden oldukça uzak sonuçlar elde edilir. Bu çalışmada 3B yazıcı ile farklı baskı yönlerinde imal edilen deney numunelerinin sonuçları kullanılarak ANSYS 2024 R1 yazılımında modelleme yapılmıştır. Böylelikle hem baskı yönünün malzeme dayanımına etkisi hem de deneysel ve nümerik sonuçların birbiri ile karşılaştırılması detaylıca incelenecektir.

2. LİTERATÜR TARAMASI

3B yazıcıların endüstrideki kullanımının artması ve farklı malzemelerin eklemeli imalata uygun hale getirilmesi ile birlikte mekanik özelliklerin etkisi ön plana çıkmıştır. Bu konuda fazlaca araştırmacı çalışmış ve sonuçlarını paylaşmışlardır. Kamaal ve ark.(2020) [6] Polilaktik asit (Polylactic Acid, PLA) kompozit malzemesinin farklı yön ve iç dolgu değerlerinde çekme ve çentik darbe deneyleri ile dayanım sonuçlarını inceledi. Bu çalışma ile birlikte çekme deneyinde iç dolgu ve katman kalınlığı arttıkça çekme dayanımının da arttığı sonucuna

vardılar. Buna karşın çentik darbe deneyinde katman kalınlığı arttıkça darbe dayanımının azaldığını gözlemlediler. Hibbert ve ark. (2019) 3B baskıda akrilonitril bütadien stiren (Acrylonitrile Butadiene Styrene, ABS) malzemesinin çekmeye karşı farklı baskı parametreleri ve farklı gerinim hızlarında mekanik özellikleri incelemiş ve birçok baskı parametresinde çekme hızı arttıkça çekme dayanımının da arttığı sonucuna ulaşmışlardır. Senthil ve ark. (2021) PLA malzemesinin farklı dolgu desenlerinde darbeye olan dayanaklıklarını araştırmış ve 12 farklı desen arasında farklı doluluklarda enerjiyi en fazla absorbe eden deseninin çizgi desen olduğunu gözlemlemişlerdir. Bunun yanında %85 doluluğun farklı desenlerde en dayanıklı doluluk olduğu sonucuna varmışlardır. Kamer ve ark. (2022) FDM yöntemi ile basılan PLA malzemesinin yazdırma hızının dayanımına olan etkisini araştırmışlardır. Bu araştırma sonucunda yazdırma hızı arttıkça dayanımın azaldığını tespit etmişlerdir. Bununla birlikte yüzey pürüzlülüğünü de incelemiş ve baskı hızının artmasıyla yüzey kalitesinin azaldığını gözlemlemişlerdir. Pang ve ark. (2022) yazdırma sıcaklığının baskı hassasiyeti ve çekme dayanımına etkisini inceledikleri bir çalışmada, sıcaklığın artmasıyla hassasiyetin düşmesine karşın dayanımın arttığını gözlemlemişlerdir. Ansari ve ark. (2021) yazdırma hızı ve sıcaklığının çekme dayanımına etkisini inceledikleri bir çalışmada düşük hızlarda sıcaklıkla birlikte dayanımın da arttığını fakat yüksek hızlarda optimum bir sıcaklık olduğunu tespit etmişlerdir. Aynı çalışma içerisinde baskı süresini de incelenmiş ve baskı süresinin sıcaklıktan bağımsız olarak baskı hızından etkilendiği görülmüştür. Saenz ve ark. (2021) ABS malzemesi kullanılarak üretilen çekme numunelerinin farklı katman kalınlıklarında, dolgu desenlerinde ve doluluk oranlarında, oda sıcaklığında ve 77 K'de elastisite modülü, akma dayanımı ve maksimum çekme dayanımını araştırmışlardır. Oda sıcaklığında numuneler elastik davranış ve pekleşme gösterirken 77K'de numunelerin kırılmaya kadar elastik davranış gösterirken daha düşük dayanım ve daha yüksek elastisite modülü gösterdiği gözlemlenmiştir. Morales ve ark. (2018) ABS malzemesinden üretilen bir numunenin katmanlar arası soğutulmasının dayanıma olan etkilerini inceledikleri çalışmada soğuma işleminin katmanlar arası kaynaşmayı azaltarak özellikle basma ve kaymaya karşı malzeme dayanımını düşürdüğü belirtilmiştir. SEA daha önce belirtildiği üzere malzemenin mekanik karakteristik özelliklerine ihtiyaç duyar. ANSYS gibi birçok SEA yazılımlarında model parametrelerini barındıran kendi malzeme kütüphaneleri mevcuttur. Buna rağmen daha güvenli sonuçlar elde edebilmek adına kullanılacak malzemelerin mekanik deneylerinin yapılması ve sonrasında malzeme özelliklerinin ANSYS yazılımına tanımlanması oldukça önemlidir. Burada yapılan deneyler sonucunda malzemenin mekanik davranışına karar verilmeli ve analiz türü için gerekli malzeme özellikleri girilmelidir.

3. DENEYSEL ÇALIŞMA

Bu çalışmada deney numuneleri ULTEM 9085 malzeme Tablo 1'deki baskı parametreleri kullanılarak STRATASYS F900 makinesi ile Türk Havacılık ve Uzay A.Ş., Eklemeli İmalat biriminde üretilmiştir. Çekme, basma ve 3 nokta deneylerinde işlem hızı 2 mm/dk olarak tercih edilmiştir.

Tablo 1. Baskı parametreleri

Model Malzemesi	Ultem 9085
Malzeme Yoğunluğu	1300 kg/m^3
Destek Malzemesi	SUP8500B
Katman Kalınlığı	0,254 mm
Model Noozle Tipi ve Çapı	T16 – 0,508 mm
Destek Noozle Tipi ve Çapı	T16 – 0,508 mm
İç Dolgu Deseni ve Doluluğu	Solid – %100
Duvar Kalınlığı	0,508 mm
Dolgu Raster Açısı	+/- 45°
Destek Tipi	Sparse
Otomatik-Destek Açısı	43°

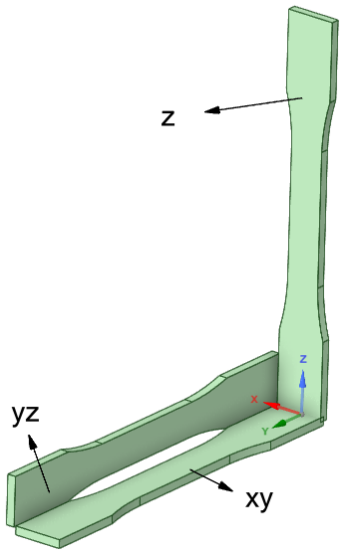
Çekme Deneyi: Çekme deneyi malzemelerin mekanik davranışlarını belirlemek için kullanılan en kapsamlı mekanik deneydir. Deneyde temel olarak standartlara göre üretilmiş olan numune deney cihazının çenelerine bağlanır. Çenelerden biri sabit, diğeri ise hareketlidir. Numune belirli bir hızla çekilir ve bu süreçte tepki kuvvetleri ve şekil değişimi ölçülür. Deney malzeme kopana kadar devam ettirilir. Akma gerilmesinden daha düşük gerilmelerde kuvvet kaldırılınca cisim başlangıç haline geri döner ve bu bölge de elastik bölge olarak adlandırılır. Akma gerilmesi aşıldığında ise malzemedeki deformasyon yük kaldırılsa dahi geri alınamaz yani plastik deformasyon başlar. Mühendislik uygulamaları genellikle yapısal elemanların elastik bölgesi ile sınırlı olsa da şekillendirme proseslerinde plastik bölge oldukça önemlidir. Çekme deneyi malzemenin hem elastik hem de plastik davranışını ortaya koyduğu için endüstride de sıklıkla kullanılmaktadır [Cabezas ve ark., 2004]. Çekme deneyinde çekme makinesinin sensörleri kuvvet-uzama grafiğini oluşturur. Malzemenin mekanik özelliklerini ortaya çıkarmak için büyüklüklerin geometriden bağımsız olması gerekir. Burada kuvvet Denklem 1'de verildiği şekilde malzemenin ilk kesit alanına bölünerek eksenel çekme gerilmesi değeri elde edilir.

$$\sigma = F/A \quad (1)$$

Uzama miktarı da numunenin ilk boyutlarına bağlıdır ve Denklem 2'de verildiği gibi toplam uzama miktarı ilk boya bölünerek geometriden bağımsızlaştırılır.

$$\varepsilon = \delta/L \quad (2)$$

Bu çalışmada numuneler 3 farklı baskı yönünde ASTM D638 standardına göre üretilmiştir. Şekil 1'de görüldüğü gibi xy düzlemine paralel olarak basılan numune xy, yz düzlemine paralel olarak basılan numune yz ve xz düzlemine paralel olarak basılan numune ise z olarak isimlenidirilmiştir. Bütün yönler için çekme deneylerden elde edilen mekanik özellikler Tablo 2'de paylaşılmıştır.



Şekil 1. Numuneleri üretiminde kullanılan baskı yönleri

Tablo 2. Çekme deneyi sonuçları

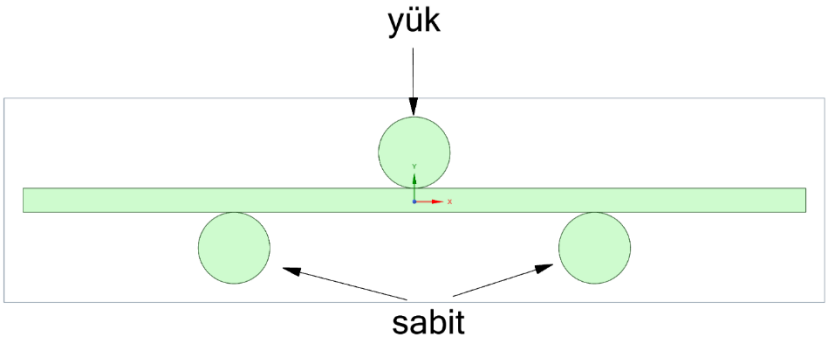
Baskı Yönü	Akma Gerilmesi (MPa)	Kopma Gerilmesi (MPa)	Kopma uzaması (%)	Elastisite Modülü (MPa)
XY	34,907	61,872	6,152	1930,4
YZ	42,252	72,33	6,0452	2098
Z	32,002	50,086	2,9682	1939

Basma Deneyi: Çelikler çekme ve basma yönünde benzer davranış sergiledikleri için çekme deneyi genellikle yeterlidir. Fakat cam, polimer, plastik gibi malzemeler basma ve çekmede farklı davranışlar sergilerler. Bu tür malzemeler için çekme deneyi yeterli olmadığından basma deneyine de ihtiyaç duyulur. Basma deneyi, bir parçaya veya numuneye etki eden basma veya sıkıştırma kuvvetlerinin ve deformasyon miktarının ölçülmesini ifade eder. Test sonucunda gerilim-birim deformasyon (gerinim) grafiği çizilir ve çekme deneyinin tersi olarak kabul edilir.

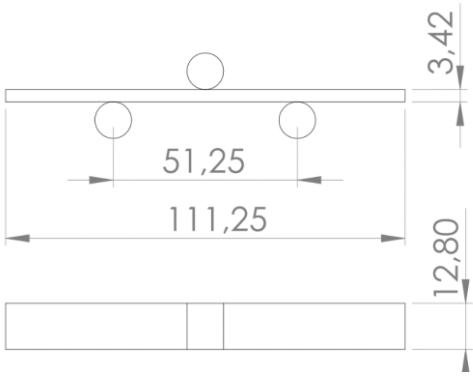
Gerekli hesaplamalar için kullanılan denklemler çekme deneyindekilerle aynıdır. [Aydemir, 2022].

Bu çalışmada 12,6 mm çapında ve 25,6 mm uzunluğunda silindirik numune kullanılmıştır. Deney sonucu numunenin 80,2 MPa basma gerilmesinde akmaya başladığı görülmüştür. Akma noktasındaki birim deformasyon değeri ise 0,564'dür.

3 Nokta Eğme Testi: 3 nokta eğme testi malzemelerin mekanik özelliklerini belirlemede kullanılan bir başka yaygın deneydir. Burada temel olarak malzeme alttan belirli uzaklıktaki 2 adet destek ile sabitlenirken orta noktasından aşağı doğru yük uygulanır ve böylelikle numune eğilir. Şekil 2'de deney şematik olarak gösterilmiştir. Numunenin alt kısma uzamaya ve çekmeye, üst kısmı ise kısalmaya ve basmaya zorlanır.

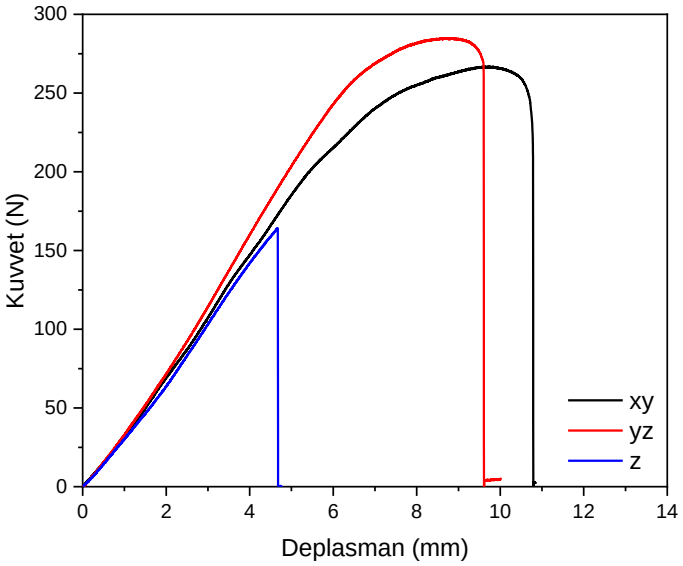


Şekil 2. 3 nokta eğme testi şematik gösterimi



Şekil 3. 3 nokta eğme testi numune ölçüleri

Eğme testinde numune ölçüleri kadar destekler arası mesafe de önemlidir ve sonuçları etkiler. Bu çalışmada Şekil 3'de görüldüğü gibi parça 111,25x3,42 mmxmm ve destek mesafesi 51,25 mm boyutlarındadır. Baskı yönlerinin isimlendirilmesi çekme numuneleri ile aynıdır. Farklı yönlerdeki 3 nokta deneylerine ait sonuçlar Şekil 4'de grafik olarak verilmiştir.



Şekil 4. 3 nokta eğme testi grafiği

4. SONLU ELEMANLAR ANALİZİ

SEA yazılımları sonlu elemanlar yönteminin kullanıldığı CAE tabanlı bir nümerik hesaplama araçlarıdır. SEA'lara fiziksel bir geometri "mesh" adı verilen bir ağ yapısı ile tanımlanır. Mesh geometriyi sonlu sayıdaki küçük elemanlara bölerek elemanların birleştiği düğüm noktalarından gerekli fiziksel denklemler ile çözüm yapmayı amaçlamaktadır. Bu sayede karmaşık geometriler bile matematiksel modele dönüştürülebilmekte ve çözümlenebilmektedir. Sonuçların hassasiyeti eleman sayısı ile doğrudan ilişkilidir. Eleman sayısı ve boyutları geometriyi doğru yansıtmalıdır. Bu durum karmaşık geometrilerde el ile hesaplamayı imkânsız hale getirmektedir. Sıradan bir doğrusal statik problem için kullanılacak olan bağıntı Denklem 3'te verilen Hooke yasasından elde edilebilir;

$$F = K.u \tag{3}$$

Burada F uygulanan kuvveti, K rijitliği ve u deformasyonu temsil etmektedir. 3 eksenli kartezyen koordinat sistemi için denklem genişletilirse matris formunda yazılabilir [Roylance, 2001]. Plastik bölgede rijitlik deformasyonun bir fonksiyonu olacağından iteratif çözüm metotlarından olan Newton-Raphson yöntemine başvurulur. Böylelikle geometrideki değişiklikler sonucu etkilenen rijitlik de simülasyona dâhil edilmiş olur. Bu çalışmada gerçekleştirilen çekme, basma ve 3 nokta eğme deneyleri plastik deformasyonları da içerdiğinden doğrusal olmayan davranış da modellenmiştir.

Doğrusal Malzeme Davranışının Modellenmesi: Doğrusal malzeme davranışı parça üzerine gelen kuvvetlerin akma gerilmesinin altında bir gerilme oluşturmasında kullanılmaktadır. Bu

durumda malzeme üzerine gelen kuvvetler kalıcı bir deformasyona yol açmayacak ve kaldırıldığında geometri ilk haline dönecektir. Aksi halde geri döndürülemeyen deformasyonlar parçaların beklenilen çalışma şartlarında kalmasını önlemektedir.

Bu çalışmada malzemenin her eksende aynı davranışı sergileyeceği kabulü ile Isotrophic Linear Elasticity malzeme modeli kullanılmıştır. Tanımlama için gerekli iki parametre vardır ve bunlar Elastisite Modülü ile Poisson oranıdır. Elastisite modülü "*E*" ile gösterilir ve formülü Denklem 4'te verildiği gibi lineer bölgede gerilmenin gerinmeye oranı şeklindedir.

$$E=\sigma/\varepsilon \tag{4}$$

Poisson oranı eksenel yüklemede kesitteki daralma miktarının boydaki uzamaya oranıdır. Kesit daralması negatif olduğundan Poisson oranının pozitif bir değer alması için (–) ile çarpılır ve "υ" ile gösterilir. X yönünde çekilen izotropik bir malzeme için Poisson oranı;

$$\upsilon=-\varepsilon_y/\ \varepsilon_x \tag{5}$$

Bu değerler kullanılarak malzemenin akma noktasına kadar olan doğrusal davranışı modellenir.

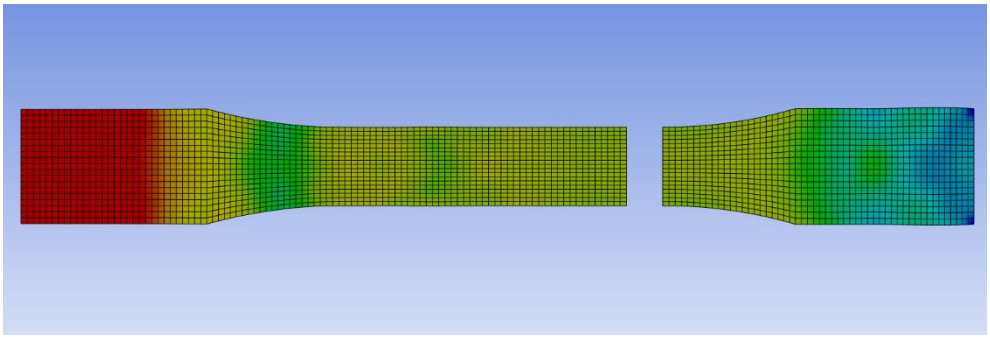
Doğrusal Olmayan Malzeme Davranışının Modellenmesi: Malzemeler akma gerilmelerinden daha yüksek gerilmelere maruz kaldıklarında gerilim ve gerinim arasında doğrusal olmayan bir bağıntı gözlenir. Bunun başlıca sebebi kesit değiştikçe şekil değişimine izin veren çizgisel kusurlar (dislokasyon) giderek yığılır ve bu durum pekleşme olarak adlandırılır. Burada malzeme rijitliği deformasyonun bir fonksiyonudur (Denklem 6). Plastik bölgeye geçen malzemeler genellikle şekillendirme işlemlerinde kullanılsa da SEA yönteminde okunacak gerilme değerlerinin doğruluğu açısından doğrusal olmayan malzeme davranışının da göz önüne alınması büyük önem arz etmektedir. Aksi halde yazılım aynı deformasyon değeri için gerçekte olduğundan çok fazla gerilmeler gösterebilir. Bunun sebebi akmadan sonra pekleşme verisi malzemede bulunmadığından doğrusal davranış kabulü ile doğrusal olmayan davranış ihmal edilir.

$$F= K.(u).u \tag{6}$$

Bu çalışmada farklı plastik gerinim değeri için gerilme değerinin tanımlandığı Multilinear Isotrophic Hardening malzeme modeli kullanılmıştır.

Malzeme Kırılmasının Modellenmesi: ANSYS içerisinde malzemenin kırılabilmesi için farklı malzeme modelleri bulunmaktadır. Bunların büyük çoğunluğu metallerin kırılmasını modellemek için denklemler ve deneysel veriler yardımı ile eklenebilir. Bu çalışma kapsamında polimer malzeme kullanıldığı için başvurulan model gerilme ve gerinimin sınırlandırılmasıdır. Gerilmenin ve gerinimin sınırlandırılması Şekil 5'te görüldüğü gibi ANSYS için girilen değere ulaşan mesh elemanlarının matematiksel modelden atılması anlamına gelmektedir. Böylelikle

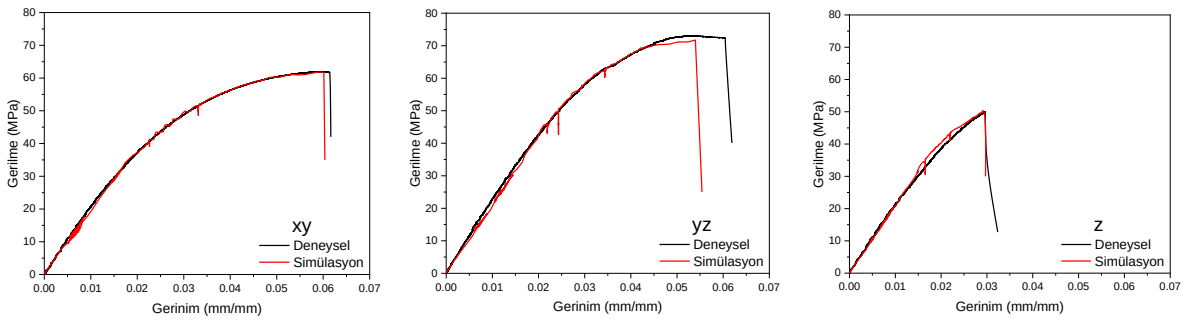
fiziksel modelde birbirine bağlı olan düğüm noktaları birbirinden koparılarak yük transferi gerçekleştiremezler. Bu adımlar ile malzemede kırılma modellenmiş olur. ANSYS içerisinde kırılma modelleri “failure” altında bulunmaktadır. Bu çalışmada gerilme tabanlı kırılma modeli kullanılmıştır.



Şekil 5. ANSYS çekme deneyi kırılma anı

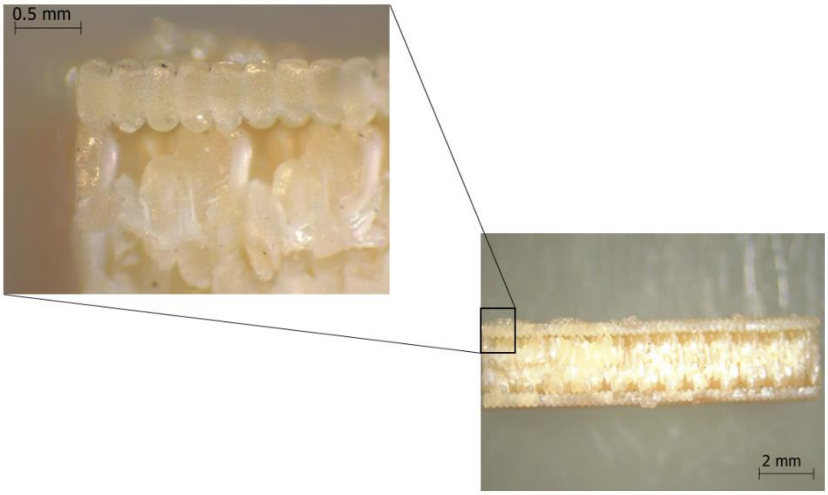
Çekme Deneyinin Sonlu Elemanlar Modeli: SEA adımlarının en başında geometri hazırlığı gelir. Burada ilk olarak CAD dosyası ANSYS Mechanical içine aktarılır ve malzeme seçimi yapılır. Farklı baskı yönleri için malzeme özellikleri Tablo 2’de verilmiştir. Buna ek olarak tüm yönlerde Poisson oranı 0,39 olarak belirlenmiştir.

Malzeme özellikleri belirlendikten sonra sonlu eleman ağı oluşturulmuştur. Geometri basit olduğundan daha hassas sonuçlar için karelerden oluşan lineer “hex8” eleman türü tercih edilmiştir ve eleman boyutu 1 mm olarak belirlenmiştir. Explicit analizler quadratic eleman desteklemediğinden hex eleman kullanılması sonuçları daha doğru yansıtacaktır. Çekme numunesi için toplam eleman sayısı 8607’dır. Mesh aşamasından sonra numune bir ucundan sabitlenmiş ve diğer ucundan çekilmiştir. Çekme deneyinin farklı yönlerde nümerik ve deneysel sonuçları Şekil 6’da verilmiştir.



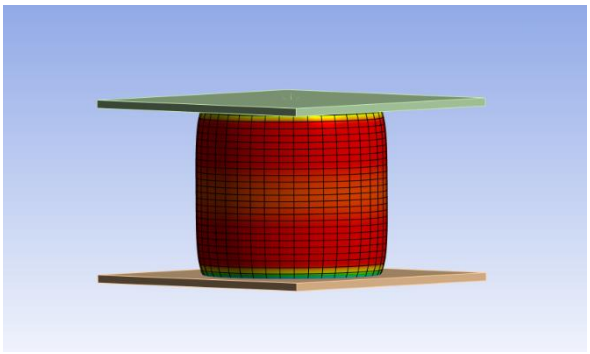
Şekil 6. Farklı yönlerde çekme deneyinin deneysel ve nümerik sonuç grafikleri

Çekme numunesinin kırılma yüzeyi mikroskop altında incelenmiştir. Bu inceleme çekme deneyi grafiklerinde de görüldüğü üzere gevrek kırılmayı doğrulamaktadır. Bunun yanı sıra malzemenin baskı kalitesi hakkında da bilgi vermektedir. Homojen bir kırılmanın olması ve katmanlar arası yapışma istenilen kalitenin sağlandığını göstermektedir. Kırılma yüzeyinin görüntüsü Şekil 7'de gösterilmiştir.

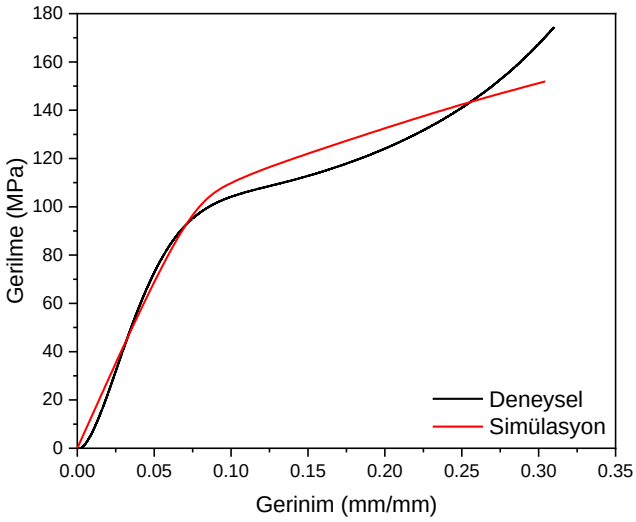


Şekil 7. Kırılma yüzeyinin mikroskop altında görüntüsü

Basma Deneyinin Sonlu Elemanlar Modeli: Çekme deneyinin analizinde de olduğu gibi öncelikle CAD dosyasına mesh örülerek fiziksel model matematiksel modele dönüştürülmüştür. Eleman boyutunun 1 mm olarak belirlendiği sistemde toplam 10740 eleman bulunmaktadır. Analizin gerçeğe yakın fiziği yakalayabilmesi için numunenin alt ve üstüne plakalar yerleştirilmiştir. Bu model için Şekil 8'de görüldüğü gibi alt plaka sabitlenmiş ve üstteki plakaya deney sonuçlarından yola çıkılarak 12 mm basma yönünde yer değiştirme uygulanmıştır. Yerleştirilen plakalar rijit olarak ve numune ile aralarındaki sürtünme katsayısı 0,1 olarak tanımlanmıştır. Simülasyona ve deneye ait sonuçlar Şekil 9'da gerilme-gerinim grafiği olarak verilmiştir.

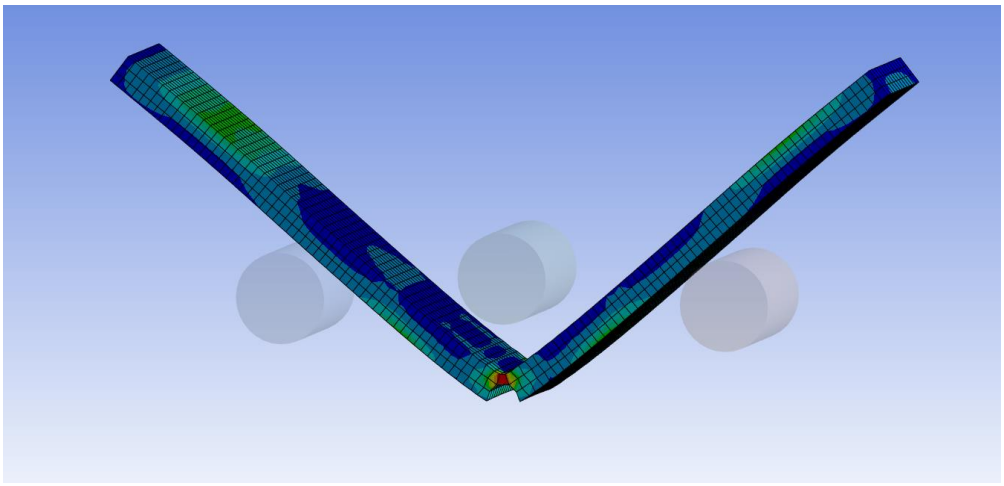


Şekil 8. ANSYS basma deneyi sonucu geomterinin son hali

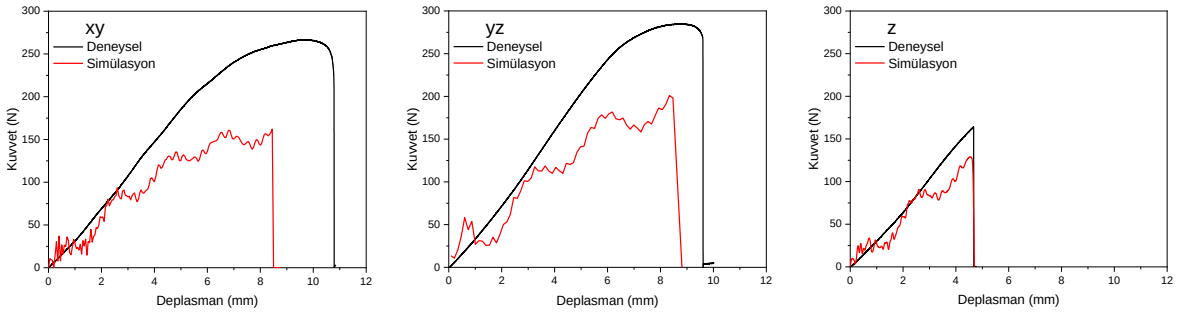


Şekil 9. Basma deneyinin nümerik ve deneysel sonuçlarının karşılaştırılması

3 Nokta Eğme Testinin Sonlu Elemanlar Modeli: 3 nokta eğme deneyinde öncelikle CAD dosyası ANSYS Mechanical içerisine aktarılır. Malzeme seçiminde aynı baskı yönündeki çekme deneyinden elde edilen veriler ile oluşturulan malzeme model parametreleri kullanılmıştır. Bu modelde 3destek ve 1 iş parçası olmak üzere 4 katı gövde bulunmaktadır. Eleman boyutu global olarak 1 mm ve toplam elaman sayısı 12480'dir. Bütün parçalar birbiri ile explicit analizlerde kullanılan ve tüm parçalar için olası etkileşim sonucu temas denklemleri kuran "body interaction" seçeneği ile temaslandırılmıştır. Tanımlanan temasların hepsi sürtünmeli temastır ve sürtünme katsayıları 0,1 olarak belirlenmiştir. Destekler üzerinde herhangi bir gerilme istenmediği için bu gövdeler rijit seçilmiştir. Numune ise esnektir. Tekli destek sabit hızla yer değiştirirken alttaki iki destek sabit tutulmuştur. Analiz sonucunda numunede meydana gelen kırılma Şekil 10'da gösterildiği gibidir. 3 nokta eğme analizlerinden elde edilen deplasman ve kopma kuvveti grafikleri Şekil 11'de verildiği gibidir.



Şekil 10. ANSYS yazılımında 3 nokta eğme numunesinin kırılma anı



Şekil 11. 3 nokta eğme deneyinin farklı baskı yönlerinde nümerik ve deneysel sonuçları

ANSYS yazılımı ile yapılan sonlu elemanlar analizinin sonuçları çekme deneyinden elde edilen sonuçlar için gerilme ve gerinim tabanlı kırılma modellerinde deneysel verilere oldukça yakındır. Burada tanımlanan Multilineer Isotropic Hardening plastisite modeli yeterli olmaktadır. Fakat aynı durum 3 nokta eğme deneyi için geçerli değildir. Bunun sebebi explicit analizin kısa süreli analizlere uygun olması, temas durumlarında ani atalet kuvvetlerinin dâhil edilmesi ve malzeme verilerinin sadece çekme deneyi referans alınarak belirlenmesidir. 3B yazıcıdan eklemeli imalatla elde edilen ürünlerin katmanlar arası dayanımı ve katman boyunca olan dayanımının farklı olması homojen, izotropik bir malzeme tanımlaması için farklı gerilme durumlarında geçerli değildir. Z baskı yönündeki numuneler için sonlu elemanlar analizi ve deneysel sonuçlar birim deformasyon olarak örtüşürken gerilme değerleri örtüşmemektedir. Diğer baskı yönleri için ise sonuçlar gerilim ve birim deformasyon için de farklılık göstermektedir. FDM yöntemi ile üretilen bu tür malzemelerin basma ve çekme yönlerindeki asimetrik davranışı deney sonuçlarında görülmektedir

5. SONUÇ

Farklı baskı yönlerinde 3B yazıcı ile üretilen numunelerin mekanik deneylerinin sonuçları işletme şartlarında uygulanan kuvvet yönünün baskı yönü ile ilişkisini ve dayanıma etkisini göstermektedir. Çekme deneyinde kuvvetin, numunelerin baskı yönünde kullanılan katmanların yönü ile aynı olması durumunda esas olarak malzeme kuvveti taşıyıp en mukavim davranışı sergilerken kuvvete dik baskı yönlerinde yapılan deneylerde gerilme katmanlar arası yapışma yüzeylerinde oluştuğu için daha düşük gerilme ve gerinim değerinde malzeme kopmaktadır. Aynı durum 3 nokta eğilme deneyinde de gözlemlenmektedir. Bu deneyde numune üzerinde hem basma hem de çekme gerilmeleri oluşmaktadır ve gerilme yönü baskının katmanları ile aynı yönde olması durumunda daha yüksek gerilmelere dayanabilmektedir. Bu durum 3B yazıcı ile elde edilen parçaların çalışma koşullarını üretimden önce öngörebilmenin ve sonlu elemanlar analizinin bu konuda önemini ortaya koymaktadır.
Nümerik ve deneysel sonuçların karşılaştırılmasında asimetrik davranış farklı gerilme durumlarında SEA doğruluğunu azaltmaktadır ve bu tür malzemeler için daha spesifik ve farklı malzeme modelleri kullanılmalıdır.

KAYNAKÇA

[1] Wong, K., Hernandez, A., A Review of Additive Manufacturing, ISRN Mechanical Engineering, vol. 2012, 2012.

[2] Zaldivar, R.J., Witkin D.B., McLouth, T., Patel, D.N., Schmitt, K, Nokes, J.P., Influence of processing and orientation print effects on the mechanical and thermal behavior of 3D-Printed ULTEM 9085 Material, Additive Manufacturing, vol. 13, s.72, 2016.

[3] Naik, M., Thakur, D.G., Chandel, S., An insight into the effect of printing orientation on tensile strength of multi-infill pattern 3D printed specimen: Experimental study, Materials Today: Proceedings, vol. 62, s.7392, 2022.

[4] Madenci, E., Güven, İ., The Finite Element Method and Applications in Engineering Using ANSYS, 2015.

[5] Sönmez, S., Kesen, U., Dalgıç, C., 3 Boyutlu Yazıcılar, 6. Uluslararası Matbaa Teknolojileri Sempozyumu, s.472, 2018, İstanbul Üniversitesi.

[6] Kamaal, M., Anas, M., Rastogi, H., Bhardwaj, N., Rahaman, A., Efect of FDM process parameters on mechanical properties of 3D-printed carbon fibre–PLA composite, Progress in Additive Manufacturing, vol. 6, s.64, 2020.

[7] Hibbert, K., Warner, G., Brown, C., Ajide, O., Owolabi, G., Azimi, A., The Effects of Build Parameters and Strain Rate on the Mechanical Properties of FDM 3D-Printed

Acrylonitrile Butadiene Styrene, Open Journal of Organic Polymer Materials, vol. 9, s. 19, 2019.

[8] Senthil, P., Mishra, P. K., Adarsh, S., Anoop, M.S., An investigation to study the combined effect of different infill pattern and infill density on the impact strength of 3D printed polylactic acid parts, Composites Communications, vol. 24, s. 4, 2021.

[9] Kamer, M.S., Temiz, S., Yaykasli, H., Kaya, A., Akay, O.E., Effect of printing speed on FDM 3D-printed PLA samples produced using different two printers, International Journal of 3D Printing Technologies and Digital Industry, vol. 6 s. 438, 2022

[10] Pang, R., Lai, M.K., Ismail, K.I., Yap, T.C., The Effect of Printing Temperature on Bonding Quality and Tensile Properties of Fused Deposition Modelling 3d-Printed Parts, IOP Conf. Ser.: Mat. Sci. And Eng., 1257, 2022.

[11] Ansari, A.A., Kamil, M., Effect of print speed and extrusion temperature on properties of 3D printed PLA using fused deposition modeling process, Materials Today: Proceedings, vol. 45, s.5462-5468 , 2021.

[12] Saenz, F., Otarola, C., Valladares, K., Rojas, J., Influence of 3D printing settings on mechanical properties of ABS at room temperature and 77 K, Additive Manufacturing, vol. 49, s.6, 2021.

[13] Morales, N.G., Fleck, T.J., Rhoads J.F., The effect of interlayer cooling on the mechanical properties of components printed via fused deposition, Additive Manufacturing, vol. 24, s. 243-248, 2018.

[14] Cabezas, E.E, Celentano, D.J., Experimental and numerical analysis of the tensile test using sheet specimens, Finite Elements in Analysis and Design, vol. 40, s. 555-575, 2004.

[15] Aydemir, B., Malzeme Basma Testlerinin Detayları ve Sonuçlarının Yorumlanması, 7th International Mediterranean Science and Engineering Congress, no. 51, s. 118-124, 2022, Antalya, Türkiye.

[16] Roylance, D., Finite Elemant Analysis, Massachusetts Institute of Technology, Department of Materials Science and Engineering, 2001.

MARTENZİTİK PASLANMAZ ÇELİKLERİN LAZER DOLGU KAYNAĞINDA ÖRTÜŞME ORANININ KALINTI GERİLMEYE ETKİSİ

Meryem ALTAY, *meryemaltay@uludag.edu.tr* Bursa Uludağ Üniversitesi, 16059, Bursa
Hakan AYDIN, *hakanay@uludag.edu.tr* Bursa Uludağ Üniversitesi, 16059, Bursa
Adem KARŞI, *akarsi@coskunoz.com.tr* Coşkunöz Ar-Ge Merkezi, 16140, Bursa

ÖZET

Lazer dolgu kaynağı, kalıp sektöründe onarım uygulamalarına yönelik bir eklemeli imalat yöntemlerinden biridir. Yüksek ilerleme hızı ve yüksek kaplama verimliliği özelliklerine sahiptir. Büyük parçaların onarımı için lazer ışınının üst üste binmesini gerektiren çok katmanlı üretim gerekmektedir. Kaplama katmanındaki kalıntı gerilme, kaplama katmanının mekanik ve fiziksel özelliklerini doğrudan etkileyerek çatlak kusurlarına neden olmaktadır. Kalıntı gerilme oluşum mekanizmaları oldukça karmaşıktır ve deformasyon üzerinde büyük etkisi olduğu için araştırılması gerekmektedir. Bu çalışmada, FGS600-3A küresel grafitli dökme demir üzerine 42C martenzitik paslanmaz çelik toz malzeme lazer kaplama teknolojisi ile kaplanmıştır. Kaynak parametreleri lazer gücü için 1,3 kW ve ilerleme hızı için 8 mm/s olacak şekilde sabit tutularak, 3 katmanlı üretim gerçekleştirilmiştir. Örtüşme oranı %20 - %50 - %80 arasında değiştirilmiştir; bu da 2.4 mm, 1,5 mm ve 0,6 mm'ye karşılık gelmektedir. Farklı bindirme oranlarına sahip kaplama katmanlarındaki kalıntı gerilme ölçümü XRD yöntemi ile, kaplama yönüne göre 0°, 45°, 90° olacak şekilde, maksimum ve minimum asal gerilme için gerçekleştirilmiştir. Sonuçlar, kaplama yönünün 0° ölçümlerinde, ısı girdisi azalırken örtüşme oranı arttığında, nispeten düşük düzeyde kalıntı çekme gerilimi oluştuğunu göstermektedir. Artan enerji girdisi ile örtüşme oranı azaldıkça kalıntı gerilmeler basınç gerilmelerine dönüşür. Kaynak ilerlemesine dik (90°) doğrultudaki kalıntı gerilmeler incelendiğinde; tüm numunelerde basma kalıntı gerilmelerinin etkili olduğu görülmüştür. Örtüşme mesafesi değeri azaldıkça (enerji girişinin artmasıyla birlikte) gerilimin değeri de azalmıştır. 45° kalıntı gerilme ölçümünde ise tüm numunelerde basma kalıntı gerilmelerinin etkili olduğu görülmektedir. Farklı örtüşme oranları için yapılan bu çalışma endüstriyel kalıpların onarım uygulamaları için uygun örtüşme oranının belirlenmesine yönelik deneysel bir çıktı sağlamaktadır.

Anahtar Kelimeler: lazer dolgu kaynağı, örtüşme oranı, kalıntı gerilme

ABSTRACT

Laser cladding is one of the additive manufacturing methods for repair applications in the mold industry. It is used in the repair of large parts in the mold industry thanks to its high scanning speed and high coating efficiency features. Residual stresses occurring in the coating layer can create deformation and cause crack defects, so it needs to be investigated. In this study, 42C martensitic stainless steel powder material was coated on FGS600-3A ductile cast iron with laser cladding technology. By keeping the welding parameters constant as 1.3 kW for laser power and 8 mm/s for feed speed, 3-layer production was carried out for different overlap rates. The overlap ratio was varied from 20% to 50% to 80%; which corresponds to 2.4 mm, 1.5 mm and 0.6 mm. Residual stress measurement in coating layers with different overlap ratios was carried out by the XRD method for at 0°, 45°, 90°, maximum and minimum principal stress depending on the coating direction. The results show that at 0° measurements of the coating direction, relatively low levels of residual tensile stress are developed as the overlap ratio increases while the heat input decreases. As the overlap ratio decreases with increasing energy input, residual stresses turn into compressive stresses. It was observed that compressive residual stresses were effective in all samples in the direction perpendicular (90°) to the welding progress. As the overlap distance value decreased, the stress value also decreased. In the 45° residual stress measurement, it is seen that compressive residual stresses are effective in all samples. This study provides an experimental output to determine the appropriate overlap ratio for repair applications of industrial molds.

Keywords: laser cladding, overlap rate, residual stress

1.GİRİŞ

Lazer dolgu kaynağı, toz malzemelerin yüksek enerjiye sahip bir lazer ışını ile ergitilerek temel malzemenin üzerine katmanlar şeklinde biriktirildiği bir yüzey modifikasyon tekniği ve eklemeli imalat yöntemidir. Lazer dolgu kaynağı yönteminde amaç, kaplanmış yüzeyin mekanik özelliklerini iyileştirmektir. Kaplama katmanı ile temel malzeme arasındaki sağlam metalurjik bağın oluşması, ince taneli ve düşük gözenekli mikro yapısı, hızlı bir katmanlı üretim yöntemi olması gibi avantajları sayesinde kalıp sektöründe hasarlı parçaların tamiratında kullanılmaktadır. Lazer kaplama yönteminin dezavantajı ise proses esnasında ya da soğuma sonrasındaki çatlak oluşumlarıdır. Çatlaklar, lazer ışınının ergiyik havuz içerisinde oluşturduğu yüksek termal gradyen nedeniyle ortaya çıkan yüksek kalıntı gerilmeler nedeniyle oluşmaktadır. Kaplamanın mekanik özellikleri proses parametrelerine

bağlıdır, istenilen özelliklerin elde edilmesi için lazer gücü, ilerleme hızı, örtüşme oranı, toz besleme hızı gibi proses parametrelerinin optimum değerlerinin belirlenmesi gerekmektedir.

Bian ve diğ. [Bian ve diğ., 2024] H13 takım çeliklerinin üzerine Ni60 alaşımını lazer dolgu kaynağı yöntemi ile kaplamışlardır. Tek katmanlı ve çok katmanlı kaplama işlemi sırasında kaplamanın mikroyapı özelliklerini ve çatlakların oluşum davranışlarını incelemişlerdir. Sonuçlar, çatlakların esas olarak kaplamanın yüzeyinden başladığını ve kalıntı gerilmeler nedeniyle derinlik yönünde alt tabakaya doğru yayıldığını göstermiştir. Çatlaksız kaplama tabakasının elde edilebilmesi için proses parametrelerinin uygun bir şekilde belirlenmesi gerektiğini; örtüşme oranı parametresinin çok katmanlı kaplama işleminde çatlak oluşumunu ve yayılmasını etkileyen önemli parametrelerden biri olduğu sonucuna varmışlardır. Nazemi ve Urbanic [Nazemi ve Urbanic, 2018] AISI 1018 çelik plaka üzerine P420 paslanmaz çelik tozunu lazer dolgu kaynağı üretim yöntemi ile kaplamışlardır. Lazer kaplama işlemini simüle etmek üzere 3 boyutlu termal-metalurjik-mekanik sayısal model oluşturmuşlardır. Farklı örtüşme oranlarının (%40, %50, %60) sıcaklık alanı gelişimi, termal döngü özellikleri, mekanik özellikler, kaplama ve temel malzemede oluşan kalıntı gerilmeler üzerindeki etkisini araştırmışlardır. %50 örtüşme konfigürasyonunun minimum distorsiyona sahip olduğunu bulmuşlardır. Sunulan simülasyon metodolojisi, lazer kaplama yönteminde mekanik ve fiziksel özellikleri tahmin etmek için kullanılabilir. Yao ve diğerleri [Yao ve diğ., 2023]. çalışmalarında çok katmanlı lazer kaplama işleminde sıcaklık alanının gelişimini ve buna bağlı olarak indüklenen kalıntı gerilmeyi tahmin etmek için bir sonlu elemanlar modeli geliştirmişlerdir. A36 yumuşak çelik temel malzeme üzerine 316L paslanmaz çelik toz malzemesi kaplama yapılmıştır. Sonlu elemanlar modelinin soğuma sonrası sonuçları, kalıntı gerilme ölçüm metodlarından X-ışını kırınım yöntemi ile deneysel ölçümlerle de doğrulanmıştır. Malzeme özelliklerinin (Young modülü, akma mukavemeti ve termal genleşme katsayısı) ve kaplama katman sayısının kalıntı gerilmeler üzerindeki etkisini araştırmışlardır; kaplama katmanlarının sayısı arttıkça enine düzlemde yüksek çekme kalıntı gerilmesinin oluştuğu, son kaplama katmanında ise boylamsal düzlemde von Mises eşdeğeri kalıntı gerilmeler oluştuğu gözlemlemişlerdir. Çalışma sonuçları lazer kaplama işleminde proses parametrelerini optimize ederek kaplama katmanlarındaki kalıntı gerilmeleri azaltmak için rehberlik sağlayabilir.

Bu çalışmada Metco42C martenzitik paslanmaz çelik toz malzemesinin FGS600-3A küresel grafitli dökme demirler üzerindeki lazer dolgu kaynağı yapılmıştır. Farklı örtüşme oranı parametrelerinin kalıntı gerilme üzerindeki etkisi XRD ölçüm metodu yöntemi ile

incelenmiştir. Elde edilen çıktıların otomotiv gövde kalıp tamiratında kullanılması ve ileriki çalışmalar için yol göstermesi hedeflenmektedir.

2.MATERYAL VE YÖNTEM

Bu çalışmada otomotiv sektöründe sac metal şekillendirme kalıplarında kullanılan FGS600-3A küresel grafitli dökme demir temel malzeme üzerine Metco 42C martenzitik paslanmaz çelik toz malzemesini (AISI 431 martensitik paslanmaz çelik) lazer dolgu kaynağı yöntemi ile kaplanmıştır. Metco 42C toz malzemesinin ve FGS600-3A sfero dökme demirin kimyasal bileşimleri Tablo 1'de gösterilmektedir.

Table 1 Metco 42C martenzitik paslanmaz çelik ve FGS600-3A küresel grafitli dökme demir malzemelerinin kimyasal kompozisyonu (wt.%)

Malzeme	C	Si	Mn	P	S	Sn	Cu	Mg	Cr	Ni
FGS600-3A	3.06	2.06	0.52	0.044	0.009	<0.01	0.68	0.049	--	--
Metco 42C	0.18	--	--	--	--	--	--	--	17	2

Lazer dolgu kaynağı işleminde KUKA KR 90 R3100 Ekstra 6 eksenli dolgu kaynağı ünitesi ve KUKA KL 1500-3T lineer table, Toplas 3D V3 yazılımıyla birlikte kullanılmıştır (Şekil 1).
Kullanılan lazer ışını LASERLINE-LDF 4000-100 teknik özellikleri: maksimum lazer gücü 4000 W, lazer dalga boyu 900-1070 nm arasında, lazer ışın çapı 3 mm, lazer ışın kalitesi 30 mm-rad, minimum odaklama 150 mm mesafede 450 µm, fiber kablo mesafesi 12 mm, optik fiber 600 m (NA 0,2). DELTATHERM LTK 1-4 Lazer Nozul Soğutma Cihazı ve ERLAS Gmbh lazer nozul kullanılmıştır. Oerlikon Twin-120A toz besleme hızı 13,6 g/dk, toz besleyici dönüş hızı 3 rpm, soğutma suyu akış hızı 1,8 l/dak, soğutma suyu basıncı 0,22-0,3 MPa'dır. Koruyucu gaz olarak Argon kullanılmıştır, besleme hızı 5 lt/dk'dır.



Şekil 1 Lazer dolgu kaynağı ünitesi

Bu çalışmada örtüşme oranının kalıntı gerilme açısından etkisini araştırmak amacıyla üç parametreli gruplar oluşturulmuştur. Örtüşme yüzdesi %20 - %50 - %80 arasında değişmiştir; hatve mesafesi olarak 2,4 mm - 1,5 mm - 0,6 mm'ye karşılık gelmektedir (Tablo 2). Numunelerin üretimi için optimum kaynak parametreleri sabit tutulmuştur: lazer gücü 1,3 kW ve ilerleme hızı 8 mm/s. Tüm numunelerde 3 katlı üretim yapılmıştır. Lazer gücü ve ilerleme hızı için belirlenen optimum proses parametrelerine ticari uygulamalarımızdaki uzmanlık ve önceki çalışmalarımız yardımcı olmuştur. Enerji girdisi lazer gücü, ilerleme hızı, lazer ışın çapı, hatve mesafesi parametrelerine göre hesaplanmıştır (Denklem 1).

$$Enerji\ Girdisi = \frac{Lazer\ Gücü}{(İlerleme\ Hızı * Lazer\ Işın\ Çapı * Hatve\ Mesafesi)} \quad (1)$$

Tablo 2 Numunelerin örtüşme oranı ve hatve mesafesi değerleri

Numune No	Örtüşme Oranı (%)	Hatve mesafesi (mm)
1	20	2.4
2	50	1.5
3	80	0.6

120 mmx30 mm boyutundaki FGS600-3A kalıp temel malzeme numuneleri prüzsüz bir yüzey elde edebilmek için CNC freze makinesinde 1 mm kalınlığa kadar işlendikten sonra üzerinde lazer kaplama uygulanmıştır. Lazer kaplama numunelerinin kalıntı gerilimi, X-Işını Difraktometresi (XRD) yöntemi ile ölçülmüştür. Kalıntı gerilme işlemi öncesinde numunelerin yüzeyini parlatmak için elektropolishing yöntemi uygulanmıştır. XRD kalıntı gerilim ölçümünde STRESSTECH X-Işını Difraktometresi kullanılmıştır. X-ışını tüpünün çalışma koşulları 30 kV, bükülme açısı ±45°X ve salınım mesafesi ±0,003 mm'dir. Numunelerin kalıntı gerilmeleri kaplama yüzeyinden 0◦, 45◦ ve 90◦ aralığında açısal açıyla ölçülmüştür.

3.ARAŞTIRMA SONUÇLARI VE TARTIŞMA

Lazer dolgu kaynağı işlemi sonrası, Metco 42 martenzitik paslanmaz çelik kaplama malzemesi FGS600-3A küresel grafitli dökme demir temel malzemeye göre daha fazla büzülmek isteyecektir. Bu nedenle kalıntı gerilme, çekme veya basma kalıntı gerilimi olarak ortaya çıkmaktadır. Kaynak yönü boyunca (0°'lik yönde) ortaya çıkan kalıntı gerilmeler incelendiğinde (Tablo 3); yüksek hatve mesafesi parametresinde düşük enerji girdisi oluşmaktadır, yüksek hatve mesafesi ile üretilen numunelerde nispeten düşük düzeyde

çekme kalıntı gerilmesi ortaya çıkmaktadır. Hatve mesafesi düştüğünde yani enerji girdisi arttığında, kalıntı gerilmeler basma gerilmelerine dönüşmektedir. Enerji girdisi artışı kaynak yönünde basma kalıntı gerilmelerinin ortaya çıkmasına sebep olmuştur.

Tablo 3. Kaynak yönünde 0° ölçülen kalıntı gerilme değerleri

Numune No	Hatve Mesafesi [mm]	Enerji Girdisi [J/mm^3]	Kalıntı Gerilme [MPa]
1	2.4	22.57	**39.2**
2	1.5	36,11	**-97.7**
3	0.6	90,28	**-56.1**

Kaynak ilerlemesine dik yönde (90°'lik yönde) ortaya çıkan kalıntı gerilmeler incelendiğinde (Tablo4); tüm numunelerde basma kalıntı gerilmelerinin etkin olduğu görülmüştür. Hatve mesafesinin azalmasıyla basma gerilmesinin değeri azalmıştır. Hatve mesafesi değerinin en yüksek, enerji girdisinin en düşük olduğu numunede soğuma hızının daha fazla olmasından dolayı kalıntı gerilme değeri daha yüksek olmuştur.

Tablo4. Kaynak yönüne dik 90° ölçülen kalıntı gerilme değerleri

Numune No	Hatve Mesafesi [mm]	Enerji Girdisi [J/mm^3]	Kalıntı Gerilme [MPa]
1	2.4	22.57	**-195.1**
2	1.5	36,11	**-159**
3	0.6	90,28	**-38.6**

Kaynak ilerlemesine göre 45°'lik yönde ortaya çıkan kalıntı gerilmeler incelendiğinde (Tablo5); yine tüm numunelerde basma kalıntı gerilmelerinin etkin olduğu görülmektedir. Orta düzeyde enerji girdisi daha düşük kalıntı gerilmelerin ortaya çıkmasına sebep olmuştur.

Tablo 5. Kaynak yönüne göre 45° ölçülen kalıntı gerilme değerleri

Numune No	Hatve Mesafesi [mm]	Enerji Girdisi [J/mm^3]	Kalıntı Gerilme [MPa]
1	2.4	22.57	**-82.3**
2	1.5	36,11	**-19.4**
3	0.6	90,28	**-177.8**

Numunelerin maksimum ve minimum kalıntı asal gerilmeleri incelendiğinde (Tablo6 ve Tablo7); genel anlamda numunelerde basma kalıntı gerilmelerinin daha etkin olduğu görülmektedir. Ortaya çıkan maksimum kalıntı asal gerilmeler 100 MPa'nın altında kalmaktadır. Diğer taraftan ortaya çıkan minimum kalıntı asal gerilmeler -250 MPa'ya yaklaşmaktadır. Bu kalıntı gerilme değerleri çatlak ve deformasyon oluşturacak değerlerden uzaktır ki numunelerin enine ve boyuna kesit yüzeyleri incelendiğinde herhangi bir çatlak oluşumuna rastlanılmamıştır. Ancak, dolgu kaynak bölgesinde ortaya çıkan basma kalıntı gerilmeleri sac metal kalıplarında yorulma dayanımı açısından riski arttırmaktadır.

Tablo 6. Maksimum kalıntı asal gerilme değerleri

Numune No	Hatve Mesafesi [mm]	Enerji Girdisi [J/mm^3]	Kalıntı Gerilme [MPa]
1	2.4	22.57	**39.3**
2	1.5	36,11	**-15,1**
3	0.6	90,28	**83.3**

Tablo 7. Minimum kalıntı asal gerilme değerleri

Numune No	Hatve Mesafesi [mm]	Enerji Girdisi [J/mm^3]	Kalıntı Gerilme [MPa]
1	2.4	22.57	**-195.2**
2	1.5	36,11	**-241.6**
3	0.6	90,28	**-178.1**

4.SONUÇLAR

Bu çalışmada, FGS600-3A küresel grafitli dökme demir temel malzeme üzerine Metco42C martenzitik paslanmaz çelik toz malzeme kaplamasının kalıntı gerilme değerleri farklı örtüşme oranı ve ısı girdisi açısından incelenmiştir.

Kaplama yönünün 0° ölçümlerinde, örtüşme oranı arttığında ısı girdisi azalırken, nispeten düşük düzeyde kalıntı çekme gerilimi oluştuğunu göstermektedir. Artan enerji girdisi ile örtüşme oranı azaldıkça kalıntı gerilmeler basınç gerilmelerine dönüşmektedir. Kaynak ilerlemesine dik doğrultudaki 90° kalıntı gerilme ölçümlerinde, tüm numunelerde basma kalıntı gerilmelerinin etkili olduğu görülmüştür. Örtüşme mesafesi değeri azaldıkça enerji

girdisinin artmasıyla birlikte, kalıntı gerilme değerleri de azalmıştır. 45° kalıntı gerilme ölçümünde ise tüm numunelerde basma kalıntı gerilmelerinin etkili olduğu görülmektedir.

Numune yüzeylerinde çatlak oluşumuna rastlanmamıştır, ancak oluşan basma kalıntı gerilmeleri sac metal kalıplarında yorulma dayanımı açısından risk teşkil etmektedir. Farklı örtüşme oranları için yapılan bu çalışma endüstriyel kalıpların onarım uygulamaları için uygun örtüşme oranının belirlenmesine yönelik deneysel bir çıktı sağlamaktadır.

TEŞEKKÜR

Yazarlar, 1505 Üniversite-Sanayi İşbirliği Destek Programı kapsamındaki desteği için Türkiye Bilimsel ve Teknolojik Araştırma Kurumu'na (TÜBİTAK) ve lazer kaplama işlemleri için olanaklar sağlayan Coşkunöz Kalıp Makina A.Ş.'ye teşekkür eder (Proje No: 5180090).

KAYNAKÇA

1. **Bian, Y., Dong, B., Chen, B., Guo, J., Li, S., Tian, C., Xu, S., He, X., Yu, G.** (**2024),** "Dynamic evolution behavior of cracks for single-track and multi-track clads in laser cladding", International Journal of Advanced Manufacturing Technology, 130(5–6), 2313–2328. https://doi.org/10.1007/s00170-023-12766-3.

2. **Nazemi, N., Urbanic, J.** [**2018),** "An Experimental and Simulation Study for Powder Injection Multitrack Laser Cladding of P420 Stainless Steel on AISI 1018 Steel for Selected Mechanical Properties", Journal of Manufacturing Science and Engineering, Transactions of the ASME, 140(1), https://doi.org/10.1115/1.4037604.

3. **Yao, M., Kong, F., Tong, W.** (**2023), "**A 3D finite element analysis of thermally induced residual stress distribution in stainless steel coatings on a mild steel by laser hot wire cladding", International Journal of Advanced Manufacturing Technology, 126(1–2), 759–776, https://doi.org/10.1007/s00170-023-11155-0.

TEMASSIZ ENERJİ SİSTEMİ İLE ÇALIŞAN 70 TON TRANSFER ARABASI

Yalçın GÜLER, *yalcin.guler@kumsan.com.tr*, KM Kümsan Vinç Sistemleri, 41455, Kocaeli

Mehmet KOÇHİSARLI, *mehmet.kochisarli@kumsan.com.tr*, KM Kümsan Vinç Sistemleri, 41455, Kocaeli

Aydoğan AKÇA, *aydogan.akca@kumsan.com.tr*, KM Kümsan Vinç Sistemleri, 41455, Kocaeli

Ece KARSLI, *ece.karsli@kumsan.com.tr*, KM Kümsan Vinç Sistemleri, 41455, Kocaeli

Engin TEKİN, *engin.tekin@kumsan.com.tr*, KM Kümsan Vinç Sistemleri, 41455, Kocaeli

Sibel SAİN ÖZDEMİR, *sibel.ozdemir@alpdanismanlik.com.tr***,** Alp İnovasyon ve Danışmanlık Hiz. Ltd. İstanbul

ÖZET

Ağır yük istiflenen çelik servislerindeki yüklerin yatay şekilde ray hattı boyunca taşınmasını sağlayan, bunu yaparken temassız enerji sistemini kullanan bir transfer arabası tasarlanmıştır. Böylece mevcut sisteme göre enerji verimliliğinin %50 artırılması, temassız enerji sistemi kullanıldığından %80 daha uzun ömürlü olması ve transfer arabası üzerindeki kablo karmaşıklığı önlenerek alan avantajı sağlanması amaçlanmıştır.

70 ton transfer arabası, endüstriyel tesislerde (demir-çelik, maden, liman ve tersane vb. endüstrilerde) ağır malzeme taşıma işlemlerinde kullanılan büyük taşıma araçlarından biridir. Bu transfer arabaları genellikle elektrikli, hidrolik veya pnömatik güç sistemleriyle çalışır. Elektrikli modeller genellikle kablolu/akülü olabilir ve uzun mesafelerde taşıma işlemlerini gerçekleştirebilirler. Hidrolik sistemler, yüksek basınçlı sıvıların kaldırılması/taşınmasında çalışırken, pnömatik sistemler basınçlı havayla hızlı ve hassas taşıma işlemlerine kullanılır.

Bu araçlar raylar üzerinde hareket eder ve programlanabilir kontrol sistemleriyle yönlendirilir. Böylece, belirli bir rotada otomatik olarak hareket edebilir ve yükleri istenilen konumlara taşıyabilirler. Ayrıca, güvenlik sensörleri ve acil durdurma sistemleri gibi önlemlerle donatılmış olabilirler.

Anahtar Kelimeler: ağır yük transfer arabası, tasarım, enerji verimliliği, temassız enerji sistemi

ABSTRACT

A transfer car has been designed that allows the loads in heavy-duty stacked steel services to be transported horizontally along the rail line, using a contactless energy system. Thus, it is aimed to increase energy efficiency by 50% compared to the current system, to have an 80% longer lifespan since the contactless energy system is used, and to provide space advantage by preventing the cable complexity on the transfer car.

70 tons transfer car is one of the large transportation vehicles used in heavy material transportation operations in industrial facilities (iron-steel, mining, port and shipyard etc. industries). These transfer cars usually operate with electric, hydraulic or pneumatic power systems. Electric models can often be corded/battery powered and can carry long distances. While hydraulic systems work in lifting/transporting high pressure liquids, pneumatic systems are used for fast and precise transportation operations with compressed air.

These vehicles move on rails and are guided by programmable control systems. Thus, they can automatically move along a specific route and transport loads to desired locations. They may also be equipped with measures such as safety sensors and emergency stop systems.

Keywords: heavy duty transfer cart, design, energy efficiency, contactless energy system

GİRİŞ

Günümüzde endüstri 4.0 ile akıllı hale gelmeye başlayan fabrikaların bir uzantısı olarak depolarda, ağır malzeme taşıyan sistemlerden biri de transfer arabalarıdır. İmalatın karmaşık üretim hatları arasında ki ağır yük transferlerinin kesintisiz sağlanması bir işletme için kuşkusuz en önemli faktörlerden biridir [Li, 2014]. Bobin taşıma arabaları; raylı, raysız ve otonom (AGV) hareket kabiliyetleri ve akülü, kablosuz ve kablo tamburlu güç besleme sistemleri ile üretilmektedir. Belirli bir düzlemde transfere ihtiyaç duyan işletmeler için raylı ağır yük taşıma arabaları uygunken değişken güzergâhlarda hareket eden taşıma arabaları için raysız ve otonom arabalar daha uygundur [Lashkari, 1986].

Raylı Transfer Arabaları, doğrusal hat üzerinde istasyonlar arası yük transferi için tasarlanmıştır. Müşterilerin ihtiyaçlarına yönelik özel çözümler sunarak taşınacak yükün ağırlığına göre tasarlanarak üretilmektedir.

Raylı yük taşıma sistemleri, işletme içerisindeki iş akışının hızlanmasını ve güvenli çalışma ortamlarının oluşmasını sağlar [Fan, 2017]. Taşınacak yükün türü ve şekline göre kişiselleştirmeler yapılabilir. Otomotiv sanayi gibi ağır sanayi kollarında öncelikli olarak kullanılan yük taşıma sistemleridir.

Literatürde gerçekleştirilen çalışmada endüktif yönteme dayalı olarak çalışan temassız elektrik güç aktarım sistemlerinin verimlilik analizi ve tasarımı ele alınmaktadır. Sistemlerin büyük kaçak endüktansları, maksimum verimlilik için rezonans koşullarını elde etmek amacıyla telafi edilmektedir. Temassız bir sistemin devre modelleri dikkate alınarak, belirli bir frekans aralığı ve bağlaşım katsayısı için dengeleme kapasitörleri de dahil olmak üzere farklı parametrelerin etkileri analiz edilmektedir. Optimum kapasitörleri ve rezonans frekansını belirlemek için bir algoritma önerilmiştir. Deneysel sonuçlarla doğrulanmıştır. Temassız enerji kullanımının verimliliğe olumlu katkılarının ortaya konmuş olması, aynı yaklaşımın transfer arabalarında da uygulanmasıyla enerji verimliliğine olumlu katkı sağlanabileceğini göstermiştir [Hasanzadeh, 2014].

2023 yılında yapılan bir çalışmada kablosuz güç aktarım teknolojisindeki son gelişmelere, zorluklara ve potansiyel uygulamalara kapsamlı bir genel bakış sunmaktadır. Manyetik dosyalı bağlantı, elektrik dosyalı bağlantı, mikrodalgalar ve lazer teknolojileri dahil olmak üzere kablosuz güç aktarımının çeşitli yönleri ele alınmıştır. Hem teorik gelişmelere hem de pratik uygulamalara odaklanarak fiziksel mekanizmalara, mevcut en son tekniklere, bunların sınırlamalarına ve hızla gelişen bu alanın beklentilerine ışık tutmaktadır [Covic, 2013]. Bu inceleme, modern teknolojik ortamda çeşitli uygulamalar için kablosuz güç aktarım sistemlerinin anlaşılmasına ve geliştirilmesine katkıda bulunmaktadır. Yalnızca elektrikli araçların kablosuz şarj edilmesi, tüketici elektroniği, vücuda yerleştirilebilir tıbbi cihazlar ve su altı ekipmanları gibi hâlihazırda uygulanmakta olan kablosuz güç iletimi alanını değil, uzay mikrodalga iletimi gibi araştırılmakta olan uygulamaları da ele almaktadır ve transfer arabalarında kullanımı kapsamında yol gösterici olmuştur [Liu, 2024].

Kablosuz güç aktarımı, elektrikli araç şarjı, akıllı telefon şarjı veya biyomedikal implantlara güç verilmesi gibi birçok alanda popüler bir teknoloji olarak halihazırda yerleşmiştir. Son yıllarda elektronik tekstillerde (e-tekstillerde) veya akıllı tekstillerde kablosuz güç aktarımı, tekstil malzemelerinin ve esnek elektronik bileşenlerin gelişmesiyle birlikte hızlı bir büyüme kaydetmiştir [Lui, 2013]. Gerçekleştirilen bir çalışmada e-tekstillerde WPT'ye ilişkin önceki literatürün karşılaştırmalı bir incelemesi verilmektedir. Tekstil tabanlı WPT sistemleri, verici

(Tx) ve alıcı (Rx) özelliklerine, Tx ve Rx üretim tekniğine, uygulanan alt katmana, çalışma frekansına, güç seviyesine ve elde edilen verimliliğe göre kategorize edilmiştir [Rahman, 2023]. Farklı parametrelerin tablo halinde analizi, araştırmacıların, üreticilerin ve endüstri personelinin farklı tekstil tabanlı WPT sistemlerini değerlendirmek için bilgi ve veri elde etmesi için bir platform görevi görmektedir. E-tekstillerde WPT uygulamalarının fırsatları ve zorlukları da bu alanın beklentilerine genel bir bakış sağlamak amacıyla ayrıntılı olarak tartışılmıştır [Lund, 2021].

Bir başka çalışmada ise pil depolamalı güneş enerjisinin, kablo ile kullanımı yerine, kablosuz güç aktarımı (WPT) arayüzü, elektrik izolasyonu, daha düşük bakım maliyeti, daha iyi güvenilirlik gibi ek avantajlarla birlikte kurulumu kolaylaştırarak karmaşık kablolama parçasını büyük ölçüde azaltılabileceğini gösterilmiştir [Ghosh, 2023]. Bu çalışma, güneş enerjili alçak gerilim (LV) güç kaynağı için akü depolamalı temassız güç aktarım sisteminin uygulamasını sunarak araştırma boşluğunu doldurmaktadır. Endüktif güç aktarımı (IPT) için çeşitli rezonans topolojileri incelenmiş ve pil enerji depolama sistemi ile entegre edilmiş LCL telafili IPT sisteminin eksiksiz bir teorik modeli sunulmuştur. Önerilen entegre IPT sisteminin LVDC düzeyinde çalışmasını anlamak için gerilim ve akım özellikleri araştırılmıştır. Kurulum ilk olarak MATLAB/Simulink kullanılarak simülasyonda gerçekleştirilip detaylı olarak analiz edilmiştir.

70 Ton Transfer Arabası Tasarımı

Temassız enerji sistemi ile çalışan bobin transfer arabasının taşıma kapasitesi 70 Ton olacak şekilde, 2 adet çelik bobini 1.5 metre ray ekseninde ve 16.5 metre çalışma yolu uzunluğunda taşıyabilecek güçte tasarlanmıştır.

Tasarım Hesaplarının Yapılması

Tasarımın ilk aşamasında bazı hesaplamlar yapılmaktadır. Bu hesapların yapılmasında Ansys2021v1, Solidworks2021 ve kiriş analizlerinde Autocad yazılımları kullanılmaktadır. Tüm hesaplamalar sonunda bir hesap raporu oluşturulmaktadır. Bu hesap raporunda aşağıda belirtilen parametreler hesaplanmaktadır:

A. İlk aşamada FEM e göre Yükleme Halleri incelenir Bu aşamada;
   - Konstrüksiyon Hesabı ile çelik yapı belirlenir
   - Mekanizma Hesapları ile tekerlek, rulman, motor, redüktör aksamları belirlenir

B. Araba Yürütme Grubu hesaplamasında ise çalışma yükü, toplam kaldırma grubu ağırlığı, toplam hareketli kütle ağırlığı, araba yürütme hızı dikkate alınarak aşağıdaki parametreler hesaplanır:

- Arabaya Etki Eden Rüzgar Kuvveti
- Tekerlek Çapı, Araba Teker Arası Mesafe, Araba Aksı
- Yürütme Grubu Toplam ve Tahrikli Teker Sayısı
- Araba Yürütme Rayı
- Araba Yürütme İvmelenmesi
- Toplam Tahrik Verimi
- Teker Sürtünme Katsayısı.

  4 tahrikli teker kullanımının yeterli olduğu bulunmuştur.

C. Yürütme Motor Kontrolü için ivmelenme ve toplam kalkış momentleri hesaplanarak Araba Yürütme Motor Seçimi gerçekleştirilir. Bu tasarım için 50 Hz için 1500 Motor Devir hızı uygun bulunmuştur.

D. Yürütme Redüktör Kontrolü için redüktör çıkış devri ve İhtiyaç Redüktör Tahvil Oranı hesaplanarak uygun redüktörler (14 çıkış devir/dak.) seçilmiştir.

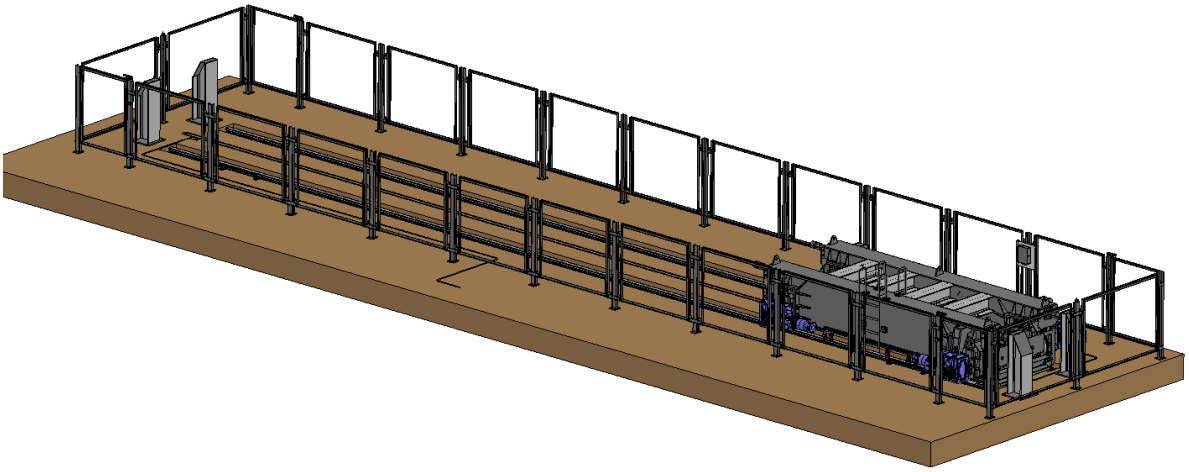
E. Yürütme freni için ihtiyaç fren torku hesaplanarak maksimum momenti 40 Nm olarak belirlenmiştir.

F. Teker Etkiyen Dikey Yüklerin Hesabı için, 13 ton araba ağırlığı dikkate alınarak; çalışma yükü, ölü ağırlık, Statik Test Katsayısı, FEM Emniyet Katsayısı, Ortalama Teker Yükü hesaplanmıştır.

G. Son aşamada ise tekere etkiyen yanal yükler hesaplanarak tekerlerin sınır basıncı kontrolü ve araba yürütme teker rulmanı kontrolü yapılır

Transfer Arabası tasarımı

Yapılan hesaplamalar sonucunda yukarıda bazı detayları verilen transfer arabasının her biri maksimum 32 Tonluk iki bobini taşıyabileceği öngörülmüştür. Şekil 1'de tasarımı gerçekleştirilen Temassız Enerji Sistemi Transfer Arabasının 3D görseli paylaşılmıştır.

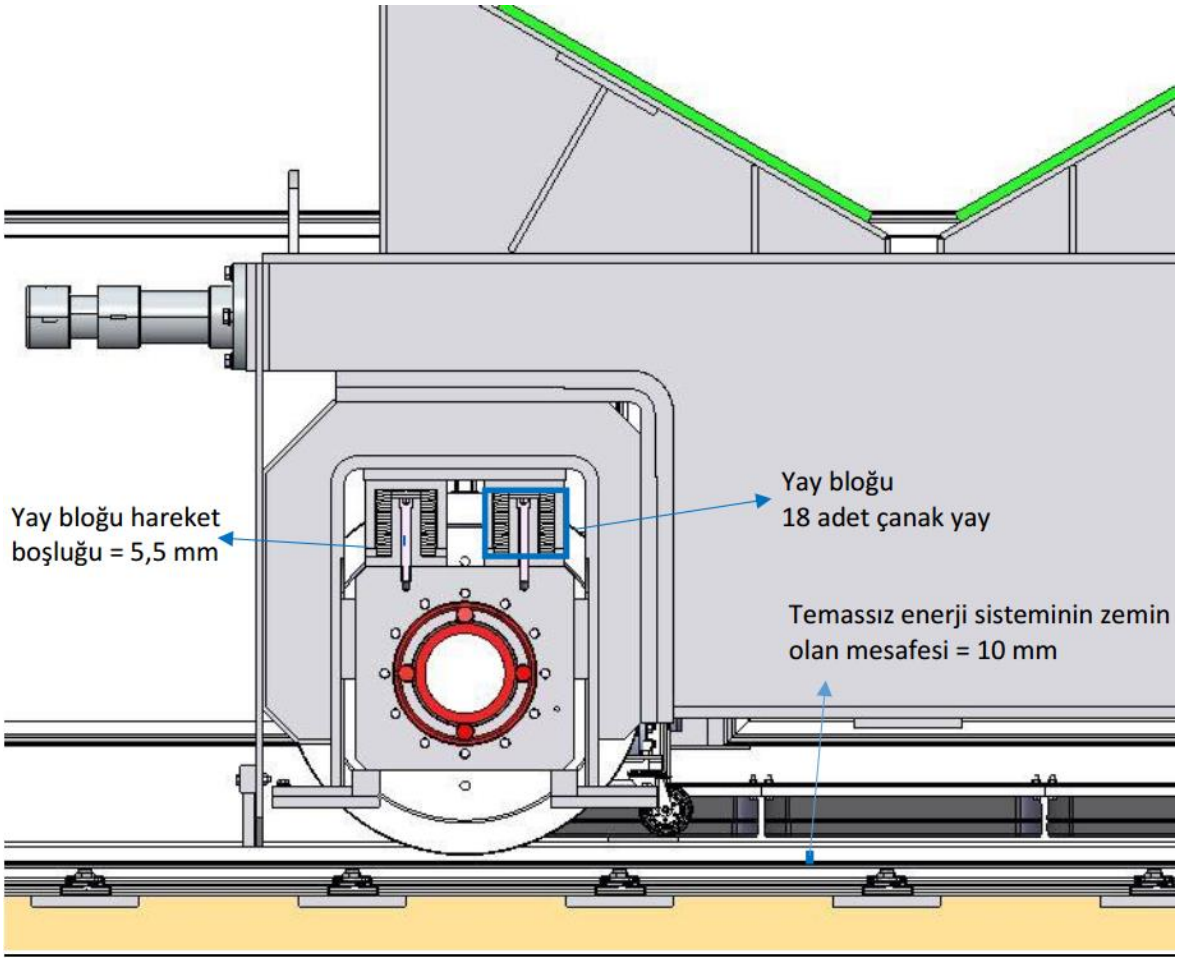


Şekil 1. Temassız Enerji Sistemi Transfer Arabası 3D resim

Ortam sıcaklığı 50 °C'nin üzerinde ve açık ve kapalı ortam şartlarında çalışabilme özeliğine sahip olarak tasarlanan transfer arabasının rayları, hemzemin olacak şekilde tasarlanmıştır. Zemin üzerinde kablo/tava geçişi olmayacaktır ve kullanılan temassız enerji sistemi sayesinde aracın üzerinde herhangi bir pil veya kablo sistemi olmadan çalışacaktır.

Transfer arabasının ön ve arka tarafına alan tarayıcı özelliği olan (radar) ve fensler arası yatay alanı komple tarayabilecek özelliğe sahip radar çarpışma sensörleri de tasarıma eklenmiştir. Ek olarak makinaların sistemlerinde çakışma vb. problemler yaratmayacak şekilde Kablosuz haberleşme sistemi de bulunacaktır.

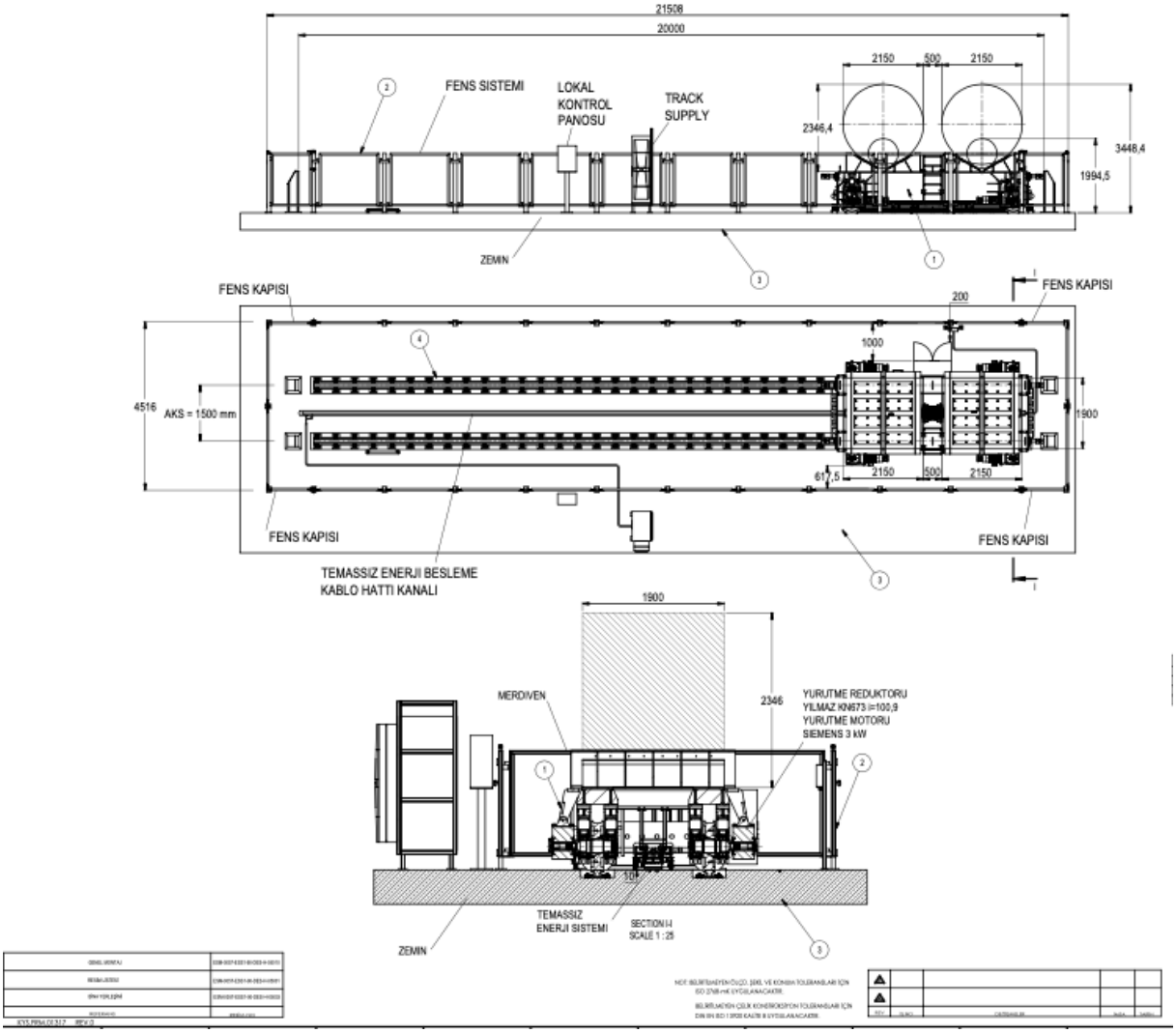
Teker yatakları ile araba şasesi arasında yaylar bulunacaktır. Bu nedenle Şekil 2'de görünen çanak yay sistemiyle ilgili hesaplamalar yapılmıştır.



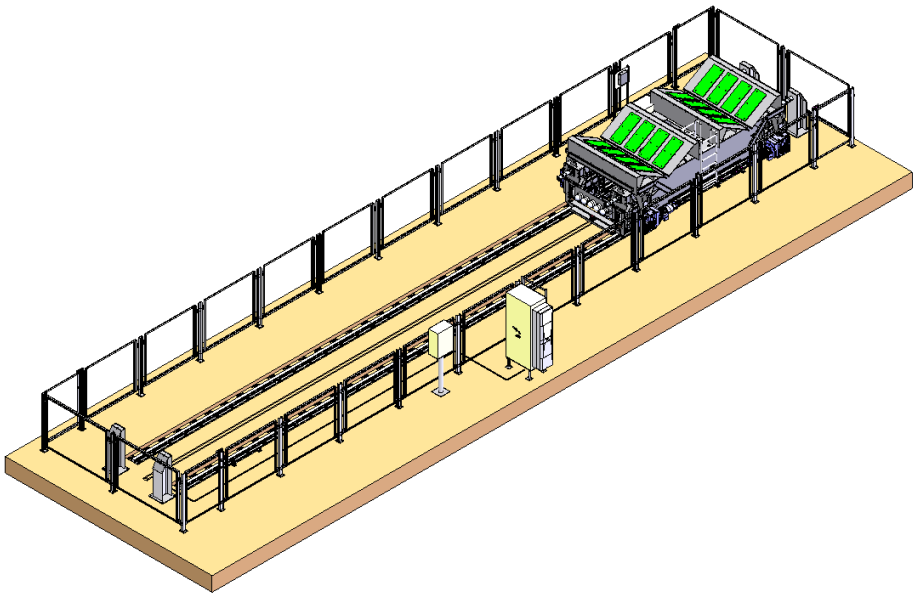
Şekil 2. Çanak Yay Sistemi

Hem manuel ve hem de otomatik olarak çalışabilecek şekilde tasarlanan transfer arabasının kontrolü lokal kontrol panelinden yapılabilecektir. Çalışma mekanizması, bobinler yüklendiğinde transfer arabası hareket edecek ve diğer tarafta arabanın yürüme yolu üzerinde her iki yönde yavaşlatma, durdurma switchleri ile duracaktır. Aynı şekilde boşaltma tamamlandığında yükleme noktasına geri dönebilecek şekilde tasarlanmıştır. Bobinleri algılama limit anahtarı sayesinde, tüm bobinler yüklenmeden veya boşaltılmadan transfer arabasının hareket etmemesi sağlanacaktır. Fren tipi olarak elektromanyetik fren kullanılacaktır. Transfer arabası hareket halindeyken hareket yönündeki hollerde çalışan vinçlerin taşıdığı yüke ve tonga çarpmasına karşın; her holde yapılacak bir şase üzerine photocell switch ve vinç kiriş altlarına reflektör montaj edilecektir.

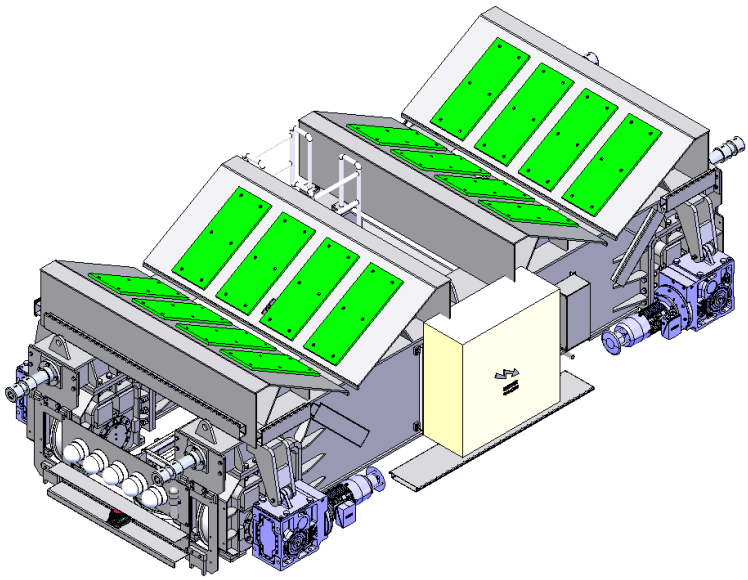
Sistemin teknik tasarımına ait detaylar Şekil 3'te, 3D görüntüleri ise Şekil 4a ve 4b'de gösterilmiştir.



Şekil 3. Transfer Arabasının Teknik Tasarım Çizimi



Şekil 4a Transfer Arabası-Ray Tasarımı



Şekil 4b Transfer Arabası 3D model perspektif görünümü

Tasarlanan Sistemin Yenilikçi Özellikleri:

Geliştirilen transfer arabası, en son teknoloji ekipmanları kullanarak üstün performans ve verimlilik sağlayacaktır.

Temassız enerji transfer sistemi, arabaya batarya veya elektrik kablosu kullanmadan enerji aktaracak ve bakım maliyetlerini azaltacaktır.

Yüksek performanslı kontrollere sahip transfer arabası, hassas kontrol ve izleme yaparak sistemini maksimum verimlilikte çalıştıracaktır. Ayrıca, araba yaylı süspansiyon sistemi sayesinde yükleme dengesizliklerini önleyecek ve böylece verimliliği ve maliyet tasarrufunu artıracaktır.

Bu projenin yenilikçi yönü, transfer arabasına güç sağlamak için kullanılan ve pil veya elektrik kablosu ihtiyacını ortadan kaldıran temassız enerji yöntemidir.

Temassız enerji sistemi kullanılarak akü veya kablo değişimine gerek kalmayacağından transfer arabasının kullanım ömrü daha uzun olacak ve akü veya busbar sistemi olmadığı için araç daha fazla alana sahip olacaktır. Ayrıca kabin üzerinde bulunan yaylar, yük farklarından kaynaklanan dengesizlikleri önleyerek verimliliğin artmasını ve maliyet tasarrufu sağlayacaktır.

Bu projede tasarlanan transfer arabası 70 ton taşıma kapasiteli 2 adet çelik rulo taşıyabilecek yapıda olacaktır. Temassız enerji sistemi ile tam yükte çalışabilecek olan ürün, çalışma esnasında farklı ağırlıklarda yüklenen bobinleri dengeli bir şekilde taşıyabilecektir.

Transfer arabasında kullanılan temassız enerji sistemi, yüksek enerji verimliliği sağlayarak sürekli bakım ihtiyacını ortadan kaldıracak ve uzun bir kullanım ömrü sunacaktır.

Projenin temel işlevselliği ve yenilikçi yönü, tasarımda akü veya bara sistemi kullanılmadığından, araba üzerinde alan kazanma avantajı sağlanmasıdır. Ayrıca akü kullanılmadığı için ürün daha uzun ömürlü olacaktır.

Kablo karmaşası olmadığından bakım kolaylığına sahip olacaktır.

Temassız Elektrik Sistemi

Yukarıda bahsedilen Transfer arabasında kullanılan Temassız Elektrik Sistemi olarak İndüktive bir elektrik sistemi kullanılmıştır. Bu systemin kullanılma nedenleri aşağıda verilmektedir:

- Bakım gerektirmez – yüksek kullanılabilirlik
- Sürekli çalışma mümkündür, dolayısıyla daha az araç gereklidir

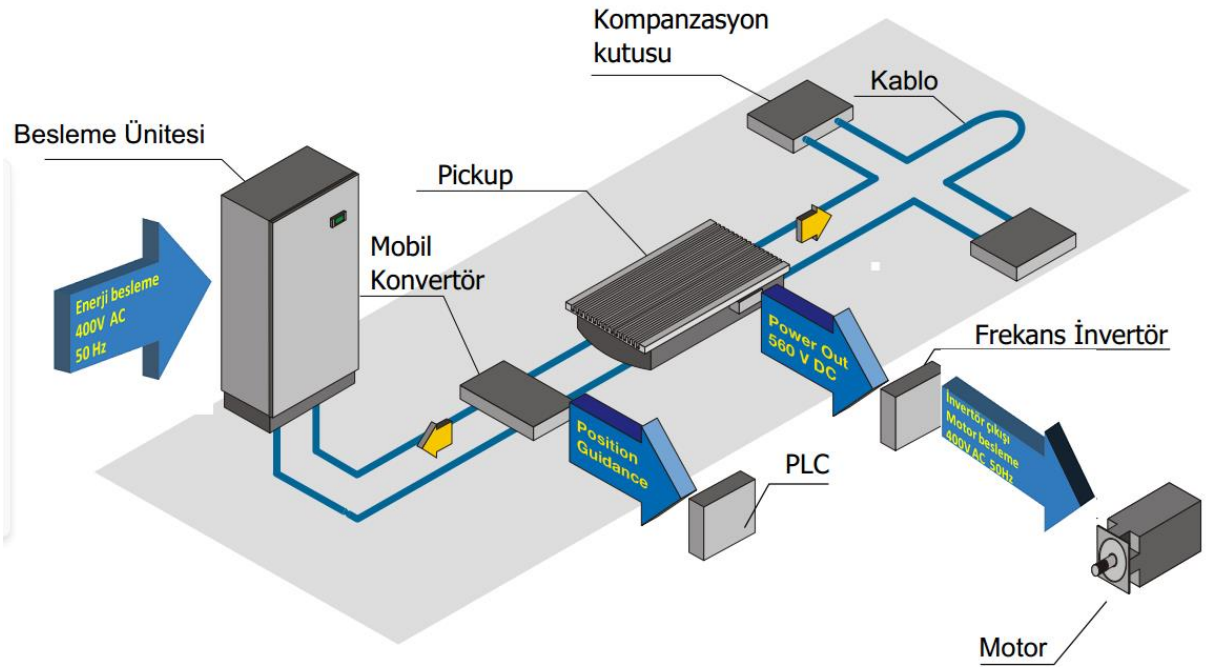
- Akümülatörlerle karşılaştırıldığında atık yönetimi yoktur
- Sınırsız zemin kullanımına imkan tanır
- Güç ve veri aktarım bileşenlerinde mekanik koruma yoktur
- Mümkün olan zorlu ortamlarda (toz, su, yağ...) kullanım mümkündür.
- Galvanik izolasyon sayesinde yüksek elektrik güvenliği sağlar
- Toprak potansiyelinden kaynaklanan tüketici yüküne sahiptir.
- Gürültüsüzdür.

Sistemin Çalışma Prensibi Şekil 5'te verilmektedir.

Endüktif Güç Transferi, güç ve dijital verilerin mekanik veya elektriksel temas olmadan aktarılmasını mümkün kılan ve yüksek hızlara ve aşınmaya karşı mutlak dirence bağlı mobil elektrifikasyon sistemlerine ihtiyaç duyan tasarımcılara birçok olasılık açan bir teknolojidir.

Zemine veya başka bir yüzeye gömülü birincil hat kablolarına sahip ve düz F-Pickup'larla kullanılan Endüktif Güç Transfer Zemin sistemleri. Öncelikle yüzeyde çalışan araçlarda kullanılır.

Otomatik Güdümlü Araç (AGV), Otonom Mobil Robot (AMR/Cobot) gibi çeşitli araçlar için otomatik, tamamen müdahalesiz ve verimli akü şarjı sağlayan temassız, endüktif bir bağlantı sistemidir.



Şekil 5. Temassız elektrik sisteminin çalışma Prensibi

Tasarımı yapılan Transfer arabasında Conductıx – Inductive Power Transfer(IPT®) temassız elektrik sistemi kullanılmıştır. Bu system (IPT®) neredeyse tüm elektrik üretimi ve iletiminin yanı sıra diğer birçok elektrikli ve elektronik cihazla aynı prensibe dayanmaktadır: elektromanyetik indüksiyon. Bir transformatör gibi, birincil devredeki alternatif elektrik akımı da alternatif bir elektromanyetik alan üretir. Elektromanyetik indüksiyon yasasına göre bu alan, yakındaki ikincil devrede alternatif bir akımı indükler [Aditya, 2014].

Klasik bir transformatörden farklı olarak (her ikisi de paylaşılan bir demir veya ferrit çekirdek ile yakından bağlanmış birincil ve ikincil parçaya sahip), IPT® ayrı birincil ve ikincil parçalardan oluşur [Lui, 2011]. Birincil kısım genellikle bir birincil bobinden değil, bir iletken halkadan oluşur. Bu iletken döngü, güç sağlanacak araçların hareket yolu boyunca bir çift kablo olarak kurulur. Birincil ve ikincil parçalar artık sabit bir çekirdek aracılığıyla bağlanmamaktadır.

İkincil Pikap serbestçe hareket edebilir. Ana iletkenlere göre hava boşluğu ve yeterli toleranslarla konumlandırılabilir ve ayrıca her hızda hareket edebilir.

Birincil iletken etrafındaki alternatif alanın frekansı, bir IPT sisteminin işlevi ve verimliliği için belirleyici bir faktördür. Normal elektrik kaynağı 50-60 Hz'de çalışırken IPT® genellikle 20.000 Hz frekansında, yani bunun yaklaşık 400 katı yükseklikte çalışır.

Bu, gücün büyük hava boşlukları üzerinden etkili bir şekilde aktarılmasını mümkün kılar.

İndüklenen alternatif akımın kullanılabilir hale getirilmesi için bir kontrol devresi ile düzenlenmesi gerekir. Bu patentli kontrol devresi, birincil hattaki istenmeyen geri beslemeyi azaltmaktan sorumludur [Rahman, 2021]. Böylece birden fazla bağımsız değişken yükün tek bir birincil yol üzerinde çalışmasını sağlar. Bu, çok sayıda bağımsız aracın bulunduğu malzeme taşıma uygulamalarının tek bir sistemde çalıştırılması için temel bir gerekliliktir.

Modern bir malzeme taşıma çözümünde güç aktarımının yanı sıra güvenilir veri aktarımı da vazgeçilmezdir. iDAT, sinyal yayılımının çok hassas bir şekilde tanımlanmasını sağlayan, diğer radyo kontrollü sistemlere müdahale etmemesini ve bunlardan etkilenmemesini sağlayan endüktif bir veri aktarım sistemidir [Zhang, 2018 – Birajdar, 1981]. Sürekli zemin tabanlı endüktif sistemlerle iDAT, araç yönlendirme ve konumlandırma işlevlerini de sağlayabilir. Araç yönlendirmesi için ana iletkenin etrafındaki alan, araç kontrolörüne hassas bir dijital sinyal sağlamak amacıyla kullanılır. Konum için, zemindeki Konum İşaretleri ana hattan gelen manyetik alandan güç alır ve bu nedenle konum kodlarını sürekli olarak iletebilirler. Araçta herhangi bir aktivasyon elektroniğine gerek yoktur.

İki temel düzenleme vardır:

1. IPT®-Ray :Sistemler, bir E-Pickup'ın her iki hat kablosunu da birkaç taraftan sardığı, çıkıntılı bir birincil hat düzenlemesine sahiptir. Öncelikle raya monteli uygulamalarda kullanılır.
2. IPT®-Zemin: zemine veya başka bir yüzeye gömülü birincil hat kablolarına sahip ve düz F-Pickup'larla kullanılan sistemler. Öncelikle yüzeyde çalışan araçlarda kullanılır.

SONUÇLAR

KÜMSAN'da temassız enerji sistemi ile çalışan bobin transfer arabası tasarlamış ve üretimine başlanmıştır. Bu transfer arabasının rayları hemzemin olarak imal edilecektir. Tasarlanan transfer arabasının, kullanılan temassız enerji sistemi sayesinde aracın üzerinde herhangi bir pil veya kablo sistemi olmayacağı için daha fazla kullanım alanı sunmaktadır.

Arabanın önüne çıkabilecek personel ve parçalar için transfer arabasının ön ve arka tarafına alan tarayıcı özelliği olan (radar) ve fensler arası yatay alanı komple tarayabilecek, mesafesi ve tarama açısı ayrıca ayarlanabilir özelliğe sahip radar çarpışma sensörleri tasarıma eklenmiştir. Böylelikle transfer arabası alandaki mesafesini ayarlayabilecek ve önüne bir engel çıkması durumunda transfer arabası durabilecektir.

Çalışma mekanizması, bobinler yüklendiğinde transfer arabası zaman gecikmeli olarak hareket edecek ve diğer tarafta arabanın yürüme yolu üzerinde her iki yönde yavaşlatma, durdurma switchleri ile duracaktır. Fren tipi olarak elektromanyetik olarak kullanılacak ve böylelikle yüksek performanslı, sessiz ve hızlı tepki veren bir fren sistemiyle transfer arabası durdurulabilecektir. Aynı şekilde boşaltma tamamlandığında zaman gecikmeli olarak yükleme noktasına geri dönebilecek şekilde tasarlanmıştır. Bobinleri algılama limit anahtarı sayesinde, tüm bobinler yüklenmeden veya boşaltılmadan transfer arabasının hareket etmemesi beklenmektedir. Şase üzerindeki switchler reflektörü 5 sn den fazla gördüğünde aktif olacak ve hareket eden transfer arabası rampalı duruşa geçecek şekilde tasarlanmıştır. Vinç uzaklaştıktan sonra switchler 10 sn reflaktörü görmediğinde araba/arabası otomatik hareketine devam etmesi beklenmektedir.

İş güvenliğini sağlamak adına fens geciş kapılarına sensörler yerleştirilerek ve otomasyon sistemine bağlı olan kapı sensörleri, kapı açık olduğunda araba hareketlerini engellenecektir. Ek olarak ransfer arabasının ön ve arka tarafında sesli, ışıklı ikaz olacak ve kumanda panelinde acil stop yerleştirilerek iş güvenliğini artırması beklenmektedir.

Tasarlanacak transfer arabası, mevcut sistemlere göre %50 daha yüksek bir enerji verimliliği sağlayacaktır.

Tasarlanacak transfer arabası, kablo karışıklığı olmadığı için bakım işlemleri oldukça kolaylaşacak ve maliyetlerde %30'a varan düşüş sağlnacaktır. Ayrıca temassız enerji sisteminin kendi bkım ihtiyacı da düşük olacağından bakım süresinde %50'ye varan azalma sağlanacaktır. Toplamda ise mevcut sistemlere göre %80 daha uzun ömre sahip olacaktır.

Tasarlanacak transfer arabası, üzerindeki yaylar sayesinde yükler arasındaki farklılıklardan kaynaklı dengesizlikleri engelleyerek, taşıma esnasında %95'e varan bir yük dengesi sağlayacaktır.

Tasarlanan transfer arabası, Temassız enerji sistemi sayesinde kullanım sırasında pil değiştirme veya şarj işlemleri gerektirmeyecektir. Bu sayede yüksek verimli enerji kullanımı sağlanarak işletme maliyetleri %40'a kadar azaltılabilir.

KAYNAKÇA

1. **Li, S., Mi, C.C. (2014),** " Wireless Power Transfer for Electric Vehicle Applications", IEEE Journal of Emerging and Selected Topics in Power Electronics, Vol. 3, ISSUE 1, pp 4 – 17.

2. **Lashkari, K., Shladover, S.E., Lechner, E.H. (1986),** "INDUCTIVE POWER TRANSFER TO AN ELECTRIC VEHICLE", Science Engineering Medicine, pp 258-267.

3. **Fan, M., Shi, L., Yin, Z., Li, Y. (2017),** " A novel pulse density modulation with semi-bridgeless active rectifier in inductive power transfer system for rail vehicle", CES Transactions on Electrical Machines and Systems, Vol. 1, ISSUE 4, pp 397 - 404.

4. **Hasanzadeh, S., Vaez-Zadeh, S. (2013),** "Efficiency analysis of contactless electrical power transmission systems", Energy Conversion and Management., Vol.65, pp 487-496.

5. **Covic, G.A., Boys, J.T. (2013),** "Inductive power transfer", Proc. IEEE., Vol.101, pp 1276-1289.

6. **Liu, Z., Li, T., Li, S., Mi, C.C. (2024),** " Advancements and Challenges in Wireless Power Transfer: A Comprehensive Review", Nexus., Vol.1, ISSUE 2.

7. **Lui, K.W., Murphy, O.H., Toumazou, C. (2013),** "A wearable wideband circularly polarized textile antenna for effective power transmission on a wirelessly-powered sensor platform", IEEE Trans. Antennas Propag, Vol.61, pp 3873-3876.

8. **Rahman, S., Haque, M.A., Solaiman, M., Ratul, R.H. (2023),** "Wireless power transfer using electronic textiles: A comparative review", Journal of Engineering Research.

9. **Lund, A., Wu, Y., Fenech-Salerno, B., Torrisi, F. (2021),** " Conducting materials as building blocks for electronic textiles", MRS Bull, Vol.46, pp 491-501.

10. **Ghosh, A., Gamage, D., Zhang, X., Ukil, A., Hu, A.P. (2023),** "Easy-to-install battery storage based residential power supply with contactless power transfer", Journal of Energy Storage, Vol.72.

11. **Aditya, K., Williamson, S.S. (2014),** " Design considerations for loosely coupled inductive power transfer (IPT) system for electric vehicle battery charging-A comprehensive review", IEEE Transportation Electrification Conference and Expo, ITEC, IEEE, pp 1-6.

12. **Lui, C., Hu, A.P., Wang, B., Nair, N. (2011),** " A capacitively coupled contactless matrix charging platform with soft switched transformer control", IEEE Trans. Ind. Electron, Vol.60, pp 249-260.

13. **Rahman, S., Kosesoy, M.A., Ozdemir, O., Simsek, M.T., Aydemir, A. (2021),** Design and Practical Implementation of a Parallel-Switched Power Factor Correction Boost Converter", Proceedings of the 2021 Fourteenth IEEE International Conference on Industry Applications (INDUSCON), IEEE, pp 395–400.

14. **Zhang, Z., Pang, H., Georgiadis, A., Cecati, C. (2018),** " Wireless power transfer—An overview", IEEE Trans. Ind. Electron, Vol. 66, pp 1044-1058.

15. **Birajdar, S.R. (1981),** " Wireless Energy Transmission", Trans. Microw. Theory Techn., Vol. 29, pp 1319-1327.

YÜKSEK HACİMLİ TALAŞ KALDIRMA KAPASİTESİNE SAHİP FREZE TEZGAHI İÇİN TAKIM DEĞİŞTİRME SİSTEMİNİN GELİŞTİRİLMESİ

Can TUNCER, *can.tuncer@gri.com.es,* Gesbey Enerji Türbini Kule Üretim San. ve Tic. A.Ş., 10680, Balıkesir

Talat Yiğit GENCEL, *talatyigit.gencel@gri.com.es,* Gesbey Enerji Türbini Kule Üretim San. ve Tic. A.Ş., 10680, Balıkesir

Enver YALÇIN, *eyalcin@balikesir.edu.tr,* Balıkesir Üniversitesi, 10145, Balıkesir

Ali ORAL, *a.oral@balikesir.edu.tr,* Balıkesir Üniversitesi, 10145, Balıkesir

ÖZET

Günümüzde CNC tezgahlarda kullanılmakta olan farklı yapılarda otomatik takım değiştirme sistemleri mevcuttur ve bu sistemler takım değiştirme sürelerinin minimize edilmesiyle imalat sürelerinin kısaltılmasına odaklanmıştır. İmalatta, süreçlerin en iyi şekilde yönetilmesi ve kaynakların verimli kullanılması günümüzün rekabetçi ortamında ayakta kalabilmenin en önemli parametreleridir. Bu çalışmada bir pasoda 30 mm kaynak ağzı açmak amacıyla geliştirdiğimiz otomatik kaynak ağzı açma makinesi takım değiştirme sistemi geliştirilmiştir. Geliştirilen tezgahta kullanılan takım tutucu boyutlarının ve kütlesinin geleneksel takımlara göre büyük oluşuna paralel olarak, otomatik takım değiştirme sistemi büyük takım tutucuların insan gücüyle değiştirilmesindeki ergonomik zorluklar ve hızlı takım değiştirme ihtiyacı nedeniyle terzi usulü-tezgaha özel takım değiştirme sistemi geliştirilmiştir.

Anahtar terimler: otomatik takım değiştirici, takım değiştirici, takım tutucu

ABSTRACT

Today, there are automatic tool change systems having different structures used in CNC machines, and these systems are focused on shortening production times by minimizing tool change times. In manufacturing, the best management of processes and efficient use of resources are the most important parameters of surviving in today's competitive environment. In this study, the automatic beveling machine tool change system, which we developed in order to open a 30 mm bevel in a pass, was developed. In parallel with the large size and mass of tool holders used in the developed machine compared to traditional tools, the automatic tool change system has been developed as a tailor-made tool-specific tool

changing system due to the ergonomic difficulties in replacing large tool holders with manpower and the need for fast tool change.

Key Words: automatic tool changer, tool changer, tool holder

1. GİRİŞ

Günümüzün çevik üretim ortamında sürekli olarak verimlilik, doğruluk ve üretkenliği artırmanın arayışları sürmektedir. Modern, hızlı ve hassas talaş kaldırma işlemlerinde kullanılan CNC tezgahlar ile üretim hızının artmasına karşın hala işlem dışı zamanlarda harcanan süreyi düşürme çabaları devam emektedir. Otomatik takım değiştirme (OTD) sistemleri CNC tezgahlar için devrim yaratan bir yenilik olarak görülmüştür. OTD sistemi, takım tezgahlarında kullanılan kesici takımların otomatik olarak değiştirilmesini sağlayan bir mekanizmadır.

Otomatik takım değiştirme işlemi tüm CNC takım tezgahlarına uygulanabilen ve üretim verimliliğine etki eden, üretimin kesintisiz ve daha düşük maliyetle gerçekleştirilebilmesine katkı sağlayan bir sistemdir [Lianzhong ve ark. 2010]. Bir CNC tezgahtaki takımların otomatik olarak değiştirilmesiyle, takım değişiminde harcanan üretken olmayan yardımcı süre büyük ölçüde en aza indirilirken aynı zamanda operasyonların hassasiyeti ve iş güvenliği de artmaktadır [Obreja ve ark., 2013; Tao ve ark., 2011].

Farklı yapıdaki CNC tezgahlarda farklı tip OTD sistemleri vardır ve OTD sistemleri genel olarak; döner tip (Şekil 1.a [Anonim-1], zincir tipi (Şekil 1.b [Anonim 2]), kavrama tipi (Şekil 1.c [Anonim 3]), lineer tip (Şekil 1.d [Anonim 4]) gibi farklı yapılarda olabilir.



Şekil 1. OTD tipleri

OTD sisteminin tasarım özellikleri CNC takım tezgahının özelliklerine ve kısıtlarına bağlı olarak belirlenir [Gökler ve ark.,1997]. Bu çalışmada 3000x14000x30 mm boyutlarına sahip rüzgar türbin kule saclarına bir pasoda 30 mm kaynak ağzı açabilen bir tezgah [TUNCER, 2022] için OTD sistemi geliştirilmiştir. Söz konusu tezgahta kullanılan kesici takım (Şekil 2) kütlesi 40 kg 'dır.



Şekil 2. Kaynak ağzı açma takımı

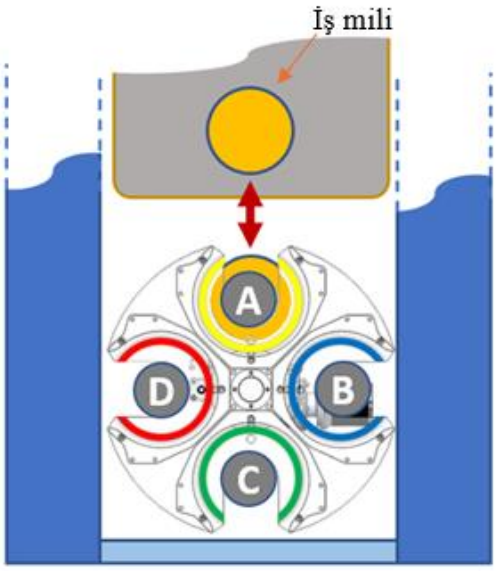
Yüksek hacimli talaş kaldırma işlemi yapan bu tür tezgahlar incelendiğinde, takım değiştirme işlemlerinin manuel olarak yapıldığı görülmüştür. Bu büyüklükte bir kesici takımın operatör marifetiyle değiştirilmesi esnasında bazı risk ve problemlerle karşılaşılabilmektedir. Bu problemlerden bazıları aşağıda örnek olarak verilmiştir.

- Söz konusu kesici takımların makine üzerinden operatör kontrolüyle manuel olarak hidrolik el kaldıraçları vasıtasıyla uzun sürede, iş ve personel sağlığını tehlikeye atacak şekilde değiştirilmektedir.
- Operasyon esnasında farklı kaynak ağızlarının oluşturulması için farklı açılarda takımlar kullanılabilmektedir. Manuel olarak yapılan takım değiştirme işlemi nedeniyle iş miline hatalı takım takılabilir.

Bu problemleri gidermek ve prosesin ihtiyaçlarını karşılamak amacıyla geliştirilen bu özel frezeleme makinesine entegre olarak çalışabilecek bir otomatik takım değiştirme mekanizmasının geliştirilmesi hedeflenmiştir. Bu çalışmada, üzerinde 4 takım depolayan döner tip OTD geliştirilmiştir.

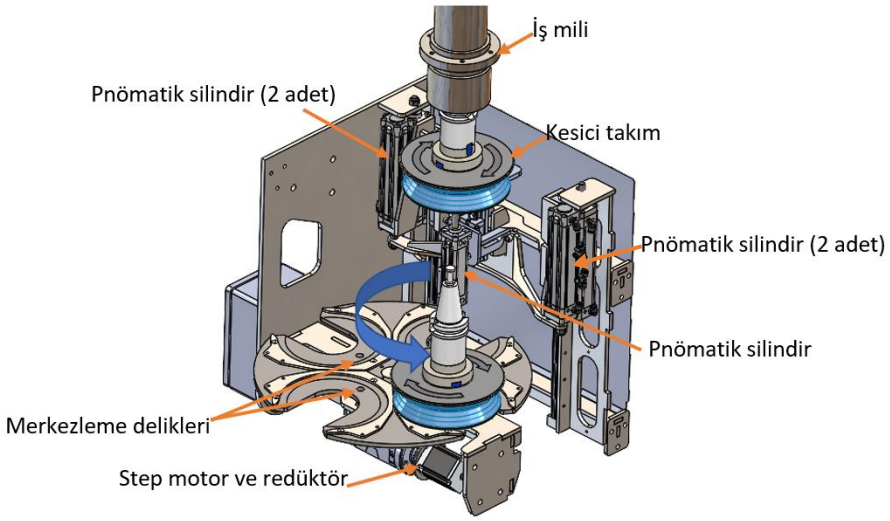
2. TASARIM VE TASARIM DOĞRULAMA ÇALIŞMALARI

Çalışmada tezgah iş milinde ve slotlar üzerindeki takımların varlık ve yokluk durumunu algılayabilen 4 slotlu bir OTD tasarım (Şekil 3) ve üretimi gerçekleştirilmiştir. Söz konusu sistem, kaynak ağzı açma/kenar frezeleme işleminde kullanılan kesici takımların otomatik olarak değiştirilmesi için makineye ve prosese özel olarak geliştirilmiş bir mekatronik sistemdir.



Şekil 3. Otomatik kesici takım değiştirme mekanizmasının şematik görseli

Mekanizmada yer alan dairesel döner tabla üzerinde 4 adet slot bulunmakta olup, kesici takımlar farklı kaynak ağzı açıları için 4 farklı slota yerleştirilmektedir. Şekil 4 'te geliştirilen OTD 'nin 3D görseli verilmiştir.

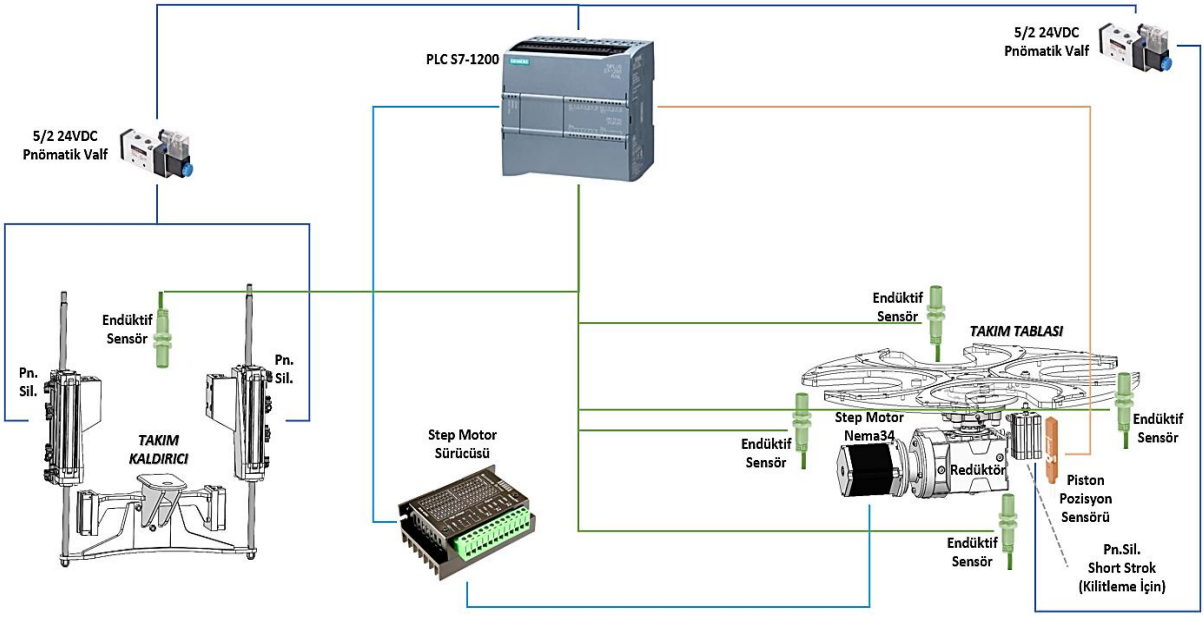


Şekil 4. OTD Sistemi 3D CAD görseli

OTD sisteminde, slotlara yerleştirilen kesici takımlar, taşıyıcı plaka ile 90° ve katları açılarla döndürülerek istenilen takımın, takım değiştirme noktasına gelmesi sağlanmaktadır. Kesici takımın iş mili ile tam olarak merkezlenmesi için plaka üzerinde bulunan deliklere, pnömatik silindir ile konik merkezleme pimleri yerleştirilmektedir. Kesici takımın değiştirme işlemi, tezgahta operatörün komut vermesiyle gerçekleştirilmektedir. Takım değiştirme komutu verildiğinde OTD üzerindeki boş slot, takım indirme pozisyonuna gelecek şekilde redüktör-motor grubu ve endüktif sensör yardımıyla doğru slotun istenen konuma geldiğine dair bir

sinyal oluşana kadar döndürülür. Spindle üzerinde bulunan takım serbest bırakılarak OTD üzerine alınır. Döner tabla üzerindeki ilgili slotta bulunan yeni kesici takımın makineye yüklenmesi istendiğinde, iş miline takılacak takım endüktif sensör tarafından algılandığında devreye giren takım kaldırma asansör grubu pnömatik silindirler tarafından yükseltilir ve iş mili üzerine montajı gerçekleşen yeni takım kilitlenerek takım değiştirme işlemi tamamlanmış olur.

Otomatik takım değiştirme sisteminin kontrol algoritmasını yürüten PLC sistemini içeren otomasyon birimi, takım kaldırma silindirleri üzerinde yer alan pnömatik silindir pozisyon sensörleri, takım tablası üzerinde yer alan takım var/yok denetimi yapan endüktif sensör, döner tablanın istenen slotunun istenen konuma gelmesinin doğrulamasını sağlayan pozisyonlama sensörleri, döner tabla kilitlemesi yapan pnömatik silindir ve üzerinde yer alan piston konum sensörlerinin tümü; algoritma gereğince doğru takımın doğru slota yerleştirilmesi, makinede takım varken takım yükleme yapılamaması, makinede takım yokken takım çıkarma yapılmaması, takım yüklenmesine/yüklenmemesine rağmen tablada takım varsa/yoksa hata sinyali oluşturması gibi çok sayıda karmaşık güvenlik doğrulamasını içermektedir. OTD sisteminin kontrol şeması Şekil 5'te verilmiştir.



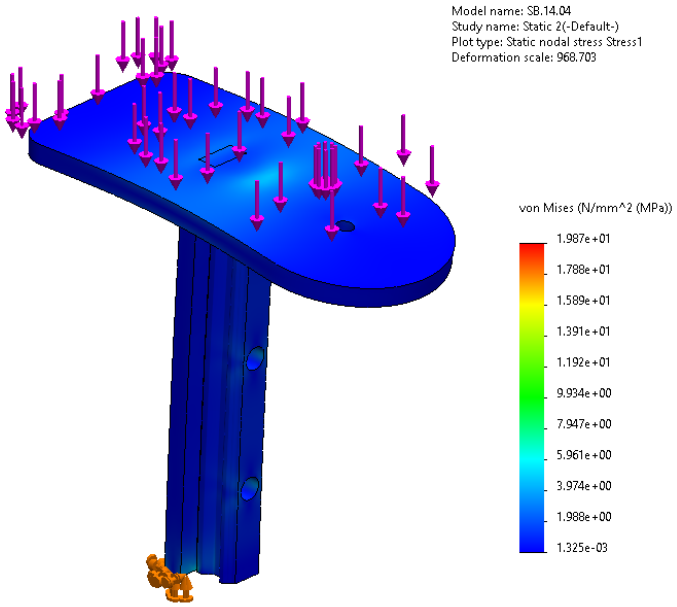
Şekil 5. OTD sisteminin kontrol şeması

Makine üzerindeki kısıtlı hacim ve erişme yükseklikleri nedeniyle kesici takım iş miline kadar yükselememektedir. Slot içinden yükselen üçüncü bir pnömatik silindir kesici takımın iş miline takılmasını sağlayacak şekilde devreye girmektedir (Şekil 6).



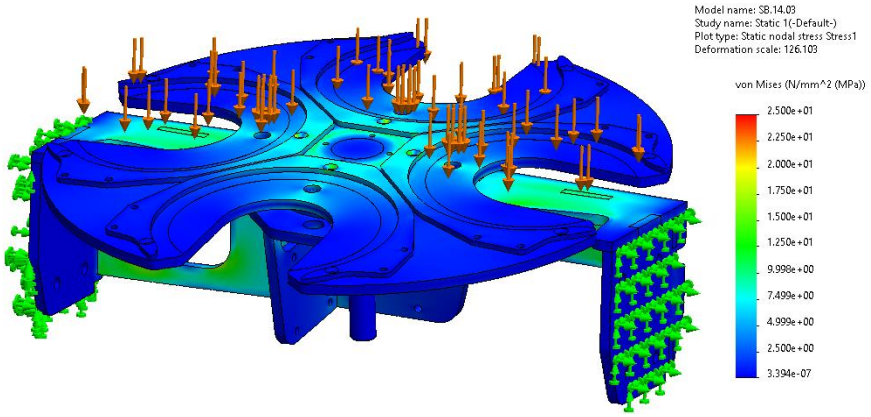
Şekil 6. Takım yükseltme sistemi

OTD' yi oluşturan çelik konstrüksiyon S235JR kalite sac malzemeden yapılmıştır. Tasarım doğrulama çalışmalarında öncelikle kritik görülen elemanlar dikkate alınmıştır. Sonlu elemanlar analizleri için SolidWorks Simulation kullanılmış olup Şekil 6 'da görülen takım taşıyıcısının analizinde taşınan yüklere karşı (400 N) 12 kat emniyetli olduğu görülmüştür (Şekil 7).



Şekil 7. Takım taşıyıcı tabla sütununun stres dağılımı

Bir diğer kritik aksam olan tabla grubu üzerinde her biri 400N yük uygulayan 4 adet takım bulunduğu varsayılarak yapılan statik analizde; yapının 9,4 kat emniyetli olduğu görülmüştür. Bu durum takım düşmesi ve diğer darbelere karşı yapının yeterince dayanıklı olduğu şeklinde yorumlanabilir.



Şekil 8. OTD tablasının stress dağılımı

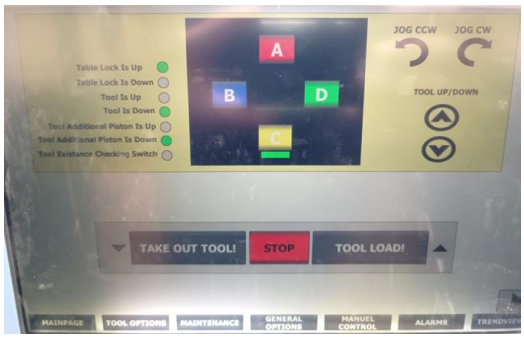
3. PROTOTİP ÜRETİMİ

Mekanizma ve otomasyon yapısının tasarım doğrulama çalışmaları tamamlandıktan sonra OTD 'nin prototip üretimi gerçekleştirilmiş ve tezgaha entegrasyonu yapılmıştır (Şekil 9).



Şekil 9. Freze makinesi üzerinde konumlanmış OTD

Takım değiştirme işlemi tezgah PLC otomasyonuna bağlı bir HMI (kontrol ekranı) üzerinden yürütülmektedir (Şekil 10).



Şekil 10. Takım değiştirici kumanda ekranı

4. SONUÇLAR

Gesbey Ar-Ge Merkezi tarafından geliştirilen Kaynak Ağzı Açma Tezgahına entegre edilen OTD sistemi, oluşan gerilmelere karşı yüksek emniyet katsayısına sahip olarak tasarlanmıştır. Başlangıçta manuel olarak, hidrolik kaldıraçlar ve operatör becerisi ile yapılan takım değiştirme işlemi iş sağlığı ve güvenliği açısından da önemli riskler içermekteydi. Geliştirilen OTD sistemi ile;

- Yanlış kesici takım kullanımının önüne geçilmesi mümkün olmuştur.
- Takım değişimi yüksek hassasiyetle pozisyonlama yapılmasıyla, el değmeden ve hatasız şekilde gerçekleştirilmektedir.
- Konvansiyonel kesici takımlara göre çok daha ağır özel yapım kesici takımlar emniyetli şekilde aktarılabilmektedir.
- Takım değişimi işlemi manuel proseste yaklaşık 10 dakikada gerçekleştirilebilirken geliştirilen OTD ile 30 saniye içinde yapılmaktadır.
- İş güvenli riskleri minimize edilmiştir.

5. KAYNAKLAR

1. **C.Tuncer, S.Türköz, A.Oral,** (2022); Determination Of Cutting Parameters For Aggressive-High Performance Chip Removal Of The Beveling Machine With Automated Workpiece Determination And Tool Path Generation System, The 19th International Conference on Machine Design and Production, Cappadocia, Turkey, s209-219

2. **Obreja, C., Stan, G., Andrioaia, D., & Funaru, M**. (2013). Design of an automatic tool changer system for milling machining centers. Applied Mechanics and Materials, 371, 69-73.

3. **Tao, Y., Chao-jian, L., Shou-quan, H., Xue-jun, J., & Wei, L.,** (2011); Design and study of control system of automatic tool changer. International Conference on Electric Information and Control Engineering, s. 4879-4881

4. **Lianzhong, Z., & Li, W.** (2010); Machining center automatic ATC analysis and research. 3rd International Conference on Information Management, Innovation Management and Industrial Engineering (Vol. 2, pp. 355-358)

5. **Gökler, M. I., & Koc, M. B.,** (1997); Design of an automatic tool changer with disc magazine for a CNC horizontal machining center. International Journal of Machine Tools and Manufacture, 37(3), 277-286.

6. **Anonim 1:** https://www.haascnc.com/haas-service-parts/tool_changer.html (E.T: 30.06.2024)

7. **Anonim 2:** https://mellowpine.com/cnc-tool-changer (E.T: 30.06.2024)

8. **Anonim 3 :** https://www.lvcnc.com/what-is-an-automatic-tool-changer-and-the-4-common-types.html (E.T: 30.06.2024)

9. **Anonim 4:** https://www.igolden-cnc.com/linear-atc-cnc-router-vs-circle-atc-cnc-router (E.T: 30.06.2024)

SİSTEMATİK KONSTRÜKSİYON YAKLAŞIMIYLA LİNEER RAY TAPASI MONTAJ APARATI TASARIMI

H. Aytuğ KURT, *hasankurt@yilmazmachine.com.tr* Yılmaz Makine, R&D Department, 41455, Kocaeli, Türkiye

Alper YETER, *alperyeter@yilmazmachine.com.tr* Yılmaz Makine, R&D Department, 41455, Kocaeli, Türkiye

Mustafa BAKKAL, *bakkalmu@itu.edu.tr* Istanbul Technical University, 34367, İstanbul,Türkiye.

ÖZET

Bu çalışmada, lineer rayların montaj deliklere takılan plastik tapaların kontrollü ve standart şekilde montajlanabilmesi için Sistematik Konstrüksiyon Yöntemiyle özel bir aparat tasarlanıp üretilmiştir. Tasarlanan aparat, ray tapalarının geleneksel metoda göre daha hızlı ve kaliteli çakılmasını sağlamış, aynı zamanda malzeme tasarrufu sağlamıştır. Yapılan 3 özdeş 1 metrelik rayda 17 adet tapanın montaj süresi ölçülmüş, aparatsız 8,058 saniye/tapa; aparatlı olarak ise 3,23 saniye/tapa olarak ölçülmüştür. Ayrıca aparatsız, 51 tapa montajında 11 adet fire verilmiştir. Aparatla yapıldığındaysa fire oluşmamıştır.

Sonuç olarak, bu teknikle yapılan tasarımların daha verimli ve yenilikçi olduğu görülmüştür. İlaveten bu teknikle sadece portatif aparatların değil aynı zamanda diğer makinelerin de tasarlanabileceği anlaşılmıştır.

Anahtar Kelimeler: Lineer Ray, Lineer Kizak, Lineer Araba, Plastik Tapa, Sistematik Konstrüksiyon.

ABSTRACT

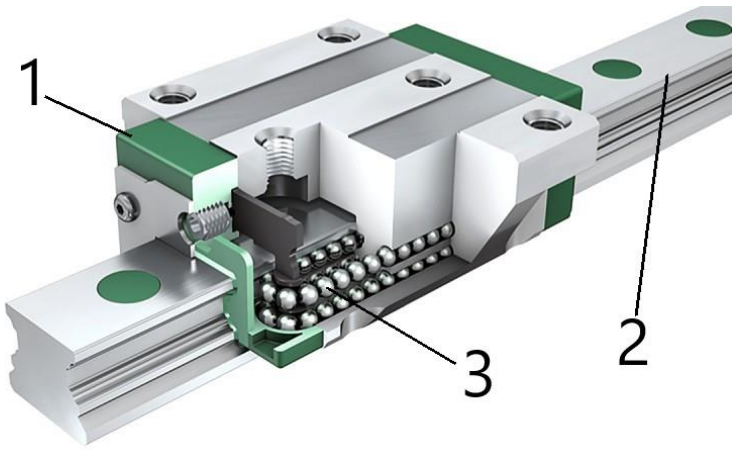
In this study, a special apparatus was designed and manufactured by Systematic Construction Method for controlled and standardized installation of plastic plugs inserted into the mounting holes of linear rails. The designed apparatus provided faster and higher quality fastening of the rail plugs compared to the traditional method, and at the same time saved material. The installation time of 17 plugs in 3 identical 1 metre rail was measured and it was measured as 8,058 seconds/tap without apparatus and 3,23 seconds/tap with apparatus. In

addition, without apparatus, 11 wastage was given in the assembly of 51 plugs. There was no wastage with apparatus. As a result, it was seen that the designs made with this technique are more efficient and innovative. In addition, it is understood that not only portable apparatus, but also other machines can be designed with this technique.

Keywords: Linear rail, Linear Guide, Linear Carriage, Plastic Plug, Systematic Construction.

1. GİRİŞ

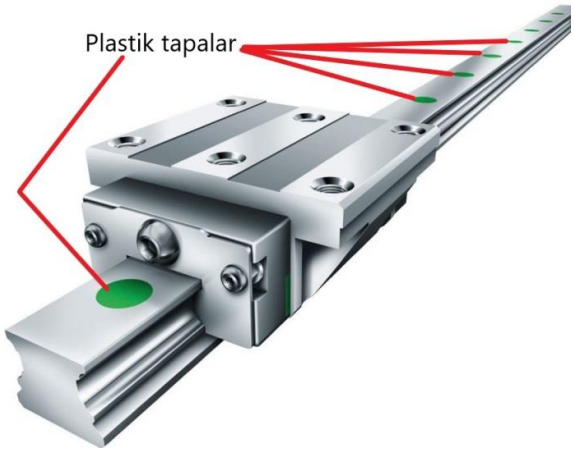
Doğrusal bir eksen boyunca yüklerin hassas biçimde taşınması için taşıyıcı görevi gören sistemler lineer kılavuz sistemi olarak tanımlanmaktadır. Lineer kılavuz sistemleri yüksek taşıma kapasitesi, yüksek hareket hassasiyeti, rijitliği ve diğer üstün özellikleri nedeniyle sanayide pek çok uygulamada kullanılmaktadır. Bu sistemler prensipte üç temel elemandan oluşmaktadır (Şekil 1.). Bunlar hareketli taşıyıcı araba/kızak (1), taşıyıcı arabayı hareket doğrultusunda destekleyen ray (2) ve taşıyıcı arabanın ray üzerinde hareketine imkan sağlayan bilyelerdir (3).



Şekil 1. Örnek bir lineer kılavuz sistemi.

Pek çok avantaja sahip bu sistemler hassas takım tezgahlarında, paketleme ve dolum makinelerinde, pek çok lojistik uygulamasında, inşaat sektöründe güvenlik kapılarında, sağlık sektöründe röntgen, MR vb. cihazlarda ve ek olarak çok çeşitli sektör ve uygulamada yaygın olarak kullanılmaktadır. Lineer kılavuz sistemlerinin tam performanslı çalışabilmesi için hassas eksen hattı boyunca montajlanması ve diğer montaj kurallarından taviz verilmemesi gerekmektedir. Bu sistemler, genellikle toz, talaş, yağ vb. hem mekanik hem de kimyasal kirliliğin olduğu ortamlarda çalışmaktadır. Yüksek hassasiyetlerde çalışan bu sistem tabii olarak kritik hareketli parçalarında mekanik/kimyasal kirliliğe karşı hassasiyete sahiptir. Özellikle taşıyıcı arabaların bilyeli yatakları, her ne kadar toz keçeleri ile korunmaya çalışılsa

da hareket ettikleri rayların üst satıhlarından şasilere bağlantı yapılan cıvata deliklerine toz, talaş vs. dolabilmektedir. Dolan bu mekanik bozucular, hassas çalışan bilye-yatak sistemine zarar verip servis dışı bırakabilmektedir. Bu tip kirlenmelere karşı hassas olan sistemin kararlı hale gelmesi için ray bağlantı delikleri, cıvatalarla montaj yapıldıktan sonra Şekil 2'deki gibi plastik tapalarla kapatılmaktadır. Dolayısıyla bu tapaların doğru çakılması, sistemin kararlı çalışması için kritik öneme sahiptir. Çalışma kapsamında tapa montajlarının hassas, kontrollü ve standardize yapılması için sistematik konstrüksiyon yönteminden faydalanılmış ve bu yöntem marifetiyle özel bir aparat tasarlanıp üretilmiştir.



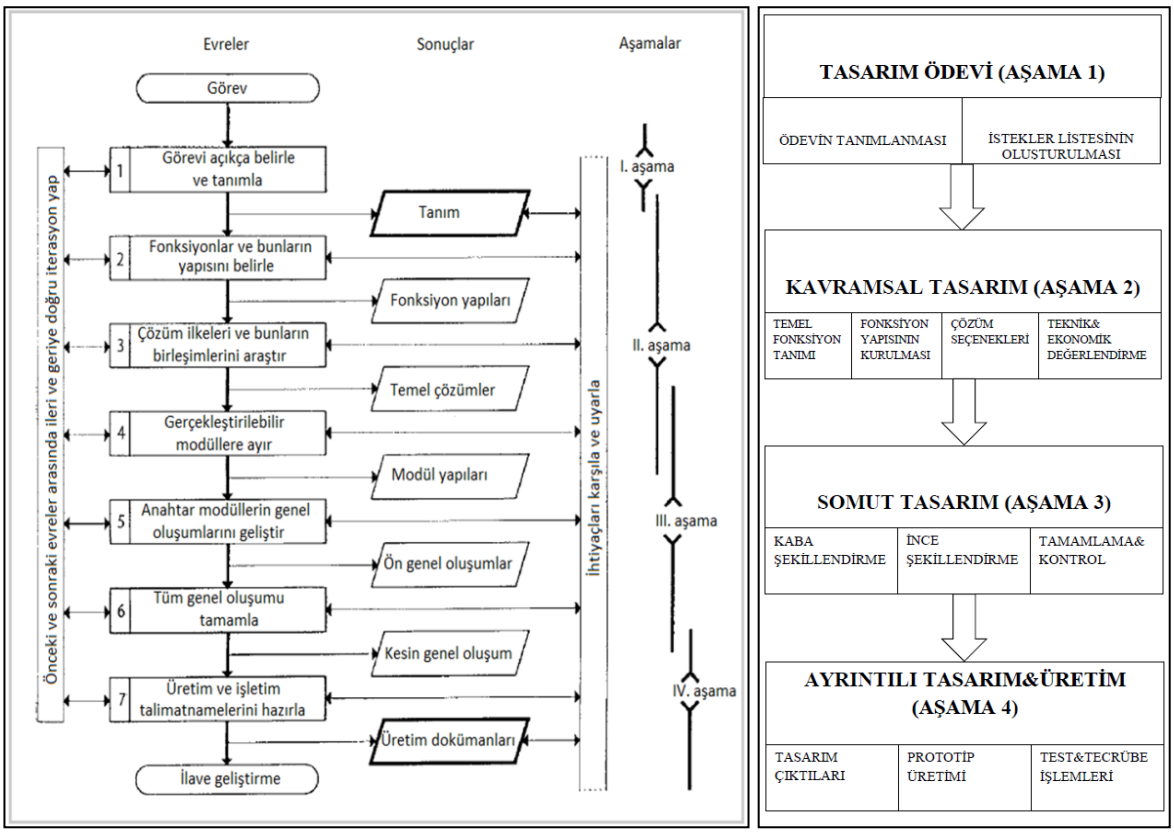
Şekil 2. Lineer ray/araba sistemlerinde kullanılan plastik tapalar.

Tasarımda kullanılan teknik olan sistematik konstrüksiyon yönteminin kökleri II. Dünya savaşı yıllarına dayanmakla beraber bu alandaki gelişmeler 1970'lerden itibaren hız kazanmıştır. Sistematik Konstrüksiyon yaklaşımı tasarım süreçlerinin tasarımcılara özel metotlardan arındırılıp standardize edilmesini; bunun yanında tasarım kalitesinin arttırılmasını ve daha hızlı tasarımcı yetiştirilmesini amaçlayan bir yöntemdir. Çalışma kapsamında sistematik konstrüksiyon tekniğine ait detaylar, bu teknikle yapılan tapa montaj aparatı tasarımı, çalışma sürecinde elde edilen sonuçlar ve yorumlar sunulacaktır.

2. SİSTEMATİK KONSTRÜKSİYON

Tasarım faaliyeti süresince çözüme yönelik tüm kriterlerin göz önünde bulundurulup bu kriterlerin her birinin bir sistem ve metoda göre değerlendirilerek uygulanmasına sistematik konstrüksiyon denmektedir [1]. 1920'li yıllarda ilk çalışmaları A. Erkens tarafından yapılan bu yaklaşım, sistematik konstrüksiyonu sürekli kontrol-karşılaştırma-değerlendirme döngüsünde adım adım çözüme ulaşma işlemi olarak ele almıştır [2,3,4]. O tarihten itibaren Prof. Wögerbauer, Kesselring, Nieman, Leyer, Rodenacker, Hansen, Roth, Koller, Hubka vd. bireysel olarak bu metodun geliştirilmesi için çalışmalar yapmıştır. 1970'lere gelindiğinde

Alman Mühendisler Birliği (VDI) tarafından aralarında Prof. Gerhard Pahl, Prof. Wolfgang Beitz ve Prof. Rudolf Koller gibi profesörlerin bulunduğu alt komisyon kurularak konu üzerinde yoğun olarak çalışılmaya başlanmıştır. Prof. Pahl&Beitz; konu üzerindeki sekiz yıllık çalışmalarını *"Konstrüksiyon Öğretisi"* kitabında yayınlamışlardır [4]. VDI o tarihlerden günümüze bu alanda yaptığı çalışmaları VDI 2221 standardında ortaya koymuş olup bu standartta bir ürün tasarımı için düzenli ve genel bir teknik sistem önermektedir [5,6]. Önerilen bu sistemin akışı Şekil 3.a'da gösterilmiştir.



(a) (b)

Şekil 3. (a) Sistematik konstrüksiyon işlem adımları [7,8].
(b) Pahl&Beitz göre sistematik konstrüksiyon aşamaları [7].

VDI'nın kurduğu alt komisyonda yer alan ve sonraki yıllarda kendi soyadlarıyla Pahl&Beitz yaklaşımı olarak da anılacak yaklaşımı ortaya koyan Prof. G. Pahl ve Prof.W.Beitz'e ait metodu gösteren şema Şekil 3.b'de sunulmuştur.

3. LİNEER KIZAK TAPA MONTAJ APARATININ SİSTEMATİK KONSTRÜKSİYON YAKLAŞIMIYLA TASARIMI

Sistematik konstrüksiyon tekniğinde yapılacak tasarım genel bir teknik ödev olarak kabul edilip bu ödev basamaklar halinde daha basit alt ödevlere ayrılarak analiz edilir [1,9]. Bu kapsamda Bölüm 2'de detaylarıyla ortaya konan sistematik konstrüksiyon aşamaları gereği

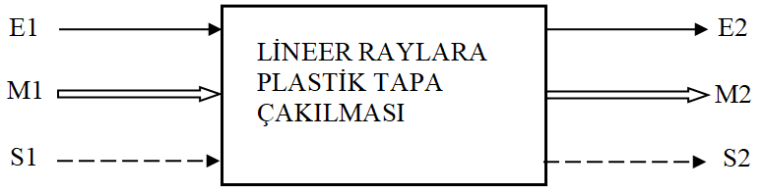
ilk etapta teknik ödevin tanımı yapılacaktır. Devamında teknik ödevin tanımına paralel olarak istekler listesi hazırlanacaktır. İstekler listesinin sentezlenip yorumlanmasıyla temel fonksiyon ortaya konacaktır. Ortaya konan temel fonksiyon, kendini oluşturan alt fonksiyonlara bölünerek fonksiyon yapısı kurulacaktır. Bu noktada her bir alt fonksiyon için çözüm seçenekleri oluşturulacaktır. Son olarak çözüm seçenekleri morfolojik tablolarla birleştirilerek değerlendirilecektir [8,10]. Bulunacak en uygun çözüme göre gerekli mühendislik hesapları yapılarak tasarım detaylandırılıp prototip için uygun tasarım çıktıları elde edilecektir [11]. Tüm tasarımların temelinde yatan ihtiyaç özünde bir problemin çözümü ya da problemin daha başarılı bir çözümüdür. Lineer kızak sistemlerinde çalışma esnasında ray cıvata bağlantı deliklerine toz, talaş vs. dolması sistemin çalışmasına zarar verip çalışma ömrünü kısaltmaktadır. Yine hatalı uygulamalarda ray deliklerinde biriken yabancı maddeler hassas çalışan bilye-yatak sisteminde çeşitli hasarlara neden olmaktadır. Bu ve benzeri sorunların önüne geçmek için ray bağlantı delikleri nitelikleri ray üreticilerince belirlenen plastik tapalarla kapatılmaktadır. Plastik tapaların kapatılması operasyonu özel evsaflı tokmaklarla manuel ve tek tek yapılmaktadır. Operasyon esnasında hatalı montajlardan kaynaklı tapaların bozulması, deliği düzgün kapatmaması, fazla çakılması vb. pek çok sıkıntı ile karşılaşılmaktadır. Teknik ödev, lineer kızak tapa çakma operasyonunun daha hızlı, daha standart, daha basit ve daha emniyetli yapılmasıdır. Teknik ödevdeki gereksinimlerin eksiksiz tarifi çalışmanın sınırlarını çizmede büyük öneme sahiptir. İsteklerin açık, doğru ve eksiksiz belirlenmesindeki başarı ile projenin başarısı birbiriyle doğru orantılıdır. Bu kapsamda projenin bu kısmında taleplerin hassas bir biçimde belirlenip tasniflenmesi projenin sınırlarını ve hedeflerini belirlemektedir. Bu aşamanın sonunda oluşturulacak “İstekler Listesi” tasarımcının temel alacağı bir tasarım şartnamesi niteliğindedir. İstekler listesinin bir diğer özelliği de dinamik yapıda olması gerekliliğidir. Bunun anlamı gerekli görüldüğü takdirde bu liste revize edilebilir, güncellenebilirdir [8,12].İstekler listesi oluşturulurken teknik ödevi tanımlayan özellikteki istekler üç tipte sınıflandırılır. Bunlar; Kesin istekler (K), Arzu Tipi İstekler (A), Hedef İsteklerdir (H). Bu istek tiplerinden kesin istekler, teknik ödevin çözümünde mutlaka yerine getirilmesi gereken, olmazsa olmaz isteklerdir. Arzu Tipi İstekler, gerçekleştirilmesi zorunlu olmayan, ancak gerçekleştirildiği takdirde pazar şansı vb. avantajlar sağlayacak isteklerdir. Hedef gösteren istekler ise, müşteri veya satış ile ilgili olmayıp ortaya konacak ürünün gelecek yıllarda gelişecek teknolojilere uyum sağlayabilmesi için konulacak isteklerdir [13]. Her ne kadar (H)’ler, istekler listesinde yer alması öngörülen istek tiplerinden biri olsa da bunların listeye konması zorunlu değildir [8,12]. Çalışma kapsamında projeye dair hazırlanan istekler listesi Tablo 1.’de verilmiştir. Kavramsal tasarım fikir düzeyindeki tasarım olup problemin tanımından soyut anlamda çözüme ulaşıncaya kadar geçen süreçtir. Bu süreçte; temel prensip tanımlanır, fonksiyon yapısı (strüktürü) kurulur, her bir alt fonksiyon için çözüm aranır ve uygun bağlantılar seçilerek çözüm

seçenekleri oluşturulur. Bu çözüm seçenekleri teknik ve ekonomik olarak değerlendirilerek karar verilir. Verilen karar neticesinde soyut kavramsal tasarım ortaya konarak çözüm tasarımı oluşturulur. Çalışmanın bu aşamasında, ortaya konan istekler listesinden hareketle teknik ödevin özünü teşkil eden temel prensip tanımlanacaktır. Temel prensip; ödevin bütün çözümlerinde bulunan, teknik yapıttaki ana özellikleri içeren nitelikte olmalıdır. Ayrıca bir temel prensip pek çok teknik ödev çözümü için geçerli olabilirken bir teknik ödev için sadece bir temel prensip tanımlanabilir [4,14].

Tablo 1. İstekler listesi

PROJE ÖDEVİ: LİNEER KIZAK PLASTİK TAPA ÇAKMA APARATI İSTEKLER			
S.Nu	**İstekler**	**İstek Düzeyi**	**Açıklama**
1	Aparatın, lineer ray üzerinde hareket edebilmesi için hassas yataklanabilir araba/kızak sistemi olmalıdır.	**K**	Kızak üzerinde aparat çalışırken önden tapayı çakıp arkadan kızak üzerinde hareket etmesi nedeniyle hem kıza geçmiş hem de tapanın kallitesini uygulamalı kontrol etmiş olacaktır.
2	Plastik tapalar, ayarlanabilir kuvvette ve mümkün olduğunca hızlı çakılmalıdır. Çevrim süresi en geç 3 saniyedir.	**K**	Sabit kuvvet, her bir plastik tapanın hiç zararsız ve tam çakılmış olması istendiği içindir.
3	Minimum 30 kg.lık baskı kuvveti sağlamalıdır.	**K**	Bu tapaların güvenle ve doğru çakılabilmesi için gerekli baskı kuvvetidir.
4	Yeterli dayanımda ve olabildiğince hafif bir gövdesi olmalıdır. Uygulamada titreşim,sehim vb. deformasyon oluşmamalıdır.	**K**	Baskı kuvvetinden kaynaklı reaksiyon kuvvetlerini taşıyabiliecek; aynı zamanda elde taşınabilmesi ve rahat hareket ettirilebilmesi hafif olması içindir.
5	Açma-kapama butonu tek elle kontrol edilebilir olmalıdır.	**K**	Tetikleme sistemi operatör tarafından kontrol edilecek bir aparat olduğu için elle kontrol imkanı sağlayan ekipmanlar olmalıdır. Aparat bu kontrolü sağlamalıdır.
6	Plastik tapa besleme kartuşu olmalıdır.	**A**	Elle çakma işi öncesi ekstra iş olarak tapa dizmek yerine tek makine ile hem dizme hem çakma yapılabilecek bir makine içindir.
7	Emniyet mekanizması bulundurmalıdır.	**K**	Sistem üzerinde herhangi bir olağandışı çalışma durumuna karşı enerjinin kesilmesine/tahliyesine yönelik emniyet sistemi.
8	Çakılan plastik tapa sayısını gösteren sayaç bulundurmalıdır.	**A**	Yapılan işin takibi için sistem.
9	Çakılacak tapanın yerini otomatik belirlemeyi sağlayacak sistem olmalıdır.	**A**	Seri operasyonlarda çakılacak kontrolün daha hızlı belirlenerek işin hızlanması için yapılacak mekanizma/sistem.
10			
K	**Kesin istek. Karşılanması zorunlu istekler.**		
A	**Arzu tipi istekler. Karşılanması zorunlu olmayan istekler. Ancak karşılandığı takdirde avantaj sağlayacak isteklerdir.**		
H	**Hedef tipi istekler. Karşılanması gelecekte avantaj sağlayabilecek isteklerdir. İstekler listesinde olması zorunlu**		

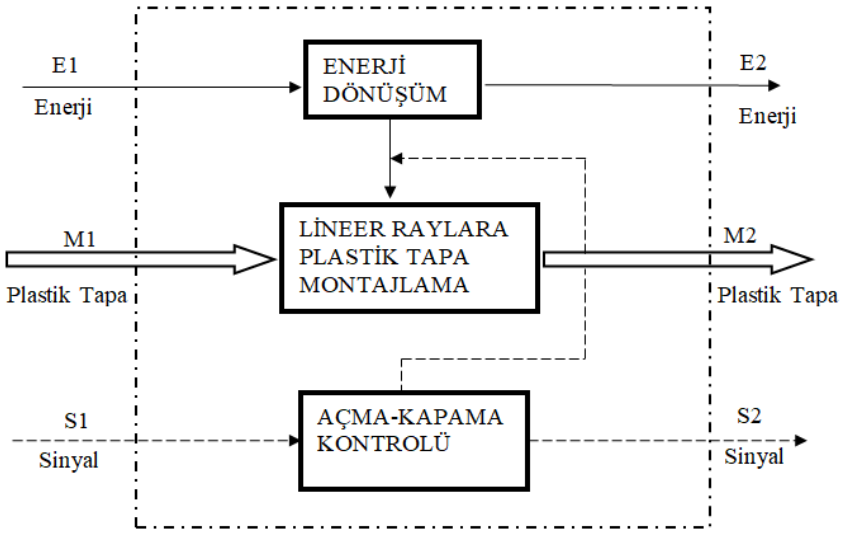
Bu çalışma kapsamında belirlenen temel prensip “Lineer raylara plastik tapa çakılması” olarak belirlenmiştir. Önceki bölümde belirlediğimiz temel prensip fonksiyon yapısının temelini oluşturmaktadır. Her ne kadar temel fonksiyonu oluştursak da yapılacak ürünün sembolik olarak içeriği belirsiz olduğundan "Kara kutu" olarak değerlendirilmektedir [1]. Bundan dolayı temel fonksiyonun tanımlanmasından sonra problemimizin kara kutu (black box) diyagramı oluşturulur. Şekil 4.’te sunulan bu diyagramda giriş-çıkış ürünleri olan enerji (E), madde (M) ve sinyal (S) akışı gösterilmektedir. Büyüklüklere özgü referans belirtmesi için kesikli dikdörtgen sistem çevresini, sürekli çizgili ok enerji, iki boyutlu ok madde, kesikli çizgili ok ise sinyali temsil etmektedir.



Şekil 4. Kara kutu diyagramında temel fonksiyon (black box)

Burada temel fonksiyon, kara kutuya giren ve çıkan büyüklükler arasındaki ilişkiyi göstermektedir. Sisteme E1-M1-S1 olarak giren büyüklükler bu fonksiyona göre değişime uğrayıp E2-M2-S2 olarak çıkmaktadır [13]. Sistemi aktive edecek enerji kaynağını temsil eden E1; elektrik ya da akışkan gücü benzeri bir kaynaktır. M1 ise sistemin çalışması esnasında tüketilen malzemeyi göstermektedir. S1 ise operatör tarafından yapılacak açma-kapama işlemini ifade etmektedir.

Temel (ana) fonksiyon da belirlendikten sonra sıra bu ana fonksiyonu gerçekleştirecek alt fonksiyonlar belirlenmiştir. Bu alt fonksiyonları gösteren detaylı fonksiyon yapısı Şekil 5.'da gösterilmiştir.



Şekil 5. Detaylı alt fonksiyon yapısı.

E1-E2; pnömatik enerji mekanik enerjiye dönüşmekte, M1-M2; dışardan alınan bir tapa sisteme çakılmaktadır ve S1-S2; kapalı durumdaki aparatı açık hale getiren dönüşümü sağlamaktadır. Detaylı fonksiyon yapısında gözüktüğü üzere plastik tapa istenilen deliğe yerleştirildikten sonra aparat operatör tarafından kontrol edilerek montaj işlemi gerçekleştirilir.

Fonksiyon yapısının kurulması, sıradaki işlem olan ana fonksiyon ve buna bağlı alt fonksiyonların kurulması için gerekli alt yapıyı sağlamaktadır. Alt fonksiyonlar, ana fonksiyonu gerçekleştirmek için gerekli birbirinden bağımsız faaliyetler olarak

tanımlanabilmektedir [1,9]. Yine bu aşamada her bir alt fonksiyonun detayları açıklanarak birbirleriyle ilişkilendirilip Tablo 2.'deki gibi fonksiyon zincirinin oluşturulması gerekir [1].

Çözüm seçeneklerinin birleştirilmesinde *"sistematik tümleme"* yöntemi kullanılmaktadır [8]. Bu yönteme göre yapılan birleştirme işlerinde gruplandırma tablolarından faydalanılmaktadır. F. Zwicky tarafından önerilen bu gruplandırma tabloları, *"morfolojik tablolar"* olarak adlandırılmaktadır [13,15]. Morfolojik tablolar oluşturulurken satırlara alt fonksiyonlar; sütunlara ise bu fonksiyonlar için çözüm prensipleri sıralanır. Bu şemalar yapıldıktan sonra tümleşik çözümü oluşturmak için her satırdan en az bir çözümün seçilmesi gerekmektedir. Seçilen çözümler birleştirilerek fonksiyon yapısı oluşturulur.

Tablo 2. Fonksiyon zincirinin kurulması

Fonksiyon Derecesi	**Fonksiyon Tarifi**
ANA FONKSİYON **1.Derece Fonksiyon**	Lineer raylara plastik tapa çakılması.
ALT FONKSİYONLAR **2. Derece Fonksiyonlar**	1. Aparatı ray üzerinde hareket ettirmek.
	2. Plastik tapaların her operasyonda aynı standartta montajlamak.
	3. Plastik tapaları hızlı montajlamak.
	4. Montaj işlemi sonrası uygunluğunun kontrol etmek.
	5. Yeterli dayanım ve olabildiğince hafif olmasını sağlamak.
	6. Operatör tarafından tek elle açılıp kapanabilmek.

F1,F2,F3,…Fn alt fonksiyonları için Ç1,Ç2,Ç3….Çn adet çözüm varsa teorik olarak X1.X2.X3…Xn kadar çözüm seçeneğinden bahsedilebilmektedir. Bu çalışmadaki alt fonksiyonlar için oluşturulan çözüm seçenekleri Tablo 3'te gösterilmiştir.

Çözüm Seçeneği Sayısı=X1.X2.X3.X4.X5.X6=4.5.5.5.4.3=**6000 Adet**

Tablo 3.'te, yapılacak aparat için 6000 farklı teorik çözüm kombinasyonu gösterilmiştir. Ancak bu aşamada uygun olmayan çözüm seçenekleri elenerek kombinasyon sayısı düşürülecektir. Eleme yapılırken çözüm seçeneğinin temel fonksiyona uygunluğu, istekler listesini karşılama durumu, pratikte uygulanabilirlik, ekonomik maliyet durumu, emniyet, tedarik durumu, çözümün uygulanmasında yeterli bilgi birikimi kriterleri değerlendirilmiş ve uygun olmayan çözüm seçenekleri elenmiştir. Elenen çözüm yöntemleri Tablo 3.'te koyu renkle gösterilmiştir.

Tablo 3. Çözüm seçeneklerinin oluşturulması ve uygun olmayan çözümlerin elenmesi.

	ÇÖZÜM SEÇENEKLERİ (Ç)				
ALT FONKSİYONLAR (F)	**Ç1**	**Ç2**	**Ç3**	**Ç4**	**Ç5**
(F1) Aparatı ray üzerinde hareket ettirmek.	Lineer arabayla	Hassas kızakla	Kırlangıç yatakla	Lineer bilyalı rulmanla	
(F2) Plastik tapaların her operasyonda aynı standartta çakmak.	Kestamit uçlu tokmak	Plastik uçlu tokmak	Aüminyum uçlu tokmak	Çelik uçlu tokmak	Ahşap uçlu tokmak
(F3) Plastik tapaların hızlı çakmak.	Elektrikli silindirle kuvvet üret	Hidrolik silindirle kuvvet üret	Hidropnömatik silindirle kuvvet üret sistemiyle	Pnömatik silindir ile kuvvet üret	Manuel mekanik tokmak sistemi ile kuvvet üret
(F4) Çakma işlemi sonrası uygunluğunun kontrol etmek.	Komparatör	Lineer arabayla	Kumpas	Lazer sensör	Kapasitif sensör
(F5) Yeterli dayanım ve olabildiğince hafif olmasını sağlamak.	Alüminyum gövde	Çelik gövde	Plastik gövde	Kompozit gövde	
(F6) Operatör tarafından tek elle açılıp kapanabilmek.	Otomatik modda seri operasyon & bir defa çevrim başlatmak için butona bas bırak & manyetik cetvelle mesafe kontrol	Yarı otomatik operasyon & her baskıda butona tek basma ile tahrik & operatörce mesafe ayarı	Manuel mekanik tokmakla operasyon & her baskıda operatörce elle tahrik & operatörce mesafe ayarı		

Yapılan elemelerden sonra oluşan çözüm seçenekleri sayısı aşağıdaki gibi hesaplanmıştır.

Kalan Çözüm Seçeneği Sayısı=X1.X2.X3.X4.X5.X6=1.2.3.2.1.1=**12 Adet**

Elemeler sonunda tapa montaj aparatı tasarımı için **12 adet** çözümümüz kalmıştır. Bu tasarımlar sırasıyla aşağıda sunulmuştur.

T1: F1Ç1, F2Ç1, F3Ç1, F4Ç2,F5Ç1,F6Ç2

T2: F1Ç1, F2Ç1, F3Ç1, F4Ç5,F5Ç1,F6Ç2

T3: F1Ç1, F2Ç1, F3Ç2, F4Ç2,F5Ç1,F6Ç2

T4: F1Ç1, F2Ç1, F3Ç2, F4Ç5,F5Ç1,F6Ç2

T5: F1Ç1, F2Ç1, F3Ç4, F4Ç2,F5Ç1,F6Ç2

T6: F1Ç1, F2Ç1, F3Ç4, F4Ç5,F5Ç1,F6Ç2

T7: F1Ç1, F2Ç2, F3Ç1, F4Ç2,F5Ç1,F6Ç2

T8: F1Ç1, F2Ç2, F3Ç1, F4Ç5,F5Ç1,F6Ç2

T9: F1Ç1, F2Ç2, F3Ç2, F4Ç2,F5Ç1,F6Ç2

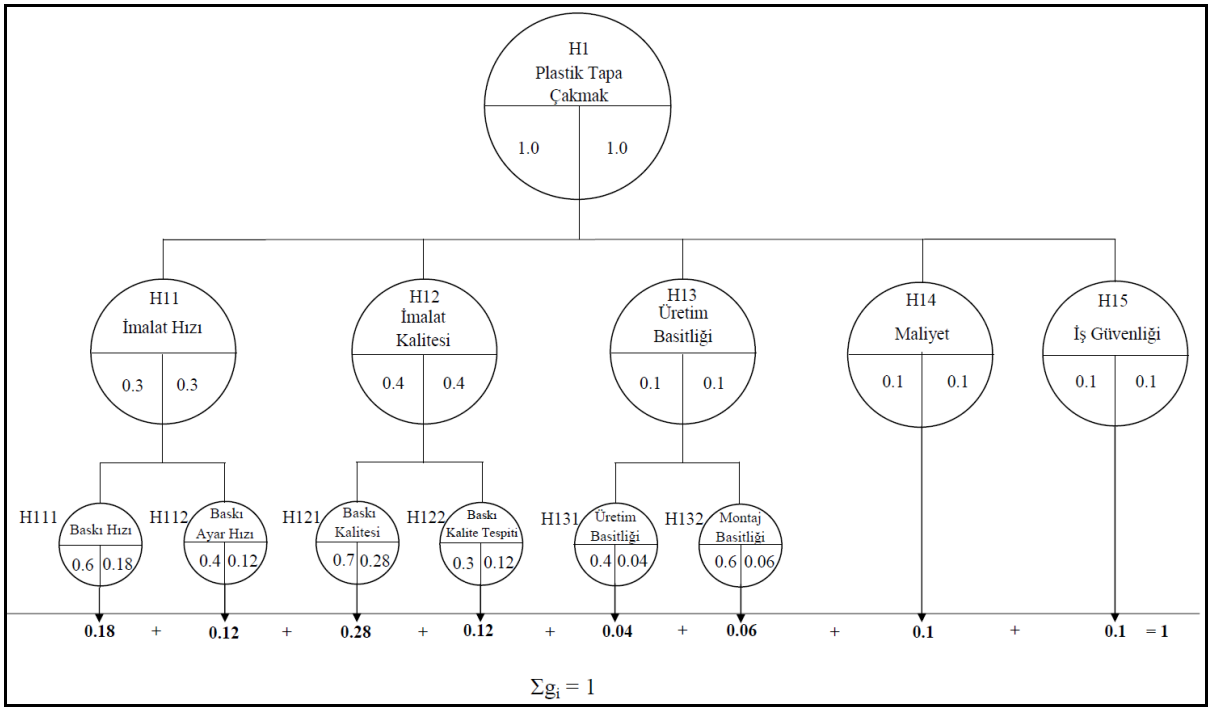
T10: F1Ç1, F2Ç2, F3Ç2, F4Ç5,F5Ç1,F6Ç2

T11: F1Ç1, F2Ç2, F3Ç4, F4Ç2,F5Ç1,F6Ç2

T12: F1Ç1, F2Ç2, F3Ç4, F4Ç5,F5Ç1,F6Ç2

Kavramsal tasarım kısmındaki son aşama olan teknik ve ekonomik değerlendirme, önceki adımlarda üretilen çözüm seçeneklerinin teknik ve ekonomik yönden analiz edilmesidir. Bu analizin yapılması esnasında Prof. Kesselring tarafından ortaya atılan *"Teknik-Ekonomik Değerlendirme"* sistemi kullanılmaktadır [13]. Bu sisteme göre daha önceki aşamalarda bulunan çözümler içerisinden daha uygun olanların belirlenebilmesi için istekler listesine göre hedeflerin tanımlanması gerekmektedir. Sonrasında bu hedeflere ulaşmada öneme sahip alt kriterler belirlenmelidir. Proje hedefleri ve hedef alt kriterlerine göre "*Hedef Ağacı*" çizilerek bu kriterlerin önemine göre tüm sistem içindeki ağırlık faktörleri belirlenmelidir.

Hedef ağacı çizilirken oluşturulacak hiyerarşi temel hedeflerin yatayda, o temel hedefe ulaşmada kullanılacak alt hedeflerin ise düşeyde sıralanmasıdır. Proje kapsamında belirlenen hedeflere göre ağırlıklandırılmış hedefler ağacı Şekil 6.'da sunulmuştur.



Şekil 6. Ağırlıklandırılmış hedefler ağacı

Şekil 6'da sunulan hedefler ait açıklamalar aşağıda belirtilmiştir.

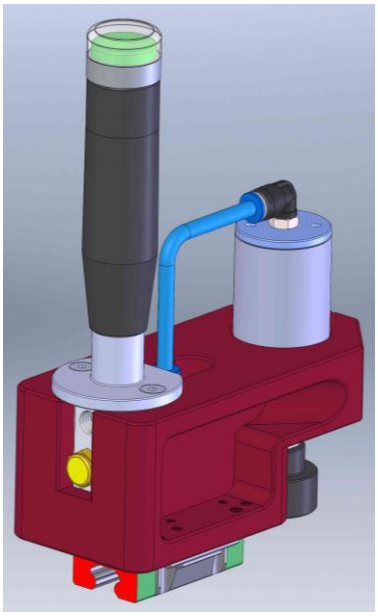
H1 : Plastik tapa çakmak
H11 : İmalat hızı
H12 : İmalat kalitesi
H13 : Üretim basitliği
H14 : Maliyet
H15 : İş güvenliği
H111 : Baskı hızı
H112 : Baskı ayar hızı
H121 : Baskı kalitesi
H122 : Baskı kalite tespiti
H131 : Üretim basitliği
H132 : Montaj basitliği

Şekilde ifade edilen hedeflerin Fayda-Değer analizinde değer tayinin yapılması için puanlamalar VDI 2225'e göre yapılmaktadır. Bu standarda göre değer puanlamaları aşağıdaki gibidir.

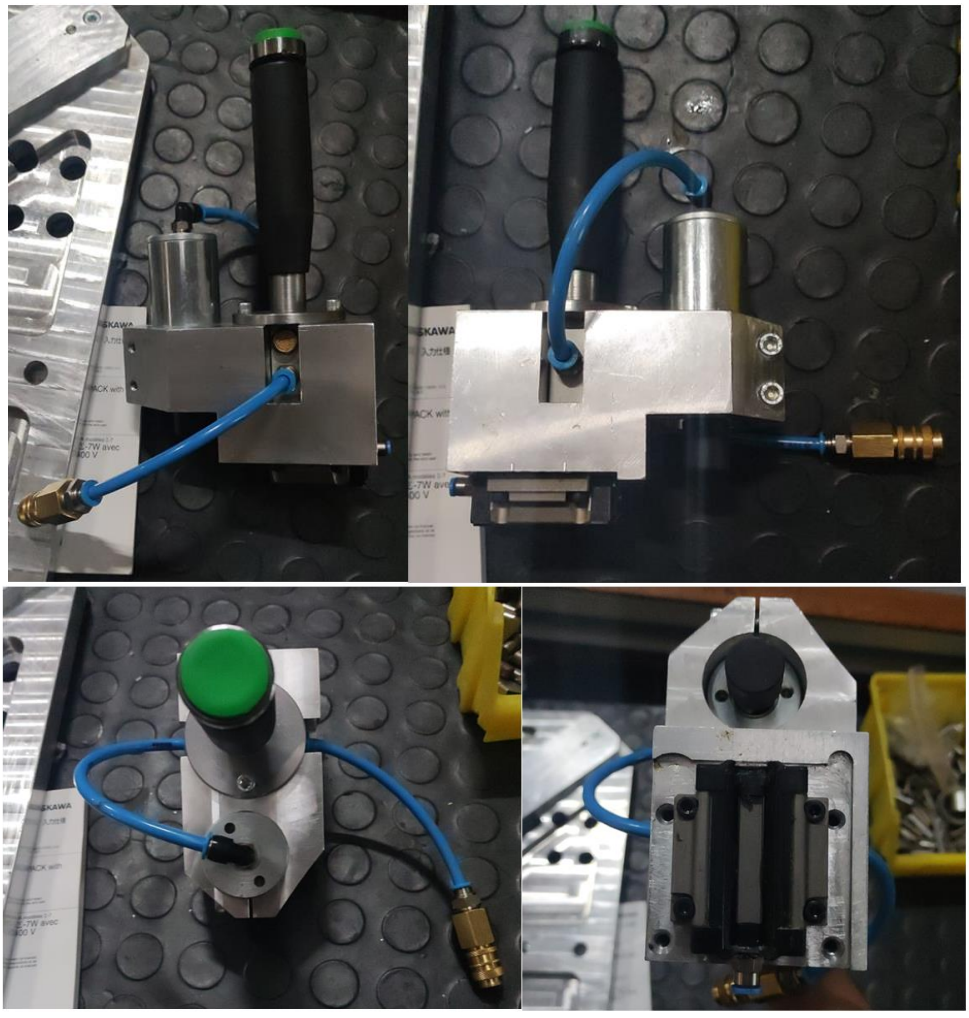
- 4: İyi
- 3: Yeterli
- 2: Orta
- 1: Zayıf
- 0: Uygun değil

VDI 2225'e göre en uygun çözüme karar verilebilmesi için Tablo 3'teki tüm çözüm seçeneklerinin puanlanması (P_i) gerekmektedir. Çalışma kapsamında yapılan puanlama Tablo 4'te gösterilmiştir. Sonrasında verilen puanlar, Şekil 6'daki ağırlıklandırmalarla (g_i) çarpılarak her bir çözüm seçeneğinin toplam değerleme puanına ulaşılmıştır. Bu toplam değerleme puanları da yine Tablo 4'te gösterilmiştir.

Toplam puanlamaya bakılarak verilen karara göre en uygun çözüm **X_i=3,74** puan alan ***"T5"*** numaralı konfigürasyon olmuştur. Tasarım olarak en uygun çözümün belirlenmesini müteakip bu elemanların yukarıda belirtilen hedefleri karşılayabilecek niteliklerde boyutlandırılması adımına geçilmiştir. Boyutlandırma sonrası üretilen CAD modele ve üretilen prototipe ait görseller Şekil 7. ve Şekil 8.'de sunulmuştur.



Şekil 7. Aparata dair somut tasarım (CAD) çıktıları.



Şekil 8. Üretimi yapılan prototip.

Tablo 4. Teknik ve ekonomik değerlendirme

Tasarım Nu	Bilgi&Analiz	Hedefler (gi)								TOPLAM (ΣXi=Pi*gi)
		H111 (0.18)	H112 (0.12)	H121 (0.28)	H122 (0.12)	H131 (0.04)	H132 (0.06)	H14 (0.1)	H15 (0.1)	
T1	Çözüm Konfig.	F1Ç1, F2Ç1, F3Ç1, F4Ç2,F5Ç1,F6Ç2								Xi = 2,9
	Çözüm Detay	Lineer arabayla hereketli, kestamit uçlu tokmak ile çakan, elektrikli silindirle kuvvet üreten, lineer arabayla kontrol eden, alüminyum gövdeli,yarı otomatik operasyonla her baskıda butona tek basımla operatörce tahrik edilip operatörce mesafe ayar yapılır aparat.								
	Hedef	Baskı hızı	Baskı ayar hızı	Baskı kalitesi	Baskı kalite tespiti	Üretim basitliği	Montaj basitliği	Maliyet	İş Güvenliği	
	Verilen Puan (Pi)	2	3	4	3	2	2	1	4	
T2	Çözüm Konfig.	F1Ç1, F2Ç1, F3Ç1, F4Ç5,F5Ç1,F6Ç2								Xi = 3,02
	Çözüm Detay	Lineer arabayla hereketli, kestamit uçlu tokmak ile çakan, elektrikli silindirle kuvvet üreten, **kapasitif sensörle kontrol eden**, alüminyum gövdeli,yarı otomatik operasyonla her baskıda butona tek basımla operatörce tahrik edilip operatörce mesafe ayar yapılır aparat.								
	Hedef	Baskı hızı	Baskı ayar hızı	Baskı kalitesi	Baskı kalite tespiti	Üretim basitliği	Montaj basitliği	Maliyet	İş Güvenliği	
	Verilen Puan (Pi)	2	3	4	4	2	2	1	4	
T3	Çözüm Konfig.	F1Ç1, F2Ç1, F3Ç2, F4Ç2,F5Ç1,F6Ç2								Xi = 3,28
	Çözüm Detay	Lineer arabayla hereketli, kestamit uçlu tokmak ile çakan, **hidrolik silindirle kuvvet üreten**, **lineer arabayla kontrol eden**, alüminyum gövdeli,yarı otomatik operasyonla her baskıda butona tek basımla operatörce tahrik edilip operatörce mesafe ayar yapılır aparat.								
	Hedef	Baskı hızı	Baskı ayar hızı	Baskı kalitesi	Baskı kalite tespiti	Üretim basitliği	Montaj basitliği	Maliyet	İş Güvenliği	
	Verilen Puan (Pi)	3	3	4	3	3	3	3	3	
T4	Çözüm Konfig.	F1Ç1, F2Ç1, F3Ç2, F4Ç5,F5Ç1,F6Ç2								Xi = 3,34
	Çözüm Detay	Lineer arabayla hereketli, kestamit uçlu tokmak ile çakan, **hidrolik silindirle kuvvet üreten, kapasitif sensörle kontrol eden**, alüminyum gövdeli,yarı otomatik operasyonla her baskıda butona tek basımla operatörce tahrik edilip operatörce mesafe ayar yapılır aparat.								
	Hedef	Baskı hızı	Baskı ayar hızı	Baskı kalitesi	Baskı kalite tespiti	Üretim basitliği	Montaj basitliği	Maliyet	İş Güvenliği	
	Verilen Puan (Pi)	3	3	4	4	3	2	3	3	
T5	Çözüm Konfig.	F1Ç1, F2Ç1, F3Ç4, F4Ç2,F5Ç1,F6Ç2								Xi = 3,74
	Çözüm Detay	Lineer arabayla hereketli, kestamit uçlu tokmak ile çakan, **pnömatik silindirle kuvvet üreten**, **lineer arabayla kontrol eden**, alüminyum gövdeli,yarı otomatik operasyonla her baskıda butona tek basımla operatörce tahrik edilip operatörce mesafe ayar yapılır aparat.								
	Hedef	Baskı hızı	Baskı ayar hızı	Baskı kalitesi	Baskı kalite tespiti	Üretim basitliği	Montaj basitliği	Maliyet	İş Güvenliği	
	Verilen Puan (Pi)	4	4	4	3	3	4	4	3	
T6	Çözüm Konfig.	F1Ç1, F2Ç1, F3Ç4, F4Ç5,F5Ç1,F6Ç2								Xi = 3,68
	Çözüm Detay	Lineer arabayla hereketli, kestamit uçlu tokmak ile çakan, **pnömatik silindirle kuvvet üreten, kapasitif sensörle kontrol eden**, alüminyum gövdeli,yarı otomatik operasyonla her baskıda butona tek basımla operatörce tahrik edilip operatörce mesafe ayar yapılır aparat.								
	Hedef	Baskı hızı	Baskı ayar hızı	Baskı kalitesi	Baskı kalite tespiti	Üretim basitliği	Montaj basitliği	Maliyet	İş Güvenliği	
	Verilen Puan (Pi)	4	3	4	4	3	3	4	3	

T7	**Çözüm Konfig.**	F1Ç1, F2Ç2, F3Ç1, F4Ç2,F5Ç1,F6Ç2							**Xi = 2,58**
	Çözüm Detay	Lineer arabayla hereketli, **plastik uçlu tokmak ile çakan, elektrikli silindirle kuvvet üreten, lineer arabayla kontrol eden**, alüminyum gövdeli,yarı otomatik operasyonla her baskıda butona tek basımla operatörce tahrik edilip operatörce mesafe ayar yapılır aparat.							
	Hedef	**Baskı hızı**	**Baskı ayar hızı**	**Baskı kalitesi**	**Baskı kalite tespiti**	**Üretim basitliği**	**Montaj basitliği**	**Maliyet**	**İş Güvenliği**
	Verilen Puan (Pi)	2	3	3	3	1	2	1	4
T8	**Çözüm Konfig.**	F1Ç1, F2Ç2, F3Ç1, F4Ç5,F5Ç1,F6Ç2							**Xi = 2,7**
	Çözüm Detay	Lineer arabayla hereketli, **plastik uçlu tokmak ile çakan**, **elektrikli silindirle kuvvet üreten**, **kapasitif sensörle kontrol eden**, alüminyum gövdeli, yarı otomatik operasyonla her baskıda butona tek basımla operatörce tahrik edilip operatörce mesafe ayar yapılır aparat.							
	Hedef	**Baskı hızı**	**Baskı ayar hızı**	**Baskı kalitesi**	**Baskı kalite tespiti**	**Üretim basitliği**	**Montaj basitliği**	**Maliyet**	**İş Güvenliği**
	Verilen Puan (Pi)	2	3	3	4	1	2	1	4
T9	**Çözüm Konfig.**	F1Ç1, F2Ç2, F3Ç2, F4Ç2,F5Ç1,F6Ç2							**Xi = 3**
	Çözüm Detay	Lineer arabayla hereketli, **plastik uçlu tokmak ile çakan, hidrolik silindirle kuvvet üreten, lineer arabayla kontrol eden**, alüminyum gövdeli,yarı otomatik operasyonla her baskıda butona tek basımla operatörce tahrik edilip operatörce mesafe ayar yapılır aparat.							
	Hedef	**Baskı hızı**	**Baskı ayar hızı**	**Baskı kalitesi**	**Baskı kalite tespiti**	**Üretim basitliği**	**Montaj basitliği**	**Maliyet**	**İş Güvenliği**
	Verilen Puan (Pi)	3	3	3	3	3	3	3	3
T10	**Çözüm Konfig.**	F1Ç1, F2Ç2, F3Ç2, F4Ç5,F5Ç1,F6Ç2							**Xi = 3,12**
	Çözüm Detay	Lineer arabayla hereketli, **plastik uçlu tokmak ile çakan, hidrolik silindirle kuvvet üreten, kapasitif sensörle kontrol eden**, alüminyum gövdeli,yarı otomatik operasyonla her baskıda butona tek basımla operatörce tahrik edilip operatörce mesafe ayar yapılır aparat.							
	Hedef	**Baskı hızı**	**Baskı ayar hızı**	**Baskı kalitesi**	**Baskı kalite tespiti**	**Üretim basitliği**	**Montaj basitliği**	**Maliyet**	**İş Güvenliği**
	Verilen Puan (Pi)	3	3	3	4	3	3	3	3
T11	**Çözüm Konfig.**	F1Ç1, F2Ç2, F3Ç4, F4Ç2,F5Ç1,F6Ç2							**Xi = 3,34**
	Çözüm Detay	Lineer arabayla hereketli, **plastik uçlu tokmak ile çakan, pnömatik silindirle kuvvet üreten, lineer arabayla kontrol eden**, alüminyum gövdeli,yarı otomatik operasyonla her baskıda butona tek basımla operatörce tahrik edilip operatörce mesafe ayar yapılır aparat.							
	Hedef	**Baskı hızı**	**Baskı ayar hızı**	**Baskı kalitesi**	**Baskı kalite tespiti**	**Üretim basitliği**	**Montaj basitliği**	**Maliyet**	**İş Güvenliği**
	Verilen Puan (Pi)	4	3	3	3	3	4	4	3
T12	**Çözüm Konfig.**	F1Ç1, F2Ç2, F3Ç4, F4Ç5,F5Ç1,F6Ç2							**Xi = 3,4**
	Çözüm Detay	Lineer arabayla hereketli, **plastik uçlu tokmak ile çakan, pnömatik silindirle kuvvet üreten, kapasitif sensörle kontrol eden**, alüminyum gövdeli,yarı otomatik operasyonla her baskıda butona tek basımla operatörce tahrik edilip operatörce mesafe ayar yapılır aparat.							
	Hedef	**Baskı hızı**	**Baskı ayar hızı**	**Baskı kalitesi**	**Baskı kalite tespiti**	**Üretim basitliği**	**Montaj basitliği**	**Maliyet**	**İş Güvenliği**
	Verilen Puan (Pi)	4	3	3	4	3	3	4	3

4. SONUÇLAR VE TARTIŞMA

Bu çalışmada, lineer kılavuz sistemlerinde bulunan raylar üzerindeki delik tapalarının hassas, kontrollü ve standart şekilde montajının yapılması için Pahl&Beitz tarafından önerilen sistematik konstrüksiyon yönteminden faydalanılarak özel bir aparat tasarlanıp prototip üretilmiştir.

İlk kısımda teknik ödev tanımlanmış, devamında istekler listesi belirlenmiş olup devamında sistemin çalışmasına dair ana ve alt fonksiyonlar belirlenerek sistemin fonksiyon yapısı ve zincirleri kurulmuştur. Ardından belirlenen ana ve alt fonksiyonlara dair çözüm seçenekleri

ortaya konulmuş olup işbu çözüm seçeneklerinin projedeki hedeflere göre ağırlıklandırılması yapılarak VDI 2225'e göre teknik ve ekonomik değerlendirmesi gerçekleştirilmiştir. Son olarak da 12 adet tasarım içerisinden en yüksek puanlı kombinasyon seçilerek konsept tasarım tamamlanmış; somut tasarım ve prototip aşamasına geçilmiştir.

Somut tasarım ve prototip aşamasında ise belirlenen kavramsal tasarıma göre detaylı mekanik hesaplamalarla sistemin, istekler listesindeki kapasitelere cevap verebilecek nitelikte olması sağlanmıştır.

İzlenen bu metotlar neticesinde ortaya konan prototip üzerinde performansın ölçümü için aparatlı ve aparatsız 3 adet 1'er metrelik ray üzerinde tapa çakma işlemi yapılmıştır. Deneyler neticesinde çıkan fire miktarları, birim zamanda çakılan tapa sayıları ve diğer sonuçlar aşağıda maddeler halinde sunulmuştur.

- Aparatsız olarak her bir raya 17 adet tapa çakılmış; bu esnada ortaya çıkan fire miktarları Tablo 5'te verilmiştir. 2 adet rayda 3 adet, diğer rayda ise 5 adet tapa çakılma esnasında fire verilmiştir.

Tablo 5. Numune raylara çakılan tapalarda verilen fire miktarları

Ray Nu	Ray Boyu [m]	Çakılan Tapa Sayısı [Adet]	Fire Sayısı	Fire Yüzdesi
Ray-1	1 m	17	3	%17,6
Ray-2	1 m	17	5	%29,4
Ray-3	1m	17	3	%17,6

Hatalı çakılan tapaların ortalama çıkarılma süresi ise yaklaşık 30 saniye olarak ölçülmüştür.

- Ayrıca çakma işlemlerinde yapılan süre ölçümlerinde elde edilen sonuçlar Tablo 6'da sunulmuştur.

Tablo 6. Aparatsız tapa çakma süreleri.

Ray Nu	Çakılan Tapa Sayısı [Adet]	Birim Süre [s]	Ortalama Süre [s]	Ağırlıklı Ortalama Süre [s]
Ray-1	1	8,12	8,12	8,136
	5	40,78	8,156	
	17	138,23	8,131	
Ray-2	1	8,44	8,44	8,058
	5	40,14	8,028	
	17	136,77	8,045	
Ray-3	1	7,96	7,96	8,19
	5	41,27	8,254	
	17	139,16	8,185	

- Tasarlanan aparatla montaj yapıldığında ise her bir rayda çakma işlemine başlamadan önce aparatın montajının yapılmasının yaklaşık 30 saniye sürdüğü ölçülmüştür.
- Aparatın tüm ray marka ve tiplerinde kullanılabilmesini sağlayan alt kısmındaki değiştirilebilir araba parçasının, iki ray arasındaki geçiş değişiminin yaklaşık 1 dakika sürdüğü ölçülmüştür.
- Yeni aparatla yapılan çakma işlemlerinde en dikkat çeken husus montaj işlemi sırasında standart bir süreç izlenebilmesi ve bu sürecin hassas olarak tekrarlanabilmesi olmuştur. Bu kapsamda işleme başlandıktan sonra her bir tapanın montaj süresi yaklaşık 3,2 saniye olarak ölçülmüştür.
- Ölçümler 3 rayda da 1, 5 ve 17 tapa ölçeklerinde tekrar edilmiş ve sonuç yine sırasıyla 3,2 saniye, 16 saniye ve 55 saniye mertebelerinde ölçülmüştür.

Sonuç olarak; hareket ve kontrol sistemlerinde yaygın kullanılan çalışmaya konu aparatın tasarımında *“Sistematik Konstrüksiyon”* metodu kullanılmış ve bu sayede kavramsal tasarım sürecinde tüm mevcut olasılıklar değerlendirmeye alınarak en uygun çözüm bulunmaya çalışılmıştır. Sistematik Konstrüksiyon tekniğinin sağladığı bu analitik çözüm yaklaşımı sayesinde kavramsal tasarım tamamlanmıştır. Bu aşamadan sonra gerçekleştirilen somut tasarım ve prototipleme aşamasıyla proje gerçekleştirilmiş olup kullanılan sistematik konstrüksiyon metodunun projenin her aşamasına tam hakimiyet sağlaması sayesinde herhangi bir malzeme, zaman, iş gücü kaybı yaşanmamıştır. Ayrıca bu tekniğin sadece portatif aparatlarda değil aynı zamanda diğer makine tasarımlarında da kullanılabileceği görülmüştür.

Bu çalışmaya konu olan *"TAPA MONTAJ APARATI'nın"* tescili için *"2022/021266"* numarasıyla patent başvurusu yapılmıştır.

5. KAYNAKÇA

[1] G. Kutay, Konstrüksiyon Sistematiği, www.guven-kutay.ch, (2009).

[2] Erkens A., "Beiträge zur konstruktionserziehung".VDI 72. 17-21, 1928.

[3] Mutlu,E., Parlar,Z.,"An apparatus design for high speed sealing application based on systematic design approach." Blucher Mechanical Engineering Proceedings, May 2014, Vol.1, Num.1.

[4]Kumru,M.M., "Konstrüktif ödevlerin sistematik geliştirilmesi ve bir uygulama örneği.", Yüksek Lisans Tezi, İTÜ Fen Bilimleri Enstitüsü, Şubat 1998.

[5] VDI 2221- "Systematic Approach to the Design of Technical Systems and Products.", VDI, Düsseldorf, 1993.

[6]"Mühendislik Tasarımı - Sistematik Yaklaşım", Prof. Dr. Hüseyin Börklü, Hatipoğlu Yayınları, Ankara, 2010.

[7] Pahl,G.,Beitz,W., Feldhusen,J.,Grote,K.H."Engineering Design-A Systematic Approach",3rd Edition, Springer Published.

[8] Azeloğlu,C.O., "MAK 5410-Sistematik Konstrüksiyon Ders Notları" YTÜ FBE, İstanbul, 2017.

[9] Gökkurt,M.A., "Anahtarla açma-kapama özelliğine sahip iki kutuplu yan topraklamalı alman tipi priz konstrüksiyonu" Yüksek Lisans Tezi, YTÜ, 2013, İstanbul.

[10] C. O. AZELOĞLU Et Al. , "Sistematik Konstrüksiyonda Bir Kavramsal Tasarım Uygulaması: Çok Amaçlı Öğütücü," 3'rd International Symposium on Industrial Design & Engineering , Antalya, Turkey, pp.434-440, 2018.

[11] Parlar, Z.,Soybora, E., Burhan, M., Davaslıgil, S., "Sistematik Konstrüksiyon ve Tasarım Odaklı Düşünme Yaklaşımı ile Yaratıcı Kavramsal Tasarım Süreci: Küçük Ev Aleti Tasarımı." SAÜ Fen Bilimleri Enstitüsü Dergisi,1-1. 10.16984/saufenbilder.307260 (2017).

[12] Azeloğlu, C. & Alper, M.. (2019). Yeni Bir Hidroterapi Egzersiz Aletinin Sistematik Konstrüksiyon Yaklaşımıyla Kavramsal Tasarımı. Gazi Üniversitesi Fen Bilimleri Dergisi Part C: Tasarım ve Teknoloji. 7. 291-302. 10.29109/gujsc.526706.

[13] Gökşenli,A., "Mercedes-Benz konsept midibüs fikrinin oluşumundan minibüsün tasarlanmasına kadar izlenen adımların sistematik konstrüksiyon ile desteklenmesi", Doktora Tezi, İTÜ, Makine Fakültesi, Makine Mühendisliği Bölümü,1999.

[14] Hansen, F.,"Konstuktionssystematik-Grundlage und Methoden",München, Carl Hanser 321-330, 1974.

[15] Zwicky, F.,"Entdecken,Erfinden,Forschen im Morphologischen Weltbild, München, Droemer-Knaur,32-38, 1971.

BÜYÜK BOYUTLU FREZE TEZGAHLARI İÇİN HİDROLİK DÖNER-İŞ BAĞLAMA SİSTEMİNİN GELİŞTİRİLMESİ

Mehmet UĞUR *mehmet.ugur@genba.com.tr,* Genba Group, 10100, Balıkesir, Turkey
Talha GİRGİN *Talha.girgin@genba.com.tr,* Genba Group, 10100, Balıkesir, Turkey
O.Talha DİNÇER *talha.dincer@genba.com.tr,* Genba Group, 10100, Balıkesir, Turkey
Cengiz OĞUZER *cengiz.oguzer@genba.com.tr,* Genba Group, 10100, Balıkesir, Turkey
Ali ORAL *a.oral@balikesir.edu.tr,* Balıkesir Üniversitesi, 10145, Balıkesir, Turkey
a.oral@argeon.com.tr , Argeon Teknoloji Mühendislik Hiz.10145 Balikesir,Turkey

ÖZET

Rüzgar türbin kulesi gibi çok büyük kütlelere sahip yapıların imalatları için büyük ölçekli imalat makineleri kullanılmaktadır. Büyük boyutlu ve büyük kütleli asimetrik iş parçaları genellikle portal freze gibi büyük tezgahlarda işlenmektedir. Bu parçaların imalatları esnasında yine büyük iş bağlama ve döndürme sistemlerine ihtiyaç duyulmaktadır. Talaşlı imalat işlemlerinin gerçekleştirilebilmesi için iş bağlama aparatlarıyla parçanın serbestlik derecesi kısıtlanarak parça sabitlenmekte ve ardından talaş kaldırma işlemleri yapılmaktadır. Tezgah tablasına sabitlenen iş parçaları, genellikle bir bağlamada işlenememekte ve çoğunlukla tezgah tablası üzerinde döndürülmektedir. Bu tür iş parçalarını döndürmek için ise vinç ve benzeri yardımcı kaldırma-taşıma araçları kullanılmaktadır. İş parçalarının vinç ile kaldırılıp döndürülmesi esnasında ergonomik problemler, iş sağlığı ve güvenliği riskleri oluşmaktadır. Ayrıca, iş parçası döndürüldükten sonra parça üzerinde tekrar referans noktaların belirlenmesi gereklidir.

Geliştirilen döndürme ve konumlandırma sistemi iş parçasının tüm yüzeyleri üzerinde işlem yapılmasına olanak sağlayacaktır. Bu amaçla öncelikle tezgah tablası üzerinde bulunan iş parçası, hidrolik tahrikli hareketli çeneler ile kavranır. Çeneler arasındaki parça, dönmenin sağlanabileceği yüksekliğe hidrolik silindirler ile çıkarılır ve istenilen açıda dönme (90°-180°) sağlandıktan sonra tekrar tabla üzerine yerleştirilir. Hareketli çeneler parçayı serbest bırakarak park konumuna geçerler ve parçanın işlenmesine başlanır.

Bu çalışmada, büyük kütleli iş parçalarının bir freze tezgahı üzerinde otomatik olarak döndürülmesini ve konumlandırılmasını sağlayacak yenilikçi bir hidrolik tahrikli bir iş bağlama sistemi geliştirilmiştir. Geliştirilen sistem ile geleneksel olarak vinçler ile yapılan kaldırma,

döndürme ve konumlandırma işlemleri esnasında iş güvenliği riskleri ortadan kaldırılmış ve tekrar referanslandırma yapılmasına olan gereksinim ortadan kaldırılmıştır.

Anahtar terimler: İş bağlama sistemleri, ergonomik problemler, döner eksenli iş bağlama mekanizması

ABSTRACT

Large-scale manufacturing machines are used for the manufacture of structures with very large masses, such as wind turbine towers. Asymmetrical workpieces with large sizes and large masses are usually machined on large machines such as gantry mills. During the production of these parts, large work clamping and rotation systems are also needed. In order to carry out machining operations, the part is fixed by restricting the degree of freedom of the part with work clamping apparatus and then machining operations are performed. Workpieces fixed to the machine table are usually not machined in a clamping and are often rotated on the machine table. In order to rotate such workpieces, cranes and similar auxiliary lifting-transport vehicles are used. Ergonomic problems, occupational health and safety risks occur during the lifting and turning of workpieces with a crane. In addition, after the workpiece has been rotated, it is necessary to determine the reference points on the part again.

The developed rotation and positioning system will allow processing on all surfaces of the workpiece. For this purpose, first of all, the workpiece on the table is grasped by hydraulically driven movable jaws. The piece between the jaws is raised by hydraulic cylinders to the height where rotation can be achieved, and after rotation at the desired angle (90°-180°) is achieved, it is placed back on the table. The moving jaws release the part, move to the parking position, and the part is started to be processed.

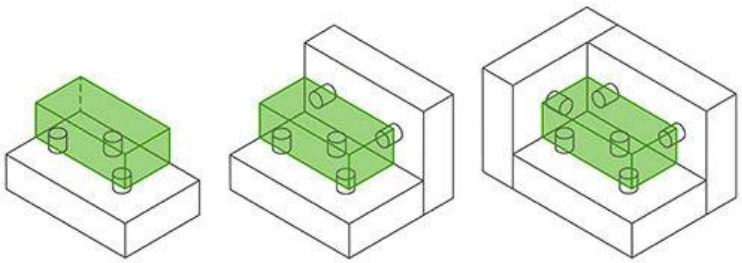
In this work, an innovative hydraulically driven work clamping system has been developed that will enable automatic rotation and positioning of large-mass workpieces on a milling machine. With the developed system, occupational safety risks have been eliminated during lifting, rotating and positioning operations traditionally performed with cranes and the need for re-referencing has been eliminated.

Keywords: Work clamping systems, ergonomic problems, rotary axis work holding mechanism

1. GİRİŞ

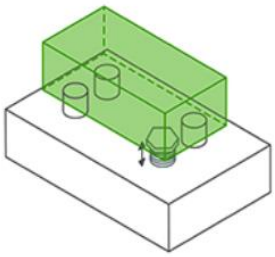
Dünya üzerindeki teknolojik gelişmeler yaşamın zorladığı ihtiyaçlar doğrultusunda ortaya çıkmıştır. Yapılmak istenen işler için mevcut kaynaklar yeterli olmadığında, eldeki olanakları geliştirmek zorunlu hale gelmiş ve bugünün teknoloji dünyası bu şekilde şekillenmiştir. İşletmeler de sahip oldukları makinelerle daha fazla üretim yapmak, durma sürelerini azaltmak ve verimliliği artırmak gibi hedeflerine ulaşmak için çözümler aramaktadırlar. Talaşlı imalat makinelerinde seri üretimi yapılan makine parçalarının aynı ölçü ve biçimde imal edilebilmesi için, çeşitli bağlama düzenleri ve iş kalıplarından yararlanılır. İşlemin başarılı olarak gerçekleşmesi için işlenecek parçaların tezgah tablasına güvenli bir şekilde sabitlenmiş olması gerekir. Aksi takdirde, iş parçasının bozulması, kesici takımın kırılması ve tezgah aksamlarının hasar görmesi söz konusu olacaktır.

İş parçasını tezgah tablasına sabitlemenin en iyi yolu 3-2-1 prensibini kullanmaktır [1,2]. Bu yöntem, işleme sırasında iş parçasının 6 serbestlik derecesinin kısıtlanmasını ve parçanın sabitlenmesini sağlar. 6 sabitleme noktası (3+2+1 = 6) kullanarak, iş parçasının tüm serbestlik dereceleri kaldırlarak, iş parçasının sabitlenmesi sağlanır [2].



Şekil 1. 3-2-1 Prensibiyle parçanın sabitlenmesi [2]

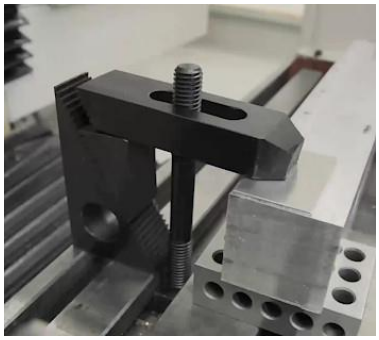
3-2-1 prensibi kullanılırken yetersiz (örneğin 2 pin) veya aşırı sabitleme pimi (örneğin 4 pim) kullanılmamalıdır (Şekil 2).



Şekil 2. Aşırı tanımlı kısıtlama [2]

İşleme sırasında bir iş parçasını doğru pozisyonda tutmak için çeşitli iş baglama yöntemleri vardır, ancak doğru yöntem büyük ölçüde iş parçasının boyutları, şekli ve malzemesine bağlıdır. Bunların yanı sıra ürün sayısı ve çeşitlilik de dikkate alınması gereken faktörlerdir.

İş parçalarının tezgah tablasına bağlamada en çok; mekanik (Şekil 3-a), hidrolik (Şekil 3-b), pnömatik (Şekil 3-c), manyetik (Şekil 3-d), vakum (Şekil 3-e) vb gibi yöntemler kullanılmaktadır.



a- Mekanik iş bağlama elemanı [3]



b- Hidrolik iş bağlama elemanı [4]



c- Pnömatik iş bağlama elemanı [5]



d- Manyetik iş bağlama elemanı[6]



e- Vakumlu iş bağlama elemanı[7]

Şekil 3. İş bağlama yöntemlerine örnekler

Bu yöntemlerin yanı sıra freze tezgahlarında divizör gibi döner eksenli iş bağlama ve konumlandırma sistemleri de sıklıkla kullanılmaktadır (Şekil 4.) [8]. Bu iş bağlama sistemleriyle 3 eksen CNC dik işleme merkezlerinin genellikle 4 eksen olarak kullanabilmesi mümkündür. Ancak bu sistemlerde genellikle küçük parçaların tezgaha hızlı ve hassas şekilde bağlanmasını ve konumlandırması yapılabilmektedir.



Şekil 4. CNC tezgahlar için döner eksen [8]

Büyük boyutlu iş parçalarının işlendiği portal/çift kolonlu frezelerde, iş parçasının çeşitli yüzeylerinin işlenmesi için iş parçası genellikle iş güvenliği riskleriyle birlikte vinçler vasıtasıyla yerinden kaldırılıp operator desteği ile çevrilerek tekrar tezgah tablasına bağlanmakta ve refesanslandırılmaktadır (Şekil 5).



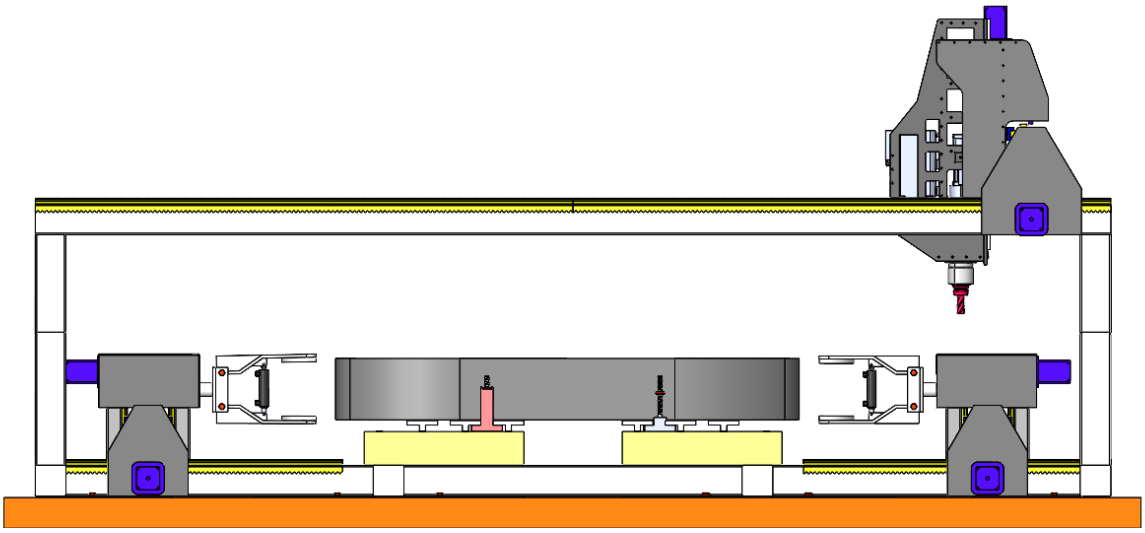
a b

Şekil 5. a-5 eksen çift kolon CNC tezgahta işlenen büyük boyutlu iş parçası b-İş parçasının taşıma-döndürme işlemi [8]

Bu çalışmada özel amaçlı ve büyük boyutlu çift kolon tezgahta büyük kütleli parçaların otomatik olarak çevrilmesi ve konumlandırılmasını yapabilecek 4. eksen sistemi geliştirilmesi hedeflenmiştir.

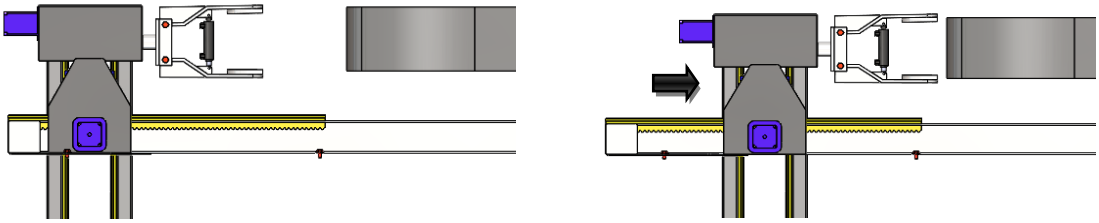
2. TASARIM VE TASARIM DOĞRULAMA

Bu çalışmada, 3 eksen çift kolonlu bir CNC tezgahta 4. eksen işlevini yerine getirecek; 1,6 ton kütleye sahip iş parçanın alt-üst ve yan yüzeylerin işlenmesine imkan sağlayacak, bağlama, çevirme ve konumlandırma işlemlerini hızlı ve güvenli bir şekilde yapılmasını sağlayacak hidrolik tahrikli bir iş bağlama ve konumlandırma sisteminin tasarımı yapılmış (Şekil 6) ve tasarım doğrulama çalışmaları gerçekleştirilmiştir.



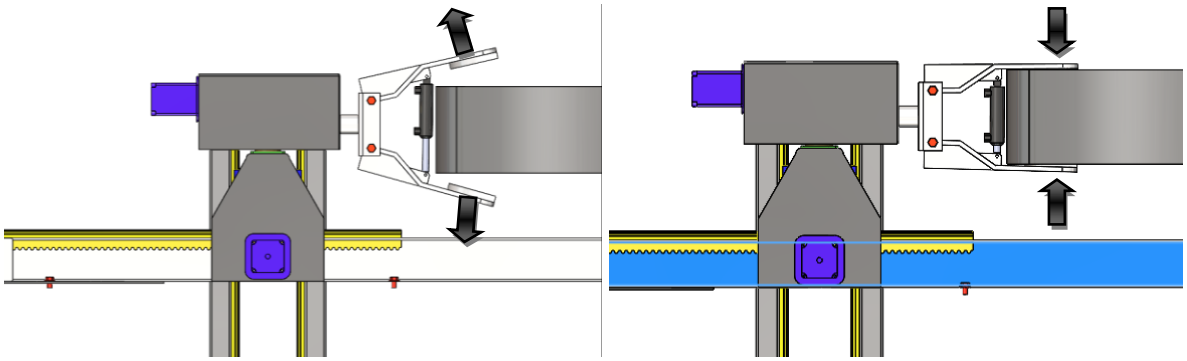
Şekil 6. Çift kolonlu freze ve hidrolik iş bağlama elemanı

Geliştirilen 4. Eksen, kendi içinde de 4 hareket eksenine sahiptir. Bu eksenler; çenelerin iş parçasına yaklaşmasını sağlayacak öteleme ekseni (Şekil 7.), iş parçasını tutacak çenelerin hareketi (Şekil 8), iş parçasının döndürülecek yüksekliğe çıkarılmasını sağlayacak yükseltme ekseni (Şekil 9) ve döndürme ekseni (Şekil 10) şeklindedir.



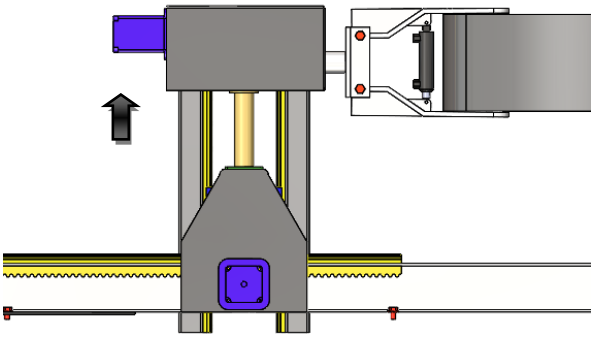
a. 4. eksen home pozisyonunda b-İş parçasına yaklaşma durumunda

Şekil 7. Öteleme ekseni (servo motor tahrikli)

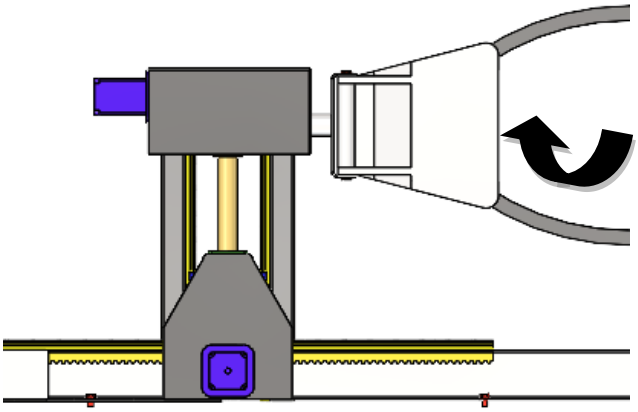


a-çene açık b-çene kapalı

Şekil 8. Çene ekseni (hidrolik tahrikli)



Şekil 9. Yükselme ekseni (hidrolik tahrikli)

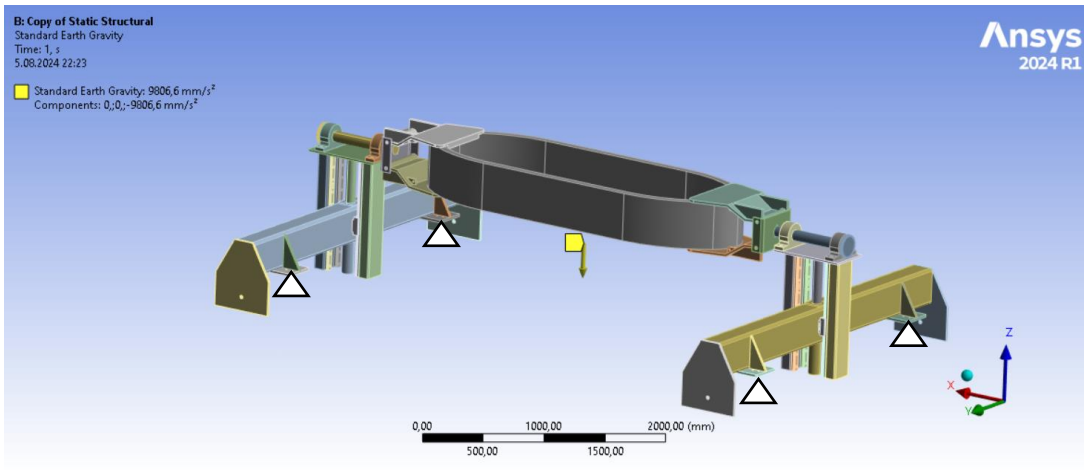


Şekil 10. Dönme ekseni (hidrolik tahrikli)

Parça döndürüldükten sonra tekrar iş parçası tekrar tabla üzerine indirilir, hidrolik bağlama elemanları parçayı sabitler ve ardından çeneler açılırak 4. Eksen home pozisyonuna geri döner.

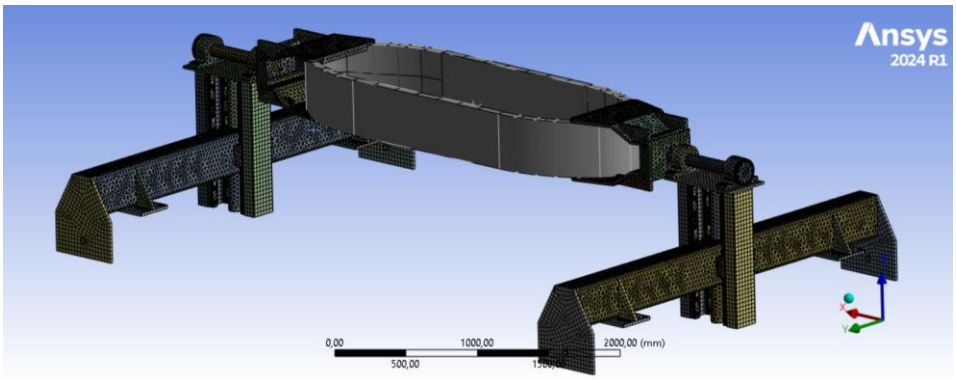
Bu işlemlerin başarı olarak gerçekleştirilmesi halinde, iş güvenliği riskleri içeren vinç ile yükün kaldırılması ve döndürülmesi işlemi bertaraf edilmiş olacak, simetrik iş parçası aynı konuma yerleştirildiğinden yeniden referanslama ihtiyacı ortadan kalkacaktır.

Bir çok araştırmacı tasarım doğrulama çalışmalarında bilgisayarların güçlü hesaplama araçlarından yararlanmaktadır [9,10]. 4 eksenli iş bağlama sisteminin tasarım çalışmalarında SolidWorks ve tasarım doğrulama çalışmalarında ANSYS 2024 kullanılmıştır. Sınır şartları Şekil 11 'de gösterildiği gibi verilmiştir. İş bağlama elemanlarına etki eden yük iş parçasının kendi ağırlığıdır (~16000 N). Lineer arabaların bağlandığı plakalar sabit mesnet olarak tanımlanmıştır (Şekil 11).



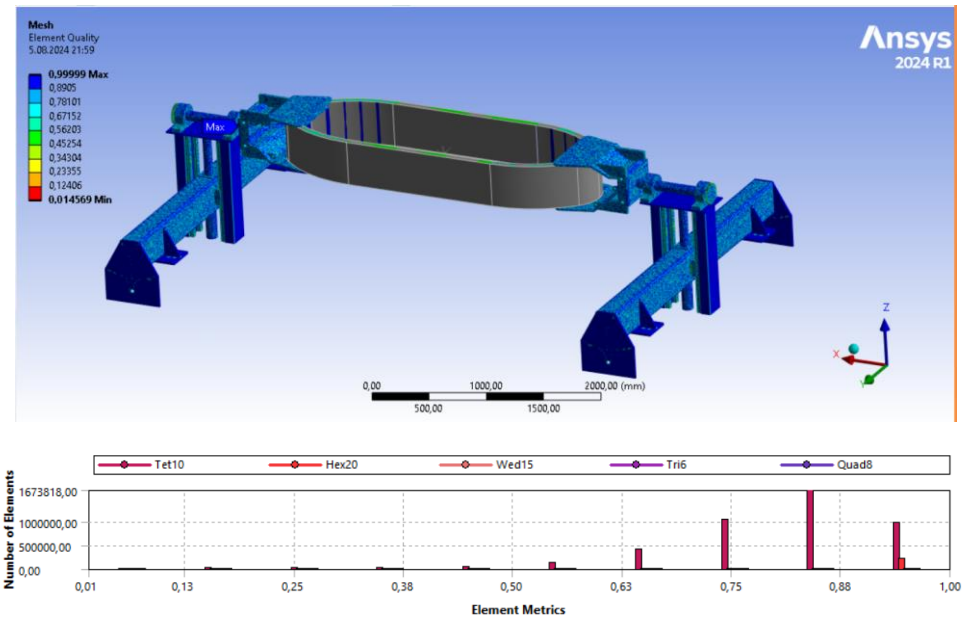
Şekil 11. Sınır şartları

Analiz yapılacak sistem üzerinde yer alan elemanlar arasında boyut farkının yüksek oluşu nedeniyle sonlu elemanlar eleman boyutları küçük seçilmiştir. Ayrıca, iş parçasının dayanımı araştırılmadığından, iş parçası sonlu elemanlar modelinde rijit olarak tanımlanmıştır (Şekil 12).



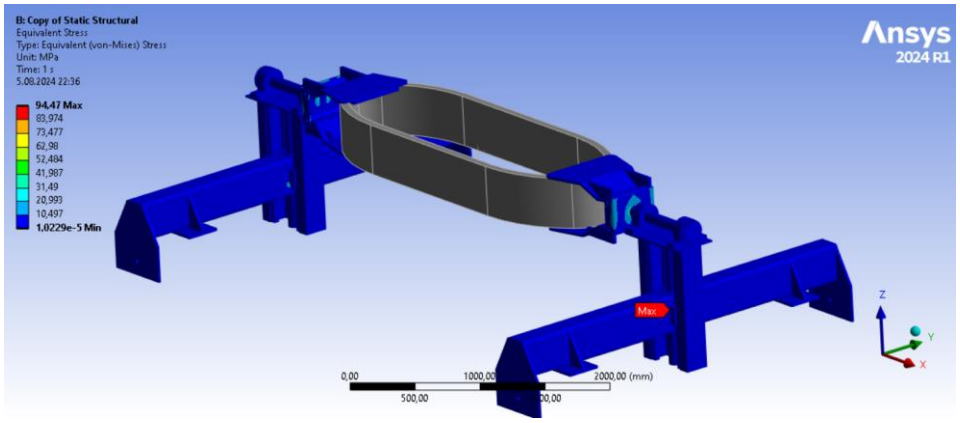
Şekil 12. Sonlu Elemanlar modeli

Sonlu elemanlar modeli üzerinde oluşan mesh kalitesi, elde edilen sonuçlar üzerinde etkili olduğundan mesh kalitesi değerlendirilmiş ve elde edilen sonlu elemanlar modelinin analiz için uygun olduğu değerlendirilmiştir.

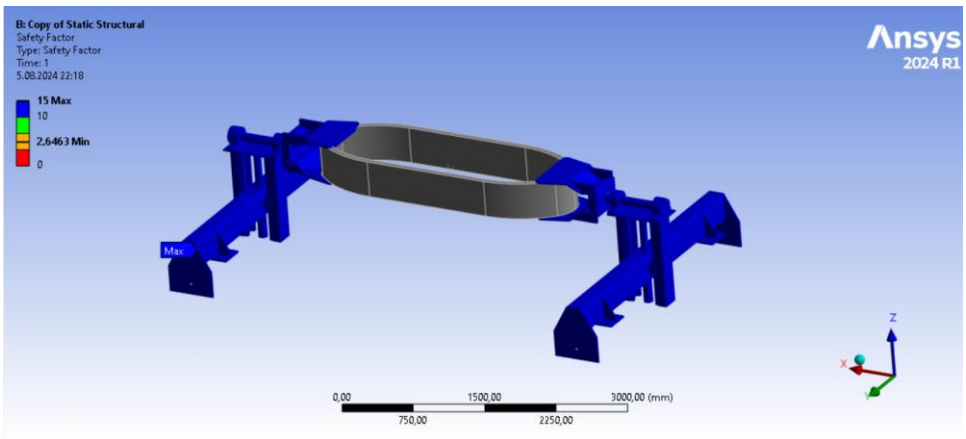


Şekil 12. Mesh kalitesi kontrolü

Yapılan analiz sonucunda maksimum gerilmenin 94,47 MPa olduğu (Şekil 13) ve bu gerilmenin, parça yükseltme ekseninde lineer araba ile temas noktasında olduğu, en düşük emniyet katsayısının da 2,64 kat olduğu görülmüştür (Şekil 14).



Şekil 13. Sistemde oluşan von-misses gerilmeleri



Şekil 14. Emniyet katsayısı

3. SONUÇLAR

Büyük boyutlu bir iş parçası üretmek amacıyla geliştirilen özel amaçlı çift kolonlu freze tezgahında iş parçasının 6 yüzeyi üzerinde işlem yapılmak istenmektedir. Büyük boyutlu iş parçasının tüm yüzeylerinin işlenebilmesi için de özel amaçlı bir iş bağlama sistemi tasarımı geliştirilmiştir. Geleneksel olarak bu tür işlemlerde, tezgah tablasıyla temas halindeki- takımın işleyemeyeceği yüzeyinin işlenebilmesi için; iş parçası vinç yardımıyla kaldırılmakta ve operator desteği ile çevrilmektedir. İş güvenliği riski ve zaman kaybına neden olan bu olumsuz durum, geliştirilmekte olan 4. eksenin devreye alınmasıyla ortadan kaldırılacaktır.
Tasarım doğrulama çalışmaları sonucunda elde edilen veriler eşliğinde sistemin güvenli şekilde çalışabileceği değerlendirilmiştir. Konuyla ilgili prototip üretim işlemleri devam etmektedir.

4. KAYNAKLAR

1- **E.Y.T. Tan, A.S. Kumar, J.Y.H. Fuh, A.Y.C (2004);** Nee, Modeling, analysis and verification of optimal fixturing design, IEEE Transactions on Automation Science and Engineering 1 (2) 121–132.
2- https://www.unisign.com/clamping-techniques/ [E.T: 01.07.2024]
3- https://www.bu.edu/epic/equipment/cnc-mill/ [E.T: 01.07.2024]
4- https://news.thomasnet.com/fullstory/clamping-devices-offer-hydraulic-and-pneumatic-operation-455498 [E.T: 01.07.2024]
5- https://www.desetec.de/en/pneumatic-clamping-elements/pneumatic-link-clamps/plp-series-pneumatic-link-clamp [E.T: 01.07.2024]
6- https://www.productionmachining.com/articles/magnetic-workholding-for-production-parts [E.T: 01.07.2024]
7- https://schunk.com/at/en/workpiece-clamping-technology/vacuum-clamping-technology/c/PUB_8323 [E.T: 01.07.2024]
8- https://madesta.lv/products/wind-power [E.T: 01.07.2024]
9- **N. Kaya (2006),** Machining fixture locating and clamping position optimization using genetic algorithms, Computers in Industry 57, 112–120
10- **N. Amaral, J.J. Rencis, Y. Rong (2004)**, Development of a finite element analysis tool for fixture design integrity verification and optimisation, International Journal of Advanced Manufacturing Technology 21, 411–419

İNCE CİDARLI ÇELİK TÜBÜLER DİREKLERİN DİNAMİK PERFORMANSI ÜZERİNE PASİF SARKAÇ AYARLI KÜTLE SÖNÜMLEYİCİLERİN ETKİLERİNİN DENEYSEL İNCELENMESİ

Sertaç ÖZDEMİR, *seozdemir@etu.edu.tr* TOBB Ekonomi ve Teknoloji Üniversitesi, 06560, Ankara

Rafet AKTEPE, *rafet.aktepe@hacettepe.edu.tr* Hacettepe Üniversitesi, 06800, Ankara

Alper ALDEMİR, *alperaldemir@hacettepe.edu.tr* Hacettepe Üniversitesi, 06800, Ankara

Erdem ACAR, *acar@etu.edu.tr* TOBB Ekonomi ve Teknoloji Üniversitesi, 06560, Ankara

ÖZET

İnce cidarlı çelik tübüler (İCÇT) direkler, sismik aktiviteler ve özellikle meteorolojik olaylar nedeniyle oluşan titreşimler sonucu büyük genliklerde döngüsel yer değiştirmeler yaşayabilir. İCÇT direklerinin hizmet ömrünü ve üzerine monte edilen ekipmanların performansını artırmak için, bu direkler aşırı titreşimlerden korunmalıdır. Bu çalışma, İCÇT direği üzerine monte edilen pasif sarkaç ayarlı kütle sönümleyicilerin (P-SAKS) performansını araştırmak için kapsamlı bir deneysel çalışma sunmaktadır. P-SAKS'lı ve P-SAKS'sız İCÇT direkleri için yapılan serbest titreşim testleri, üç farklı başlangıç uç deplasman genliği kullanılarak gerçekleştirilmiştir. Ayrıca ortam titreşim testleri gerçekleştirilmiştir. Dinamik performanslar, yer değiştirme ve ivme tepkileri üzerinden işlemsel modal analiz (İMA) yöntemleri ile değerlendirilmiştir. Deneylerden elde edilen sonuçlar, P-SAKS'ın titreşimleri etkin bir şekilde azalttığını ve İCÇT direklerinin çeşitli uyarımlar altında dinamik performansını iyileştirdiğini göstermektedir.

Anahtar Kelimeler: Titreşim kontrolü, Pasif sarkaç ayarlı kütle sönümleyici, Çelik direk

ABSTRACT

Thin-walled steel tubular (TWST) poles may undergo significant cyclic displacements due to vibrations caused by seismic activities and especially meteorological events. To enhance the service life of TWST poles and improve the performance of mounted equipment, these poles need protection from excessive vibrations. This study presents a comprehensive experimental study to investigate the performance of passive pendulum-tuned mass dampers (P-TMD) mounted on TWST poles. Free vibration tests were conducted on TWST poles with and without P-TMD, using three different initial end displacement amplitudes. Additionally, ambient vibration tests were performed. The dynamic performances were evaluated using operational modal analysis (OMA) techniques based on displacement and acceleration responses. The results obtained from the experiments demonstrate that P-TMD effectively reduces vibrations and enhances the dynamic performance of TWST poles under various excitations.

Keywords: Vibration control, Passive pendulum tuned mass damper, Steel pole

1. GİRİŞ

İnce cidarlı çelik tübüler (İCÇT) direkler, çeşitli endüstrilerde ve çevrelerde hafif, çok yönlü ve dayanıklı yapıları nedeniyle yaygın olarak kullanılmaktadır [Dexter ve Ricker, 2002]. Bu direkler, engellerin hızlı bir şekilde aşılmasını sağlayarak, dalgaların ve ışığın serbestçe yayılmasına olanak tanır ve bu sayede üzerlerine monte edilen çeşitli cihazların performansını artırır. Tübülar direkler, rüzgâr türbinleri ve güneş panelleri gibi yenilenebilir enerji kaynaklarını desteklemek, güvenlik ve gözetleme kameraları, haberleşme ve aydınlatma ekipmanları, reklam panoları gibi çeşitli yapılar için montaj yapıları olarak görev yaparlar.

İCÇT direklerinin ince yapıları ve düşük sönümleme oranları nedeniyle, meteorolojik, sismik ve mekanik olaylardan kaynaklanan titreşimlere karşı hassas oldukları bilinmektedir [Christie ve diğerleri, 2019]. Özellikle, şiddetli rüzgârların neden olduğu büyük titreşimler, bu yapıların potansiyel olarak başarısız olmasına yol açabilir. Ayrıca, sürekli titreşimler, yapısal yorgunluğa ve hizmet süresinde azalmaya neden olabilir [Gutierrez Soto, 2013].

Bu nedenle, bu tür yapıların titreşimlerini kontrol etmek ve yapıların stabilitesini artırmak için çeşitli sistemler önerilmiştir. Bu sistemler pasif, yarı-aktif ve aktif kontrol yöntemleri olarak tasarlanabilmektedir. Pasif titreşim kontrol sistemleri genelde tek bir frekansta (genellikle ilk mod frekansında) rezonansa ayarlanır ve yapısal yanıtı izleme veya dış güç gerektirmez. Bu nedenle en basit ve güçlü sistemlerdir [Elias ve Matsagar, 2017]. Depremler arasındaki baskın frekansın değişkenliği nedeniyle, pasif cihazlar bu tür olayların potansiyel frekans spektrumu boyunca sınırlı etkililik gösterir.

Pasif titreşim sönümleyiciler tiplerinden biri olan kütle sönümleyiciler basit ve düşük maliyetleri sebebiyle birçok alanda yaygın olarak kullanılmaktadır. Pasif kütle sönümleyicilerin bir türü ise bağlantılar veya kablolarla desteklenen büyük bir salınımlı kütleyi içeren pasif sarkaç ayarlı kütle sönümleyicilerdir [Gutierrez Soto, 2013; Gerges ve Vickery, 2005]. İkinci bir türü ise, içinde bulunan sıvının hareketinden yararlanarak yapının titreşimini sönümleyebilen ayarlanabilir sıvı kolonu sönümleyicilerdir [Gutierrez Soto, 2013]. Bir başka tür ise birden fazla sönümleyici tipinin üstün özelliklerini birleştiren darbe ayarlı kütle damperleridir [Zhang ve diğerleri, 2013; Zhao ve diğerleri, 2018].

Literatürde bulunan çalışmaların çoğunda P-SAKS ve İCÇT direklerinin bireysel sönümleme performansını incelenmiş olmasına rağmen P-SAKS'lı İCÇT direklerin dinamik performansını değerlendiren kapsamlı bir çalışma yapılmamıştır. Bu çalışma ile, deneysel yöntemler kullanılarak P-SAKS'ın İCÇT direklerinin dinamik davranış üzerindeki etkileri araştırılmıştır. Bu amaçla, ilk olarak P-SAKS'lı ve P-SAKS'sız İCÇT direklerinin serbest ve ortam titreşim yanıtları, deneysel çalışmalarda ivme ölçerler ve deplasman ölçerler kullanılarak ölçülmüştür. Bu titreşim yanıtları daha sonra, mod frekansı, sönümleme oranı ve mod şeklini belirlemek için Gelişmiş Frekans Alanı Dekompozisyonu (GFAD) ve Alt Uzay Tanımlama (AUT) gibi işlemsel modal analiz (İMA) yöntemleri kullanılarak titizlikle değerlendirilmiştir.

2. DENEYSEL PROGRAM

2.1 Deney Numunesinin Tanımı

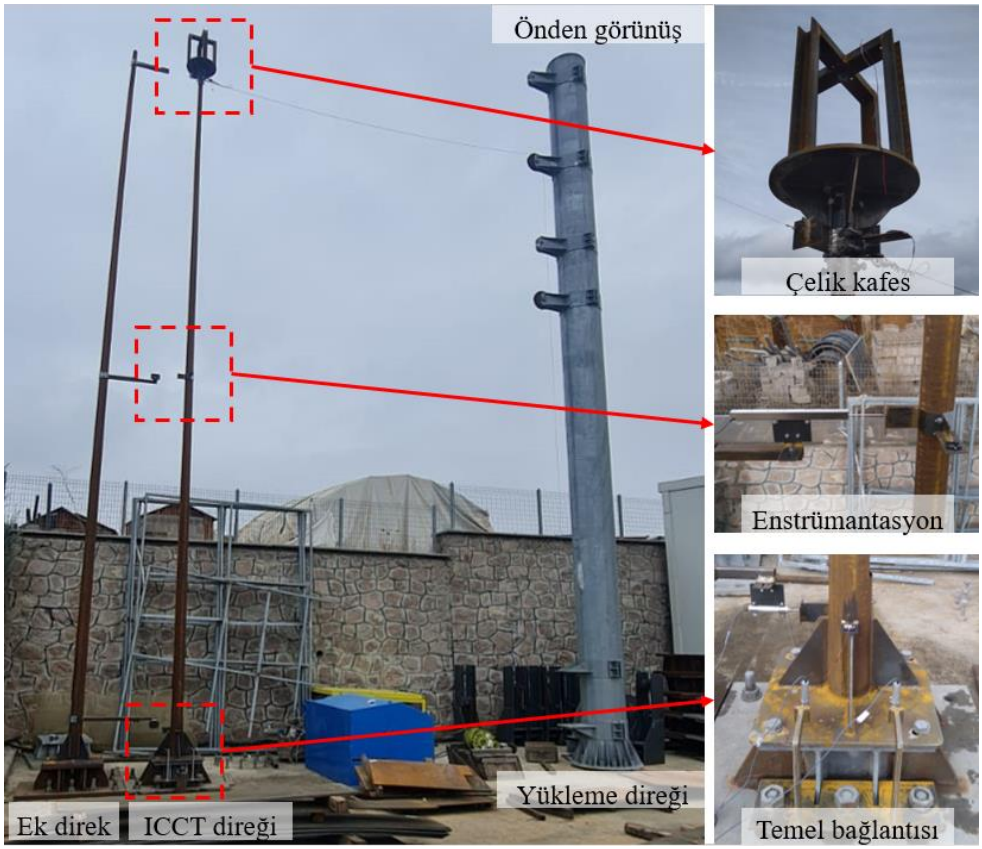
P-SAKS'lı İCÇT direğinin dinamik performansını belirlemek için, 10 metre yüksekliğinde bir dairesel çelik direk ve P-SAKS sistemi, çelik plakalar ve çelik profillerden imal edilmiştir. Dairesel çelik direk, 3 mm kalınlığında çelik kullanılarak pres bükme ve daldırma ark kaynağı ile üretilmiştir. Dairesel çelik direk konik yapıda tasarlanmıştır. Her bir metrede çapı yukarıdan aşağıya doğru 10 mm artmaktadır (taper=10mm/m). Dairesel çelik direğin alt çapı

160 mm iken üst çapı 60 mm'dir. Dairesel çelik direğin kütlesi yaklaşık 81 kg'dır. Dairesel çelik direğin alt ucuna 650×650×16 mm ölçülerinde bir çelik taban plakasına kaynatılmıştır. 200×300 mm ölçülerinde 6 mm kalınlığında olan 4 adet takviye plakası, bağlantının dayanımını ve rijitliğini artırmak için taban plakasına ve dairesel çelik direğin alt ucuna kaynatılmıştır. P-SAKS sistemi, dairesel çelik direğin üst ucuna monte edilmiştir.

P-SAKS sistemi 450 mm çapında ve 500 mm yüksekliğinde 36 kg ağırlığında silindirik boş bir çelik kafes ve 120 mm çapında ve 240 mm yüksekliğinde 22 kg ağırlığında silindirik bir çelik kütle olmak üzere iki parçadan oluşmaktadır. Çelik kafes, silindirik çelik kütlenin yerleştirilmesi ve serbestçe salınım yapması için kullanılmıştır. Çelik kafes, UNP65 profillerden ve 12 mm kalınlığında bir çelik taban plakasından imal edilmiştir. Çelik taban plakanın altında, çelik kafesi çelik direğe bağlamak için 76 mm çapında, 300 mm yüksekliğinde ve 4 mm kalınlığında çelik bir boru kaynatılmıştır (spigot borusu). Silindirik çelik kütle, bir göz cıvatası ile çelik kafesin içine asılmaktadır. İCÇT direği ve P-SAKS sistemi, S235JR sınıfı çelikten üretilmiştir. Seçilen çeliğin akma dayanımı ve nihai dayanımı sırasıyla 235 MPa ve 360-510 MPa'dır. Seçilen çelik sınıfı kolayca kaynaklanabilir ve şekillendirilebilir özelliktedir.

2.2 Deneylerde Kullanılan Ekipmanlar

Test kurulumunun detayları ve enstrümantasyonu Şekil 1'de gösterilmiştir. İCÇT direği, dört adet M24 cıvata ile zemine sabitlenmiştir. Yatay yükleme yani başlangıç deplasmanı, İCÇT direğinin üst noktasından 200 mm aşağıdaki bir noktaya çelik kablo ile uygulanmıştır. Çelik kablo yönü, uzun bir çelik yükleme direği üzerine monte edilmiş bir makara yardımıyla yataydan dikeye değiştirilmiştir. Böylece, yükleme, çelik kablonun ucuna asılan, önceden belirlenmiş kütleler ile kolayca uygulanmıştır.



Şekil 1 Deney Kurulumunun Detayları ve Ekipmanlar.

Enstrümantasyon, 5 adet deplasmanölçer (LVDT), 3 adet ivmeölçer ve bir veri toplama sistemini içermektedir. LVDT'ler, test edilen İCÇT direğinden 1.25 metre uzakta konumlandırılmış bir ek çelik direğe sabitlenmiştir. İCÇT direğinin uç deplasmanı, 500 mm nominal kapasiteye sahip LVDT 1 tarafından ölçülmüştür. Ayrıca, İCÇT direğinin orta ve tabanına yakın noktalarında bulunan sırasıyla LVDT 2 ve LVDT 3 ile ölçülen yanal deplasmanlar kullanılaarak direğin test anındaki eğilme şekli belirlenmiştir. Son olarak direğin taban plakasının dönüşünü ve taban plakasının yükselmesini ölçmek amacıyla 2 adet LVDT (LVDT 4 ve LVDT 5) kullanılmıştır. Tüm bunların yanında, çelik direğin titreşim tepkisini ölçmek için LVDT1, LVDT 2 ve LVDT 3'ün ölçüm yaptığı yerlere üç adet G-Link 200 OEM ivmeölçer yerleştirilmiştir. (Şekil 1).

P-SAKS'lı ve P-SAKS'sız İCÇT direklerin serbest titreşim davranışını araştırmak için yapılan testlerde uygulanan prosedürde, direkler temelden 10 m yükseklikten 10 kg, 20 kg ve 30 kg olmak üzere üç farklı kütleye denk gelen yanal deplasmana tabii tutulmuştur. Deplasman, önceden ölçülmüş kütleler kullanılarak çelik kablo aracılığıyla İCÇT direğine uygulanmıştır. Uygulanan kütlenin büyüklüğü belirlenirken, çelik kablo'nun dikey parçası, cıvataları ve ekstra

bağlantı parçalar gibi tüm aletlerin kütlesi hesaba katılmıştır. İCÇT direği yüklendiğinde ve statik denge durumu sağlandığında, uygulanan yük aniden kaldırılmış ve İCÇT direğinin serbest titreşim anındaki hareketi kaydedilmiştir.

3.DENEYSEL SONUÇLAR

P-SAKS'lı ve P-SAKS'sız İCÇT direklerin, üç farklı başlangıç deplasmanına göre serbest titreşim tepkileri, LVDT'ler ve ivmeölçerler aracılığıyla elde edilmiştir. Bu tepkiler Şekil 2 ve Şekil 3'te gösterilmiştir. Elde edilen yer değiştirme ve ivme verileri yatay rijitliği, tepki frekansı ve sönümleme oranı gibi modal parametrelerin belirlenmesi için kullanılmıştır. Sistemlerin yatay rijitliği, malzemenin elastik özellikleri, geometri ve destek koşullarına bağlı olmakta ve elastik bölgede dinamik yüklemelerden etkilenmemektedir. Frekans, yapıların deprem, rüzgâr gibi dinamik yükler altında nasıl tepki verdiğini belirleyen kritik bir faktördür. Düşük frekansa sahip yapılar, daha esnektir ve daha yüksek yer değiştirme talepleriyle karşılaşırlar. Bir diğer önemli faktör olan sönümleme oranı, dinamik yüklemeler altında enerji emilimi kapasitesi ve titreşim genliklerini belirlemede önemli rol oynamaktadır.

İCÇT direğinin çeşitli başlangıç deplasmanları için etkili sönümleme oranları (ξ_{eff}), tek serbestlik dereceli (TSD) bir sistemle serbest titreşim tepkisinin alanlarının eşitlenmesiyle hesaplanmıştır. TSD sistemlerinin serbest titreşim denklemi ve bu denklemin çözümü denklemler (1) ve (2)'de verilmiştir.

$$m\ddot{u} + c\dot{u} + ku = 0 \quad \textbf{(1)}$$

$$u(t) = e^{-\zeta_{eff}\omega_n t}[u(0)\cos\omega_D t + \frac{\dot{u}(0) + \zeta_{eff}\omega_n u(0)}{\omega_D}\sin\omega_D t] \quad \textbf{(2)}$$

Burada, $\ddot{u}$, $\dot{u}$, ve u sırasıyla ivme, hız ve yer değiştirme matrislerini ifade etmektedir. ω_n ve ω_D sırasıyla P-SAKS'sız ve P-SAKS'lı İCÇT direklerinin doğal frekanslarını belirtmektedir. Son olarak, "t" zamanı temsil etmektedir.

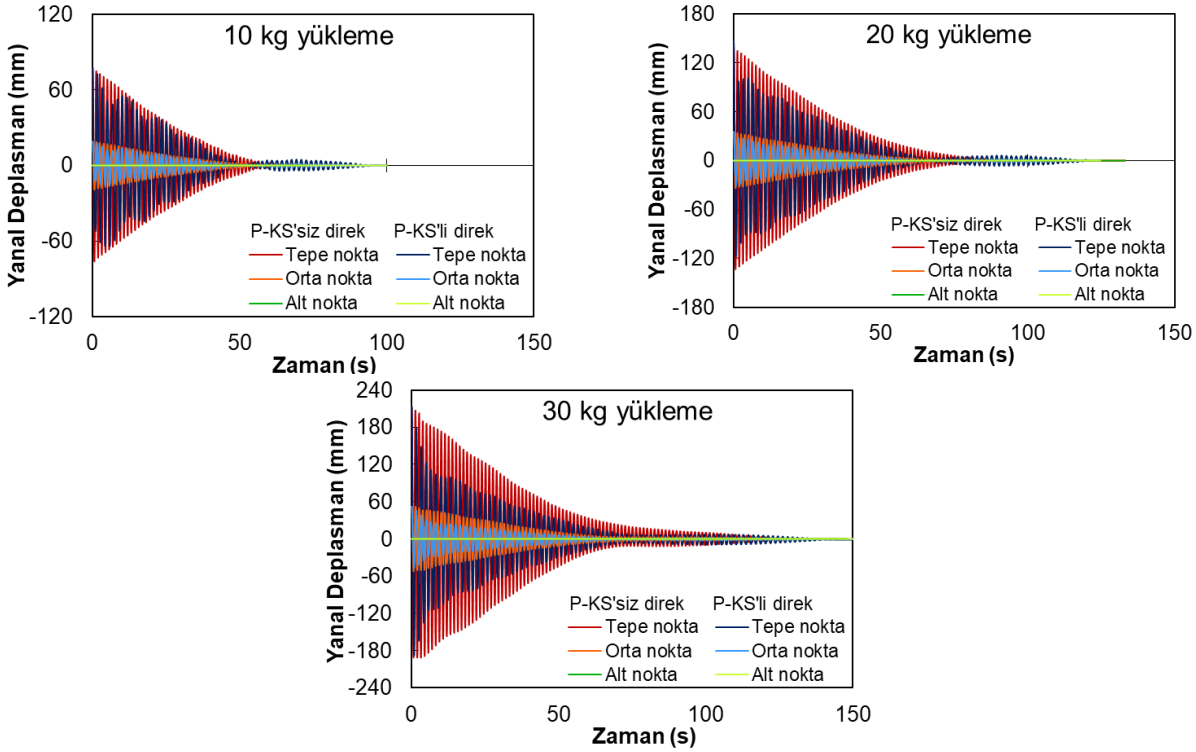
Etkili sönümleme oranı, yer değiştirme genliğindeki azalma oranı ve bu azalmayı sağlamak için gerekli olan döngü sayısına göre belirlenmiştir. Yer değiştirmeye dayalı etkili sönümleme oranı hesaplama yöntemi, sistemlerin dinamik davranışını anlamak için kullanılmaktadır. Bu

nedenle, maksimum yer değiştirme genliğinde %50 azalma sağlayan sönümleme oranları ($\xi_{0.5}$) Denklem (3) kullanılarak hesaplanmıştır.

$$\zeta_{0.5} = \frac{1}{2\pi j} \ln \frac{u_i}{u_{0.5i}} \quad \textbf{(3)}$$

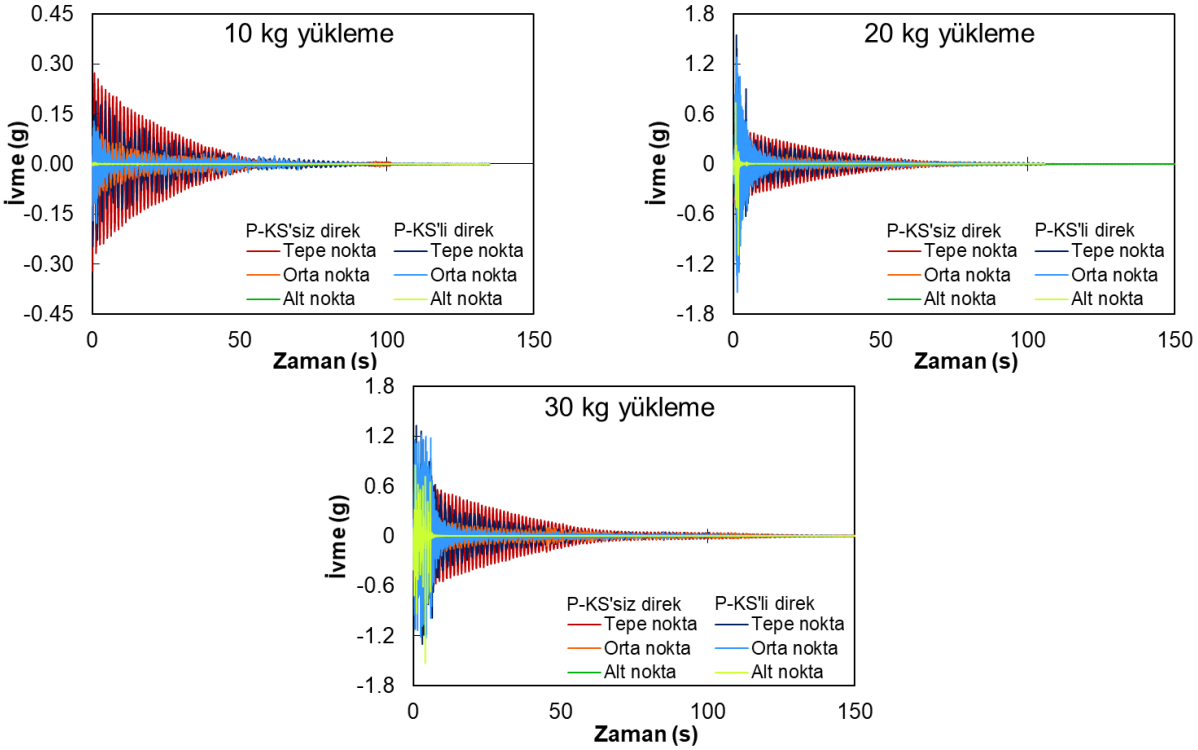
$\zeta_{0.5}$, maksimum yer değiştirme genliğinde %50 azalmaya karşılık gelen sönümleme oranını ifade etmekte. j, yer değiştirme genliğini %50 azaltmak için gereken döngü sayısını, u_i ve $u_{0.5i}$ ise sırasıyla maksimum ve maksimumun %50'si yer değiştirme genliklerini belirtmektedir.

İCÇT direklerin çeşitli başlangıç deplasmanı koşulları altında zamana bağlı yanal yer değiştirme tepkileri Şekil 2'de gösterilmiştir. P-SAKS bulunan İCÇT direği, bulunmayanlara göre daha düşük yer değiştirme tepkisi sergilemiştir. P-SAKS, yer değiştirme genliklerini azaltmanın yanı sıra, pozitif ve negatif yönlere eşit olmayan yer değiştirme genlikleri de oluşturmuştur. Ayrıca, 20 kg ve 30 kg yükler altında yapılan serbest titreşim testlerinin ilk döngülerinde yer değiştirme genliğinde belirgin bir azalma sağlamıştır. Daha sonra azalma oranı düşmekte ve testler boyunca neredeyse sabit kalmıştır. Şekilde görüldüğü üzere, 30 kg yük altında, P-SAKS'lı İCÇT direğinin yer değiştirme tepkisi, yükün serbest bırakılmasından kısa bir süre sonra, İCÇT kütlesi ile çelik kafes arasındaki çarpışma nedeniyle belirgin bir azalma yaşamıştır. Ek olarak, çelik kütlenin titreşimi, yer değiştirme genliklerinin sıfıra yaklaştığı ilk andan kısa bir süre sonra yer değiştirme genliğinde küçük bir artışa neden olmuştur.



Şekil 2 Çeşitli Başlangıç Deplasmanlarına Maruz Kalan İCÇT Direklerin Zamana Bağlı Yer Değiştirme Tepkileri.

Şekil 3, çeşitli başlangıç deplasmanları altında P-SAKS'lı ve P-SAKS'sız İCÇT direklerinin zamana bağlı ivme tepkilerini göstermektedir. P-SAKS'lı İCÇT direğinin ivme tepkileri genellikle P-SAKS'sız olanlara göre daha düşüktür. Ancak, 20 kg ve 30 kg yüklerle yapılan serbest titreşim testlerinde, P-SAKS'lı İCÇT direğinin orta ve alt noktalarda ölçülen ilk 10 sn'deki ivme değerleri, çelik kütlenin titreşimi nedeniyle ani ve yüksek genlikli değişiklikler göstermektedir. İCÇT direği ve P-SAKS arasındaki frekans farklılıkları nedeniyle, P-SAKS'lı İCÇT direğinin ivme tepkisi tam bir sinüs şekli almamıştır, bu durum diğer ivme tepkileri ile karşılaştırıldığında fark edilmektedir.



Şekil 3 Çeşitli Başlangıç Deplasmanlarına Maruz Kalan İCÇT Direklerin Zamana Bağlı İvme Tepkileri.

Yer değiştirme verilerinden elde edilen yanal rijitlik, frekans ve sönümleme oranı gibi parametreler ayrı ayrı Tablo 1'de listelenmiştir. P-SAKS'sız ve P-SAKS'lı İCÇT direklerin yanal rijitlik değerleri (k) sırasıyla ortalama 1351 N/m ve 1326 N/m'dir. İhmal edilebilecek derecedeki yanal rijitlik farkı, sönümleyicinin kütlesi ve direğin başlangıç geometrik kusurların kombinasyonu sonucu kaynaklanabilmektedir. P-SAKS'ın sisteme dahil edilmesi, frekansı 0.80 Hz'den 0.60 Hz'ye düşürmüştür. Sistemdeki toplam kütlenin %18.7 artışı frekansta %25 azalmaya neden olmuştur. Etkili sönümleme oranı (ξ_{eff}) ve maksimum yer değiştirme genliğinde %50 azalma için sönümleme oranları ($\xi_{0.5}$), 30 kg yükleme altında P-SAKS'lı İCÇT direği hariç benzer değerler vermiştir. 30 kg yükleme altında P-SAKS'lı İCÇT direğinin sönümleme oranında gözlemlenen bu fark, yük bırakıldıktan hemen sonra serbest titreşimin ilk döngüsünde çelik kütlenin ve çelik kafesin çarpışmasından kaynaklanmıştır. Ortalama olarak, P-SAKS olmayan İCÇT direği %0.68 (0.69%) etkili bir sönümleme oranına sahipken, P-SAKS'lı İCÇT direği %1.19 (1.44%) etkili bir sönümleme oranına sahiptir. P-SAKS'ın sisteme dahil edilmesi, ortalama %75 (108%) bir sönümleme oranı artışı sağlamıştır. P-SAKS'ın sönümleme oranı üzerindeki etkisi, başlangıç yer değiştirme genliği büyük olduğunda daha belirgindir. En büyük yer değiştirme talebinde, P-SAKS'lı İCÇT direğinin sönümleme oranı %2'ye kadar çıkmıştır.

Tablo 1 Elde Edilen Performans Parametrelerinin Özeti.

Deney	U_{max} (mm)	k (N/m)	t (s) (5%)	f_1 (Hz)	A_0 (g)	ζ_{eff} (%)	$\zeta_{0.5}$ (%)
Dampersiz (10 kg LL)	77.30	1269.08	54.85	0.80	0.007-0.229-0.060	0.80	0.79
Dampersiz (20 kg LL)	139.80	1403.43	73.65	0.80	0.149-0.461-0.940	0.66	0.68
Dampersiz (30 kg LL)	213.20	1380.39	99.75	0.80	0.618-0.796-1.476	0.58	0.59
Ortalama		**1350.97**	**76.08**	**0.80**		**0.68**	**0.69**
Damperli (10 kg LL)	77.80	1260.93	48.10	0.59	0.013-0.304-0.433	1.23	1.23
Damperli (20 kg LL)	146.30	1341.08	61.35	0.60	1.797-2.760-2.674	1.14	1.09
Damperli (30 kg LL)	213.70	1377.16	69.50	0.60	2.366-2.433-2.624	1.19	2.00
Ortalama		**1326.39**	**59.65**	**0.60**		**1.19**	**1.44**

4. MODAL ANALİZ SONUÇLARI

P-SAKS'lı ve P-SAKS'sız İCÇT direklerin hem serbest hem de ortam titreşim testleri yapılmış, bu testlerde direklerin ivme tepkileri toplanmıştır. Testler sırasında ivme tepkileri yaklaşık 150 saniye boyunca kaydedilmiştir. Yapının modal parametrelerini yani; mod şekli, doğal frekans ve sönümleme oranını belirlemek için GFAD ve AUT olmak üzere iki İMA yöntemi, ARTEMIS Modal Pro adlı ticari yazılım yardımıyla kullanılmıştır.

İMA, yapısal çıktıları ölçümlemek ve ortam kuvvetlerini ölçülmeyen girdi olarak kullanmak üzerine kurulu bir tekniktir. İMA; parametik ve parametrik olmayan yöntemler olarak iki kategoriye ayrılabilir. Parametrik olmayan yöntemler, ölçülen verileri kullanarak frekans alanında bir dizi matematiksel işlem yaparak yapının dinamik özelliklerini tespit ederken; parametrik yöntemler, zaman alanındaki bir parametrik modeli tahmin ederek modal parametreleri optimize eder ve hesaplanan tepkileri gözlemlerle uyumlu hale getirir.

GFAD, frekans alanı dekompozisyonu (FAD) yönteminin parametrik bir genişlemesidir ve doğrudan uygulanabilen parametrik olmayan bir yaklaşımdır. Bu yöntemle, zaman alanından frekans alanına dönüştürülen ham verilerden spektral yoğunluk matrisleri tahmin edilir. Bu matrisler daha sonra, tekil değer dekompozisyonu gibi algoritmalar kullanılarak bireysel frekans bileşenlerine ayrılır [Brincker ve diğerleri, 2000]. GFAD, FAD metodunu doğal

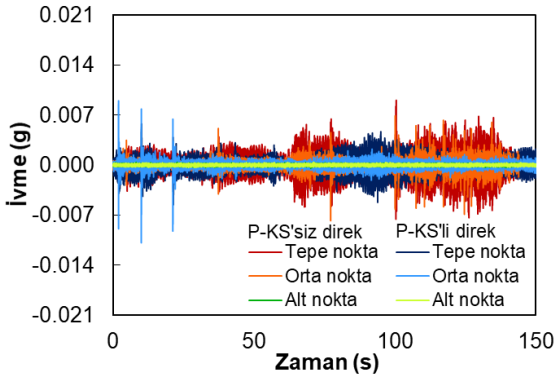
frekanslar, mod şekilleri ve sönümleme oranları için daha kesin tahminler sağlayacak ek adımlarla geliştirir.

AUT ise, yapıların modal parametrelerini yalnızca çıktı kullanarak tespit etmek için geniş bir uygulama alanına sahip olan çok değişkenli bir tanımlama yöntemidir. AUT, sayısal olarak stabil, gürültü bozulmalarına dayanıklı ve ortam uyarılmalarındaki zamana bağlı değişimleri incelemek için uygun olan bir yöntemdir [Liu ve diğerleri, 2013]. İlk olarak Van Overschee ve De Moor tarafından geliştirilen (1991) ve daha sonra Peeters ve De Roeck tarafından geliştirilen (1999) veriye dayalı AUT genel algoritması, ölçülen verilerin olasılıksal durum uzay sistemini dekompoze ederek modal parametreleri çıkarmaktadır. Bu çalışmada, AUT'nin Genişletilmiş Ağırlıksız Temel Bileşen uygulaması kullanılmıştır.

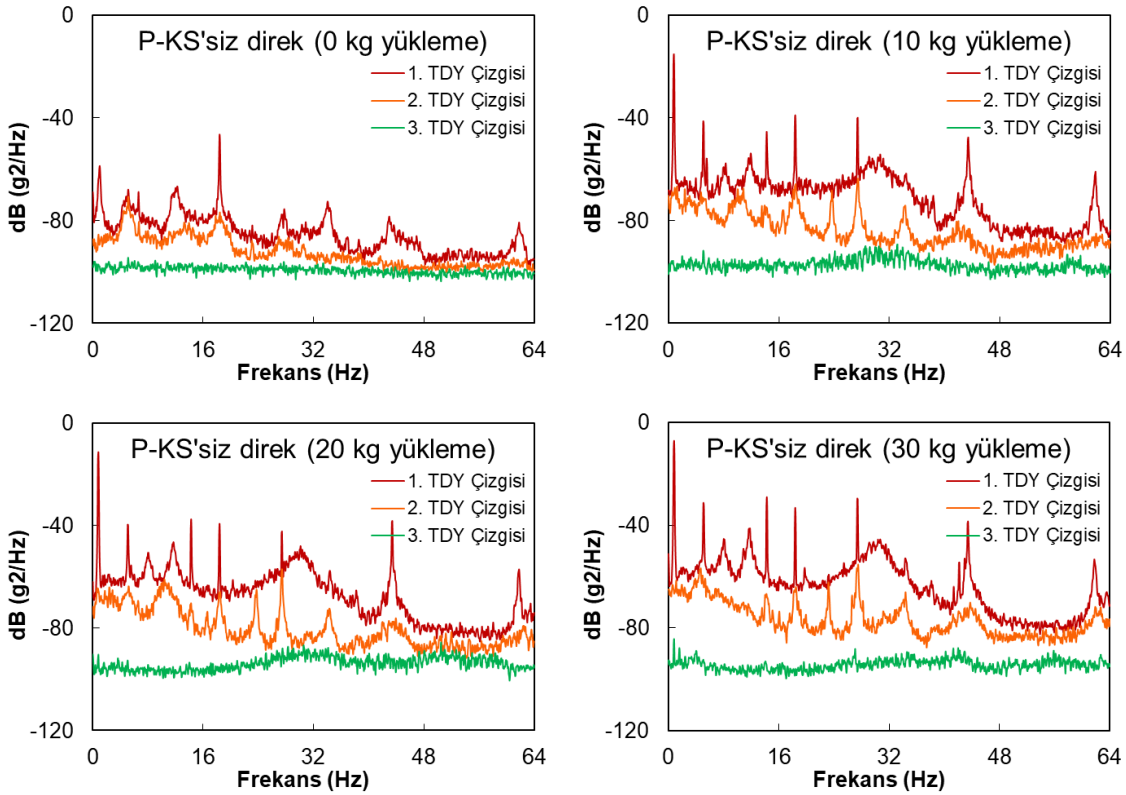
P-SAKS'lı ve P-SAKS'sız İCÇT direklerin ortam titreşim ölçümleri Şekil 4'te gösterilmektedir. Sistemin ince yapısı nedeniyle İCÇT direklerinin döngüsel titreşimi ortam titreşimi ivme yanıtlarından kolayca gözlemlenebilmektedir. P-SAKS'sız İCÇT direğinin ivme genlikleri, P-SAKS'lı olanlara göre biraz daha yüksektir. Doğal ve insan kaynaklı uyarılmalar, ölçülen titreşim yanıtlarındaki zirvelerin gözlemlenmesini önemli ölçüde etkiler. Tekil değer yoğunluk grafikleri, P-SAKS'sız ve P-SAKS'lı İCÇT direkleri için sırasıyla Şekil 5 ve Şekil 6'de gösterilmiştir. Yaklaşık olarak 18 Hz, 33 Hz ve 63 Hz'de gözlenen üç zirve, çift ve kopya modlar olarak tanımlandığı için tercih edilen modlar olarak dikkate alınmamıştır. Beş belirgin zirve modları tanımlamak için seçilmiş ve ilgili frekansları, sönümleme oranları, sönümleme oranı tahminlerinin standart sapmaları ve karmaşıklıkları P-SAKS'sız ve P-SAKS'lı durumlar için sırasıyla Tablo 2 ve Tablo 3'te özetlenmiştir. Örnekleme aralığının kısalığı nedeniyle kısmen gürültülü grafikler elde edilmiştir. İMA tarafından tahmin edilen temel mod frekansları, ortam ve serbest titreşim testleri arasında farklılık göstermektedir. P-SAKS'sız İCÇT direği için temel mod frekansları, ortam titreşiminde 0.99 Hz ve serbest titreşim durumlarında 0.80 Hz olarak ölçülmüştür. Benzer şekilde, P-SAKS'lı bir İCÇT direği için temel mod frekansları, ortam titreşiminde yaklaşık 0.72 Hz ve serbest titreşim durumlarında 0.60 Hz olarak ölçülmüştür.

Her iki durumda da serbest titreşim testlerinden elde edilen temel mod frekansları, yer değiştirme ölçümlerinden elde edilen sonuçlarla yakından örtüşmektedir. İMA'nın ilk mod frekansı tahminlerindeki farklılık, gerekli olan süreden daha kısa bir süre boyunca veri kaydedilmesinden kaynaklanmış olabilir. P-SAKS'sız İCÇT direği için serbest titreşim

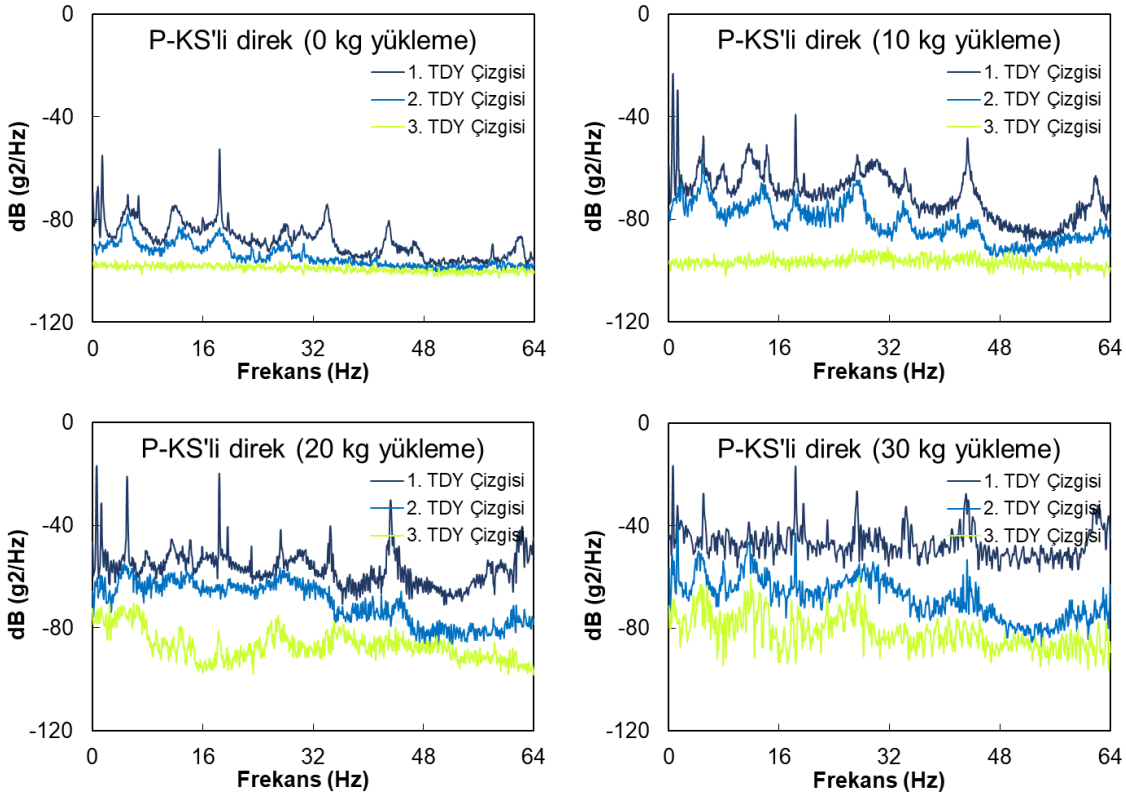
testlerinde GFAD (AUT) tarafından tahmin edilen ikinci moddan beşinci moda kadar frekanslar ortalama olarak şöyledir: 5.09 (5.08), 14.25 (14.26), 27.41 (27.43), ve 43.41 (43.41). P-SAKS'lı İCÇT direği için, serbest titreşim testlerinde GFAD (AUT) tarafından tahmin edilen ikinci moddan beşinci moda kadar frekanslar ortalama olarak şöyledir: 5.02 (5.09), 14.23 (13.99), 27.31 (27.25), ve 43.23 (43.28). Gözlemlendiği üzere hem GFAD hem de AUT, mod frekansları için benzer tahminler sunmakta ve P-SAKS'ın yüksek mod frekansları üzerindeki etkisi minimal düzeyde olduğu gözlemlenmektedir. Ek olarak, P-SAKS'ın doğal titreşim frekansı tekil değer yoğunluk grafiklerinden belirlenmiş ve 1.37 Hz olarak bulunmuştur.



Şekil 4 Ortam Koşulları Altında P-SAKS'lı ve P-SAKS'sız İCÇT Direklerinin Zamanla Değişen İvme Tepkileri.



Şekil 5 Çeşitli Yükleme Durumları Altında P-SAKS'sız İCÇT Direği İçin Tekil Değer Yoğunluk Grafikleri.



Şekil 6 Çeşitli Yükleme Durumlarında P-SAKS'lı İCÇT Direği İçin Tekil Değer Yoğunluk Grafikleri.

İMA tarafından elde edilen sönümleme oranı tahminleri, P-SAKS'sız ve P-SAKS'lı İÇÇT direkleri için sırasıyla Tablo 2 ve Tablo 3'te sunulmuştur. Her iki durumda da mod numarası arttıkça sönümleme oranlarının azaldığı gözlemlenmiştir, bu da sönümlemenin büyük ölçüde kütleyle orantılı olduğunu göstermiştir. Ortam titreşim testlerinin serbest titreşim testlerine kıyasla daha yüksek sönümleme oranları ve karmaşıklık değerleri verdiği belirlenmiştir. Daha yüksek karmaşıklık değerleri, kısa süreli ve gürültülü ölçümlerin ya da zayıf modal parametre tahminlerinin varlığını önermekte, bu da tahminlerin karşılaştırılmasını mantıksız kılabilmektedir. Bu nedenle, sadece serbest titreşim testlerinden elde edilen İMA tahminleri karşılaştırılmıştır.

Tablo 2 P-SAKS'sız İÇÇT Direği İçin GFAD ve AUT Yöntemleri Kullanılarak Elde Edilen Modal Parametreler.

	GFAD			AUT		
	Frekans [Hz]	**Sönümleme Oranı [%]**	**Sönümleme Oranı SS. [%]**	**Frekans [Hz]**	**Sönümleme Oranı [%]**	**Sönümleme Oranı SS. [%]**
Ortam Titreşimi	0.989	9.703	N/A	0.991	11.336	4.102
	5.125	0.000	N/A	5.413	6.677	2.382
	12.103	2.436	N/A	12.129	2.585	0.459
	27.694	0.948	N/A	27.558	1.279	0.131
	43.091	0.851	N/A	43.269	1.581	0.199
Serbest Titreşim (10 kg yükleme)	0.801	4.360	N/A	0.797	1.214	1.835
	5.083	0.696	N/A	5.090	0.865	0.143
	14.246	0.226	N/A	14.259	0.796	0.140
	27.408	0.133	N/A	27.403	0.139	0.035
	43.420	0.115	N/A	43.428	0.135	0.013
Serbest Titreşim (20 kg yükleme)	0.801	4.319	N/A	0.797	0.980	0.944
	5.089	0.756	N/A	5.084	1.031	0.123
	14.253	0.232	N/A	14.267	0.379	0.047
	27.412	0.132	N/A	27.425	0.232	0.029
	43.410	0.072	N/A	43.411	0.096	0.003
Serbest Titreşim (30 kg yükleme)	0.801	4.315	N/A	0.797	1.066	1.018
	5.084	0.730	N/A	5.071	1.023	0.127
	14.250	0.216	N/A	14.256	0.242	0.025
	27.405	0.127	N/A	27.407	0.128	0.021
	43.416	0.084	N/A	43.395	0.154	0.013

Tablo 3 P-SAKS'lı İCÇT Direği İçin GFAD ve AUT Yöntemleri Kullanılarak Elde Edilen Modal Parametreler.

	GFAD			AUT		
	Frekans [Hz]	**Sönümleme Oranı [%]**	**Sönümleme Oranı SS. [%]**	**Frekans [Hz]**	**Sönümleme Oranı [%]**	**Sönümleme Oranı SS. [%]**
Ortam Titreşimi	0.724	10.175	N/A	-	-	-
	5.063	0	N/A	5.741	15.949	1.527
	-	-	-	-	-	-
	27.877	1.16	N/A	27.796	1.952	0.184
	42.844	0.787	N/A	42.794	1.560	0.790
Serbest Titreşim (10 kg yükleme)	0.599	5.693	N/A	-	-	-
	5.031	1.185	N/A	5.098	3.146	1.272
	14.256	1.117	N/A	14.205	0.701	0.084
	27.373	0.662	N/A	27.347	1.471	1.039
	43.336	0.148	N/A	43.368	0.205	0.005
Serbest Titreşim (20 kg yükleme)	0.599	5.673	N/A	-	-	-
	5.021	0.753	N/A	5.010	0.522	0.120
	14.193	1.043	N/A	13.358	4.219	2.984
	27.279	0.177	N/A	27.160	0.980	0.144
	43.230	0.106	N/A	43.260	0.214	0.066
Serbest Titreşim (30 kg yükleme)	0.5990	5.704	N/A	-	-	-
	5.0200	0.967	N/A	5.159	7.238	2.359
	14.2530	0.682	N/A	14.415	4.890	1.802
	27.2860	0.257	N/A	27.228	0.499	0.128
	43.1360	0.355	N/A	43.207	0.513	0.050

5. SONUÇLAR

Bu bildiri, P-SAKS'ların İCÇT direklerin dinamik performansına olan etkilerinin araştırılması üzerine detaylı bir deneysel çalışma sunmaktadır. P-SAKS'lı ve P-SAKS'sız İCÇT direklerini temsil eden iki çelik direk, 3 farklı başlangıç deplasman değeri için serbest titreşim ve ortam titreşim koşulları altında test edilmiştir. İCÇT direklerinin yer değiştirme ve ivme tepkileri, LVDT'ler ve ivmeölçerler yardımıyla kaydedilmiştir. İncelenen direklerin mod şekli, doğal frekans ve sönüm oranı gibi modal parametrelerinin belirlenmesi amacıyla İMA yöntemleri olan GFAD ve AUT kullanılmıştır. Ayrıca yer değiştirme-zaman eğrileri kullanılarak sönümleme oranı ve mod şekilleri elde edilmiş ve GFAD ve AUT yöntemlerinden elde edilen sonuçlarla karşılaştırılmıştır. Bu çalışmada sunulan bulgular ve tartışmalar temel alındığında, aşağıdaki temel sonuçlar çıkarılabilir:

- P-SAKS'ın uygulanması, sönüm oranında ortalama %75 ila %108 arasında bir artışa yol açmaktadır.
- Serbest titreşim testlerinde, P-SAKS'sız İCÇT direğin sönüm oranı başlangıç deplasman değeri arttıkça azalmaktadır.
- P-SAKS'lı ve P-SAKS'sız İCÇT direklerde mod sayısı artıkça moda karşılık gelen sönüm oranı azalmıştır. Bu, İCÇT direklerin sönüm oranının temel olarak direğin havayla etkileşimi ile ilişkili olduğunu göstermektedir.
- Ortam titreşim testlerinden elde edilen İMA sonuçları, serbest titreşim testlerinden elde edilen sonuçlara kıyasla daha yüksek sönüm oranları ve karmaşıklık değerleri vermektedir. Bunun birinci nedeninin ortam titreşimlerinin kısa bir süre boyunca ölçülmesi düşünülmektedir. Dolayısıyla, sınırlı veriler için, serbest titreşim testleri, İMA için ortam titreşim testlerine kıyasla daha güvenilir sonuçlar sunabilir sonucuna varılabilir.

TEŞEKKÜR

Test alanı, test ekipmanı ve teknik destek sağladığı için Hacettepe Üniversitesi ve Mitaş Endüstri'ye teşekkür ederiz.

KAYNAKÇA

1. **Dexter, R. J., & Ricker, M. J. (2002),** Fatigue resistant design of cantilevered signal, sign, and light supports. NCHRP Rep. No. 469, National Cooperative Highway Research Program, Transportation Research Board, Washington, D.C.
2. **Christie, M. D., Sun, S., Deng, L., Ning, D. H., Du, H., Zhang, S. W., & Li, W. H. (2019),** A variable resonance magnetorheological-fluid-based pendulum tuned mass damper for seismic vibration suppression. Mechanical Systems and Signal Processing, 116, 530–544
3. **Gutierrez Soto, M., & Adeli, H. (2013),** Tuned mass dampers. Archives of Computational Methods in Engineering, 20, 419-431.
4. **Elias, S., & Matsagar, V. (2017),** Research developments in vibration control of structures using passive tuned mass dampers. Annual Reviews in Control, 44, 129–156.

5. **Gerges, R. R., & Vickery, B. J. (2005),** Optimum design of pendulum-type tuned mass dampers. The Structural Design of Tall and Special Buildings, 14(4), 353–368.
6. **Zhang, P., Song, G., Li, H.-N., & Lin, Y.-X. (2013),** Seismic Control of Power Transmission Tower Using Pounding TMD. Journal of Engineering Mechanics, 139(10), 1395–1406.
7. **Zhao, N., Lu, C., Chen, M., Luo, N., & Liu, C. (2018),** Parametric Study of Pounding Tuned Mass Damper Based on Experiment of Vibration Control of a Traffic Signal Structure. Journal of Aerospace Engineering, 31(6), 04018108.
8. **Brincker, R., Zhang, L., & Andersen, P. (2000),** Modal Identification from Ambient Responses using Frequency Domain Decomposition. In İMAC 18: Proceedings of the International Modal Analysis Conference (İMAC), San Antonio, Texas, USA, February 7-10, 2000 (pp. 625-630)
9. **Liu, Y. C., Loh, C. H., & Ni, Y. Q. (2013),** Stochastic subspace identification for output-only modal analysis: application to super high-rise tower under abnormal loading condition. Earthquake engineering & Structural dynamics, 42(4), 477-498.

AKILLI MÜCEVHERLERDE İNOVASYON: TEKNOLOJİ VE TASARIMIN BİRLEŞİMİ

Sevban AKIN, *akinsevban@gmail.com*, Mimar Sinan Güzel Sanatlar Üniversitesi, 34427, İstanbul

Hüseyin Özkal ÖZSOY, *ozkal.ozsoy@msgsu.edu.tr*, Mimar Sinan Güzel Sanatlar Üniversitesi, 34427, İstanbul

ÖZET

Bu bildiri, estetik ve teknolojinin buluştuğu akıllı mücevherleri kapsamlı bir şekilde incelemektedir. Giyilebilir teknolojiler hızla gelişerek günlük yaşamın bir parçası haline gelmiştir. Akıllı mücevherler hem estetik hem de fonksiyonel özellikleriyle büyük ilgi çekmektedir. Çalışmamızda, akıllı mücevherlerin tanımı, tarihsel gelişimi, teknolojik bileşenleri ve işlevleri ele alınacaktır. Ayrıca, tasarım ilkeleri, malzeme seçimi ve modayla entegrasyon tartışılacak; gelecekteki potansiyel gelişimler ve kullanıcı beklentileri değerlendirilecektir. Bu bildiri, tasarımcılar ve mühendisler için önemli öngörüler sunmayı amaçlamaktadır.

Anahtar Kelimeler: Akıllı Mücevher, Giyilebilir Teknoloji, Estetik ve Fonksiyonellik

ABSTRACT

This paper comprehensively examines smart jewellery where aesthetics and technology meet. Wearable technologies have developed rapidly and have become a part of daily life. Smart jewellery attracts great interest with both aesthetic and functional features. Our study will discuss the definition, historical development, technological components and functions of smart jewellery. Furthermore, design principles, material selection and integration with fashion will be discussed; potential future developments and user expectations will be evaluated. This paper aims to provide important insights for designers and engineers.

Keywords: Smart Jewelry, Wearable Technology, Aesthetics and Functionality

1. GİRİŞ

Teknolojinin hızla ilerlemesiyle birlikte, geleneksel mücevher anlayışı da önemli bir dönüşüm geçirerek akıllı mücevherler çağına geçiş yapmıştır. Akıllı mücevherler, estetik ile fonksiyonelliği bir araya getirerek kullanıcıların günlük yaşamlarını kolaylaştıran ve

zenginleştiren önemli bir teknolojik yenilik olarak öne çıkmaktadır [Song, 2019]. Bu çalışma, akıllı mücevherlerin geçmişi, teknolojik bileşenleri, kullanım alanları ve gelecekteki potansiyelleri üzerine derinlemesine bir derleme sunmayı hedeflemektedir. Akıllı mücevherlerin evrim süreçleri, kullanılan teknolojilerin detaylı analizi ve kullanıcı beklentilerinin nasıl karşılandığı üzerine odaklanacak olan bu çalışmada, bu teknolojilerin takı sektöründeki rolü detaylı bir şekilde tartışılacaktır. Tasarımcılar ve mühendisler için öngörülerde bulunurken, karşılaşılan zorluklar da ele alınacak ve bu alandaki gelecek vizyonu çeşitli açılardan değerlendirilecektir.

2. AKILLI MÜCEVHER

Akıllı mücevherler, geleneksel mücevherlerin estetik özelliklerini taşıyan ve aynı zamanda çeşitli teknolojik özelliklerle donatılmış takılar olarak tanımlanmaktadır [Song, 2019]. Bu takılar genellikle giyilebilir teknoloji kategorisinde yer alır ve kullanıcıya çeşitli fonksiyonlar sunar [MacLean, 2013]. Estetik ve teknolojiyi başarılı bir şekilde birleştiren bu takılar, hem moda dünyasında hem de günlük yaşamda kullanıcıların ilgisini çekmektedir [Pala, İ. E. 2020].

Akıllı mücevherler, geleneksel takılardan önemli ölçüde ayrılır. Geleneksel mücevherler genellikle estetik ve süsleme amaçlı iken, akıllı mücevherler modern teknoloji ile entegre edilmiş işlevselliğiyle öne çıkmaktadır [Rantala, 2018]. Akıllı mücevherler, kullanıcıya sağlık izleme, iletişim özellikleri veya güvenlik uyarıları gibi pratik fonksiyonlar sunabilirken, geleneksel mücevherler genellikle yalnızca görsel çekicilik amacı taşır [Rantala, 2018]. Bu nedenle, akıllı mücevherler teknoloji ve estetiği birleştirerek farklı bir kullanım deneyimi sunar, geleneksel mücevherlerden belirgin bir şekilde ayrılır.

3. AKILLI MÜCEVHERLERİN TARİHSEL EVRİMİ

Akıllı mücevherler, geçmişten günümüze önemli bir değişim ve gelişim gösteren teknolojik takılardır. İlk ortaya çıktıkları dönemde, bu mücevherler genellikle temel işlevleri basitleştirmeyi amaçlamıştır. Örneğin, akıllı takılar kategorisinde yer alan 1975 yılında tasarlanan hesap makineli kol saati, bu alandaki ilk önemli örnektir [Aydın, 2019]. Teknolojinin ilerlemesiyle birlikte, mücevherlerde kullanılan sensörlerin ve bağlantı teknolojilerinin gelişmesi ile birlikte fonksiyonel özellikleri önemli ölçüde genişlemiştir [Pala, İ. E. 2020]. Akıllı mücevherler alanında önemli bir ilerleme, 2000 yılında yüzüğün içine entegre edilen algılayıcılar sayesinde hastaların sağlık durumlarını sürekli olarak izlemelerine olanak tanıyan bir yüzüğün geliştirilmesiyle yaşanmıştır [Yang ve Rhee, 2000]. Son yıllarda, bu teknolojik takılar sağlık izleme, fitness takibi, iletişim araçları ve güvenlik uygulamaları gibi çeşitli alanlarda yaygın bir şekilde kullanılmaktadır [Brown, 2019]. Örneğin, 2008 yılında piyasaya sürülen Fitbit Classic aktivite bilekliği, aktivite sıklığı ve kaybedilen kalori hesaplama özellikleriyle dikkat çeken ilk

örneklerden biridir [Tu, 2017]. Kolye, bilezik ve broş gibi farklı tasarımlarda sunulan bu ürünlere örnek olarak, Beatbella markasının "Leaf" adlı ürünü verilebilir. Bu ürün, geleneksel mücevherlerden farklı görünmemesine rağmen, aktivite takibi ve uyku izleme gibi işlevleriyle kullanıcılarına değerli bir deneyim sunmaktadır [Seneviratne, 2017]. Bu gelişmeler, kullanıcıların günlük yaşamlarını daha sağlıklı bir şekilde yönetmelerine yardımcı olmaktadır.



Şekil 1. Kolye ve yüzül olarak farklı tasarımları olan Leaf adlı akıllı mücevher ürün örneği [Alıntılanma adresi: https://bellabeat.com/product/leaf-urban/]

Akıllı mücevher tasarımında malzeme seçimi, estetik detaylar ve moda trendleri gibi unsurlar, bu teknolojik takıların benzersiz bir evrim geçirmesine olanak sağlamıştır [Jackson, 2023]. Motiv Ring gibi titanyumdan yapılan şık, dayanıklı ve su geçirmez akıllı mücevherler, aktivite takibi, kalp atış hızı ölçümü ve uyku izleme gibi özellikler sunarak kullanıcılarına gelişmiş fonksiyonlar sağlamaktadır [Akıncı, 2021; Seneviratne, 2017]. Ayrıca estetik açıdan dikkat çekici olan bu ürünler, online güvenlikte ekstra koruma sağlar.



Şekil 2. Günlük aktivite ve sağlık takibi yapılmasına olanak sağlayan Motiv Ring adlı ürün. [Alıntılanma adresi: https://mymotiv.com/]

Akıllı mücevherlerin kullanım alanları sadece aktivite takibi ve sağlık izleme ile sınırlı değildir; aynı zamanda günlük yaşamı kolaylaştırmaya da hizmet ederler. Bu bağlamda geliştirilen inovatif ürünlerden biri olan McLEAR Ring, yüzük aracılığıyla temassız ödeme yapılabilmesini sağlamaktadır [Aktaş, 2023].



Şekil 3. Günlük yaşamı kolaylaştıran ve temassız ödeme imkânı sağlayan McLEAR Ring isimli ürün. [Alıntılanma adresi: https://mclear.com/product/payment-ring/#description]

Akıllı mücevherler, düzenli bir yaşam sürdürmede önemli bir rol oynayabilir. Bunun güzel bir örneği olan "Senstone", şık bir dijital mücevherdir. Bu akıllı ses kayıt cihazı, bileklik, kolye veya broş olarak kullanılabilir ve tek dokunuşla sesli notlar almayı sağlar. Alınan notlar, etiketlenerek akıllı telefonlara aktarılabilir ve kolayca erişilebilir [Jarusriboonchai, 2019].



Şekil 4. Sesli notlar oluşturma ve bunları uygun bir şekilde arşivleme özelliği olan Senstone isimli ürün. [Alıntılanma adresi: https://www.senstone.io/.]

Son zamanlarda dikkat çeken bir diğer ürün ise JOULE isimli küpedir [Jackson, 2023]. Günlük aktivite takibi, kalori hesabı ve kalp atış hızını belirleme gibi işlevlerle donatılan bu küpe, aynı zamanda hafif ve kullanıcı dostu tasarımıyla öne çıkar. Bu özellikleriyle, kullanıcıların hem

sağlıklarını takip etmelerini hem de konforlu bir kullanım deneyimi yaşamalarını sağlar [Ran Noh, 2019]



Şekil 5. Küpenin arkasında yer alan mekanizması sayesinde günlük aktivite ve sağlık takibi özelliklerinin yanı sıra tasarımı ile dikkat çeken JOULE isimli ürün [Alıntılanma adresi: https://shopjoule.com/]

Akıllı mücevherlerin tarih boyunca geçirdiği değişimler, teknolojinin takı dünyasına kattığı yenilikleri ve bu yeniliklerin kullanıcıların yaşam tarzlarına nasıl entegre edildiğini açıkça göstermektedir. Gelecekte, akıllı mücevherlerin daha da gelişmesi ve kullanıcıların ihtiyaçlarına daha uygun hale gelmesi beklenmektedir. Bu gelişmeler, kullanıcıların günlük yaşamlarını daha da kolaylaştıracak ve kişisel sağlık, güvenlik ve iletişim gibi birçok alanda daha etkili çözümler sunacaktır. Akıllı mücevherlerin hem estetik hem de fonksiyonellik açısından daha sofistike ve kullanışlı hale gelmesi öngörülmektedir [Song, 2019].

4. AKILLI MÜCEVHERLERİN TEKNOLOJİK BİLEŞENLERİ VE İŞLEVLERİ

Akıllı mücevherler, geleneksel takıların estetik ve zarafetini modern teknolojinin sunduğu yenilikçi özelliklerle birleştirerek, kullanıcıların günlük yaşamlarını önemli ölçüde zenginleştiren ve kolaylaştıran bir yenilik sunmaktadır. Bu teknolojik bileşenler, mücevherlerin sadece dış görünüşlerini değil, aynı zamanda işlevselliğini de büyük ölçüde artırmaktadır [Choudhury ve Pentland, 2002].

Akıllı mücevherlerin temel teknolojik bileşenleri arasında sensörler yer almaktadır. Sensörler, mücevherin işlevselliğini ve kullanıcı deneyimini artıran önemli bileşenler olarak öne çıkmaktadır [Özgüner Kılıç, 2017]. İşte akıllı mücevherlerde kullanılan bazı sensörler ve bu sensörlerin kullanım alanlarına örnekler:

1. **İvmeölçer**: İvmeölçerler, cihazın hareketini algılamak ve bu hareketleri ölçmek için kullanılır. Akıllı mücevherlerde ivmeölçerler adım sayma, hareket izleme, yüzme veya koşu gibi aktiviteleri takip etmek için kullanılır [Choudhury ve Pentland, 2002].
2. **Kalp Atış Hızı Sensörü**: Kalp atış hızı sensörleri, kullanıcının nabzını ölçmek için kullanılır. Bu sensörler genellikle optik olarak çalışır ve mücevherin yüzeyine yerleştirilmiştir. Kalp atış hızı takibi, kullanıcının egzersiz sırasında veya günlük yaşamında kalp sağlığını izlemesine yardımcı olur [Ghandi ve Wang, 2014; Glatter, 2014].
3. **GPS (Global Positioning System):** Bazı akıllı mücevherler, GPS sensörleri sayesinde konum belirleme özelliği sunar. Bu sensörler, kullanıcının konumunu belirlemek ve aktivitelerini haritalamak için kullanılır. Örneğin, açık hava aktiviteleri veya yolculuk sırasında konum takibi için kullanılabilir [Song, 2019].
4. **Termal Sensörler:** Vücut sıcaklığını ölçmek için kullanılan termal sensörler, akıllı mücevherlerde kullanıcının sağlık durumunu izlemek ve vücut sıcaklığı değişikliklerini takip etmek için kullanılır [Chiu, 2018].
5. **Pil ve Şarj Sensörleri:** Bazı akıllı mücevherlerde, batarya ömrünü ve şarj seviyesini izlemek için pil ve şarj sensörleri bulunur. Kullanıcıya batarya durumu hakkında bilgi verir ve şarj seviyesini gösterir [Seneviratne, 2017].

Bu teknolojik bileşenlerin entegrasyonu sayesinde akıllı mücevherler, diğer cihazlarla iletişim kurabilir, mesajları gösterebilir veya ödeme yapma gibi işlevleri yerine getirebilir. Böylece kullanıcılar, daha bağlantılı ve işlevsel bir deneyim yaşarlar.

Sonuç olarak, akıllı mücevherlerin teknolojik bileşenleri ve işlevleri, kullanıcıların günlük yaşam kalitesini artırırken sağlık takibi ve güvenlik gibi kritik alanlarda da önemli katkılar sağlar. Bu teknolojilerin ilerlemesiyle birlikte, akıllı mücevherlerin kullanım alanları ve potansiyelleri sürekli genişlemekte ve gelişmektedir [Song, 2019]. Tasarımcılar ve mühendisler, bu yenilikçi ürünlerin gelecekteki uygulamalarını keşfetmek ve kullanıcıların beklentilerine daha fazla uygun hale getirmek için çalışmalarını sürdürmektedirler.

5. AKILLI MÜCEVHERLERİN TASARIM İLKELERİ VE ESTETİK

Akıllı mücevherler, teknoloji ile estetik ve işlevselliği başarılı bir şekilde harmanlayan yenilikçi ürünlerdir [Wang, 2024]. Tasarım ilkeleri ve estetik unsurlar, bu mücevherleri geleneksel takılardan ayıran ve kullanıcı deneyimini önemli ölçüde derinleştiren faktörler olarak öne çıkar.

1. **Minimalist ve Zarif Tasarım Anlayışı:** Akıllı mücevherler genellikle minimalist bir estetik ile tasarlanır. Az detaylı ve sade bir görünüm, kullanıcıların günlük yaşamlarına kolayca uyum sağlamasını ve mücevherin teknolojik özelliklerini daha estetik bir şekilde

sunmasını sağlar. Bu tasarım yaklaşımı, mücevherin hem görsel olarak çekici olmasını hem de kullanıcıya pratik bir işlevsellik sunmasını sağlar [Vesilind, 2015].

2. **İşlevselliği Öne Çıkaran Tasarım Yaklaşımı:** Tasarım sürecinde, mücevherin teknolojik işlevselliği ön planda tutulur. Sensörlerin ve diğer teknolojik bileşenlerin entegrasyonu, mücevherin kullanım alanını genişleterek kullanıcıya önemli avantajlar sunar [Wang, 2024]. Bu sayede, mücevher sadece estetik bir aksesuar olmaktan öte, günlük yaşamda pratik bir araç olarak da işlev görür.
3. **Kullanıcı Deneyimine Odaklı Ergonomik Tasarım:** Akıllı mücevherlerin tasarımında kullanıcı memnuniyeti ve konforu ön planda tutulur. Mücevherin vücuda uyumu, rahat kullanımı ve güvenliği, tasarım sürecinde dikkate alınan temel unsurlardır. Bu sayede kullanıcılar, mücevherleri uzun süre rahatça kullanabilirler [Jarusriboonchai, 2019].
4. **Malzeme Seçimi ve Kalite Standartları:** Estetik görünümün yanı sıra, mücevherlerde kullanılan malzemelerin kalitesi ve dayanıklılığı da önemlidir. Yüksek kaliteli malzemelerin tercih edilmesi, mücevherin uzun ömürlü olmasını sağlar ve kullanıcıya güven verir. Ayrıca, malzeme seçimi mücevherin prestijini ve stilini belirleyen unsurlardan biridir [Rantala, 2018].
5. **Modüler Tasarım ve Kişiselleştirme Seçenekleri:** Bazı akıllı mücevherler, modüler tasarım özellikleri sunar. Kullanıcılar, bilezik, kolye veya yüzük gibi farklı parçaları birleştirerek mücevherlerini kişiselleştirebilirler. Bu özellik, kullanıcıların kendi tarzlarına ve ihtiyaçlarına göre mücevherlerini özelleştirmelerine olanak tanır [Wang, 2024].
6. **Estetik ve Teknoloji Dengesi:** Akıllı mücevherlerde estetik unsurlarla teknolojik bileşenlerin uyumlu bir şekilde entegre edilmesi önemlidir. Mücevherin dış görünümü, teknolojinin sağladığı işlevsellikle birlikte estetik bir bütünlük içinde olmalıdır [Wang, 2024]. Bu, kullanıcıların mücevheri hem görsel olarak çekici bulmalarını hem de teknolojinin sağladığı faydayı hissetmelerini sağlar [Jarusriboonchai, 2019].

Sonuç olarak, akıllı mücevherlerin tasarım ilkeleri, teknoloji ile estetik ve işlevselliğin başarılı bir şekilde entegre edilmesini hedefler. Minimalist yaklaşım, işlevselliği öne çıkaran tasarım, kullanıcı odaklı ergonomi, yüksek kaliteli malzeme seçimi, modülerlik ve kişiselleştirme seçenekleri ile estetik ve teknoloji dengesi, bu tasarımların başarısını ve kullanıcı memnuniyetini belirleyen önemli unsurlardır.

6. AKILLI MÜCEVHERİN KULLANIM ALANLARI VE UYGULAMALAR

Akıllı mücevherler, geleneksel takıların estetik ve zarafetini modern teknolojinin sunduğu yenilikçi özelliklerle birleştirerek, çeşitli günlük yaşam uygulamalarında kullanıcıya katkı sağlar

[Özgüner Kılıç, 2017]. Akıllı mücevherlerin yaygın kullanım alanları ve uygulamaları aşağıda listelenmiştir.

1. **Sağlık ve Fitness Takibi:**
   - **Kalp Atış Hızı Ölçümü:** Akıllı mücevherler genellikle kalp atış hızı sensörleriyle donatılmıştır. Egzersiz sırasında kullanıcının nabzını sürekli olarak izleyerek antrenman verimliliğini artırır [Özgüner Kılıç, 2017].
   - **Aktivite Takibi:** İvmeölçerler ve adım sayma sensörleri sayesinde günlük aktivitelerin takibini yapar. Yürüme, koşma gibi aktivitelerin yanı sıra günlük adım sayısını ölçer [Ghandi ve Wang, 2014; Glatter, 2014].
   - **Uyku İzleme:** Uyku kalitesini ve süresini takip ederek kullanıcıya uyku düzeni hakkında bilgi verir [Büyükgöze, 2019].
2. **Navigasyon ve Konum Belirleme:**
   - **GPS Özelliği:** Bazı akıllı mücevherler GPS sensörleri ile konum belirleme özelliği sunar [Özgüner Kılıç, 2017]. Seyahat sırasında kullanıcıya yol tarifi sağlar ve konumunu doğru bir şekilde belirler [Song, 2019].
3. **Güvenlik ve Acil Durumlar:**
   - **Acil Durum Bildirimi:** Özel tasarlanmış uygulamalar veya butonlar aracılığıyla acil durumlar için hızlı bildirim gönderme özelliği sunar [Büyükgöze, 2019]. Kullanıcı düşme veya rahatsızlık durumunda acil yardım çağırabilir.
4. **Ödeme ve Kimlik Doğrulama:**
   - **NFC Teknolojisi:** NFC özelliği sayesinde akıllı mücevherler, ödeme yapma ve erişim kontrolü gibi işlemleri kolaylıkla gerçekleştirebilir [Seneviratne, 2017].
   - **Kimlik Doğrulama:** Erişim kontrolü gerektiren yerlerde kimlik doğrulama için kullanılabilir [Seneviratne, 2017].
5. **Gündelik Yaşam Bilgileri:**
   - **Bildirim Yönetimi:** Akıllı mücevherler, akıllı telefonlardan gelen bildirimleri kullanıcıya ileterek önemli mesajları veya çağrıları kaçırmasını önler [Özgüner Kılıç, 2017].
   - **Hava Durumu ve Zaman:** Bazı modeller hava durumu bilgisi ve saat gibi temel bilgileri anlık olarak kullanıcıya sunabilir [Jarusriboonchai, 2019].
6. **Eğlence ve İfadeler:**
   - **Kişiselleştirilmiş Ekranlar:** Renkli ekranlar veya LED ışıklar aracılığıyla kullanıcıların kişiselleştirilmiş mesajlar veya simgeler göstermesine olanak tanır [Jarusriboonchai, 2019].

Bu kullanım alanları ve uygulamalar, akıllı mücevherlerin günlük yaşamı kolaylaştıran ve daha bağlantılı bir deneyim sunmasını sağlar. Her geçen gün teknolojinin ilerlemesiyle birlikte, akıllı mücevherlerin sunduğu fonksiyonlar ve kullanım alanları da giderek genişlemektedir.

7. AKILLI MÜCEVHERLERİN GELECEĞİ

Akıllı mücevherler, teknolojinin hızla gelişmesiyle birlikte gelecekte çok çeşitli ve etkileyici özelliklere sahip olabilir. Bu gelişim potansiyeli, mücevherlerin teknoloji entegrasyonu ve kullanım alanlarının genişlemesi ile ilgilidir. Gelecekteki akıllı mücevherlerin birçok önemli özelliği olması öngörülmektedir [Song, 2019]. Bu özellikler:

1. **Gelişmiş Sensörler ve Teknoloji Entegrasyonu:** İvmeölçerler, kalp atış hızı sensörleri, GPS, termal sensörler gibi teknolojilerin yanı sıra, biyometrik ölçümler ve oksijen seviyesi takibi gibi ileri düzey sensörler gelecekte akıllı mücevherlerde daha yaygın olarak kullanılacaktır [Wang, 2024]. Bu sensörlerin entegrasyonu, kullanıcıların sağlık durumlarını daha kapsamlı ve gerçek zamanlı olarak izlemelerine olanak tanıyacaktır [Jarusriboonchai, 2019].
2. **Yapay Zeka ve Veri Analitiği:** Akıllı mücevherlerin topladığı büyük veri setlerinin yapay zeka algoritmalarıyla analiz edilmesi, kullanıcılara kişiselleştirilmiş sağlık önerileri sunabilecek potansiyele sahiptir [Wang, 2024]. Örneğin, kullanıcının günlük aktivite düzeyine göre önerilerde bulunmak veya sağlık parametrelerini sürekli olarak izlemek gibi işlevler, yapay zekanın sağladığı veri analitiğiyle desteklenebilir [Hu, 2023].
3. **Enerji Verimliliği ve Pil Teknolojileri:** Gelecekte akıllı mücevherlerin enerji tüketiminin optimize edilmesi ve daha uzun pil ömrüne sahip olmaları beklenmektedir. Gelişmiş pil teknolojileri, mücevherlerin sürekli kullanılabilir olmasını sağlayacak ve kullanıcıların günlük yaşamında daha fazla konfor sunacaktır [Seneviratne, 2017].
4. **Modüler Tasarım ve Kişiselleştirme:** Gelecekteki akıllı mücevherlerin modüler tasarımı, kullanıcıların mücevherlerini kolayca kişiselleştirmelerine olanak verebilecektir. Bu modülerlik, kullanıcıların bilezik, kolye veya yüzük gibi parçaları değiştirerek mücevherlerini tarzlarına ve ihtiyaçlarına göre özelleştirmelerine imkân tanıyacaktır [Jarusriboonchai, 2019].

5. **Güvenlik ve Gizlilik:** Veri güvenliği ve kullanıcı gizliliği, gelecekteki akıllı mücevherlerin gelişiminde kritik öneme sahiptir. Kullanıcı verilerinin güvenliği sağlanarak, mücevherlerin güvenilirliği artırılacak ve kullanıcıların bu teknolojiye olan güveni artacaktır [Salmela ve Vimm, 2018].
6. **Yeni Kullanım Alanları ve İnovasyon:** Akıllı mücevherlerin geleceği, sağlık izleme ve günlük yaşam kolaylığı sağlamanın ötesine geçerek yeni kullanım alanlarına yönelebilir [Wang, 2024]. Örneğin, ödeme yapma, iletişim kurma, sanal gerçeklik deneyimleri gibi alanlarda kullanım potansiyelleri genişleyebilir. Bu da mücevherlerin sadece kişisel sağlık takibi aracı olmaktan çıkıp, günlük yaşamın birçok yönünde kullanılabilecek çok yönlü araçlar haline gelmelerini sağlayabilir [Salmela ve Vimm, 2018].

Bu noktalar göz önüne alındığında, akıllı mücevherlerin geleceği, teknolojinin ilerlemesi ve kullanıcı ihtiyaçları doğrultusunda önemli bir evrim geçirebilir. Bu teknolojilerin, bilimsel ve teknolojik ilerlemelerin ışığında, kullanıcı deneyimini zenginleştirme potansiyeli büyük önem taşımaktadır [Wang, 2024]. Gelecekte, akıllı mücevherlerin sağlık takibinden günlük yaşam kolaylıklarına kadar geniş bir yelpazede kullanılabileceği öngörülmektedir [Song, 2019]. Özellikle yapay zeka destekli analizler ve kişiselleştirilmiş veri sunumlarıyla, bu teknolojilerin kullanıcıların yaşam kalitesini artırmada kritik bir rol oynayabileceği düşünülmektedir [Wang, 2024]. Akıllı mücevherler, teknolojinin sınırlarını zorlayarak, gelecekte daha entegre, daha kullanışlı ve daha kişisel deneyimler sunabilirler [Jarusriboonchai, 2019].

8. SONUÇ VE TARTIŞMA

Bu bildiri, estetik ve teknolojinin birleştiği akıllı mücevherlerin geniş bir incelemesini sunmuştur. Akıllı mücevherler, geleneksel takılardan farklı olarak estetik özelliklerini modern teknoloji ile birleştirerek kullanıcılarına hem görsel hem de işlevsel avantajlar sağlamaktadır. Bu çalışma, akıllı mücevherlerin tanımı, tarihsel gelişimi, teknolojik bileşenleri ve işlevleri üzerine detaylı bir derleme sunarak, bu alandaki önemli gelişmeleri ve potansiyelleri ele almıştır.

Akıllı mücevherlerin geçmişten günümüze olan evrim süreci incelendiğinde, teknolojinin ilerlemesiyle birlikte sensörlerin ve bağlantı teknolojilerinin gelişiminin, bu mücevherlerin fonksiyonel özelliklerini önemli ölçüde artırdığı görülmektedir. Sağlık izleme, aktivite takibi, iletişim araçları ve güvenlik uygulamaları gibi çeşitli alanlarda kullanılan akıllı mücevherler, kullanıcıların günlük yaşamlarını kolaylaştırma potansiyeline sahiptir.

Teknolojik bileşenler ve işlevler açısından, akıllı mücevherlerin sensörlerden GPS'e, kalp atış hızı ölçümünden NFC teknolojisine kadar geniş bir yelpazede özellikler sunduğu

görülmektedir. Bu bileşenlerin entegrasyonu, mücevherlerin sadece estetik bir aksesuardan öteye geçerek kullanıcıya gerçek bir değer sağlamasını sağlar. Özellikle sağlık ve güvenlik gibi kritik alanlarda akıllı mücevherler, kullanıcıların yaşam kalitesini artırmakta ve günlük yaşamlarını daha bağlantılı hale getirmektedir.

Tasarım ilkeleri ve estetik unsurlar açısından, akıllı mücevherler minimalist ve zarif bir görünüme sahip olacak şekilde tasarlanmakta ve kullanıcı deneyimini maksimize etmektedir. İşlevselliği öne çıkaran tasarım yaklaşımı, sensörlerin ergonomik entegrasyonu ve malzeme seçimi gibi unsurlar, mücevherlerin kullanıcılar tarafından rahatlıkla benimsenmesini sağlamaktadır.

Gelecekteki potansiyeller açısından, akıllı mücevherlerin daha gelişmiş sensörlerle donatılması, yapay zeka ve veri analitiğiyle desteklenmesi ve enerji verimliliği açısından iyileştirilmesi beklenmektedir. Bu gelişmeler, kullanıcı deneyimini daha da zenginleştirecek ve akıllı mücevherlerin günlük yaşamda daha yaygın olarak kullanılmasını sağlayacaktır.

Sonuç olarak, bu bildiri akıllı mücevherlerin bugünü ve geleceği hakkında kapsamlı bir bakış sunmuş, tasarımcılar ve mühendisler için önemli öngörüler ortaya koymuştur. Teknoloji ve estetiği başarılı bir şekilde birleştiren akıllı mücevherler, kullanıcıların yaşam tarzlarına değer katmaya devam edecektir.

9. KAYNAKÇA

1. Song, Y., (2019), “Innovation of Smart Jewelry for the Future”, International Journal of Performability Engineering”, 15(2): 591-601 doi: 10.23940/ijpe.19.02.p23.591601.

2. Wang, Y., (2024), “Design and Application of Intelligent Jewelry Products”, Academic Journal of Science and Technology, Vol. 10, No. 1, 2024.

3. Hu, J., (2023), “Research on Innovative Design Method and Evaluation of Jewelry Based on CiteSpace & Playgound AI”, Design Studies and Intelligence Engineering, Doı: 10.3233/FAIA231424

4. Aydın, N., (2019), Giyilebilir Teknolojiler, İksad Yayınevi, Ankara

5. Özgüner Kılıç, H., (2017), Giyilebilir Teknoloji Ürünleri Pazarı ve Kullanım Alanları, Aksaray Üniversitesi İktisadi ve İdari Bilimler Fakültesi Dergisi**,** 9 (4) 99-112.

6. Tu, L., (2017), FitBeat: A Lightweight System for Accurate Heart Rate Measurement during Exercise, 2017 IEEE International Conference on Smart Computing (SMARTCOMP), Doı: 10.1109/SMARTCOMP.2017.7947009

7. Jackson, C., (2023), The smart jewellery you need to know for 2023, Traveller, Alıntılanma adresi: https://www.cntraveller.com/article/smart-jewellery, Alıntılanma tarihi: 22.06.2024

8. MacLean, D., (2013), MoodWings: a wearable biofeedback device for real-time stress intervention. Proceedings of the 6th International Conference on Pervasive Technologies Related to Assistive Environments (p. 66). ACM.

9. Pala, İ. E., (2020), Giyilebilir Teknoloji Girişimlerinin Ürün Geliştirme Süreçlerinde Endüstriyel Tasarımın Yeri: Türkiye'deki Teknoloji Geliştirme Bölgeleri Üzerine Bir Araştırma, Doktora Tezi, İstanbul Teknik Üniversitesi Endüstri Ürünleri Tasarımı Anabilim Dalı, İstanbul

10. Rantala, I., *ve ark.* (2018) Smart Jewelry: Augmenting Traditional Wearable Self-Expression Displays, PerDis '18: Proceedings of the 7th ACM International Symposium on Pervasive Displays, June 6–8, 2018, Munich, Germany, Doı: 10.1145/3205873.3205891.

11. Yang, B. H., ve Rhee, S., (2000), Development of the ring sensor for healthcare automation, Robotics and Autonomous Systems, 30(3), 273-281.

12. Brown, B., (2019), Global Wearable Technology Market to Accelerate, Alıntılanma adresi: https://healthtechinsider.com/2019/05/22/globalwearable-technology-market-to-accelerate-15/, Alıntılanma tarihi: 14 Haziran, 2023.

13. Seneviratne, S., *ve ark.* (2017), A Survey of Wearable Devices and Challenges, IEEE Communications Surveys & Tutorials, Doı: 10.1109/COMST.2017.2731979.

14. Akıncı, B*., ve ark.* (2021), Hipertansiyon Hastaları İçin Giyilebilir Sağlık Teknolojileri Seçimi, H.Ü. Sağlık Bilimleri Fakültesi Dergisi, Cilt: 8, No: 2, 2021, Doı: 10.21020/husbfd.767834.

15. Aktaş, P. (2023), Bir sanat nesnesi olan mücevherin teknolojik inovasyon bağlamında incelenmesi, Yüksek Lisans Tezi, Altınbaş Üniversitesi Sanat ve Tasarım Bölümü, İstanbul.

16. Jarusriboonchai, P., ve Häkkilä, J., (2019), Customisable Wearables: Exploring the Design Space of Wearable Technology, 18th International Conference, Doı: 10.1145/3365610.3365635

17. Ran Noh, Y., ve Jeong Choi, Y,(2019), An Analysis of the Emotional Design Types of Smart Jewelry, Journal of Digital Convergence, Vol. 17. No. 8, pp. 423-428, Doı: 10.14400/JDC.2019.17.8.423.

18. Choudhury, T., ve Pentland, A.. (2002). The sociometer: A wearable device for understanding human networks. In CSCW'02 Workshop: Ad hoc Communications and Collaboration in Ubiquitous Computing Environments..

19. Ghandi, M., ve Wang, T., (2014). The Future of Biosensing Wearables, Rock Health, Alıntılanma adresi: https://rockhealth.com/reports/the-futureof-biosensing-wearables/, Alıntılanma tarihi: 12 Haziran, 2024.

20.Glatter, R. (2014). Wearable Technology and Digital Healthcare Strategies Should Shift Focus to Chronic Medical Illness, Alıntılanma adresi: https://www.forbes.com/sites/robertglatter/2014 /11/20/wearable-technology-and-digitalhealthcare-strategies-should-shift-focus-tochronic-medical-illness/#450501c0b7b2, Alıntılanma tarihi: 12 Haziran, 2024.

21. Chiu, Yu-Tzu (2018). Wristify: Thermo electric Wearable Would Reduce Energy Consumption, Alıntılanma adresi: https://spectrum.ieee.org/energywise/energy/environment/

wristifythermoelectric-bracelet-would-reduce-energy-consumption, Alıntılanma tarihi: 12 Haziran, 2024.

22. Vesilind, E. (2015). Cool New Wearable: Altruis' Modular Smart Jewelry, Erişim adresi: https://www.jckonline.com/editorial-article/cool-new-wearablealtruis-modular-smart-j, Alıntılanma tarihi: 10 Haziran, 2024.

23. Büyükgöze, S. (2019). Giyilebilir Teknolojilerden Sağlık Alanındaki Sensör Yamalar Üzerine Bir İnceleme. Avrupa Bilim ve Teknoloji Dergisi, (17), 1239-1247, Doı: 10.31590/ejosat.658020.

24. Salmela, E. ve Vimm, I. (2018), Digital Smart Jewelry: Next Revolution of Jewelry Industry?, Doı:10.5772/intechopen.71705

ÜRÜN DOĞRULAMA VE SAHA TESTLERİNDE KULLANIMA YÖNELİK ANDROID TABANLI CANLI VERİ TOPLAMA ARAYÜZÜ GELİŞTİRME

Sedat TARAKÇI, *s.tarakci@tirsankardan.com.tr* Tirsan Kardan A.S, 45030, Manisa

Oğuzhan ALDEMİR, *o.aldemir@tirsankardan.com.tr* Tirsan Kardan A.S, 45030, Manisa

Efe IŞIK, *e.isik@tirsankardan.com.tr* Tirsan Kardan A.S, 45030, Manisa

ÖZET

Otomotiv endüstrisinde araç üzerindeki sensörlerden veri toplama ihtiyacı gün geçtikçe artmaktadır. Kardan mili gibi dinamik parçalar üzerinden de araç testleri sırasında anlık olarak veri toplanmaktadır. Bu kapsamda, sensörler veya veri toplama sistemlerinden gelen verilerin gözlemlenebilmesi amacıyla veri izleme yazılımı ihtiyacı oluşmaktadır.

Bu çalışma kapsamında, kara taşıtları saha testlerinde dinamik aktarma organları üzerinden veri toplanması amacıyla geliştirilmiş bir ölçüm sisteminden gelen farklı tipteki gerçek zamanlı verilerin izlenebileceği android tabanlı bir kullanıcı arayüzü geliştirilmesi amaçlanmıştır. Geliştirilen veri izleme arayüzü yazılımının, saha testlerinde elde edilen tüm verileri cep telefonu veya tablet gibi mobil cihazlar üzerinden okunmasına yönelik kullanılması amaçlanmıştır.

Anahtar Kelimeler: Veri toplama, Kullanıcı arayüzü, android uygulama

ABSTRACT

In the automotive industry, the need to collect data from sensors on the vehicle is increasing day by day. Dynamic parts such as cardan shaft are used to collect data instantaneously during vehicle tests. In this context, there is a need for data monitoring software to monitor the data from sensors or data acquisition systems.

Within the scope of this study, it is aimed to develop an android-based user interface to monitor real-time data from a measurement system on dynamic drivetrain components in vehicle field tests. The data monitoring interface is used to read all data obtained in field tests on mobile devices.

Keywords: Data acquisition, Graphical User Interface, Android application

1. GİRİŞ

Otomotiv endüstrisi giderek daha fazla sensörlerin kullanıldığı ve ölçümlerin gerçekleştirildiği bir alan haline gelmektedir. Buna bağlı olarak daha fazla otomotiv bileşeni birbirine bağlanmakta ve dolayısıyla hem araç bilgisayarları hem de sürücülerle iletişim halinde olmaktadır. Birbirine bağlı bu araç bileşenleri, istatistik, durum izleme, temelinde takip edilmektedir [Aldemir,2020].

Bilgisayar kontrollü araç sistemleri önem kazandıkça, farklı sensörler kontrolörler hakkında bilgi sağlamada önemli bir role sahiptir. Sensör sayıları giderek artmakta ve otomotiv sensörleri büyümeye devam etmektedir [Persson,2015 Erda,1983]. Kardan mili ve diğer aktarma organları, ölçüme ihtiyaç duyulan önemli bileşenler arasındadır [Ulukan,1984].

Bu çalışmada, kardan mili saha testlerinde gerçekleştirilen veri toplama çalışmalarında kullanılmak üzere, bu veri toplama sistemlerinden edinilen verinin anlık olarak izlenebileceği android tabanlı bir kullanıcı arayüzü geliştirme çalışması amaçlanmıştır. Geliştirilecek kullanıcı arayüzü yazılımı ile saha testlerinde elde edilen tüm veriler cep telefonu veya tablet gibi bir cihaz üzerinden izlenebilecektir. Veri toplama sisteminin sensör sayısı ve tipi, iletişim protokolü gibi özelliklerine göre Tirsan Kardan bünyesinde geliştirilen tüm veri toplama sistemleriyle uyumlu çalışacak, verilerin anlık olarak izlenebildiği ve sonrasında kaydedilerek ardıl işlemler yapılmasına da izin veren bir kullanıcı arayüzü geliştirilmesi amaçlanmıştır.

2. KULLANICI ARAYÜZÜ GELİŞTİRME

2.1 Arayüz Tasarımının Oluşturulması

İhtiyaç duyulan ekranlar ve her ekranın sahip olması gereken fonksiyonlar belirlenerek kavramsal tasarım ve ekran mimarisi oluşturulmuştur. Arayüzün ilk olarak bir açılış ekranına sahip olması planlanmıştır. Bu ekranda kullanıcı girişi ve şifre ile arayüz erişimi gerçekleşecektir. Bu sayede yetkisiz kullanımlar engellenmiştir.

Sisteme giriş sonrası iki buton ile yeni bir test başlatma ve daha önce gerçekleşen testlerin liste görünümüne erişim imkanı bulunması planlanmıştır. Yeni bir test yaratıldığında veri toplama sistemi ile bağlantı kurulacaktır. Test listesi seçeneğinden ise eski testlerin excel çıktıları alınma imkanı olacaktır. Test listesindeki testleri excele kaydedebildiğimiz gibi istenen testler silinebilecektir.

Canlı test oluşturma ekranında, ilgili veri toplama sistemi seçilerek bağlantı kurulacak ve bu veri toplama sistemine bağlı sensörlerden veri okunmak istenenleri, alt pencerelerden seçilecektir. Seçimlerin tamamlanmasının ardından canlı veri ekranına geçilecektir.

Canlı veri ekranında seçilen tüm sensörlerin verdiği değerler ekrandaki ilgili bölümlere yazdırılacaktır. Bununla birlikte veri trendini izleyebilmek adına grafik çıktıları verilecektir. Canlı test sonlandırıldıktan sonra okunan veriler otomatik olarak veri tabanına kaydedilecektir.

İstenildiği takdirde ardıl işlemler için excel çıktısı alma seçeneği de bulunacaktır. Şekil 1'de programın akış şeması verilmektedir.



Şekil 1 Arayüz Akış Şeması.

Uygulama başlatıldığında gelen ilk ekran olan oturum açma ekranı firma logosu da kullanılarak tasarlanmıştır. Güvenliği sağlama açısından kullanıcı adı ve şifre girdileri oluşturulmuştur. Doğru kombinasyon girilmediğinde hangi girdinin yanlış olduğu belirtilecektir. Uygulama arayüzü tasarlanırken popüler mobil uygulamalardan yararlanılmış, kullanıcı beklentilerini de karşılayacak görsellik ve kullanım kolaylığı getirecek fonksiyonlar göz önünde bulundurulmuştur. Uygulamada çoğunlukla firmanın sahip olduğu renk kodları kullanılmıştır. Açılış ekranı Şekil 2'de verilmiştir.



Şekil 2 Arayüz Açılış Ekranı.

Giriş yapıldıktan sonra ana sayfa ekranına geçilmektedir. Ana sayfa ekranında test oluşturma ve test listesi ekranlarına erişecek butonlar yer almaktadır. Ekranın alt kısmında ise kaydı alınmış son 6 test yer almaktadır. Kullanıcı bu ekrandan yeni bir test başlatabilecek veya eski testlerden çıktı alarak ardıl işlemler gerçekleştirebilecektir. Şekil 3'te ana ekranın bir görüntüsü yer almaktadır.



Şekil 3 Ana Kullanıcı Ekranı.

Şekil 4'te ise ana ekranı oluştururken geliştirilen kodlar verilmektedir.

```
// Test oluşturma ve test listesi ekranlarına geçişi sağlayan kod bloğu
val listebuttonBinding = binding.testListButton
val olusturbuttonBinding = binding.testOlusturButton
olusturbuttonBinding.setOnClickListener { it: View!
    Navigation.findNavController(it).navigate(R.id.action_anasayfa_to_testolusturFragment)
}
listebuttonBinding.setOnClickListener { it: View!
    Navigation.findNavController(it).navigate(R.id.action_anasayfa_to_testlistesiFragment)
}
```

```
// Ekran açıldığında Tablo yükleme fonksiyonunu çalıştıran fonksiyon
override fun onViewCreated(view: View, savedInstanceState: Bundle?) {
    super.onViewCreated(view, savedInstanceState)
    loadTests(requireContext())
}
```

Şekil 4 Ana Ekran Kodları.

Yeni bir test başlatmak için «Create New Test» butonu tıklanmaktadır. Bu buton tıklandığında test oluşturma ekranı açılmakta ve «Test Input» başlığı altında test adı, test açıklaması, cihaz ve sensör seçimleri gerçekleştirilmektedir. Bu seçimlere göre bluetooth bağlantısı kurulduğunda alınacak veri ve kaynaklar ortaya koyulmaktadır ve veri olarak gönderilmektedir. Ardından sonraki ekranda argüman olarak alınır. «Create Test» butonuna basıldığında bluetooth bağlantısı kurulması için arka planda kod çalışmaktadır. Bağlantı kurulduğunda canlı test ekranına geçilir ve veri okunmaya başlanır. Test oluşturma ekranı Şekil 5'te verilmektedir.



Şekil 5 Test Oluşturma Ekranı

Test oluşturma ekranı hazırlanırken oluşturulan bazı kod satırları Şekil 6'da verilmektedir.

```
bundle.putString("DEVICE_ADDRESS1", selectedDeviceAddress1.toString())
bundle.putString("Selected_Device", selectedDevice1.toString())
bundle.putString("Selected_Data3", selectedData3.toString())
bundle.putString("Selected_Data4", selectedData4.toString())
bundle.putString("Test_Name", testName1.toString())
bundle.putString("Test_Description", testName2.toString())
try {
    findNavController().navigate(
        R.id.action_testolusturFragment_to_canlitestFragment,
        bundle
    )
```

Şekil 6 Test Oluşturma Ekranı Kodları

Canlı test ekranında; verilerin yanında cihaz ismi ve anlık test süresi bilgileri de tabloda yer almaktadır. Seçimi yapılan sensörlere göre ekranda belirlenen yerlere veri toplama sisteminden gelen veriler yazdırılmaktadır. Testi kaydetme, durdurma ve veri ölçekleme butonları tablonun hemen altında bulunmaktadır. Bu ekranlar için oluşturulan kodların bir bölümü Şekil 7'de verilmektedir.

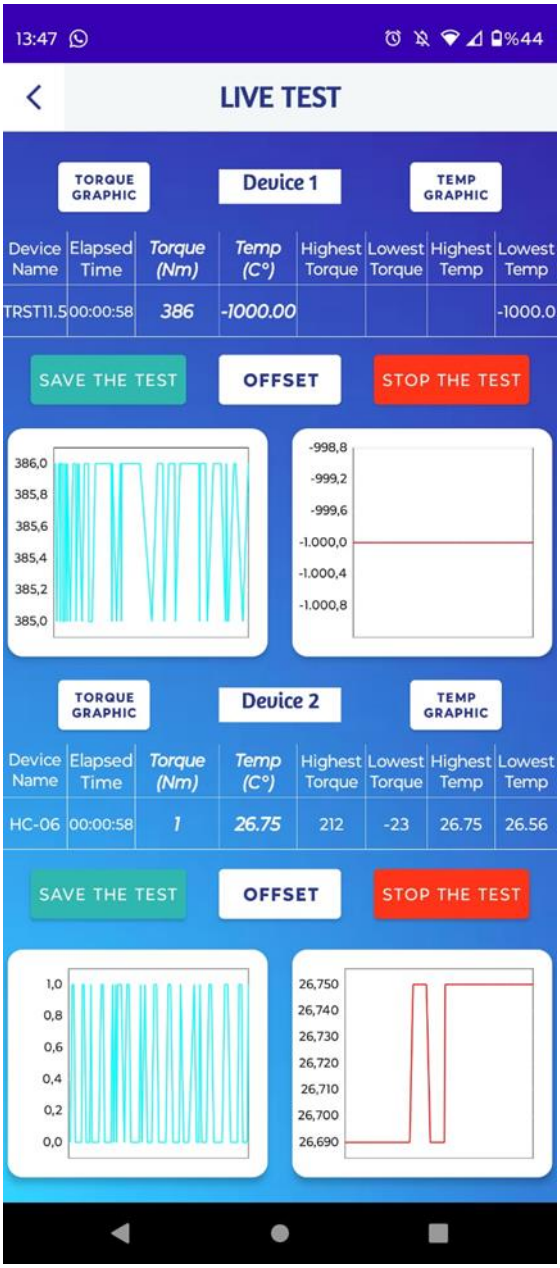
```
// Stop Test butonuna basıldığında çalışan fonksiyon
private fun finishTest() {
    // Veri okumayı durduran değişkenler
    stopStatus = true
    stopReading = true
    testFinished = true
    // Süre akışı durdurulur
    handler.removeCallbacks(runnable)
```

```
// Tork verisinin ölçeklendiği fonksiyon
private fun offsetTorqueValue(offsetTorque: String, sabitTork: Int, deviceIndex: Int) {
    if (offsetTorque.isNotEmpty()) {
        if (deviceIndex == 1) {
            textViewDiff.text = ("$offsetTorque, $sabitTork")
            val offsetTorque1 = ((offsetTorque.toInt() - sabitTork) / div).toString()
            textViewTorque.text = offsetTorque1
```

Şekil 7 Canlı Test Ekran Kodları

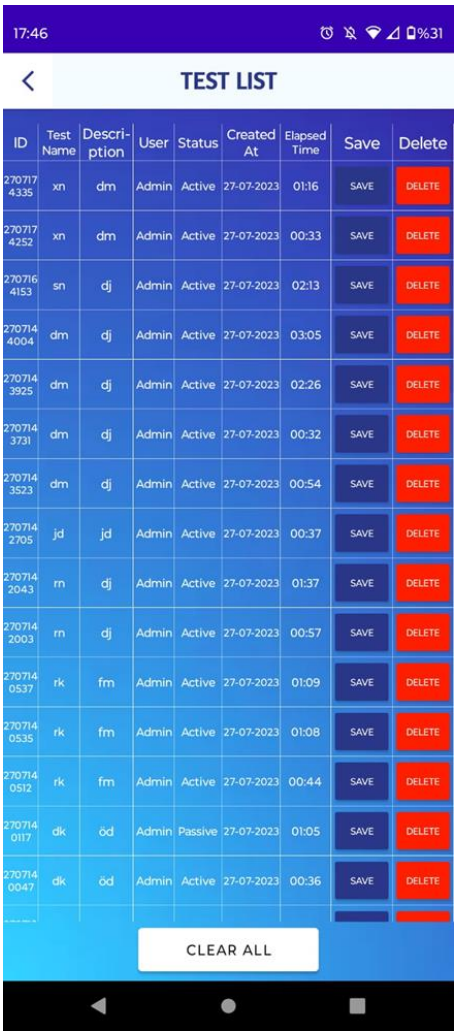
Veri ölçekleme butonu tork verisi toplanırken kullanılmaktadır. Araç altı veya test cihazına montajda bağlantı kaynaklı gelen ek yükler veri toplama sisteminde kendini artık tork değerleri olarak göstermektedir. Bu değerleri kaldırmak için veri ölçekleme butonundan faydalanılmaktadır.

Ekranlardaki «stop test» butonu ile testi tamamlamak, «save test» butonuyla da testi kaydetmek mümkün olmaktadır. Arayüze eş zamanlı olarak iki sistem ve her sisteme bağlı ikişer sensör bağlanabilmektedir. Toplanan verilere ait gerçek zamanlı grafikler çizdirilebilmekte ve veri trendi takip edilebilmektedir. Şekil 8'de canlı test ekranı görülmektedir.



Şekil 8 Canlı Test Ekranı

Testler tamamlandıktan sonra ardıl işlemler için test listesi üzerinden bir excel dosyası üzerine kaydetme seçeneği oluşturulmuştur. Test listesinde geçmişte gerçekleştirilen tüm testlere erişim imkanı bulunmaktadır. İstenildiği takdirde «delete» butonuyla veri tabanından kaldırma seçeneği eklenmiştir. Şekil 9'da test listesi ekranı görülmektedir.



Şekil 9 Test Listesi

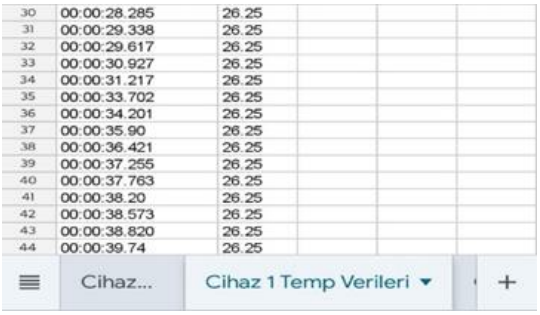
Bununla birlikte tüm ekran mimarileri kurulmuştur. Arka planda bluetooth bağlantısını kurmak için fonksiyonlar tanımlanmıştır. Beklenmeyen bir durumda bluetooth bağlantısı koptuğunda hata vermesini önleyecek şekilde tekrar bağlantı denemeleri gerçekleştirilir.

2.2 Fonksiyonlar

Arka planda yer alan bazı önemli fonksiyonlar şu şekildedir.

2.2.1 DownloadExcelFile

Bu fonksiyon daha önce bahsedilen «save test» butonuna tıklandığında çalışmaktadır. Kaydedilen testin id'sini baz alarak testi Excel dosyası halinde indirir. Şekil 10'da çıktı örneği verilmektedir.



Şekil 10 Excel Çıktıları

2.2.2 ConnectWithRetry

Bu fonksiyon bluetooth bağlantısını kurmaktadır. Eğer ilk denemede adaptör bağlanamamışsa bunu 2 kez daha denemektedir.

2.2.3 ConnectWithRetry2

Bu fonksiyon olası bir bluetooth bağlantısı kopması durumunda o ana kadar ki testi kaydedip sonsuza kadar tekrar bağlantı denemesi yapılmasını sağlamaktadır.

2.2.4 CancelLiveTestFragment

Bu fonksiyon eğer «connectWithRetry» fonksiyonunda denemeler sonucu bağlantı kurulamazsa test oluşturma ekranını yeniden başlatır.

2.2.5 ProcessedRecievedData

Bu fonksiyon, cihazdan gelen verinin tork ve sıcaklık ayrımını yapıp hangi kısımlarının ekranda yansıtılacağını ayıklamaktadır. Ardından ise numerik biçime veriyi dönüştürmektedir.

2.2.6 AddTorqueDataToExcel/addTempDataToExcel

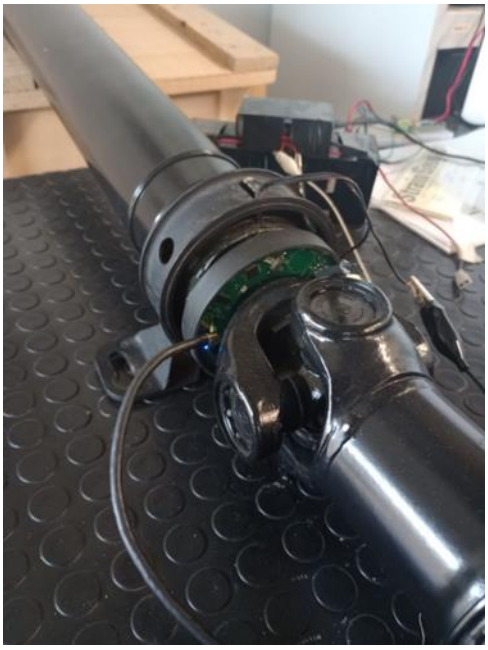
Bu fonksiyon oluşturulan Excel sayfalarını süreyi de katarak sürekli güncellemektedir.

2.2.7 UpdateTorqueData

Bu fonksiyon işlenmiş veriyi tabloda yazmakla yükümlüdür. Eğer veri ölçekleme açıksa tabloya yazmadan önce «offsetTorqueValue» fonksiyonuna gitmekte ve ölçeklenmiş veriyi yazdırmaktadır.

2.3 Testler

Arayüzün, kardan miline entegre ölçüm ve veri toplama sistemi üzerinden testleri gerçekleştirilmiştir. Tork ve sıcaklık verilerinin arayüz üzerinden takibi gerçekleştirilmiştir. Olası hata senaryoları üzerinden veri kaybı ve izleme durumları takip edilmiştir. Birden fazla cihazın bağlandığı durumlar, birden fazla sensörün bağlandığı durumlar, veri yoğunlukları, farklı frekanslarda veri ileten cihazlarla bağlantı denemeleri gerçekleştirilerek sistemin sorunsuz şekilde çalıştığı ortaya koyulmuştur. Şekil 11'de entegre ölçüm sistemi görülmektedir.



Şekil 11 Entegre Ölçüm Sistemi

3. SONUÇLAR

Bu çalışmada, kardan mili saha testlerinde gerçekleştirilen veri toplama çalışmalarında kullanılmak üzere, bu veri toplama sistemlerinden edinilen verinin anlık olarak izlenebileceği android tabanlı bir kullanıcı arayüzü geliştirilmiştir.

Projede 5 ekran sınıfı, 1 ana yönlendirici sınıfı ve 1 veritabanı sınıfı olmak üzere 7 class bulunmaktadır. Bu classların içinde 58 tane fonksiyon bulunuyor olup, yazılan toplam kod satır sayısı yaklaşık 3000'dir.

Veriler her 7.5 salisede bir yenilenir. Bu hızlar bağlantı kalitesine göre hassasiyet değişeceğinden farklılıklar gösterebilmektedir.

Kullanıcı arayüzü yazılımı ile saha testlerinde elde edilen tüm veriler cep telefonu veya tablet gibi bir cihaz üzerinden izlenebilecektir. Veri toplama sisteminin sensör sayısı ve tipi, iletişim protokolü gibi özelliklerine göre Tirsan Kardan bünyesinde geliştirilen tüm veri toplama

sistemleriyle uyumlu çalışan, verilerin anlık olarak izlenebildiği ve sonrasında kaydedilerek ardıl işlemler yapılmasına da izin veren bir kullanıcı arayüzü geliştirilmiştir.

Testler sonucunda arayüzün yeterliliği ortaya koyulmuştur ve android cihazlara indirmek üzere PlayStore'a yüklenmiştir.

Teşekkür: Bu çalışmanın gerçekleştirilmesinde desteklerini esirgemeyen Tirsan Kardan Ar-Ge Merkezi'ne ve Test Merkezi'ne sonsuz teşekkürlerimizi sunarız.

KAYNAKÇA

1. **Aldemir, O., Tarakçı, S., Solmaz, T., Işık, E. (2020),** " External system design for real time monitoring of temperature and torque data on the driveshaft", 1. 10th International Automotive Technologies Congress Book, 769-776, 2020.

2. **Persson, G., Persson, O., (2015),** "Torque Sensor for Automotive applications", Lund University,2015

3. **Muftah, H., Haris, S.M., Petroczki, K., Khidir, E.A., (2013),** "An Improved Strain Gauge-Based Dynamic Torque Measurement Method", International Journal Of Circuits, Systems And Signal Processing, Volume 7, Issue 1, 66-73

4. **Tarakçı, S., Aldemir, O., Işık, E., (2023),** "Savunma Sanayi Saha Testlerinde Kullanılmak Üzere Kardan Miline Entegre bir Tork Ölçüm Sistemi" ICNASEN 2023 Bildiriler Kitabı sf. 72-78.

ALÜMİNYUM 7075 T6 MALZEMESİNİN FREZELENMESİNDE KESME PARAMETRELERİNİN EN İYİLENMESİ

Sinan GÖKÇE,*sinangokce188@gmail.com,* Paksan Makine Sanayi Tic. AŞ, 10600, Balıkesir,

S**emin KAYA**, *skaya@balikesir.edu.tr* Balıkesir Üniversitesi, 10145, Balıkesir

ÖZET

Bu çalışmada, Al alaşımlarında işleme parametrelerinin en doğru şekilde seçilmesine odaklanılmıştır. Taguchi yöntemi ile belirlenen 9 farklı deney, 3 farklı parametre kullanılarak yapılmıştır. Deneyler sonucunda elde edilen takım yan yüzey aşınmaları ölçülerek kayıt edilmiştir. Oluşturulan deney tasarımı ile alınan ölçüm değerleri değerlendirilmiştir. Bu çalışma sonuncunda Al 7075-T6 malzemesi için takım yan yüzey aşınmasına en çok etki eden parametrenin ilerleme olduğu görülmüş, diğer parametrelerde sırasıyla kesme hızı ve talaş derinliği olarak belirlenmiştir.

Anahtar Kelimeler: Frezeleme, Taguchi yöntemi, takım aşınması

ABSTRACT

This study focused on selecting the most accurate processing parameters for Al alloys. 9 different experiments were conducted using the Taguchi method and three different parameters. The tool flank wear obtained from the experiments was measured and recorded. The measurement values obtained from the designed experiments were evaluated. As a result of this study, it was observed that the parameter with the most significant effect on tool flank wear for Al 7075-T6 material was the feed rate, followed by cutting speed and then depth of cut.

Keywords: Milling, Taguchi method, tool wear

1. GİRİŞ

Talaşlı imalat yapan firmaların rekabet edebilmelerinin temelinde, üretim teknikleri ve düşük maliyetler yer almaktadır. Bu rekabet ortamının sağlanması adına üretim yöntemlerinin tasarımları gün geçtikçe önem kazanmaktadır. Kesici takımların yüksek maliyetleri

sonucunda, üretimde birim maliyetlerinin azaltılması büyük önem taşımaktadır. Bu sebeple doğru kesici takım ve doğru parametre seçimi önemlidir.

Kesici takımlar, markaları, malzemeleri, tipleri, kullanım yerleri ne olursa olsun fark etmeksizin aşınacaklardır. Bu aşınma takım ömrünün sonuna kadar devam edecektir. Talaşlı üretim esnasında belirlenen yöntem ve parametreler, takım aşınmasını doğrudan etkilemektedir ve takım ömrünün azalmasına sebep olabilecek yöntem ve parametreler birim maliyetleri doğrudan artıracaktır. Talaş kaldırma yöntemi, iş parçası malzemesi, kesici takım malzemesi, kesici takım geometrisi, kesme hızı, ilerleme, kesme derinliği vb. faktörleri takım ömrüne etki eden faktörler olarak değerlendirebiliriz.

Kesme hızı, ilerleme, kesme derinliğini en önemli talaşlı imalat işleme parametreleri olarak sayabiliriz. Kesme hızının düşük seçilmesi işleme süresini artıracak ve bununla beraber üretim süresini etkileyecek ve dolayısıyla birim maliyeti de etkileyecektir. Kesme hızının fazla seçilmesi sürtünmeden dolayı oluşan ısıyı artıracak ve yüzey pürüzlülüğünü artırmanın yanında takım ömrünü de olumsuz yönde etkileyecektir. İlerleme miktarının seçimi de aynı şekilde büyük öneme sahiptir. Düşük ilerleme hızlarının seçilmesi, işlem süresini artıracaktır, birim maliyetlerin artmasına sebep olacaktır. Ancak ilerleme hızlarının yüksek seçilmesi yüzey pürüzlülüğünü olumsuz etkilenecektir.

Tüm bu parametreler ve kesme şartları düşünüldüğünde, en uygun kesici takımların ve takım tezgâhlarının seçimi büyük önem taşınmaktadır. Rekabet içinde bulunan firmaların üretim maliyetlerini düşürme konusunda bu parametrelere dikkat etmeleri zorunluluk haline gelmiştir.

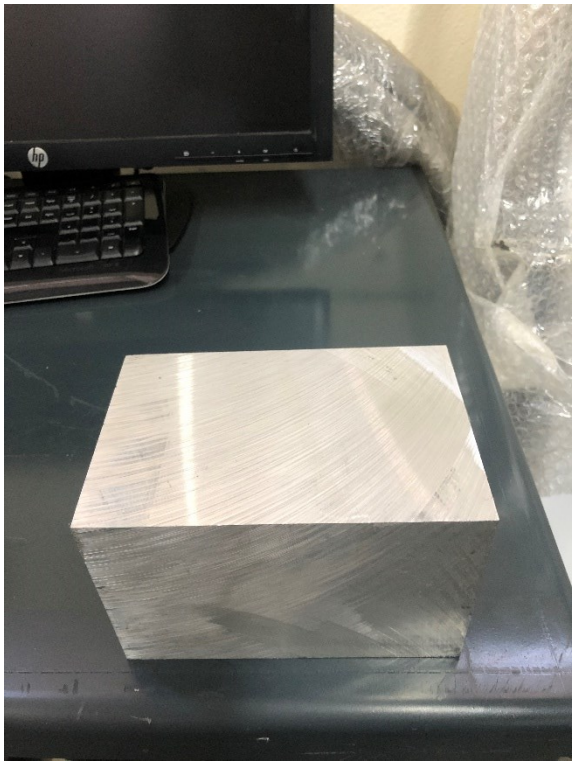
Bu çalışmada Alüminyum 7075-T6 malzemesinin; frezelenmesi için gerekli en iyi kesme parametreleri araştırılmıştır. Deneylerde 3 farklı kesme parametresi olarak; kesme hızı, ilerleme ve talaş derinliği kullanılmıştır. Her biri için 3’ er adet değer belirlenmiş ve Taguchi metodu ile 9 deneyden oluşan tasarım elde edilmiştir.

Wang ve Li, TC17 titanyum alaşımının frezelenmesinde, 80-100-120 m/dk kesme hızlarında, 0,04-0,08-0,12 mm/dev ilerleme hızlarında, 0,8-1,6-2,4 kesme kalınlıklarında ve 0,4-1-1,6 kesme derinliklerinde deneyler gerçekleştirmiş ve deneyler sonucunda yan yüzey aşınmasına ve yüzey pürüzlülüğüne etkileri incelenmiştir. Yan yüzey aşınmasında en etkili parametrenin sırasıyla, kesme kalınlığı, ilerleme, kesme hızı ve kesme derinliği olduğu sonucuna varılmıştır **[Wang & Li, (2021]**. Chaudhari, AISI H11 malzemesinin tornalamasında kesme parametrelerinin takım yan yüzey aşınmasına etkilerini araştırmıştır.

Bu çalışmada 3 farklı kesici takım, 3 farklı malzeme sertliği, 3 farklı kesme ve ilerleme hızı seçerek 9 deney yapmıştır. Bu deneyler sonucunda ANOVA verilerine göre yan yüzey aşınmasında en etkili parametrelerin sırasıyla sertlik, ilerleme, kesme hızı ve kesici takım olduğu sonucuna varılmıştır **[Özbek, Özbek, Kara 2017].** Özbek ve arkadaşları, AISI 420 çeliğinin tornalanmasında Taguchi yöntemi ile kesme parametrelerinin optimizasyonu üzerine çalışmışlardır. 3'er seviye ve 3 parametre ile deneyler gerçekleştirmişler ve yan yüzey aşınması ölçümleri almışlardır. Bu ölçüm sonuçlarını göre ANOVA analizi kullanarak hangi parametrenin yan yüzey aşınmasında daha etkili olduğunu araştırmışlardır. Bunun sonucunda yapılan çalışmada en etkili parametrenin %47.04 ile ilerleme olduğu ve daha sonra sırasıyla %36,28 kesme hızı ve %4,1 kesme derinliği olduğu sonucuna ulaşmışlardır

2. MATERYAL VE YÖNTEM

Bu deney için hazırlanan Alüminyum 7075 – T6 deney numunesi boyutları 100x100x150 mm olarak seçilmiştir. CNC freze tezgâhına mengene yardımı ile bağlanan deney numunelerine farklı işleme parametreleri ile kesme sıvısı olmadan işleme yapılmıştır.



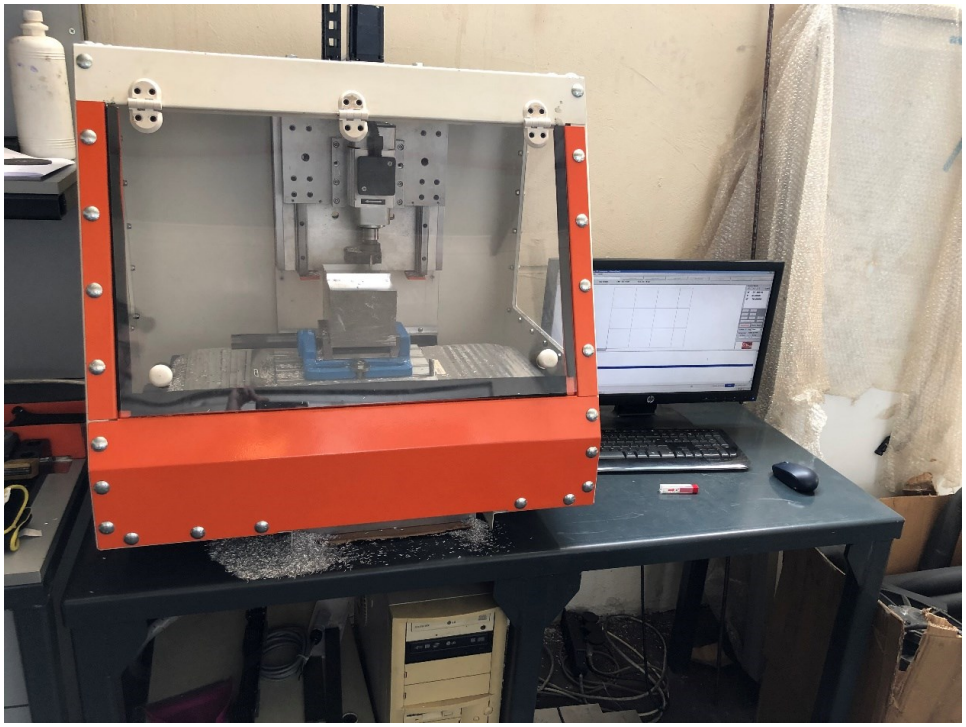
Şekil 1: Deneylerde kullanılan deney numunesi

Tablo 1: Malzemenin kimyasal bileşimi **[Anonim, 2024]**.

Al	Fe	Si	Cu	Mn	Mg	Zn	Cr	Ti	Diğer
Kalan	0.50	0.40	1.2 – 2.0	0.30	2.1 – 2.9	5.1 – 6.1	0.18 – 0.28	0.20	0.05

Tablo 2: Malzemenin mekanik özellikleri [4].

Akma Dayanımı (MPa)	Çekme Dayanımı (MPa)	Yüzde Uzama (%)	Brinell Sertliği (HB)
505	570	11	150



Şekil 2: Deneysel çalışmada kullanılan takım tezgâhı

Tablo 3: Deneylerde kullanılan parmak freze teknik özellikleri.

Parmak Freze Kısımları	Detayları
Parmak freze cinsi	KARCAN 123 Serisi Alu-Mac
Kesici uç sayısı	3
Helis açısı	45°
Köşe radyusu	0.2 mm
Kesme hızı	Max. 350 – 400 m/dk

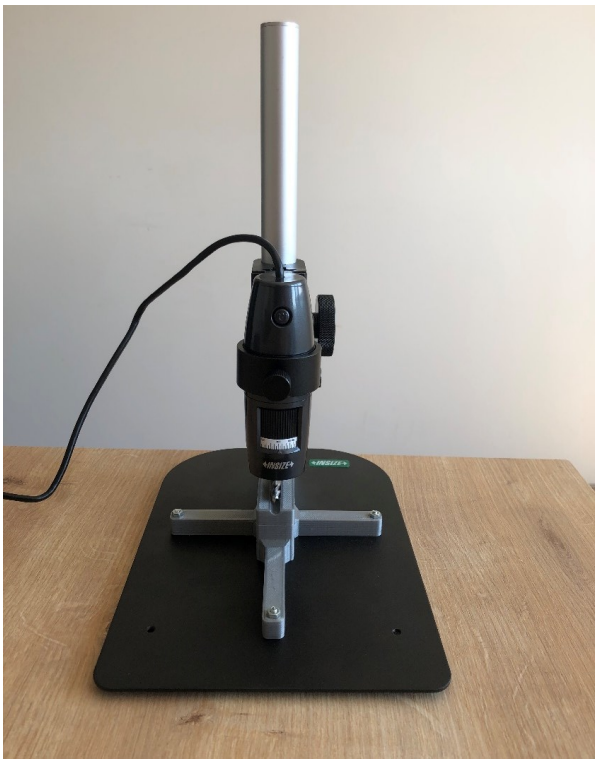
Tablo 4: Deneylerde kullanılan parmak freze diş başı ilerleme (fz:mm/diş) değerleri [**Oral, Çelik, 2009**].

Ø5	ap=1.5Ø	ap=1Ø	ae=0.3Ø	ae=0.2Ø	ae=0.1Ø
fz	0.062	0.076	0.152	0.19	0.24



Şekil 3: Deneylerde kullanılan 45° helis açısına sahip parmak freze.

Yapılan deneyler sonucunda elde edilen takım aşınması değerleri insize marka ısm-pm200 model dijital mikroskop ile elde edilmiştir. Mikroskop ile birlikte gelen yazılım sayesinde değerler hassas olarak elde edilmiş ve kayıt altına alınmıştır.



Şekil 4: Frezelerin incelendiği ISM-PM200 Dijital Mikroskop.

Deneysel çalışma için belirlediğimiz işleme parametreleri Tablo 5’ de verilmiştir. Deney tasarımı ve faktörleri Tablo 6’ da verilmiştir.

Tablo 5: Deneysel çalışmanın işleme parametreleri ve seviyeleri.

Kod	Faktörler	Sembol	Birim	1.Seviye	2.Seviye	3.Seviye
A	İlerleme	F	mm/dk	1000	1500	2000
B	Kesme hızı	Vc	m/dk	125	150	175
C	Talaş derinliği	ae	mm	0.5	1	1.5

Tablo 6: Deney faktörleri ve L9 ortogonal dizin.

Deney No	Değişkenler	İlerleme	Kesme Hızı	Talaş Derinliği
1	A1B1C1	1000	125	0.5
2	A1B2C2	1000	150	1
3	A1B3C3	1000	175	1.5
4	A2B1C2	1500	125	1
5	A2B2C3	1500	150	1.5
6	A2B3C1	1500	175	0.5
7	A3B1C3	2000	125	1.5
8	A3B2C1	2000	150	0.5
9	A3B3C2	2000	175	1

3. DENEYSEL SONUÇLAR VE TARTIŞMA

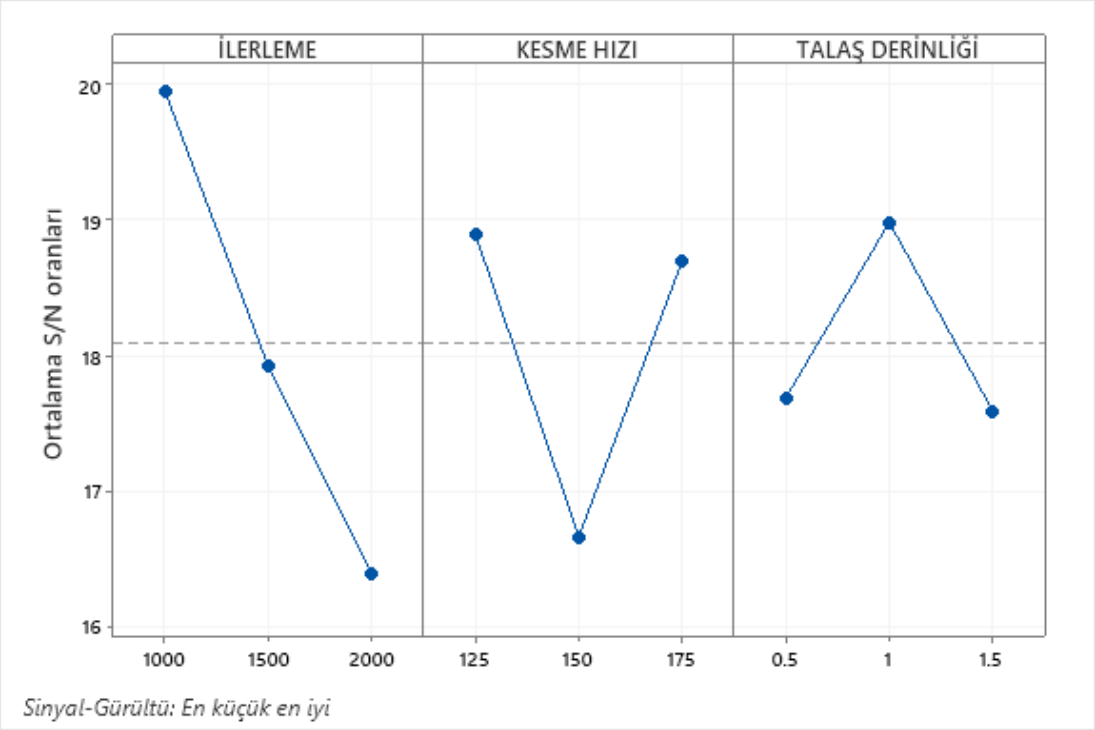
Yapılan çalışmada; deney numunesi 5mm derinlik sabit tutularak işleme yapılmıştır. Her bir deney numunesinden 200 cm3 talaş kaldırılmıştır. Her bir deney numunesi ve parametre için farklı parmak freze çakısı kullanılmıştır. Taguchi L9 ile oluşturulan parametreler ile yapılan deneyler sonucunda elde edilen Vb değerleri ve bu değerler ile hesaplanan S/N oranları Tablo 7’ de verilmiştir. Ayrıca parametreler arasında en etkili olanının belirlenmesinde kullanılan S/N yanıt tablosu Tablo 8’ de verilmiştir. Bu tablonun grafik ile gösterimi Şekil 5’ te verilmiştir.

Tablo 7: Takım aşınması deney sonuçları ve S/N oranları.

Deney No	İlerleme (F) [mm/dk]	Kesme hızı (Vc) [m/dk]	Talaş Derinliği (ae) [mm]	Yan Yüzey Aşınması (Vb) [mm]	S/N (dB)
1	1000	125	0.5	0,101	19,9136
2	1000	150	1	0,106	19,4939
3	1000	175	1.5	0,095	20,4455
4	1500	125	1	0,100	20,0000
5	1500	150	1.5	0,167	15,5457
6	1500	175	0.5	0,123	18,2019
7	2000	125	1.5	0,145	16,7726
8	2000	150	0.5	0,179	14,9429
9	2000	175	1	0,134	17,4579

Tablo 8: S/N yanıt tablosu.

Seviyeler	İlerleme	Kesme Hızı	Talaş Derinliği
Seviye 1	19,95	18,90	17,69
Seviye 2	17,92	16,66	18,98
Seviye 3	16,39	18,70	17,59
Delta	3,56	2,23	1,40
Sıralama	1	2	3



Şekil 5: Her bir parametre için ortalama S/N oranları.

Takım aşınması deney sonuçlarına göre en iyi kesme parametreleri; ilerlemenin birinci seviyesi olan 1000 mm/dk' da, kesme hızının birinci seviyesi olan 125 m/dk'da, talaş derinliğinin ikinci seviyesi olan 1 mm' de elde edilmiştir.

Ortalama S/N oranlarını gösteren Şekil 5 incelendiğinde; en büyük S/N değerleri o parametreye ait en iyi kesme koşullarını göstermektedir. Yine aynı tablo üzerinden yola çıkarsak, takım aşınmasında en iyi parametreler sırasıyla; ilerlemenin 1. seviyesi, kesme hızının 1. seviyesi ve kesme derinliğinin 2. seviyesi olduğu görülmüştür.

ANOVA (Varyans Analizi) deney tasarımında kullanılan kontrol faktörlerinin birbirleri ile etkileşimlerini ve performans karakteristiği üzerinde etki seviyelerini belirlemek için kullanılan istatiksel bir yöntemdir **[Özbek, Özbek, Kara 2017].**

Deneylerden elde edilen sonuçlara göre yan yüzey aşınmasındaki etkilerini belirlemek için yapılan ANOVA sonuçlar Tablo 9' da verilmiştir. F değerleri ve parametrelerin etki oranları tabloda görülmektedir. Yapılan bu analiz sonucunda en etkili parametrenin %53,96 ile ilerleme olduğu görülmüştür. Kesme hızı ise %31,27 oran ile ikinci en etkili parametre olarak belirlenmiştir. Yan yüzey aşınması üzerinde en az etkili olan parametre ise %12,46' lık oran ile kesme derinliği olduğu belirlenmiştir.

Tablo 9: ANOVA tablosu.

Parametreler	Serbestlik derecesi (DF)	Kareler toplamı (SS)	Kareler ortalaması (MS)	F oranı	Katkı oranı (%)
İlerleme	2	0,004078	0,002039	23,41	53,96
Kesme hızı	2	0,002364	0,001182	13,57	31,27
Kesme derinliği	2	0,000942	0,000471	5,40	12,46
Hata terimi	2	0,000174	0,000087		2,31
Toplam	8	0,007558			100,00

ANOVA sonuçları incelendiğinde, her bir parametrenin etki oranları değerlendirilmiştir. Oluşan tabloya göre takım yan yüzey aşınmasında en etkili parametrenin ilerleme olduğu ve sonrasında sırasıyla kesme hızı ve kesme derinliği olduğu görülmüştür.

4. SONUÇLAR

Elde edilen deney sonuçlarına göre genel olarak ilerlemenin artmasıyla yan yüzey aşınmasının arttığı gözlenmiştir. Tablo 9.' da verilen ANOVA sonuçları incelendiğinde, her bir

parametrenin etki oranları değerlendirilmiştir. Oluşan tabloya göre takım yan yüzey aşınmasında en etkili parametrenin ilerleme olduğu ve sonrasında sırasıyla kesme hızı ve kesme derinliği olduğu görülmüştür.

Elde edilen S/N oranlarına bakılarak en iyi takım yüzey aşınması değerlerini elde etmek için her bir parametreden seçilmesi gereken değerlerin ilerleme için 1000 mm/dk, kesme hızı 125 m/dk, talaş derinliği 1 mm olarak seçilmiştir.

Bu çalışmada, literatürde karşılaşılan deneysel tartışmalarda benzer sonuçlara rastlanmıştır. Bunlara örnek olarak, sertleştirilmiş AISI 420 çeliğinin tornalanması ile yapılan çalışmada ANOVA sonuçlarına göre yan yüzey aşınmasında en çok etkiye sahip olan parametrenin %47,04 ile ilerleme ve sırasıyla %26,28 kesme hızı, %4,1 kesme derinliği olduğu belirlenmiştir **[Özbek, Özbek, Kara 2017]**. Başka bir çalışmada, Inconel 625 süper alaşımının frezelenmesinde kesme parametrelerinin Taguchi yöntemi ile optimizasyon çalışması yapılmış ve yan yüzey aşınmasında etkili olan parametreler sırasıyla %41,5 ilerleme, %28,86 kesme hızı ve %15,01 kesme derinliği olarak belirlenmiştir **[Akgün, Demir, 2021]**.

Bahsedilen 2 çalışmada da elde edilen sonuçlar, yapmış olduğumuz deneysel çalışmanın sonuçlarına oldukça benzerlik göstermektedir.

KAYNAKÇA

1. **Wang, Z., & Li, L. (2021),** Optimization of process parameters for surface roughness and tool wear in milling TC17 alloy using Taguchi with grey relational analysis. Advances in Mechanical Engineering, 13(2).
2. **Chaudhari, Y. D. (2013),** Investigation Of Tool Wear In Hard Turning Using Taguchi Method. International Journal Of Engineering Research and Applications, 3(2), 317-321
3. **Özbek, N. A., Özbek, O., & Kara, F. (2017)** “Sertleştirilmiş AISI 420 çeliğinin tornalanmasında Taguchi yöntemi kullanılarak takım aşınması için kesme parametrelerinin optimizasyonu”, Düzce Üniversitesi, Düzce,
4. **Anonim,** “7075 aluminum alloy properties, AA 7075-T6, T7351, T651, Density, Composition, Yield Strength” https://www.theworldmaterial.com/al-7075-aluminum-alloy/ (E.T:01.06.2024)
5. **Oral, A. Ve Çelik, S. (2009),** “Küçük ölçekli işletmeler için sayısal denetimli çok amaçlı kesme makinası tasarımı”, Mühendis ve Makine, 50, 8-17

6. **Akgün, M., & Demir, H. (2021),** Optimization and finite element modelling of tool wear in milling of Inconel 625 superalloy. Politeknik Dergisi, 24(2), 391-400 (2021).

SERTLEŞTİRİLMİŞ ÇELİKLERİN FREZELEME İŞLEMLERİNDE KESİCİ TAKIM KARBÜR KALİTESİ VE KAPLAMANIN İŞLEME PERFORMANSINA ETKİSİ

Hasan KUŞ, *h.kus@karcan.com* Karcan Kesici Takım San. ve Tic. A.Ş., 26110, Eskişehir

Çağla GÖKBULUT AVDAN, *c.avdan@karcan.com* Karcan Kesici Takım San. ve Tic. A.Ş., 26110, Eskişehir

Çağlar YAVAŞ, *c.yavas@karcan.com* Karcan Kesici Takım San. ve Tic. A.Ş., 26110, Eskişehir

ÖZET

Sertleştirilmiş çelikler yüksek mukavemetleri ve iyi aşınma direnci nedeniyle kalıpçılık endüstrisinde yaygın kullanılır. Sert işleme, malzemenin yüksek mukavemeti nedeniyle zor bir işlem olarak kabul edilir. Bu çalışma kapsamında; 1.2379 çeliğinin frezeleme işlemleri için geliştirilen kesici takımlarda, karbür kalitesi ve kaplamanın işleme performansına etkisi araştırılmıştır. %8 Co ve %6 Co submicron karbür kalitesi bazında kıyaslanmış, %6 Co kalitenin daha iyi performans gösterdiği görülmüştür. Ardından %6 Co kaliteye (nc-AlTiN)/(a-Si3N4), TiSiN, AlTiN-TiSiXN ve TiAlSiN bazlı kaplamalar uygulanarak sertleştirilmiş çeliklerin işlenmesindeki performansları test edilmiştir. Çalışma sonunda, %6 Co kalite ve Yüksek Güçte Darbeli Magnetron Püskürtme (HiPIMS) teknolojisiyle yapılan TiAlSiN bazlı kaplamanın önerilebileceği sonucuna varılmıştır.

Anahtar Kelimeler: Sertleştirilmiş Çelikler, İşlenebilirlik, Kesici Takım, Kanal Frezeleme, Karbür Hammadde Kalitesi, Kaplama Uygulamaları

THE EFFECT OF CUTTING TOOL CARBIDE QUALITY AND COATING ON MACHINING PERFORMANCE IN MILLING PROCESSES OF HARDENED STEELS

ABSTRACT

Hardened steels are widely used in the mold industry due to their high strength and good wear resistance. Hard machining is considered a challenging process due to the high strength of the material. In this study, the impact of carbide quality and coating on the machining performance of cutting tools developed for milling operations of 1.2379 steel was

investigated. Submicron carbide qualities containing 8% Co and 6% Co were compared, revealing that the 6% Co quality performed better. Subsequently, (nc-AlTiN)/(a-Si3N4), TiSiN, AlTiN-TiSiXN, and TiAlSiN-based coatings were applied to the 6% Co quality and their performance in machining hardened steels was tested. The study concluded that the 6% Co quality and TiAlSiN-based coating made using High Power Impulse Magnetron Sputtering (HiPIMS) technology could be recommended.

Keywords: Hardened Steels, Machinability, Cutting Tool, Slot Milling, Carbide Material Quality, Coating Applications

1. GİRİŞ

Sertleştirilmiş çelikler yüksek sertlikleri, yüksek mukavemetleri ve iyi aşınma direnci nedeniyle özellikle kalıpçılık endüstrisinde yaygın kullanılır [Davim, 2010]. Sert işleme olarak da adlandırılan sert malzemelerin işlenmesi, malzemenin yüksek mukavemeti nedeniyle zor bir işlem olarak kabul edilir. Aynı zamanda sert işleme, yüksek kesme kuvvetlerine ve kesme sıcaklığına sebep olmaktadır. Bu durumda kesici takımlar için daha yüksek performans gereksinimi ortaya çıkmaktadır [Wang ve Liu, 2016]. Sert işleme için iş parçası malzemesinin iyi işlenebilirliğe sahip olması önemlidir. Bu iş parçası malzemenin işleme kabiliyetinin belirlenmesinde kesme kuvvetleri ve yüzey kalitesi büyük önem taşımaktadır. Kesme kuvvetleri, kesme işlemi, takım aşınması, iş parçası malzemesi, takım tutucu, sabitleme elemanları ve takım tezgahının kendisi sert malzemelerin işlenebilirliğini etkiler [Boogert vd., 1996]. Düşük kesme kuvvetleri, yüksek malzeme kaldırma oranı, iyi yüzey bütünlüğü, doğru ve tutarlı iş parçası geometrik özellikleri ve düşük takım aşınma oranı, bir malzemenin yüksek işlenebilirliğini gösterir [Noordin vd., 2004].

Frezeleme işlemi endüstride büyük bir öneme sahiptir. Makine, otomotiv, havacılık, kalıpçılık ve silah sanayi frezeleme işlemini yoğun olarak kullanan alanlardandır [Yaşar, 2020]. Kalıpçılık sektöründe de en yaygın kullanılan operasyonlardan biri frezeleme işlemidir. Kalıpçılık sektöründe kullanılan soğuk veya sıcak iş takım çeliklerinin sertleştirme işlemleri sonrasında da işlenmesine ihtiyaç duyulmaktadır. Frezeleme işlemlerinde kesici takım performansını etkileyen birçok parametre vardır. Bu parametreler işleme sürecinin verimliliğini, yüzey kalitesini ve takım ömrü üzerinde önemli bir etkiye sahiptir. Kang MC ve arkadaşları AISI D2 soğuk iş takım çeliğini yüksek performansta frezelenmesinde TiAlN ve TiSiAlN kaplamalar üzerinde çalışarak, TiSiAlN kaplamanın daha iyi sonuç verdiğini gözlemlemiştir [Kang vd., 2008]. Literatürdeki bulgulardan hareketle bu çalışma kapsamında; 1.2379 çeliği olarak da bilinen, çeşitli endüstriyel uygulamalarda yaygın olarak kullanılan çok yönlü bir takım çeliği olan 60 HRC sertliğe sahip, ısıl işlem görmüş D2 soğuk iş takım

çeliğinin frezeleme işlemleri için geliştirilen kesici takımlarda, kesici takım karbür kalitesi ve kaplamanın işleme performansına etkisi deneysel olarak araştırılması amaçlanmıştır.

2. MALZEME VE METOT

Bu çalışma kapsamındaki deneysel çalışmalarda iş parçası malzemesi olarak kullanılan 60 HRC'ye kadar setleştirilmiş 1.2379 (X153CrMoV12) malzemenin kimyasal bileşimleri Tablo 1'de verilmiştir.

Tablo 1. 1.2379 malzemenin kimyasal kompozisyonu (wt%)

	C	Mo	V	Cr
Max-Min	1.5-1.65	0.70-0.90	0.80-1	11.8-12.2
Actual Value	1.55	0.80	0.9	12

Bu çalışmada Ø12 karbür parmak frezeler ile 2379 60 HRC malzemesinde son yüzey frezeleme operasyonu yapılarak aşınma, eğilme momenti ve talaş oluşumları incelenmiştir. Çalışmada karbür kalitesinin takım performansına etkisinin görülmesi için 2 farklı karbür kalitesi denemesi gerçekleştirilmiştir. Hammadde içerikleri Tablo 2'de verilmiştir.

Tablo 2. Kullanılan 2 farklı sementit karbür takım malzemesi kalitesinin özellikleri

	ISO Grade	Tane Boyutu (mμ)	Kobalt Miktarı (%)	Sertlik (HRA)	Sertlik (HV30)	Özkütle (g/cm³)	Enine Kopma TRS (N/mm²)
Kalite 1	K05-K10	0,5-0,8	6	93,1	1820	14,8	3600
Kalite 2	K10-K20	0,2-0,5	8,2	93,7	1930	14,55	4400

2 farklı karbür kalitesinde üretilen takımların performans denemelerinin ardından, kullanılacak karbür kalitesi belirlenerek farklı kaplama kompozisyonlarında takım üretimi gerçekleştirilmiştir. Kaplama firmaları kullandıkları farklı reçete ve kaplama yöntemleri ile birbirinden ayrılmaktadır. Çalışma kapsamında 4 farklı firmanın 4 farklı kaplama türü kullanılmıştır. Kullanılan kaplama tipleri ve içerikleri Tablo 3'te verilmiştir.

Tablo 3. Çalışmada kullanılan kaplama türleri ve içerikleri

Kaplama İçeriği	Kaplama Tekniği
(nc-AlTiN)/(a-Si3N4)	Katodik-Ark Biriktirme

TiSiN	Katodik-Ark Biriktirme
AlTiN-TiSiXN	Katodik-Ark Biriktirme
TiAlSiN-based	HiPIMS

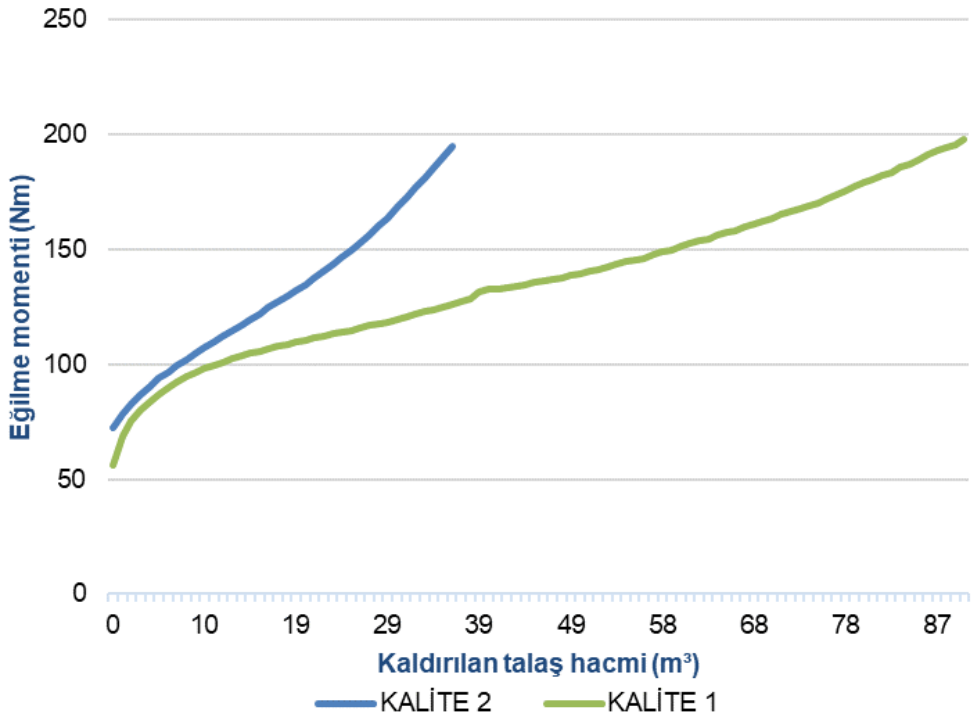
Testlerde kullanılan takım tezgahı Karcan ARGE test merkezi bünyesinde bulunan Mikron VCP 800 tezgahıdır. Deneylerde Spike mobile 1.2. versiyon dinamometre tutucu kullanılarak takımlara ait eğilme momenti ölçümleri, takım aşınması ve kuvvet analizleri yapılmıştır. Karbür kalitesini karşılaştırmak için yapılan deneylerde Karcan firmasının geliştirerek ürettiği bu takımlara TiAlSiN bazlı kaplama uygulanmıştır. Bu kaplama HiPIMS (Yüksek Güçlü İtkili Magnetron Püskürtme) yöntemiyle yapılmıştır. Takımlara ortalama 6-8 µ köşe yuvarlama uygulanmıştır. Frezeler için 45° helis açısı ve kesici ağız sayısı 6 olarak seçilmiştir. Ø12 takımların boyu 82 mm'dir. Tablo 4'te testlerde kullanılan kesme parametreleri gösterilmiştir.

Tablo 4. Takımlara ait test parametreleri

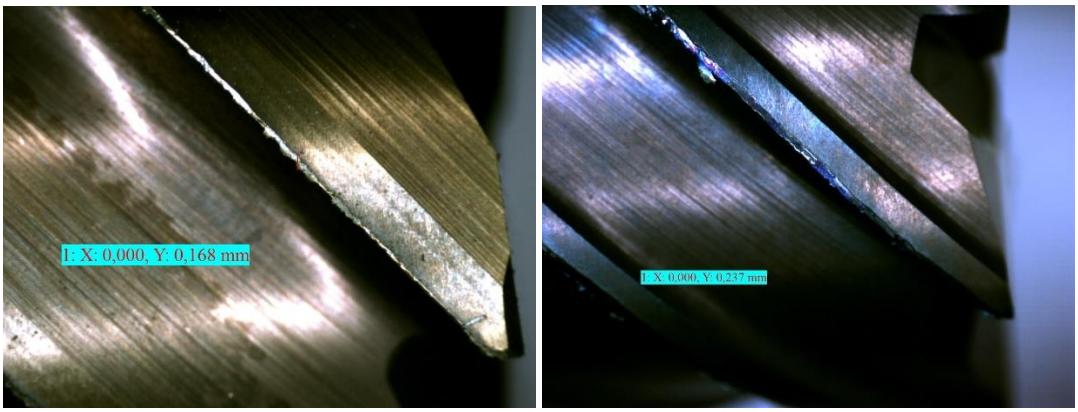
Malzeme	1.2379 (60HRC)
Takım Çapı	Ø12
Kesme hızı	150,8 m/dk
Diş başı ilerlemesi	0,1 mm/diş
Tabla ilerlemesi	2400 mm/dk
Ap	12 mm
Ae	0,3 mm
Tutucu	Bilyalı tutucu (spike)
Spindle Tipi	HSK 63
Soğutma şekli	Hava (dıştan akış)
Makine Modeli	MIKRON VCP800

3. BULGULAR VE TARTIŞMA

Çalışma kapsamında sertleştirilmiş çelik malzemenin işlenmesinde en iyi performansı sergileyecek takım karbür kalitesini ve kaplaması belirlenmek amacıyla aynı geometriye sahip 2 farklı hammaddede freze üretimi gerçekleştirilmiştir. Frezeler belirlenen test parametrelerinde 1.2379 (60Hrc) sertleştirilmiş çelik malzemede performans testine tabii tutulmuştur. Hammadde denemeleri sonucu eğilme momentleri grafiği Şekil 1'de verilmiştir. Takım ömrüne en büyük etken eğilme momenti olduğu için bu değerler baz alınmıştır.



Şekil 1. 2 farklı karbür kaliteleri için eğilme momentindeki değişim

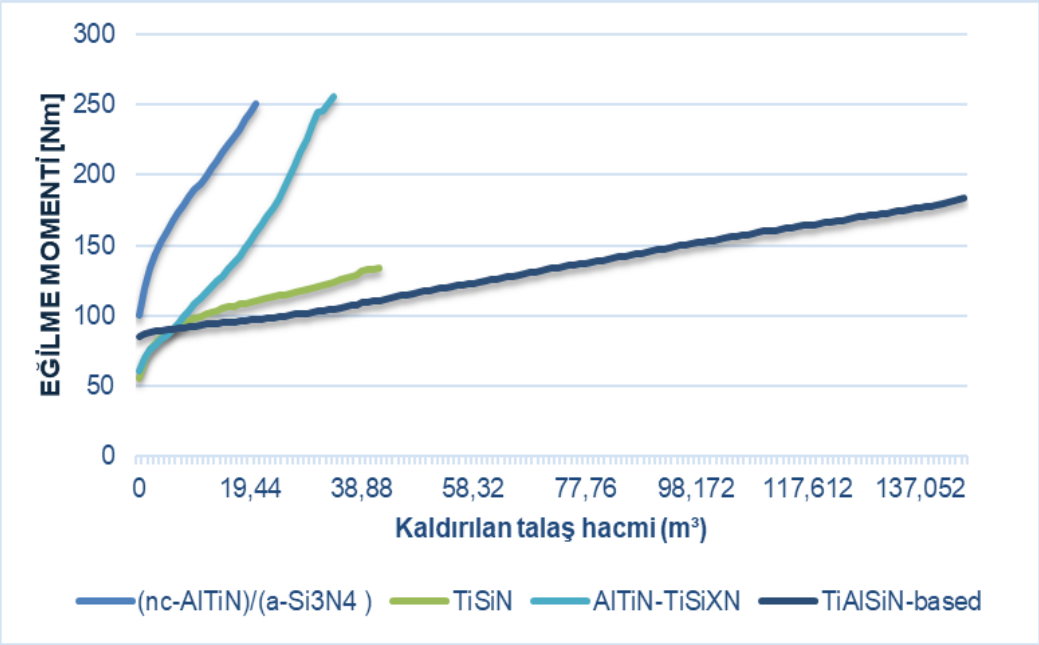


a) b)

Şekil 2.Takımlara ait aşınma görüntüleri a) Kalite 1, b) Kalite 2

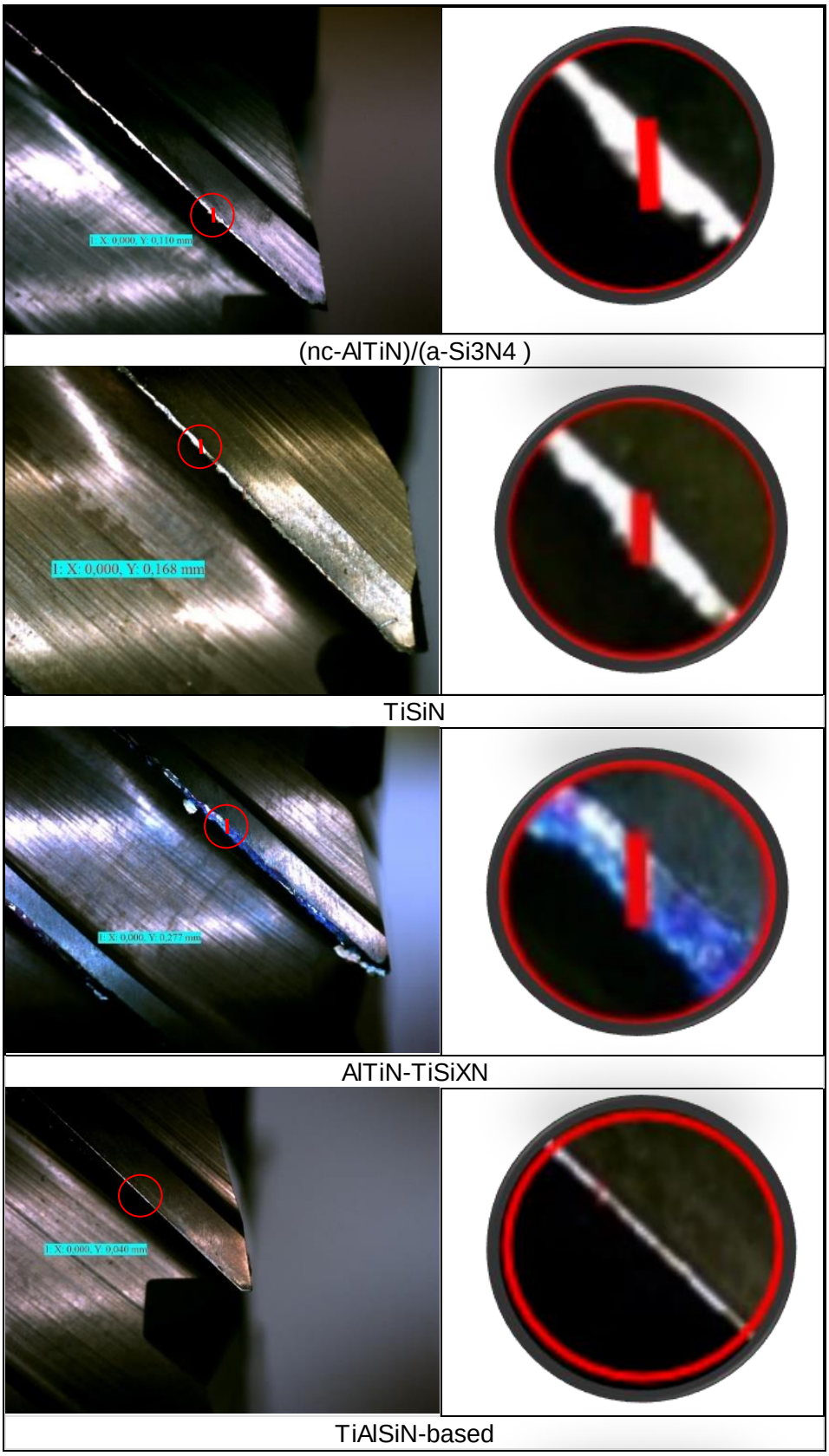
Aşınma görüntüleri incelendiğinde, Kalite 1'in Kalite 2'ye kıyasla %50 oranda daha az aşındığı görülmüştür. Kalite 1'in 87,48 m³ talaş kaldırmasına rağmen, 36,936 m³ talaş kaldıran kalite 2'ye göre 50,544 m³ daha fazla talaş kaldırmıştır.

Kalite 1'in yüksek performansı doğrultusunda yapılacak kaplama denemeleri için bu hammaddeden üretilmiş frezeler ile çalışma devam ettirilmiştir. Farklı kaplama firmalarının sertleştirilmiş çelik işlemede önerdiği kaplama çeşitlerinde frezeler kaplatılmıştır. Kaplama sonucunda yapılan performans testlerine göre takımların eğilme moment grafikleri Şekil 3'de verilmiştir.



Şekil 3.Farklı kaplama uygulanmış takımların eğilme momenti grafiği

Şekil 3 incelendiğinde, farklı firmaların farklı reçete ve kaplama şekilleriyle kaplama yaptığı takımların performansında farklılıklar olduğu görülmüştür. Farklı kaplama uygulamaları için gözlenen takım aşınmaları Şekil 4'te gösterilmiştir. Eğilme momenti, kaldırılan talaş hacmi ve takım aşınma değerleri dikkate alındığında TiAlSiN bazlı kaplamanın öne çıktığı görülmüştür.



Şekil 4.Farklı kaplama uygulamalarında görülen maksimum takım aşınmaları

4. SONUÇ

Bu çalışma kapsamında, 60 HRC sertlikte ısıl işlem 1.2379 görmüş malzemenin işlenmesi için farklı karbür kaliteleri ve farklı kaplama uygulamalarının takım performansına etkisi incelenmiştir. Testler sonunda %6 kobalt içeren kalitenin daha iyi performans gösterdiği görülmüş ve bu kalitedeki takım daha sonra, (nc-AlTiN)/(a-Si3N4), TiSiN, AlTiN-TiSiXN ve TiAlSiN bazlı kaplamalar uygulanarak performansları değerlendirilmiştir. Yüksek güçte darbeli magnetron püskürtme (HiPIMS) teknolojisiyle yapılan TiAlSiN bazlı kaplamalı takım, daha yüksek hacimde talaş kaldırarak daha uzun ömür sergilemiştir. Çalışma sonunda, sertleştirilmiş çeliklerin işlenmesi için düşük kobalt oranına sahip kalite ve HiPIMS teknolojisiyle kaplanan yapılan TiAlSiN bazlı kaplamanın önerilebileceği sonucuna varılmıştır. Bu çalışma, farklı kaplama türlerinin performansını değerlendirmek için bir adım olup endüstriyel uygulamalarında kullanılan takımların seçiminde rehberlik edebileceği düşünülmektedir.

KAYNAKÇA

1. **Davim, J.P. (2010),** "Surface integrity in machining", Springer.

2. **Wang, B. and Liu, Z. (2016), "**Cutting performance of solid ceramic end milling tools in machining hardened AISI H13 steel" International Journal of Refractory Metals and Hard Materials, 55, 24-32.

3. **Boogert, R. M., Kals, H. J. J., and van Houten, F. J. (1996),** "Tool paths and cutting technology in computer-aided process planning", The International Journal of Advanced Manufacturing Technology, 11, 186-197.

4**. Noordin, M. Y., Venkatesh, V. C., Sharif, S., Elting, S., Abdullah, A. (2004),** " Application of response surface methodology in describing the performance of coated carbide tools when turning AISI 1045 steel" Journal of materials processing technology, 145(1), 46-58.

5. **Yaşar, S. A. (2020)**, "17-4 PH ve 15-5 PH Paslanmaz Çeliklerinin Tornalanmasında Kesme Parametrelerinin Kesme Kuvveti ve Yüzey Pürüzlülüğüne Etkilerinin Araştırılması" Karaelmas Fen ve Mühendislik Dergisi 10, 71-81

6. **Kang, M. C., Kim, K. H., Shin, S. H., Jang, S. H., Park, J. H., & Kim, C. (2008), "**Effect of the minimum quantity lubrication in high-speed end-milling of AISI D2 cold-worked die steel (62 HRC) by coated carbide tools" Surface and Coatings Technology, 5621-5624.

AUTHORS INDEX

AUTHOR	Page Number
ACAR, Erdem	525
ACER, Durmuş Can	127
AKÇA, Aydoğan	471
AKDENİZ, Özgür	321, 373, 387
AKIN, Sevban	543
AKKÖK, Metin	145
AKTEPE, Rafet	525
ALDEMİR, Alper	525
ALDEMİR, Oğuzhan	561
ALTAY, Meryem	463
ALTAY, Özkan	213
ANFLOR, Carla	233
ASHIZAWA, Yuya	85
AVDAN, Çağla GÖKBULUT	579
AYDIN, Hakan	463
BAKAN, Aykut	169
BAKKAL, Mustafa	271, 497
Bayar, Kerem	319
BAYRAMOĞLU, Melih	357
BESIR, Meliksah	401
BİLBAY, Fahri Berk	243
BÜYÜK, Murat	259
ÇAKIR, Hasan	271
CAKIR, Mustafa Cemal	243
ÇALIŞKAN, Hakan	183
CANBOLAT, I. Melih	401
CANKURT, Tolga	285
ÇELİKCAN, Emre	373
ÇETİN, Ahmet	127
DİKER, İbrahim	127
DİNÇER, O. Talha	515
DİZECİ, Şehram	207
DOYMUS, Eren	401
DURMAZ, Hafize	271
ECE, Remzi Ecmel	447
EMİN, Ali	339, 373

AUTHOR	Page Number
EROL, Mustafa	387
GENCEL, Talat Yiğit	487
GEREN, Necdet	127, 357
GİRGİN, Talha	515
GÖKÇE, Sinan	569
GÖKCİLER, O. Cem	127, 357
GÖKLER, Mustafa İ.	155
GÖLBAŞI, Umut Can	425
GÜLER, Yalçın	471
GÜLTEKİN, Mustafa	437
GÜRLER, A. Ali	301
HAKTANIR, Umut B.	373
HASKİLİT, Emre Can	447
HIRAO, Akinari	51
HIROTA, Sumire	99
HOKKAÖMEROĞLU, Cemal Emre	387
İBEKCİ, M. Burak	357
İBRAHİMOĞLU, Fatih	207
İLME, Mert	183
IŞIK, Efe	561
KANDEMİR, Berkay	373
KARPAT, Yiğit	169
KARŞI, Adem	463
KARSLI, Ece	471
KATO, Takeo	51, 65
KAYA, Semin	569
KHABAZ-AGHDAM, Ata	207
KIDA, Yuki	65, 75
KILIÇ, S. Engin	145
KILKIŞ, Birol	19
KOÇHİSARLI, Mehmet	471
KONUKSEVEN, E. Ilhan	301, 401
KORKMAZ, Habip Gökay	447
KURT, Berk	285
KURT, H. Aytuğ	497
KUŞ, Hasan	579

AUTHOR	Page Number
LEKESİZ, Hüseyin	192
MATSUOKA, Kei	65
Matsuoka, Yoshiyuki	51
MIYACHI, Hideo	85, 99
MIYASHITA, Tomoyuki	37
NATORI, Teru	37
NAZLIER, Umut	373
OGI, Tetsuro	65, 75
OĞUZER, Cengiz	515
ORAL, Ali	487, 515
ÖZBAKIŞ, Murat	425
ÖZBAYOĞLU, A. Murat	213
ÖZBOZ, Ö. Dehan	213
ÖZDEMİR, Sertaç	525
ÖZDEMİR, Sibel SAİN	471
ÖZKAN, Abdullah	437
ÖZKAN, Göktürk M.	127
ÖZSOY, Hüseyin Özkal	543
ÖZTÜRK, Fahrettin	447
SANTANNA, Euclides	233
SARTIN, Karla	233
SAVAŞ, V. Emre	259
ŞEN, Onur	425
SHIBANO, Toma	99
SUBAŞI, Levent	155
TANIKAWA, Tomohiro	111
TARAKÇI, Sedat	561
TEKİN, Engin	471
TOROS, Serkan	447
TUNCER, Can	487
UĞUR, Mehmet	515
ULUER, M. Ural	145
ÜNVER, H. Özgür	213
UYSAL, Ö. Faruk	285
UZAY, Çağrı	357
YALÇIN, Enver	487

AUTHOR	Page Number
YAMAN, Ulaş	145, 155
YAVAŞ, Çağlar	579
YETER, Alper	271, 497
YILDIZ, Seda	192